

Universidade Federal de Minas Gerais
Instituto de Ciências Exatas
Departamento de Química

SUNDAY JOSEPH OLUSEGUN

SYNTHESIS AND CHARACTERIZATION OF MAGNETIC NANOCOMPOSITES AS ADSORBENTS
FOR THE SEQUESTRATION OF DYES AND ANTIBIOTIC

Belo Horizonte

2020

UFMG/ICEX/DQ 1393
T 633

SUNDAY JOSEPH OLUSEGUN

SYNTHESIS AND CHARACTERIZATION OF MAGNETIC NANOCOMPOSITES AS ADSORBENTS
FOR THE SEQUESTRATION OF DYES AND ANTIBIOTIC

Tese apresentada ao
Departamento de Química do
Instituto de Ciências Exatas da
Universidade Federal de Minas
Gerais como requisito parcial
para a obtenção do grau de
Doctor em Ciências - Química

Orientator: Prof. Nelcy Della Santina Mohallem

Belo Horizonte

2020

Ficha Catalográfica

O529s Olusegun, Sunday Joseph
2020 Synthesis and characterization of magnetic
T nanocomposites as adsorbents for the sequestration of
dyes and antibiotic = Síntese e caracterização de
compósitos magnéticos como adsorventes para o
sequestro de corantes e antibióticos [manuscrito] /
Sunday Joseph Olusegun. 2020.
[xix], 148 f. : il.

Orientadora: Nelcy Della Santana Mohallem.

Tese (doutorado) - Universidade Federal de Minas
Gerais - Departamento de Química.
Inclui bibliografia.

1. Físico-química - Teses 2. Compósitos - Teses 3.
Nanopartículas magnéticas - Teses 4. Adsorção - Teses
5. Quitosana - Teses 6. Corantes - Teses 7.
antibióticos - Teses I. Mohallem, Nelcy Della Santana,
Orientadora II. Título.


CDU 043

**"Synthesis and Characterization of Magnetic Nanocomposites as Adsorbents for
the Sequestration of Dyes and Antibiotic"**

Sunday Joseph Olusegun

Tese aprovada pela banca examinadora constituída pelos Professores:

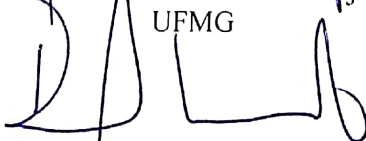

Prof. Nelcy Della Santina Mohallem - Orientadora
UFMG


Prof. Angela de Mello Ferreira
CEFET-MG


Prof. Mônica Cristina Teixeira
UFOP


Prof. Virgínia Sampaio Teixeira Ciminelli
DEMET/UFMG


Prof. Maria Helena de Araújo
UFMG


Prof. Rochel Montero Lago
UFMG

Belo Horizonte, 28 de fevereiro de 2020.

DEDICATION

This research is dedicated to the lovely memory, sacrifice and prayers of my late mother
(Mrs. Adunni Olusegun)

Also to the fatherly role and input of my dad, Mr Olusegun Dare

ACKNOWLEDGMENT

There is no such thing as a “self-made” man. We are made up by thousands of others. Everyone who has ever done for us, or spoken one word of encouragement to us, has entered the make-up of our character and thought as well as our success” - George Matthew Adams.

Prof. Nelcy Della Santana Mohallem, my sincere appreciation goes to you. You made the journey of my PhD program and research very smooth and interesting. You welcome my ideas and add your inputs, through a constructive criticism. You are not only concern about my research, you are much more concern about my well-being. You are an excellent mentor, sincere supervisor, and a caring mother.

I cannot forget the piece of advice and suggestions from Prof. Rochel Montero Lago, who decide to work behind the scene by adding “spices” that could make my research more colorful and attractive. Prof. Luiz C. A. Oliveira, thanks for the suggestions and inputs that you gave during my qualifying examination.

The financial support from CNPq, Brazilian National Council for Scientific and Technological Development – Brazil and TWAS, the academy of sciences for the developing world is highly appreciated.

Thanks to the Head of Department of the Department of Chemistry, UFMG, and other members of staff for making the Department a conducive place for me. Specifically, I appreciate (Alesandra (former secretary), Simone Regina (present secretary) Lilian, Fabiana, and others) of Chemistry Postgraduate unit for their immeasurable support towards my PhD program. The immense contribution and support that I received from every member of our research group (Luiz, Magnum, Gustavo, Hellen) cannot be quantified. Thank you, guys.

The support that I received from my extended family are wonderful. Likewise, the magnanimous contributions of my lovely wife, Christiana F. Olusegun cannot be forgotten, her passion towards the success of this work is enormous. Thank you for all the kind gesture. Ifeoluwa Thais J Olusegun, my lovely daughter, thanks for not giving me unnecessary stress that would have made the program burdensome.

Above all, I give all glory and honour to God for seeing me through this program. Father without you, I will be nowhere.

TABLE OF CONTENTS

ABSTRACT	ix
LIST OF FIGURES	xiii
LIST OF TABLES	xvii
LIST OF ABBREVIATIONS	xix
CHAPTER ONE: GENERAL INTRODUCTION AND OBJECTIVES	
1.0 Introduction	1
1.1 Aims and Objective	3
1.1.1 Aim of the Research	3
1.1.2 Specific Objectives	3
CHAPTER TWO: LITERATURE REVIEW	
2.0. Introduction	4
2.1 Wastewater	4
2.1.1 Dyes based wastewaters	4
2.1.2 Antibiotics based wastewaters	6
2.2 Techniques for wastewater treatment	7
2.3 Wastewater treatment through adsorption	7
2.4 Magnetic adsorbents	11
2.4.1 Spinel ferrite composites	13
CHAPTER THREE	
3.0 Materials and methods	14
3.1 Materials	14
3.2 Cobalt ferrite synthesis	14
3.3 Preparation of spray-dried cobalt ferrite	14
3.4 Calcination process	14
3.5 Preparation of CoFe ₂ O ₄ /chitosan composite	15
3.6 Production of rice husk silica	16
3.7 Synthesis of CoFe ₂ O ₄ /rice husk silica	16
3.8 Preparation of SDS- modified raw kaolinite	17
3.9 Preparation of spray dried kaolinite	17
3.10 Synthesis of CoFe ₂ O ₄ /kaolinite nanocomposite	17

3.11	Characterization of the samples	19
3.12	Adsorption studies	20
3.12.1	pH studies	20
3.12.2	Kinetic studies	20
3.12.3	Dosage studies	20
3.12.4	Temperature and concentration studies	20
3.13	Adsorption kinetics	21
3.14	Adsorption isotherm	21
3.15	Adsorption thermodynamics	22
3.16	Computational details for the adsorption of CoFe_2O_4 /chitosan	22

CHAPTER FOUR: RESULTS AND DISCUSSION

4.1	Effect of drying process and calcination on the structural and magnetic properties of cobalt ferrite.	24
4.1.1	Brief introduction	24
4.1.2	X-ray diffraction analysis of the synthesized CoFe_2O_4	25
4.1.3	TEM and HRTEM analysis	26
4.1.4	Scanning electron microscopy (SEM)	28
4.1.5	BET specific surface area analysis	28
4.1.6	Magnetization versus Temperature	29
4.1.7	Magnetization versus Field	31
4.1.8	Adsorption analysis	35
4.1.9	EFTEM images of SD-700 after adsorption	37
4.1.10.	Conclusion	38
4.2	Experimental and theoretical studies for the adsorption of acid orange II and methylene blue using spray dried crosslinked CoFe_2O_4 /chitosan composite	39
4.2.1.	Brief introduction	39
4.2.2	Characterization of CoFe_2O_4 /chitosan composite	40
4.2.3	Effect of pH, surface charge and adsorbent dosage on adsorption of acid orange II (AO) and methylene blue (MB)	43
4.2.4.	Kinetic study for the adsorption of AO and MB on CoFe_2O_4 /chitosan composite	45
4.2.5	Adsorption isotherms for the adsorption of AO and MB on CoFe_2O_4 /chitosan composite	47

4.2.6 Adsorption thermodynamic for the adsorption of AO and MB on CoFe ₂ O ₄ /chitosan composite	50
4.2.7 Computational studies	51
4.2.7.1 Geometry and electronic structure of the Dyes	51
4.2.7.2 Interaction of the Dyes and the magnetic chitosan models	54
4.2.8 Conclusion	59
4.3 Synthesis of CoFe ₂ O ₄ /bio silica composite for the adsorption of doxycycline	60
4.3.1 Brief introduction	60
4.3.2 XRD of CoFe ₂ O ₄ /rice husk silica	61
4.3.3 Scanning electron microscopy (SEM) of CoFe ₂ O ₄ /rice husk silica composite and rice husk silica	62
4.3.4 Transmission electron microscopy (TEM) of CoFe ₂ O ₄ /rice husk silica composite and rice husk silica	63
4.3.5 Magnetization versus Field of CoFe ₂ O ₄ /rice husk silica composite	65
4.3.6 BET specific surface area	66
4.3.7 FTIR spectra of CoFe ₂ O ₄ /rice husk silica composite and rice husk silica	67
4.3.8 Influence of pH on the adsorption of doxycycline	68
4.3.9 Effect of contact time, and kinetic studies of adsorption of DOX on CoFe ₂ O ₄ /rice husk silica	70
4.3.10 Adsorption isotherm for the adsorption of DOX on CoFe ₂ O ₄ /rice husk silica	72
4.3.11 Thermodynamic of adsorption	74
4.3.12 Mechanism of adsorption	75
4.3.13 Recovery of the adsorbent through thermal treatment	77
4.3.14 Characterization of CFS-700 after adsorption	78
4.3.15 Conclusion	79
4.4 Synergistic effect of CoFe ₂ O ₄ on the adsorption capacity of nano bio-silica for the removal of methylene blue	81
4.4.1 Influence of pH on amount adsorbed by CoFe ₂ O ₄ /rice husk silica and rice husk silica	81
4.4.2 Effect of adsorbent dosage on adsorption of MB by BSIL, CFS-100 and CFS-700	82
4.4.3 Kinetic study for adsorption of MB on BSIL, CFS-100 and CFS-700	83
4.4.4 Adsorption isotherm for the adsorption of MB on BSIL, CFS 100 and 700	84

4.4.5	Effect of temperature and thermodynamic of adsorption of MB on BSIL, CFS 100 and 700	87
4.4.6	Effect of ionic strength on the adsorption of MB on BSIL and 700	89
4.4.7	Regeneration and reusability of BSIL and SCOF-700	90
4.4.8	Characterization of BSIL and CFS-700 after adsorption	90
4.4.9	Conclusion	92
4.5	Comparative adsorption mechanism of doxycycline and Congo red using synthesized kaolinite/CoFe ₂ O ₄ composites	94
4.5.1.	Brief introduction	94
4.5.2.	Characterization on the synthesized nanocomposites	96
4.5.3.	Effect of pH and ionic strength on the removal of Congo red and doxycycline	100
4.5.4.	Effect of adsorbent dose on the adsorption of CR and DOX on KCF nanocomposites	103
4.5.5.	Contact time and adsorption kinetic of CR and DOX on KCF nanocomposites	104
4.5.6	Adsorption isotherm of CR and DOX on KCF nanocomposites	106
4.5.7.	Thermodynamic of adsorption of CR and DOX on KCF nanocomposites	111
4.5.8	FTIR after adsorption and mechanism of adsorption of CR and DOX on KCF nanocomposites	113
4.5.9	Conclusion	115
4.6	Enhancement of adsorption capacity of kaolinite through spray drying and surface modification process for adsorption of methylene blue	116
4.6.1	characterization of raw, modified and spray dried kaolinite	116
4.6.2	Effect of pH of the adsorption of MB on RK, SMK and SDK	117
4.6.3	Effect of dosage	119
4.6.4	Effect of contact time and adsorption kinetics	119
4.6.5	Adsorption isotherm for the adsorption of MB on RK, SMK and SDK	122
4.6.6	Adsorption thermodynamic	124
4.6.7	Conclusion	125
CHAPTER FIVE: GENERAL CONCLUSION		
	Conclusion	126
	References	128
	Appendix	

ABSTRACT

Nowadays, the removal of contaminants like dyes and antibiotics from wastewater has become an urgent task. Enhancing the performance of adsorbents to facilitate the adsorption process and projecting an easy method of separating adsorbent after removal of contaminants is of great scientific and industrial interest. In this research, cobalt ferrite composite with chitosan, biosilica, and kaolinite were synthesized and employed as adsorbents for the removal of methylene blue, acid orange II, Congo red and doxycycline. The obtained composites were characterized by powder X-ray diffraction (XRD), scanning electron microscopy (SEM) transmission electron microscopy (TEM), Fourier-transform infrared spectroscopy technique, a SQUID magnetometer, and N₂ gas adsorption technique.

Pure CoFe₂O₄ nanoparticles were synthesized using a co-precipitation method. The resulting precipitate was dried by employing the conventional method (oven) and spray drying process. Cobalt ferrite samples obtained from the two drying processes were briefly applied to adsorb methylene blue solution as a cationic dye model to know the effect of the drying process on the adsorption of dye. The studies showed that all the spray-dried samples performed better than other samples in adsorbing methylene blue (MB) solution.

Spray-dried cross-linked chitosan/ CoFe₂O₄ composite was also synthesized and applied as an adsorbent for the removal of acid orange II and methylene blue. The magnetic composite was in the form of microspheres with cobalt ferrite encapsulated in chitosan. Adsorption studies revealed that acid orange II was more favorably adsorbed (542 mg g⁻¹) s on the composite than methylene blue (173 mg g⁻¹). The adsorption process is spontaneous and exothermic. Computational studies showed that the formation of hydrogen bond between acid orange II and the magnetic composite (at both acidic and alkaline pH) contributed to its better adsorption than methylene blue.

The removal of doxycycline hydrochloride (DOX), a widely used antibiotic, from wastewater by CoFe₂O₄/rice husk silica nanocomposite was studied. The adsorbent was synthesized through co-precipitation of iron and cobalt salt mixed with a suspension of rice husk silica, whose precipitate was dried and calcined at different temperatures. The as-prepared nanocomposite has the highest specific surface area (283 m² g⁻¹). The mechanism of adsorption entails electrostatic and n- π interaction. Adsorption data fitted well with

Langmuir isotherm, having the monolayer adsorption capacity of 835 and 581 mg g⁻¹ for the as-prepared and sample calcined at 700 °C, respectively. The removal of DOX is entropy-driven, spontaneous in nature. CoFe₂O₄/rice husk silica nanocomposite was also used to adsorb methylene blue. The adsorption capacity of the composite (253 mg g⁻¹) was higher than that of bio-silica (52 mg g⁻¹), and the process was exothermic and spontaneous. Langmuir and Freundlich models were applied to explain the adsorption isotherm, while pseudo-second-order is best applicable for the kinetics mechanism. The amount of removed methylene blue increased with an increase in ionic strength due to the dimerization of MB. Regeneration and reusability of the adsorbents showed that they are economically viable.

Lamellar kaolinite supported CoFe₂O₄ nanoparticle was synthesized and employed to adsorb doxycycline and Congo red (CR) from aqueous solution. Comparative adsorption mechanism of the two targeted contaminants showed that adsorption of DOX was influenced by hydrogen bond and n- π interaction, while that of CR was due to hydrophobic interaction and hydrogen bond. However, the adsorption of the two contaminants was best fitted to the Langmuir isotherm, with a monolayer maximum adsorption capacity of 400 mg g⁻¹ at 333 K for DOX, and 547 mg g⁻¹ at 298 K for CR. The removal of DOX from aqueous solution was favored by an increase in temperature (endothermic), while that of CR was exothermic. Thermodynamics studies confirmed that the adsorption of two contaminants is feasible and spontaneous. Another study showed that the adsorption capacity of kaolinites for the removal of methylene blue was improved by spray drying a clay dispersion and through surface modification. The spray-dried kaolinites have the highest specific surface area of 102 m² g⁻¹ and better performance than the modified and raw kaolinites with an adsorption capacity of 168 mg g⁻¹ (at 333 K). The calculated thermodynamics parameters revealed that the adsorption process is spontaneous at all the studied temperatures for spray-dried kaolinite.

RESUMO

Hoje em dia, a remoção de contaminantes como corantes e antibióticos de águas residuais tornou-se uma tarefa necessária. Melhorar o desempenho dos adsorventes para facilitar o processo de adsorção e projetar métodos de separação destes adsorventes após a remoção de contaminantes é de grande interesse científico e industrial. Nesta pesquisa, compósitos formados por ferrita de cobalto com quitosana, biosílica e caulinita foram sintetizados e empregados como adsorventes de azul de metileno, alaranjado II, vermelho do congo e doxiciclina. Os compósitos obtidos foram caracterizados por difração de raios-X (DRX), microscopia eletrônica de varredura (MEV) microscopia eletrônica de transmissão (MET), espectroscopia na região do infravermelho, magnetômetro SQUID e adsorção de gás N_2 .

Nanopartículas puras de $CoFe_2O_4$ foram sintetizadas por co-precipitação. O precipitado resultante foi secado empregando-se o método convencional (forno), e o processo de secagem por nebulização. Amostras de cobalto de ferritas obtidas a partir dos dois processos de secagem foram brevemente aplicadas à solução de azul de metileno, usado como um modelo de corante catiônico para se conhecer o efeito do processo de secagem sobre a adsorção de corantes. Os estudos mostraram que todas as amostras secas por nebulização tiveram melhor desempenho do que as outras na adsorção de azul de metileno (AM).

Compósitos interligados de quitosana/ $CoFe_2O_4$ obtidos por nebulização também foram sintetizados e utilizados como adsorventes para a remoção de alaranjado II e azul de metileno. O compósito magnético foi obtido na forma de microesferas com ferrita de cobalto encapsulada em quitosana. Os estudos da adsorção revelaram que o alaranjado II foi adsorvido mais favoravelmente do que o azul do metileno. O processo de adsorção é espontâneo e exotérmico. Estudos computacionais mostraram que a formação de ligações de hidrogênio entre o alaranjado II e o composto magnético (em pH ácido e alcalino) contribuiu para sua melhor adsorção do que o azul metileno.

A remoção de hidrocloreto de doxiciclina (DOX), um antibiótico amplamente utilizado, de águas residuais pelo nanocompósito formado por $CoFe_2O_4$ /sílica de casca de arroz foi estudada. O adsorvente foi sintetizado pela co-precipitação de sais de ferro e cobalto misturados com uma solução de sílica de casca de arroz, cujo precipitado foi seco e calcificado em várias temperaturas. O nanocompósito recém preparado tem a área superficial específica

mais elevada ($283 \text{ m}^2 \text{ g}^{-1}$). O mecanismo de adsorção envolve interações n- π eletrostáticas. Os dados de adsorção se ajustaram com a isoterma de Langmuir, tendo a capacidade de adsorção de monocamada de 835 e 581 mg g^{-1} para a amostra recém preparada e a calcinada a 700 °C, respectivamente. A remoção do DOX é entropicamente impulsionada e de natureza espontânea. A capacidade de adsorção do compósito (253 mg g^{-1}) foi maior do que a da biosílica (52 mg g^{-1}), com processo exotérmico e espontâneo. Os modelos de Langmuir e Freundlich foram aplicados para explicar a isoterma de adsorção, cuja pseudo segunda ordem é mais aplicável para a cinética do mecanismo. A quantidade de azul de metileno removido aumentou com um aumento na força iônica devido à sua dimerização. A regeneração e reutilização dos adsorventes mostraram que eles são economicamente viáveis.

Nanopartículas de CoFe_2O_4 suportada sobre caulinita lamelar foram sintetizadas e empregadas na adsorção de doxiciclina e vermelho do congo a partir de solução aquosa. Os mecanismos comparativos da adsorção dos dois contaminadores mostraram que a adsorção de DOX foi influenciada pela ligação do hidrogênio e pela interação n- π , enquanto a do vermelho do congo foi devido à interação hidrofóbica e à ligação do hidrogênio. No entanto, a adsorção dos dois contaminantes teve um ajuste melhor à isoterma de Langmuir, com uma capacidade máxima de adsorção de 400 mg g^{-1} a 333 K para DOX, e 547 mg g^{-1} em 298 K para o vermelho do congo. A remoção do DOX da solução aquosa foi favorecida por um aumento da temperatura (endotérmico), enquanto a do vermelho do congo foi exotérmica. Estudos termodinâmicos confirmaram que a adsorção dos dois contaminantes é viável e espontânea. A capacidade de adsorção das caulinitas foi melhorada pela secagem por nebulização de uma dispersão de argila e através de sua modificação superficial. As caulinitas secas por nebulização tiveram a maior área superficial específica, de $102 \text{ m}^2 \text{ g}^{-1}$ e um melhor desempenho do que as caulinitas modificadas superficialmente e as naturais, com capacidade de adsorção de 168 mg g^{-1} (a 333 K). Os parâmetros termodinâmicos revelaram que o processo de adsorção é espontâneo em todas as temperaturas estudadas para as argila secas por nebulização.

LIST OF FIGURES

Fig. 2.1: Basic terms of adsorption	8
Fig.2.2. Schematic representative of spinel ferrite structure	12
Fig. 3.1. Scheme of cobalt ferrite synthesis	15
Fig.3.2. Scheme of the cobalt ferrite/chitosan composite synthesis	15
Fig. 3.3. Scheme of the cobalt ferrite/rice husk silica nanocomposite synthesis	17
Fig. 3.4. Scheme of the cobalt ferrite/kaolinite nanocomposite synthesis	18
Fig. 3.5: Optimized structures of MB (top) and AO (bottom) with respective numbering of atoms	22
Fig. 3.6. Protonated (top), non-protonated (middle) and deprotonated (bottom) models to simulate the chitosan polymer	23
Fig. 4.1. XRD pattern of cobalt ferrite samples calcined at different temperatures	26
Fig. 4.2. TEM images of spray-dried cobalt ferrite calcined at different temperature, showing agglomeration	27
Fig. 4.3. HRTEM images of various cobalt ferrite samples. The inset in each image shows the Fast Fourier Transform (FFT)	27
Fig. 4.4. SEM images of SD-700 (SEM images of SD-100 and SD-500 not shown)	28
Fig. 4.5. Nitrogen adsorption-desorption isotherm at 77K of the for various cobalt ferrite	29
Fig. 4.6. Magnetization versus applied field at 10 and 300 K for cobalt ferrite samples	32
Fig. 4.7: UV-Vis spectra of the original MB dye solution and the respective MB after adsorption processes. (0.1 g of cobalt ferrite was added to 12 mL of MB solution (50 mg L^{-1} .)	36
Fig. 4.8: Methylene blue solution before and after immersion	36
Fig. 4.9: Bright field TEM image of the cobalt ferrite with adsorbed methylene blue (a). The EEL spectra (b) performed at the cobalt ferrite performed in a particle in (a) under vacuum. The RBG color map (c) show the distribution of each individual element (d-f).	37
Fig. 4.10. Crosslinked chitosan	40
Fig. 4.11. XRD pattern (A) and SEM image with EDS (B) of magnetic chitosan composite	41
Fig. 4.12. TEM bright field image (i), EEL spectrum (ii), and EFTEM images of crosslinked magnetic chitosan composite. The EEL spectrum was recorded in a region with no overlapping between the cobalt ferrite and the C-support film	42
Fig. 4.13. TGA curves (A) Magnetization versus applied field at 300 K (B) of magnetic chitosan composite	43

Fig. 4.14. The effect of pH on the removal of 100 mg L ⁻¹ AO and MB using 10 mg of magnetic chitosan	44
Fig. 4.15. Zeta potential of cobalt ferrite/chitosan composite as a function of pH	44
Fig. 4.16. AO and MB solutions before and after immersion in magnetic chitosan composite	45
Fig. 4.17. Variation of amount adsorbed with respect to dosage	45
Fig. 4.18. Kinetics plots for AO and MB adsorption on magnetic chitosan	46
Fig. 4.19. Langmuir isotherm for the adsorption of AO and MB on magnetic chitosan	47
Fig. 4.20. Freundlich isotherm for the adsorption of AO and MB on magnetic chitosan	48
Fig. 4.21. Liu isotherm for the adsorption of AO and MB on magnetic chitosan	48
Fig. 4.22. Frontier Kohn-Sham orbitals obtained with the solvent polarized electronic density for MB and AO molecules	52
Fig. 4.23. Electron density plot map of the dual descriptor Fukui function, $\Delta f(r)$, for MB (top) and AO (bottom), obtained from the calculated SCF electronic densities	53
Fig. 4.24. Optimized structures for the interaction between (A) acid orange II + non-protonated chitosan model, (B) acid orange II + protonated chitosan model and (C) acid orange II + deprotonated chitosan model	58
Fig. 4.25: Optimized structures for the interaction between (A) methylene blue + non-protonated chitosan model and (B) methylene blue + deprotonated chitosan model	58
Fig. 4.26: Proposed mechanism pathway for interactions between magnetic chitosan and the two dyes molecules	59
Fig. 4.27: Diffractograms of cobalt ferrite/rice husk silica: as prepared, CFS-300, CFS-500 and CFS-700	62
Fig. 4.28: SEM images of cobalt ferrite/rice husk silica composite: CFS- 100 (A), CFS-300 (B), CFS-500 (C) and CFS-700 °C (D), rice husk silica (D)	63
Fig. 4.29: TEM images (a, c, e) with the electron diffraction (b, d, f) of BSIL, CFS-100 and 700	64
Fig. 4.30: Magnetization versus applied field at 300 K for CoFe ₂ O ₄ /rice husk silica Composite	65
Fig. 4.31: N ₂ adsorption and desorption of the composite (A) and their pore size distribution curves (B)	66
Fig.4.32: FTIR spectra of CoFe ₂ O ₄ /rice husk silica composite and rice husk silica	68

Fig. 4.33: (A) Effect of pH on the adsorption capacity of CFS-100, CFS-300, CFS-500 and CFS-700; (B) Zeta potential of CFS-100 (a representative of CFS-300, CFS-500 and CFS-700)	69
Fig. 4.34. The structure of doxycycline hydrochloride	70
Fig. 4.35: Kinetic plots of the adsorption of DOX on CoFe ₂ O ₄ /rice husk silica	71
Fig. 4.36. Langmuir and Freundlich isotherms for the adsorption of DOX on CFS 100	72
Fig. 4.37. Langmuir and Freundlich isotherms for the adsorption of DOX on CFS 700	73
Fig. 4.38: FTIR spectra of Doxycycline (DOX), CFS-700 before adsorption and after adsorption(A) and effect of ionic strength (B)	76
Fig. 4.39: XRD before and after adsorption (A) and effect of phosphate (B)	77
Fig. 4.40. Reusability of cobalt ferrite/rice husk silica composite	78
Fig. 4.41. TGA of CFS-700 before and after adsorption	78
Fig. 4.42. The RGB color map showing the distribution of each individual element	79
Fig. 4.43. The effect of pH (A) on the adsorption of MB on BSIL, COF, CFS-100 and SCF-700, with zeta potential (B)	81
Fig. 4.44: Electrostatic attraction between MB and the adsorbents	82
Fig. 4.45: Amount of MB adsorbed with respect to dosage of the adsorbents (CFS 100 and 700 (A) and BSIL (B))	82
Fig. 4.46: Kinetic plots of the adsorption of MB on BSIL (A), CSF 100 (B) and CFS 700 (C)	83
Fig. 4.46. Langmuir and Freundlich isotherms for the adsorption of MB on BSIL	84
Fig. 4.48. Langmuir and Freundlich isotherms for the adsorption of MB on SCOF100	85
Fig. 4.49. Langmuir and Freundlich isotherms for the adsorption of MB on SCOF 700	85
Fig.4.50. Effect of temperature on adsorption capacity of BSil, CFS 100 and 700 for the adsorption of MB	88
Fig. 4.51. Effect of ionic strength on the adsorption of MB on SIL and CFS-700 (A), Monomer (B) and dimers molecules (C) of MB	89
Fig. 4.52: Reusability of BSIL and CFS-700 (A) and Images of BSIL before adsorption, after adsorption and calcination (B)	90
Fig. 4.53: FTIR spectra before and after adsorption. BSIL (A) and CFS-700 (B)	91
Fig. 4.54: Elemental mapping of SCOF 700 after adsorption	92
Fig. 4.56. Structure of kaolinites	94
Fig.4.56. FTIR spectra (A) and XRD patterns (B) of KCF nanocomposites calcined at different temperature	97

Fig.4.57. SEM images and EDS spectra of KCF nanocomposites	98
Fig.4.57. TEM images of KCF-100 and 700	99
Fig.4.58: Magnetization versus applied field at 300 K (A) and N ₂ adsorption and desorption (B) of the KCF-100 and 700	99
Fig. 4.59: Effect of pH on the adsorption of CR and DOX (10 mg of the adsorbent and 100 ppm of the adsorbate)	102
Fig. 4.60: Zeta potential of KCF-100 (a representative of the nanocomposite)	102
Fig. 4.61: Effect of ionic strength on the adsorption of CR and DOX	102
Fig. 4.62: Effect of adsorbent dosage on the adsorption CR and DOX	103
Fig. 4.63: Effect of contact time on the adsorption of CR and DOX on KCF nanocomposites	103
Fig. 4.64: Kinetic plots of the adsorption of CR on KCF nanocomposites	105
Fig. 4.65: Kinetic plots of the adsorption of DOX on KCF nanocomposites	105
Fig.4.66: Langmuir and Freundlich plots for the adsorption of CR on KCF-100	108
Fig.4.67: Langmuir and Freundlich plots for the adsorption of CR on KCF-700	108
Fig.4.68: Langmuir and Freundlich plots for the adsorption of DOX on KCF-100	108
Fig.4.69: Langmuir and Freundlich plots for the adsorption of DOX on KCF-700	109
Fig. 4.70: FTIR spectra of before and after adsorption of CR and DOX	115
Fig. 4.71: Adsorption mechanism of CR and DOX on KCF nanocomposites	115
Fig. 4.72: Nitrogen adsorption-desorption isotherm at 77K (A) and volume of equal mass (B) of RK, SMK and SDK	117
Fig. 4.73: Effect of pH on the adsorption of MB on RK, SMK and SDK (A) zeta potential (B)	118
Fig.4.74: Effect of contact time on the adsorption of MB on RK, SMK and SDK	120
Fig. 4.75: Pseudo-second-order kinetic plot (A) and intra particle diffusion (B) of MB adsorption on RK, SMK and SDK	121

LIST OF TABLES

Table 1. Crystallite size and Lattice constant for cobalt ferrite	26
Table 2. BET specific surface area	29
Table 3. Magnetic anisotropy and squareness ratio at 10 and 300 K	34
Table 4. Saturation magnetization, coercivity and remanence values obtained at 10 and 300 K	34
Table 5. Comparison of saturation magnetization (at room temperature) reported by some authors	35
Table 6. Parameters for kinetics models for the adsorption of AO and MB on magnetic chitosan	46
Table 7. Langmuir and Freundlich isotherms parameters for the adsorption of MB at 303 -333 K	49
Table 8. Comparison of the maximum monolayer adsorption (q_{max}) of different adsorbents for the removal of AO and MB at room temperature	48
Table 9. Thermodynamics parameters for the adsorption of AO and MB at 303 -333 K	51
Table 10. Electronic structure descriptors for MB and AO	54
Table 11: Distances (in Å) between the center-of-mass (CM_{dye}) of the dyes molecules and the center-of-mass of the chitosan (CM_{chito}) models, interaction energies (ΔE_{SCF}) and dispersion corrections for the dye-chitosan systems at the optimized geometries. All the energies were calculated using the C-PCM continuum solvation model as detailed in the SI	55
Table 12. Saturation magnetization, coercivity and remanence values obtained at 300 K	65
Table 13. BET specific surface area	67
Table 14. Parameters for kinetics models	71
Table 15. Langmuir and Freundlich isotherms parameters for the adsorption of DOX at 298 - 333 K	73
Table 16. Comparison of the maximum monolayer adsorption (q_{max}) of different adsorbents for the removal DOX	74
Table 17. Thermodynamics parameters for the adsorption of DOX at 298 - 333 K	75
Table 18. Parameters of kinetics models for the adsorption of MB on BSIL, CFS-100 and CFS-700	84

Table 19. Langmuir and Freundlich isotherms parameters for the adsorption of MB at 303 - 333 K	86
Table 20. Comparison of the maximum monolayer adsorption (q_{max}) of different adsorbents for the removal of MB	87
Table 21. Thermodynamics parameters for the adsorption of at 303 -333 K	88
Table 22. d-spacing of the composite major peaks at different temperature	97
Table 23. Parameters for kinetics models of the adsorption of CR and DOX on KCF Composites	106
Table 24. Langmuir and Freundlich isotherms parameters for the adsorption of CR	109
Table 25. Langmuir and Freundlich isotherms parameters for the adsorption of DOX	110
Table 26: Comparison of the maximum monolayer adsorption (q_{max}) of different adsorbents for the removal of R and DOX	111
Table 27: Thermodynamic parameters for CR	112
Table 28: Thermodynamic parameters for DOX	112
Table 29: Parameters for kinetics models of adsorption of MB on RK, SMK, and SDK	122
Table 30: Langmuir and Freundlich isotherms parameters for the adsorption of MB at 303 - 333 K	123
Table 31: Comparison of the maximum monolayer adsorption (q_{max}) of different adsorbents for the removal of Methylene blue at room temperature	124
Table 32: Thermodynamics parameters for the adsorption of MB at 303 -333 K	125

LIST OF ABBREVIATIONS

MB	Methylene blue
CR	Congo red
AO II	Acid orange II
DOX	Doxycycline
CFS	Cobalt ferrite/rice husk silica
OD	Oven dried
SD	Spray dried
M_s	Magnetic saturation
BET	Brunauer-Emmett-Teller
BSIL	Bio silica
KCF	Kaolinites/cobalt ferrite
RK	Raw kaolinite
SMK	Surface modified kaolinite
SDK	Spray dried kaolinite
FIG	Figure
BJH	Barrett-Joyner-Halenda
EELS	Electron energy loss spectroscopy

CHAPTER ONE: GENERAL INTRODUCTION AND OBJECTIVES

1.0 Introduction

Technological advancement and industrialization though a driving force behind nation's economic, has led to the generation of huge amounts of effluent (especially among industries that use a large volume of water) into the water body and this has brought harmful consequences on the ecosystem [1]. Due to this, clean water that is regarded as an essential commodity is scarcely available due to the depletion of groundwater and contamination of surface water.

Recycling or recovery of fresh water from dirty, contaminated, polluted water is one of the feasible solutions to curb the problems that are associated with water. Sadly enough, many hazardous chemical compounds (dyes, pharmaceuticals, heavy metal ions) whose origin are traced to industrial wastewater, are responsible for some chronic diseases in humans and animals, also damage to the environment [2]. As a result of this, different techniques have been developed for the purification of water, with a singular purpose of making water available at a clean state [3]. Adsorption technique has been widely used for sequestration of contaminants from wastewater due to its easy implementation, low energy consumption, simple maintenance, affordability, and environmentally friendly application [4].

Different materials (non-magnetic) have been studied as adsorbents for the removal of various contaminants [5]. However, pollutant-loaded adsorbents must be separated from aqueous solution through filtration or centrifugation, these inconvenient separation procedures prevent their large-scale applications in water treatment [6]. Filters that are being used for the separation can be blocked, more so, with the advancement in the use of nano adsorbents, it connotes that the removal of the adsorbents from aqueous solutions after adsorption is difficult and leads to loss of materials [4]. It is stated that an ideal adsorbent for commercial applications should not only have high performance, rapid removal of contaminants, cost-effectiveness, environmentally friendly, it must also be easy to separate from aqueous solution [4,7].

In view of this, focus has been on the development of magnetic adsorbents for wastewater treatment. In recent years, magnetic separation using magnetic composites has been

studied as an effective method for the elimination of biological molecules, organic pollutions, and heavy metal ions, having the advantage of being easily separated from aqueous solutions [8]. Therefore, this research focuses on the synthesis and characterization of magnetic composites for the adsorption of dyes and antibiotic. The adsorption mechanism and characteristics of the composites (cobalt ferrite with chitosan, bio-silica, and kaolinite) were studied for the removal of methylene blue, Congo red, acid orange II and doxycycline. A brief introduction about each material and the gap that this research is aiming to bridge with respect to what is available in the literature can be found in chapter four. This is to make the entire thesis interesting to the readers.

1.1 Aims and Objective

1.1.1 Aim of the Research

The study is aimed at synthesis and characterization of cobalt ferrite nanocomposites as absorbents for the sequestration of dyes and antibiotic.

1.1.2 Specific Objectives

The aim of this research will be achieved through the following specific objectives:

- i. synthesis of cobalt ferrite and its composite with chitosan, silica extracted from rice husk and kaolinite;
- ii. characterization of the produced magnetic nanocomposites using XRD, TGA, Brunauer Emmett Teller (BET), scanning electron microscopy with EDS, magnetic analyser and TEM;
- iii. evaluation of the efficiency and adsorption capacity of the synthesized magnetic composites for sequestration of cationic dye, anionic dye and doxycycline;
- iv. theoretical studies of chitosan magnetic composite;
- v. evaluate the kinetic, thermodynamic, isotherm parameters of the sorption process and reusability of the synthesized magnetic composites.

CHAPTER TWO: LITERATURE REVIEW

2.0. Introduction

Water is acknowledged as a vital ingredient in all facets of life. While it is possible to survive for a month without food, it is difficult to survive without water. It provides a number of physical and chemical processes that are essential to humans, animals, and plants [9]. Water is an indispensable resource in virtually all the economic sectors. The importance of water in domestic, industrial and agriculture activities among others, cannot be overemphasized. The sustenance of terrestrial and aquatic lives is pivoted on water. Rivers, lakes, oceans, and streams provide an avenue for recreation such as swimming and fishing, this help to generate income for driving an economic forward [10]

However, progression in industrial growth, though a boost to nations' economy, has resulted to depletion in human health due to contamination of water through the waste from the various industries that use a large amount of water to carry out their day to day activities [11]. Water is significantly polluted by various human and industrial activities that encompass the dumping of untreated domestic sewage and industrial effluents into water bodies [12]. In view of this, water becomes contaminated, unsafe to drink, results to the death of humans and plants. This necessitates the need for clean and safe water for domestic, agriculture and industrial activities.

2.1 Wastewater

Wastewater generally encompasses effluents from domestic, industrial, commercial and agriculture activities. Wastewaters from these activities comprise of different concentrations of both organic and inorganic matters. Specifically, industrial effluents contain acids, material with high biological oxygen demand, color, antibiotics, and different toxic materials [13,14] . Textile and pharmaceutical industries are among industries that release toxic waste into water bodies.

2.1.1 Dyes based wastewaters

Dyes are colored and organic compounds that have their usefulness in industries such as; textiles, printing, plastics, rubber, and leather for coloring of their finished products. Dyes

are classified based on their chemical structures, solubility in water and applications [15]. Structure wise, they are classified as anionic (acid and reactive dyes); cationic (basic dyes); and nonionic (disperse dyes) [16]. They are also classified as natural dyes and synthetic dyes. Natural dyes are obtained from animals and minerals. Meanwhile, the rapid growth among industries that use dyes, makes it impossible for natural dyes to meet up with demands. In view of this, synthetic dyes are developed and have gradually replaced natural dyes in fabrics and textile industries [17]. Dyes attach themselves to the surface of materials and fabrics, to impart color. They are stable and difficult to degrade biologically due to their complex aromatic structures [18]. It has been estimated that more than 10 percent of the dyes used in dyeing fabrics may be directly lost into waterways [19].

Textile industries consume a large volume of water for various processing such as washing, bleaching, wetting of fibers, dissolving of dyes among others [20]. Textile effluents (highly polluted and dangerous) happen to be one of the major contaminants that affect the water body. This effluent contains a large volume of dyes and other chemicals that are used during the dyeing process [21]. The aftermath of this leads to water pollution. Consequently, it makes water to have poor quality. In addition, due to the organic substances that the effluents carry along with it, there is an occurrence of biological and chemical changes during which makes water to be depleted of oxygen [22].

The presence of dyes in water even in small quantities is highly visible and affects its aesthetic values [23]. The complex aromatic structures that most dyes possess, makes it resistant to light, biological activity and ozone thus making it difficult to be removed by the ordinary waste treatment process [24]. It has been established that dyes have mutagenic, carcinogenic and allergenic effects [25,26]. When effluents containing dyes are discharged into the water body, it results in unpleasant odor, leading to hemorrhage, dermatitis, irritation of skin among others [27]. The presence of dyes in water can significantly affect photosynthetic activity in aquatic lives due to a reduction in light penetration and may also be toxic to certain forms of aquatic lives [16,28]. Dye containing effluents are characterized as having low pH, high color and organic content which leads to high BOD and COD [24].

2.1.2 Antibiotics based wastewaters

The production of different groups of pharmaceutical products is increasing daily due to the geometric increase in population and the dwindling health status of the populace. Antibiotics happen to be an important group of pharmaceuticals that are referred to as substances with antibacterial, anti-fungal, or anti-parasitical activity [29]. They are divided into different sub-groups such as β -lactams, quinolones, tetracyclines, macrolides, sulphonamides and others [29]. They are often complex molecules which may possess different functionalities within the same molecule, due to this, under different pH conditions antibiotics can be neutral, cationic, anionic, or zwitterionic [29,30].

However, as good as antibiotics are in treating bacteria-related infections in humans and animals, the incomplete metabolization of the active ingredients of this class of drug in the body system has led to their release into the environment through excretion; thereby increasing the pollutants load in the ecosystem [31]. In view of this, there is a great concern over the detrimental effects that antibiotics, which has been estimated to be averagely consumed more than 100×10^6 kg per year in the entire globe, could have on the environment and various organisms if not treated before being discharged into the environment [32]. Antibiotics are released into the ecosystem from different point sources (such as households, hospitals, and pharmaceutical industries) and lead to the contamination of clean water, rapid spread of bacteria resistant to antibiotics and death of important bacteria in the ecosystem [33].

Doxycycline is among the group of antibiotics that are classified under tetracycline (characterized as broad-spectrum antibiotics) [34]. It is a potent drug that has been tested and confirmed to have satisfactory activity against a broad range of Gram-negative and Gram-positive and for the treatment of sexually transmitted diseases, upper respiratory tract infections and lots more [35,36]. Just like every antibiotic, the presence of doxycycline in surface water, groundwater and sediments are hazardous to the environment hence the need to remove them and make the environment pollutant-free [29]. The complex structure and the antibacterial nature of this class of drugs make it technically impossible to be degraded by a micro-organism, hence resulted in the antibiotics-contaminated environment [37].

2.2 Techniques for wastewater treatment

In an effort to combat the problem of water pollution, rapid and significant progress in wastewater treatment has been made, which are photocatalytic, chemical precipitation, oxidation, adsorption, lime coagulation, membrane filtration, ion exchange, reverse osmosis and bioremediation [38–43]. However, some of these techniques have associated shortcomings. Biological techniques of treating textile effluents although attested to be a feasible method, it is not commonly applied in real scale due to significant variation in wastewater composition, including the presence of high salinity levels among others [44]. More so, this process takes a long time and cannot degrade complicated dyes. [45]. More so, coagulation cannot remove all types of dyes. It has been affirmed that acid and basic dyes do not respond favorably to this treatment, it leads to the generation of a huge amount of toxic sludge which disposal becomes a major problem [46]. It has also been stated that the addition of coagulants to wastewater that contains cationic dyes was not fruitful; therefore, this method cannot remove cationic dyes. Membrane separation techniques encompass nanofiltration (NF), microfiltration (MF), ultra-filtration (UF) and reverse osmosis (RO) process. As promising as this technique is, it has shortcomings in the area of the initial cost of investment, it generates other wastes that contain insoluble dyes that will be required to be treated further, and has a possible tendency to foul [47]. Electrochemical treatment that involved a coupled coagulation and flotation process for the removal of doxycycline has also been reported to lead to sludge generation [48]. The application of advanced oxidation processes (AOPs) has been affirmed to be a viable and effective attenuation option due to the oxidation of a wide range of trace organic chemicals such as pharmaceuticals, consumer products, and industrial chemicals that are discharge to surface water [49]. Meanwhile, this method (AOPs) of treating wastewater is capital intensive [50].

2.3 Wastewater treatment through adsorption.

Adsorption is one of the viable methods that has been used to remove dyes, antibiotics and other contaminants from wastewater. It has been able to meet the needs of wastewater treatment because of its good performance, affordability, and friendliness to the environment [4].

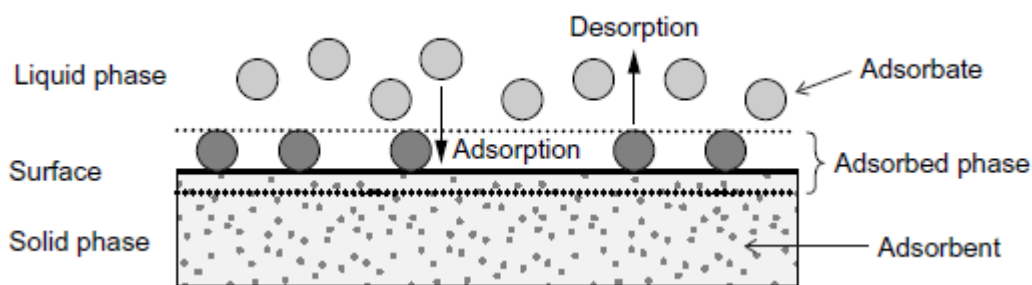


Fig. 2.1: Basic terms of adsorption [51]

Adsorption is change in concentration of a given substance at the interface as compared with the neighbouring phases, while the material in the adsorbed state is defined as the 'adsorbate', but that in the bulk gas or vapour phase prior to being adsorbed is called the 'adsorptive' (**Fig 2.1**) [52]. The history of adsorbents has been traced down to the use of activated carbon. The application of charcoal for medicinal purposes to adsorb odorous vapors from putrefactive wounds and from the intestine was first recorded in 1550 BC [52]. Gradually there is an advancement in the adsorption studies with the use of different adsorbents (natural, agricultural, industrial, etc.) for the removal of various contaminants [5]. The adsorption of adsorbate on the surface of adsorbent could be physical or chemical; homogeneous or heterogeneous adsorption. Among the factors that are considered before choosing any material as adsorbent are; cost-effectiveness, chemical stability, availability, environmental friendliness among others. However, the specific surface area, pore size, surface charge, affinity for the adsorbate, and molecular structure are among the important characteristics that make an adsorbent to perform effectively [32].

Adsorption of contaminants is influenced by many factors such as; solution pH. It (pH) may influence the adsorption of contaminants by changing the surface charge of the adsorbent, and the ionization of the adsorbate. Meanwhile, it is not in all cases that pH determines the adsorption of contaminants because in some cases, adsorption is totally independent of

solution pH. Another factor is contact time, this helps to know the optimum time when equilibrium adsorption is reached. The information obtained from contact time could be helpful in the wastewater treatment plant. Temperature is another factor that influences the adsorption of contaminants. It helps to know the type of adsorption that took place with respect to the increase or decrease of the adsorption capacity with temperature. Another factor is adsorbent dosage, which helps to determine a minimum amount of adsorbent that is economically viable in wastewater treatment processes. The effect of the adsorbent properties such as porosity, specific surface area, and surface charge cannot be overemphasized. It is well known that industrial wastewaters always have pollutants such as inorganic salts, the availability of such salts in solution influences the adsorption process at large [53], in view of this, ionic strength is a factor is an important parameter to investigate this.

A wide range of adsorbents has been used to remove contaminants. Adsorption of doxycycline hydrochloride (DOX) adsorption on copper nitrate modified biochar (Cu-BC) was investigated by Liu et al.[54]. According to the authors, Cu-BC adsorbent was synthesized through the calcination of peanut shells biomass at 450 °C and then impregnated with copper nitrate. The synthesized Cu-BC exhibited excellent sorption efficiency of about 93.22% of doxycycline hydrochloride from aqueous solution. The DOX removal by Cu-BC was greatly pH-dependent and the optimal pH was 8.0. According to the authors, the kinetics and isotherm data were well described by the pseudo-second-order kinetic model and Langmuir model. Thermodynamic results indicated the sorption process was spontaneous and endothermic. In their conclusion, they opined that the experimental results suggest that the adsorption efficiency of DOX on the Cu-BC was dominated by the strong complexation and electrostatic interactions between DOX molecules and the Cu-BC samples.

Zinc oxide functionalized with silica zeolitic particles (ZnO@Ze) that were synthesized via precipitation method by Shubhangi et al., [55] showed excellent adsorption of Congo red (CR) dye from polluted water. The morphology and structure of synthesized composite were characterized by Scanning electron microscopy, Transmission electron microscopy, X-ray diffraction, and Fourier transform infrared spectroscopy and its performance towards adsorption and photodecomposition of CR was evaluated. The adsorption dynamics studied

by time and concentration variation indicated that the adsorption data follows pseudo-second-order kinetics and Langmuir isotherm model with a maximum adsorption capacity of 161.3 mg g^{-1} , thus indicating homogeneous physiochemical adsorption of CR dye on the adsorbent surface. They concluded that the synthesized composite is easily regenerable and reusable and is capable of removing CR dye from the polluted water up to 90% (for 5 regeneration cycles) and hence proved to be a highly efficient and viable material for the water purification industries.

In addition, Biochar that was generated from municipal sludge and tea waste through co-pyrolysis, characterized by Scanning Electron Microscope (SEM) and Fourier Transform Infrared Spectroscopy (FTIR), was used as an adsorbent for the removal of methylene blue (MB) dye by Shisuo et al., [56]. The effect of dosage, contact time, pH, temperature on the adsorption properties of methylene blue (MB) onto biochar were investigated. The adsorption kinetics, isotherm, thermodynamic and mechanism also were also studied by the authors. Their results showed that pseudo-second-order kinetics was the most suitable model for describing the adsorption of MB onto biochar. Equilibrium data were well fitted to the Langmuir isotherm model. A rise in operating temperature was found to enhance MB adsorption on biochar. Adsorption thermodynamic of MB on biochar showed that the adsorption was a spontaneous and endothermic process under higher temperature conditions. The mechanism between MB and biochar involved electrostatic interaction, ion exchange, surface complexation, physical function according to the authors.

Activated carbon (AC) that was prepared from sawdust through co-calcinations with limestone was employed to remove acid orange from aqueous solution by Lingjun et al., [57]. Acid Orange II (AOII) was utilized as an anionic dye to study the potential of the prepared AC. Their results revealed that the surface area and total pore volume were both increased greatly. When the activated carbon was prepared in mass ratios of 1:2 and 1:1 (calcium carbonate to sawdust), the surface area increased to 611.4 and $706.9 \text{ m}^2/\text{g}$, respectively, and the adsorption capacities increased to 310.89 and 389 mg/g . They wrote that the enhancements indicated efficient activation, resulting in energy-saving and environmentally friendly activated carbon production.

Even though the above adsorbents among others have proven to be effective in removing contaminants from wastewater, it is difficult to separate them in a continuous system. In view of this, studies are focusing on the use of magnetic adsorbents which could be easily separated from wastewater by using a magnet. Magnetic adsorbents that have a high surface area, efficiency and easy to separate after adsorption process, have been the focused materials, due to this, spinel ferrites have been the number one choice for the treatment of wastewater [4].

2.4 Magnetic adsorbents

Magnetic adsorbents are referred to a new class of adsorbents where a base adsorbent is embedded with magnetic particles which are oxides of metals such as Fe, Co, Ni and Cu [58], and on the application of an external magnetic field, they can be easily separated from water [59]. The use of these classes of adsorbents to purify wastewater is a concept that is attracting the attention of researchers from day to day [59]. Meanwhile, the challenges of using Fe_3O_4 magnetic nanoparticles are; phase changes into other oxides (which significantly influence the magnetic characteristics of the particles) and stability at low pH [4]. Due to this, MFe_2O_4 nanoparticles (spinel ferrite) have attracted attention because of their strong magnetic features, higher chemical resistance to oxidation and stability in acidic medium (they can be used throughout a broad pH range) [4].

Ferrites can be classified according to their crystalline structure: hexagonal ($\text{MFe}_{12}\text{O}_{19}$), garnet ($\text{M}_3\text{Fe}_5\text{O}_{12}$) and spinel (MFe_2O_4), where M represents one or more divalent transition metals (Mn, Fe, Co, Ni, Cu, and Zn) [60]. Kebede et al., [8] stated that spinel ferrites are homogeneous materials with a general chemical formula of AB_2O_4 , where A and B are metallic cations positioned at two different crystallographic sites, tetrahedral (A sites) and octahedral (B sites) and composed of Fe(III) as one of the main constituents in their structure (**Fig 2.2**). The cations of both positions are tetrahedrally and octahedrally coordinated to oxygen atoms, respectively. Valenzuela et al., [61] commented that the formula MFe_2O_4 , depending on the position of M(II) and Fe(III) site preference, three possible spinel ferrite structures are known, namely normal, inverse and mixed. In a normal spinel structure of ferrite, M(II) located at tetrahedral sites while Fe (III) at octahedral sites. In an inverse spinel structure of ferrite, Fe (III) equally distributed at both sites while M(II)

occupies only at octahedral sites. In a mixed spinel structure of ferrite, both ions randomly occupy the tetrahedral and octahedral sites. Spinel ferrite nanoparticles (SFNPs) have received special attention among the crystalline structure of ferrites. This is mainly due to their excellent magnetic properties, simple chemical composition, and wide applications in several areas which include wastewater treatment, biomedical, catalyst and electronic device [8].

Cobalt ferrite is a typical example of inverse spinel ferrite [62]; found to be an interesting magnetic material that has magnetic properties that encompass large magnetic anisotropy ($1.8 - 3 \times 10^5 \text{ J m}^{-3}$) and moderate magnetization saturation (80 emu g^{-1}) [63,64]. It is chemically stable, with encouraging mechanical hardness [65]. These properties made cobalt ferrite a useful material for different applications. Nanocrystalline cobalt ferrite is regarded as an essential material due to its inherent thermal, magnetic, chemical and electrical properties [66]. Various contaminants such as heavy metals and dyes among others have been successfully removed from wastewater by cobalt ferrite [67,68]. It has also been combined with adsorbents and photocatalytic materials in treating wastewater due to its ability to be easily separated from solutions by external magnetic field after being used to remove toxic pollutants [8]. A study carried out by Kooti and Afshari [69] showed that it could act as an excellent catalyst for the conversion of alkenes to aldehydes or epoxides. Furthermore, it has been proven to be an effective material for drug delivery systems. It is an appropriate magnetic material for hyperthermia application, clinical practice and for isolating and purifying genomic DNA [70,71]. Application of Co-ferrite in drug delivery systems by using the hyperthermia method has brought a significant breakthrough and provided a broader view on releasing a drug to a targeted location [72].

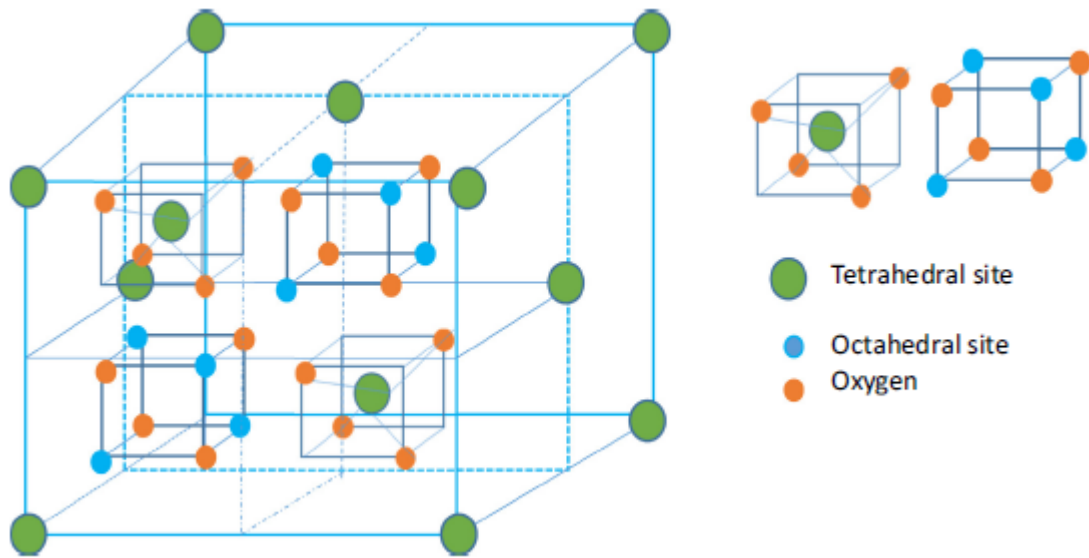


Fig.2.2. The schematic representative of spinel ferrite structure [8].

2.4.1 Spinel ferrite composites

One of the problems that are associated with ferrites nanoparticles is that they tend to agglomerates as a result of their high surface energy, van der Waals forces, and magnetic dipolar interactions [73]. Furthermore, it has been observed that dissolution/leaching of metal ions from pure spinel ferrites can occur. To combat these issues, spinel ferrites have been combined with various matrix materials to fabricate magnetically responsive composites. Reddy and Yun [4] stated that their hybrid combination yields various types of spinel ferrite composites (SFCs), which may lead to a performance that could not be attained by individual materials and exhibit fewer limitations. It was further stated that the combination of spinel ferrites magnetic particles with materials such as polymers, biomaterials, carbonaceous materials, and inorganic oxides, has led to composites with improved performance.

CHAPTER THREE

3. Materials and methods

3.1 Materials

Iron and cobalt sulfate ($\text{FeSO}_4 \cdot 7\text{H}_2\text{O}$ (assay: 99%) and $\text{CoSO}_4 \cdot 7\text{H}_2\text{O}$ (assay: 98.102%)) were purchased from Dinamica Quimica Contemporanea Ltd., Brazil. Chitosan with the degree of deacetylation (87.4 %), viscosity (176 cPs at 20 °C), pH (8.7) and an apparent density (0.25 g mL^{-1}) was purchased from Polymar/Brazil, while methylene blue and acid orange II were purchased from Labsynth and Sigma Aldrich respectively. Congo red is a product of BDH Chemicals, United Kingdom. The rice husk that we used was collected from a local rice mill in Ajaokuta steel city, Kogi State, Nigeria. Doxycycline (DOX, assay: 98.3, yellow powder, 1.4 to 2.8% water) from TRB Pharma in Brazil. Kaolinite was obtained from Chapada do Norte, Minas Gerais, Brazil.

3.2 Cobalt ferrite synthesis

CoFe_2O_4 was prepared by chemical co-precipitation method [64]. In this case, $\text{FeSO}_4 \cdot 7\text{H}_2\text{O}$ and $\text{CoSO}_4 \cdot 7\text{H}_2\text{O}$ were mixed in ratio 2:1 and dissolved in distilled water by gently heating the solution and stirred for one hour. An aqueous solution of NaOH (sodium hydroxide) was added to the mixture and stirred continuously until the pH reached 12. Digestion was carried out at 90 °C on a hot plate for 2 hours, after which the gelatinous precipitate formed was washed with distilled water till pH 7 was attained. Part of the neutralized precipitate was oven-dried at 100 °C, while the rest was spray dried.

3.3 Preparation of spray-dried cobalt ferrite

The neutralized cobalt ferrite solution was continuously stirred throughout the spray drying period. Spray dryer with 1 mm nozzle was used for the drying process. The process was performed by setting an inlet temperature at 120°C and airflow rate at 50 L min^{-1} pressure. The dried product was collected in a collection bottle.

3.4 Calcination process

The respective oven and spray-dried cobalt ferrite samples were further calcined at 500 and 700 °C for 2 h. The scheme of the synthesis is shown in **Fig. 3.1**.

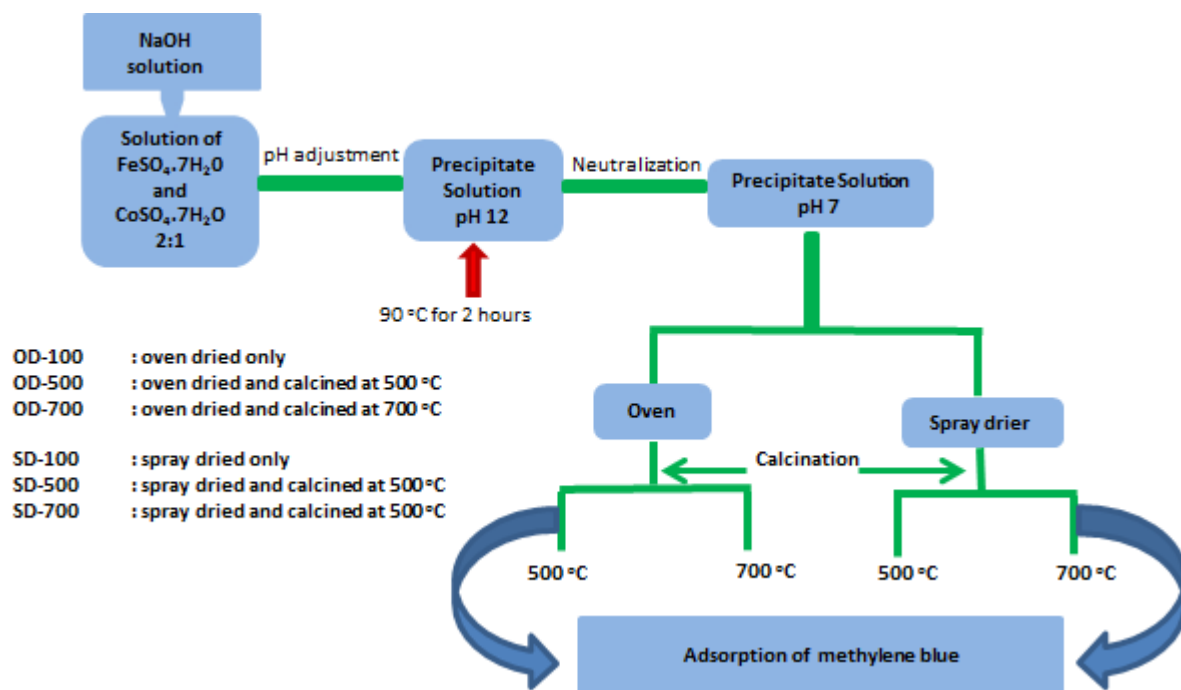


Fig. 3.1. Scheme of cobalt ferrite synthesis.

3.5 Preparation of CoFe₂O₄/chitosan composite

Firstly, 4 g of chitosan was dissolved in 120 mL of 2% (v/v) acetic acid and stirred for 30 minutes. Then, 1 g of cobalt ferrite was added and the mixture was sonicated for another 30 minutes. Subsequently, 1 ml aqueous solution of 25 wt.% glutaraldehyde was added to the mixture and mechanically stirred for 1 hour. The resulted magnetic composite was spray-dried, characterized and used as adsorbent. The inlet temperature of the spray drier was set at 120 °C and airflow rate at 30 L min⁻¹. Fluxogram of the synthesis is shown in **Fig. 3.2**.

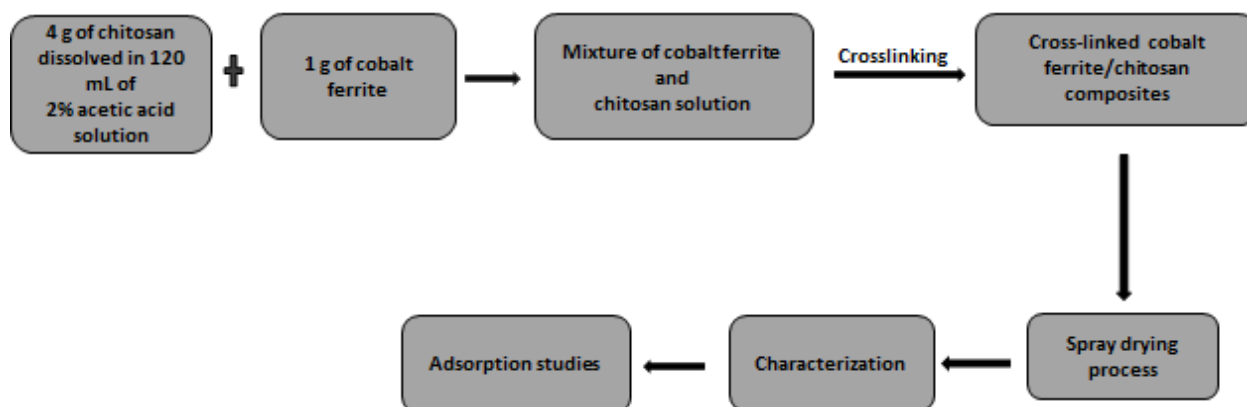
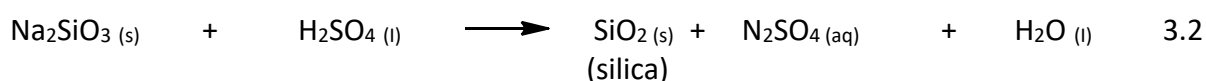
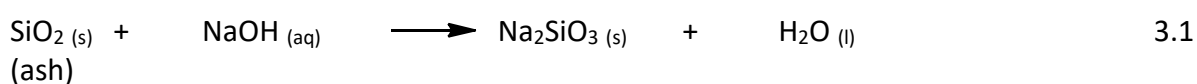


Fig. 3.2. Scheme of the cobalt ferrite/chitosan composite synthesis.

3.6 Production of rice husk silica

Silica was extracted from rice husk ash according to the method reported by Daramola et al [74]. The husk was adequately washed using water and dried in the oven at 80 °C for 24 h. Firstly, the husk was turned into ash in a muffle furnace programmed at 650 °C for 5 h. Approximately 10 g of the ash was thoroughly mixed with 100 mL of 1 M sodium hydroxide solution, boiled in shaking water bath at 100°C in a beaker for 1 h, cooled and filtered. Concentrated tetraoxosulphate (VI) (H₂SO₄) acid (assay: 97%) was added to neutralize the filtrate and the precipitate obtained was incubated for 48 h to facilitate the formation of silica gel. Vacuum filtration was used to separate the silica from suspension, which was dried at above 100 °C in an oven. The summary of the extraction process is shown in equations 3.1 and 3.2 [75]



3.7 Synthesis of CoFe₂O₄/rice husk silica

An approximately 1.0 g of rice husk silica was put into 250 mL beaker, containing 100 mL of distilled water. The mixture was sonicated in a water bath for 30 min. FeSO₄.7H₂O (1.0 g) and CoSO₄.7H₂O (0.5 g) were added to the dispersed rice husk silica suspension in the beaker and placed on magnetic hot plate stirrer for 30 min, after which the pH was adjusted to 11 using NH₄OH (28% NH₃, assay 99.99%) and digested for 2 h at 90 °C. NH₄OH (ammonium hydroxide) was used as precipitant due to the presence of impurities in the cobalt ferrite that was precipitated with NaOH. The precipitate formed was filtered through a vacuum filtration process, washed with distilled water until the pH reached 7. The product formed (CoFe₂O₄/rice husk silica nanocomposite) was dried in an oven at 100 °C and calcined at 300, 500 and 700 °C for 2 h. Each sample was designated as cobalt ferrite/rice husk silica as-prepared (CFS-100), cobalt ferrite/rice husk silica calcined at 300 °C (CFS-300), cobalt ferrite/rice husk silica calcined at 500 °C (CFS-500), cobalt ferrite/rice husk silica calcined at 700 °C (CFS-700). The scheme of the cobalt ferrite/rice husk silica nanocomposite synthesis is shown in **Fig. 3.3**.

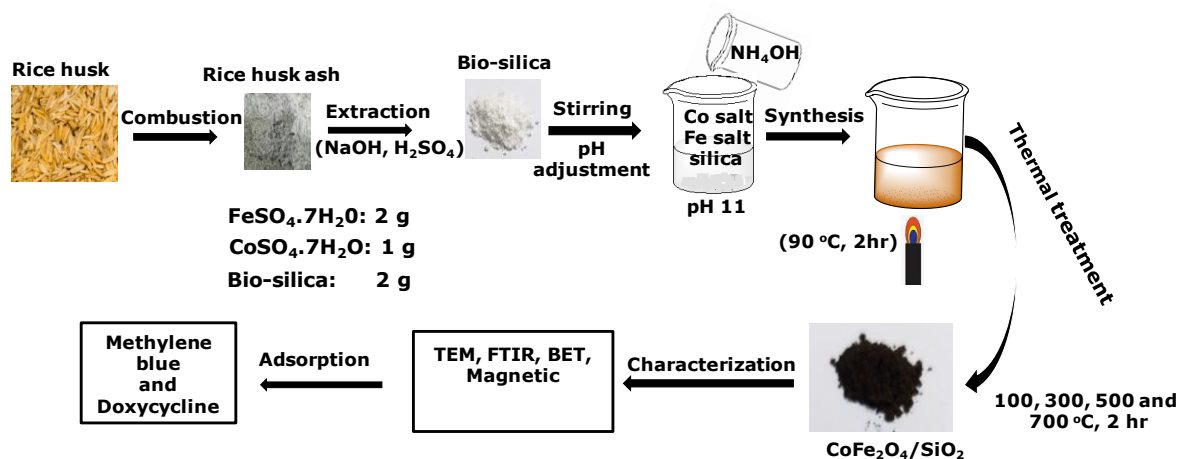


Fig. 3.3. Scheme of the cobalt ferrite/rice husk silica nanocomposite synthesis.

3.8 Preparation of SDS- modified raw kaolinite

Sodium dodecyl sulfate (SDS) modified raw kaolinite was prepared accordingly, 1g of raw clay was dispersed into 100 mL of 0.01M of SDS. The mixtures were stirred for 3h at 80 °C and left overnight at room temperature. The modified raw clay was centrifuged and dried in the oven at 100 °C.

3.9 Preparation of spray-dried kaolinite.

10g of raw kaolinite sample was dispersed in 1L of distilled water containing 0.1 g of dispersant (Logospense 4262). The mixture was continuously stirred during the spray drying period. Spray Dryer MSD 0.5 with 0.7mm nozzle was used to dry the suspended clay. The process was performed by setting an inlet temperature at 120°C and airflow rate at 50 L min^{-1} pressure. The dried product (spray-dried kaolinite) was collected in a collection bottle.

3.10 Synthesis of CoFe_2O_4 /kaolinite nanocomposite

Spray-dried kaolinite (2 g) was dispersed in 25 mL solution containing 2 g of Iron (II) sulfate heptahydrate and 1 g of cobalt (II) sulfate heptahydrate. The mixture was stirred for 30 minutes and precipitated at pH 11 using ammonium hydroxide (28% NH_3 , assay 99.99%), boiled at 90 °C for 2 hours, filtered and dried. Part of the dried nanocomposites was calcined at 300, 500 and 700 °C for 2 h. Each sample was designated as kaolinite/ CoFe_2O_4 nanocomposite as-prepared (KCF-100), kaolinite/ CoFe_2O_4 nanocomposite calcined at 300 °C (KCF-300), kaolinite/ CoFe_2O_4 nanocomposite at 500 °C (KCF-500), kaolinite/ CoFe_2O_4

nanocomposite calcined at 700 °C (KCF-700). The scheme of the cobalt ferrite/kaolinite nanocomposite synthesis is shown in Fig. 3.4.

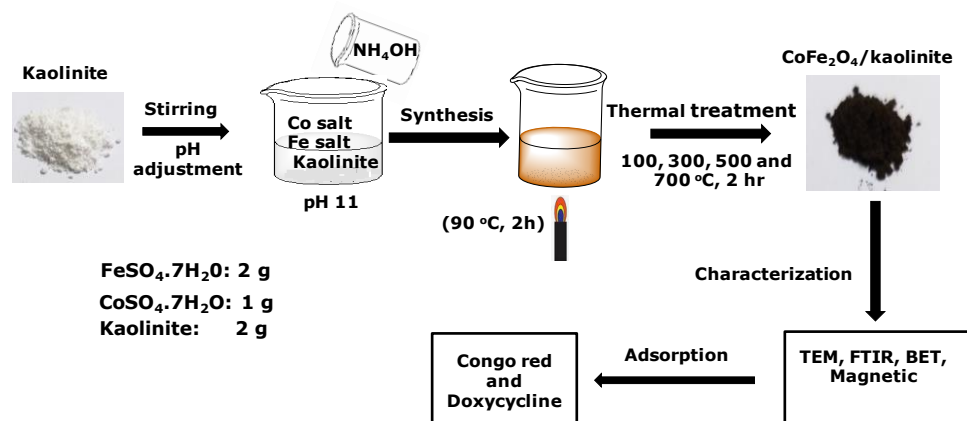


Fig. 3.4. Scheme of the cobalt ferrite/kaolinite nanocomposite synthesis.

3.11 Characterization of the samples

X-ray diffraction (XRD) was performed in a X-ray diffractometer (Shimadzu, XRD 7000) using CuK α radiation [$\lambda = 1.5418 \text{ \AA}$, scanning step = 0.05° , scanning speed 2° min^{-1}]. The powder samples were prepared by packing them to a flat surface in a separate sample holder. The data obtained were analyzed using Search-match software.

Morphology of the nanocomposite was assessed in a thermionic (W filament) scanning electron microscope (SEM), FEI Quanta 200 FEG coupled with an EDX silicon drift detector (Bruker). The powders were put on a stub, fixed with carbon tape.

The sample for transmission electron microscopy (TEM) analysis was prepared by dispersing a small quantity of the powder inside isopropanol and sonicated for 10 minutes. A drop of the suspension was pipetted and placed on the carbon-coated copper grid. The solvent evaporates while the particles settled on a carbon film. The sample was inserted into the sample holder and the image taken on FEI Tecnai G2-20 (200 kV) coupled with a Si (Li) EDAX detector and a Quantum SE system with Gatan Energy Filter.

The textural characteristics of the samples were determined by nitrogen adsorption in a Quantachrome Autosorb. Approximately, 50 – 60 mg of the nanocomposite was weighed inside the sample cell and degassed at 200 °C to remove adsorbed gases and water. The sample was cryogenically cooled with liquid nitrogen (77 K), while the adsorbate gas (nitrogen) is dose into the system at the series of reduced pressures. The gas adsorbed and

the system is allowed to equilibrate, after which time the resultant pressure over the sample is measured. The amount of gas adsorbed by the sample at each reduced pressure point is then used to construct an isotherm. The data obtained were analyzed using multipoint points BET for the evaluation of the specific surface area. The pore size distribution curves were obtained by BJH.

Fourier Transform Infrared (FTIR) spectroscopy was used to study the functional groups that were present in the nanocomposites. The FTIR spectra were recorded via a Varian FTIR 660 spectrometer between 400 and 4000 cm^{-1} , 64 accumulations, and 4 cm^{-1} resolution using the standard KBr method. For this analysis, each sample and KBr powder was dried in an oven at 200 C for 2 h to remove moisture. 200 mg of KBr was mixed with 2 mg of each sample, crushed using a mortar and pestle and then pressed to form transparent pellets that were used for the characterization. The pellet was placed in the FTIR sample holder and analysis.

NETZSCH– STA 409EP (Netzsch Inc., Germany)-type thermogravimetric (TGA) was used to detect mass loss with respect to the amount that was adsorbed on the magnetic composites. Before carrying out the test, the samples were evenly distributed in an alumina sample pan. The analysis was performed in synthetic air at 50 $\text{cm}^3 \text{min}^{-1}$ flow rate starting from 40°C to 600°C $\pm 10^\circ\text{C}$ with 10°C/min heating rate.

The study of magnetic measurements was performed on a magnetometer and susceptometer equipped with SQUID (Superconducting Quantum Interference Device) sensor. The Cryogenic S700X magnetometer was used in the Laboratory of Magnetism of the Chemistry Department of UFMG. This equipment has field application capacity of up to 7 tesla, and continuous standard temperature control from 1.6 K to 300 K. All measurements was performed on samples previously dried in powder form (2 to 6 mg). The sample was placed inside a capsule used in a pharmacy handling, which in turn is placed and inside a small plastic tube. The data were interpreted using the molar masses obtained from the chemical analyzes

3.12 Adsorption studies

3.12.1 pH studies

Optimum pH was determined by adding 10 mg of the respectively adsorbent to 15 mL of 100 mg L⁻¹ of each of the adsorbate solution (acid orange II, Methylene blue, Congo red and Doxycycline) inside 50 mL beaker for 24 hours. The pH of the solution was adjusted to 2, 4, 6, 8 and 10 with dilute HCl and NaOH.

3.12.2 Kinetic studies

Kinetic studies were carried out for 24 hours, while the amount adsorbed was measured at regular intervals to know the optimum time. In these studies, the pH of the solution was fixed (optimum pH), 10 mg of the adsorbents was added to fixed volume (15 mL) of 100 mg/L the adsorbate solutions.

3.12.3 Dosage studies

The amount of each adsorbent added to 15 mL of 100 mg L⁻¹ of the adsorbate was varied from 2, 4, 6, 8 and 10 mg). Optimum pH and time were used for this study.

3.12.4 Temperature and concentration studies

The temperature of the solution was varied from 298, 303, 313, 323 and 333 K by placing the beakers containing a fixed volume of the respective concentration (50, 100,150, 200, 250, 300 350, 400, 450 and 500 mg L⁻¹) of the respective adsorbate inside a temperature-controlled water bath and allowed to stay for the optimum time that had been earlier determined.

After each of the study listed above, reasonable quantity of the solution was withdrawn and the final unabsorbed concentration of the adsorbate was measure by a UV–Vis spectrophotometer (U-2010, Hitachi) at a wave-length of λ_{\max} 345 nm (Doxycycline), 664 nm (Methylene blue), 500 nm (Congo red) and 485 nm (Acid orange II). The amount adsorbed (mg g⁻¹) was calculated using equation 3.3

$$q = \frac{(C_o - C_e)V}{m} \quad 3.3$$

3.13 Adsorption kinetics

The importance of the kinetic study cannot be overemphasized as it helps to know the equilibrium time and how fast the composites could attain the highest adsorption capacity with respect to the initial concentration. The data obtained from contact time were further subjected to a nonlinear form of pseudo-first-order, pseudo-second-order, and general order kinetic models, shown in equations 3.4 and 3.5 respectively.

$$q_t = q_e [1 - \exp(-k_1 t)] \quad 3.4$$

$$q_t = q_e - \frac{q_e}{[k_2 (q_e) t + 1]} \quad 3.5$$

Where, q_t and q_e are amount of contaminant adsorbed at time 't' and at equilibrium time respectively, k_1 and k_2 are the rate constant of pseudo-first-order and second-order kinetic models respectively.

3.14 Adsorption isotherm

Adsorption isotherm is a graphical expression of the adsorbate concentration against its residual concentration at a constant pH and temperature, it provides understanding about the mechanism of adsorption. Therefore, the data obtained from temperature studies were subjected to two commonly isotherms which are Langmuir and Freundlich. Langmuir isotherm assumes monolayer adsorption on a homogeneous surface with a definite number of adsorption sites, maximum adsorption capacity is determined through it. Freundlich model is suitable for heterogeneous surfaces and can be applied to multilayer adsorption and it helps to understand that the vacant sites on the adsorbent are having distinct energy [5]. The non-linear equations of Langmuir and Freundlich are shown in equations 3.6 and 3.7 respectively.

$$q_e = \frac{q_{max} C_e K_L}{(1 + K_L C_e)} \quad 3.6$$

$$q_e = K_F C_e^{1/n_F} \quad 3.7$$

where C_e is the equilibrium concentration in bulk solution (mg L^{-1}), q_e is the amount of contaminants that was adsorbed (mg g^{-1}), q_{max} is the maximum adsorption capacity (mg g^{-1}), K_L is an equilibrium constant of Langmuir (L g^{-1}), K_F is the Freundlich constant ($\text{mg g}^{-1} (\text{mg L}^{-1})^{-1/n_F}$), n_F is the dimensionless exponent of Freundlich.

3.15 Adsorption thermodynamics

The values of thermodynamic parameters (changes in Gibbs-free energy (ΔG^o), changes in enthalpy (ΔH^o) and changes in entropy (ΔS^o)) were calculated using equations 3.8 and 3.9

$$\log Ke = \frac{\Delta S^o}{2.303R} - \frac{\Delta H^o}{2.303RT} \quad 3.8$$

$$\Delta G^o = \Delta H^o - T\Delta S^o \quad 3.9$$

It is worthy to note that Ke is a dimensionless thermodynamic equilibrium constant, which was obtained from Langmuir equilibrium constant (K_L) as shown in equation (3.10), [76]. where the activity coefficient of adsorbate is the standard concentration of the adsorbate (1 mol L⁻¹).

$$Ke = \frac{1000 * K_L * \text{molecular weight of the adsorbate} * \text{standard concentration of the adsorbate}}{\text{activity coefficient of adsorbate}} \quad 3.10$$

3.16 Computational details for the adsorption of CoFe₂O₄/chitosan

To have a better understanding of the adsorption mechanism, reactivity and the interactions involving the dyes and chitosan magnetic composite, quantum chemical calculations were carried out at the DFT level theory using the ORCA software [77,78]. Geometry optimizations of the dye molecules in which electronic properties were investigated using the Fukui functions, including the solvation effects are shown in **Fig 3.5**.

Three chitosan models were built as pentameric structures as shown in **Fig. 3.6**. The protonated model (charge +5), has the five amino groups in -NH₃⁺ form; the neutral model keeps the hydroxyl and amino groups in neutral states and, the deprotonated model (charge -2) has two OH groups deprotonated. These three models simulate the chitosan in acidic, neutral or basic pH respectively. The interaction of the dyes with the chitosan models was investigated through geometry optimization at the DFT/PBE-3c level of theory. Hydrogen bond formation of the dyes in water solution was investigated using Monte Carlo (MC) statistical mechanical simulation in an NPT ensemble at 298K using a classical pair potential composed of Coulomb plus 12-6 Lennard Jones terms [79] in a box with 599 molecules of water described by the TIP3P model[80]. All MC simulations were done using the DICE(v3.0beta) software developed by Coutinho and Canuto [81].

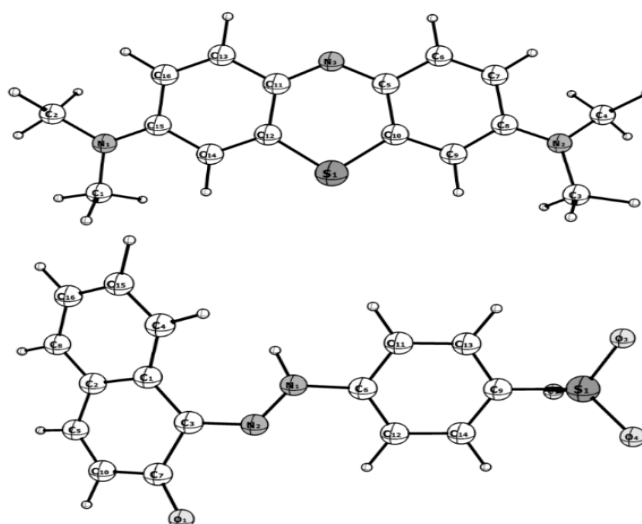


Fig. 3.5: Optimized structures of MB (top) and AO (bottom) with the respective numbering of atoms.

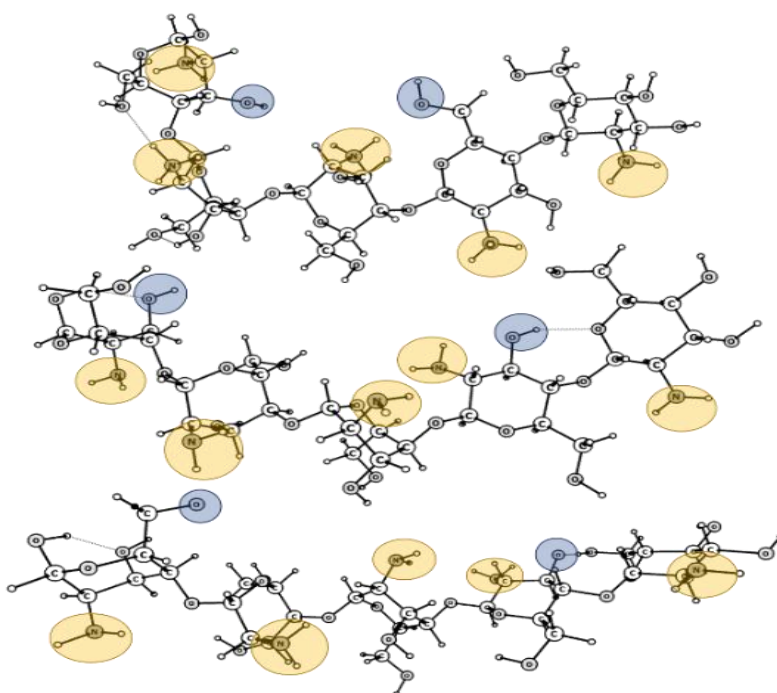


Fig. 3.6. Protonated (top), non-protonated (middle) and deprotonated (bottom) models to simulate the chitosan polymer. The yellow circles highlight the amino groups that are protonated ($-NH_3^+$) in the top or non-protonated ($-NH_2$) in the middle and bottom structures, while the blue circles highlight the OH groups that are protonated ($-OH$) in top and middle or deprotonated ($-O^-$) in the bottom structure comprising the three chitosan models.

CHAPTER FOUR: RESULTS AND DISCUSSION

4.1 Effect of drying process and calcination on the structural and magnetic properties of cobalt ferrite.

4.1.1 Brief introduction

It was gathered from the literature that the characteristics of magnetic nanoparticles depend on the synthesis route and drying process [64]. Given this, several authors have carried out various researches on cobalt ferrites and its synthesis route [82–84]; this is to provide a well viable and cost-effective means of synthesizing spinel ferrites. Mahboubeh et al., [85], utilized combustion, co-precipitation and Stöber (precipitation) methods to synthesize cobalt ferrite, and discovered that co-precipitated cobalt ferrite has moderate crystal size (49.5 nm) and saturation magnetization (55.8 emu g⁻¹). Also, Ristic et al. [86], used a co-precipitation method to synthesize cobalt ferrite and studied the influence of pH and autoclaving time on the crystallite size and magnetic measurement of CoFe₂O₄. According to their report, both the crystallite size and magnetic saturation increased with the increase in precipitated pH.

In view of this, chemical co-precipitation method was used to prepare cobalt ferrite used in this study. This process has been noted to be a suitable method for the synthesis of nanoparticles; it is less time consuming and cost-effective [87]. However, the significant effect that drying process could have on magnetic, textural, morphological and structural properties of cobalt ferrite and its effectiveness in treating contaminants has not been reported and this propelled our curiosity. Therefore, we employed spray drying and conventional oven drying method to dry co-precipitated cobalt ferrite used for the study. Agnese Stunda-Zujeva et al [88] wrote that spray drying method is one of the most convenient and fast techniques that could be used to produce particles of high surface area. The performance of the oven and spray dried cobalt ferrite on the adsorption of the methylene blue was studied (in brief) before and after calcination process.

4.1.2 X-ray diffraction analysis of the synthesized CoFe_2O_4

The diffractograms of the synthesized cobalt ferrite are shown in **Fig. 4.1**. The pattern matched with card number 22-1086 of the Joint Committee on Powder Diffraction Standards (JCPDS), which is a typical pattern of cubic spinel ferrite having space group of $Fd\bar{3}m$ (N^o 227). The diffractograms of the as-received samples: OD-100 and SD-100 showed the presence of two phases: CoFe_2O_4 and $\text{Co}_{0.33}\text{Fe}_{0.67}(\text{OOH})$ (card #14-558). Meanwhile, $\text{Co}_{0.33}\text{Fe}_{0.67}(\text{OOH})$ phase disappeared after calcination. Phase transformation was observed after the samples were calcined at 500°C , leading to the appearance of hematite phase.

Another observation was the slight shift of peak (311) in both OD-100 and SD-100 diffractograms after calcining at 500°C . Dehydroxylation of the Cobalt-iron (oxy) hydroxide ($\text{Co}_{0.33}\text{Fe}_{0.67}(\text{OOH})$) phase at this temperature could have been responsible for the shift. Thermal decomposition of this phase could have initiated the movement of a certain amount of Co^{2+} ions from octahedral to the tetrahedral sites, and equivalent transfer of Fe^{3+} ions from tetrahedral to octahedral sites. Rao et al [89] as well reported a shift in peak due to an increase in annealing temperature. The lattice parameters (a) are itemized in **Table 1**. The values obtained for both OD-700 and SD-700 are closed to the reported lattice constant of pure cobalt ferrite in the literature ($8.396 \pm 0.001 \text{ \AA}$) [90].

The impure phase, Fe_2O_3 disappeared completely after the samples were calcined at 700°C , leading to the formation of single-phase cobalt ferrite. This shows that the presence of hematite (an antiferromagnetic) in cobalt ferrite can be thermally decomposed giving rise to pure cobalt ferrite. Calcination process has effect on the purification, crystal growth and crystallization of the synthesized CoFe_2O_4 . This structural change resulted in change in the magnetic properties of the samples. However, the drying process does not have a significant effect on its structure.

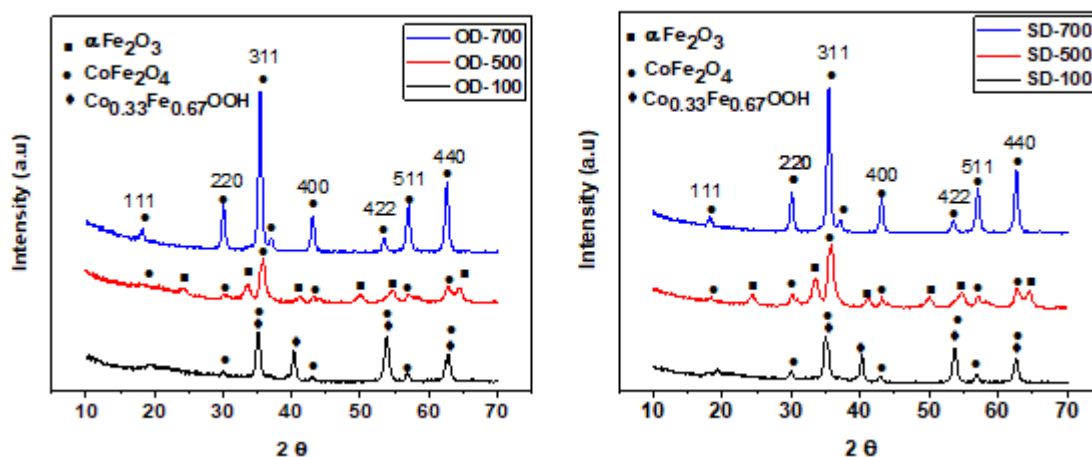


Fig. 4.1. XRD pattern of cobalt ferrite samples calcined at different temperatures.

Table 1. Crystallite size and Lattice constant for cobalt ferrite.

Cobalt ferrite	Crystallite size (nm)	Lattice parameter (Å)
OD-100	8	8.47
OD-500	10	8.32
OD-700	14	8.40
SD-100	9	8.47
SD-500	10	8.36
SD-700	14	8.40

4.1.3 TEM and HRTEM analysis

Transmission electron microscopy (TEM) images of SD-100, SD-500, and SD-700, show distinct agglomeration (**Fig. 4.2**). The reason for the agglomeration was due to the interaction that exists among the particles. This feature was only observed in the spray-dried images. Bright-field TEM images of all the samples are displayed in **Fig. A1** (Appendix). The images are plate-like structure of different orientation and morphology.

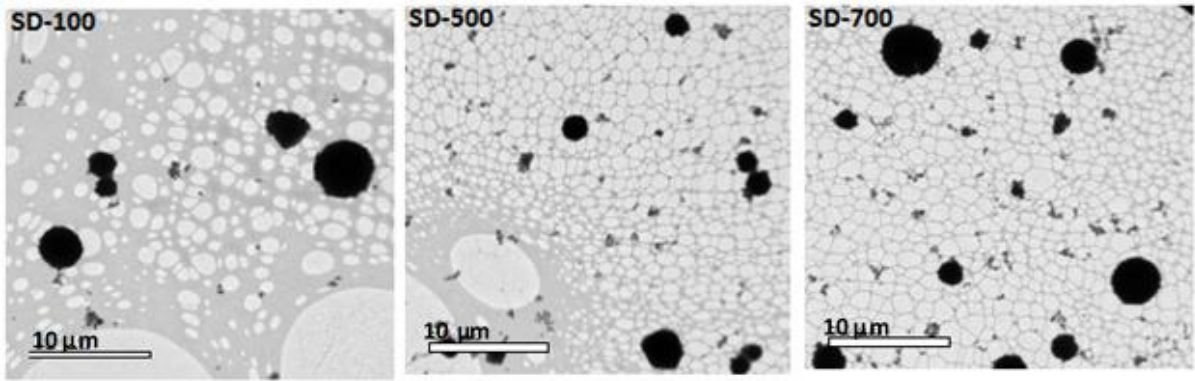


Fig. 4.2. TEM images of spray-dried cobalt ferrite calcined at a different temperature, showing agglomeration.

High resolution-transmission electron microscopy (HR-TEM) images of all the samples show the degree of crystallinity through the appearance of clear lattice fringes of crystalline planes in the particles (**Fig. 4.3**). The clear appearance of the fringes (observed at the Fast Fourier Transform in each image) increases with the increase in the calcination temperature. This is in accordance with the X-ray diffractogram results, which show an increase in the crystallite size with respect to an increase in temperature.

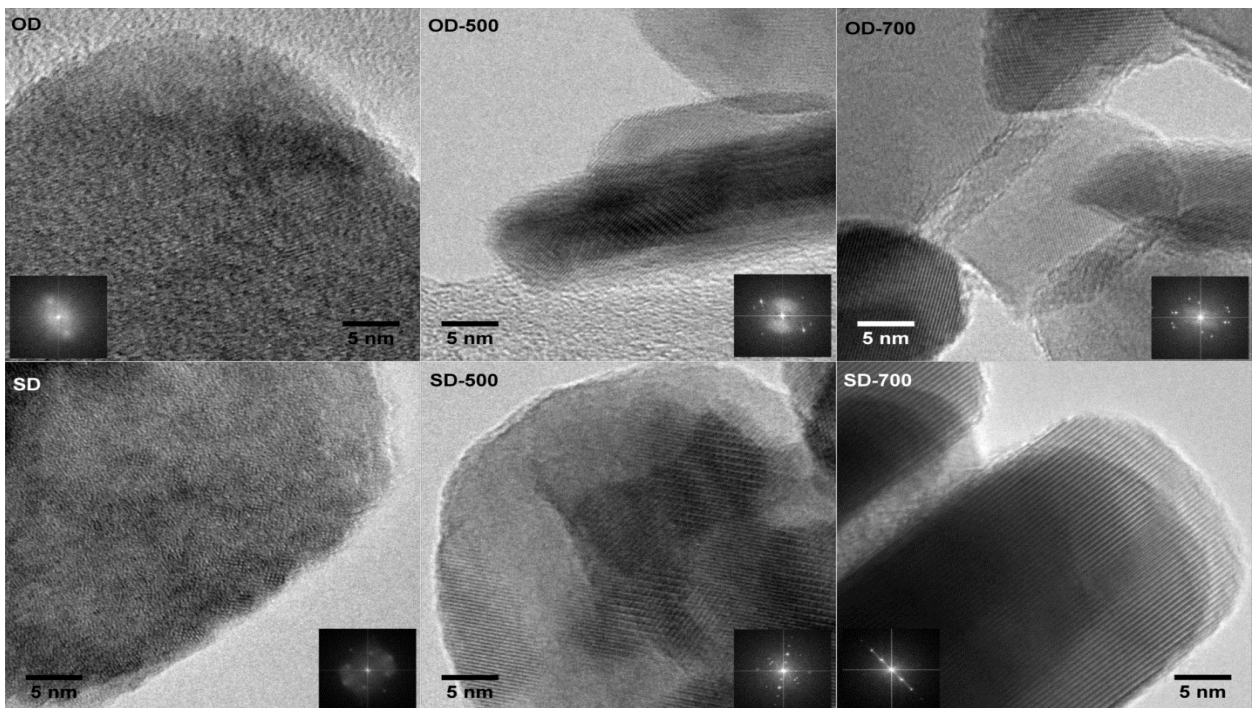


Fig. 4.3. HRTEM images of various cobalt ferrite samples. The inset in each image shows the Fast Fourier Transform (FFT).

4.1.4 Scanning electron microscopy (SEM)

Scanning electron microscopy analysis of the spray-dried sample (**Fig. 4.4**) was performed to assess the morphology of the agglomerate observed at TEM. Averagely, the image of SD-700 shows particles with a spherical shape and a high degree of agglomeration among the fine particles (spray-dried powder). It is well documented that particles with the large surface area to volume ratios tend to agglomerate so as to reduce their high surface energies [91].

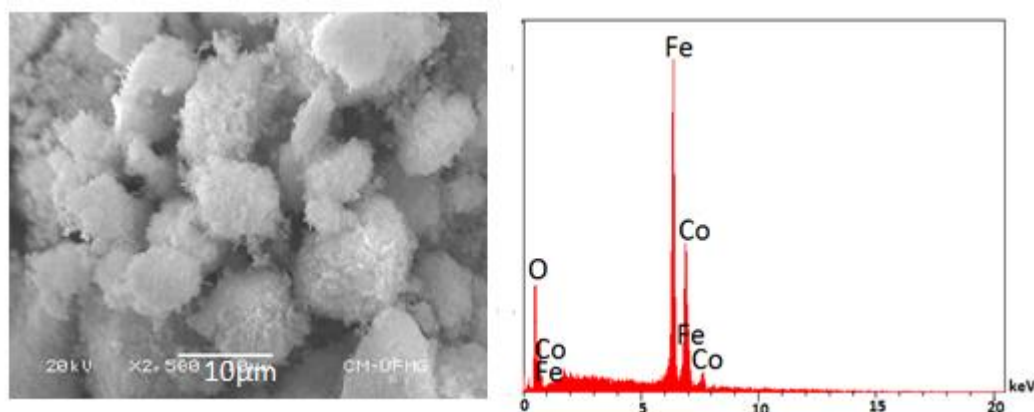


Fig. 4.4. SEM images of SD-700 (SEM images of SD-100 and SD-500 not shown).

4.1.5 BET specific surface area analysis

Nitrogen adsorption and desorption isotherms are shown in **Fig. 4.5**, while the specific surface areas (SSA) are itemized in **Table 2**. The specific surface areas of SD-100, SD-500, and SD-700 are higher than the respective oven-dried samples. This signifies that spray drying process can improve the SSA of cobalt ferrite and perhaps other powder samples. More so, the cost of surfactant can as well be reasonably reduced or avoided by employing spray drying process to produce powder of high surface area. The results also show that the values of SSA reduce as the calcination temperature increases, which could be due to phase transformation and dehydroxylation as observed in XRD diffractogram. This is expected because calcination leads to lower surface area as decomposition of some compounds could take place. The isotherm is typical of nonporous or macroporous material.

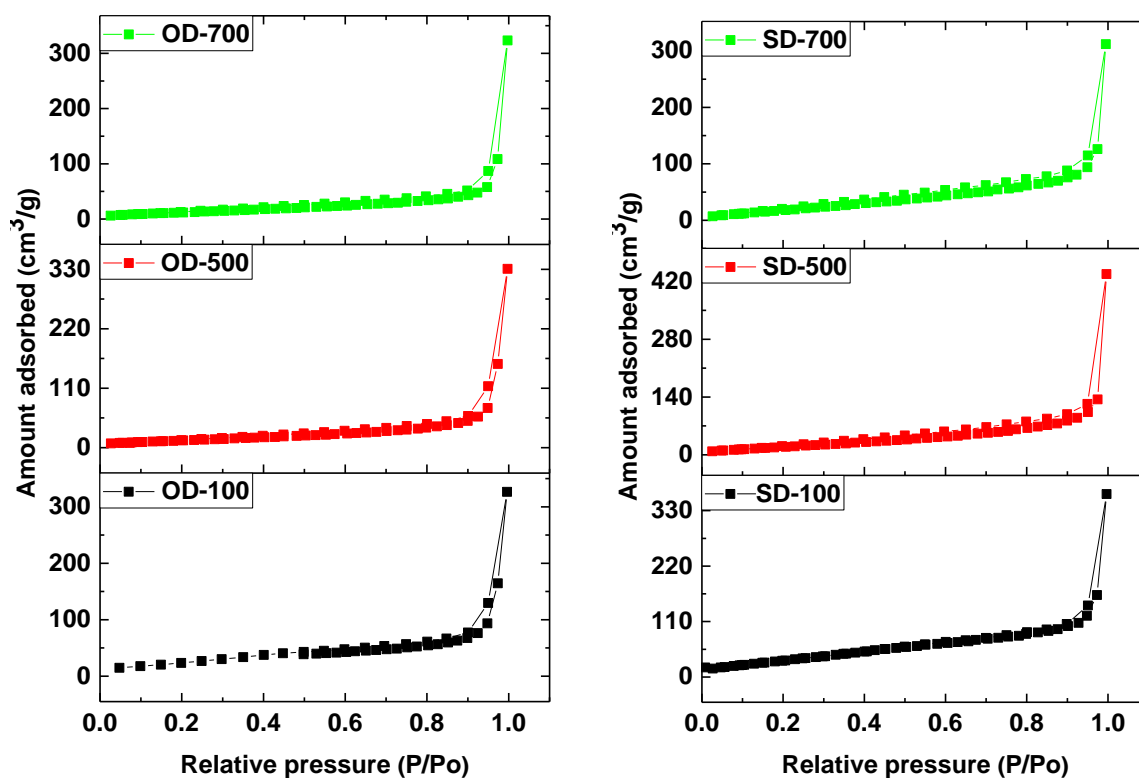


Fig. 4.5. Nitrogen adsorption-desorption isotherm at 77K of the for various cobalt ferrite

Table 2. BET specific surface area

Cobalt ferrite	Parameters	
	SSA ($\text{m}^2 \text{g}^{-1}$)	C constant
OD-100	92	27
OD-500	52	38
OD-700	47	28
SD-100	138	21
SD-500	86	14
SD-700	82	13

4.1.6 Magnetization versus Temperature

The magnetic profile of synthesized cobalt ferrite (OD-100, OD-500, OD-700, SD-100, SD-500, and SD-700) was characterized by measuring the zero-field cooled (ZFC) and field cooled (FC). The results of the measurement are shown in Fig. A2. The maximum point on

the ZFC curve is the blocking temperature (T_B) [92]. As shown in the Fig., ZFC of both OD-100 and SD-100 increases with temperature and attained maximum values (T_B) at 240 and 164 K respectively, after which it decreases with further increase in temperature. This type of behavior is associated with the characteristic behavior of superparamagnetic materials [93], meanwhile considering their coercivity values which are far greater than zero (**Fig. 4.6**), they cannot be regarded as pure superparamagnetic.

The presence of cobalt–iron (oxy) hydroxide in the two samples would have influence weak magnetic interaction within the particles hereby leading to the attainment of blocking temperature. This infers that the presence of cobalt–iron (oxy) hydroxide hindered the response of the magnetic moment to the magnetic field which leads to a low magnetic anisotropy barrier (**Table 3**). It has been stated that anisotropy energy acts as an energy barrier that prevents free rotation of the magnetic moments away from the easy axis [63].

The value of T_B corresponds to the particles size interaction; hence for SD-100 to have attained lower T_B than OD-100, it means that the particles have higher interaction and this could have propelled the agglomeration of the particles which was noticed in the TEM images. It was stated that, above the blocking temperature, the interaction between magnetic nanoparticles is very weak, while the interaction between the particles is strong below T_B [94,95]. This implies that the lower the T_B , the higher the magnetic interaction within the nanoparticles. Spray drying process enhanced the magnetic interaction (evidence in the agglomeration) of the particles which resulted to lower T_B .

The decomposition of cobalt–iron (oxy) hydroxide as confirmed from the XRD results, leads to a high magnetic anisotropy energy barrier after calcination and became difficult to be overcome by thermal activation within the temperature range (10 - 300 K). The values of T_B are well too high to be determined, this indicates that the materials (OD-500, OD-700, SD-500 and SD-700) are still magnetically blocked at room temperature.

4.1.7 Magnetization versus Field

The result of magnetization as a function of the applied field (**Fig. 4.6**) was carried out at 10 and 300 K. In the curves of hysteresis, the saturation magnetization (M_s) increased with an increase in calcination temperature (due to the disappearance of $\alpha\text{-Fe}_2\text{O}_3$ and $\text{Co}_{0.33}\text{Fe}_{0.67}(\text{OOH})$ phase) as listed in **Table 4**. The M_s of OD-100, OD-500, SD-100 and SD-500 are lower than the bulk M_s of cobalt ferrite (80 emu g^{-1}) [90], meanwhile, values obtained for SD-700 and OD-700 are close to the bulk M_s of cobalt ferrite. The lower saturation magnetization values reported for OD-100, OD-500, SD-100 and SD-500 are attributed to the presence of alpha hematite and cobalt-iron (oxy) hydroxide impurities which reduced the number of moments contributing to magnetic saturation.

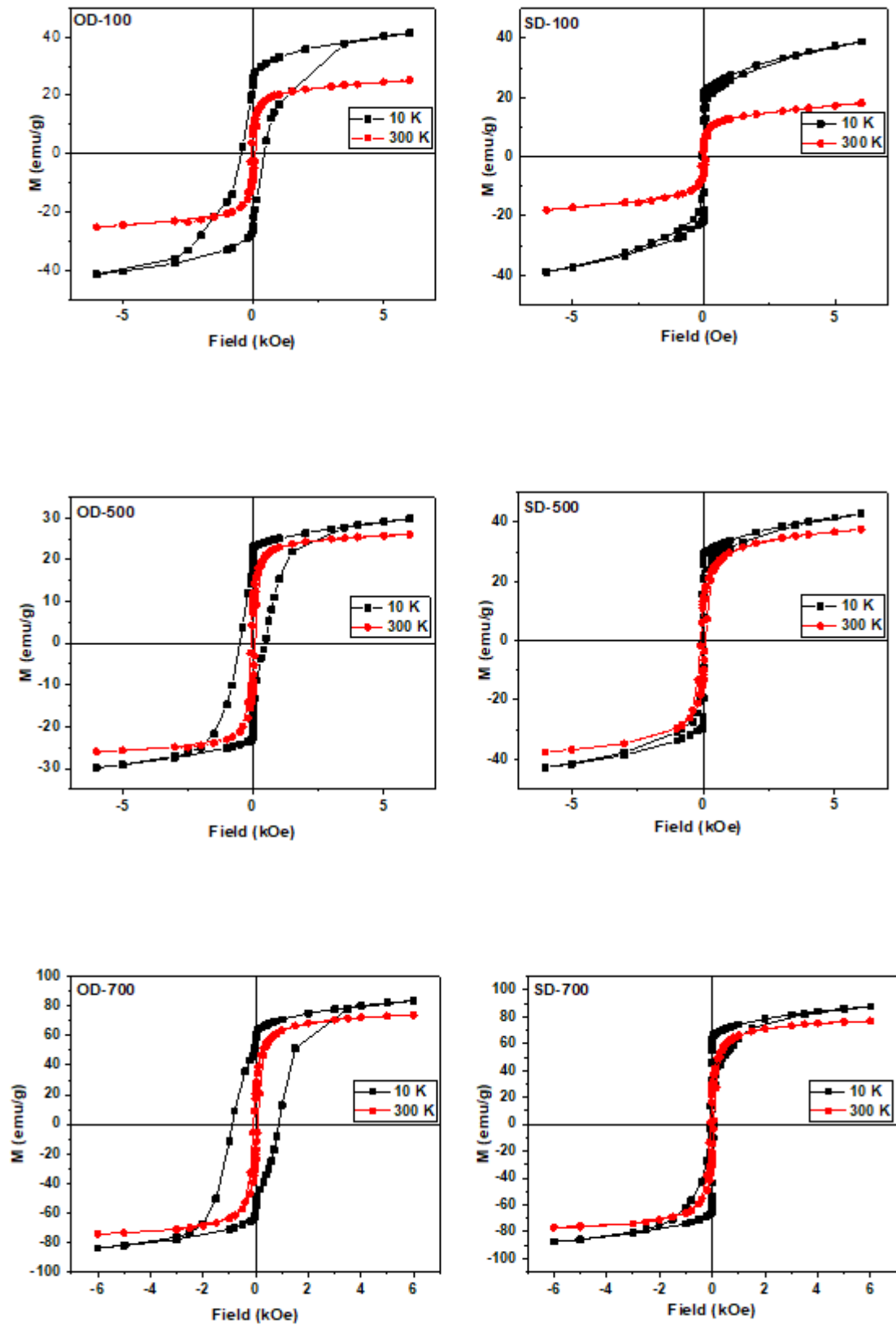


Fig. 4.6. Magnetization versus applied field at 10 and 300 K for cobalt ferrite samples.

Increase in crystallite size (itemized in **Table 1**) could as well be responsible for higher M_s at 700 °C. Magnetic domain size is directly proportional to crystallite size. Whenever the magnetic domain size increases, there will be a corresponding increase in the number of atomic spins that align themselves in the direction of the applied magnetic field, thereby enhancing the magnetic saturation of the material [96].

It was also observed from **Table 4** that the magnetic saturation of all the samples is higher at 10 K (low temperature) than 300 K (room temperature) because of a reduction in thermal vibration [92]. The high values of coercivity (H_C) and a lower value of M_r at 10K are attributed to the increased in magnetic anisotropy of the particles which prevent magnet moment from aligning in an applied field [96]. At low temperature, magnetic spin freezes and reversal of magnetization becomes difficult, resulting to high anisotropy and coercivity [97]. The coercivity of SD-100, SD-500 and SD-700 are less than their respective oven-dried samples due to agglomeration which was caused by mutual interaction within particles. The respective coercivity values of this synthesized cobalt ferrite, make its applications differ at low (10 K) and room (300 K) temperature. The magnetic anisotropy (K) values shown in **Table 3** are calculated from equation 4.1 below [97].

$$K = \frac{M_s \times H_C}{0.96} \quad 4.1$$

Squareness ratio (R_S) calculated from equation 4.2 below is a measure of how easy it is for the direction of magnetization to re-orient to the closet easy axis after withdrawing of the magnetic field [98].

$$R_S = \frac{M_r}{M_S} \quad 4.2$$

Squareness ratio obtained at room temperature for all the samples is within 0.3 – 0.39 implying that at 300 K the magnetic properties of the synthesized cobalt are not direction-dependent (isotropic). This is a typical example of a soft magnet with a characteristic of single-domain nanoparticles. Meanwhile, at 10 K, R_S range from 0.55 – 0.78, which indicates a hard magnet property, comprising of multi-domain nanoparticles with high anisotropy behavior and high coercivity [96].

Table 3. Magnetic anisotropy and squareness ratio at 10 and 300 K.

Cobalt ferrite	10k		300K	
	K x 10 ³ (erg cm ⁻³)	Rs	K x 10 ³ (erg cm ⁻³)	Rs
OD-100 °C	19.27	0.68	2.11	0.34
OD-500°C	14.21	0.78	2.22	0.39
OD-700°C	79.06	0.74	6.22	0.35
SD-100 °C	1.49	0.55	1.45	0.3
SD-500°C	1.73	0.68	3.53	0.35
SD-700°C	6.81	0.76	4.38	0.37

Table 4. Saturation magnetization, coercivity and remanence values obtained at 10 and 300 K.

Cobalt ferrite	10k			300K		
	Hc (Oe)	Mr (emu g ⁻¹)	Ms (emu g ⁻¹)	Hc (Oe)	Mr (emu g ⁻¹)	Ms (emu g ⁻¹)
OD-100 °C	449	28.12	41.21	79.95	8.6	25.5
OD-500°C	465	22.87	29.35	82.36	10.35	25.8
OD-700°C	913	61.39	83.14	80.8	26.05	73.0
SD-100 °C	36.44	24.13	39.27	65.6	6.29	21.2
SD-500°C	38.75	29.25	42.86	89.5	13.42	37.8
SD-700°C	74.7	67.04	87.64	54.6	28.75	77.0

The difference in drying process did not have a significant effect on the squareness ratio. A comparison of saturation magnetization obtained at room temperature reported by some authors are listed in **Table 5**.

Table 5. Comparison of saturation magnetization (at room temperature) reported by some authors

Ms (emu g ⁻¹)	Reference
77	This work
73	This work
60.6	[99]
59.4	[69]
54	[72]
20	[96]
56.2	[100]
58.4	[101]
50	[102]
50	[103]
45	[104]
70.4	[105]

4.1.8 Adsorption analysis

The various cobalt ferrite samples were tested for the adsorption of methylene blue. Displayed in **Fig. 4.7** is the UV-Vis spectra of methylene blue before and after the adsorption process. The absorbance intensity at λ_{\max} reduces gradually with an increase in the calcination temperature of the samples. Considering the drying process, SD and OD-700 performed better than the rest samples. We could recall that it was at the diffractograms of OD-700 and SD-700 that no trace of impurities (α -Fe₂O₃ and Co_{0.33}Fe_{0.67}(OOH)) was noticed. Given this, it could be inferred that the presence of α -Fe₂O₃ and Co_{0.33}Fe_{0.67}(OOH) phase were responsible for the lower adsorption performance in the samples in which they are present. Another interesting observation again was that, although OD-700 and SD-700 have the lower specific surface area, yet due to the absence of impurity, they adsorbed methylene blue solution better than the other samples (related to the same drying process).

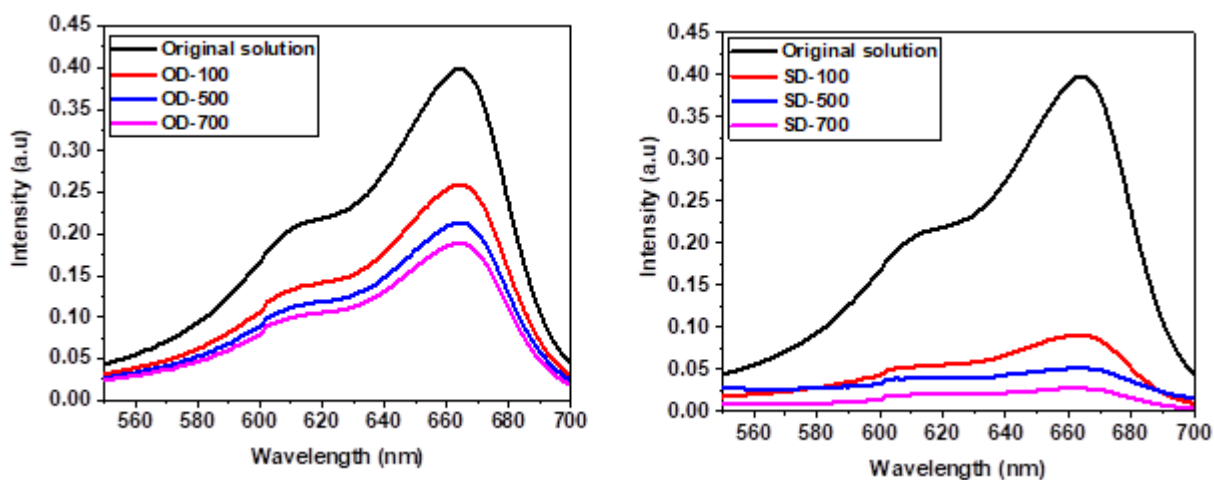


Fig. 4.7: UV-Vis spectra of the original MB dye solution and the respective MB after adsorption processes. (0.1 g of cobalt ferrite was added to 12 mL of MB solution (50 mg L^{-1}).

Now, comparing the two-drying process, it was also observed that SD-100, SD-500, and SD-700 adsorbed MB better than OD-100, OD-500 and OD-700, respectively. This is due to their higher specific surface areas. SD-700 adsorbed 93 % of the initial methylene blue solution while OD-700 adsorbed 52%. This shows the significant effect that spray drying process has over the texture of the material dried in the oven. The respective pictures of methylene blue solutions before and after adsorption are shown in **Fig. 4.8**.

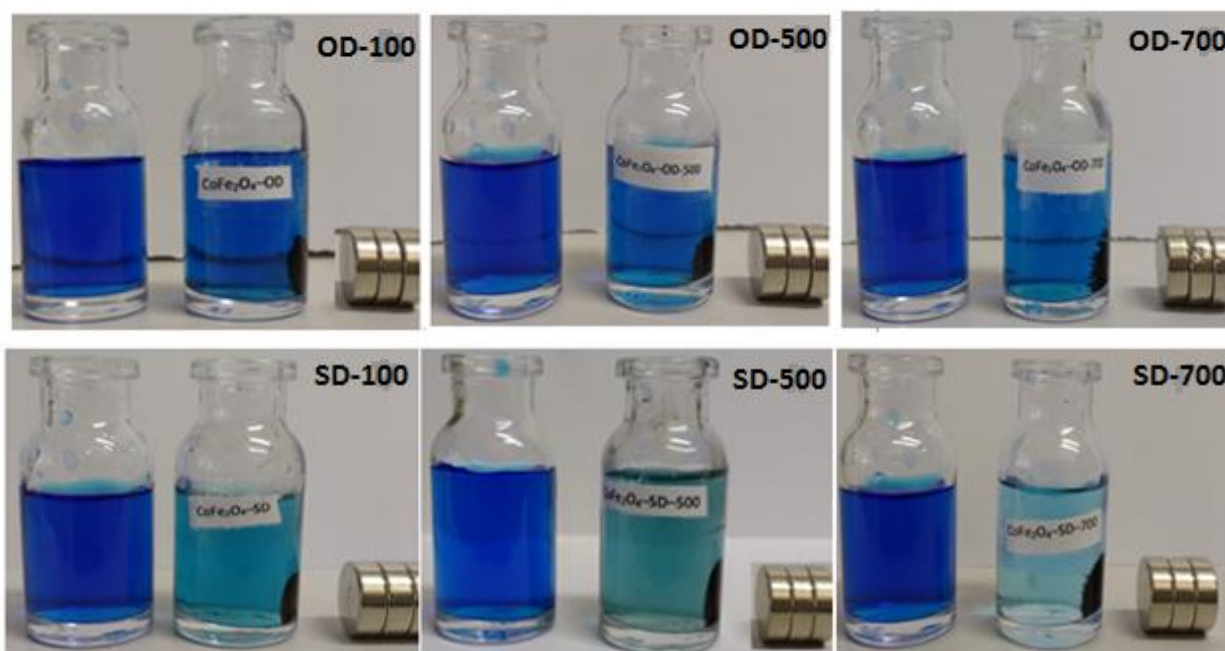


Fig. 4.8: Methylene blue solution before and after immersion

4.1.9 EFTEM images of SD-700 after adsorption

The adsorption of methylene blue (MB) on the surface of SD-700 (having the highest percentage adsorbed) was confirmed through energy-filtered TEM (EFTEM) images, which was critically examined after the adsorption process. The EELS mapping of the Fe, Co, and C were performed by using the three-window method, in which only the signal above the background at each ionization edge contributed to the EFTEM images (Fig. 4.9). The C signal outlining the nanoparticle was due to the C from methylene blue. This ascertained the adsorption of MB on SD-700.

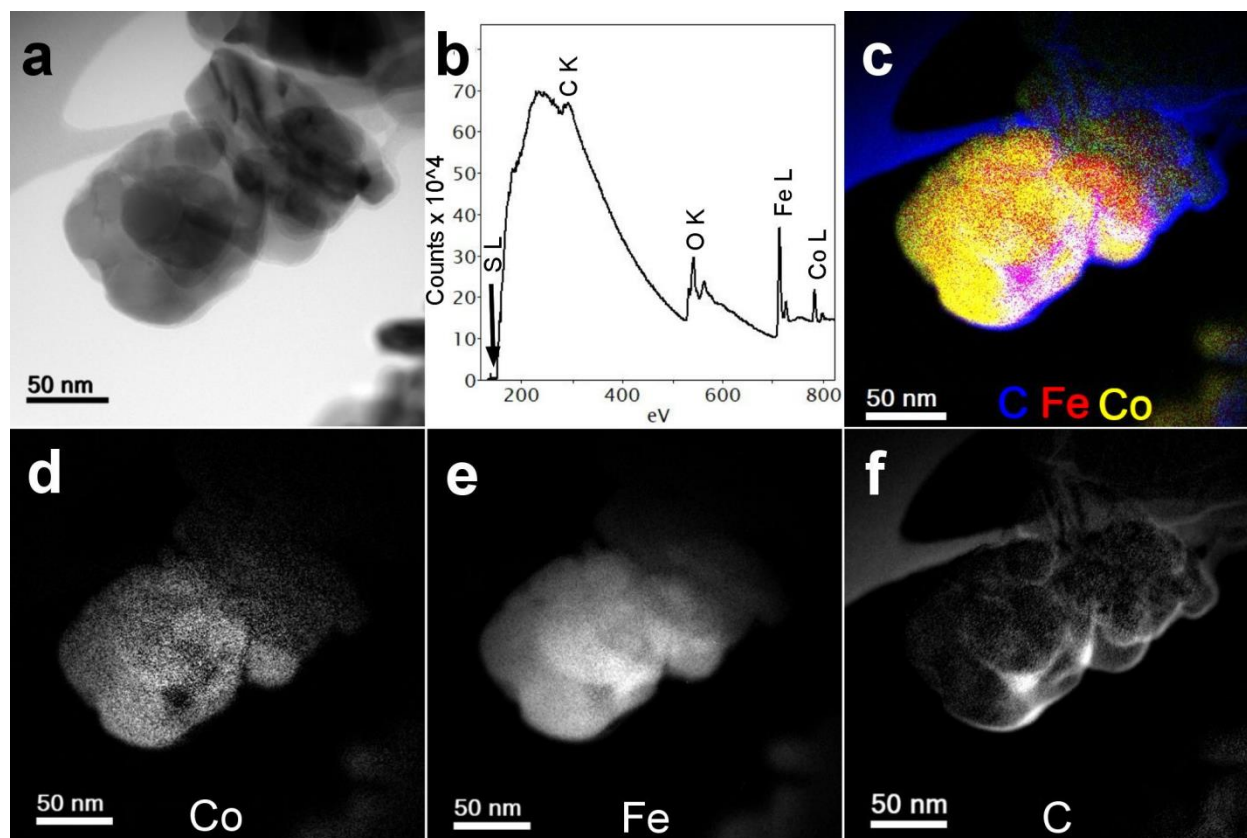


Fig. 4.9: Bright-field TEM image of the cobalt ferrite with adsorbed methylene blue (a). The EEL spectra (b) performed at the cobalt ferrite performed in a particle in (a) under vacuum. The RBG color map (c) shows the distribution of each individual element (d-f).

4.1.10. Conclusion

Cobalt ferrite nanoparticles were successfully synthesized by using a co-precipitation method, followed by two different drying processes (oven and spray). Two phases of impurities (α Fe_2O_3 and $\text{Co}_{0.33}\text{Fe}_{0.67}(\text{OOH})$) were observed in the samples before they were calcined at 700 °C. These phases drew back the potential of the synthesized cobalt ferrite to adsorb methylene blue. The drying process seems not to have significant effects of the diffractogram, but on the magnetic, specific surface area, the morphology of the samples and their ability to adsorb higher percentage of methylene blue solution. Although the calcined samples (oven and spray dried) at 700 °C has the lowest specific surface area, they adsorbed methylene blue better than non-calcined and calcined at 500. This was due to the absence of impurities which resulted to single/pure phase CoFe_2O_4 . This implies that the crystallite growth of the samples did not have negative effects on their ability to adsorb methylene blue solution. SD-700 has the overall best performance, implying that spray drying method could be employed to produce powder of high surface area and adsorption capacity.

4.2 Experimental and theoretical studies for the adsorption of acid orange II and methylene blue using spray-dried crosslinked CoFe₂O₄/chitosan composite

4.2.1. Brief introduction

Chitosan was first discovered and discussed by Rouget in 1859 as a deacetylated form of natural polymer chitin [106]. It is a natural polycationic, polysaccharide derived from chitin, which is found in the crustacean's shells, insect's cuticle and cell wall of fungi [107]. Structurally it is composed of (copolymer) N-acetyl-d-glucosamine and D-glucosamine units with one amino (NH₂) group and two hydroxyls (OH) groups in each repeating glycosidic units [106]. At low pH, chitosan remains as a polycationic species, due to protonation of the amino group with increased soluble property [106]. It is friendly to the environment, readily available, does not have any toxic effect, biodegradable and cheap to obtain [108]. There is continuous extensive research to improve chitosan characteristics for specific applications. It finds its applications in wound dressings, drug delivery, antimicrobial agent and adsorption.

It has been under consideration due to its high amount of amino and hydroxyl functional groups with potential for the adsorption of dyes, metal ions and proteins [109]. In acid solutions, the amino groups of chitosan are much easier to be protonated and they adsorb the anionic dyes strongly by electrostatic attraction [110]. However, the use of chitosan as an adsorbent has many flaws because of its low surface area, coagulation in water, dissolution in acidic solutions. To increase its stability in acidic solutions and to impart mechanical strength during adsorption, crosslinking of chitosan has proven to be very helpful (**Fig 4.10**) [109].

In this study, the setback in separating crosslinked chitosan after adsorption was overcome by synthesized crosslinked chitosan/cobalt ferrite magnetic composite. An innovative approach (spray drying process) was used to dry the glutaraldehyde cross-linked chitosan-cobalt ferrite composite used for this study. The obtained spray-dried magnetic composite was used to adsorb acid orange II (an azo and anionic dye) and methylene blue (cationic dye) from simulated wastewater. Acid orange II (AO) and methylene blue (MB) are chosen

as our target organic dyes due to their usage in textile, cosmetic, paper and food industries [111]. They are toxic, cause nausea, high blood pressure, and respiratory discomfort in humans [112,113].

The use of magnetic chitosan is not a new approach in adsorption studies but, combining experimental with theoretical studies for the proper understanding of the adsorption mechanism has not been reported in the literature. In view of this, a computational chemistry approach was utilized to complement experimental studies. This is to enable a proper understanding of the mechanism of adsorption. The interaction between the dyes molecules and glutaraldehyde cross-linked chitosan-cobalt ferrite composite in the terms of the possibility of charge transferred was unraveled from the quantum chemical descriptors and discussed with respect to the amount of each dye adsorbed.

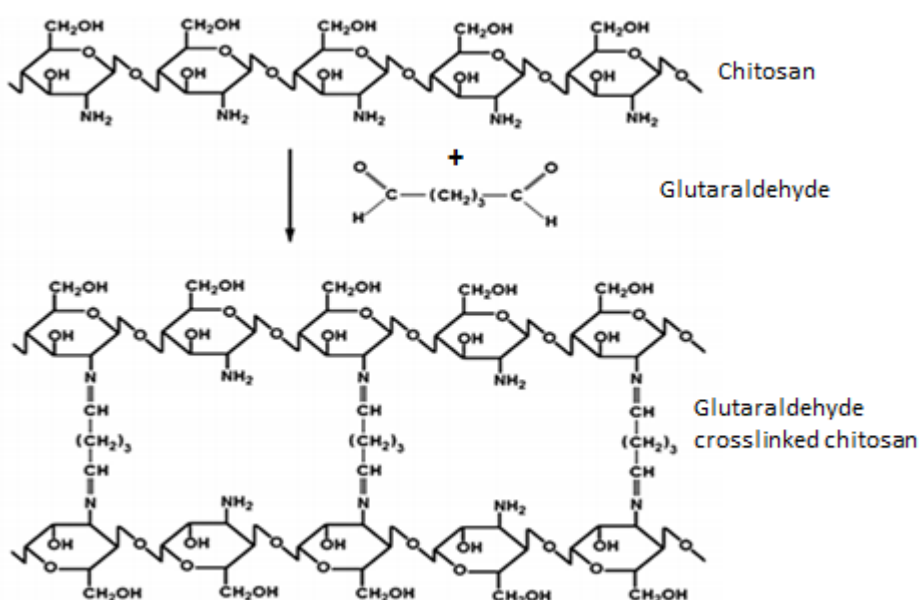


Fig. 4.10. Crosslinked chitosan [114].

4.2.2 Characterization of CoFe_2O_4 /chitosan composite

The diffractogram of CoFe_2O_4 and chitosan/ CoFe_2O_4 (magnetic composite) presented in **Fig. 4.11 A** reflects the pure cubic spinel crystal structure of CoFe_2O_4 . All the peaks in the pure cobalt ferrite are present in the magnetic composite, this shows that the presence of chitosan did not in any way change the structure of cobalt ferrite. The observed change between 20 and 25 ° in the pattern of the composite is due to the presence of amorphous

chitosan. The same observation was reported for amorphous silica with cobalt ferrite [115]. The scanning electron microscope image of the magnetic chitosan is shown in **Fig. 4.11 B**. The particles are spherical and their size ranges from 2 to 5 μm diameter. The secondary electron image suggests that crosslinked chitosan probably formed a coat around cobalt ferrite.

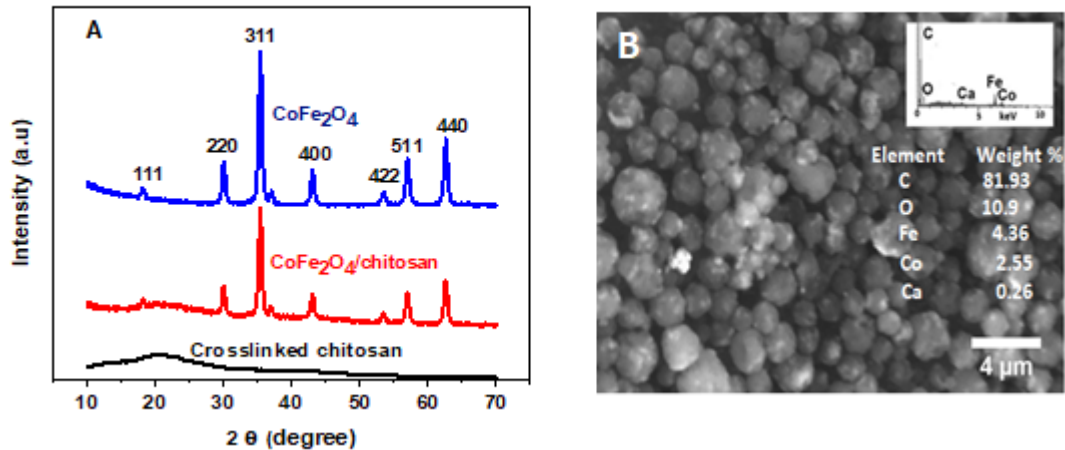


Fig. 4.11. XRD pattern (A) and SEM image with EDS (B) of magnetic chitosan composite.

TEM analysis shows that the magnetic chitosan is aggregates of nanoparticles (**Fig. 4.12-i**). The energy filtered TEM (EFTEM) images in **Fig. 4.12** displays the elemental mapping of the composite. Each EFTEM image was recorded by using the three-window method which integrates only the core-loss signal above the background for each of the edges, C-K, Ca-L, O-K, Fe-L, and Co-L, shown in the electron energy-loss (EEL) spectrum (**Fig. 4.12-ii**). It is clearly seen that the C is homogeneously distributed within the composite along with O, Co, and Fe, thus confirming the covering of crosslinked chitosan onto cobalt ferrite.

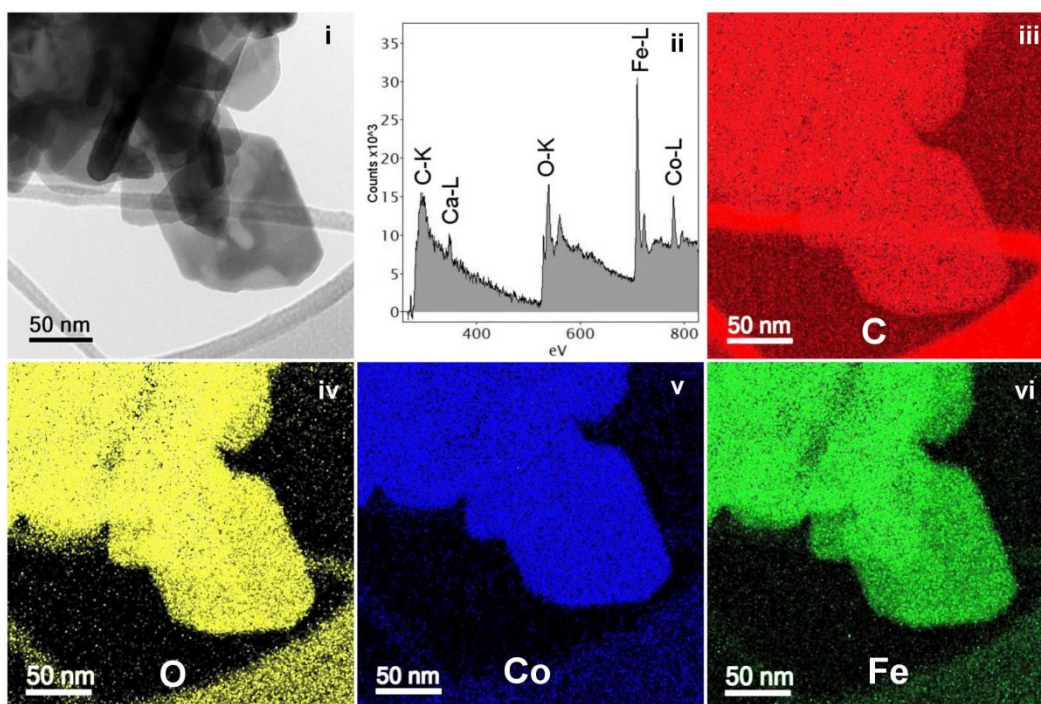


Fig. 4.12. TEM bright-field image (i), EEL spectrum (ii), and EFTEM images of crosslinked magnetic chitosan composite. The EEL spectrum was recorded in a region with no overlapping between the cobalt ferrite and the C-support film.

TGA curves of chitosan and magnetic chitosan composite are shown in **Fig. 4.13 A**. The initial mass loss in chitosan up to 100 °C was due to the removal of adsorbed water molecules. After this, it was thermally stable up to 250 °C. More so, there was a significant mass loss from 300 °C to 590 °C due to the complete decomposition of chitosan. However, in the case of magnetic chitosan composite, there is a continuous mass loss up to 500 °C. This could be because of loss of water, breaking of the bond between chitosan and glutaraldehyde and decomposition of chitosan structure. The estimated amount of cobalt ferrite that was found in the composite after complete decomposition of chitosan was 19.94 wt %, which is approximately equal to the amount in grams of cobalt ferrite that was added to chitosan as mentioned in the experimental section.

The result of magnetization as a function of an applied field carried out at 300 K is shown in **Fig. 4.13 B**. The presence of chitosan on the surface of cobalt ferrite formed a magnetically dead layer and thereby affecting the saturation magnetization. However, the saturation

magnetization (10.79 emu g^{-1}) is higher than M_s value of 7.6 emu g^{-1} reported by Ai et al., [116] for cobalt ferrite/activated carbon composite.

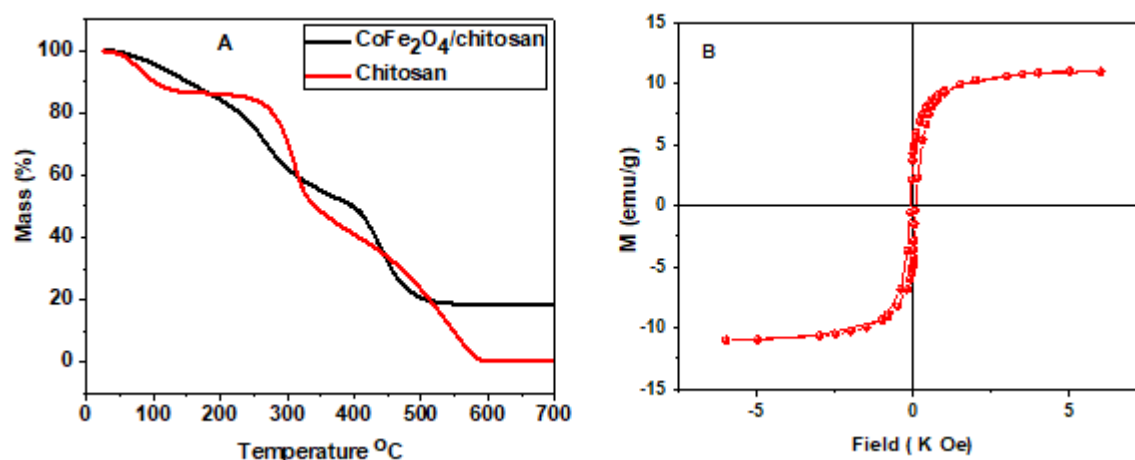


Fig. 4.13. TGA curves (A) Magnetization versus applied field at 300 K (B) of magnetic chitosan composite

4.2.3 Effect of pH, surface charge and adsorbent dosage on adsorption of acid orange II (AO) and methylene blue (MB)

Fig. 4.14 shows the influence of pH on the adsorption capacity of the magnetic chitosan composite. The result clearly shows that the efficiency of the composite depends on pH, this is because the percentage adsorbed decreases with an increase in the pH of AO solution, whereas it increases with an increase in the pH of MB solution. Considering the adsorption of AO, 95 % of the initial 100 ppm was adsorbed at pH 2 and 3, while a lower value of 30 % was adsorbed at pH 10. Whereas for MB a very negligible amount was adsorbed between pH 2 to 10, while 68 % was adsorbed at pH 12. Linking this with the result obtained from zeta potential measurement of the adsorbent, which is presented in **Fig 4.15**, insight into the mechanism of the adsorption was obtained. The net charge on the surface of the adsorbent is zero at pH 9, below this pH, zeta potential values are positive while they are negative above it This implies that anionic dye should be favorably adsorbed at lower pH while cationic dye at pH above 9, as shown in **Fig 4.14**. It can be affirmed that electrostatic attraction/repulsion between the composite and the dye molecules contributed to the mechanism of adsorption of the two dyes. At lower pH, there is an attraction between the surface of the adsorbent and AO. This attraction decreases as the pH of AO solution

increases leading to a decrease in amount adsorbed due to the net surface charge that tends towards negative values and vice-versa for MB. The mechanism of adsorption, though mainly due to electrostatic attraction/repulsion for the adsorption of MB, is not limited to this for the adsorption of AO. This is because at pH 10 when the surface was positively charged, approximately 30 % of AO was removed, which implies that other mechanisms could possibly contribute to the adsorption process. This was further confirmed from the results obtained from theoretical studies. The picture of AO and MB solutions that shows the magnetic separation before and after adsorption is shown in **Fig 4.16**.

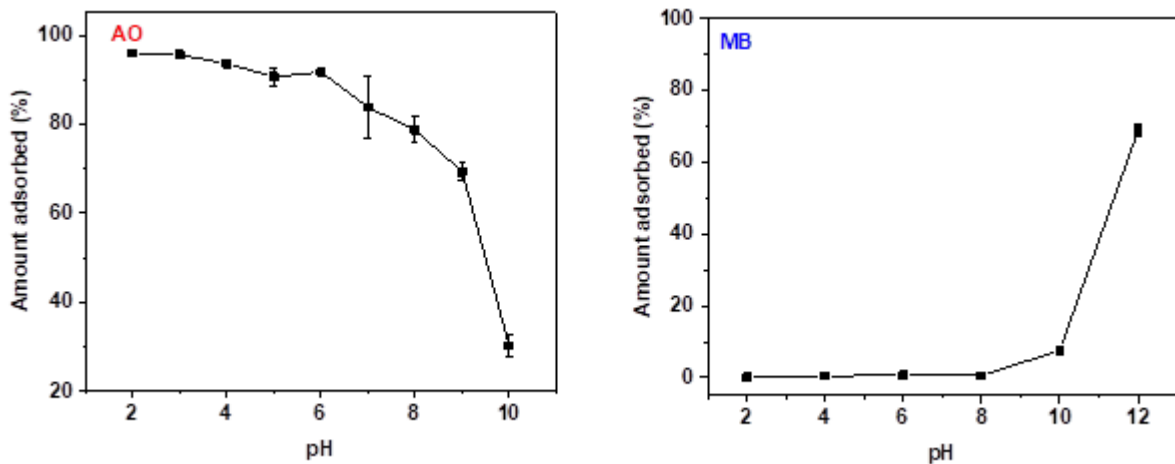


Fig. 4.14. The effect of pH on the removal of 100 mg L⁻¹ AO and MB using 10 mg of magnetic chitosan.

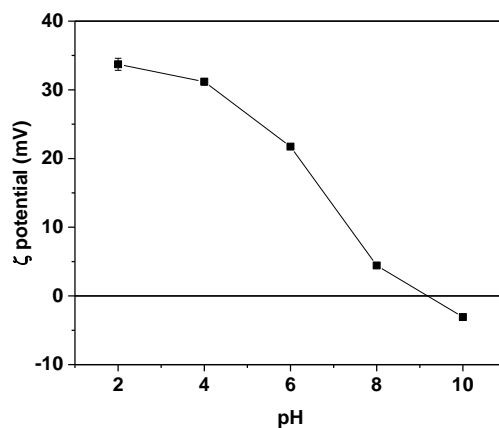


Fig. 4.15. Zeta potential of cobalt ferrite/chitosan composite as a function of pH.

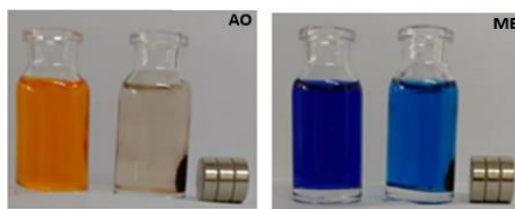


Fig. 4.16. AO and MB solutions before and after immersion in magnetic chitosan composite.

The result of the effect of dosage on the amount of AO (100 ppm, pH 3) and MB (100 ppm, pH 12) adsorbed are shown in **Fig. 4.17**. The amount adsorbed attained saturation at 8 mg dosage for AO adsorption, meanwhile, MB did not attain an equilibrium within the dosage range that was studied. This could be because of the better affinity that the composite has for AO.

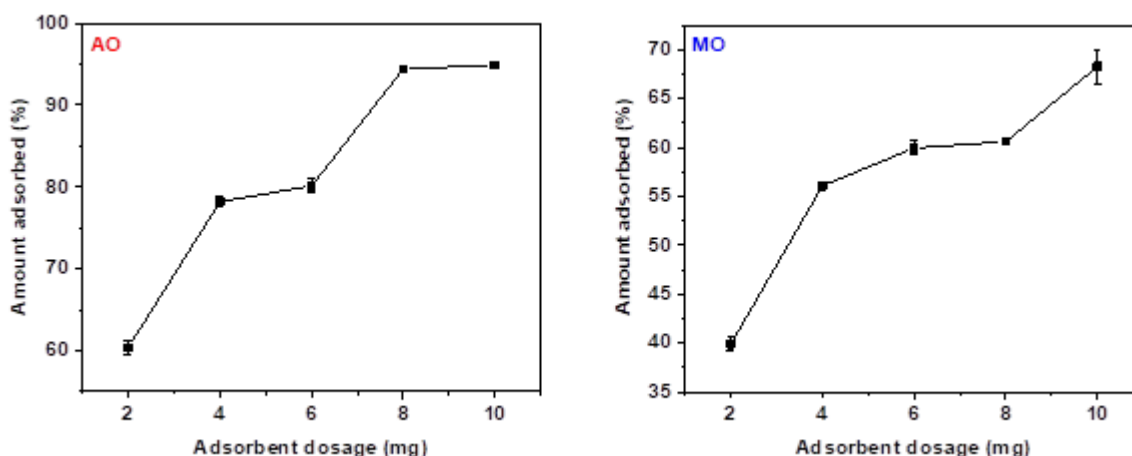


Fig. 4.17. Variation of amount adsorbed with respect to dosage.

4.2.4. Kinetic study for the adsorption of AO and MB on $\text{CoFe}_2\text{O}_4/\text{chitosan}$ composite

The kinetic investigation was carried out with 100 mg L^{-1} of the adsorbates, 10 mg of adsorbent at 30 min interval for 240 min. The adsorption of AO attained equilibrium at 90 mins whereas, MB adsorption could not attain equilibrium until 210 mins. The analysis of the kinetic data was done using pseudo-first order and pseudo-second order. Kinetic parameters are itemized in **Table 6**, while the nonlinear fit curves of the two models for the two dyes are shown in **Fig. 4.18**. It has been established that the model with the best fit exhibits the lowest SD and highest R^2_{adjusted} that is close to unity [117]. The SD values obtained from pseudo-second order for the two dyes are lower than the respective values

obtained from pseudo-first order, in addition to this, R^2_{adjusted} for the pseudo-second-order model is close to unity. The implication of this is that pseudo-second-order is more suitable to explain the kinetic process for the adsorption of the two dyes and that the rate-limiting step of the adsorption is chemisorption and adsorption rate decreases as the surface coverage increases [118]. The lower the SD (obtained from the square root of Reduced Chi-squared), the closer the theoretical q_e to experimental q_e [76].

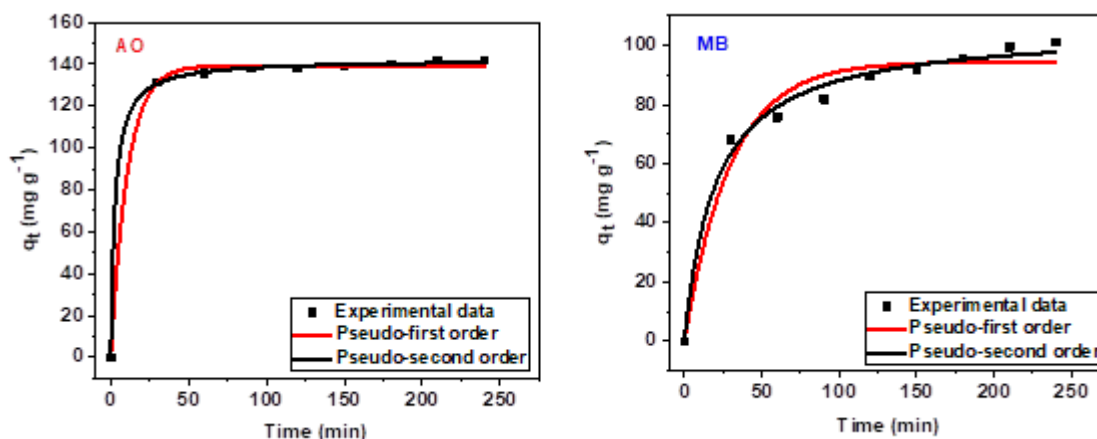


Fig. 4.18. Kinetics plots for AO and MB adsorption on magnetic chitosan.

Table 6. Parameters for kinetics models for the adsorption of AO and MB on magnetic chitosan

Model	parameters	Acid orange II	Methylene blue
Pseudo-first order	q_e (mg g ⁻¹)	139.27	94.47
	k_1 (min ⁻¹)	0.093	0.033
	R^2_{adjusted}	0.9981	0.9624
	SD (mg g ⁻¹)	2.001	6.058
Pseudo-second order	q_e (mg g ⁻¹)	159.55	93.39
	k_2 (g mg ⁻¹ min ⁻¹)	0.3355	0.0564
	R^2_{adjusted}	0.9994	0.9859
	SD (mg g ⁻¹)	1.041	3.701

4.2.5 Adsorption isotherms for the adsorption of AO and MB on CoFe₂O₄/chitosan composite

Langmuir, Freundlich and Liu isotherms were employed for the understanding of the adsorption mechanism of the two dyes. Langmuir and Liu isotherms help to establish the maximum adsorption capacity of the magnetic chitosan, which is expressed in terms of the amount of dye adsorbed per unit mass of the adsorbent. **Fig. 4.19 – 4.21** show the experimental data and nonlinear fitting of the isotherms for AO and MB respectively, while their respective parameters are displayed in **Table 7**. Base on the values of SD and R^2_{adjusted} for the three isotherms, Liu was found to more fitted to explain the adsorption mechanism which speculates that active sites of adsorbent possess different energy [119]. The decrease in the values q_{max} , K_g and K_L (as shown in Table 2) with respect to temperature shows that adsorption process is exothermic. The maximum adsorption capacity for AO are more than the counterpart MB, this signifies that the magnetic chitosan composite has a better affinity for AO than MB and coupled with the fact that mechanism of AO adsorption was not limited to electrostatic attraction. Comparison of the maximum adsorption capacity (q_{max}) of different adsorbents for the removal of AO and MB are listed in **Table 8**. The magnetic chitosan used in this study performed better than other adsorbents reported in the literature (Table 8).

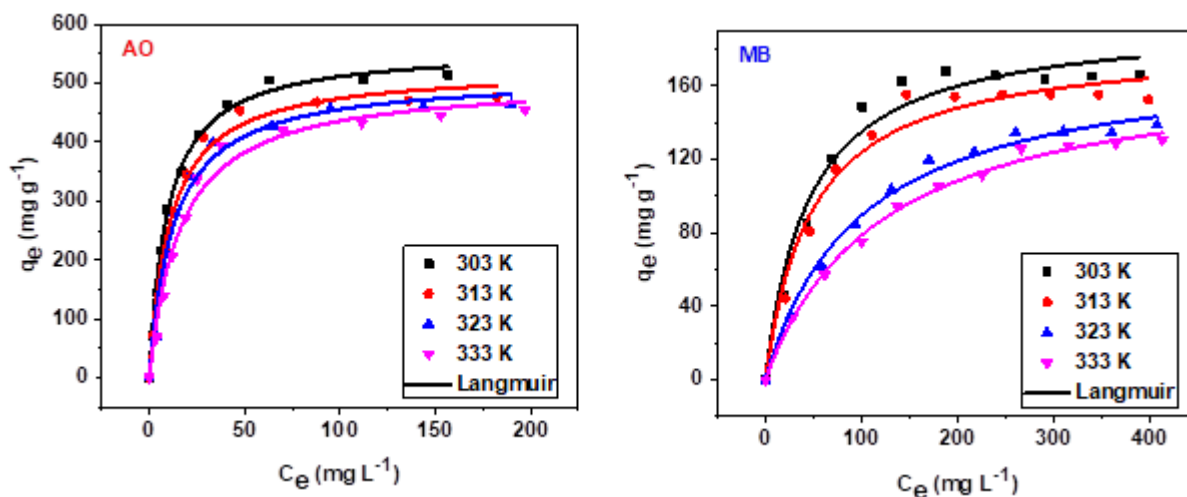


Fig. 4.19. Langmuir isotherm for the adsorption of AO and MB on magnetic chitosan.

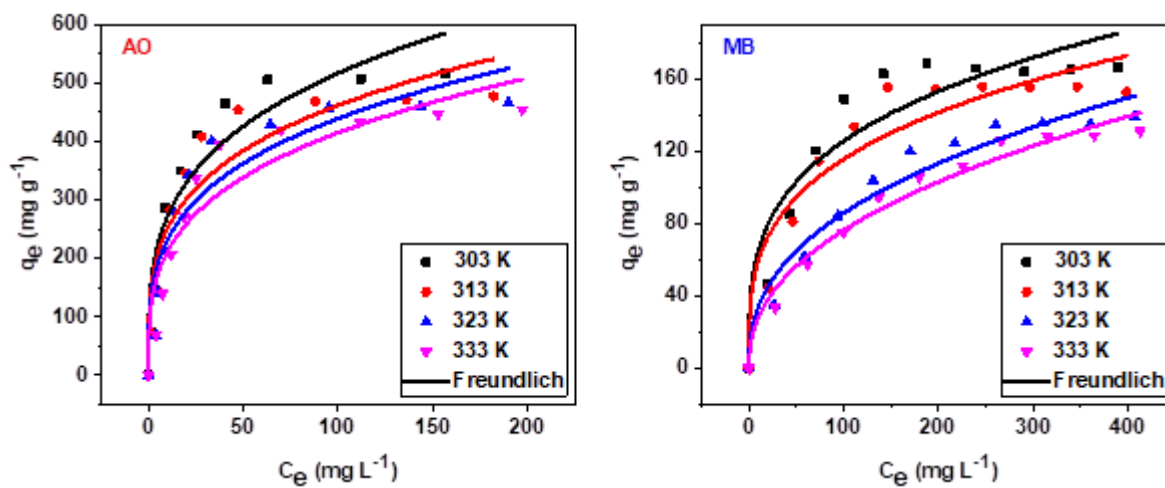


Fig. 4.20. Freundlich isotherm for the adsorption of AO and MB on magnetic chitosan.

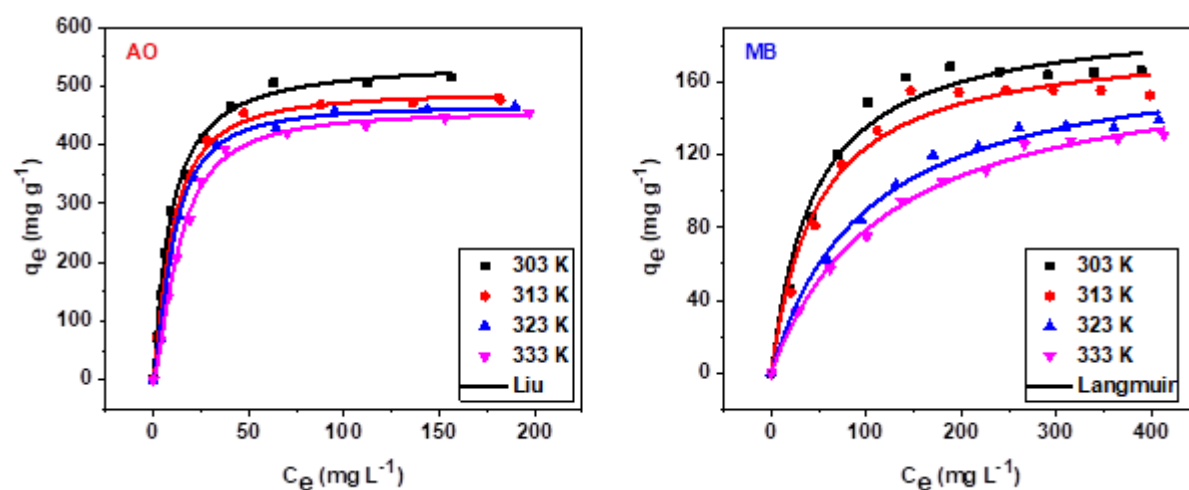


Fig. 4.21. Liu isotherm for the adsorption of AO and MB on magnetic chitosan.

Table 7. Langmuir and Freundlich isotherms parameters for the adsorption of MB at 303 - 333 K.

Acid orange II				
	303 K	313 K	323 K	333 K
Langmuir				
q_{\max} (mg g ⁻¹)	560	525	512	506
K_L (L mg ⁻¹)	0.101	0.093	0.08	0.062
R^2_{adjusted}	0.9957	0.9881	0.9826	0.9810
SD (mg g ⁻¹)	12.08	18.86	22.09	22.41
Freundlich				
K_F (mg g ⁻¹ (mg L ⁻¹) ^{-1/n_F})	143.01	135.78	122.01	107.27
n_F	3.588	3.766	3.599	3.407
R^2_{adjusted}	0.9045	0.8769	0.8787	0.8822
SD (mg g ⁻¹)	57.28	60.85	58.49	55.81
Liu				
q_{\max} (mg g ⁻¹)	543	492	468	458
K_g (L mg ⁻¹)	0.1133	0.10416	0.0967	0.0740
n_L	1.111	1.328	1.472	1.502
R^2_{adjusted}	0.9965	0.9958	0.9968	0.9966
SD (mg g ⁻¹)	10.95	11.19	9.38	9.44
Methylene blue				
Langmuir				
q_{\max} (mg g ⁻¹)	196.31	18	178	173
K_L (L mg ⁻¹)	0.022	0.0205	0.0101	0.0083
R^2_{adjusted}	0.9708	0.9720	0.9914	0.9948
SD (mg g ⁻¹)	9.92	9.01	4.33	3.16
Freundlich				
K_F (mg g ⁻¹ (mg L ⁻¹) ^{-1/n_F})	33.76	30.38	13.53	10.34
n_F	3.507	3.448	2.494	2.305
R^2_{adjusted}	0.8943	0.8991	0.9553	0.9732
SD (mg g ⁻¹)	18.86	17.12	9.91	7.15
Liu				
q_{\max} (mg g ⁻¹)	174	163	158	166
K_g (L mg ⁻¹)	0.0252	0.0238	0.0128	0.0092
n_L	1.664	1.632	1.292	1.075
R^2_{adjusted}	0.9894	0.9887	0.9946	0.9944
SD (mg g ⁻¹)	5.94	5.71	3.42	3.26

Table 8. Comparison of the maximum monolayer adsorption (q_{max}) of different adsorbents for the removal of AO and MB at room temperature.

Dyes	Adsorbents	q_{max} (mg g ⁻¹)	References
Acid orange	MnO ₂ /MCM-41	218	[120]
	CuFe ₂ O ₄ /activated carbon composite	392	[121]
	ODTMA-palygorskite	99	[122]
	Iron-benzenetricarboxylate (Fe(BTC))	435	[123]
	Carbon-modified TiO ₂	24	[124]
	Calcium carbonate/sawdust (AC-1)	310	[57]
	C ₃ H ₉ N treated <i>S. marginatum</i>	71	[125]
	Magnetic graphene chitosan	42	[126]
	CoFe ₂ O ₄ /chitosan	542	This work
Methylene blue	Magnetic cellulose/graphene oxide composite	70	[127]
	Surface-functionalized silica aerogels	68	[128]
	EDTA-modified bentonite	160	[129]
	RMAC nodules	187	[130]
	Activated biochar	33	[131]
	Acid washed black cumin seEDX	73	[132]
	CMt nanocomposites	138	[133]
	CO ₂ -biochar.	161	[134]
	CoFe ₂ O ₄ /chitosan	174	This work

4.2.6 Adsorption thermodynamic for the adsorption of AO and MB on CoFe₂O₄/chitosan composite

The thermodynamic parameters are listed in **Table 9**. The values of enthalpy (ΔH) are negative for the two dyes which confirms the exothermic nature of the adsorption process. This agrees with the adsorption capacity listed in **Table 7**, which decreases with an increase in temperature. It was also observed that entropy is positive for AO and negative for MB this means that there is an increase and decrease in the disorder of the system at the interface of the magnetic chitosan composite and the dye solution respectively [135]. Negative values of ΔG show that the adsorption of the two dyes are feasible and spontaneous. It was

obvious that the magnitude of ΔG obtained for AO tends to higher negative values than that of MB. The implication is that the adsorption of AO on the surface of chitosan magnetic composite is more spontaneous than that of MB.

Table 9. Thermodynamic parameters for the adsorption of AO and MB at 303 -333 K.

Adsorbents	ΔH° (kJ mol ⁻¹)	ΔS° (J K ⁻¹ mol ⁻¹)	ΔG° (kJ mol ⁻¹)			
			303 K	313 K	323 K	333 K
AO	-11.22	51.31	-26.77	-27.28	-27.80	-28.31
MB	-30.57	-24.36	-23.19	-22.95	-22.71	-22.46

4.2.7 Computational studies

4.2.7.1 Geometry and electronic structure of the Dyes

Table 10 presents the values of common reactivity descriptors related to HOMO and LUMO orbitals for the dye molecules. The data shows that AO and MB have similar HOMO and LUMO energies, and consequentially a similar gap $\Delta E_{\text{HOMO-LUMO}}$. This results in very close values of electron affinity, hardness, and softness, which in theory describe two molecules with very similar reactivity for covalent interactions. However, the adsorption of AO is much higher than that of MB and this can be explained not only by electrostatic attraction but also by the molecular dipole moment.

Since chemical bonding usually happens by electronic density exchange between the LUMO and HOMO orbitals of the involved species [136,137], to increase the interactions between two bonding molecules, they usually approach in a way that maximizes the superposition of LUMO and HOMO orbitals of each other. Analysis of **Fig. 4.22**, shows that the HOMO and LUMO orbitals of AO and MB are very similar for both molecules, being distributed along the molecule through the π system involving the aromatic rings. Therefore, to increase the interactions, both dye molecules should approach parallel to the surface of the adsorbent through the plane of the aromatic rings, maximizing the surface contact with the adsorbent. As can be seen from **Fig. 4.23** the yellow to red areas shows regions with more electrophilicity (greater contribution from the $f^+(r)$ function) and the cyan to blue areas

shows regions with more nucleophilicity (greater contribution from $f^-(r)$ function), while blank regions show small reactivity. The picture shows that many sites with more nucleophilic or electrophilic characters are placed in a non-uniform way in both molecules and, adsorption interactions should not have a strong covalent character. Therefore, the weaker inter-molecular interactions should be maximized along the plane of the aromatic rings, increasing the surface contact with the adsorbent.

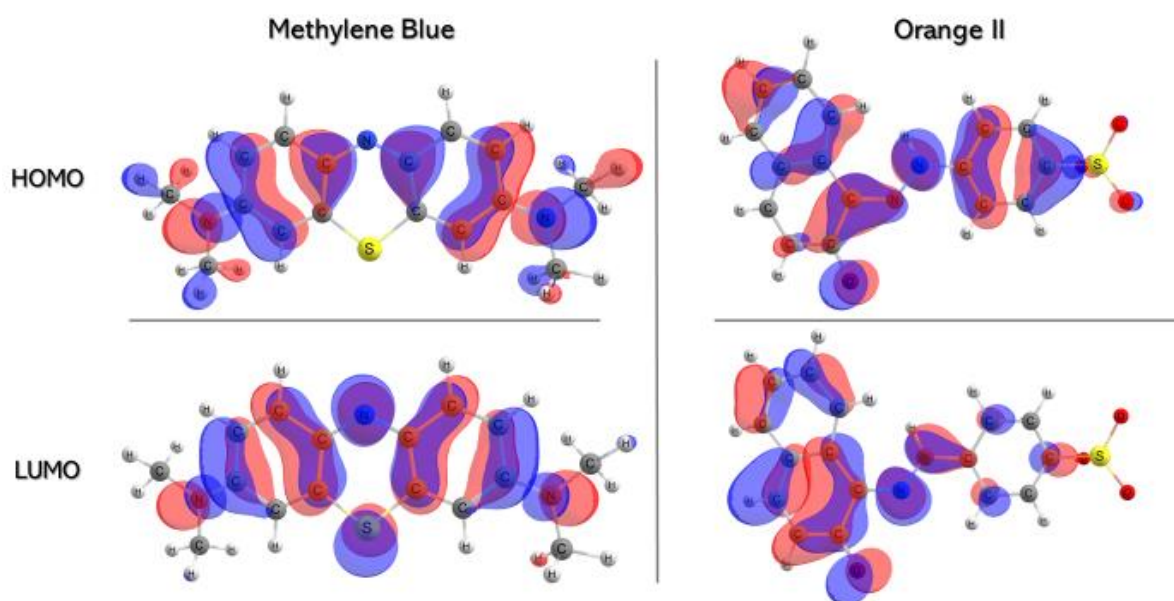


Fig. 4.22. Frontier Kohn-Sham orbitals obtained with the solvent polarized electronic density for MB and AO molecules.

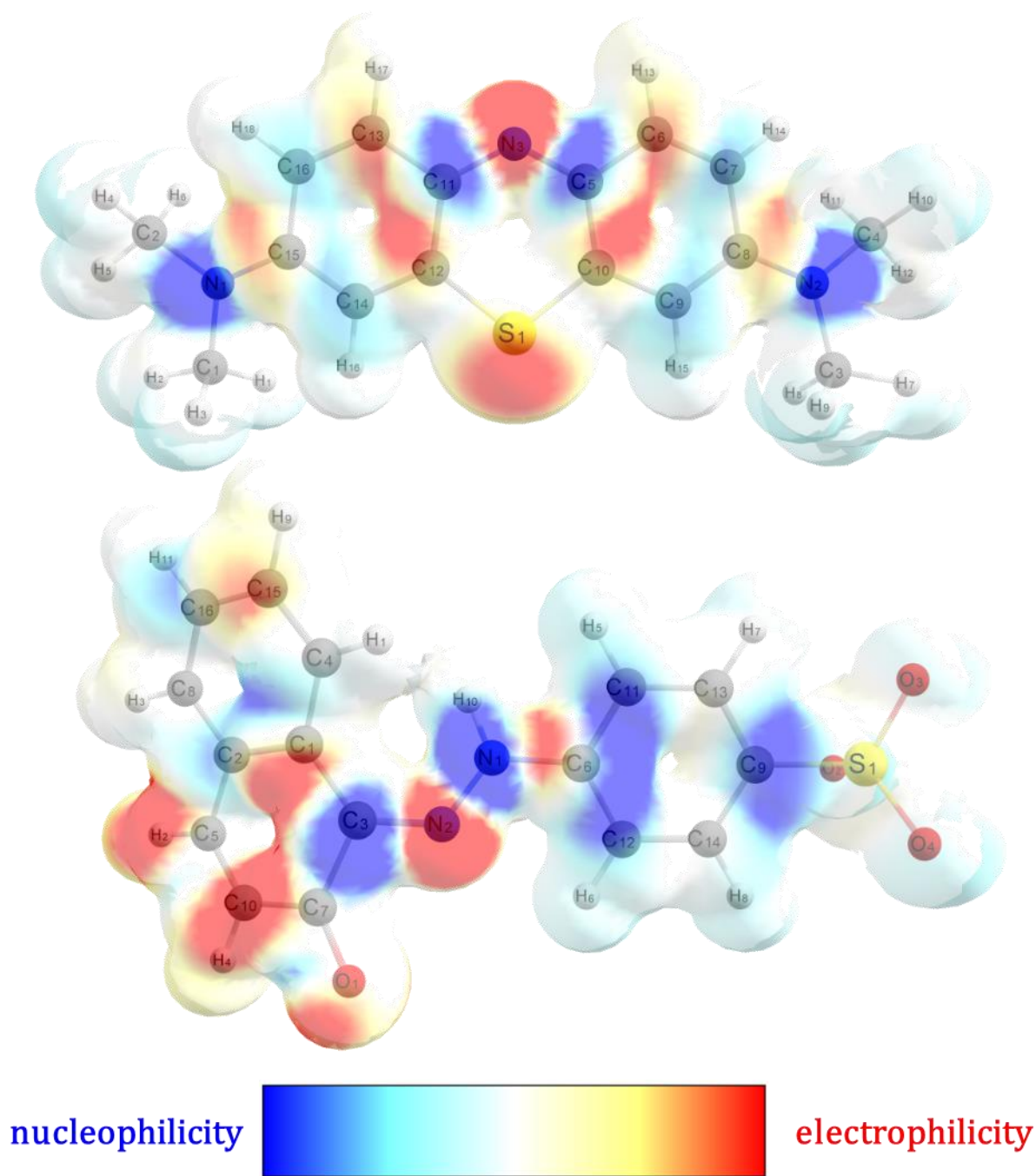


Fig. 4.23. Electron density plot map of the dual descriptor Fukui function, $\Delta f(r)$, for MB (top) and AO (bottom), obtained from the calculated SCF electronic densities.

Table 10. Electronic structure descriptors for MB and AO.

	Acid orange II	Methylene blue
E_{HOMO} (eV)	-5.82	-5.68
E_{LUMO} (eV)	-2.69	-3.30
$\Delta E_{\text{HOMO-LUMO}}$ (eV)	3.13	2.39
χ (eV)	4.26	4.49
η (eV)	1.56	1.19
σ (eV ⁻¹)	0.64	0.84
μ (Debye)	32.24	3.46
$\mu^{\text{exp.}}$ (Debye ^a)	N.A.	1.63/2.46/3.79

^a Experimental data obtained from absorption and fluorescence shifts in various media using three different methods as explained in reference [138]. Each value corresponds to one of the methods used.

4.2.7.2. Interaction of the Dyes and the magnetic chitosan models.

The optimized structures for the interaction of the dye molecules with the chitosan models are shown in **Figs 4.24 and 4.25**. AO dye interacts with the non-protonated (structure A), protonated (structure B) and deprotonated (structure C) chitosan models. However, MB dye interacts only with the neutral (structure A) and deprotonated (structure B) chitosan models. Interaction of MB with the protonated chitosan model is not favorable and, the optimization leads to separate structures too far from each other. This result is in line with the experimental results since, under experimental conditions, no significant amount of MB is adsorbed in the pH range of 0 to 8, when the composite is positively charged.

Analyzing the structures shown in **Fig. 4.24** it is possible to see that when the chitosan model is very positive the interaction mode between it and the AO changed drastically. The negative SO^{3-} group is perpendicular to the polymer surface, being pointed directly towards it to maximize the attractive electrostatic interactions, following the dipole moment vector of the molecule. When the surface changed to neutral or negative the AO molecule interacts with the chitosan along the plane of the aromatic rings, maximizing the weak interactions like hydrogen bonding (hbond), and van der Waals (dispersion forces). However, as expected, for the interaction of the MB dye with the negatively charged model of the chitosan (**Fig 4.25**), the two molecules are close to each other due to the electrostatic attraction resulted by the two opposite charges. However, this electrostatic attraction is

distributed throughout the entire molecule due to its small dipole moment. This distance can also be quantitatively viewed in **Table 11**.

Table 11: Distances (in Å) between the center-of-mass (CM_{dye}) of the dyes molecules and the center-of-mass of the chitosan (CM_{chito}) models, interaction energies (ΔE_{SCF}) and dispersion corrections for the dye-chitosan systems at the optimized geometries. All the energies were calculated using the C-PCM continuum solvation model as detailed in the SI.

System	$r(CM_{dye}-CM_{chito})$ (Å)	ΔE_{SCF}^* (kcal mol ⁻¹)	$E_{disp.}$ (kcal mol ⁻¹)	$\Delta E_{dif.}^{**}$ (kcal mol ⁻¹)
AO + magnetic chitosan (0)	3.59	-23.86	-12.71	-11.16
AO + magnetic chitosan (+)	9.44	-17.84	-4.30	-13.55
AO + magnetic chitosan (-)	4.91	14.22	-12.06	26.28
MB + magnetic chitosan (0)	4.76	-4.10	-9.96	5.86
MB + magnetic chitosan (+)	-----	-----	-----	-----
MB + magnetic chitosan (-)	3.96	-32.84	-12.26	-20.59

* The interaction energies were obtained from the expression $\Delta E_{SCF} = E_{Total} - (E_{dye} + E_{chitosan})$, in which E_{Total} is the dye-chitosan cluster total SCF energy, E_{dye} is the SCF energy of the dye in the cluster geometry and $E_{chitosan}$ is the SCF energy of the chitosan model in the cluster geometry. ** $\Delta E_{dif} = \Delta E_{SCF} - E_{disp}$

Table 11 shows some energy values for the interacting systems. We would emphasize that these come only from the DFT/PBE-3c SCF energies and, thus, have limited quantitative value. Analysis of the data on **Table 11** shows that the dispersion energy is similar for all the systems in which the interaction between the dye and the chitosan happens when the two molecules are aligned with each other. This is expected, although we should take into account that the distances between the two molecules are very different from each other considering dispersion forces that are proportional to r^{-6} . So, for the AO with negative chitosan, even though the interaction energy is similar, the much larger distance implies bigger dispersion forces than the MB with negative chitosan, as an example. The AO with the protonated chitosan system has much smaller dispersion energy. This is also expected when we look at the interaction mode, that has low surface contact areas, as was previously discussed. Therefore, most of the interaction in this system should come from the electrostatic energy term, which is roughly covered by the values in the last column of **Table 11**, that shows the difference between the total interaction energy and the dispersion energy (ΔE_{dif}) if one considers that there is no significant amount of covalent bonding between the two molecules. In fact, support for this is the observation that ΔE_{dif} is

stabilizing for AO with positive chitosan and for MB with negative chitosan, which are molecules with opposite charges, and it is destabilizing for AO with negative chitosan and MB with positive chitosan, which are molecules with same charges.

Another observation is that the $r(\text{CM-CM})$ distance is much smaller for the interaction of AO and the neutral model than for the interaction with the negative model, due to the electrostatic repulsion between the molecules in the latter case. However, there are still strong dispersion forces between the AO molecule and the negative chitosan model illustrated by the dispersion energies and the optimized structure, which explains why AO adsorbs on the composite surface even when they have the same charge signal.

The same cannot be said about the interaction of MB with the positive chitosan model since the interaction is not favorable and the system dissociates. Comparing the MB with AO, the CM-CM distances for the interaction with the chitosan models, in the former are larger than in the latter, showing that MB is not able to interact as efficiently as AO with the magnetic chitosan composite. The optimized structures clearly show that there should be no hydrogen bond interactions between MB and the chitosan model as we will discuss. As expected, the $r(\text{CM}_{\text{dye}}-\text{CM}_{\text{chitosan}})$ is smaller for the interaction of MB with the negative model of chitosan than for the interaction with the neutral model, when one should expect stronger and attractive Coulomb interactions due to the opposite charges, confirmed by the larger value of ΔE_{dif} . If we qualitatively use the recommendation from IUPAC for the definition of hydrogen bond [139], and the geometric criteria established in the computational details section, the AO molecule can act as a hydrogen bond acceptor through all its oxygens from the SO^{3-} group or the C=O group, with hydrogen bond distances between 1.8 to 3.0 Å, and also as a hydrogen bond donor through its N-H group, with hydrogen bond distances around 2.3 Å. These observations were further analyzed via Monte Carlo simulations of the isolated dyes in aqueous solution. The hydrogen bond analysis from the MC simulations revealed that while indeed the MB molecule is not capable to form hydrogen bonds in solution, the AO dye is capable of accepting multiple hydrogen bonds through its S-O and C=O groups. In all MC simulation configurations, the AO dye formed an average of 6 h-bonds per molecule with an average energy of $-36.54 \text{ kJ mol}^{-1}$. This reinforces the capability of the AO molecule to make stronger and more numerous intermolecular interactions through hydrogen bonding, opposite to MB which is not capable to form these

interactions. Furthermore, the larger amount of intermolecular interactions is what should make AO adsorb more in most of the situations, especially considering the strong hydrogen bonds that it is able to make with chitosan. The scheme of the overall mechanism of the adsorption process is presented in **Fig 4.26**. Mechanism of adsorption had been proposed to be through electrostatic attraction, hydrogen bond among others [140,141]. FTIR of the composite before and after adsorption of the two dyes (Appendix **Fig. A3**). IR spectra after adsorption of AO revealed new peaks at 1512, 823, and 723 cm^{-1} which correspond to the presence of azo chromophore and fingerprint of AO.

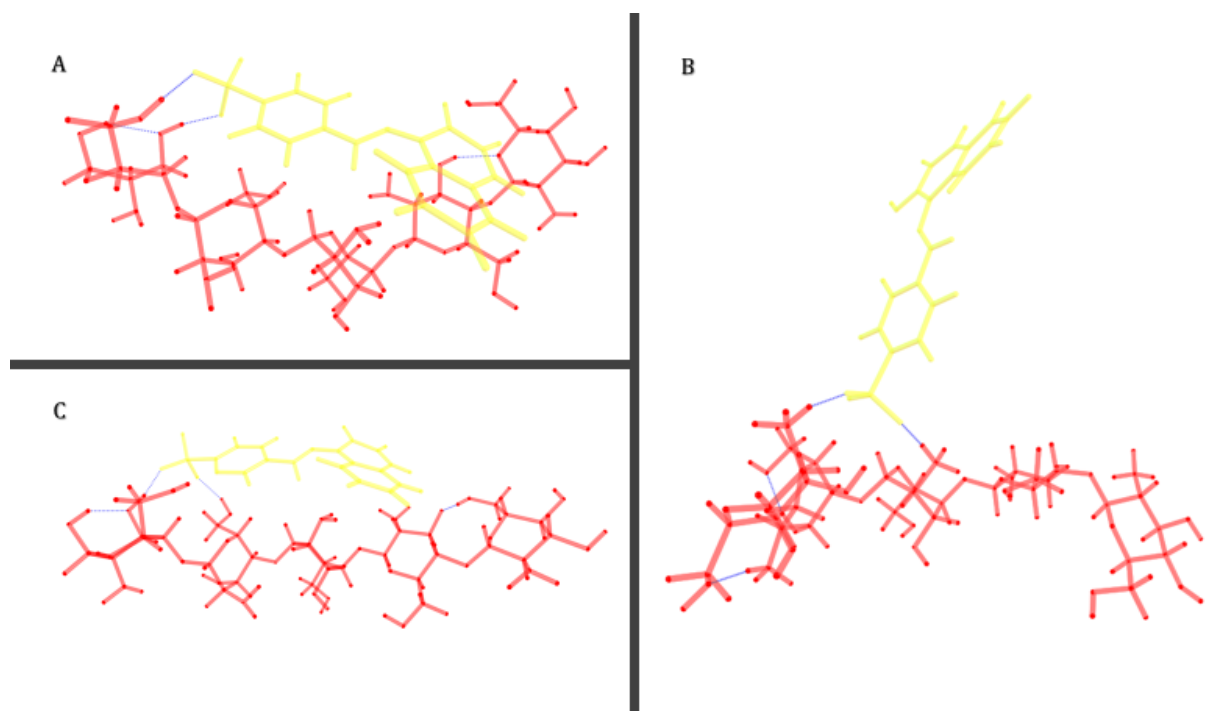


Fig. 4.24. Optimized structures for the interaction between (A) acid orange II + non-protonated chitosan model, (B) acid orange II + protonated chitosan model and (C) acid orange II + deprotonated chitosan model.

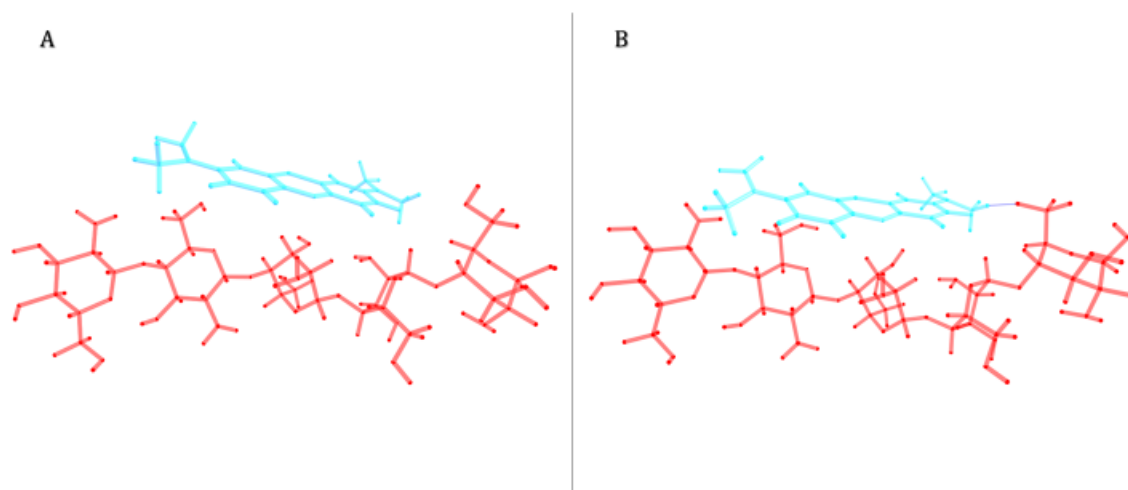


Fig. 4.25: Optimized structures for the interaction between (A) methylene blue + non-protonated chitosan model and (B) methylene blue + deprotonated chitosan model.

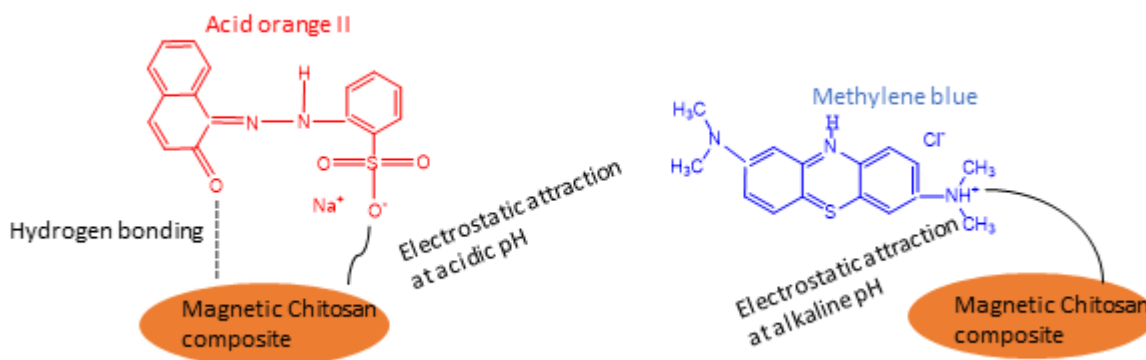


Fig. 4.26: Proposed mechanism pathway for interactions between magnetic chitosan and the two dyes molecules.

4.2.8 Conclusion

Chitosan/cobalt ferrite composite was synthesized and employed as an adsorbent for the removal of both acid orange II and methylene blue. The ease of separating the magnetic composite after adsorption was demonstrated by using an external magnet. The results obtained from the characterization of the composite showed that chitosan was well distributed around the surface of cobalt ferrite. Adsorption studies showed that the pH of the solution plays a significant role in the removal of the two dyes. Methylene blue adsorption was found to be limited to the surface charge of the composite; this was not the case for the adsorption of acid orange II. The adsorption of the two dyes was spontaneous and exothermic in nature. The theoretical observations of the phenomena are in good agreement with the experimental data. The results from the computational studies showed that the two dyes have similar reactive sites, however, the huge molecule dipole moment and strong dispersion forces of acid orange II enhanced its interaction with the magnetic chitosan. The theoretical results presented here provide a descriptive molecular view of these systems and insight into the mechanism of adsorption.

4.3 Synthesis of CoFe₂O₄/bio silica composite for the adsorption of doxycycline

4.3.1 Brief introduction

Silica particles have found its usefulness in numerous industrial applications which encompasses using as filler material in composites, raw material for the synthesis of shear thickening fluid, electronic devices, catalysts, drug delivery systems, thermal insulators, energy storage, chemical, and biological separations and the engineering fields of rubber and ceramics [142,143], and also as adsorbent (either as composite with other materials, raw or functionalized form) for the removal of contaminant from water [144–146]. Owing to the increasing importance of silica for various applications, different methods have been adopted to produce silica, which includes flame synthesis, hydrothermal process, sol-gel synthesis route, microwave reactor process, microemulsion methods, combustion method [147]. Meanwhile, sol-gel is the most common method of synthesizing silica. This technique involves the use of silica precursors, alkoxides (tetramethyl orthosilicate (TMOS), tetraethyl orthosilicate (TEOS) or sodium silicate solution (SSS). However, TEOS is the most studied precursor in the sol-gel process presumably due to its low reactivity towards hydrolysis making it possible to follow and control the reaction more easily[148].

Sad enough, the chemical route of synthesizing silica is supposedly expensive, environmentally hazardous and demands rigorous synthesis conditions [149]. It has been documented that silicon is the second most abundant element (approximately 32% of the total weight of soil) in Earth's crust [150]. Aqueous silicic acid (Si(OH)₄) in the soil is transported to plants, with the increasing concentration of silicic acid and as a result of polymerization, silicon is deposited in the plant tissues[150]. In view of this, bio-silica from agricultural waste like rice husk has been another source of silica production for different industrial uses [151].

Rice is the second-largest cereal crop in the world and its grain consists of about 20 wt% of rice husks [152]. Rice husks are costless and a widely available agricultural waste which is produced from the processing and refining of rice, it was estimated by The Food and Agriculture Organization of the United Nations (FAO) that about 89,000 tons of rice husk was burnt in 2012 [145]. Since most of the rice husk usually ends up either being dumped or

burned in open spaces, which causes damage to the land and environmental pollution, efforts have been made to use it as raw material for manufacture of industrial chemicals based on silica and silicon compounds, hence is excellent and the most efficient source of high-grade amorphous silica [145,153]. This does not only reduce environmental pollution but also of a great economic benefit.

Nano adsorbents like nano bio-silica with small sizes could be difficult to sort out after attaining their optimum adsorption capacity [4]. Therefore, incorporating magnetic particles into the biosilica matrix could ease the stress of separation after the adsorption process. More so, silica coating enhances the coulomb repulsion of the magnetic nanoparticles thereby improves its stability, prevents the aggregation of magnetic nanoparticles in solution and promotes the binding of various biological ligands to the surface of the nanoparticles [154]. In view of this, in this research, CoFe_2O_4 /bio silica was synthesized for the first time and applied for the adsorption of doxycycline and methylene blue.

4.3.2 XRD of CoFe_2O_4 /rice husk silica

The diffractogram of rice husk silica (BSIL), as prepared CoFe_2O_4 /rice husk silica composite (CFS-100) and those calcined at 300 (CFS-300), 500 (CFS-500) and 700 °C (CFS-700) are shown in **Fig 4.27**. The high-intensity peak of BSIL was between 15° and 32° centered at 22° this confirms the amorphous nature of BSIL. The absence of no other sharp peak on the diffractogram of BSIL implies that the extracted silica is pure. Considering the diffractogram of the composites, calcination of the composite up to 700 °C leads to an increase in the intensity of peaks of the CoFe_2O_4 phase and the appearance of some peaks which are recessive in the diffractogram below this calcined temperature (700 °C). The diffractogram of CFS-100, CFS-300, and CFS-500 are similar and exhibit the nature of nanocrystalline materials. This implies that calcination temperature (below 700 °C) could not promote noticeable movement of atoms within the composite, which could lead to the transformation of cobalt ferrite with the appearance of designated peaks. The obtained diffractogram of CFS-700 corresponds with card number 22-1086 of the Joint Committee on Powder Diffraction Standards (JCPDS) which is a typical pattern of cubic spinel ferrite having space group of $Fd-3m$ (N° 227) and devoid of impurities. Crystallite size of CFS-100 and CFS-

700 at peak 311 calculated using Scherrer's equation is 2 nm and 5 nm. The hump between 17 and 23 (2θ) is due to the presence of amorphous rice husk silica.

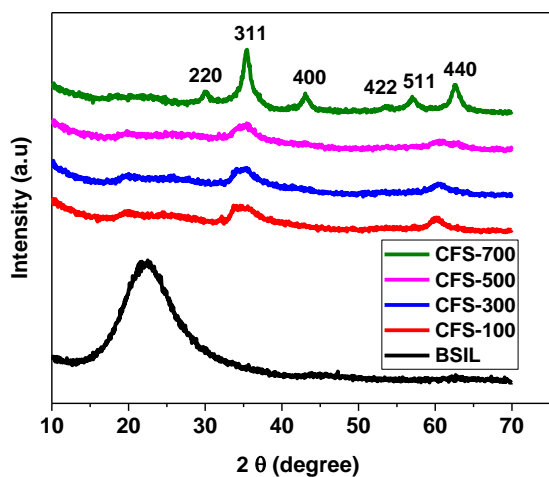


Fig. 4.27: Diffractograms of cobalt ferrite/rice husk silica: as prepared, CFS-300, CFS-500, and CFS-700.

4.3.3 Scanning electron microscopy (SEM) of CoFe_2O_4 /rice husk silica composite and rice husk silica.

SEM images of CFS-100 (A) CFS-300 (B), CFS-500 (C), CFS-700 °C (D) and rice husk silica (D) are shown in **Fig. 4.28**. There is no significant difference in the morphology of the images (CoFe_2O_4 /rice husk silica), meaning that calcination did not have any negative effect on the samples' morphology.

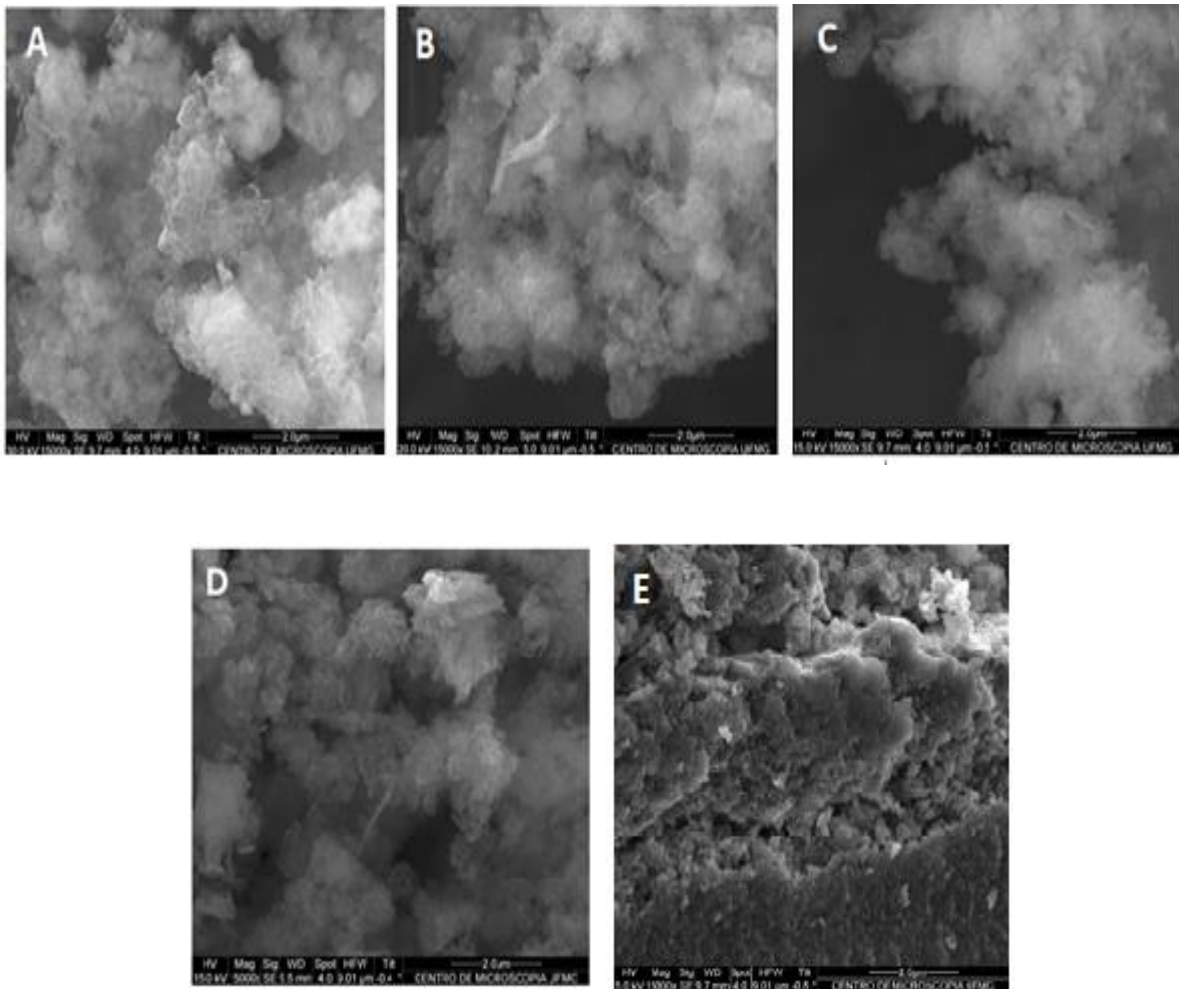


Fig. 4.28: SEM images of cobalt ferrite/rice husk silica composite: CFS- 100 (A), CFS-300 (B), CFS-500 (C) and CFS-700 °C (D), rice husk silica (E).

4.3.4 Transmission electron microscopy (TEM) of CoFe_2O_4 /rice husk silica composite and rice husk silica.

Transmission electron microscopy (TEM) images of CoFe_2O_4 /rice husk silica composite and rice husk silica are shown in **Fig 4.29**. Since the XRD and SEM results of the composite calcined at CFS-300 and CFS-500 did not show any significant difference, TEM analysis was conducted on CFS-100, CFS-700 and bio silica. The image of rice husk silica (BSIL) showed a well dispersed nanoparticles of both spherical and longitudinal morphology, while those of CFS 100 and 700 shown typical agglomerates of sponge-like structure. Electron diffraction (ED) image of silica (b) shows that the extracted silica is amorphous which agrees with XRD result. There is a remarkable difference in the ED of CFS 100 and 700. The crystal growth of

the composite was prompted by calcination temperature. The diffraction pattern of CFS 700 shows distinct d-spacings which are characteristic of cobalt ferrite while fewer d-spacings are seen on CFS 100, which means that at this temperature cobalt ferrite has not been fully formed within the composite. More so, the spots on the diffraction pattern of CFS 700 shows that that sample is more crystalline than SCOF 100 whose diffraction pattern shows evenly intensity diffracted rings.

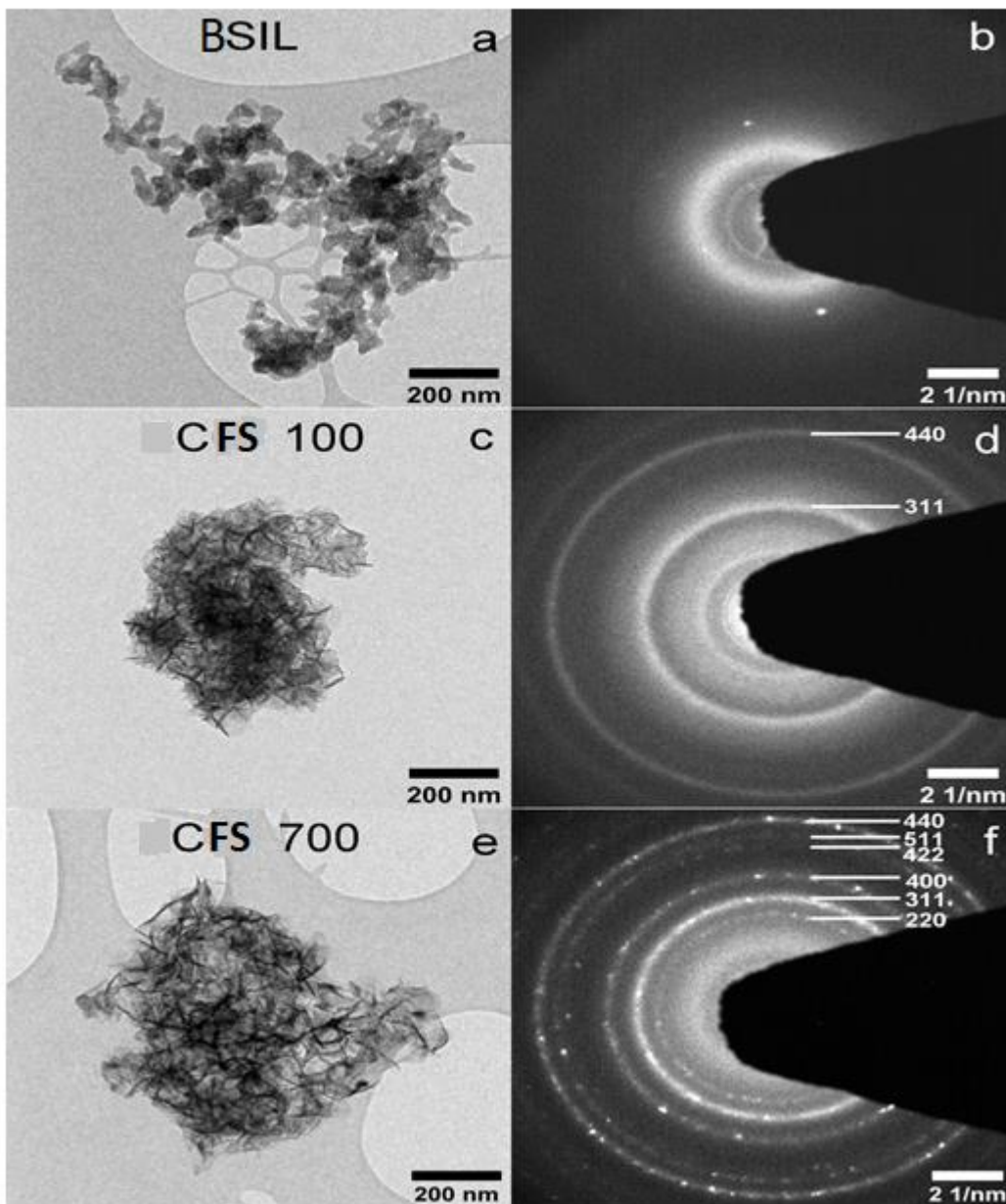


Fig. 4.29: TEM images (a, c, e) with the electron diffraction (b, d, f) of BSIL, CFS-100 and 700

4.3.5 Magnetization versus Field of CoFe₂O₄/rice husk silica composite

The result of magnetic saturation (M_s) values of CFS -100 and 700 with respect to applied field are displayed in **Fig 4.30**. There is a sharp and noticeable increase in the M_s of the composite after calcined at 700 °C, which could be due to the magnitude of thermal vibrations of atoms that increases with the increase in temperature [155]. It is stated that migration of Fe³⁺ ions to octahedral sites due to increase in the calcination temperature could induces increase in magnetic saturation in addition, the overall magnetic moment of Fe³⁺ ions due to migration is greater that of Co²⁺ ions [156]. In addition to this, the sharp increase in M_s could be due to increase in crystallite size with calcination, as seen in the XRD results. Magnetic domain is differently proportion to crystallite size, which results to increase in magnetic saturation Both coercivity and magnetic remanence increases with increase in calcination temperature. Magnetic parameters are listed in **Table 12**.

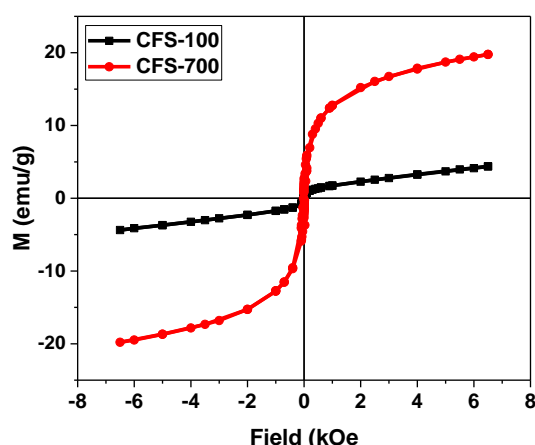


Fig. 4.30: Magnetization versus applied field at 300 K for CoFe₂O₄/rice husk silica composite.

Table 12. Saturation magnetization, coercivity and remanence values obtained at 300 K

	Hc (Oe)	Mr (emu g ⁻¹)	Ms (emu g ⁻¹)
CFS-100	10.2	0.27	4.38
CFS-700	34.65	3.01	20.33

4.3.6 BET specific surface area

The N_2 adsorption and desorption of the $CoFe_2O_4$ /rice husk silica composite and rice husk silica and their respective pore size distribution curves are shown in **Fig 4.31**. The isotherms of the composite are type IIb, which is a characteristic of a mesoporous material with pore diameter > 2 nm. Isotherms with type H3 hysteresis are affirmed not to exhibit any limiting adsorption at high P/P_0 (P is the pressure of the adsorbate gas (N_2) while P_0 saturation pressure), the behavior which have been associated with the existence of agglomerates of particles forming slit pores with non-uniform shape [157,158]. Regardless of the same isotherm and hysteresis shown by all the samples (CFS-100, CFS-300, CFS-500 and CFS-700), the volume of N_2 adsorbed differs significantly. **Table 13** contains the specific surface area (SSA) of the composites and rice husk silica. The values of SSA of the composites decrease with increase in calcination temperature, close to 50 % of the SSA was reduced when calcined at 700 °C. More so, as the calcination temperature increases, there is a shrinkage and collapsed of pores which as well leads to decrease in pore volumes as shown in Table 1. Positive value of C constant infers interaction between the N_2 molecules and the nanocomposite [159]. The various SSA values obtained for the composites are higher than that of rice husk silica ($55 \text{ m}^2 \text{ g}^{-1}$).

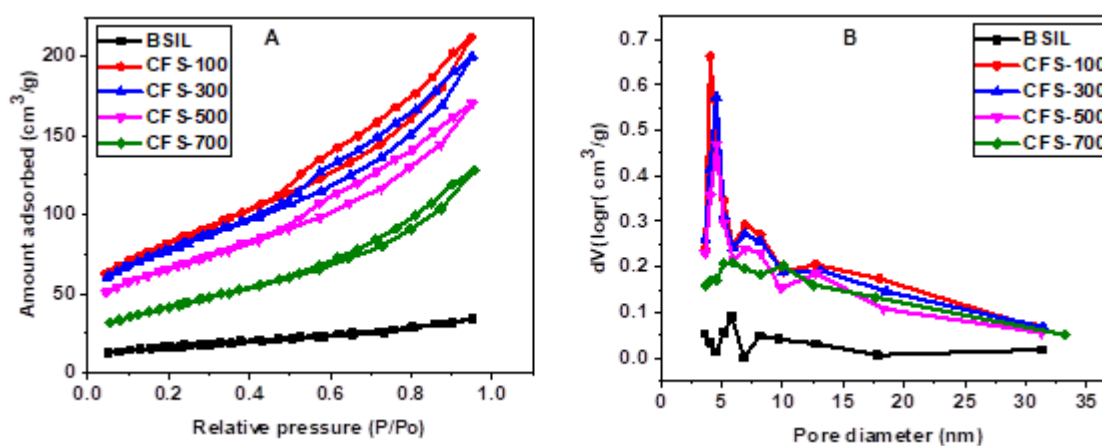


Fig. 4.31: N_2 adsorption and desorption of the composite (A) and their pore size distribution curves (B).

Table 13. BET specific surface area

CoFe ₂ O ₄ / rice husk silica	Parameters		
	SSA (m ² g ⁻¹)	*Total pore volume (cm ³ g ⁻¹)	C constant
BSIL	55	0.032	-210
CFS-100 °C	283	0.33	511
CFS-300 °C	270	0.31	379
CFS-500 °C	229	0.26	389
CFS-700 °C	148	0.2	116

* Single point pore volume was calculated at P/P₀ of 0.95.

4.3.7 FTIR spectra of CoFe₂O₄/rice husk silica composite and rice husk silica.

The IR spectra of the composite is presented in **Fig. 4.32**. The broad band at 3490 cm⁻¹ (1) correspond to OH group, which could be due to the presence of absorbed water. However, the intensity of the band decreases with increase in the calcination temperature (CFS-700), because of loss of water (dehydration) during the calcination process. The same observation occurred at peak 1637 cm⁻¹ (2) assigned to OH group for CFS-700 as well. The peak at 1023 cm⁻¹ (3) is for vibrational band of Si-O-Si [147,152]. The peak at 585 cm⁻¹ (4) is attributed to stretching vibration in metal-oxide (CoFe₂O₄) which becomes more distinct in intensity due to increase in temperature. This correlate with the XRD results in Fig. 1, which shows appearance of new peaks and increase in intensity of peaks with respect to temperature. The peak at 490 cm⁻¹ (5) present in all the spectra is assigned to Si-O vibrational bond. The 1086 cm⁻¹ band with the shoulder at 1160 cm⁻¹ (of the sample CFS-700) is due to the asymmetric stretching bonds Si-O-Si of the SiO₄ tetrahedron associated with the motion of oxygen in the Si-O-Si anti-symmetrical stretching which could be promoted by cobalt ferrite [160].

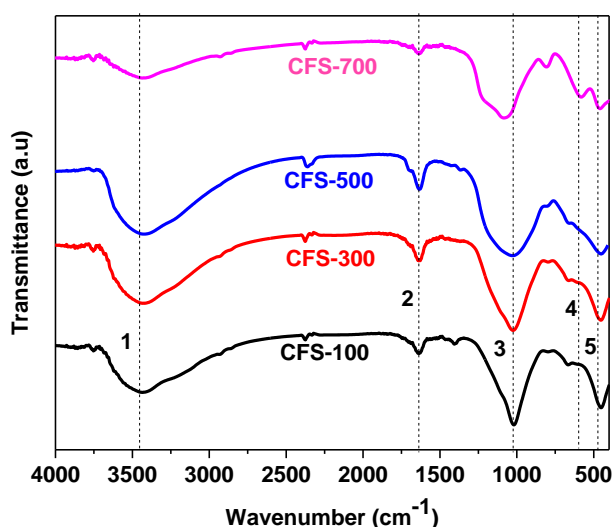


Fig.4.32: FTIR spectra of CoFe_2O_4 /rice husk silica composite and rice husk silica.

4.3.8 Influence of pH on the adsorption of doxycycline

The results obtained from the effect of pH on the adsorption capacity of cobalt ferrite/rice husk silica nanocomposite calcined at various temperature, rice husk silica only, cobalt ferrite only and zeta potential values are shown in **Fig. 4.33**. The trend of the amount of DOX that was adsorbed (with initial concentration of 100 ppm) on the composite is not consistent with variation in the pH of aqueous doxycycline hydrochloride. It increases from pH 2 to 4, maintains equilibrium up till pH 8 and slightly decline at pH 10. The amphoteric nature of DOX molecules (**Fig. 4.34.**) with different ionizable functional groups such as phenol, alcohol and amino groups, that exist as cations, anions and zwitterion at different pH has made its electrostatic attraction and repulsion between its molecules and the adsorbent to be complex [161]. The surface of the adsorbent is dominated by negative charge (**Fig 4.33 B**). At $\text{pH} \leq 3$, DOX is protonated which makes it to exists in cationic form (DOX^+) [162], and adsorbed on the negative charge surface of the nanocomposites through electrostatic attraction. Meanwhile between pH 4 – 9 its exists as zwitterions [30] which implies that electrostatic interaction is not the mechanism of adsorption within the range of these pHs. The slight and insignificant decrease in amount adsorbed at pH 10 could be attributed to the repulsion between the negatively charge surface of the adsorbent and the anionic site of some functional groups on DOX. However, electrostatic interaction between

the adsorbents and DOX molecules is not enough to explain the mechanism of adsorption of DOX on the synthesized cobalt ferrite/rice husk silica. More so, the reduction in SSA (itemized in Table 1) with respect to calcination temperature did not show a significant effect on the amount of DOX that was adsorbed. The amount of DOX adsorbed by CFS-100, CFS-300 and CFS-500 are almost the same despite the difference in specific surface area (SSA). In addition to this, the SSA of CFS-700 is almost half of CFS-100, ordinarily one would expect the amount adsorbed to follow suit, but this is not the case. It could be stated that the adsorption capacity of the various calcined samples was not completely influence by their SSA. One of the factors that has been documented to favor the adsorption of antibiotics (large molecular size) is the presence of mesopores in the entire bulk of the adsorbent [163]. This could have promoted the adsorption capacity notwithstanding the variation in calcination temperature. Considering the adsorption behavior of cobalt ferrite (COF) and rice husk silica (BSIL), the amount adsorbed are much lower than those of the composite. Among the reasons for the low values, are non-porosity of COF, micro porosity of SIL and low surface area of both samples. In view of these low values, further studies were focused on the nanocomposite (CFS-100, CFS-300, CFS-500 and CFS-700).

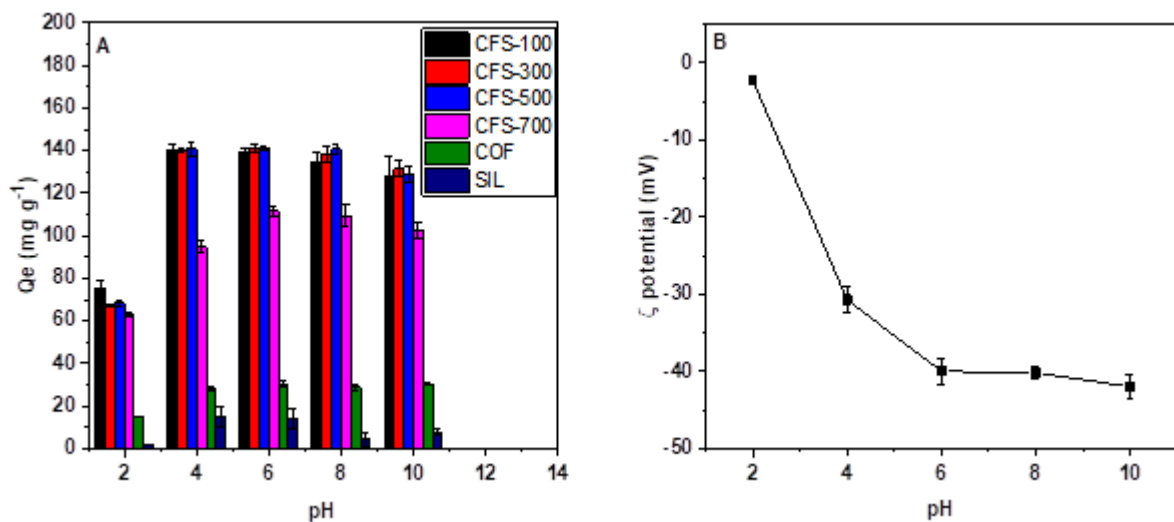


Fig. 4.33: (A) Effect of pH on the adsorption capacity of CFS-100, CFS-300, CFS-500 and CFS-700; (B) Zeta potential of CFS-100 (a representative of CFS-300, CFS-500 and CFS-700).

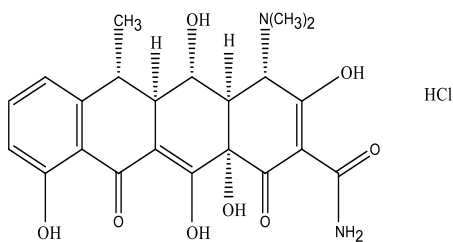


Fig. 4.34. The structure of doxycycline hydrochloride.

4.3.9 Effect of contact time, and kinetic studies of adsorption of DOX on CoFe₂O₄/rice husk silica

The contact time studies were carried for 10 h as can be seen in **Fig. 4.35**, the adsorption of DOX was rapid within 1 h contact time. More than 80 mg g⁻¹ was adsorbed by all the samples except CFS-700 which adsorbed approximately 50 mg g⁻¹. The availability of active sites at the initial stage of the adsorption process, facilitate rapid adsorption of the antibiotic. Meanwhile, as the time proceeds, less active sites are available for the unoccupied adsorbate, which led to lower rate of adsorption.

The data obtained from contact time were further subjected to nonlinear form of pseudo-first order and pseudo-second order

The plots of these models are shown in **Fig. 4.35** while the respective kinetics parameters are listed in **Table 14**. Pseudo second order kinetic model is best appropriate for the adsorption process. The R^2_{adjusted} of this model for all the samples are higher than the respective values obtained for pseudo first order and general order. More so, the values of standard deviation (SD) obtain from this model, is lower than that of the other two models. This implies that it is more reliable to relate q_e calculated from pseudo second order to the experimental q_e . The values of q_e obtained from CFS-100, CFS-300 and CFS-500 are within the same range except for CFS-700. This shows that calcination temperature up to 500 °C did not have any significant effect on the amount (mg g⁻¹) of DOX that was removed from the bulk solution. In view of this, further study was carried out on CFS 100 and CFS 700 only.

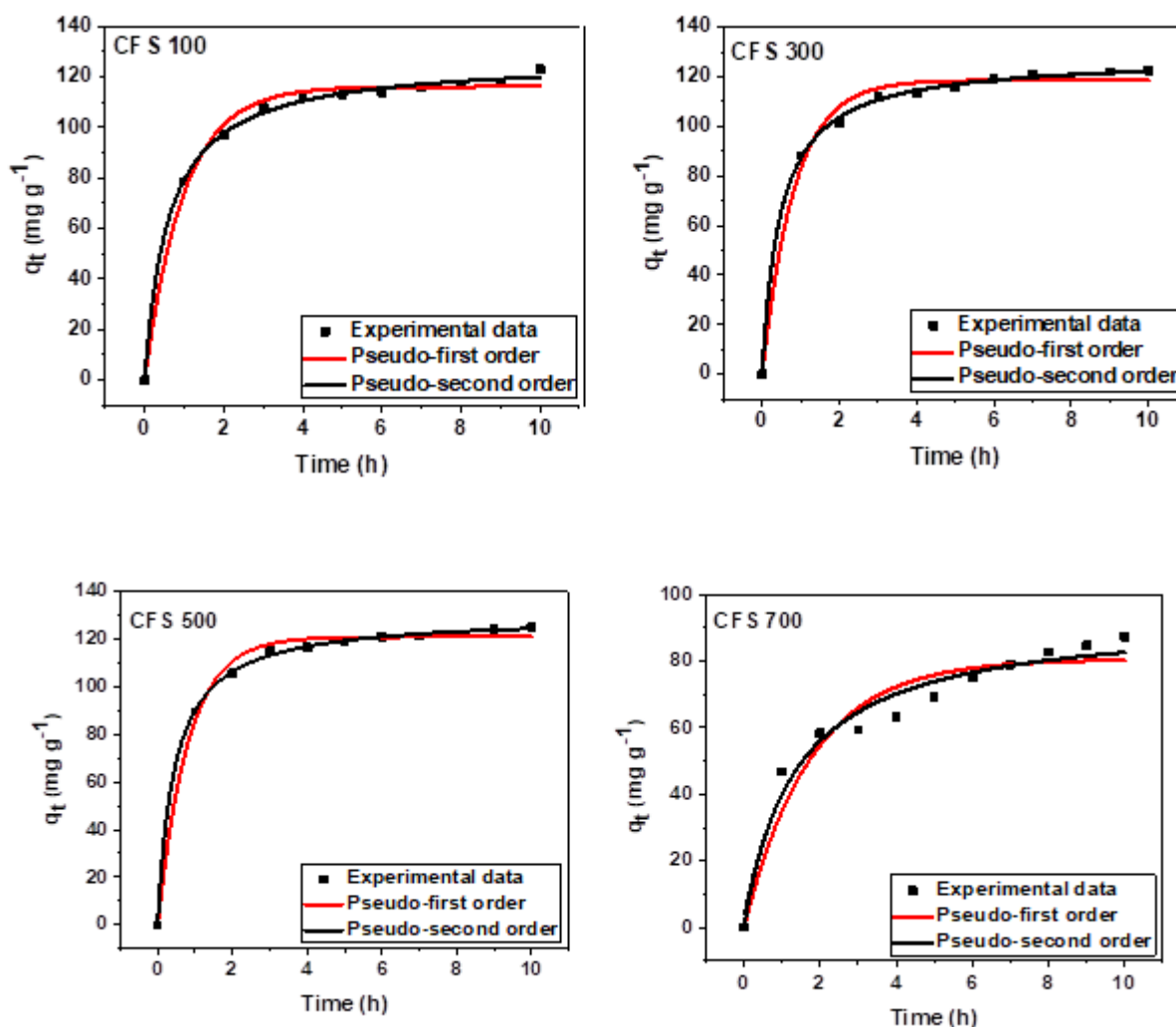


Fig. 4.35: Kinetic plots of the adsorption of DOX on CoFe₂O₄/rice husk silica

Table 14. Parameters for kinetics models.

Model	Parameters	CFS-100	CFS-300	CFS-500	CFS-700
Pseudo-first order	q_e (mg g ⁻¹)	116.09	118.57	120.74	80.49
	k_1 (min ⁻¹)	1.017	1.203	1.233	0.568
	R^2_{adjusted}	0.9906	0.9881	0.9924	0.9256
	SD (mg g ⁻¹)	3.414	3.906	3.156	6.763
Pseudo-second order	q_e (mg g ⁻¹)	127.16	127.84	129.76	93.72
	k_2 (g mg ⁻¹ min ⁻¹)	0.013	0.016	0.017	0.007
	R^2_{adjusted}	0.9977	0.9989	0.9993	0.9654
	SD (mg g ⁻¹)	1.687	1.191	0.991	4.613

4.3.10 Adsorption isotherm for the adsorption of DOX on CoFe₂O₄/rice husk silica

The curve fits of the Langmuir and Freundlich isotherms for adsorption of DOX on CFS 100 and CFS 700 are shown in **Fig. 4.36 and 4.37** respectively, while the various isotherms parameters are itemized in **Table 15**. The monolayer adsorption capacity obtained from Langmuir isotherm increases with increase in temperature, which is similar to the findings of Brigante and Avena, 2016 [144]. Adsorption of DOX on the adsorbent is favored with increase in temperature which is a typical endothermic adsorption process. Rather than DOX molecule to be desorbed at higher temperature, it was kinetically favored. Its migration and binding to the surface of the adsorbent occurred more faster than desorption which do occur in many adsorption studies. Considering the values of SD and $R^2_{adjusted}$ the experimental data fitted well with Langmuir than Freundlich isotherm. This implies there is monolayer adsorption of DOX on the surface of the nanocomposite without any interaction between the adsorbed species. The adsorption capacities obtained were further normalized by the surface area of each material (CFS 100 and 700) [164], and the values obtained are 2.95 and 3.93 mg m² for CFS 100 and CFS 700 respectively. Based on this normalization result one could opine that the adsorption of DOX on these two nanocomposites was not directly influenced by specific surface. Itemized in **Table 15** is the comparison of the adsorption capacity with other adsorbents in the literature for the adsorption of DOX.

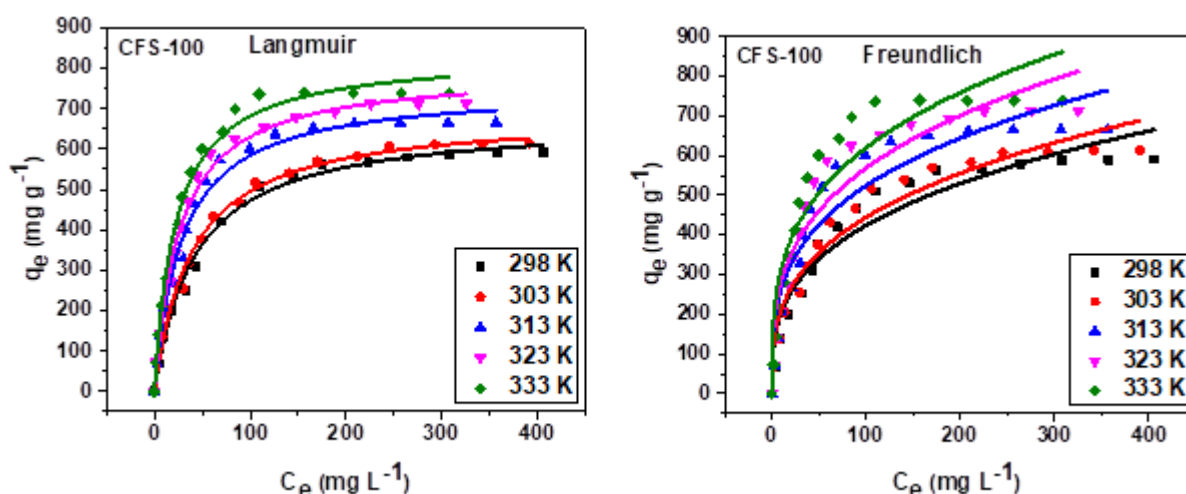


Fig. 4.36. Langmuir and Freundlich isotherms for the adsorption of DOX on CFS 100.

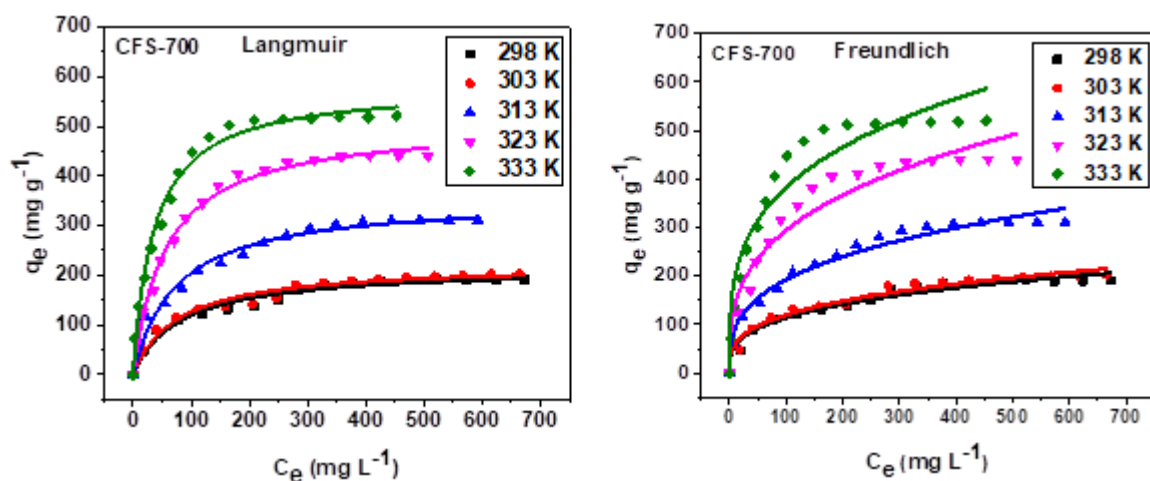


Fig. 4.37. Langmuir and Freundlich isotherms for the adsorption of DOX on CFS 700.

Table 15. Langmuir and Freundlich isotherms parameters for the adsorption of DOX at 298 - 333 K

CFS 100					
	298 K	303 K	313 K	323 K	333 K
Langmuir					
q_{\max} (mg g ⁻¹)	672.97	689.72	752.31	794.96	835.47
K_L (L mg ⁻¹)	0.024	0.026	0.035	0.038	0.044
R^2_{adjusted}	0.9921	0.9933	0.9851	0.9925	0.9888
SD (mg g ⁻¹)	17.81	17.34	28.18	21.12	27.26
Freundlich					
K_F (mg g ⁻¹ (mg L ⁻¹) ^{-1/n_F})	96.63	101.43	133.13	141.29	160.83
n_F	3.11	3.11	3.36	3.36	3.41
R^2_{adjusted}	0.9321	0.9461	0.8987	0.9111	0.8921
SD (mg g ⁻¹)	52.02	47.92	73.44	72.87	84.93
CFS-700					
Langmuir					
q_{\max} (mg g ⁻¹)	216.22	222.98	355.27	507.76	581.44
K_L (L mg ⁻¹)	0.012	0.013	0.014	0.018	0.028
R^2_{adjusted}	0.9754	0.9764	0.9806	0.9929	0.9863
SD (mg g ⁻¹)	8.89	9.05	13.47	12.22	20.61
Freundlich					
K_F (mg g ⁻¹ (mg L ⁻¹) ^{-1/n_F})	27.48	29.41	44.33	68.32	105.09
n_F	3.22	3.26	3.13	3.15	3.55
R^2_{adjusted}	0.9672	0.9748	0.9739	0.9356	0.9272
SD (mg g ⁻¹)	10.27	9.37	15.64	36.83	47.46

Table 16. Comparison of the maximum monolayer adsorption (q_{max}) of different adsorbents for the removal DOX.

Adsorbents	q_{max} (mg g ⁻¹)	References
Cu(II) impregnated biochar	93	[54]
MFO-0.5-700	308.51	[161]
Lignin xanthate resin–bentonite clay	438.75	[165]
Electro-generated adsorbents	31.35	[166]
MIL- 53(Fe)/Fe ₃ O ₄	477	[167]
Graphene-MoS ₂ .	555.56	[30]
NaY zeolite	252.12	[168]
Rice straw biochars	170.36	[169]
Fe ₃ O ₄ magnetic nanoparticles	61.35	[162]
graphene nanosheet	110	[170]
CFS-100	835.47	This work
CFS-700	581.44	This work

4.3.11 Thermodynamic of adsorption

Thermodynamic parameters are listed in **Table 17**. The values of ΔH° being positive implies that DOX adsorption on the nanocomposite is endothermic process. This depicts that by increasing the temperature of the system, the forces of adsorption that exist between DOX molecules and the adsorbents (CFS-100 and CFS-700) become higher. This is in accordance with the adsorption capacity obtained from Langmuir isotherm which is directly proportional to increase in temperature. Negative values of ΔG° confirms that the process is spontaneous. The values of ΔG° are more negative with increase in the temperature, this implies that spontaneity of adsorption of DOX is stronger [171]. The positive values of ΔS° signifies that the adsorption process of the antibiotic is entropy-driven [172]. In addition, the value of ΔS° for CSF-100 being higher than CFS-700 shows increasing randomness.

Table 17. Thermodynamics parameters for the adsorption of DOX at 298 - 333 K.

Adsorbents	ΔH° (kJ mol ⁻¹)	ΔS° (J K ⁻¹ mol ⁻¹)	ΔG° (kJ mol ⁻¹)				
			298 K	303 K	313 K	323 K	333 K
CFS-100	15.76	127.31	-22.17	-22.81	-24.08	-25.36	-26.63
CFS-700	12.21	109.50	-20.41	-20.96	-22.05	-23.15	-24.24

4.3.12 Mechanism of adsorption

FTIR analysis is one of the techniques that helps to understand the mechanism of adsorption through the interaction between the adsorbent and adsorbate. **Fig. 4.38 (A)** is the FTIR spectra of Doxycycline (DOX), CFS-700 before adsorption and after adsorption (CFS-700 + DOX). Analyzing the major peaks on the DOX, the broad peak at 3418 cm⁻¹ is assigned to the phenolic -OH stretching, while 2920 cm⁻¹ is attributed to -CH asymmetric stretching. The band at 1610 cm⁻¹ is due to the presence of C=O, while the peak at 1445 cm⁻¹ is attributed to C-C. More so, the band at 1079 cm⁻¹ is assigned to C-O. The peaks at the CFS-700 before adsorption, had been discussed under section 3.5. The increase in intensity of C=O after adsorption shows that there is interaction between oxygens on the surface of the nanocomposites and the aromatic rings of DOX which results to n- π interaction [173].

Effect of ionic strength on the adsorption capacity was further investigated for better understanding of adsorption mechanism. This was carried out by adding 0.2 to 1.0 mol L⁻¹ NaCl to 100 ppm of DOX. The result obtained is presented in **Fig. 4.38 (B)** and shows that the amount (mg g⁻¹) adsorbed decreases slightly with increase in amount (mol L⁻¹) of NaCl that was added to DOX solution. This confirms that electrostatic interaction also plays a role in the mechanism of adsorption.

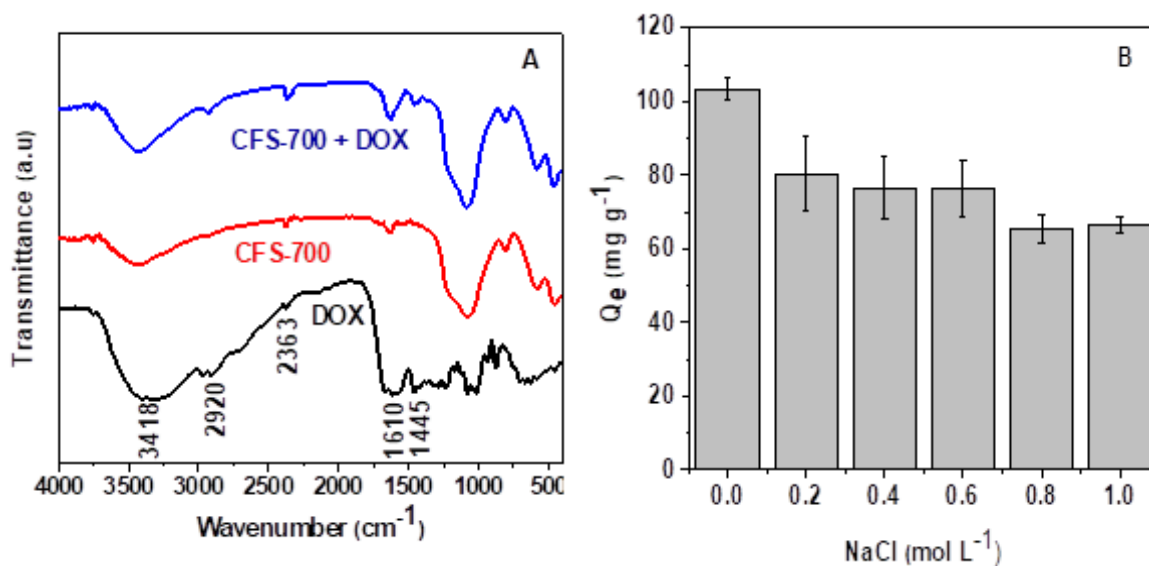


Fig. 4.38: FTIR spectra of Doxycycline (DOX), CFS-700 before adsorption and after adsorption(A) and effect of ionic strength (B).

The XRD pattern of CFS-700 before and after adsorption presented in **Fig. 4.39 (A)** are similar. The adsorption of DOX is mainly on the surface of the composite, no ion exchange was involved. The result was similar to what was obtained by [174] in their study on the adsorption of rhodamine 6G on kaolinite and palygorskite clay minerals. The result obtained from the effects of phosphate on the adsorption of DOX is displayed in **Fig. 4.39 (B)**. Phosphate can be chemically adsorbed on the iron sites through complexation via exchange of ligands and hinder the complexation of other organic ligands on the iron sites [175,176]. The result from this study shows that the presence of phosphate does not have significant effect on the adsorption of DOX despite remarkable concentration of phosphate that was added to fixed concentration (100 mg L⁻¹) DOX solution. This infers that the adsorption of DOX is not through the exchange of ligands on the iron sites as confirm from the XRD.

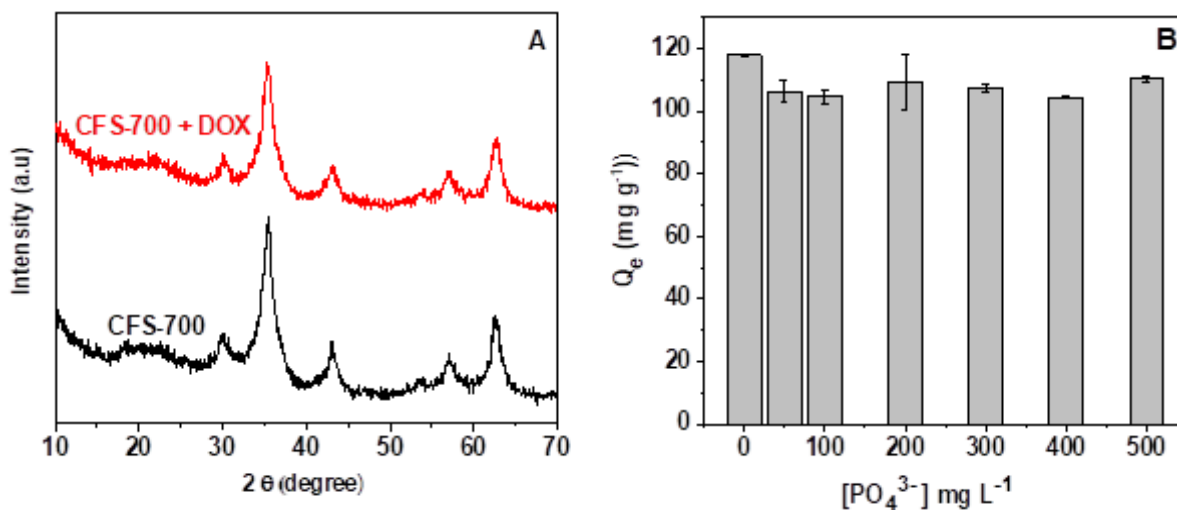


Fig. 4.39: XRD before and after adsorption (A) and effect of phosphate (B).

4.3.13 Recovery of the adsorbent through thermal treatment.

Thermal recovery of the adsorbent (CFS-700) was carried by thermally treating the composite at 500 °C for 2 h after each process of adsorption with initial concentration of 500 ppm of DOX. The recovery of the adsorbent (CFS-700) using thermal treatment up to 5 cycles show the reusability of the composites without remarkable reduction in the amount adsorbed in each subsequent cycle (**Fig. 4.40**). Economically, the composite is viable to use in industrial scale. The cost of procuring new material will be greatly reduced as the thermally treated composite could be used repeatedly use for the adsorption of the antibiotic. More so, desorbing DOX from DOX-loaded adsorbent by thermal degradation could as well prevent the antibiotic from finding its way into the environment.

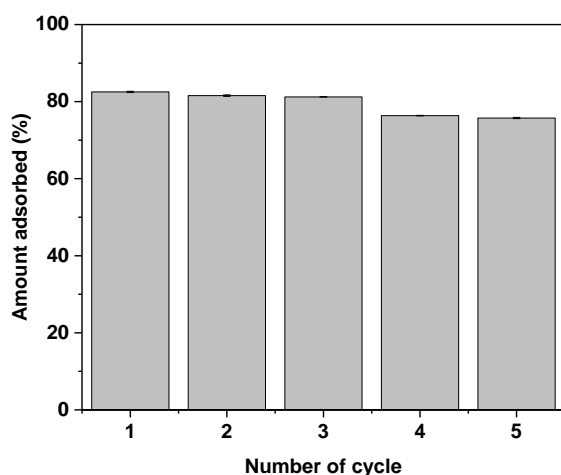


Fig. 4.40. Reusability of cobalt ferrite/rice husk silica composite

4.3.14 Characterization of CFS-700 after adsorption

Thermogravimetry analysis (TGA) was carried on CFS-700 to confirm the adsorption of DOX.

Fig. 4.41 below shows that there is no weight loss in the nanocomposite before adsorption this is expected, since it has been earlier calcined at 700. However, after adsorption there is an appreciable mass loss which is due to the presence of adsorbed DOX. Approximately 40% of mass loss was recorded. This analysis confirmed adsorption of DOX and that, the adsorbent can be thermally treated and reuse. The initial stage of mass loss up to 200 °C is associated with the presence of adsorbed and bound water, while the mass loss from 200 until 450 °C is due to the thermal degradation of DOX molecules.

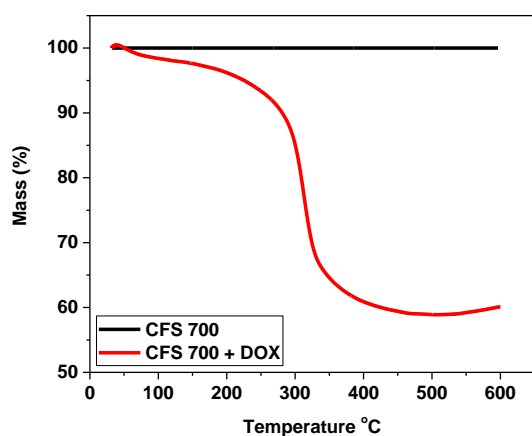


Fig. 4.41. TGA of CFS-700 before and after adsorption.

The presence of DOX in the nanocomposite after adsorption was established through energy-filtered-TEM (EFTEM). Elemental mapping of the images is presented in **Fig. 4.42**. The Carbon (C) signal is due to the presence of DOX which was adsorbed on the surface of the nanocomposite.

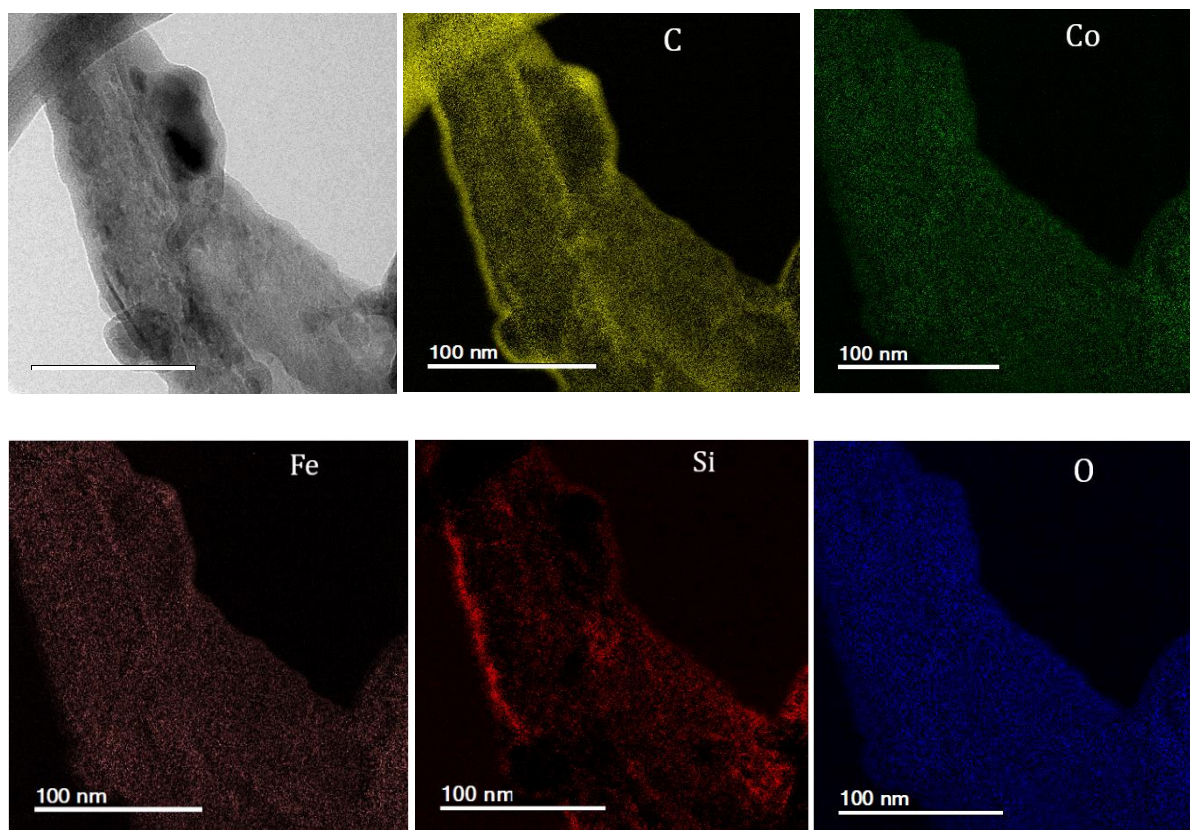


Fig. 4.42. The RGB color map showing the distribution of each individual element

4.15 Conclusion

We have successfully synthesized a novel cobalt ferrite/bio silica nanocomposite for the first time, with high adsorption capacity and investigated its adsorption capacity for the removal of doxycycline hydrochloride, a hazardous contaminant through batch process. The synthesized nanocomposite was calcined at 300, 500 and 700 °C. The as-prepared nanocomposite has the highest surface area ($283 \text{ m}^2 \text{ g}^{-1}$) while the nanocomposite calcined at 700 °C has the lowest ($148 \text{ m}^2 \text{ g}^{-1}$). Optimum pH for the adsorption was found to be 6, while equilibrium time was 10 h. Adsorption process was complexed and affected by temperature which made maximum adsorption capacity of 835.47 and 581.44 mg g^{-1} to be

attained by as-received and CFS-700 respectively, at 333 K. Addition of phosphate up to 500 mg L⁻¹ did not have any significant effects on the adsorption of DOX, which implies that the mechanism of adsorption is not through complexation with iron species of the nanocomposite. DOX-loaded nanocomposite was desorbed at 500 °C, while the DOX-desorbed nanocomposite was reused until 5 cycles. Thermal degradation of the adsorbed DOX was interesting since it could prevent the antibiotic from finding its way to the environment and save cost of procuring new adsorbent. Increased in temperature favored the adsorption process and was spontaneous. Langmuir isotherm was best applicable to explain the adsorption process among the two isotherms used. TGA and EFTM analysis clearly ascertain the adsorption of DOX on the nanocomposite.

4.4 Synergistic effect of CoFe_2O_4 on the adsorption capacity of nano bio-silica for the removal of methylene blue

4.4.1 Influence of pH on amount adsorbed by CoFe_2O_4 /rice husk silica and rice husk silica

Solution pH plays an indispensable role in adsorption process by influencing the adsorbent surface charge and ionization of the adsorbate [177,178]. pH study was carried out by varying the pH of the solution from 2 – 10, and the results obtained are shown in **Fig. 4.43 A**. Meanwhile, prior to this, the zeta potential of BSIL and CFS-700 were investigated (representative of the composite) and found the values to be negative **Fig. 4.43 B**. It was on this premise that methylene blue (MB), a model cationic dye was used as an adsorbate. The result shows an increase in the amount of MB that was adsorbed on the surface of the adsorbents with respect to pH, which is as a result of electrostatic attraction between MB and the adsorbents. There is an increase in the amount adsorbed by CFS-100 and 700 compared to BSIL despite the same negative surface charge that both exhibit. In addition to this, the amount adsorbed by both COF (cobalt ferrite) and BSIL are almost the same, it then implies that the alarming increase in the amount adsorbed by the composite is not due to only COF, but due to their synergistic effect and difference in specific surface area (SSA). The results obtained with respect to SSA of the adsorbents show that SSA plays an important role in the adsorption on MB. SSA of CFS-100 is 5 times more than that of BSIL which is equivalent to 5 times the amount adsorbed by BSIL. Worthy of note, is that cobalt ferrite aside offering a magnetic separation to the composite, enhanced the adsorption capacity. Further study was carried out on BSIL, CFS-100 and CFS 700 only.

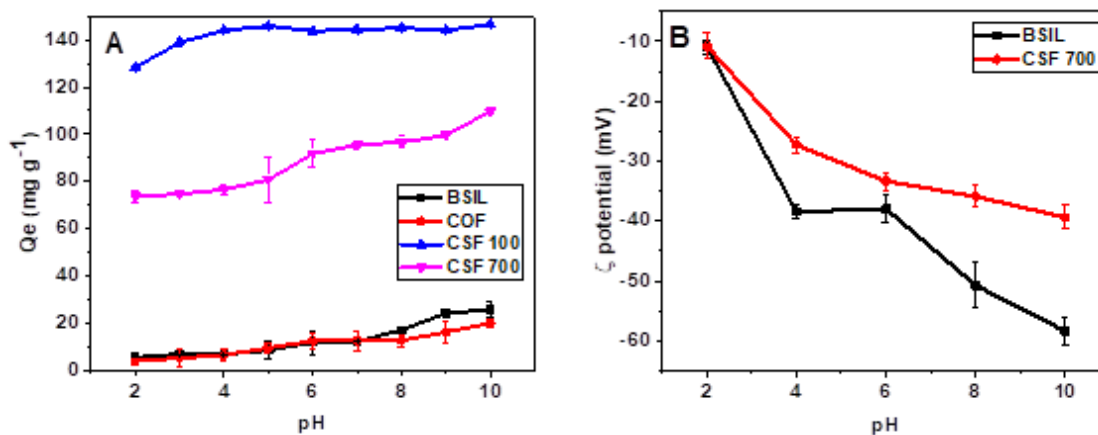


Fig. 4.43. The effect of pH (A) on the adsorption of MB on BSIL, COF, CFS-100, and SCF-700, with zeta potential (B).

All silicas have different types of silanol groups (isolated, geminal, and vicinal) on their surfaces [179]. Deprotonation of this group occurs in water with increasing pH which, leads to negative charge (SiO^-) [180,181] and becomes an active site for the adsorption of MB through electrostatic attraction (**Fig 4.44**). Meanwhile, due to the large specific surface area and negative charge on the surface of the composite, the adsorption of MB was synergistically enhanced.

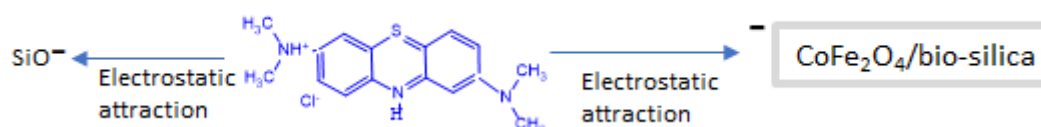


Fig. 4.44: Electrostatic attraction between MB and the adsorbents.

4.4.2 Effect of adsorbent dosage on adsorption of MB by BSIL, CFS-100, and CFS-700

The amount of MB (initial concentration of 100 mg L^{-1} and pH 9) that was adsorbed increases with the dosage of the adsorbents as shown in **Fig. 4.45**. The dosage of CFS-100 and 700 was varied from 2 – 10 mg; while that of BSIL was varied from 10 – 100 mg. The amount (%) of MB adsorbed by 2 mg of CFS-100 was equivalent to that of 10 mg of BSIL. As the dosage of CFS-100 and 700 increases, the amount adsorbed follow suit, which is due to the availability of more active sites for the adsorption of the dye. CFS-100 almost attain saturation at 8 mg, while CFS-700 could not. More so, BSIL attained equilibrium at 60 mg of the adsorbent. In the overall, both CFS-100 and 700 offer a better adsorption capacity than BSIL.

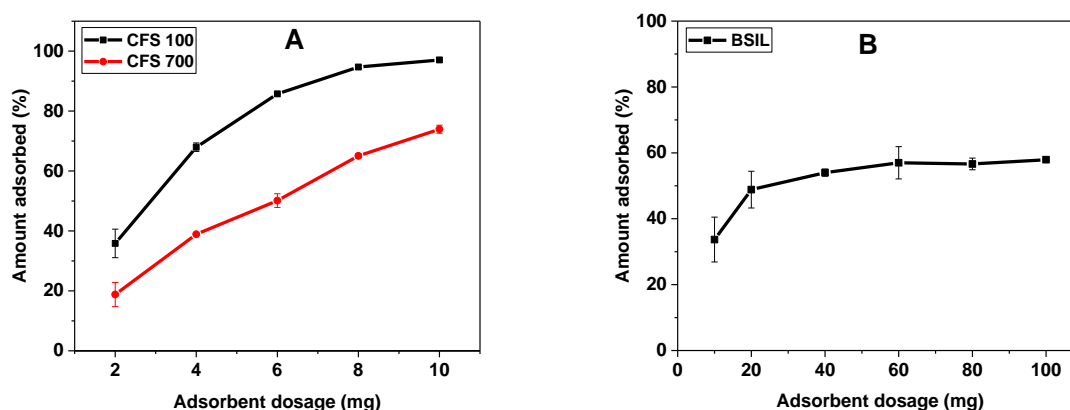


Fig. 4.45: Amount of MB adsorbed with respect to the dosage of the adsorbents (CFS 100 and 700 (A) and BSIL (B)).

4.4.3 Kinetic study for adsorption of MB on BSIL, CFS-100 and CFS-700

As shown in Fig. 4.46, approximately 133 and 103 mg g⁻¹ of MB was adsorbed by CFS-100 and 700 respectively, while for BSIL, 19 mg g⁻¹ was adsorbed after initial 30 mins contact time. After this, the adsorption was slow due to the covering of the active sites of the adsorbents by MB molecules. It is economical and time-saving in the wastewater treatment for adsorbents to adsorb the targeted contaminants within a short period of contact time [182]. The optimum time for CFSF 100 and 700 was found to be 120 mins., that of BSIL was more than this.

Pseudo-first order and pseudo-second order models were employed for the proper understanding of adsorption kinetic. The parameters of the models are itemized in Table 18.

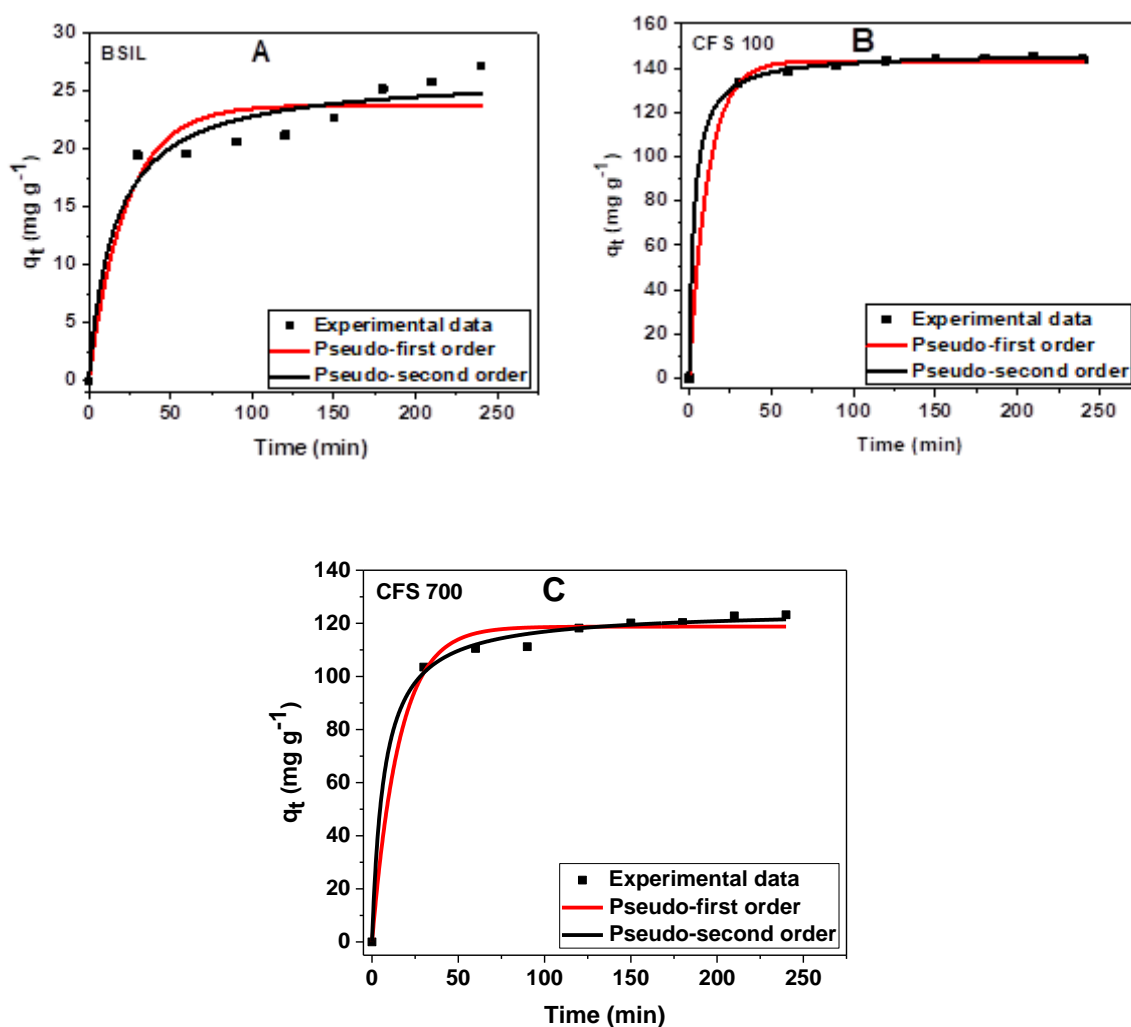


Fig. 4.46: Kinetic plots of the adsorption of MB on BSIL (A), CSF 100 (B) and CFS 700 (C).

Table 18. Parameters of kinetics models for the adsorption of MB on BSIL, CFS-100 and CFS-700

Model	Parameters	BSIL	CFS-100	CFS-700
Pseudo-first order	q_e (mg g ⁻¹)	23.75	143.26	118.76
	k_1 (min ⁻¹)	0.0439	0.0868	0.0641
	$R^2_{adjusted}$	0.9068	0.9981	0.9880
	SD (mg g ⁻¹)	2.46	2.06	4.30
Pseudo-second order	q_e (mg g ⁻¹)	23.32	164.54	130.92
	k_2 (g mg ⁻¹ min ⁻¹)	0.0716	0.2810	0.1365
	$R^2_{adjusted}$	0.9386	0.9997	0.9960
	SD (mg g ⁻¹)	1.99	0.82	2.47

4.4.4 Adsorption isotherm for the adsorption of MB on BSIL, CFS 100 and 700

The behavior of how BSIL, CFS 100 and 700 interact with different concentration of MB in the solution at a constant temperature, were examined by employing two commonly use isotherms (Langmuir and Freundlich). **Fig. 4.47, 4.48** and **4.49** depict the curve fits of the two isotherms, while their parameters are listed in **Table 19**. The trend of the adsorption capacity which decreases with an increase in temperature signifies exothermic adsorption of MB on BSIL and the composites. The adsorption capacity of the composites is higher than BSIL reason for this is the higher values of the specific surface area of the composites, which implies the availability of more active sites for adsorption. In addition, Langmuir isotherm is more appropriate to explain the mechanism of adsorption of MB on the composites. Comparison of the maximum monolayer adsorption (q_{max}) of different adsorbents for the removal of MB are listed in **Table 20**.

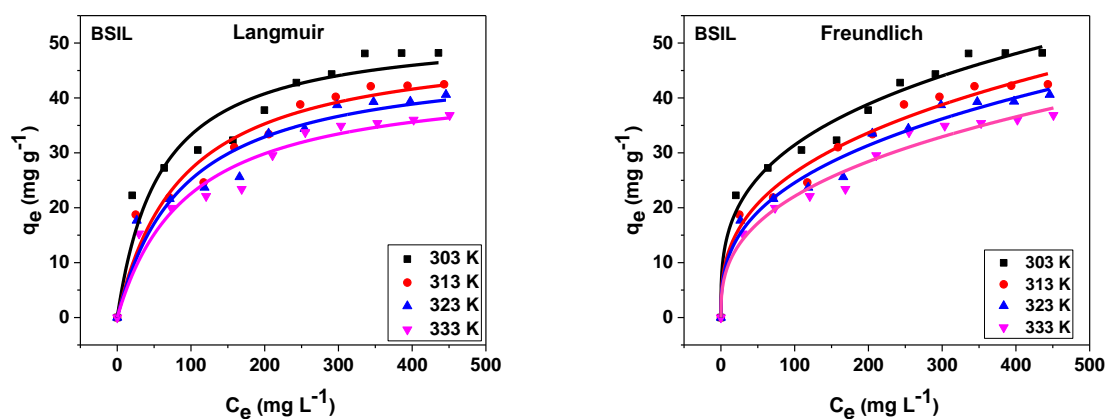


Fig. 4.46. Langmuir and Freundlich isotherms for the adsorption of MB on BSIL.

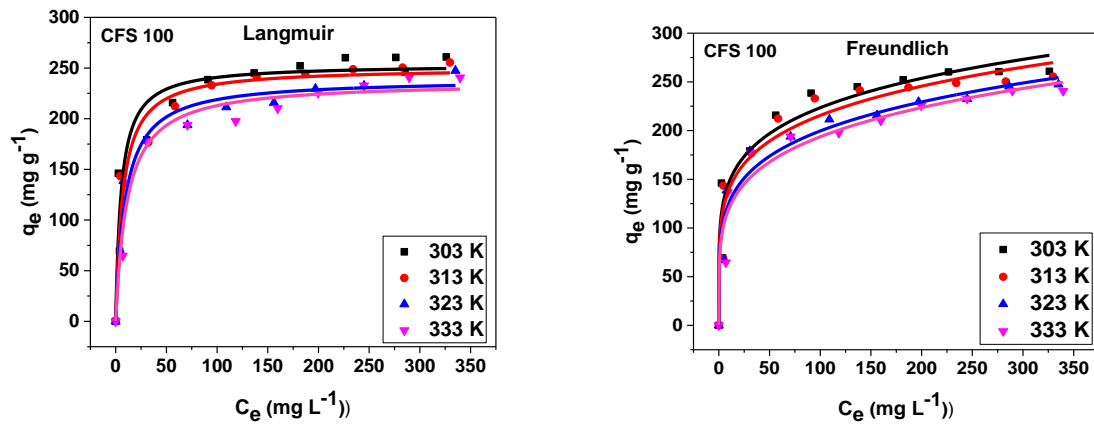


Fig. 4.48. Langmuir and Freundlich isotherms for the adsorption of MB on CFS 100

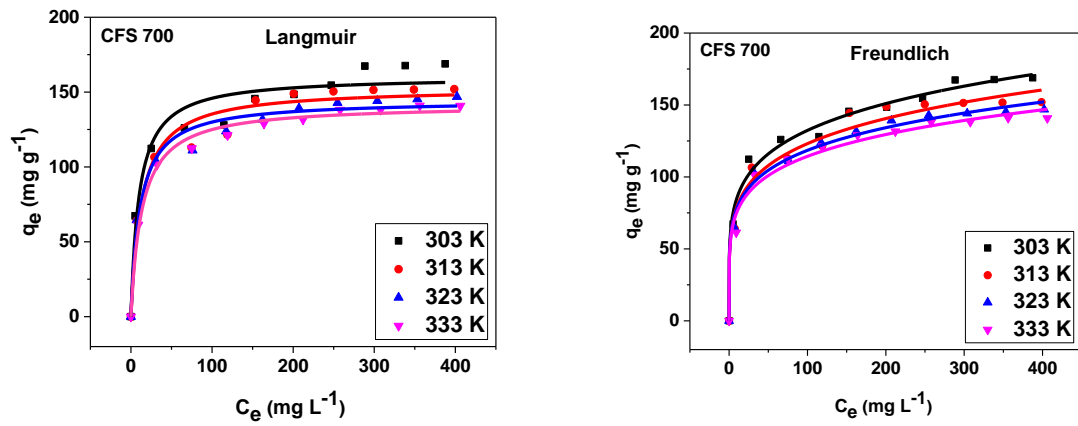


Fig. 4.49. Langmuir and Freundlich isotherms for the adsorption of MB on CFS 700.

Table 19. Langmuir and Freundlich isotherms parameters for the adsorption of MB at 303 - 333 K.

BSIL				
	303 K	313 K	323 K	333 K
Langmuir				
q_{\max} (mg g ⁻¹)	52	50	47	44
K_L (L mg ⁻¹)	0.016	0.012	0.011	0.01
R^2_{adjusted}	0.9152	0.9433	0.9320	0.9499
SD (mg g ⁻¹)	4.33	3.16	3.24	2.55
Freundlich				
K_F (mg g ⁻¹ (mg L ⁻¹) ^{-1/n_F})	7.14	5.29	4.82	4.14
n_F	3.11	2.86	2.83	2.75
R^2_{adjusted}	0.9825	0.9779	0.9726	0.9762
SD (mg g ⁻¹)	1.96	1.97	2.06	1.76
CFS-100				
Langmuir				
q_{\max} (mg g ⁻¹)	253	250	239	236
K_L (L mg ⁻¹)	0.187	0.14	0.11	0.089
R^2_{adjusted}	0.894	0.9373	0.9596	0.9527
SD (mg g ⁻¹)	28.53	21.32	15.99	16.95
Freundlich				
K_F (mg g ⁻¹ (mg L ⁻¹) ^{-1/n_F})	96.30	90.50	79.20	74.39
n_F	5.47	5.307	4.982	4.81
R^2_{adjusted}	0.9302	0.9333	0.9470	0.9370
SD (mg g ⁻¹)	23.23	21.99	18.32	19.57
CFS-700				
Langmuir				
q_{\max} (mg g ⁻¹)	160	152	144	141
K_L (L mg ⁻¹)	0.099	0.076	0.088	0.074
R^2_{adjusted}	0.9487	0.9625	0.9731	0.9898
SD (mg g ⁻¹)	11.66	9.29	7.40	4.39
Freundlich				
K_F (mg g ⁻¹ (mg L ⁻¹) ^{-1/n_F})	55.12	51.08	51.75	49.98
n_F	5.258	5.234	5.56	5.567
R^2_{adjusted}	0.9873	0.9743	0.9878	0.9803
SD (mg g ⁻¹)	5.80	7.70	4.97	6.101

Table 20. Comparison of the maximum monolayer adsorption (q_{max}) of different adsorbents for the removal of MB.

Adsorbents	q_{max} (mg g ⁻¹)	References
nFMBO	72.32	[183]
Magnetic cellulose/GO composite	70.03	[127]
Surface-functionalized silica aerogels	68.15	[128]
HSC	297.6	[184]
CNT	64.7	[185]
MGS	140.57	[186]
Activated biochar	33.33	[131]
Poly-amide modified vermiculite	111.95	[187]
Biochar	33	[188]
Lava	10.32	[189]
BSIL	52	This study
CFS -100	253	This study
CFS -700	160	This study

4.4.5 Effect of temperature and thermodynamic of adsorption of MB on BSIL, CFS 100 and 700

The results of the effects of temperature on the adsorption capacity are shown in **Fig. 4.50**. The adsorption capacity of the three adsorbents decreased with an increase in temperature. The amount adsorbed by BSIL, CFS 100 and CFS 700 at 303 K are 52.6, 253.6 and 160.48 mg g⁻¹ respectively, meanwhile, when the temperature was raised to 333 K it decreased to 44.07, 236.84 and 141.78 g g⁻¹ for BSIL, CFS 100 and CFS 700 respectively. The reason could be summarized as follow: there is increasing tendency of MB molecules to escape from the solid phase (adsorbent) to bulk phase (solution) due to increase in temperature, more so, with increase in temperature, MB molecules that are physically adsorbed on the surface of the adsorbent could gain kinetic energy which made them overcome the electrostatic force of attraction between them and the adsorbents, due to this they get desorbed at higher temperature [172]. This is an example of an exothermic adsorption process in which an increase in temperature results in to decrease in adsorption capacity.

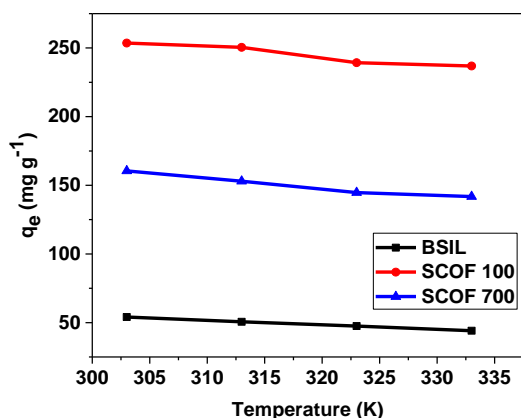


Fig.4.50. Effect of temperature on adsorption capacity of BSil, CFS 100 and 700 for the adsorption of MB.

The effect of temperature on the adsorption of the MB was further examined by calculating the thermodynamic parameters. Premise on the values of ΔH° for BSIL, CFS-100 and CFS-700 that are negative (**Table 21**), it implies that the adsorption of MB on three adsorbents is enthalpy driven. This supports the adsorption capacity obtained from Langmuir isotherm that decreases with an increase in temperature. More so, the values of ΔG° that is negative shows that adsorption of MB is spontaneous and feasible. Meanwhile, the positive values of ΔS° imply an increase in randomness of the system due to the high affinity that MB molecules have for the adsorbents.

Table 21. Thermodynamic parameters for the adsorption of at 303 -333 K.

Adsorbents	ΔH° (kJ mol ⁻¹)	ΔS° (J K ⁻¹ mol ⁻¹)	ΔG° (kJ mol ⁻¹)			
			303 K	313 K	323 K	333 K
BSIL	-12.65	28.81	-27.68	-27.91	-28.14	-28.36
CFS-100	-20.74	22.91	-28.27	-29.83	-31.39	-32.95
CFS-700	-6.35	64.802	-25.99	-26.63	-27.28	-27.93

4.4.6 Effect of ionic strength on the adsorption of MB on BSIL and 700

The effect of ionic strength on the adsorption capacity of an adsorbate may affect electrostatic and hydrophobic interactions [190]. The results show a slight increase (9 mg g^{-1}) in the amount of MB adsorbed on CSF-700 when the concentration of NaCl was varied from 0.2 to 1 mol L^{-1} (Fig. 4.51 A). Meanwhile, there is a notable and consistent increase in the adsorption of MB on BSIL with an increase in ionic strength. An increase in ionic strength modifies adsorption capacity either by diminishing it (in case of electrostatic attraction) or enhancing it (in case of electrostatic reduction) [191]. However, our results did not follow this assertion. Despite the existence of an electrostatic attraction between MB molecules and the adsorbents, the presence of NaCl did not bring about a reduction in the adsorption capacity but rather increases it. The presence of salt in dye solution increases the intermolecular, van der waals' forces between dyes' molecules which could lead to the formation of dimers and consequently aggregation of the molecules [192]. The aggregated molecules were adsorbed on the surface of BSIL and CFS-700, thereby leading to an increase in adsorption capacity. Monomer and dimers molecules of MB are shown in Fig 4.51 B and C respectively. The good thing about this result is that both adsorbents can perform effectively in a salty dye solution without any reduction in their adsorption capacity.

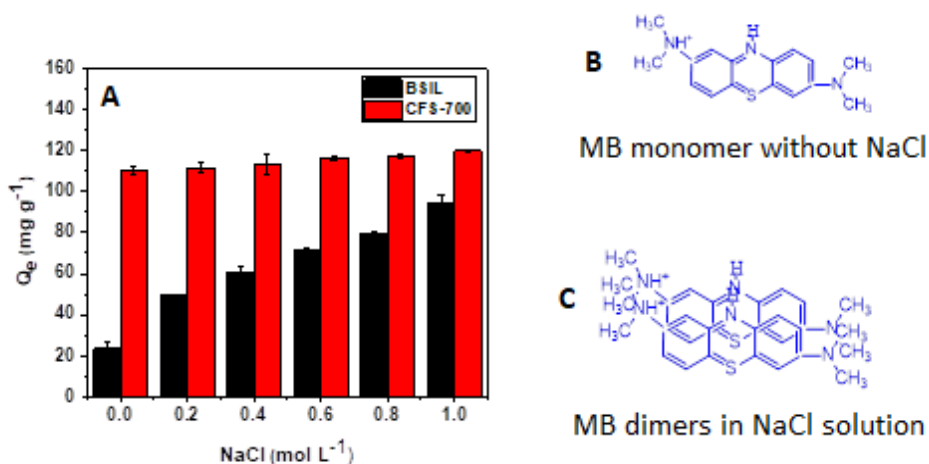


Fig. 4.51. Effect of ionic strength on the adsorption of MB on SIL and CFS-700 (A), Monomer (B) and dimers molecules (C) of MB.

4.4.7 Regeneration and reusability of BSIL and CFS-700

One of the economic benefits that adsorbents could offer is their ability to be regenerated and reused after successive adsorption process without losing much of their active sites and adsorption capacities. The adsorbed MB molecules were desorbed through calcination at 500 °C for 2 h after each adsorption process, while the adsorbents (BSIL and CFS-700) were reused. The amount adsorbed remains virtually constant after each successive cycle and till the 5th cycle (**Fig 4.52 A**). In this regard, using the adsorbents for adsorption of cationic dyes is economically viable. It has been documented that silanol groups on the surface of silica are the active adsorption sites, which were not inactive after subjected to calcination following each adsorption test. [145]. This made BSIL and CFS-700 retain their adsorption capacity after calcination. Images of BSIL before adsorption, after adsorption and calcination are shown in **Fig 4.52 B** that of CFS-700 was not shown due to its original color (dark brown) before adsorption that makes it impossible for the color of MB to be appreciably noticed after adsorption, unlike BSIL that is white.

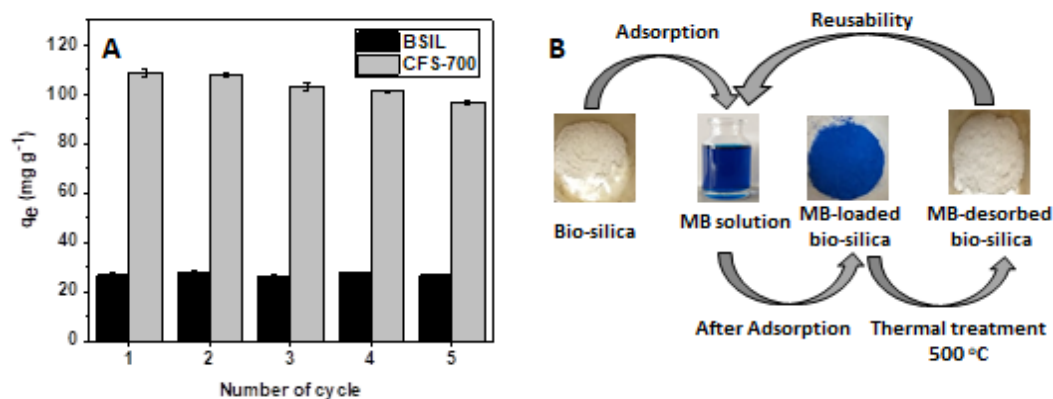


Fig. 4.52: Reusability of BSIL and CFS-700 (A) and Images of BSIL before adsorption, after adsorption and calcination (B).

4.4.8 Characterization of BSIL and CFS-700 after adsorption

BSIL and CFS-700 were characterized after adsorption. CFS-700 was chosen instead of CFS-100 because of its high value of magnetic saturation and presence of distinct d-spacings that are characteristics features of cobalt ferrite. These two adsorbents (BSIL and CFS-700) were characterized using FTIR and EFTEM techniques. **Fig. 4.53** shows their FTIR spectra of before

and after adsorption including that of MB. The small peak (A) located at 3791 cm^{-1} is acclaimed to be presence of hydrogen bond which was explained to be as result of interaction between it and silanol groups (Si-OH) [193], while the peaks labeled B and C appearing at 3465 and 1637 cm^{-1} are assigned OH (of adsorbed water molecule) stretching and bending vibration respectively [194]. The band at 1101 cm^{-1} labeled D is attributed to the symmetric stretching vibration of Si-O-Si from SiO_4 [147,152]. Furthermore, the peaks marked E and F at 798 and 498 cm^{-1} are attributed to symmetric Si-O bending [195]. Another obvious peak is at X with wavenumber 635 cm^{-1} typical fingerprint of cobalt ferrite [196]. The small peak tags Y at 950 cm^{-1} on BSIL's spectra is due to Si-OH, related to the presence of a high amount of silanol groups [193] This peak could not be found on CFS-700 spectra, which may affirm interaction between cobalt ferrite and silica. There is no noticeable peak at the spectra of BSIL after adsorption (probably due to weak interaction between it and MB), on the other hand, peaks labeled as 1 and 2 on CFS-700 after adsorption could be related to the MB. In addition, there is a small increase in the band 1637 cm^{-1} on the spectrum of CFS-700 after adsorption suggesting that hydrogen bonding could be involved in the adsorption process.

There are several peaks on the spectrum of MB in the region $1600 - 610\text{ cm}^{-1}$. The bands in between $1035 - 610\text{ cm}^{-1}$ correspond to axial-deformation of C-H vibration in polynuclear aromatic rings, while the peaks in the region between 1600 and 1136 cm^{-1} were associated with axial deformation C-N vibration in both aromatic and aliphatic ring of MB molecules [197].

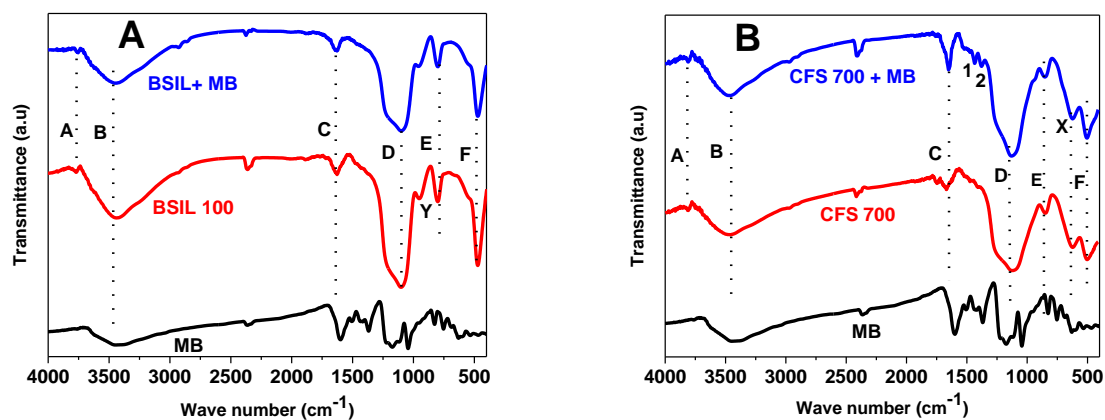


Fig. 4.53: FTIR spectra before and after adsorption. BSIL (A) and CFS-700 (B)

Further confirmation of the adsorption of MB on the adsorbents was carried out on CFS-700 through energy-filtered-TEM, by mapping elements that are present after adsorption. **Fig 4.54** shows images of the elemental mapping of Fe, Co, Si, O and C. The presence of carbon was due to the adsorption of methylene blue (MB).

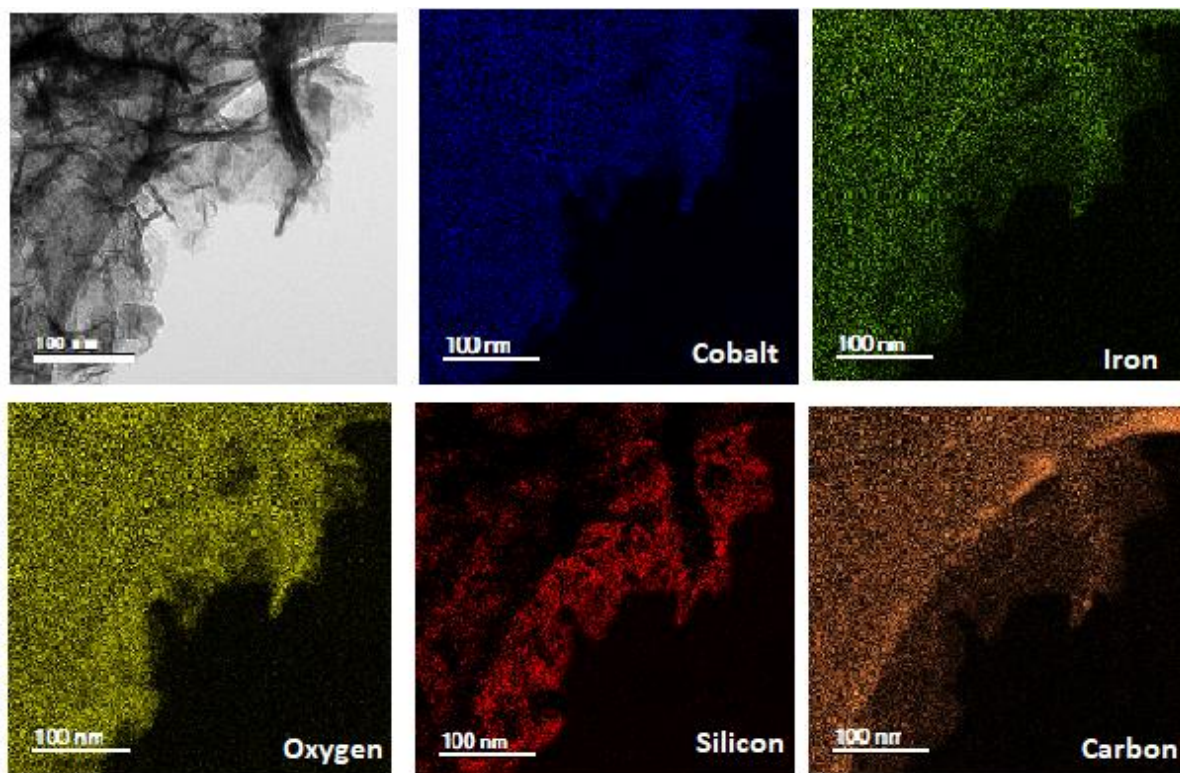


Fig. 4.54: Elemental mapping of CFS 700 after adsorption.

4.4.8 Conclusion

This novel study showed that adsorption capacity of amorphous nano bio-silica extracted from rice husk for the removal of methylene blue can be synergistically enhanced by compositing it with cobalt ferrite, which also induced magnetic properties on the composite for easy separation after adsorption process. Both surface charge and the specific surface area of the adsorbents have direct influence on their adsorption capacity. The optimum pH and equilibrium time were 9 and 120 min respectively. Adsorption data are well fitted to isotherms that were

proposed by Langmuir and Freundlich, while pseudo-second-order and Elovich are best applicable to explain the adsorption kinetics. CFS 100 has the highest adsorption capacity of 253.6 mg g⁻¹. Increment in ionic strength led to favorable adsorption which was due to the dimerization of methylene blue. Adsorption of methylene blue on the bio-silica and the composite, which was confirmed by FTIR and TEM, spontaneous and exothermic in nature. Both BSIL and the composite could be effectively reused and regenerated up to 5 cycles.

4.5 Comparative adsorption mechanism of doxycycline and Congo red using synthesized kaolinite/CoFe₂O₄ composites

4.5.1. Brief introduction

Clays are hydrous aluminosilicates broadly defined as those minerals that make up the colloid fraction of soils, sediments, rocks and water and may be composed of mixtures of fine-grained clay minerals and clay-sized crystals of other minerals such as quartz, carbonate and metal oxides [198]. The prominent ions found on the clay surface are Ca²⁺, Mg²⁺, H⁺, K⁺, NH₄⁺, Na⁺, SO₄²⁻, Cl⁻, PO₄³⁻, and NO₃⁻. The listed ions can be exchanged with other ions, yet the structure of clay mineral would not be affected [199]. Basically, clay materials fall under three important groups which are Smectite, kaolin, and mica [198]. They as well contain organic compounds, soluble salts, quartz particles, pyrite, calcite, other non-clay minerals and amorphous components [200].

Kaolinite is one of the most common clay minerals, structurally it consists of two layers, tetrahedral Si layer and octahedral Al layer which are interlinked (**Fig 4.55**), this structure is highly organized and well balanced, with little or no ionic substitution and thus low cation exchange capacity (3 to 15 meq/100 g) [200]. It has negatively charge surface and it is white. However, kaolinite has low adsorption capacity, which is as a result of the small number of exchange sites and its relatively small specific surface area [174,201].

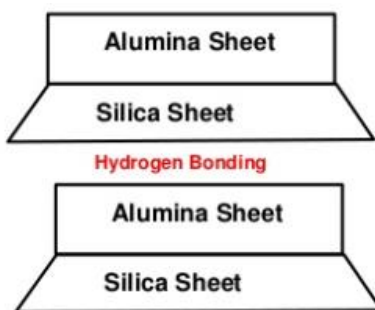


Fig. 4.56. Structure of kaolinites.

This has limited the use of kaolinites (in raw form) in comparison with montmorillonites as an adsorbent for the removal of different contaminants [202]. In view of these different

approaches have been applied to improve the adsorption capacity of kaolinites for the removal of contaminants.

Huang et al., [201], improved the efficiency of kaolinite for the adsorption of methylene by modified its surface with poly (sodium p-styrene sulfonate hydrate) (PSPSH), using a facile method combined with dopamine self-polymerization and Michael addition reaction. The results obtained by the authors showed that modification of kaolinite could effectively increase its adsorption capacity when compared with the raw kaolinite. More so, Zhang et al.,[203] prepared a modified kaolinite nanolayer from two-dimensional (2D) raw kaolin through a combination of calcination, acid leaching, and ultrasonic dispersion. The obtained nanolayers were subjected to effective modification with amino functional groups through grafting with (3-aminopropyl) triethoxysilane (APTES). Their results revealed that the chemically modified materials exhibited increased specific surface area and pore structures, and the organic modified kaolinite exhibited excellent adsorption performance for Congo red and efficient regeneration. The separation of kaolinites from solution after adsorption is another main challenge.

Therefore, introducing inorganic particles like spinel ferrites into the matrix of kaolinites could improve its adsorption capacity and enhance the ease of separation (after removal of contaminants) from aqueous solution by external magnet [204]. This process does not only reinforce the physical and chemical properties of kaolinites, it also prevents the agglomeration of inorganic nanoparticles leading the nanocomposite to have a high adsorption capacity [204]. Coprecipitation of inorganic nanoparticles in the presence of supporting materials like kaolinites helps to prevent agglomeration which could result from nanoparticles interaction [205]. Therefore, we studied the adsorption mechanism of Congo red (CR) and Doxycycline (DOX) using novel kaolinite supported cobalt ferrite calcined at 300, 500 and 700 °C. The study examined the effects of pH, ionic strength, contact time and temperature among other things on the adsorption of the CR and DOX.

4.5.2. Characterization of the synthesized nanocomposites.

FTIR spectra of KCF nanocomposites calcined at different temperatures are shown in **Fig.4.56 A**. Peaks labeled A (3700 cm^{-1}) and B (3605 cm^{-1}) which gradually decreased with increase in calcination temperature due to dehydroxylation are assigned to OH stretching of kaolinite [206]. The two peaks at 1124 and 1013 cm^{-1} (C and D respectively) were attributed to Si-O stretching. Interestingly these two peaks together with the peak at 915 cm^{-1} became broaden with an increase in temperature. The reason for broadened peaks was as a result of progressive disordering of metakaolin and the increase of the mean bond angle in the Si-O-Si network [207]. Peak 915 cm^{-1} (E), which is attributed to inner surface Al-OH deformation [208], disappeared gradually and completely (on KCF 700), which could due to dehydroxylation at a higher temperature. The bands at 698 , 541 and 476 cm^{-1} (F, G, H respectively) are characteristic of kaolinites, which are assigned to bending vibration of Al-O, Si-O-Al and Si-O, respectively. These peaks decreased with an increase in calcination temperature, whose reason has been ascribed to dehydroxylation that was accompanied by the destruction of Al-O-Si linkages of kaolinite [207]. Cobalt ferrite peak is at 594 cm^{-1} .

XRD patterns of the nanocomposite are shown in **Fig. 4.56 B**. The pattern of KCF-100 is predominant of several peaks of kaolinite mineral, which matched with card JCPDS 80-885, with few peaks of alpha-quartz. Meanwhile, the pattern of KCF-700 is dominated by peaks CoFe_2O_4 of card number JCPDS 22-1086. An increase in calcination temperature resulted in to decrease in intensity of peaks 001, 110 and 002 related to kaolinites up till $500\text{ }^\circ\text{C}$. The observation is stated to be as result of a decrease in crystal order of the mineral [207]. The peak 011 related to α -quartz was not affected by calcination. Noteworthy again is the disappearance of kaolinite peaks at the diffractogram of KCF-700. This behavior is ascribed to structural damage of kaolinite ($\text{Al}_2\text{O}_3 \cdot 2\text{SiO}_2 \cdot 2\text{H}_2\text{O}$) through dehydroxylation which resulted to the octahedral layer of kaolinite to reorganize to meta kaolinite ($\text{Al}_2\text{O}_3 \cdot 2\text{SiO}_2$) [209]. This confirmed the results of FTIR that has been earlier discussed. While temperature brought structural damage to kaolinite, it leads to the appearance of CoFe_2O_4 peaks. Calcination has a positive effect on the crystal growth of cobalt ferrite. The itemized d-spacing of the major peaks are shown in **Table 22**.

There is a decrease in d_{002} of kaolinite due to the reorganization of the octahedra layer, while d_{101} of α -quartz remains unchanged. The d_{311} of sample KCF-100 related to cobalt ferrite is lower than calcined samples, which could be as a result of a certain movement of Co^{2+} ions from octahedral to the tetrahedral sites, and equivalent transfer of Fe^{3+} ions from tetrahedral to octahedral sites, which was initiated by thermal treatment.

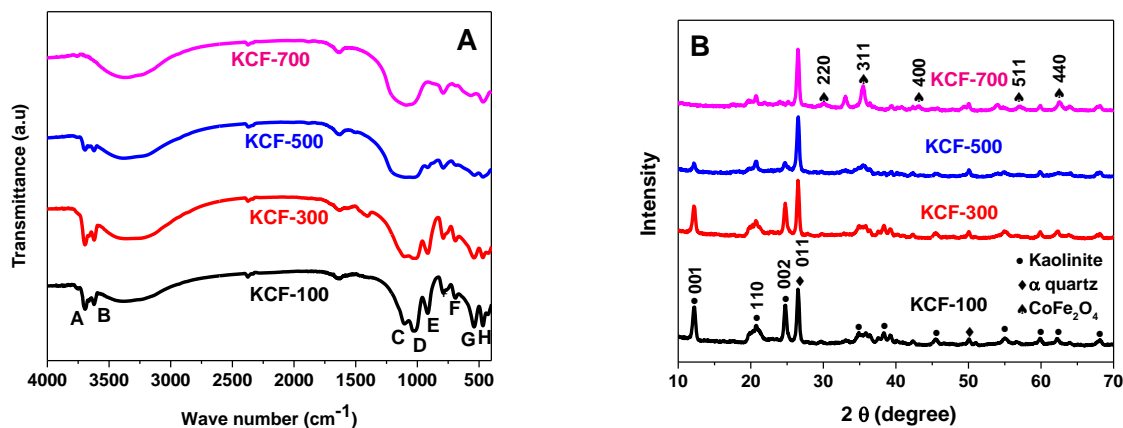


Fig.4.56. FTIR spectra (A) and XRD patterns (B) of KCF nanocomposites calcined at different temperatures.

Table 22. d-spacing of the composite major peaks at different temperatures.

Samples	d_{001} (Å)	d_{110} (Å)	d_{002} (Å)	d_{101} (Å)	d_{311} (Å)
KCF-100	7.253	6.057	7.181	4.748	8.344
KCF-300	7.260	6.080	7.183	4.748	8.392
KCF-500	7.263	6.087	7.104	4.747	8.395
KCF-700				4.749	8.394

Scanning electron microscopy (SEM) images and Energy-dispersive X-ray spectroscopy (EDS) spectra of the synthesized KCF nanocomposites are shown in **Fig. 4.57**. Comparing the images of all the samples, there is no distinct difference in their morphology, likewise in their EDS spectra. Elements present are from kaolinite and cobalt ferrite, devoid of any impurities. More information was obtained from TEM images shown in **Fig. 4.58**.

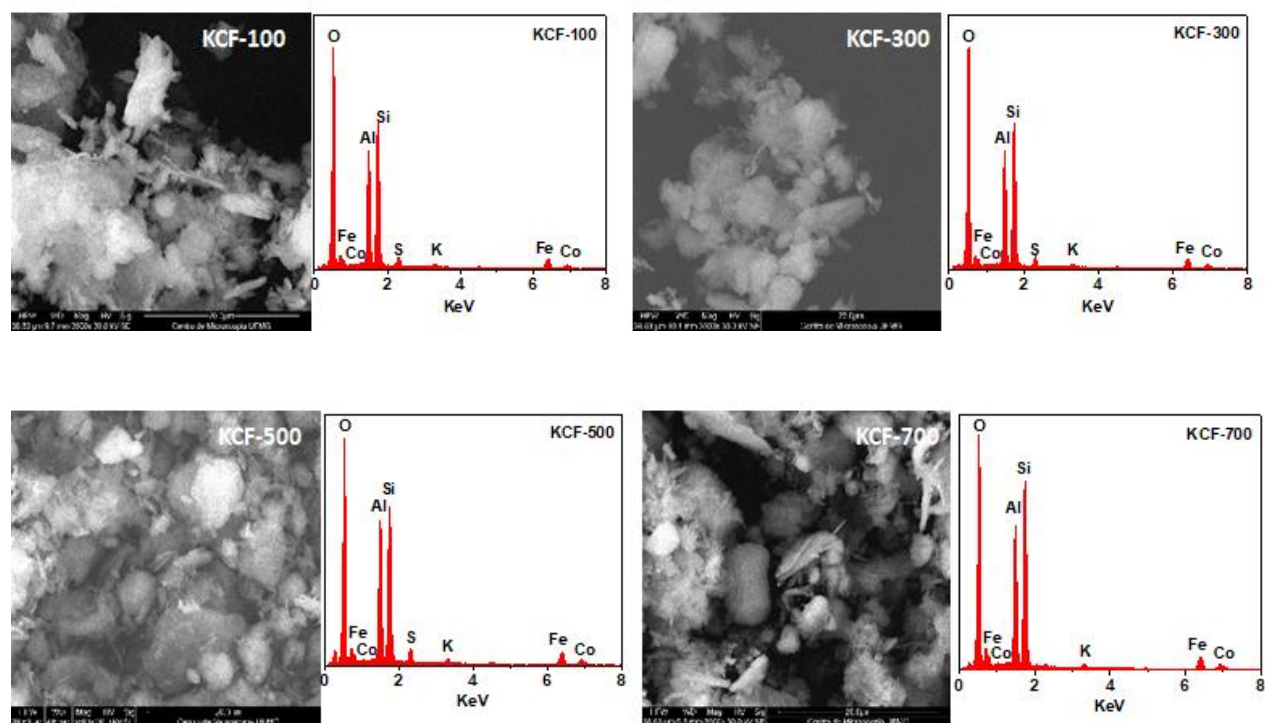


Fig.4.57. SEM images and EDS spectra of KCF nanocomposites.

Transmission electron microscopy images of KCF-100 and 700 are presented in **Fig. 4.57**. The images showed a lamellar structure of kaolinite that supported cobalt ferrite. The presence of kaolinite increases the dispersion of cobalt ferrite within the matrix. KCF-700 showed distinct particles of cobalt ferrite due to crystal growth. This is in accordance with the XRD diffractogram shown in **Fig. 4.56 B**. The images also show that the presence of kaolinite prevents agglomeration of cobalt ferrite nanoparticles, leading to smaller sizes in comparison with the cobalt ferrite that synthesized without kaolinite.

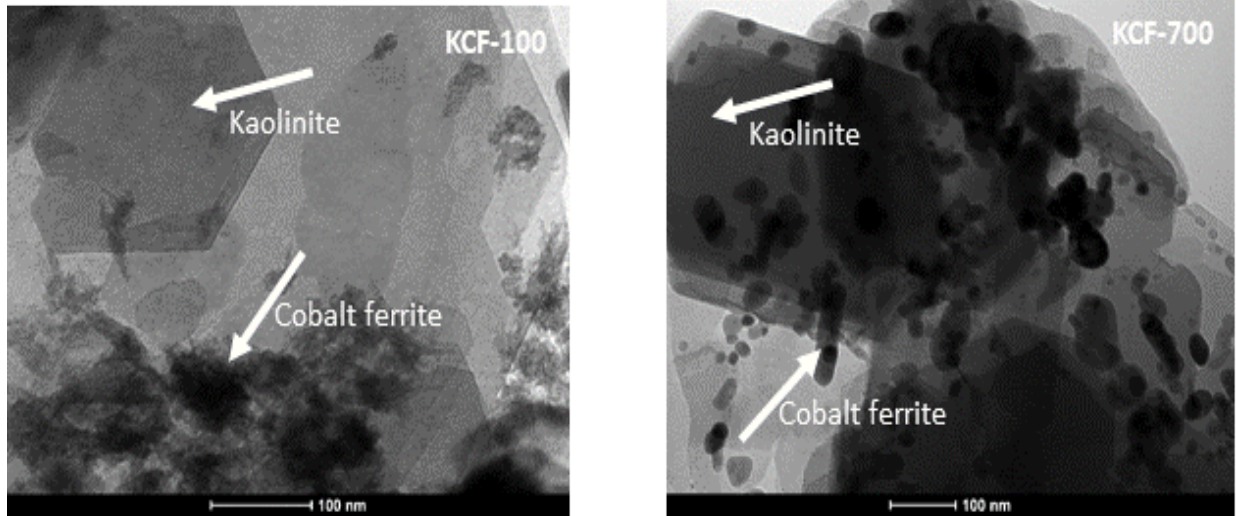


Fig.4.57. TEM images of KCF-100 and 700.

The result of magnetization versus applied field at 300 K and N_2 adsorption and desorption of the KCF-100 and 700 are shown in **Fig. 4.58 A and B** respectively. The magnetic saturation of KCF-700 is more than KCF-100 due to increase in crystallite size. Amount ($cm^3 g^{-1}$) of nitrogen gas that was adsorbed by KCOF-100 is more than that of the corresponding KCOF-100. This is expected due to shrinkage of pores due to calcination. BET specific surface area of KCOF-100 and 700 are 24 and $11 m^2 g^{-1}$ respectively. Although relatively low, but highly effective for the removal of both studied dye and the antibiotic.

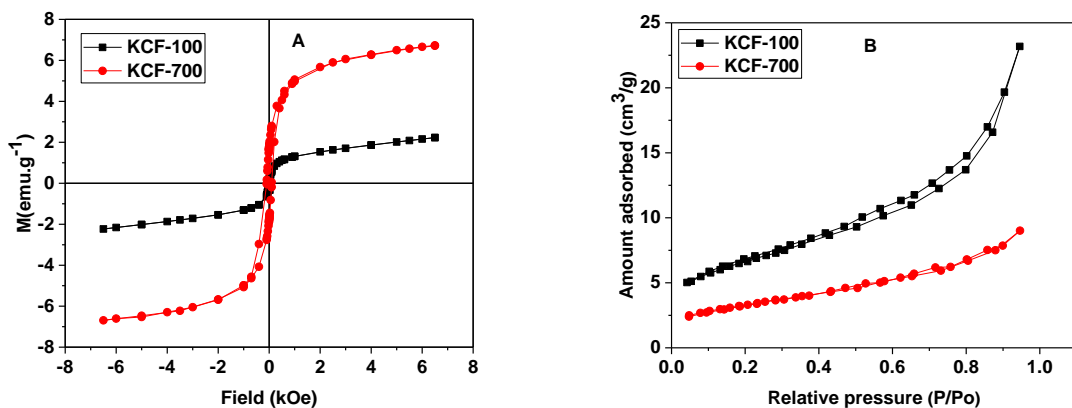


Fig.4.58: Magnetization versus applied field at 300 K (A) and N_2 adsorption and desorption (B) of the KCF-100 and 700.

4.5.3. Effect of pH and ionic strength on the removal of Congo red and doxycycline

One of the variables that could affect the interaction between adsorbate and adsorbent is the solution pH. It influences the surface charge of the adsorbent and the ionization of the adsorbate. However, adsorption could as well be influenced by hydrophobic interaction, π - π interaction, n- π interaction, hydrogen bond among others [190]. In view of this, we investigated the influence of pH on the adsorption capacity of the synthesized nanocomposites (KCF-100 and KCF-700) for the removal of CR and DOX. The results of this study are presented in **Fig. 4.59**. Likewise, the surface charge of KCF-100 was studied at the adjusted pH of 2 to 10 (**Fig. 4.60**). Surface charge of the nanocomposite at pH 2 is positive while from pH 4 – 10, it exhibits a negative charge. The adsorption of both CR and DOX is not consistent with an increase in solution pH. Agglomeration of Congo red was observed at pH 2 before adsorption and due to this, the result at this pH could not be reported. This is in accordance with the report of Mozumder and Islam [210] that Congo red agglomerated at low pH and then settle down.

The amount (mg g^{-1}) of CR that was adsorbed at pH 6 and 8 were higher than 4 and 10. The mechanism of adsorption does not seem to be influenced by electrostatic interaction. Congo red being a dipolar molecule will exist in the form of positive charge (cationic) in acidic pH <5.5 and negative charge (anionic) in alkaline pH > 5.5 [211]. Electrostatic attraction between the cationic form of the dye and negative charge surface of the nanocomposites could be responsible for the adsorption at pH at 3 and 4, meanwhile at 6 and 8 that one should expect electrostatic repulsion between the anionic form of the dye and negative charge surface of the adsorbent, this did not occur, occurring at pH 10 and 12. This implies that the adsorption of CR on the nanocomposites at pH 6 and 8 is not influenced by the electrostatic interaction. This then led us to further investigation on the adsorption behavior of CR in the presence of ionic strength to ascertain the contribution of hydrophobic interaction to the adsorption process. When adsorption is a result of electrostatic attraction, an increase in ionic strength can diminish the attraction, while it can increase the attraction in the case of electrostatic repulsion [191]. The result (effect of ionic strength on the adsorption of CR) as presented in **Fig. 4.61 A**, shows that the addition of NaCl (increase in ionic strength) leads to an increase in the adsorption of the dye. This phenomenon has been credited to an increase in hydrophobic interaction

(attraction between the non-polar groups of the dye with a non-polar group of KCF nanocomposite) in which shielding of intermolecular repulsion between the dye and the nanocomposite occurs [212,213]. This result is very advantageous during adsorption process in textile industries where their wastewater contains a high amount of salt which is used during pre and post-treatment of fabrics [213].

Considering the influence of pH on the adsorption of DOX, the result was not consistent with pH as well. DOX being an amphoteric molecule has different functional groups that ionize into cations, anions and zwitterion at different pH [161]. This makes the electrostatic interaction between its molecule and the nanocomposites to be complex and not consistent with pH. The lower amount of DOX (mg g^{-1}) that was adsorbed at pH 2 shows that there is a strong electrostatic repulsion between the positively charge KCF nanocomposites and cationic form of DOX. It is documented that at $\text{pH} \leq 3$, DOX is protonated, which makes it to exists in a cationic form (DOX^+) [162]. Meanwhile between pH 4 – 9 it exists as zwitterions which implies that electrostatic interaction is not the mechanism of adsorption within the range of these pHs. However, at pH 10, some of the functional groups ionized to anionic form, which resulted to slight electrostatic repulsion. The result gotten from the effect of ionic strength shows that the adsorption of DOX is not influenced by electrostatic interaction and that hydrophobic interaction may not be directly involved in the adsorption process. The alarming sharp difference between the amount adsorbed on KCF-100 and KCF-700 implies that the specific surface area of the nanocomposite plays a role in the adsorption of DOX. The case was not the same for the adsorption of CR. Further studies were done at pH 6 for both contaminants. The structures of Congo red and doxycycline are shown in **Fig. A4**

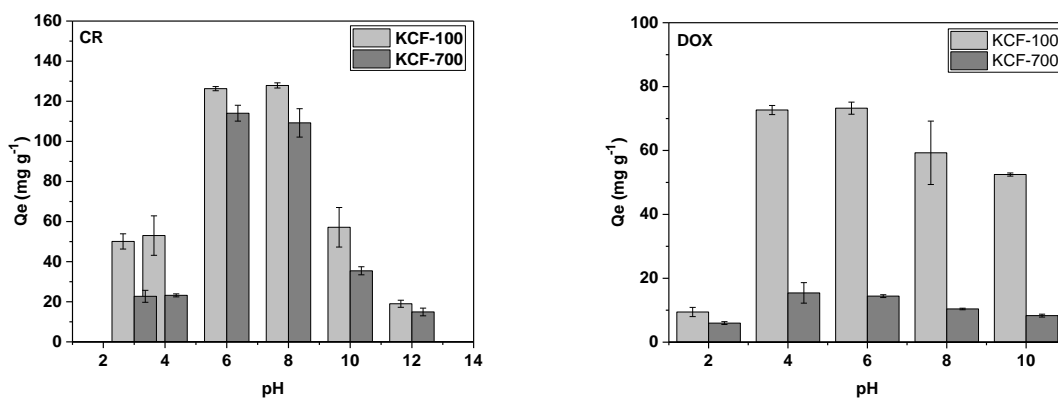


Fig. 4.59: Effect of pH on the adsorption of CR and DOX (10 mg of the adsorbent and 100 ppm of the adsorbate)

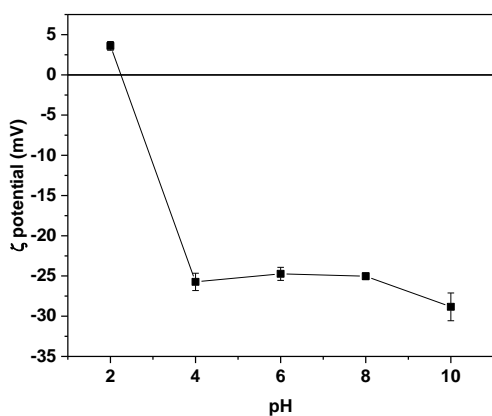


Fig. 4.60: Zeta potential of KCF-100 (a representative of the nanocomposite).

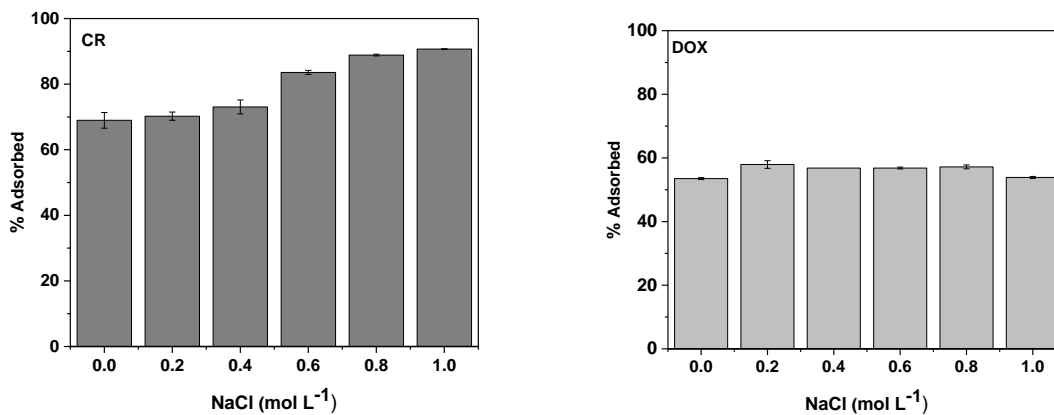


Fig. 4.61: Effect of ionic strength on the adsorption of CR and DOX.

4.5.4. Effect of adsorbent dose on the adsorption of CR and DOX on KCF nanocomposites

One of the importance of the study on adsorbent dosage is to avoid wastage of material after equilibrium has been reached with respect to the amount of the adsorbent that would be used. The results obtained from the effect of dosage for both CR and DOX are presented in **Fig. 4.62**. Examining the impact of dosage variation on the amount of CR that was adsorbed from the initial 100 ppm concentration of CR, an insignificant amount was adsorbed at 2 and 4 mg of the nanocomposite. There is a sharp increase in the amount adsorbed from 6 to 8 mg dosage, whereas there is no significant difference in the amount adsorbed within the range of 8 and 10 mg dosage. In the case of DOX, the amount increased from 25 to 50% when the dosage (KCF-100) was increased from 2 to 6 mg. It further increased gradually until it reached equilibrium at 15 mg of the nanocomposite, meanwhile, KCF-700 for the absorption of DOX did not attain an equilibrium within the dosage variation. 86% was adsorbed from 100 ppm CR solution when 10 mg of the nanocomposite was used, while 68% was adsorbed from 100 ppm of DOX when 20 mg of the adsorbent was used at room temperature. The implication is that the adsorption of CR was more favorable at the room temperature than DOX and that the nanocomposite has a better affinity for CR than DOX. Generally, an increase in adsorbent dosage, which implies the availability of more active sites for the interaction between the contaminants (DOX and CR) and KCF nanocomposite leads to an increase in percentage removed from the initial concentration of the dye and antibiotic.

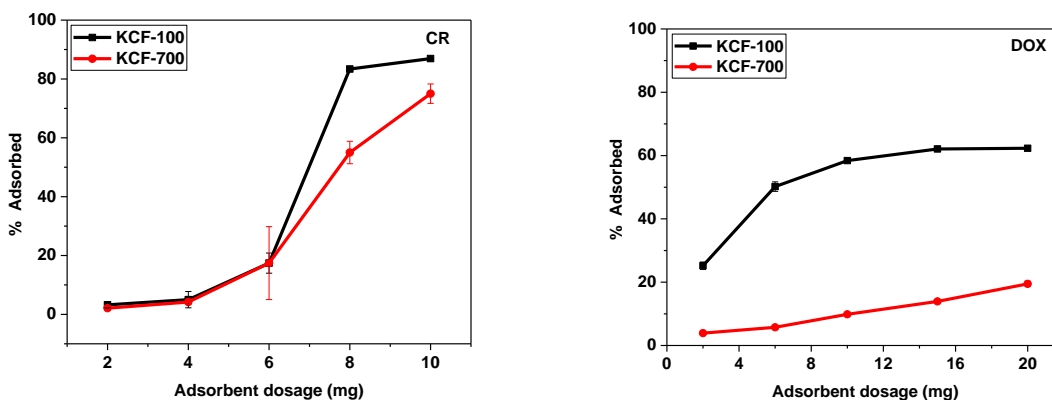


Fig. 4.62: Effect of adsorbent dosage on the adsorption CR and DOX.

4.5.5. Contact time and adsorption kinetic of CR and DOX on KCF nanocomposites

The results obtained from the effect of contact time on the adsorption of CR and DOX on KCF nanocomposites are shown in **Fig. 4.63**. This study is important for the purpose of knowing the equilibrium time for the adsorption process. Firstly, for the adsorption of CR, the amount adsorbed within the first 1 h of contact time was almost half of the total amount adsorbed during the entire duration (12 h). This is due to the collision of CR molecules in the solution which results to their rapid migration to the surface of the nanocomposite hereby leading to high adsorption. After 1 h, the adsorption of CR increases steadily and slowly until equilibrium was attained at 12 h. Since reasonable quantity was adsorbed within the first 1 h, the collision of CR molecules would have reduced, more so, less active sites are available for the unadsorbed molecules. This then could result in to slow adsorption rate. The adsorption of DOX within the first 1 h was not as rapid as that of CR. However, the adsorption of DOX attained equilibrium at 12 h. There is a sharp difference in the amount of DOX that was adsorbed by KCF-100 comparing to KCF-700. This is due to the influence of specific surface area; this was not the case for CR.

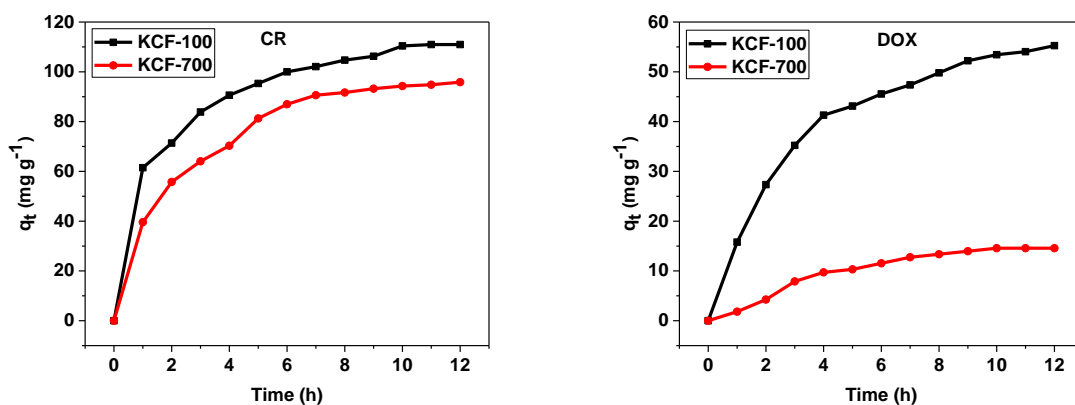


Fig. 4.63: Effect of contact time on the adsorption of CR and DOX on KCF nanocomposites.

For a better understanding of the adsorption kinetics, data from the effect of contact time were used to plot nonlinear form of pseudo-first-order and pseudo-second-order kinetic models.

Presented in **Fig. 4.64** and **4.65** are the plots of the kinetic models. The best model has been described as the one whose values of R^2_{adjusted} is near unity and has the lowest standard deviation (SD). Looking at the parameters of the two models listed in **Table 23**, it is obvious that pseudo-second-order is the best to describe the adsorption kinetic. In view of this, is it more reliable to relate q_e calculated from pseudo-second-order to the experimental q_e . Although is it well reported in the literature to ascribe chemisorption as adsorption that fits to pseudo-second-order model, this should not be affirmed without confirmation from other techniques, such as FTIR. Due to this, FTIR analysis was onducted after adsorption.

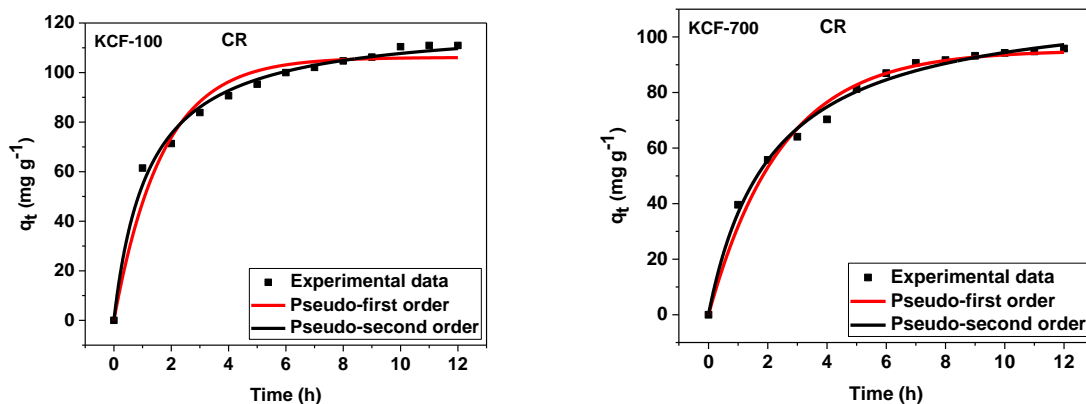


Fig. 4.64: Kinetic plots of the adsorption of CR on KCF nanocomposites.

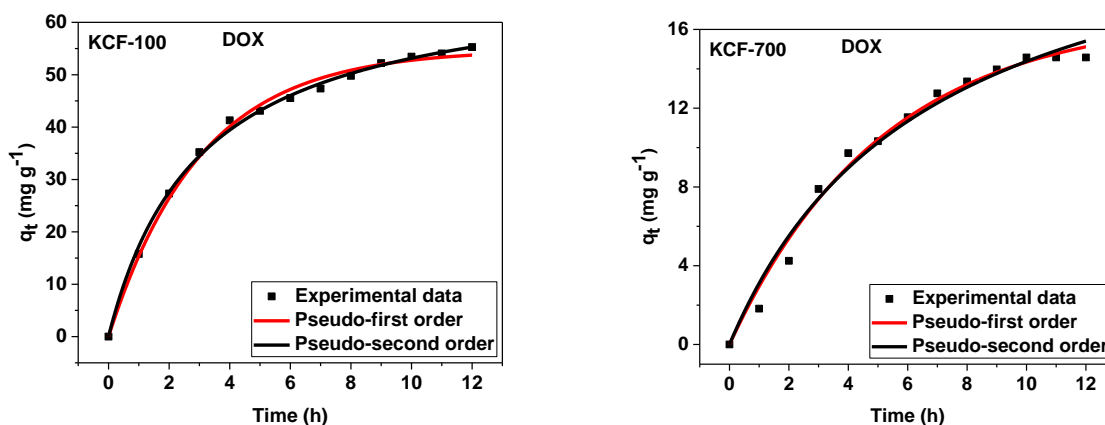


Fig. 4.65: Kinetic plots of the adsorption of DOX on KCF nanocomposites.

Table 23. Parameters for kinetics models of the adsorption of CR and DOX on KCF composites.

Model	Parameters	KCF-100	KCF-700
Congo red			
Pseudo-first order	q_e (mg g ⁻¹)	106.11	96.19
	k_1 (min ⁻¹)	0.5939	0.4067
	R^2_{adjusted}	0.9648	0.9862
	SD (mg g ⁻¹)	5.76	3.32
Pseudo-second order	q_e (mg g ⁻¹)	120.74	114.39
	k_2 (g mg ⁻¹ min ⁻¹)	0.0068	0.0041
	R^2_{adjusted}	0.9914	0.9935
	SD (mg g ⁻¹)	2.84	2.27
Doxycycline			
Pseudo-first order	q_e (mg g ⁻¹)	54.80	16.74
	k_1 (min ⁻¹)	0.329	0.194
	R^2_{adjusted}	0.9949	0.9863
	SD (mg g ⁻¹)	1.18	0.588
Pseudo-second order	q_e (mg g ⁻¹)	69.16	24.04
	k_2 (g mg ⁻¹ min ⁻¹)	0.0047	0.0061
	R^2_{adjusted}	0.9974	0.9801
	SD (mg g ⁻¹)	0.839	0.695

4.5.6 Adsorption isotherm of CR and DOX on KCF nanocomposites

The study of adsorption isotherm helps to know the adsorption capacity of the adsorbents (KCF 100 and 700) at various concentrations of the adsorbates (CR and DOX) at a fixed temperature of the system. In addition, the ratio of the quantity adsorbed and the amount remaining in the solution at equilibrium is also known. The nearness of R^2 to unity informs whether the experimental data obtained conforms to Langmuir model or not

The curve fit of Langmuir and Freundlich isotherms for the two targeted contaminants (CR and DOX) are presented in **Fig. 4.66 – 4.69**.

The parameters of both isotherms are listed in **Table 24 and 26**. As shown in these tables, the adsorption capacity of CR decreases with the increase in temperature, with maximum

adsorption of 547.12 and 391.61 mg g⁻¹ obtained for KCF 100 and 700 respectively at 298 K. This is a typical exothermic adsorption process in which increase in temperature do not favors the adsorption of the adsorbate on the adsorbent. This occurred because as temperature increases, the adsorbed CR molecules gain kinetic energy which made them to overcome forces of adsorption, due to this, desorption of the adsorbed molecule occurred leading to decrease in adsorption capacity [172].

In the case of DOX, the adsorption capacity increases with an increase in the temperature of the system, with maximum adsorption capacity recorded as 399.74 and 220.47 mg g⁻¹ for KCF-100 and 700, respectively at 333 K. This is opposite to the result obtained for CR. Now, for the adsorption capacity of DOX to have increased as temperature increases, means that the favorable intermolecular forces between DOX and KCF nanocomposites become stronger than those between DOX and water, leading to favorable adsorption with an increase in temperature. More so, it could result from the increase in the mobility of DOX, acquiring enough energy to undergo an interaction with KCF nanocomposites [214] In the industrial application of KCF nanocomposites for the adsorption of CR, cost of energy could be eliminated since it does not involve an increase in temperature. However, this would not be the scenario for DOX. Meanwhile, this is not a limitation for the application of KCF nanocomposites for the adsorption of DOX. The majority of adsorption studies on DOX reported that it was favorably adsorbed at a higher temperature.

Based on the values of adjusted R² and standard deviation (SD), the experimental data for the adsorption of the two contaminants is appropriately described by the model prescribed by Langmuir, which implies that the coverage of CR and DOX on the homogeneous surface of the synthesized KCF nanocomposite is monolayer and each adsorbate does not interact with the neighboring one. The adsorption capacity of our materials for the adsorption of CR and DOX are compared (**Table 26**) with other adsorbents that were reported in the literature. The synthesized KCF nanocomposite performed better than some of the materials reported in the literature

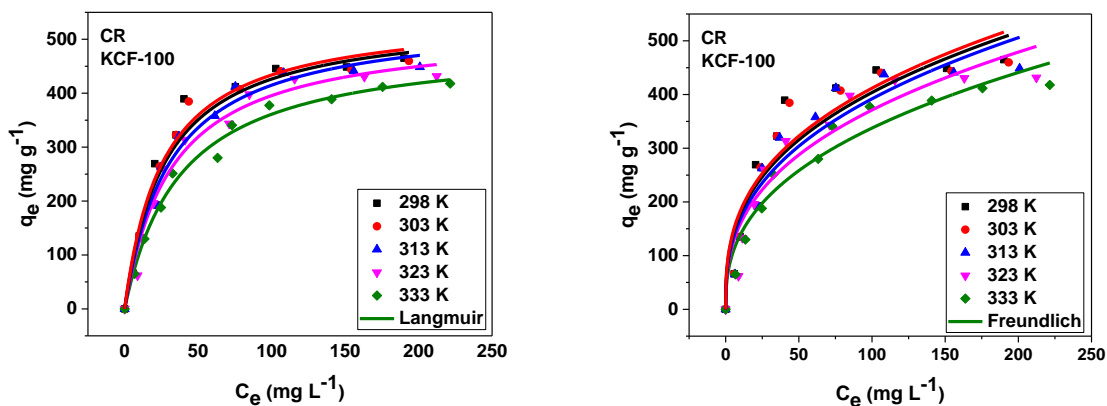


Fig.4.66: Langmuir and Freundlich plots for the adsorption of CR on KCF-100.

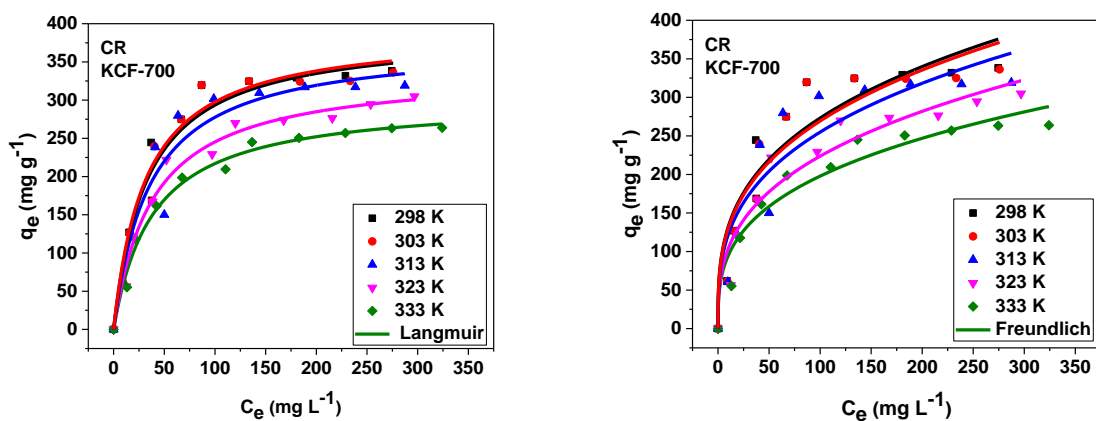


Fig.4.67: Langmuir and Freundlich plots for the adsorption of CR on KCF-700.

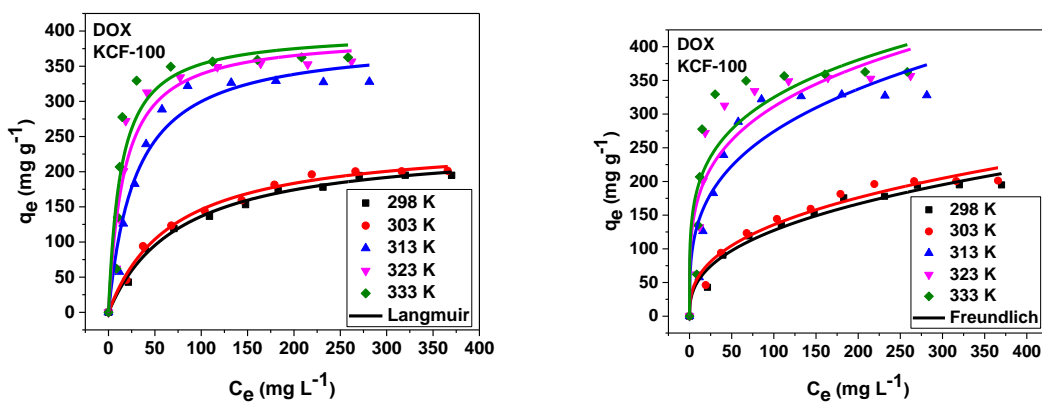


Fig.4.68: Langmuir and Freundlich plots for the adsorption of DOX on KCF-100.

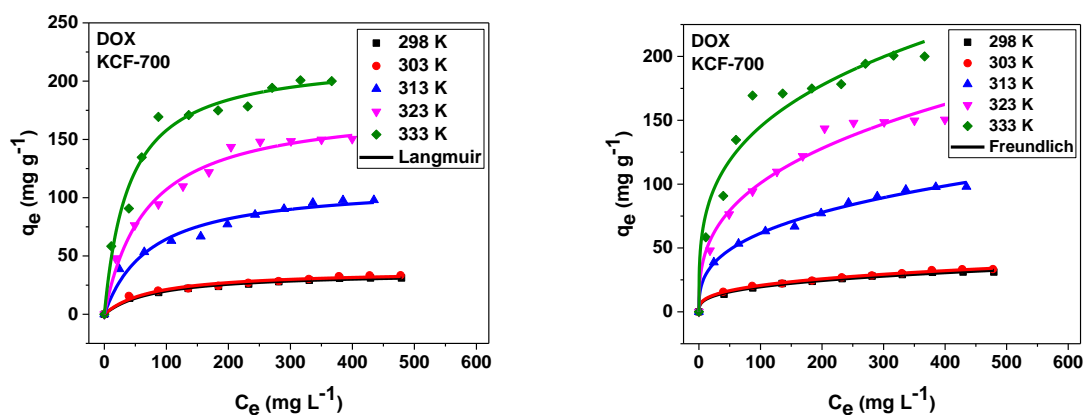


Fig.4.69: Langmuir and Freundlich plots for the adsorption of DOX on KCF-700. **Table 24.**

Langmuir and Freundlich isotherms parameters for the adsorption of CR.

CR KCF-100					
	298 K	303 K	313 K	323 K	333 K
Langmuir					
q_{\max} (mg g ⁻¹)	547	543	541	520	497
K_L (L mg ⁻¹)	0.038	0.037	0.033	0.031	0.026
R^2_{adjusted}	0.9711	0.9711	0.9796	0.9771	0.9888
SD (mg g ⁻¹)	32.29	27.75	22.94	23.49	15.38
Freundlich					
K_F (mg g ⁻¹ (mg L ⁻¹) ^{-1/n_F})	81.47	78.70	72.07	68.16	57.06
n_F	2.84	2.81	2.71	2.7	2.59
R^2_{adjusted}	0.8848	0.8954	0.9098	0.9084	0.9480
SD (mg g ⁻¹)	56.14	52.80	48.24	46.91	33.26
CR KCF-700					
Langmuir					
q_{\max} (mg g ⁻¹)	391	389	375	339	300
K_L (L mg ⁻¹)	0.032	0.03	0.028	0.026	0.025
R^2_{adjusted}	0.9613	0.9612	0.9246	0.9785	0.9873
SD (mg g ⁻¹)	23.82	23.62	31.95	15.04	10.20
Freundlich					
K_F (mg g ⁻¹ (mg L ⁻¹) ^{-1/n_F})	63.86	62.62	58.3	48.13	45.33
n_F	3.16	3.15	3.12	2.99	3.12
R^2_{adjusted}	0.8866	0.8825	0.8557	0.9297	0.9383
SD (mg g ⁻¹)	40.78	41.15	44.21	27.21	22.53

Table 25. Langmuir and Freundlich isotherms parameters for the adsorption of DOX.

DOX KCF-100					
	298 K	303 K	313 K	323 K	333 K
Langmuir					
q_{\max} (mg g ⁻¹)	240	246	388	395	400
K_L (L mg ⁻¹)	0.013	0.015	0.034	0.059	0.075
R^2_{adjusted}	0.9919	0.9922	0.9538	0.9222	0.8854
SD (mg g ⁻¹)	6.12	6.029	25.92	36.18	45.16
Freundlich					
K_F (mg g ⁻¹ (mg L ⁻¹) ^{-1/n_F})	21.24	24.3	69.34	97.57	113.61
n_F	2.57	2.67	3.35	3.97	4.38
R^2_{adjusted}	0.9638	0.9618	0.8503	0.8221	0.7808
SD (mg g ⁻¹)	12.54	13.54	46.70	54.67	62.49
DOX KCF-700					
Langmuir					
q_{\max} (mg g ⁻¹)	36	37	112	179	220
K_L (L mg ⁻¹)	0.012	0.013	0.014	0.015	0.026
R^2_{adjusted}	0.9914	0.9727	0.9665	0.9829	0.9753
SD (mg g ⁻¹)	0.87	1.63	5.53	6.48	10.34
Freundlich					
K_F (mg g ⁻¹ (mg L ⁻¹) ^{-1/n_F})	4.42	4.75	12.84	20.56	37.86
n_F	3.09	3.13	2.93	2.89	3.43
R^2_{adjusted}	0.9948	0.9966	0.9937	0.9751	0.9471
SD (mg g ⁻¹)	0.68	0.57	2.39	7.82	15.14

Table 26: Comparison of the maximum monolayer adsorption (q_{max}) of different adsorbents for the removal of R and DOX.

Contaminants	Adsorbents	q_{max} (mg g ⁻¹)	References
Congo red	GM III-5	211.1	[215]
	Activated carbon	6.72	[216]
	Water nut modified carbon	38.8	[217]
	Reagent NiO nanoparticles	39.7	[218]
	Magnetic core–manganese oxide shell	43	[219]
	FSP	39.28	[220]
	ZnO@Ze Composite	161.3	[55]
	NMFO-10	129.06	[221]
	Ni(OH) ₂	384.6	[222]
	KCF-100	547	This work
KCF-700	391	This work	
Doxycycline	Iron loaded sludge biochar	128.98	[223]
	Cu(II) impregnated biochar	93	[54]
	MFO-0.5-700	308.51	[161]
	Lignin xanthate resin–bentonite clay	438.75	[165]
	Electro-generated adsorbents	31.35	[166]
	MIL- 53(Fe)/Fe ₃ O ₄	477	[167]
	NaY zeolite	252.12	[168]
	Rice straw biochars	170.36	[169]
	KCF-100	400	This work
	KCF-700	220	This work

4.5.7. Thermodynamic of adsorption of CR and DOX on KCF nanocomposites

In order to further establish the response of the adsorption of CR and DOX to changes in temperature, thermodynamic parameters such as changes in Gibbs-free energy (ΔG°), changes in enthalpy (ΔH°) and changes in entropy (ΔS°) were calculated and itemized in **Table 27 and 28**.

The values of ΔH° is negative for the adsorption of CR and positive for DOX, showing exothermic and endothermic adsorption processes, respectively. This is in accordance with the adsorption capacity from Langmuir isotherm, which is inversely and directly proportional to

increment in temperature for CR and DOX, respectively. While the forces of adsorption of CR on the surface of KCF nanocomposites becomes weaker, not being favored by temperature, it became stronger for the adsorption of DOX. Despite different adsorption behavior of CR and DOX to changes in temperature, negative values of ΔG° obtained from their adsorption studies confirms that the adsorption process of CR and DOX is feasible and spontaneous. Positive ΔS° for the adsorption of the contaminants implies that there is an increase in the randomness at the solid/solution interface during the process of adsorption [224].

Table 27: Thermodynamic parameters for CR

Adsorbents	ΔH° (kJ mol ⁻¹)	ΔS° (J K ⁻¹ mol ⁻¹)	ΔG° (kJ mol ⁻¹)				
			298 K	303 K	313 K	323 K	333 K
KCF-100	-8.61	61.66	-26.99	-27.29	-27.91	-28.53	-29.14
KCF-700	-5.76	57.27	-22.84	-23.12	-23.70	-24.27	-24.84

Table 28: Thermodynamic parameters for DOX.

Adsorbents	ΔH° (kJ mol ⁻¹)	ΔS° (J K ⁻¹ mol ⁻¹)	ΔG° (kJ mol ⁻¹)				
			298 K	303 K	313 K	323 K	333 K
KCF-100	44.77	222.11	-21.41	-22.52	-24.75	-26.97	-29.19
KCF-700	122.97	15.53	-21.11	-21.72	-22.95	-24.18	-25.41

4.5.8 FTIR after adsorption and mechanism of adsorption of CR and DOX on KCF nanocomposites

FTIR spectra of CR, DOX and KCF-100 after adsorption are presented in **Fig. 4.70**. Starting with CR, the peak at 3428 cm^{-1} is due to the N-H stretching of primary amine, while the peaks at 1587 cm^{-1} is for N=N stretching vibration of azo group, 1372 cm^{-1} is for C-N bending, the peak at 1186 and 1036 cm^{-1} is due to asymmetric vibration of S-O ($\text{SO}_3\text{-H}$) group [225,226]. The shaded portion A shows alteration from broad peak to almost sharp peak at 3463 cm^{-1} which could possibly be due to hydrogen bond between Os from KCF nanocomposite and Hs from NH_2 group of CR. Likewise, also the shaded portion B on the spectrum of KCF-100 + CR after adsorption shows the presence of new peaks, more so the two peaks at 1124 and 1013 cm^{-1} at KCF-100 became one sharp peak after adsorption. This implies that there is a strong interaction between CR and the nanocomposite, possibly a chemical interaction.

Analyzing the major peaks on the DOX, the broad peak at 3475 and 3315 cm^{-1} are assigned to the phenolic -OH stretching and amino group, respectively, while 2920 cm^{-1} is attributed to -CH asymmetric stretching. The band at 1675 cm^{-1} is due to the presence of C=O, while the peak at 1462 cm^{-1} is attributed to C-C [161]. The shaded portion could also infer interaction between oxygens from the nanocomposite and hydrogens from the phenolic and amino group of DOX resulting to hydrogen bond. In addition, there is presence of a sharp peak at 1636 cm^{-1} that corresponds to C=O, implying there is an interaction between oxygens on the surface of the nanocomposites and the aromatic rings of DOX which lead to n- π interaction [173].

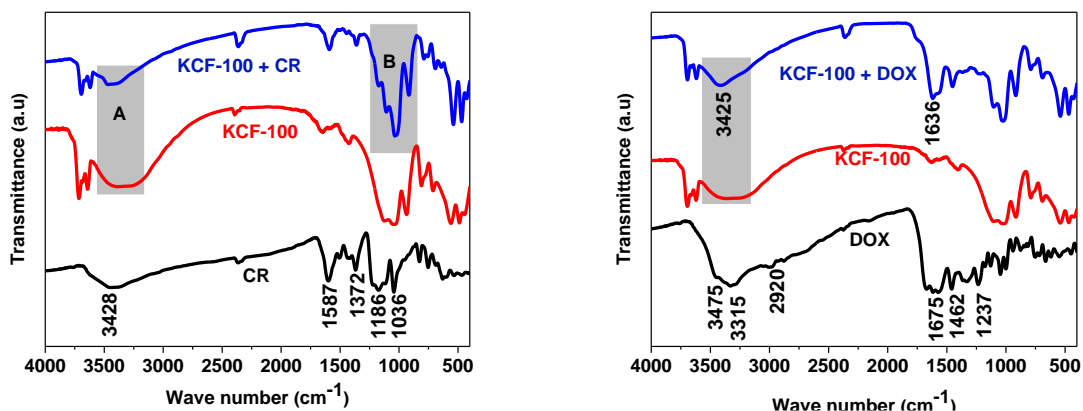


Fig. 4.70: FTIR spectra of before and after adsorption of CR and DOX.

Based on the result obtained from the pH studies, ionic strength and FTIR, the mechanism of adsorption of Congo red on KCF nanocomposites is mainly due to hydrogen bond and hydrophobic interaction, while that of doxycycline is due to n- π interaction and hydrogen. This is summarized in **Fig 4.71**.

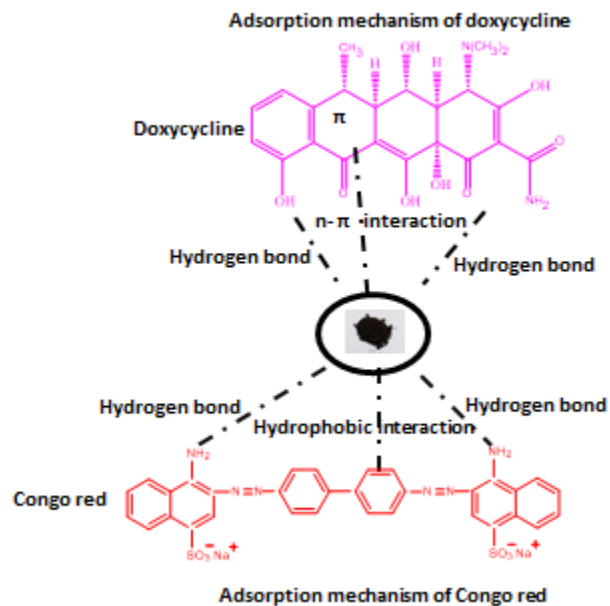


Fig. 4.71: Adsorption mechanism of CR and DOX on KCF nanocomposites

4.5.10 Conclusion

Comparative adsorption mechanism of doxycycline (DOX) and Congo red (CR) using synthesized kaolinite supported CoFe_2O_4 (KCF) nanoparticles have been successfully carried out. KCF nanocomposites despite having low specific surface areas (KCF-100: 24 mg g^{-1} , KCF-700: 11 mg g^{-1}), showed better adsorption capacity for DOX and CR when compared with other adsorbents in the literature. KCF-100 performed better than KCF-700 for the removal of the two contaminants. Basically, the adsorption of the two contaminants was not influenced by electrostatic interaction, but rather by hydrogen bond and $n-\pi$ interaction for DOX, while that of CR was as a result of hydrophobic interaction and hydrogen bond. Calcination temperature up to $700 \text{ }^\circ\text{C}$ resulted to structural damage of kaolinite ($\text{Al}_2\text{O}_3 \cdot 2\text{SiO}_2 \cdot 2\text{H}_2\text{O}$) leading to the formation of meta kaolinite ($\text{Al}_2\text{O}_3 \cdot 2\text{SiO}_2$), meanwhile, it was favorable for the formation of CoFe_2O_4 with the appearance of distinct peaks. Monolayer maximum adsorption capacity of KCF-100 (as prepared) nanocomposites for CR, 547.12 mg g^{-1} at 298 K was more than that of DOX, 399.98 mg g^{-1} at 333 K . Adsorption isotherm conformed with Langmuir, while the kinetic followed pseudo-second-order. Thermodynamics studies confirmed that the adsorption contaminants are feasible and spontaneous. The adsorption of CR is exothermic while that of DOX is endothermic.

4.6 Enhancement of adsorption capacity of kaolinite through spray drying and surface modification process for adsorption of methylene blue

4.6.1 characterization of raw, modified and spray dried kaolinite

The XRD patterns of raw kaolinite (RK), surface modified kaolinite (SMK) and spray dried kaolinite (SDK) are shown in **Fig A5**. The main mineral components of the studied clay are the kaolinite ($\text{Al}_2\text{Si}_2\text{O}_5(\text{OH})_4$) and alpha-quartz (SiO_2). The peaks at $2\theta = 12.3^\circ$ and 24.7° correspond to the (001) and (002) planes of kaolinite (Joint Committee on Powder Diffraction Standards (JCPDS) card number 80-885), The SDK diffractogram presents peaks related to alpha-quartz less intense due to the decrease of these particles. The intensity of the peaks 001 and 002 related to kaolinite did not change, showing that the size of the kaolinite plates does not decrease. Surface modification did not affect the diffractogram as well.

FTIR of the materials is presented in **Fig A6**. The peaks related to kaolinite has been earlier discussed. There is no notable difference in the spectra of RK and SDK. However, there are some new peaks on the spectrum of SMK. The sharp peak at 1045 cm^{-1} on the modified clay is assigned to Si–O–C stretching. The bands due to 2924 and 2841 cm^{-1} exhibited by the surface modified clay are due to CH_3 asymmetric stretching and CH_2 symmetric stretching.

Fig. 3.72 A shows the nitrogen adsorption-desorption isotherm of RK, SMK and SDK, whose curves are characteristic of macroporous materials. The formed mesoporous are due to the interstices of the agglomerated material. The specific surface area of the materials using BET theory is as follows 14 , 35 and $102\text{ m}^2\text{ g}^{-1}$ respectively. As the raw clay is formed by agglomerate particles, the spray drying process separates part of these agglomerates producing a particulate material with a higher specific surface area. The surfactant used to modify the raw kaolinite also increased the interaction between its surface and nitrogen gas hence leading to the increased in specific surface area in comparison with the raw kaolinite. These two processes (spray drying and surface modification) have successfully resulted to increase in specific surface area. These results are confirmed by the apparent densities of RK, SMK and SDK of $0.824 \pm$

0.018, 0.815 ± 0.015 and 0.282 ± 0.007 g cm³, respectively, whose volumes measured are shown in **Fig. 4.72 B**.

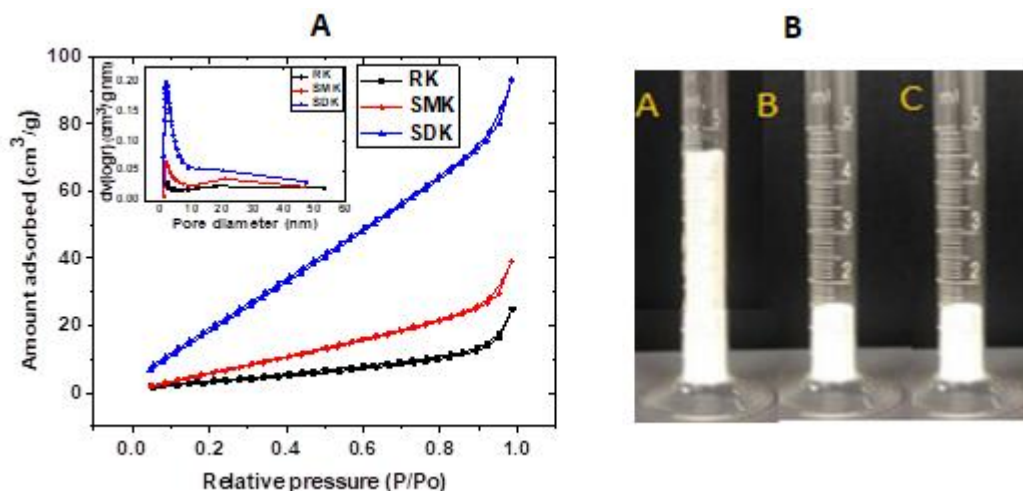


Fig. 4.72: Nitrogen adsorption-desorption isotherm at 77K (A) and volume of equal mass (B) of RK, SMK and SDK

The respective SEM images with EDS spectra and TEM of the adsorbents are displayed in **Fig A7** and 6A respectively. The images confirm that the RK and SMK are compacted materials, formed by an agglomerate of lamellar (kaolinite) and small particles (alpha-quartz). Meanwhile, SDK consists of exfoliated lamellar kaolinite and smaller particles TEM (**Fig. A8**).

The elemental constituents like Al, Si and O showed on the EDS spectra of all samples agree with XRD results, which show that clay is formed by kaolinite and alpha-quartz minerals, without other contaminants. The presence of Na and S on the EDS spectrum of SMK is an indication of the modification of clay using sodium dodecyl sulfate, in accordance with FTIR results.

4.6.2 Effect of pH of the adsorption of MB on RK, SMK and SDK

The pH of methylene blue (MB) solutions was varied from 2 - 10, while the amount of adsorbent used was kept constant, 0.1 g/50 mL of 100 mg L⁻¹ dye solutions and studied for 4 h. The graphical representation of the results is presented in **Fig. 4.73 A**. The adsorption of MB was more favorable at pH > 4 and the percentage that was removed increases with an increase

in pH. The variation of the zeta potential of the kaolin solutions depends highly on the pH of the suspension as displayed in **Fig. 4.73 B**. RK showed an isoelectric point at pH below 4, while SMK and the SDK samples showed an isoelectric point at pH below 2. As the pH increases, the surface charge of the particles becomes more negative. This explains why the adsorption of MB molecules was better at higher pH, and the SDK performed better than others (RK and SMK) because it exhibits higher negative zeta potential and specific surface area values. All the samples have the most negative value of surface charge at pH 10; this implies that adsorption process is basically due to the coulombic attraction between the negatively charged surface and the positive charge of the MB molecules

The study carried out by Yan et al., [227] revealed that the surface of kaolin is rich in silica with a small percentage of alumina. In view of this, its surface charge will likely be Si-OH^+_2 and Si-O^- in acidic and alkaline medium respectively. The adsorption of MB being a cationic dye was favorable at higher pH due to the electrostatic attraction that exists between the MB molecules and the negatively charged clay surface. Spray-dried clay (SDK) performed better than raw clay (RK) and surface-modified clay (SMK) with the highest MB removal of 72%. This result is due to the increase in the specific surface area related to the disaggregation of the lamellas produced by the spray drying process, thereby exposing more of the active surface of the SDK to the MB solution.

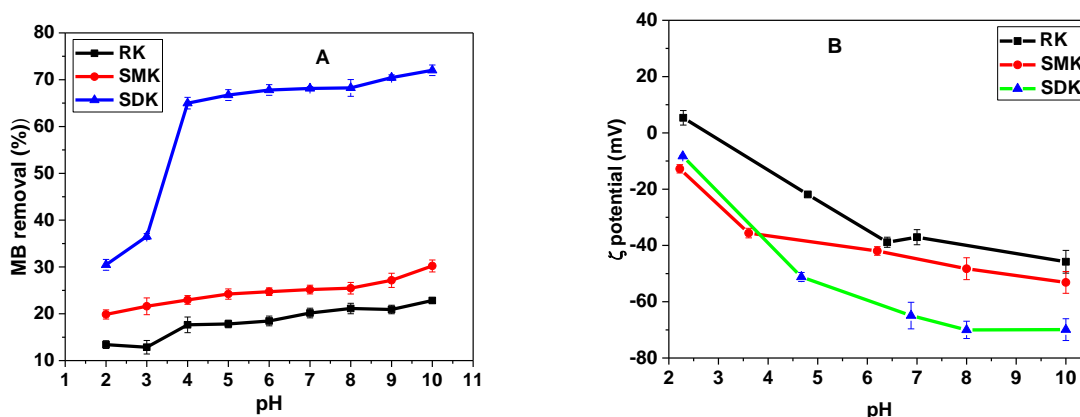


Fig. 4.73: Effect of pH on the adsorption of MB on RK, SMK and SDK (A) zeta potential (B)

4.6.3 Effect of dosage

Fig. A9 represents the influence of adsorbent mass on the removal of MB. The mass of the adsorbent was varied from 0.05 – 0.25 g per 50 mL of the dye solution and maintained for 2 h. The percentage removal of MB increases as the amount of the RK and SMK and SDK added to the fixed concentration of the dye solution increases. SDK takes the lead. The linear behavior of the adsorption process indicates that the active sites of the adsorbent can still accommodate the dye molecules on its surface. More so, 0.25 g/50 mL of SDK effectively remove 96% of the dye solution and performed almost more twice than RK.

4.6.4 Effect of contact time and adsorption kinetics

Fig. 4.74 illustrates the amount of MB absorbed at the time range of 30 - 240 mins, initial concentration of 100 mg g⁻¹ of MB, 0.1 g of the adsorbents and at pH 10. This was to ascertain the adsorption equilibrium time for the removal of MB from the solution. Effective adsorbent must not only have a high capacity but, also rapid in removing contaminants. The adsorption process increased rapidly during the first 30 minutes for SDK. However, all the adsorbents attained equilibrium at 120 minutes, after which there is no significant uptake in the percentage of MB that was removed.

The rapid initial stage of the adsorption process shows that a large amount of active vacant sites are available and that the concentration gradient between the adsorbate in solution and adsorbate on the adsorbent is high [228]. The concentration gradient becomes almost constant after the attainment of the equilibrium time. This observation has been affirmed to be as a result of limitation in the mass transfer of MB molecules to the surface of the adsorbent and reduction in the intra-particle diffusion.

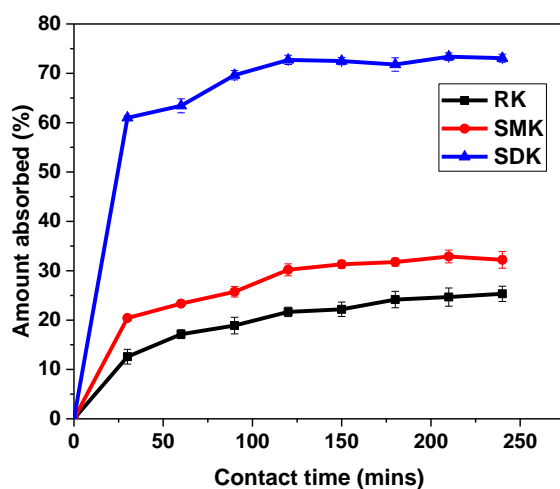


Fig.4.74: Effect of contact time on the adsorption of MB on RK, SMK and SDK

The data obtained were fitted into pseudo-first-order and second-order, and intraparticle diffusion kinetic models. This enabled a proper understanding of the control mechanism of the process of the adsorption.

The linear form of pseudo-first-order is given by equation 4.3 below

$$\log(q_e - q_t) = \log q_e - \frac{k_1 t}{2.303} \quad 4.3$$

Where q_e , q_t , k_1 and t are adsorption capacity at equilibrium (mg/g), amount of MB removed at time t , rate constant and contact time (min) respectively. The plot of $\log(q_e - q_t)$ versus t (not shown) is not linear, signifying that the experimental results are not consistent with this model. More so, the large deviation in experimental and calculated q_e , also the values of the correlation coefficient showed in **Table 30** imply that the model is not applicable for the mechanism. The values of q_e and k_1 are extrapolated from the intercept and the slope respectively.

Pseudo-second order is expressed by the equation 4.4 below

$$\frac{t}{q_t} = \frac{1}{k_2 q_e^2} + \frac{t}{q_e} \quad 4.4$$

This model proposes an adsorption mechanism in which the interaction between the adsorbate molecules on the site on the adsorbent is mainly due to the physio-chemical interaction [229].

The plot of $\frac{t}{q_t}$ against t is linear (**Fig. 4.75 A**). The respective values of k_2 (pseudo-second-order rate constant) and q_e are obtained from the intercept and slope of the Figure. The calculated

values of q_e are considerably close to the experimental values. The correlation coefficient of the plot is close to unity. Therefore, the experimental data is properly fitted into this model.

The last kinetic model that was used is the intra-particle diffusion, which describes that the adsorption rate mechanism hinges on how quick the adsorbate diffuses towards adsorbent [230]. The model is described by equation 4.5

$$q_t = k_d t^{1/2} + c \quad 4.5$$

The linear plot of q_t versus $t^{1/2}$ is represented in **Fig. 4.75 B**. The linearity of the plot indicates that the process is diffusion controlled. The value of k_d (rate constant of intra-particle diffusion) for each adsorbent are listed in **Table 29**.

It is affirmed that if the plot of q_t versus $t^{1/2}$ is multi-linear plots, it implies that two or more steps are involved in the adsorption process [231]. The intraparticle diffusion plot of this study having two linear plots (**Fig. 4.75 B**) reflects that the adsorption process was accompanied by two phases. This means that the mechanism of MB adsorption on the surface of the adsorbents entails surface adsorption and intra-particle diffusion.

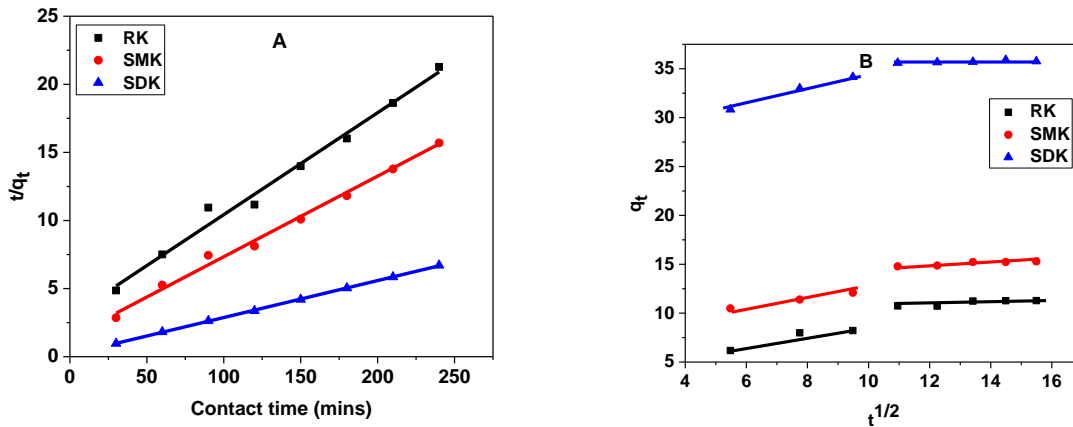


Fig. 4.75: pseudo-second-order kinetic plot (A) and intraparticle diffusion (B) of MB adsorption on RK, SMK and SDK.

Table 29: Parameters for kinetics models of adsorption of MB on RK, SMK, and SDK.

Model	Parameters	RK	SMK	SDK
Pseudo-first-order	q_e exp (mg/g)	11.27	15.29	35.9
	q_e cal (mg/g)	32.78	18.38	10.89
	k_1	0.0353	0.0278	0.0244
	R	0.8954	0.9280	0.9248
	χ^2	14.1147	0.5194	57.4380
Pseudo-second-order	q_e cal (mg/g)	13.36	17.08	36.85
	k_2	0.0165	0.0051	0.0001
	R	0.9938	0.9964	0.9998
	χ^2	0.3269	0.1875	0.0244
Intra-particle diffusion	k_d	0.5399	0.5461	0.4876
	R	0.9464	0.9407	0.9186

4.6.5 Adsorption isotherm for the adsorption of MB on RK, SMK and SDK

The suitability of Langmuir and Freundlich adsorption Isotherms was examined by fitting the data obtained at different temperatures to the linear form of both isotherm models. Langmuir and Freundlich isotherms are represented by equation 4.6 and 4.7 respectively

$$\frac{C_e}{q_e} = \frac{1}{q_{max}b} + \frac{C_e}{q_{max}} \quad 4.6$$

$$\log q_e = \log K_F + \frac{1}{n} \log C_e \quad 4.7$$

Where C_e is the equilibrium concentration in solution (mg/L), q_e is the amount of MB adsorbed per unit mass of the adsorbent (mg g^{-1}), q_{max} is the maximum adsorption capacity (mg/g) and b is Langmuir equilibrium constant (L mg^{-1}). where K_F is the Freundlich constant and $\frac{1}{n}$ is the heterogeneity factor.

The plot of $\frac{C_e}{q_e}$ against C_e at 303 - 333 K is presented in **Fig. A 10**.

The linear plot of $\log q_e$ versus $\log C_e$ at different temperatures is shown in **Fig. A 11**. The values of K_F and $\frac{1}{n}$ were obtained from the intercept and the slope respectively

The isotherms parameters are listed in Table 30. The applicability of the isotherms based on the values of the correlation coefficient (R^2) shows that Freundlich is more applicable than Langmuir because kaolin has a heterogeneous charge distribution on its surface [232,233]. The

Langmuir constant b is not consistent with increase in temperature for RK and SMK, however it increases steadily with temperature for SDK. More so, SDK having the highest surface area, resulted to high q_{max} , adsorption capacity at all temperature. The values of adsorption capacity obtained increases with temperature, signifying the endothermic nature of the adsorption process.

The values of $\frac{1}{n}$ heterogeneity factor in Freundlich isotherm less than 1, is evidence that the adsorption of MB on the adsorbents is greatly favorable. Zhao et al., [234] affirmed that molecules of an adsorbate can favorably adsorb on the surface on an adsorbent when the value of $\frac{1}{n}$ falls within range of 0.1 to 0.5, but value of $\frac{1}{n}$ greater than 2 connotes difficulty in adsorption. Comparison of the maximum monolayer adsorption (q_{max}) of different adsorbents for the removal of Methylene blue at room temperature is listed in **Table 31**.

Table 30: Langmuir and Freundlich isotherms parameters for the adsorption of MB at 303 -333 K.

Adsorbent	Temp. (K)	Langmuir			Freundlich		
		q_{max} (mg g ⁻¹)	b (mg L ⁻¹)	R	K_F (mg L ⁻¹)	$\frac{1}{n}$	R
RK	303	23	0.0561	0.995	6.132	0.229	0.965
	313	51	0.0164	0.963	4.804	0.378	0.992
	323	92	0.0165	0.987	4.601	0.518	0.998
	333	147	0.0200	0.986	6.294	0.583	0.998
SMK	303	30	0.0476	0.996	7.309	0.245	0.990
	313	55	0.0222	0.970	6.400	0.353	0.994
	323	96	0.0248	0.989	6.776	0.473	0.997
	333	144	0.0289	0.987	8.541	0.539	0.996
SDK	303	140	0.0210	0.893	9.352	0.469	0.986
	313	140	0.0282	0.938	10.626	0.468	0.995
	323	143	0.0335	0.953	11.709	0.464	0.997
	333	168	0.0399	0.935	16.290	0.433	0.987

Table 31: Comparison of the maximum monolayer adsorption (q_{max}) of different adsorbents for the removal of Methylene blue at room temperature.

Adsorbents	q_{max} (mg/g)	References
Montmorillonite/CoFe ₂ O ₄	97.75	[235]
Palm kernel fiber	95.4	[236]
Graphene/magnetite	43.82	[237]
DNPH- γ -alumina)	32.8	[238]
Kaolin-PDA-PSPSH	96.79	[201]
Modified bamboo	606	[239]
Spray-dried kaolinite (SDK)	140	This work
Surface modified kaolinite (SMK)	30	This work
Raw kaolinite (RK)	23	This work

4.6.6 Adsorption thermodynamic

Thermodynamic parameters like enthalpy, ΔH , (kJ/mol) and entropy, ΔS , (kJ/mol K) were evaluated from Van't Hoff plot by using equation 4.8 below.

$$\log \frac{q_e}{C_e} = \frac{\Delta S}{2.303R} - \frac{\Delta H}{2.303RT} \quad 4.8$$

While the Gibbs free energy, ΔG (kJ/mol) was evaluated based on equation 4.9

$$\Delta G = \Delta H - T\Delta S \quad 4.9$$

Where R is the gas constant (8.314 J/mol K), T is the temperature. The plot of $\log \frac{q_e}{C_e}$ against $\frac{1}{T}$ is shown in **Fig. A12**. The values of ΔH and ΔS are extrapolated from the slope and the intercept respectively.

The enthalpy of adsorption, ΔH , as shown in Table 4 is positive, affirming that the adsorption process is endothermic in nature.

The values of ΔS being positive connotes that the randomness of the MB molecules during the adsorption process increased at the interface of adsorbent/adsorbate solution. The values of Gibbs free energy, ΔG , as listed in Table 32, decrease with an increase in temperature,

meaning that the adsorption process will become more favorable and spontaneous when the temperature of the system is raised, according to results reported by [240]. Whenever the Gibbs free energy is positive at a specific temperature, it implies that the adsorption process is non-spontaneous and the adsorption capacity will become lower, however increasing the temperature will lead to a spontaneous process [241,242]. The negative value of ΔG obtained for SDK at all temperatures reveal a spontaneous adsorption process of MB.

Table 32: Thermodynamic parameters for the adsorption of MB at 303 -333 K.

Adsorbents	ΔH (kJ/mol)	ΔS (kJ/mol K)	ΔG (kJ/mol)			
			303 K	313 K	323 K	333 K
RK	60.28	0.1854	4.104	2.249	0.396	-1.458
SMK	58.98	0.1839	3.258	1.419	-0.418	-2.258
SDK	22.66	0.0774	-0.792	-1.566	-2.340	-3.114

4.6.7 Conclusion

This research has been able to establish that adsorption capacity can be enhanced through the spray drying dispersed clay solutions and surface modification of raw clay, although the performance of SDK is better than that of SMK. The higher specific surface area coupled with high negative surface charge values exhibited by SDK enhanced its performance over the raw and modified clay. The additional functional group on the surface-modified clay was responsible for its better adsorption capacity than raw clay. The removal of methylene blue was sensitive to the pH of the solution. Among the three kinetics models that the experimental data were fitted to, the pseudo-second model was best applicable. Adsorption isotherm model proposed by Freundlich was best fitted for the adsorption mechanism. The thermodynamic analysis revealed that adsorption of MB is endothermic and spontaneous at higher temperatures. Among the three adsorbents, spray-dried clay is highly efficient in removing methylene blue. This strategy could be employed to produce high surface area adsorbents for the removal of contaminants.

CHAPTER FIVE: GENERAL CONCLUSION

5.0 Conclusion and Recommendation

In this research, cobalt ferrite and its composite with chitosan, rice husk silica and cobalt kaolinite were successfully synthesized, characterized and applied to adsorb methylene blue, Congo red, acid orange II and doxycycline. Result obtained from each magnetic composite are unique. It was gathered from the study that spraying drying process could be used to obtain cobalt ferrite with high specific surface area and good efficiency in removing methylene blue. Result obtained from cobalt ferrite/chitosan show that combining experimental with theoretical could provide better and in-depth understanding on the mechanism of adsorption of methylene blue and acid orange II. Specific surface area of cobalt ferrite/rice husk silica was found not directly proportional to the its adsorption capacity for the removal of doxycycline, more so, the result of this composite (cobalt ferrite/rice husk) showed that adsorption capacity of cobalt ferrite and rice husk silica can be synergistically enhance by the composite of the two materials for the removal of methylene blue. Comparative study of the adsorption mechanism of Congo red and doxycycline using cobalt ferrite/kaolinite showed that the mechanism of adsorption of the two contaminants differs. The two contaminants were effectively removed by cobalt ferrite/kaolinite composite. Adsorption capacity of kaolinite for the removal of methylene blue was also enhanced by spray drying process.

The optimum pH for the adsorption of methylene blue and acid orange II using cobalt ferrite/chitosan were 4 and 12 respectively, while for the removal of doxycycline and methylene blue using cobalt ferrite/rice husk silica it was 6 and 9 respectively, meanwhile for the adsorption of Congo red and doxycycline on cobalt ferrite/kaolinite, it was pH 6. The adsorption kinetics studies for the removal of each contaminant by the respective composite are best fitted into pseudo second order model. Langmuir isotherm was best applicable to explain the adsorption mechanism for the removal of all the contaminants. Adsorption process of all the dyes on all the magnetic composites was exothermic, while that of doxycycline is endothermic. However, the adsorption of all the contaminants are spontaneous and feasible.

Cobalt ferrite/rice husk silica performed better in adsorbing doxycycline with adsorption capacity of 835 mg g^{-1} at 333 K, and in adsorbing methylene blue 253 mg g^{-1} at 303 K. Although the adsorption of acid orange II and Congo red could not be compared among the composite, the amount these dyes that were removed from the aqueous solution were better than some adsorbent that were reported in the literature.

5.1 Recommendation

- It is recommended that adsorption should be performed in continuous-flow reactor systems with magnetic separation.
- Comparative studies could be carried out on other types of spinel ferrites
- More focus should be directed towards the use of magnetic composite from agricultural and industrial wastes as adsorbents for the removal of contaminants.
- Competitive adsorption of different contaminants should be studied.

REFERENCES

- [1] E. Brillas, C.A. Martínez-Huitle, Decontamination of wastewaters containing synthetic organic dyes by electrochemical methods. An updated review, *Appl. Catal. B Environ.* 166–167 (2015) 603–643.
- [2] K.P. Singh, D. Mohan, S. Sinha, R. Dalwani, Impact assessment of treated / untreated wastewater toxicants discharged by sewage treatment plants on health , agricultural , and environmental quality in the wastewater disposal area, *55 (2004) 227–255.*
- [3] J. Mo, Q. Yang, N. Zhang, W. Zhang, Y. Zheng, Z. Zhang, A review on agro-industrial waste (AIW) derived adsorbents for water and wastewater treatment, *J. Environ. Manage.* 227 (2018) 395–405.
- [4] D.H.K. Reddy, Y.S. Yun, Spinel ferrite magnetic adsorbents: Alternative future materials for water purification?, *Coord. Chem. Rev.* 315 (2016) 90–111.
- [5] N.B. Singh, G. Nagpal, S. Agrawal, Rachna, Water purification by using Adsorbents: A Review, *Environ. Technol. Innov.* 11 (2018) 187–240.
- [6] C. Jia, J. Zhao, L. Lei, X. Kang, R. Lu, C. Chen, S. Li, Y. Zhao, Q. Yang, Z. Chen, Novel magnetically separable anhydride-functionalized Fe₃O₄@SiO₂@PEI-NTDA nanoparticles as effective adsorbents: synthesis, stability and recyclable adsorption performance for heavy metal ions, *RSC Adv.* 9 (2019) 9533–9545.
- [7] S. Tamjidi, H. Esmaeili, Application of magnetic adsorbents for removal of heavy metals from wastewater : a review study Application of magnetic adsorbents for removal of heavy metals from wastewater : a review study, (2019).
- [8] K.K. Kefeni, B.B. Mamba, T.A.M. Msagati, Application of spinel ferrite nanoparticles in water and wastewater treatment: A review, *Sep. Purif. Technol.* 188 (2017) 399–422.
- [9] I. Miljkovic, M. Kolega, S. Fratric, The Effects of Drinking Water on Attention, *Procedia - Soc. Behav. Sci.* 159 (2014) 577–583.
- [10] EPA, The Importance of Water to the U.S. Economy, (2013).
- [11] V.R. Reddy, B. Behera, Impact of water pollution on rural communities : An economic analysis, *Ecol. Econ.* 58 (2006) 520–537.
- [12] L. Santucci, E. Carol, C. Tanjal, Industrial waste as a source of surface and groundwater pollution for more than half a century in a sector of the Río de la Plata coastal plain (Argentina), *Chemosphere.* 206 (2018) 727–735.

- [13] M. Drahansky, M.. Paridah, A. Moradbak, A.. Mohamed, F. Abdulwahab taiwo Owolabi, M. Asniza, S.H.. Abdul Khalid, *Treatment Technologies for Organic Wastewater*, Intech. i (2016) 13.
- [14] R.S. Rana, P. Singh, V. Kandari, R. Singh, R. Dobhal, S. Gupta, A review on characterization and bioremediation of pharmaceutical industries' wastewater: an Indian perspective, *Appl. Water Sci.* 7 (2017) 1–12.
- [15] V.K. Gupta, Suhas, Application of low-cost adsorbents for dye removal - A review, *J. Environ. Manage.* 90 (2009) 2313–2342.
- [16] U. Tahir, A. Yasmin, U.H. Khan, Phytoremediation: Potential flora for synthetic dyestuff metabolism, *J. King Saud Univ. - Sci.* 28 (2016) 119–130.
- [17] Y. Zhou, J. Lu, Y. Zhou, Y. Liu, Recent advances for dyes removal using novel adsorbents: A review, *Environ. Pollut.* 252 (2019) 352–365.
- [18] A. Srinivasan, T. Viraraghavan, Decolorization of dye wastewaters by biosorbents: A review, *J. Environ. Manage.* 91 (2010) 1915–1929.
- [19] R. Elmoubarki, F.Z. Mahjoubi, H. Tounsadi, J. Moustadraf, M. Abdennouri, A. Zouhri, A. El Albani, N. Barka, Adsorption of textile dyes on raw and decanted Moroccan clays: Kinetics, equilibrium and thermodynamics, *Water Resour. Ind.* 9 (2015) 16–29.
- [20] C. Fersi, L. Gzara, M. Dhahbi, Treatment of textile effluents by membrane technologies, *Desalination.* 185 (2005) 399–409.
- [21] Ratna and Padhi B. S., Pollution due to synthetic dyes toxicity & carcinogenicity studies and remediation, *Int. J. Environ. Sci.* 3 (2012) 940–955.
- [22] A.E. Ghaly, R. Ananthashankar, M. Alhattab, V.V. Ramakrishnan, Production, Characterization and Treatment of Textile Effluents: A Critical Review, *J. Chem. Eng. Process Technol.* 05 (2013) 1–19.
- [23] L. Pereira, A. V. Coelho, C.A. Viegas, M.M.C. dos Santos, M.P. Robalo, L.O. Martins, Enzymatic biotransformation of the azo dye Sudan Orange G with bacterial CotA-laccase, *J. Biotechnol.* 139 (2009) 68–77.
- [24] M. Joshi, R. Bansal, R. Purwar, Colour removal from textile effluents, *Indian J. Fibre Text. Res.* 29 (2004) 239–259.
- [25] A. Appusamy, I. John, K. Ponnusamy, A. Ramalingam, Removal of crystal violet dye from aqueous solution using triton X-114 surfactant via cloud point extraction, *Eng. Sci. Technol. an Int. J.* 17 (2014) 137–144.

- [26] R.O. Alves de Lima, A.P. Bazo, D.M.F. Salvadori, C.M. Rech, D. de Palma Oliveira, G. de Aragão Umbuzeiro, Mutagenic and carcinogenic potential of a textile azo dye processing plant effluent that impacts a drinking water source, *Mutat. Res. - Genet. Toxicol. Environ. Mutagen.* 626 (2007) 53–60.
- [27] N. Tüfekci, N. Sivri, İ. Toroz, Pollutants of Textile Industry Wastewater and Assessment of its Discharge Limits by Water Quality Standards, *Turkish J. Fish. Aquat. Sci.* 103 (2007) 97–103.
- [28] O. Keskinan, M.Z.L. Göksu, Assessment of the dye removal capability of submersed aquatic plants in a laboratory-scale wetland system using ANOVA, *Brazilian J. Chem. Eng.* 24 (2007) 193–202.
- [29] K. Kümmerer, Antibiotics in the aquatic environment - A review - Part I, *Chemosphere.* 75 (2009) 417–434.
- [30] Y. Chao, W. Zhu, X. Wu, F. Hou, S. Xun, P. Wu, H. Ji, H. Xu, H. Li, Application of graphene-like layered molybdenum disulfide and its excellent adsorption behavior for doxycycline antibiotic, *Chem. Eng. J.* 243 (2014) 60–67.
- [31] R. Shokoohi, A. Dargahi, R. Khamutian, Y. Vaziri, Evaluation of the Efficiency of Wastewater Treatment Plants in the Removal of Common Antibiotics from Municipal Wastewater in Hamadan, Iran, *Avicenna J. Environ. Heal. Eng.* 4 (2017) 1–6.
- [32] L. Nielsen, T.J. Bandosz, Analysis of the competitive adsorption of pharmaceuticals on waste derived materials, *Chem. Eng. J.* 287 (2016) 139–147.
- [33] S.D. Costanzo, J. Murby, J. Bates, Ecosystem response to antibiotics entering the aquatic environment, *Mar. Pollut. Bull.* 51 (2005) 218–223.
- [34] M.O. Griffin, E. Fricovsky, G. Ceballos, F. Villarreal, Tetracyclines: a pleiotropic family of compounds with promising therapeutic properties. Review of the literature, *AJP Cell Physiol.* 299 (2010) C539–C548.
- [35] J. Gao, Y. Gao, Z. Sui, Z. Dong, S. Wang, D. Zou, Hydrothermal synthesis of BiOBr/FeWO₄ composite photocatalysts and their photocatalytic degradation of doxycycline, *J. Alloys Compd.* 732 (2018) 43–51.
- [36] N.E. Holmes, P.G.P. Charles, Safety and Efficacy Review of Doxycycline, *Clin. Med. Ther.* (2009) 471–482.

- [37] Z. Liu, M. Zhu, Z. Wang, H. Wang, C. Deng, K. Li, Effective degradation of aqueous tetracycline using a nano-TiO₂/carbon electrocatalytic membrane, *Materials (Basel)*. 9 (2016) 1–14.
- [38] M.S. Mahmoud, J.Y. Farah, T.E. Farrag, Enhanced removal of Methylene Blue by electrocoagulation using iron electrodes, *Egypt. J. Pet.* 22 (2013) 211–216.
- [39] A.M.S. Solano, S. Garcia-Segura, C.A. Martínez-Huitle, E. Brillas, Degradation of acidic aqueous solutions of the diazo dye Congo Red by photo-assisted electrochemical processes based on Fenton's reaction chemistry, *Appl. Catal. B Environ.* 168–169 (2015) 559–571.
- [40] H. Ramlow, R.A.F. Machado, A.C.K. Bierhalz, C. Marangoni, Dye synthetic solution treatment by direct contact membrane distillation using commercial membranes, *Environ. Technol. (United Kingdom)*. (2019) 1–12.
- [41] M.A. Khan, Z.A. AlOthman, M. Naushad, M.R. Khan, M. Luqman, Adsorption of methylene blue on strongly basic anion exchange resin (Zerolit DMF): kinetic, isotherm, and thermodynamic studies, *Desalin. Water Treat.* 53 (2015) 515–523.
- [42] M. Tagliavini, A.I. Schäfer, Removal of steroid micropollutants by polymer-based spherical activated carbon (PBSAC) assisted membrane filtration, *J. Hazard. Mater.* 353 (2018) 514–521.
- [43] S.O. Ganiyu, E. Vieira dos Santos, E.C. Tossi de Araújo Costa, C.A. Martínez-Huitle, Electrochemical advanced oxidation processes (EAOPs) as alternative treatment techniques for carwash wastewater reclamation, *Chemosphere*. 211 (2018) 998–1006.
- [44] F.M. Amaral, M.T. Kato, L. Florêncio, S. Gavazza, Color, organic matter and sulfate removal from textile effluents by anaerobic and aerobic processes, *Bioresour. Technol.* 163 (2014) 364–369.
- [45] A. Pirkarami, M.E. Olya, Removal of dye from industrial wastewater with an emphasis on improving economic efficiency and degradation mechanism, *J. Saudi Chem. Soc.* 21 (2017) S179–S186.
- [46] S. Gaydardzhiev, J. Karthikeyan, P. Ay, Colour removal from model solutions by coagulation--surface charge and floc characterisation aspects., *Environ. Technol.* 27 (2006) 193–9.
- [47] C.R. Holkar, A.J. Jadhav, D. V. Pinjari, N.M. Mahamuni, A.B. Pandit, A critical review on textile wastewater treatments: Possible approaches, *J. Environ. Manage.* 182 (2016) 351–366.

- [48] S. Zaidi, T. Chaabane, V. Sivasankar, A. Darchen, R. Maachi, T.A.M. Msagati, Electro-coagulation coupled electro-flotation process: Feasible choice in doxycycline removal from pharmaceutical effluents, *Arab. J. Chem.* (2015) 0–11.
- [49] D.B. Miklos, C. Remy, M. Jekel, K.G. Linden, U. Hübner, Evaluation of advanced oxidation processes for water and wastewater treatment e A critical review, *139* (2018) 118–131.
- [50] S. Sharma, J.P. Ruparelia, M.L. Patel, A general review on Advanced Oxidation Processes for waste water treatment, (2011) 8–10.
- [51] E. Worch, *Adsorption Technology in Water Treatment: Fundamentals, Processes, and Modeling*, 2012.
- [52] A. Dabrowski, *Adsorption - From theory to practice*, *Adv. Colloid Interface Sci.* *93* (2001) 135–224.
- [53] T. Ngulube, J. Ray, V. Masindi, A. Maity, An update on synthetic dyes adsorption onto clay based minerals : A state-of-art review, *191* (2017).
- [54] S. Liu, W. hua Xu, Y. guo Liu, X. fei Tan, G. ming Zeng, X. Li, J. Liang, Z. Zhou, Z. li Yan, X. xi Cai, Facile synthesis of Cu(II) impregnated biochar with enhanced adsorption activity for the removal of doxycycline hydrochloride from water, *Sci. Total Environ.* *592* (2017) 546–553.
- [55] S. Madan, R. Shaw, S. Tiwari, S. Kumar, Adsorption dynamics of Congo red dye removal using ZnO functionalized high silica zeolitic particles, *Appl. Surf. Sci.* *487* (2019) 907–917.
- [56] S. Fan, J. Tang, Y. Wang, H. Li, H. Zhang, J. Tang, Z. Wang, X. Li, Biochar prepared from co-pyrolysis of municipal sewage sludge and tea waste for the adsorption of methylene blue from aqueous solutions : Kinetics , isotherm , thermodynamic and mechanism, *220* (2016) 432–441.
- [57] L. Kong, M. Su, Y. Peng, L. Hou, J. Liu, H. Li, Z. Diao, K. Shih, Y. Xiong, D. Chen, Producing sawdust derived activated carbon by co-calcinations with limestone for enhanced Acid Orange II adsorption, *J. Clean. Prod.* *168* (2017) 22–29.
- [58] O. Philippova, A. Barabanova, V. Molchanov, A. Khokhlov, Magnetic polymer beads: Recent trends and developments in synthetic design and applications, *Eur. Polym. J.* *47* (2011) 542–559.
- [59] D. Mehta, S. Mazumdar, S.K. Singh, Magnetic adsorbents for the treatment of water/wastewater-A review, *J. Water Process Eng.* *7* (2015) 244–265.

- [60] B.I. Kharisov, H.V.R. Dias, O. V. Kharissova, Mini-review: Ferrite nanoparticles in the catalysis, *Arab. J. Chem.* (2014).
- [61] R. Valenzuela, Novel applications of ferrites, *Phys. Res. Int.* 2012 (2012).
- [62] S.K. Gore, S.S. Jadhav, V. V. Jadhav, S.M. Patange, M. Naushad, R.S. Mane, K.H. Kim, The structural and magnetic properties of dual phase cobalt ferrite, *Sci. Rep.* 7 (2017) 1–9.
- [63] S. Yoon, Determination of the Temperature Dependence of the Magnetic Anisotropy Constant in Magnetite Nanoparticles, *J. Korean Phys. Soc.* 59 (2011) 3069–3073.
- [64] J.B. Silva, W. de Brito, N.D.S. Mohallem, Influence of heat treatment on cobalt ferrite ceramic powders, *Mater. Sci. Eng. B.* 112 (2004) 182–187.
- [65] M. V. Limaye, S.B. Singh, S.K. Date, D. Kothari, V.R. Reddy, A. Gupta, V. Sathe, R.J. Choudhary, S.K. Kulkarni, High coercivity of oleic acid capped CoFe_2O_4 nanoparticles at room temperature, *J. Phys. Chem. B.* 113 (2009) 9070–9076.
- [66] A. Almasian, F. Najafi, M. Mirjalili, M.P. Gashti, G.C. Fard, Zwitter ionic modification of cobalt-ferrite nanofiber for the removal of anionic and cationic dyes, *J. Taiwan Inst. Chem. Eng.* 67 (2016) 306–317.
- [67] L. Wang, J. Li, Y. Wang, L. Zhao, Q. Jiang, Adsorption capability for Congo red on nanocrystalline MFe_2O_4 (M=Mn, Fe, Co, Ni) spinel ferrites, *Chem. Eng. J.* 181–182 (2012) 72–79.
- [68] B. Viltušnik, A. Košak, Y.L. Zub, A. Lobnik, Removal of Pb(II) ions from aqueous systems using thiol-functionalized cobalt-ferrite magnetic nanoparticles, *J. Sol-Gel Sci. Technol.* 68 (2013) 365–373.
- [69] M. Kooti, M. Afshari, Magnetic cobalt ferrite nanoparticles as an efficient catalyst for oxidation of alkenes, *Sci. Iran.* 19 (2012) 1991–1995.
- [70] M. Amiri, A. Akbari, M. Ahmadi, A. Pardakhti, M. Salavati-Niasari, Synthesis and in vitro evaluation of a novel magnetic drug delivery system; proecological method for the preparation of CoFe_2O_4 nanostructures, *J. Mol. Liq.* 249 (2018) 1151–1160.
- [71] S. Amiri, H. Shokrollahi, The role of cobalt ferrite magnetic nanoparticles in medical science, *Mater. Sci. Eng. C.* 33 (2013) 1–8.
- [72] C. Dey, K. Baishya, A. Ghosh, M.M. Goswami, A. Ghosh, K. Mandal, Improvement of drug delivery by hyperthermia treatment using magnetic cubic cobalt ferrite nanoparticles, *J. Magn. Magn. Mater.* 427 (2017) 168–174.

- [73] A.A. Rooygar, M.H. Mallah, H. Abolghasemi, J. Safdari, New “magmolecular” process for the separation of antimony(III) from aqueous solution, *J. Chem. Eng. Data.* 59 (2014) 3545–3554.
- [74] O.O. Daramola, I.O. Oladele, B.O. Adewuyi, Influence of Submicron Agro Waste Silica Particles and Vinyl Acetate on Mechanical Properties of High Density Polyethylene Matrix Composites, *West Indian J. Eng.* 38 (2015) 96–107.
- [75] N. Sapawe, N. Surayah Osman, M. Zulkhairi Zakaria, S. Amirul Shahab Syed Mohamad Fikry, M. Amir Mat Aris, Synthesis of green silica from agricultural waste by sol-gel method, *Mater. Today Proc.* 5 (2018) 21861–21866.
- [76] F.M. Kasperiski, E.C. Lima, C.S. Umpierres, S. Glaydson, P. Silas, D. Ramos, S.L.P. Dias, C. Saucier, B. Janaina, Production of porous activated carbons from *Caesalpinia ferrea* seed pod wastes : Highly efficient removal of captopril from aqueous solutions, *J. Clean. Prod.* 197 (2018) 919–929.
- [77] F. Neese, Software update: the ORCA program system, version 4.0, *Wiley Interdiscip. Rev. Comput. Mol. Sci.* (2017) e1327.
- [78] R.G. Parr, W.T. Yang, *Density-Functional Theory of Atoms and Molecules*, Oxford University Press, New York, 1989.
- [79] M.P. Allen, D.J. Tildesley, *Computer Simulation of Liquids*, *Liq. Oxford Univ. Press.* New York. 18 (1987) 385.
- [80] W.L. Jorgensen, J. Chandrasekhar, J.D. Madura, R.W. Impey, M.L. Klein, Comparison of simple potential functions for simulating liquid water, *J. Chem. Phys.* 79 (1983) 926.
- [81] H.M. Cezar, S. Canuto, K. Coutinho, DICE(v3.0beta) A general Monte Carlo program for liquid simulation, (2018).
- [82] N. Dong, F. He, J. Xin, Q. Wang, Z. Lei, B. Su, Preparation of CoFe₂O₄ magnetic fiber nanomaterial via a template-assisted solvothermal method, *Mater. Lett.* 141 (2015) 238–241.
- [83] L.J. Cote, A.S. Teja, A.P. Wilkinson, Z.J. Zhang, Continuous hydrothermal synthesis of CoFe₂O₄ nanoparticles, *Fluid Phase Equilib.* 210 (2003) 307–317.
- [84] T. Prabhakaran, J. Hemalatha, Combustion synthesis and characterization of cobalt ferrite nanoparticles, *Ceram. Int.* 42 (2016) 14113–14120.

- [85] M. Houshiar, F. Zebhi, Z.J. Razi, A. Alidoust, Z. Askari, Synthesis of cobalt ferrite (CoFe₂O₄) nanoparticles using combustion, coprecipitation, and precipitation methods: A comparison study of size, structural, and magnetic properties, *J. Magn. Mater.* 371 (2014) 43–48.
- [86] M. Ristic, S. Krehula, M. Reissner, M. Jean, B. Hannoyer, S. Musić, Synthesis and properties of precipitated cobalt ferrite nanoparticles, *J. Mol. Struct.* 1140 (2017) 32–38.
- [87] S. Irfan, M. Ajaz-Un-Nabi, Y. Jamil, N. Amin, Synthesis of Mn_{1-x}Zn_xFe₂O₄ ferrite powder by co-precipitation method, *IOP Conf. Ser. Mater. Sci. Eng.* 60 (2014) 012048.
- [88] A. Stunda-Zujeva, Z. Irbe, L. Berzina-Cimdina, Controlling the morphology of ceramic and composite powders obtained via spray drying – A review, *Ceram. Int.* 43 (2017) 11543–11551.
- [89] K.S. Rao, G.S.V.R.K. Choudary, K.H. Rao, C. Sujatha, Structural and Magnetic Properties of Ultrafine CoFe₂O₄ Nanoparticles, *Procedia Mater. Sci.* 10 (2015) 19–27.
- [90] A. Franco, V. Zapf, Temperature dependence of magnetic anisotropy in nanoparticles of Co_xFe_(3-x)O₄, *J. Magn. Mater.* 320 (2008) 709–713.
- [91] S.P. Yeap, J.K. Lim, B.S. Ooi, A.L. Ahmad, Agglomeration, colloidal stability, and magnetic separation of magnetic nanoparticles: collective influences on environmental engineering applications, *J. Nanoparticle Res.* 19 (2017) 368.
- [92] A.G. Kolhatkar, A.C. Jamison, D. Litvinov, R.C. Willson, T.R. Lee, Tuning the magnetic properties of nanoparticles, 2013.
- [93] C. Liu, B. Zou, A.J. Rondinone, Z.J. Zhang, Chemical control of superparamagnetic properties of magnesium and cobalt spinel ferrite nanoparticles through atomic level magnetic couplings, *J. Am. Chem. Soc.* 122 (2000) 6263–6267.
- [94] K. Praveena, K. Sadhana, Ferromagnetic Properties of Zn substituted Spinel Ferrites for High Frequency Applications, *Int. J. Sci. Res. Publ.* 5 (2015) 1–21.
- [95] K. Rumpf, P. Granitzer, P.M. Morales, P. Poelt, M. Reissner, Variable blocking temperature of a porous silicon/Fe₃O₄ composite due to different interactions of the magnetic nanoparticles, *Nanoscale Res. Lett.* 7 (2012) 445–448.
- [96] T. Prabhakaran, R. V. Mangalaraja, J.C. Denardin, J.A. Jiménez, The effect of reaction temperature on the structural and magnetic properties of nano CoFe₂O₄, *Ceram. Int.* 43 (2017) 5599–5606.

- [97] U. Khan, N. Adeela, K. Javed, S. Riaz, H. Ali, M. Iqbal, X.F. Han, S. Naseem, Influence of cobalt doping on structural and magnetic properties of BiFeO₃ nanoparticles, *J. Nanoparticle Res.* 17 (2015) 429.
- [98] S. Xavier, S. Thankachan, B. Jacob, E. Mohammed, Effect of Sintering Temperature on the Structural and Magnetic Properties of Cobalt Ferrite Nanoparticles, *Nanojournal.Ifmo.Ru.* 4 (2013) 430–437.
- [99] A.A. and A.B.A.H. 1Refractory M. F. Zawrah, M. M. El-Okr, Characterization of Sol-gel Fabricated Cobalt Ferrite CoFe₂O₄ Nanoparticles, *Middle East J. Appl. Sci.* ISSN. 6 (2014) 362–366.
- [100] Y.M. Abbas, S.A. Mansour, M.H. Ibrahim, S.E. Ali, Microstructure characterization and cation distribution of nanocrystalline cobalt ferrite, *J. Magn. Magn. Mater.* 323 (2011) 2748–2756.
- [101] I. Sharifi, H. Shokrollahi, M. Mahdi, R. Safi, Magnetic and structural studies on CoFe₂O₄ nanoparticles synthesized by co-precipitation , normal micelles and reverse micelles methods, *J. Magn. Magn. Mater.* 324 (2012) 1854–1861.
- [102] V. Kaliyamoorthy, D.R. Babu, M. Saminathan, Impact of ignition temperature on particle size and magnetic properties of CoFe₂O₄ nanoparticles prepared by self-propagated MILD combustion technique, *J. Magn. Magn. Mater.* 418 (2016) 280–288.
- [103] X.-H.H. Xing-Hua Li, Cai-Ling Xu, F.-S. Li, Liang Qiao, Tao Wang, Synthesis and Magnetic Properties of Nearly Monodisperse CoFe₂O₄ Nanoparticles Through a Simple Hydrothermal Condition, *Nanoscale Res Lett.* 5 (2010) 1039–1044.
- [104] T. Shahjuee, S.M. Masoudpanah, S.M. Mirkazemi, Coprecipitation Synthesis of CoFe₂O₄ Nanoparticles for Hyperthermia, *J. Ultrafine Grained Nanostructured Mater.* 50 (2017) 105–110.
- [105] M.C.C.N. Anumol, V.A. Baidyanath, S. Subasa, Tailoring magnetic properties of cobalt ferrite nanoparticles by different divalent cation substitution, *J. Mater. Sci. Mater. Electron.* 29 (2018) 813–822.
- [106] A. Ali, S. Ahmed, A review on chitosan and its nanocomposites in drug delivery, *Int. J. Biol. Macromol.* 109 (2018) 273–286.

- [107] A.P. Martínez-Camacho, M.O. Cortez-Rocha, J.M. Ezquerro-Brauer, A.Z. Graciano-Verdugo, F. Rodríguez-Félix, M.M. Castillo-Ortega, M.S. Yépiz-Gómez, M. Plascencia-Jatomea, Chitosan composite films: Thermal, structural, mechanical and antifungal properties, *Carbohydr. Polym.* 82 (2010) 305–315.
- [108] R. Huang, Q. Liu, J. Huo, B. Yang, Adsorption of methyl orange onto protonated cross-linked chitosan, *Arab. J. Chem.* 10 (2017) 24–32.
- [109] F. Marrakchi, W.A. Khanday, M. Asif, B.H. Hameed, Cross-linked chitosan/sepiolite composite for the adsorption of methylene blue and reactive orange 16, *Int. J. Biol. Macromol.* 93 (2016) 1231–1239.
- [110] A. Shajahan, S. Shankar, A. Sathiyaseelan, K.S. Narayan, V. Narayanan, V. Kaviyarsan, S. Ignacimuthu, Comparative studies of chitosan and its nanoparticles for the adsorption efficiency of various dyes, *Int. J. Biol. Macromol.* 104 (2017) 1449–1458.
- [111] A. Salima, K.S. Ounissa, M. Lynda, B. Mohamed, Cationic dye (MB) removal using polymer inclusion membrane (PIMs), *Procedia Eng.* 33 (2012) 38–46.
- [112] V.K. Gupta, A. Mittal, V. Gajbe, J. Mittal, Removal and recovery of the hazardous azo dye acid orange 7 through adsorption over waste materials: Bottom ash and de-oiled soya, *Ind. Eng. Chem. Res.* 45 (2006) 1446–1453.
- [113] G. Zhou, Z. Chen, F. Fang, Y. He, H. Sun, H. Shi, Fenton-like degradation of Methylene Blue using paper mill sludge-derived magnetically separable heterogeneous catalyst: Characterization and mechanism, *J. Environ. Sci. (China)*. 35 (2015) 20–26.
- [114] G.Z. Kyzas, E.A. Deliyanni, Mercury(II) removal with modified magnetic chitosan adsorbents, *Molecules*. 18 (2013) 6193–6214.
- [115] S. Rohilla, S. Kumar, P. Aghamkar, S. Sunder, A. Agarwal, Investigations on structural and magnetic properties of cobalt ferrite/silica nanocomposites prepared by the coprecipitation method, *J. Magn. Magn. Mater.* 323 (2011) 897–902.
- [116] L. Ai, H. Huang, Z. Chen, X. Wei, J. Jiang, Activated carbon/CoFe₂O₄ composites: Facile synthesis, magnetic performance and their potential application for the removal of malachite green from water, *Chem. Eng. J.* 156 (2010) 243–249.
- [117] A.J.B. Leite, C.S. A., P.S. Thue, G.S. dos Reis, S.L. Dias, E.C. Lima, J.C.P. Vaghetti, F.A. Pavan, W.S. de Alencar, Activated carbon from avocado seeds for the removal of phenolic compounds from aqueous solutions, *Desalin. Water Treat.* 71 (2017) 168–181.

- [118] D. Pathania, S. Sharma, P. Singh, Removal of methylene blue by adsorption onto activated carbon developed from *Ficus carica* bast, *Arab. J. Chem.* 10 (2017) S1445–S1451.
- [119] É.C. Lima, M.A. Adebayo, M.M. Fernando, *Carbon Nanomaterials as Adsorbents for Environmental and Biological Applications*, 2015.
- [120] S. Yang, Y. Wu, Y. Wu, L. Zhu, Optimizing decolorization of Acid Fuchsin and Acid Orange II solution by MnO₂ loaded MCM-41, *J. Taiwan Inst. Chem. Eng.* 50 (2015) 205–214.
- [121] G. Zhang, J. Qu, H. Liu, A.T. Cooper, R. Wu, CuFe₂O₄/activated carbon composite: A novel magnetic adsorbent for the removal of acid orange II and catalytic regeneration, *Chemosphere.* 68 (2007) 1058–1066.
- [122] B. Sarkar, Y. Xi, M. Megharaj, R. Naidu, Orange II adsorption on palygorskites modified with alkyl trimethylammonium and dialkyl dimethylammonium bromide - An isothermal and kinetic study, *Appl. Clay Sci.* 51 (2011) 370–374.
- [123] E. García, R. Medina, M. Lozano, I. Hernández Pérez, M. Valero, A. Franco, Adsorption of Azo-Dye Orange II from Aqueous Solutions Using a Metal-Organic Framework Material: Iron- Benzenetricarboxylate, *Materials (Basel).* 7 (2014) 8037–8057.
- [124] S. Jafari, B. Tryba, E. Kusiak-Nejman, J. Kapica-Kozar, A.W. Morawski, M. Sillanpää, The role of adsorption in the photocatalytic decomposition of Orange II on carbon-modified TiO₂, *J. Mol. Liq.* 220 (2016) 504–512.
- [125] M. Kousha, E. Daneshvar, M.S. Sohrabi, M. Jokar, A. Bhatnagar, Adsorption of acid orange II dye by raw and chemically modified brown macroalga *Stoechospermum marginatum*, *Chem. Eng. J.* 192 (2012) 67–76.
- [126] S. Sheshmani, A. Ashori, S. Hasanzadeh, Removal of Acid Orange 7 from aqueous solution using magnetic graphene/chitosan: A promising nano-adsorbent, *Int. J. Biol. Macromol.* 68 (2014) 218–224.
- [127] H. Shi, W. Li, L. Zhong, C. Xu, Methylene Blue Adsorption from Aqueous Solution by Magnetic Cellulose/Graphene Oxide Composite: Equilibrium, Kinetics, and Thermodynamics, *Ind. Eng. Chem. Res.* 53 (2014) 1108–1118.
- [128] N. Saad, M. Al-Mawla, E. Moubarak, M. Al-Ghoul, H. El-Rassy, Surface-functionalized silica aerogels and alcogels for methylene blue adsorption, *RSC Adv.* 5 (2015) 6111–6122.

- [129] M.L.F.A. De Castro, M.L.B. Abad, D.A.G. Sumalinog, R.R.M. Abarca, P. Paoprasert, M.D.G. de Luna, Adsorption of Methylene Blue dye and Cu(II) ions on EDTA-modified bentonite: Isotherm, kinetic and thermodynamic studies, *Sustain. Environ. Res.* 28 (2018) 197–205.
- [130] G.B. Kunde, B. Sehgal, A.K. Ganguli, Synthesis of mesoporous rebar MWCNT/alumina composite (RMAC) nodules for the effective removal of methylene blue and Cr (VI) from an aqueous medium, *J. Hazard. Mater.* 374 (2019) 140–151.
- [131] Y. Wang, Y. Zhang, S. Li, W. Zhong, W. Wei, Enhanced methylene blue adsorption onto activated reed-derived biochar by tannic acid, *J. Mol. Liq.* 268 (2018) 658–666.
- [132] S.I. Siddiqui, G. Rathi, S.A. Chaudhry, Acid washed black cumin seed powder preparation for adsorption of methylene blue dye from aqueous solution: Thermodynamic, kinetic and isotherm studies, *J. Mol. Liq.* 264 (2018) 275–284.
- [133] D.S. Tong, C.W. Wu, M.O. Adebajo, G.C. Jin, W.H. Yu, S.F. Ji, C.H. Zhou, Adsorption of methylene blue from aqueous solution onto porous cellulose-derived carbon/montmorillonite nanocomposites, *Appl. Clay Sci.* 161 (2018) 256–264.
- [134] M.A. Franciski, E.C. Peres, M. Godinho, D. Perondi, E.L. Foletto, G.C. Collazzo, G.L. Dotto, Development of CO₂activated biochar from solid wastes of a beer industry and its application for methylene blue adsorption, *Waste Manag.* 78 (2018) 630–638.
- [135] Y. Liu, Y. Liu, Biosorption isotherms, kinetics and thermodynamics, *Sep. Purif. Technol.* 61 (2008) 229–242. doi:10.1016/j.seppur.2007.10.002.
- [136] G. Frenking, S. Shaik, *The Chemical Bond*, Wiley-VCH Verlag GmbH & Co. KGaA, Weinheim, Germany, 2014. doi:10.1002/9783527664696.
- [137] F. De Proft, P.W. Ayers, P. Geerlings, *The Conceptual Density Functional Theory Perspective of Bonding*, in: *Chem. Bond*, Wiley-VCH Verlag GmbH & Co. KGaA, Weinheim, Germany, 2014: pp. 233–270. doi:10.1002/9783527664696.ch7.
- [138] A.G. Gilani, M. Salmanpour, T. Ghorbanpour, Solvatochromism, dichroism and excited state dipole moment of azure A and methylene blue, *J. Mol. Liq.* 179 (2013) 118–123.
- [139] J.J. Dannenberg, D.C. Clary, R.A. Klein, R.H. Crabtree, P. Hobza, A.C. Legon, I. Alkorta, S. Scheiner, B. Mennucci, G.R. Desiraju, H.G. Kjaergaard, D.J. Nesbitt, J. Sadlej, E. Arunan, Definition of the hydrogen bond (IUPAC Recommendations 2011), *Pure Appl. Chem.* 83 (2011) 1637–1641.

- [140] Z. Hasan, S.H. Jhung, Removal of hazardous organics from water using metal-organic frameworks (MOFs): Plausible mechanisms for selective adsorptions, *J. Hazard. Mater.* 283 (2015) 329–339.
- [141] Z. Du, S. Deng, Y. Bei, Q. Huang, B. Wang, Adsorption behavior and mechanism of perfluorinated compounds on various adsorbents — A review, *J. Hazard. Mater.* 274 (2014) 443–454.
- [142] U. Zul, T. Subhani, S.W. Husain, Towards tunable size of silica particles from rice husk, *J. Non. Cryst. Solids.* 429 (2015) 61–69
- [143] V. Sanklecha, W. Limited, Mesoporous Silica : A Review Mesoporous Silica : A Review, *Int. J. Pharm. DRUG Anal.* 6 (2019) 0–12.
- [144] M. Brigante, M. Avena, Biotemplated synthesis of mesoporous silica for doxycycline removal. Effect of pH, temperature, ionic strength and Ca²⁺ concentration on the adsorption behaviour, *Microporous Mesoporous Mater.* 225 (2016) 534–542.
- [145] G.M.K. Tolba, N.A.M. Barakat, A.M. Bastaweesy, E.A. Ashour, W. Abdelmoez, M.H. El-Newehy, S.S. Al-Deyab, H.Y. Kim, Effective and highly recyclable nanosilica produced from the rice husk for effective removal of organic dyes, *J. Ind. Eng. Chem.* 29 (2015) 134–145.
- [146] R. Darvishi Cheshmeh Soltani, A.R. Khataee, H. Godini, M. Safari, M.J. Ghanadzadeh, M.S. Rajaei, Response surface methodological evaluation of the adsorption of textile dye onto biosilica/alginate nanobiocomposite: thermodynamic, kinetic, and isotherm studies, *Desalin. Water Treat.* 56 (2015) 1389–1402.
- [147] S. Mor, C.K. Manchanda, S.K. Kansal, K. Ravindra, R.H. Ash, Nanosilica extraction from processed agricultural residue using green technology, *J. Clean. Prod.* 143 (2017) 1284–1290.
- [148] L.T. Gibson, Mesosilica materials and organic pollutant adsorption : part B removal from aqueous solution, *Chem Soc Rev.* 43 (2014) 5173–5182.
- [149] Y. Shen, Rice husk silica derived nanomaterials for sustainable applications, *Renew. Sustain. Energy Rev.* 80 (2017) 453–466.
- [150] Ç.K. Pınar Terzioğlu, Sevil Yücel, Review on a novel biosilica source for production of advanced silica - based materials : Wheat husk, *Asia-Pac J Chem Eng.* 14 (2018) 1–14.
- [151] J.A. Santana Costa, C.M. Paranhos, Systematic evaluation of amorphous silica production from rice husk ashes, *J. Clean. Prod.* 192 (2018) 688–697.

- [152] S. Azat, A. V Korobeinyk, K. Moustakas, V.J. Inglezakis, Sustainable production of pure silica from rice husk waste in Kazakhstan, *J. Clean. Prod.* 217 (2019) 352–359.
- [153] R. Abu, R. Yahya, S. Neon, Production of High Purity Amorphous Silica from Rice Husk, *Procedia Chem.* 19 (2016) 189–195.
- [154] S. Laurent, D. Forge, M. Port, a Roch, C. Robic, L. V Elst, R.N. Muller, Magnetic Iron Oxide Nanoparticles: Synthesis, Stabilization, Vectorization, Physicochemical Characterizations, and Biological Applications (vol 108, pg 2064, 2008), *Chem. Rev.* 108 (2008) 2064–2110.
- [155] R.P. Pal Singh, I.S. Hudiera, S.B. Rana, Effect of calcination temperature on the structural, optical and magnetic properties of pure and Fe-doped ZnO nanoparticles, *Mater. Sci. Pol.* 34 (2016) 451–459.
- [156] B. Purnama, A.T. Wijayanta, Suharyana, Effect of calcination temperature on structural and magnetic properties in cobalt ferrite nano particles, *J. King Saud Univ. - Sci.* (2018).
- [157] P.L. and G.M. F. Rouquerol, J. Rouquerol, K.S.W. Sing, *Adsorption by Powders and Porous Solids*, 2014.
- [158] G. Leofanti, M. Padovan, G. Tozzola, B. Venturelli, Surface area and pore texture of catalysts, 41 (1998) 207–219.
- [159] B. Azom, Calculation of BET Area of Microporous Materials with Automated Software from Quantachrome, (2013) 1–8.
- [160] T. Dippong, O. Cadar, E.A. Levei, I. Bibicu, L. Diamandescu, C. Leostean, M. Lazar, G. Borodi, L. Barbu Tudoran, Structure and magnetic properties of $\text{CoFe}_2\text{O}_4/\text{SiO}_2$ nanocomposites obtained by sol-gel and post annealing pathways, *Ceram. Int.* 43 (2017) 2113–2122.
- [161] J. Li, D.H.L. Ng, R. Ma, M. Zuo, P. Song, Eggshell membrane-derived MgFe_2O_4 for pharmaceutical antibiotics removal and recovery from water, *Chem. Eng. Res. Des.* 126 (2017) 123–133.
- [162] M. Ghaemi, G. Absalan, Fast removal and determination of doxycycline in water samples and honey by Fe_3O_4 magnetic nanoparticles, *J. Iran. Chem. Soc.* 12 (2015) 1–7.
- [163] A.B. Salviano, M.R.D. Santos, L.M. de Araújo, J.D. Ardisson, R.M. Lago, M.H. Araujo, Iron Oxide Nanoparticles Supported on Mesoporous MCM-41 for Efficient Adsorption of Hazardous β -Lactamic Antibiotics, *Water, Air, Soil Pollut.* 229 (2018) 59.

- [164] M.A. Khan, W.T. Wallace, S.Z. Islam, S. Nagpure, J. Strzalka, J.M. Littleton, S.E. Rankin, B.L. Knutson, Adsorption and Recovery of Polyphenolic Flavonoids Using TiO₂-Functionalized Mesoporous Silica Nanoparticles, *ACS Appl. Mater. Interfaces*. 9 (2017) 32114–32125.
- [165] Y. Kong, L. Wang, Y. Ge, H. Su, Z. Li, Lignin xanthate resin–bentonite clay composite as a highly effective and low-cost adsorbent for the removal of doxycycline hydrochloride antibiotic and mercury ions in water, *J. Hazard. Mater.* 368 (2019) 33–41.
- [166] S. Zaidi, V. Sivasankar, T. Chaabane, V. Alonzo, K. Omine, R. Maachi, A. Darchen, M. Prabhakaran, Separate and simultaneous removal of doxycycline and oxytetracycline antibiotics by electro-generated adsorbents (EGAs), *J. Environ. Chem. Eng.* 7 (2019).
- [167] S. Naeimi, H. Faghihian, Application of novel metal organic framework, MIL-53(Fe) and its magnetic hybrid: For removal of pharmaceutical pollutant, doxycycline from aqueous solutions, *Environ. Toxicol. Pharmacol.* 53 (2017) 121–132.
- [168] M.M.M. Ali, M.J. Ahmed, Adsorption behavior of doxycycline antibiotic on NaY zeolite from wheat (*Triticum aestivum*) straws ash, *J. Taiwan Inst. Chem. Eng.* 81 (2017) 218–224.
- [169] Z. Zeng, X. Tan, Y. Liu, S. Tian, G. Zeng, L. Jiang, S. Liu, J. Li, N. Liu, Z. Yin, Comprehensive Adsorption Studies of Doxycycline and Ciprofloxacin Antibiotics by Biochars Prepared at Different Temperatures, *Front. Chem.* 6 (2018) 1–11.
- [170] R. Rostamian, H. Behnejad, Insights into doxycycline adsorption onto graphene nanosheet: a combined quantum mechanics, thermodynamics, and kinetic study, *Environ. Sci. Pollut. Res.* 25 (2018) 2528–2537.
- [171] F. Esmaeeli, S.A. Gorbanian, N. Moazezi, Removal of Estradiol Valerate and Progesterone using Powdered and Granular Activated Carbon from Aqueous Solutions, *Int. J. Environ. Res.* 11 (2017) 695–705.
- [172] H.N. Tran, S.J. You, H.P. Chao, Thermodynamic parameters of cadmium adsorption onto orange peel calculated from various methods: A comparison study, *J. Environ. Chem. Eng.* 4 (2016) 2671–2682.
- [173] W. Huang, J. Chen, J. Zhang, Adsorption characteristics of methylene blue by biochar prepared using sheep, rabbit and pig manure, *Environ. Sci. Pollut. Res.* 25 (2018) 29256–29266.

- [174] Z. Li, N. Potter, J. Rasmussen, J. Weng, G. Lv, Removal of rhodamine 6G with different types of clay minerals, *Chemosphere*. 202 (2018) 127–135.
- [175] J. Kim, W. Li, B.L. Philips, C.P. Grey, Phosphate adsorption on the iron oxyhydroxides goethite (α -FeOOH), akaganeite (β -FeOOH), and lepidocrocite (γ -FeOOH): A31P NMR Study, *Energy Environ. Sci.* 4 (2011) 4298–4305.
- [176] P.S. Pinto, T.P.V. Medeiros, J.D. Ardisson, R.M. Lago, Role of [FeOx(OH)y] surface sites on the adsorption of β -lactamic antibiotics on Al₂O₃ supported Fe oxide, *J. Hazard. Mater.* 317 (2016) 327–334.
- [177] R.K. Anantha, S. Kota, An evaluation of the major factors influencing the removal of copper ions using the egg shell (*Dromaius novaehollandiae*): chitosan (*Agaricus bisporus*) composite, *3 Biotech.* 6 (2016) 1–16.
- [178] J. Heo, Y. Yoon, G. Lee, Y. Kim, J. Han, C.M. Park, Enhanced adsorption of bisphenol A and sulfamethoxazole by a novel magnetic CuZnFe₂O₄-biochar composite, *Bioresour. Technol.* 281 (2019) 179–187.
- [179] B.M. Lowe, C.K. Skylaris, N.G. Green, Acid-base dissociation mechanisms and energetics at the silica-water interface: An activationless process, *J. Colloid Interface Sci.* 451 (2015) 231–244.
- [180] L. Dalstein, E. Potapova, E. Tyrode, The elusive silica/water interface: Isolated silanols under water as revealed by vibrational sum frequency spectroscopy, *Phys. Chem. Chem. Phys.* 19 (2017) 10343–10349.
- [181] H. Wu, P. Li, D. Pan, Z. Yin, Q. Fan, W. Wu, Interactions between silicon oxide nanoparticles (SONPs) and U(VI) contaminations: Effects of pH, temperature and natural organic matters, *PLoS One*. 11 (2016) 1–17.
- [182] N. Liu, Y. Wu, H. Sha, Characterization of EDTA-cross-linked β -cyclodextrin grafted onto Fe-Al hydroxides as an efficient adsorbent for methylene blue, *J. Colloid Interface Sci.* 516 (2018) 98–109.
- [183] K. Lu, T. Wang, L. Zhai, W. Wu, S. Dong, S. Gao, L. Mao, Adsorption behavior and mechanism of Fe-Mn binary oxide nanoparticles: Adsorption of methylene blue, *J. Colloid Interface Sci.* 539 (2019) 553–562.

- [184] R. Li, W. Liang, J.J. Wang, L.A. Gaston, D. Huang, H. Huang, S. Lei, M.K. Awasthi, B. Zhou, R. Xiao, Z. Zhang, Facilitative capture of As(V), Pb(II) and methylene blue from aqueous solutions with MgO hybrid sponge-like carbonaceous composite derived from sugarcane leafy trash, *J. Environ. Manage.* 212 (2018) 77–87.
- [185] Y. Yao, F. Xu, M. Chen, Z. Xu, Z. Zhu, Adsorption behavior of methylene blue on carbon nanotubes, *Bioresour. Technol.* 101 (2010) 3040–3046.
- [186] S. Liu, X. Chen, W. Ai, C. Wei, A new method to prepare mesoporous silica from coal gasification fine slag and its application in methylene blue adsorption, *J. Clean. Prod.* 212 (2019) 1062–1071.
- [187] A.A. Basaleh, M.H. Al-Malack, T.A. Saleh, Methylene Blue removal using polyamide-vermiculite nanocomposites: Kinetics, equilibrium and thermodynamic study, *J. Environ. Chem. Eng.* 7 (2019).
- [188] N. Chaukura, E.C. Murimba, W. Gwenzi, Sorptive removal of methylene blue from simulated wastewater using biochars derived from pulp and paper sludge, *Environ. Technol. Innov.* 8 (2017) 132–140.
- [189] J. Ma, J. Zhang, D. Li, Removal of Methylene Blue by lava adsorption and catalysis oxidation, *Environ. Technol.* 31 (2010) 267–276.
- [190] Y. Hu, T. Guo, X. Ye, Q. Li, M. Guo, H. Liu, Z. Wu, Dye adsorption by resins: Effect of ionic strength on hydrophobic and electrostatic interactions, *Chem. Eng. J.* 228 (2013) 392–397.
- [191] Y.S. Al-degs, M.I. El-barghouthi, A.H. El-sheikh, G.M. Walker, Effect of solution pH, ionic strength, and temperature on adsorption behavior of reactive dyes on activated carbon, *Dye. Pigment.* 77 (2008) 16–23.
- [192] M.K. Gofar, K. Moradi, N.M. Kor, N. Moradi, Spectroscopic studies on aggregation phenomena of dyes, *Eur. J. Exp. Biol.* 4 (2014) 72–81.
- [193] A. Mourhly, M. Khachani, A. El Hamidi, M. Kacimi, M. Halim, S. Arsalane, The Synthesis and Characterization of Low-Cost Mesoporous Silica SiO₂ from Local Pumice Rock, *Nanomater. Nanotechnol.* 5 (2015) 35.
- [194] L.N. Anh Tuan, L.T. Kim Dung, L.D. Thanh Ha, N.Q. Hien, D. Van Phu, B.D. Du, Preparation and characterization of nanosilica from rice husk ash by chemical treatment combined with calcination, *Vietnam J. Chem.* 55 (2017) 455–459.

- [195] S. Sankar, S.K. Sharma, N. Kaur, B. Lee, D. Young, S. Lee, H. Jung, Biogenerated silica nanoparticles synthesized from sticky, red, and brown rice husk ashes by a chemical method, *Ceram. Int.* 42 (2016) 4875–4885.
- [196] O. Karaagac, B. Bilir, H. Köçkar, The influence of synthesis parameters on one-step synthesized superparamagnetic cobalt ferrite nanoparticles with high saturation magnetization, *J. Magn. Mater.* 473 (2019) 262–267.
- [197] A.M.M. Vargas, A.L. Cazetta, M.H. Kunita, T.L. Silva, V.C. Almeida, Adsorption of methylene blue on activated carbon produced from flamboyant pods (*Delonix regia*): Study of adsorption isotherms and kinetic models, *Chem. Eng. J.* 168 (2011) 722–730.
- [198] M.K. Uddin, A review on the adsorption of heavy metals by clay minerals, with special focus on the past decade, *Chem. Eng. J.* 308 (2017) 438–462.
- [199] Momina, M. Shahadat, S. Isamil, Regeneration performance of clay-based adsorbents for the removal of industrial dyes: A review, *RSC Adv.* 8 (2018) 24571–24587.
- [200] J.D.D. Moraes, S.R.A. Bertolino, S.L. Cuffini, D.F. Ducart, P.E. Bretzke, G.R. Leonardi, Clay minerals: Properties and applications to dermocosmetic products and perspectives of natural raw materials for therapeutic purposes—A review, *Int. J. Pharm.* 534 (2017) 213–219.
- [201] Q. Huang, M. Liu, J. Chen, K. Wang, D. Xu, F. Deng, H. Huang, X. Zhang, Y. Wei, Enhanced removal capability of kaolin toward methylene blue by mussel-inspired functionalization, *J. Mater. Sci.* 51 (2016) 8116–8130.
- [202] H. Xu, J. Liu, P. Chen, G. Shao, B. Fan, H. Wang, D. Chen, H. Lu, R. Zhang, Preparation of Magnetic Kaolinite Nanotubes for the Removal of Methylene Blue from Aqueous Solution, *J. Inorg. Organomet. Polym. Mater.* 28 (2018) 790–799.
- [203] Q. Zhang, Z. Yan, J. Ouyang, Y. Zhang, H. Yang, D. Chen, Chemically modified kaolinite nanolayers for the removal of organic pollutants, *Appl. Clay Sci.* 157 (2018) 283–290.
- [204] A. Tadjarodi, M. Imani, M. Salehi, ZnFe₂O₄ nanoparticles and a clay encapsulated ZnFe₂O₄ nanocomposite: synthesis strategy, structural characteristics and the adsorption of dye pollutants in water, *RSC Adv.* 5 (2015) 56145–56156.
- [205] G. Peng, T. Li, B. Ai, S. Yang, J. Fu, Q. He, G. Yu, S. Deng, Highly efficient removal of enrofloxacin by magnetic montmorillonite via adsorption and persulfate oxidation, *Chem. Eng. J.* 360 (2019) 1119–1127.

- [206] A. Spence, B.P. Kelleher, FT-IR spectroscopic analysis of kaolinite-microbial interactions, *Vib. Spectrosc.* 61 (2012) 151–155.
- [207] X. Liu, X. Liu, Y. Hu, Investigation of the thermal behaviour and decomposition kinetics of kaolinite, *Clay Miner.* 50 (2015) 199–209.
- [208] I. Fatimah, Preparation, characterization and physicochemical study of 3-amino propyl trimethoxy silane-modified kaolinite for Pb(II) adsorption, *J. King Saud Univ. - Sci.* 30 (2018) 250–257.
- [209] S. Yuan, Y. Li, Y. Han, P. Gao, G. Gong, Investigation on Calcination Behaviors of Coal Gangue by Fluidized Calcination in Comparison with Static Calcination, *Minerals.* 7 (2017) 19.
- [210] M.S.I. Mozumder, M.A. Islam, Development of Treatment Technology for Dye Containing Industrial Wastewater, *J. Sci. Res.* 2 (2010) 567.
- [211] M.K. Purkait, A. Maiti, S. DasGupta, S. De, Removal of congo red using activated carbon and its regeneration, *J. Hazard. Mater.* 145 (2007) 287–295.
- [212] B. Samiey, F. Ashoori, Adsorptive removal of methylene blue by agar: Effects of NaCl and ethanol, *Chem. Cent. J.* 6 (2012) 14. doi:10.1186/1752-153X-6-14.
- [213] M.R.R. Kooh, M.K. Dahri, L.B.L. Lim, The removal of rhodamine B dye from aqueous solution using *Casuarina equisetifolia* needles as adsorbent, *Cogent Environ. Sci.* 2 (2016) 1–14. doi:10.1080/23311843.2016.1140553.
- [214] M. Doğan, M. Alkan, Adsorption kinetics of methyl violet onto perlite, *Chemosphere.* 50 (2003) 517–528. doi:10.1016/S0045-6535(02)00629-X.
- [215] X. Zhang, Y. Li, M. Li, H. Zheng, Q. Du, H. Li, Y. Wang, D. Wang, C. Wang, K. Sui, H. Li, Y. Xia, Preparation of improved gluten material and its adsorption behavior for congo red from aqueous solution, *J. Colloid Interface Sci.* 556 (2019) 249–257.
- [216] C. Namasivayam, D. Kavitha, Removal of Congo Red from water by adsorption onto activated carbon prepared from coir pith, an agricultural solid waste, 54 (2002) 47–58.
- [217] R. Ahmad, P.K. Mondal, Application of modified water nut carbon as a sorbent in congo red and malachite green dye contaminated wastewater remediation, *Sep. Sci. Technol.* 45 (2010) 394–403.
- [218] B. Cheng, Y. Le, W. Cai, J. Yu, Synthesis of hierarchical Ni(OH)₂ and NiO nanosheets and their adsorption kinetics and isotherms to Congo red in water, *J. Hazard. Mater.* 185 (2011) 889–897.

- [219] Y. Zhai, J. Zhai, M. Zhou, S. Dong, Ordered magnetic core–manganese oxide shell nanostructures and their application in water treatment, *J. Mater. Chem.* 19 (2009) 7030–35.
- [220] Q.B. Zhang, Y.X. Hua, Corrosion inhibition of mild steel by alkylimidazolium ionic liquids in hydrochloric acid, *Electrochim. Acta.* 54 (2009) 1881–1887.
- [221] T. Luo, X. Hou, Q. Liang, G. Zhang, F. Chen, Y. Xia, Q. Ru, L. Yao, Y. Wu, The influence of manganese ions doping on nanosheet assembly NiFe₂O₄ for the removal of Congo red, *J. Alloys Compd.* 763 (2018) 771–780. doi:10.1016/j.jallcom.2018.05.203.
- [222] Y. Zheng, B. Zhu, H. Chen, W. You, C. Jiang, J. Yu, Hierarchical flower-like nickel(II) oxide microspheres with high adsorption capacity of Congo red in water, *J. Colloid Interface Sci.* 504 (2017) 688–696.
- [223] J. Wei, Y. Liu, J. Li, Y. Zhu, H. Yu, Y. Peng, Adsorption and co-adsorption of tetracycline and doxycycline by one-step synthesized iron loaded sludge biochar, *Chemosphere.* 236 (2019) 124254.
- [224] Q. Huang, M. Liu, L. Mao, D. Xu, G. Zeng, H. Huang, R. Jiang, F. Deng, X. Zhang, Y. Wei, Surface functionalized SiO₂ nanoparticles with cationic polymers via the combination of mussel inspired chemistry and surface initiated atom transfer radical polymerization: Characterization and enhanced removal of organic dye, *J. Colloid Interface Sci.* 499 (2017) 170–179.
- [225] R. Lafi, I. Montasser, A. Hafiane, Adsorption of congo red dye from aqueous solutions by prepared activated carbon with oxygen-containing functional groups and its regeneration, *Adsorpt. Sci. Technol.* 37 (2019) 160–181.
- [226] X.J. Jia, J. Wang, J. Wu, Y. Du, B. Zhao, D. Den Engelsen, Bouquet-like calcium sulfate dihydrate: A highly efficient adsorbent for Congo red dye, *RSC Adv.* 5 (2015) 72321–72330.
- [227] Z. Yan, D.I. Gittins, D. Skuse, T. Cosgrove, J.S. Van Duijneveldt, Nonaqueous suspensions of surface-modified kaolin, *Langmuir.* 23 (2007) 3424–3431. doi:10.1021/la063033m.
- [228] P.S. Kumar, C. Vincent, K. Kirthika, K.S. Kumar, kinetics and equilibrium studies of Pb²⁺ ion removal from aqueous solutions by use of nano-silversol-coated activated carbon, 27 (2010) 339–346.
- [229] Y.S. Ho, G. McKay, Pseudo-second order model for sorption processes, *Process Biochem.* 34 (1999) 451–465.

- [230] D. Robati, Pseudo-second-order kinetic equations for modeling adsorption systems for removal of lead ions using multi-walled carbon nanotube, *J. Nanostructure Chem.* 3 (2013) 55.
- [231] Z.S. and L.D. Zhiyan Zou, Highly efficient removal of Cu (II) from aqueous solution using a novel magnetic EDTA functionalized CoFe₂O₄, *RSC Adv.* 7 (2017) 5195–5205.
- [232] J. Liu, R. Gaikwad, A. Hande, S. Das, T. Thundat, Mapping and Quantifying Surface Charges on Clay Nanoparticles, *Langmuir.* 31 (2015) 10469–10476.
- [233] E. Tombácz, M. Szekeres, Surface charge heterogeneity of kaolinite in aqueous suspension in comparison with montmorillonite, *Appl. Clay Sci.* 34 (2006) 105–124.
- [234] Z. Zhao, X. Wang, C. Zhao, X. Zhu, S. Du, Adsorption and desorption of antimony acetate on sodium montmorillonite, *J. Colloid Interface Sci.* 345 (2010) 154–159.
- [235] L. Ai, Y. Zhou, J. Jiang, Removal of methylene blue from aqueous solution by montmorillonite/CoFe₂O₄ composite with magnetic separation performance, *Desalination.* 266 (2011) 72–77. doi:10.1016/j.desal.2010.08.004.
- [236] G.O. El-Sayed, Removal of methylene blue and crystal violet from aqueous solutions by palm kernel fiber, *Desalination.* 272 (2011) 225–232. doi:10.1016/j.desal.2011.01.025.
- [237] L. Ai, C. Zhang, Z. Chen, Removal of methylene blue from aqueous solution by a solvothermal-synthesized graphene/magnetite composite, *J. Hazard. Mater.* 192 (2011) 1515–1524.
- [238] W.T. Al-rubayee, O.F. Abdul-rasheed, N.M. Ali, Preparation of a Modified Nanoalumina Sorbent for the Removal of Alizarin Yellow R and Methylene Blue Dyes from Aqueous Solutions, 2016 (2016).
- [239] J.Z. Guo, B. Li, L. Liu, K. Lv, Removal of methylene blue from aqueous solutions by chemically modified bamboo, *Chemosphere.* 111 (2014) 225–231.
- [240] K. Chinoune, K. Bentaleb, Z. Boubberka, A. Nadim, U. Maschke, Adsorption of reactive dyes from aqueous solution by dirty bentonite, *Appl. Clay Sci.* 123 (2016) 64–75.
- [241] R.M. Schneider, C.F. Cavalin, M.A.S.D. Barros, C.R.G. Tavares, Adsorption of chromium ions in activated carbon, 132 (2007) 355–362. doi:10.1016/j.cej.2007.01.031.
- [242] L. Cottet, C.A.P. Almeida, N. Naidek, M.F. Viante, M.C. Lopes, N.A. Debacher, Adsorption characteristics of montmorillonite clay modified with iron oxide with respect to methylene blue in aqueous media, *Appl. Clay Sci.* 95 (2014) 25–31.

APPENDIX

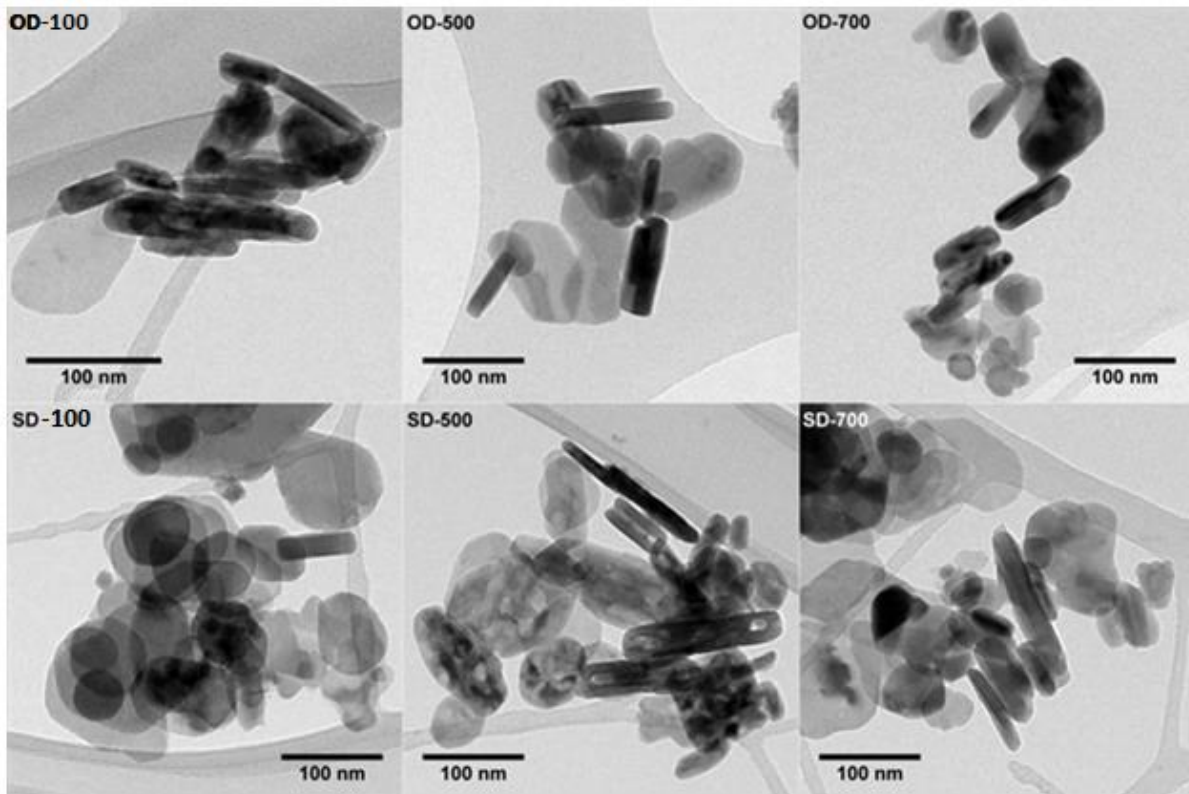


Fig. A1. Bright field TEM images of all the oven and spray dried cobalt ferrite.

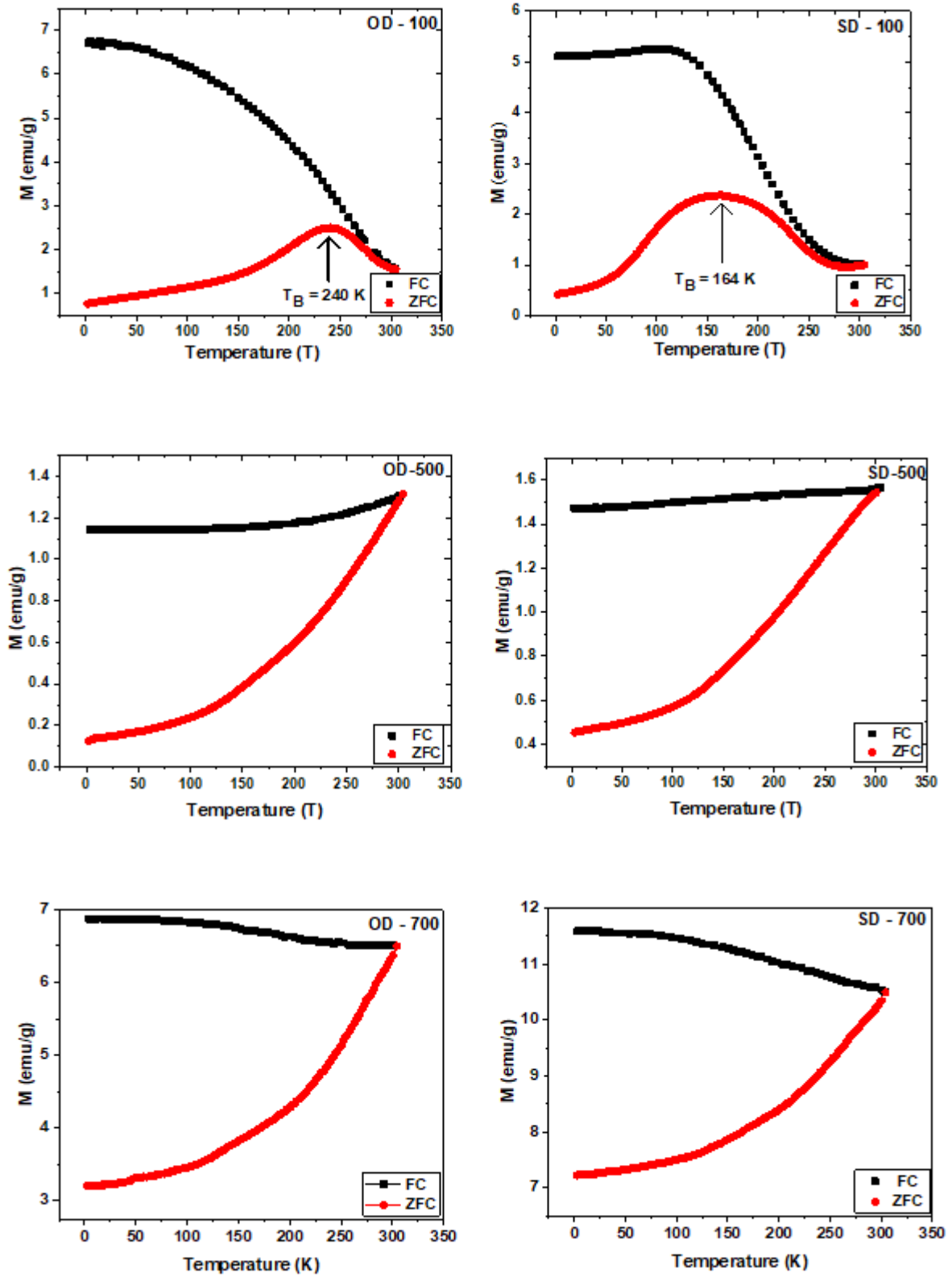


Fig. A2. ZFC and FC magnetic curves of cobalt ferrite under an applied magnetic field of 50 Oe

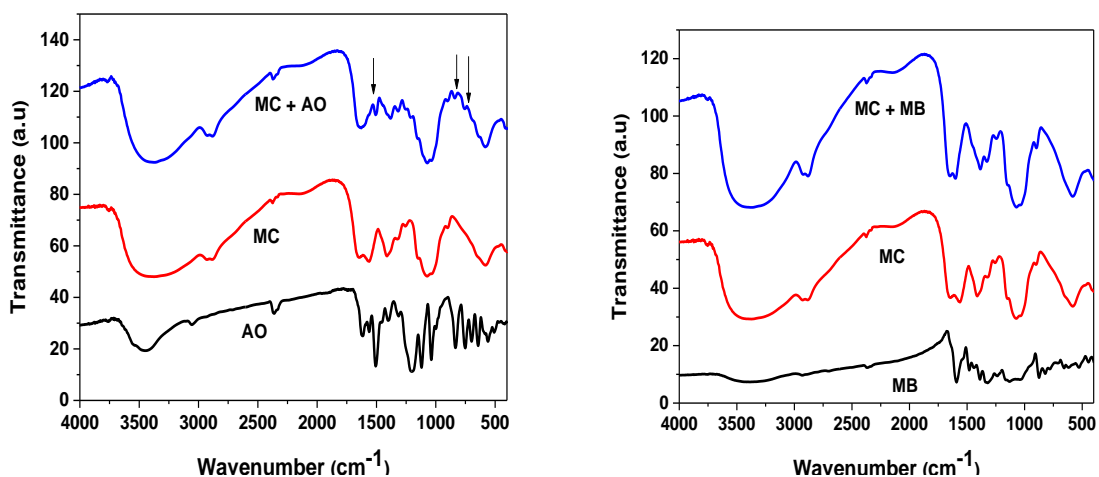


Fig. A3. FTIR spectra of acid orange (AO), methylene blue (MB), magnetic chitosan (MC), magnetic chitosan after adsorption of acid orange (MC + AO), and magnetic chitosan after adsorption of methylene blue (MC + MB),

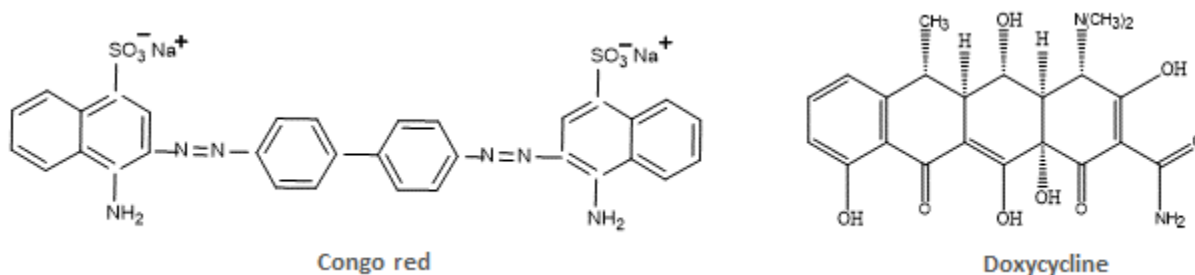


Fig. A4. The structure of Congo red and doxycycline.

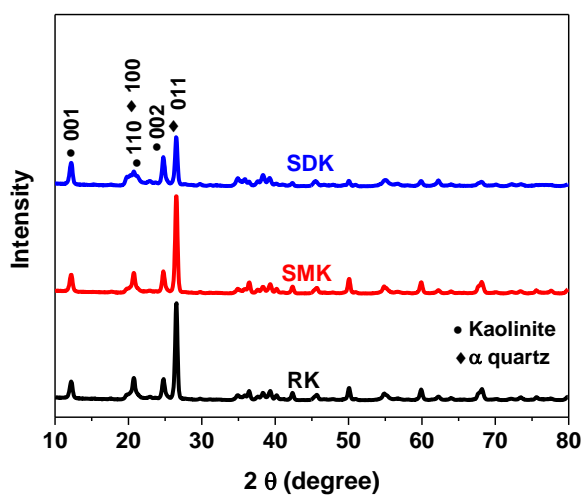


Fig. A5: XRD of RK, SMK and SDK.

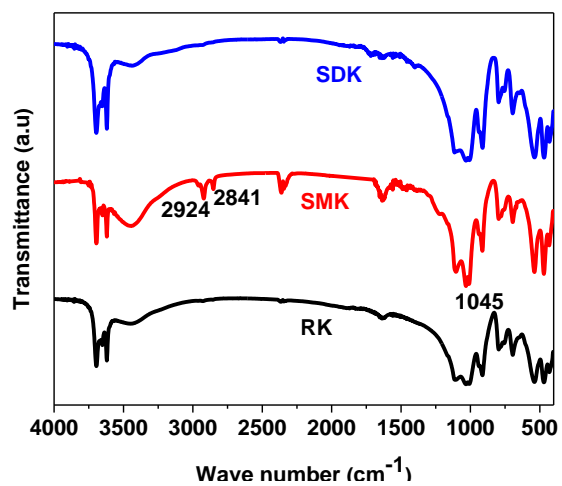


Fig. A6: FTIR of RK, SMK and SDK.

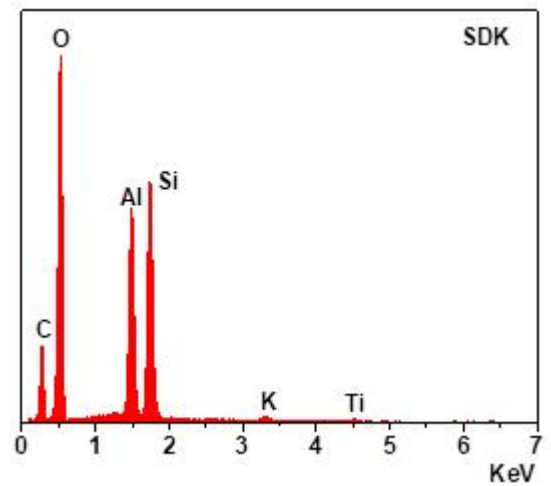
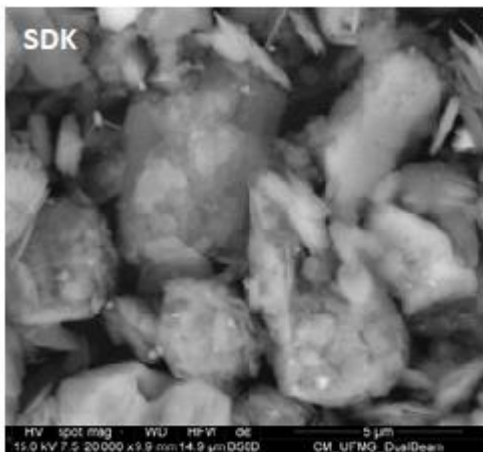
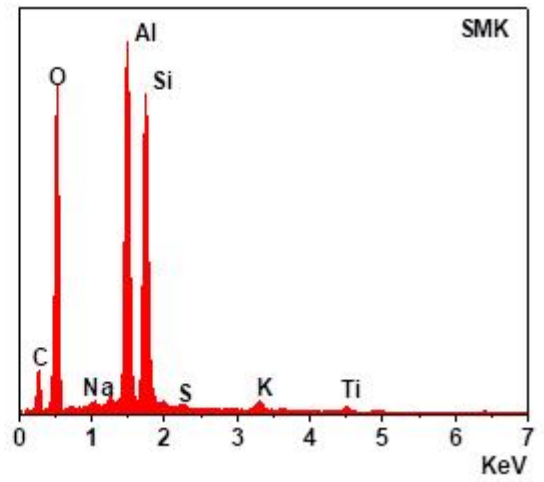
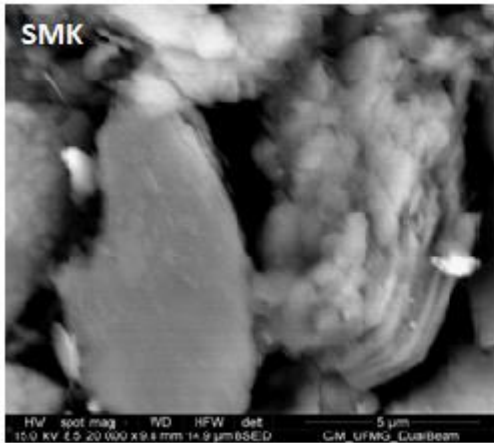
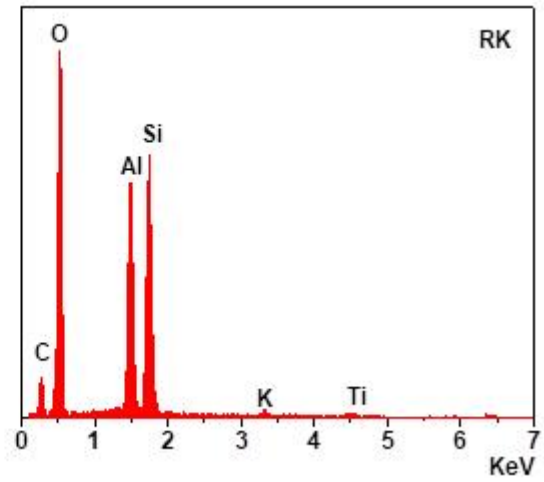
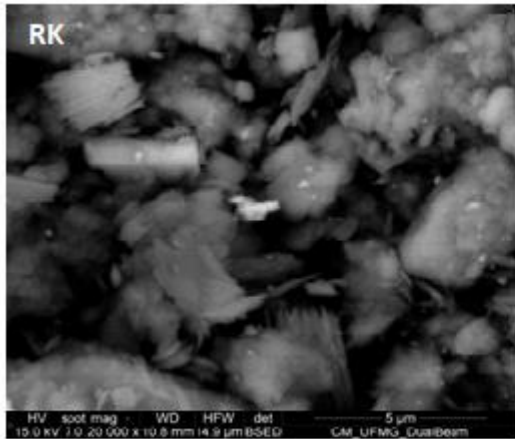


Fig. A7: SEM of RK, SMK and SDK.

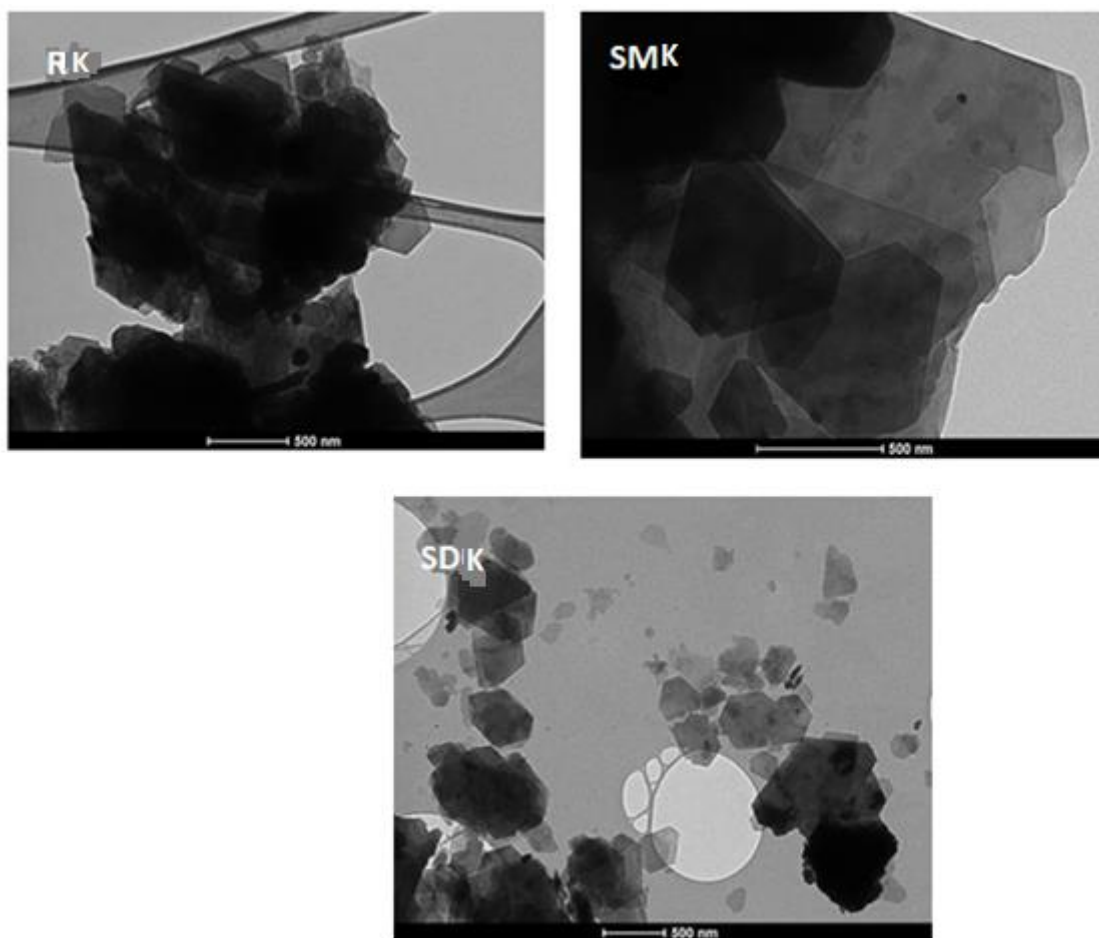


Fig. A8: TEM of RK, SMK and SDK.

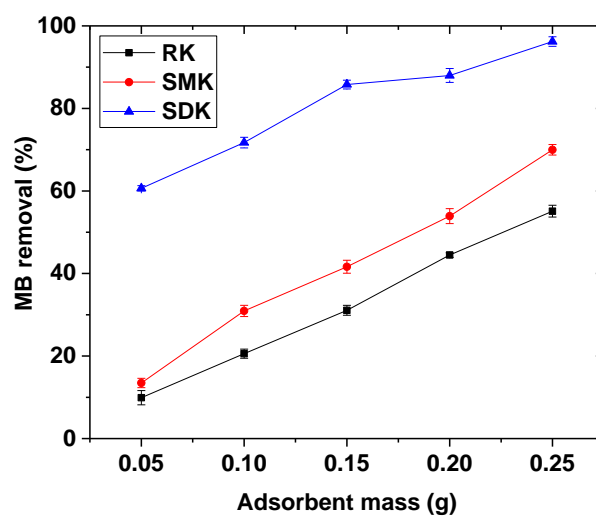


Fig. A9: Effect of dosage of RK, SMK and SDK on the adsorption of MB

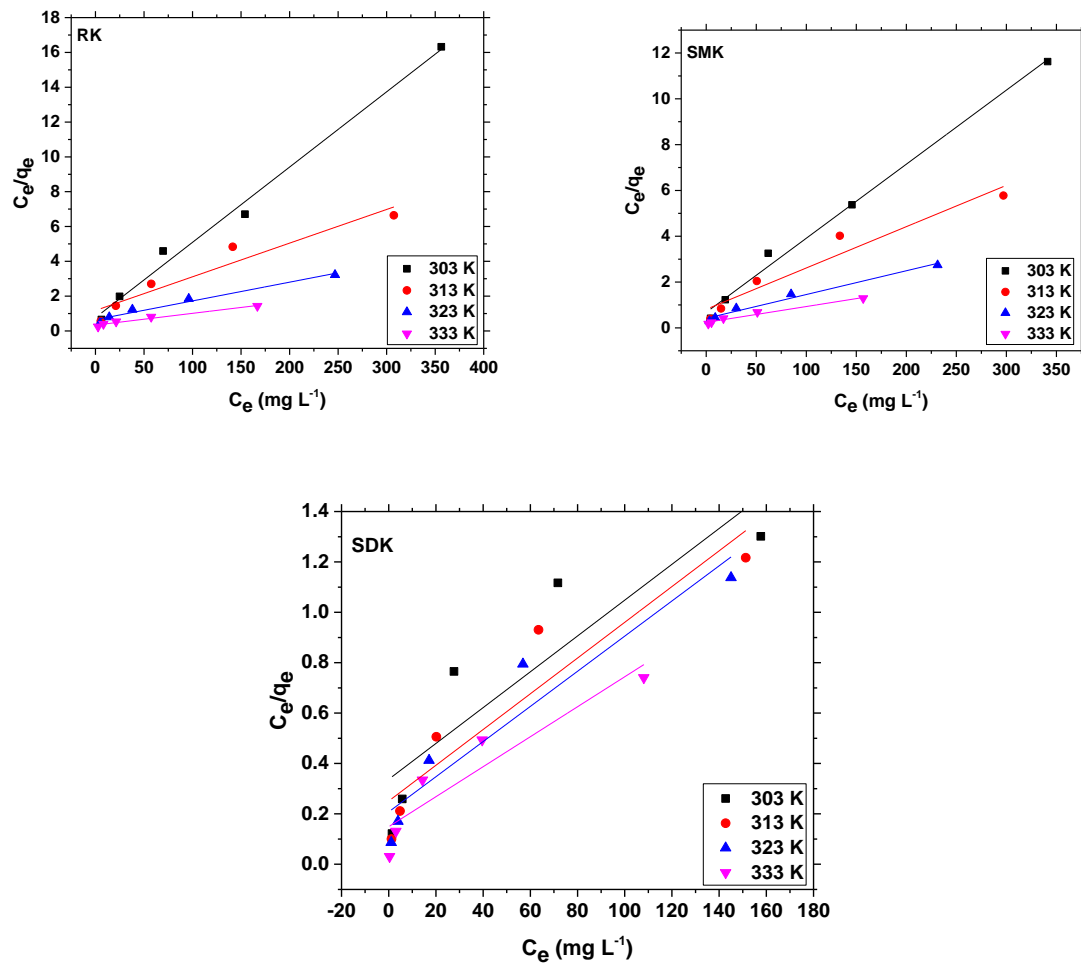


Fig. A10: Langmuir isotherm for the adsorption of MB on RK, SMK and SDK as a function of temperature.

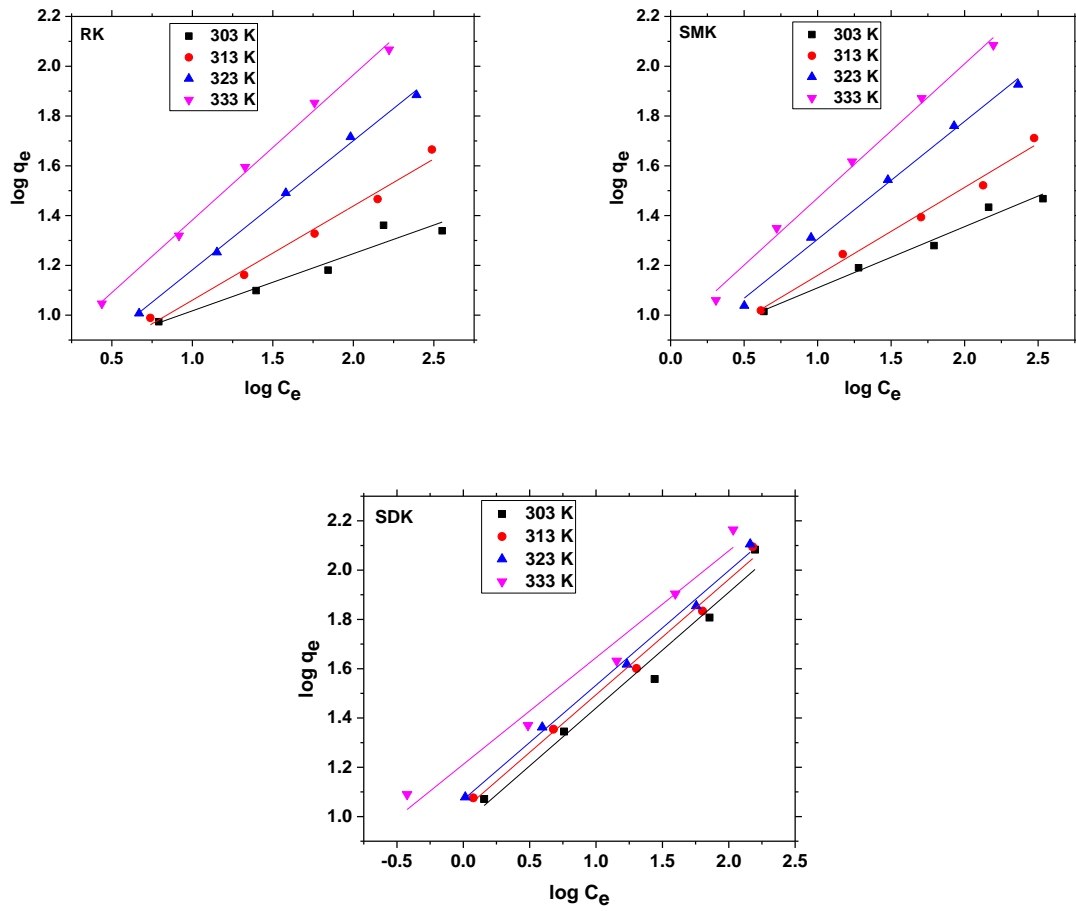


Fig. A11: Freundlich isotherm for the adsorption of MB on RK, SMK and SDK as a function of temperature.

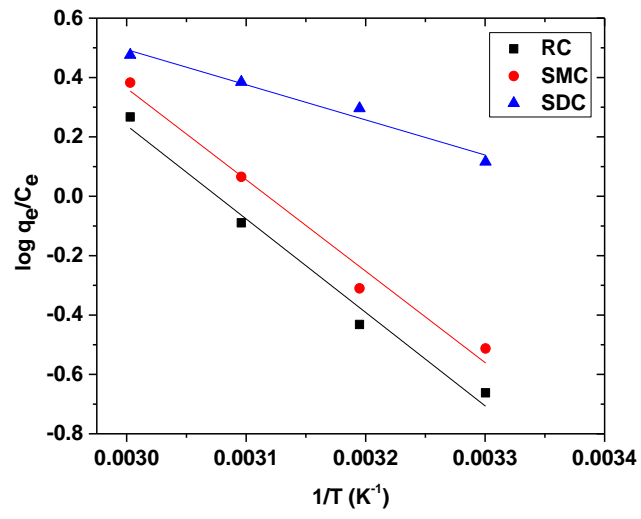
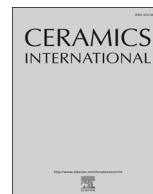


Fig. A12: Plot of $\log \frac{q_e}{C_e}$ versus $\frac{1}{T}$ for the estimation of the thermodynamic parameters for MB the adsorption.

ANEXOS

List of publications

1. **Olusegun, S.J.**, Mohallem, N.D.S., (2020). Comparative adsorption mechanism of doxycycline and Congo red using synthesized kaolinite supported CoFe_2O_4 nanoparticles. *Environ. Pollut.* 260, 114019.
<https://doi.org/10.1016/j.envpol.2020.114019>.
2. **Olusegun Sunday J.**, Erico T. F. Freitas, Luciano R. S. Lara, Nelcy D. S. Mohallem (2019). Synergistic effect of a spinel ferrite on the adsorption capacity of nano bio-silica for the removal of methylene blue. *Environ. Technol.* 0, 1–10.
<https://doi.org/10.1080/09593330.2019.1694083>.
3. **Olusegun S.J.** and Nelcy D. S. Mohallem, (2019). Insight into the adsorption of doxycycline hydrochloride on different thermally treated hierarchical CoFe_2O_4 /bio-silica nanocomposite. *Journal of Environmental Chemical Engineering. J. Environ. Chem. Eng.* 7,103442. <https://doi.org/10.1016/j.jece.2019.103442>.
4. **Olusegun, S.J.**, Rodrigues, G.L.S., Freitas, E.T.F., Lara, L.R.S., Rocha, W.R., Mohallem, N.D.S., (2019): Sequestering anionic and cationic dyes from wastewater using spray dried biopolymeric magnetic composite: Experimental and theoretical studies. *J. Hazard. Mater.* 380, 120872.
<https://doi.org/10.1016/j.jhazmat.2019.120872>.
5. **Olusegun, S. J.**, Freitas, E.T.F., Lara, L.R.S., Stumpf, H.O., Mohallem, N.D.S., (2019): Effect of drying process and calcination on the structural and magnetic properties of cobalt ferrite. *Ceram. Int.* 45, 8734–8743.
<https://doi.org/10.1016/j.ceramint.2019.01.197>.
6. **Olusegun, S.J.**, de Sousa Lima, L.F., Mohallem, N.D.S., (2018): Enhancement of adsorption capacity of clay through spray drying and surface modification process for wastewater treatment. *Chem. Eng. J.* 334, 1719–1728.
<https://doi.org/10.1016/j.cej.2017.11.084>.



Effect of drying process and calcination on the structural and magnetic properties of cobalt ferrite



Sunday Joseph Olusegun^{a,b,*}, Erico Tadeu Fraga Freitas^c, Luciano Roni Silva Lara^a, Humberto Osório Stumpf^a, Nelcy Della Santina Mohallem^{a,**}

^a Universidade Federal de Minas Gerais, Departamento de Química, Laboratório de Materiais Nanoestruturados, Belo Horizonte, Brazil

^b Department of Metallurgical and Materials Engineering, Federal University of Technology, PMB 704, Akure Ondo, Nigeria

^c Universidade Federal de Minas Gerais, Centro de Microscopia, 31.270-901, Belo Horizonte, Brazil

ARTICLE INFO

Keywords:

Spray drying process
Specific surface area
Methylene blue adsorption and magnetic properties

ABSTRACT

Synthesis of CoFe_2O_4 nanoparticles was carried out using a co-precipitation method. The resulting precipitate was dried by using conventional method (oven), and spray drying process. The products obtained from the two drying processes were calcined at 500 and 700 °C; and characterized by powder X-ray diffraction (XRD), scanning electron microscopy (SEM) transmission electron microscopy (TEM), and N_2 gas adsorption technique. Magnetic measurements were performed on a SQUID magnetometer. The magnetic saturation value (76 emu g^{-1}) of the spray dried cobalt ferrite calcined at 700 °C (SD-700) was higher than its corresponding oven-dried sample. The as-received spray dried CoFe_2O_4 nanoplates (SD-100) has the highest BET specific surface area ($138 \text{ m}^2 \text{ g}^{-1}$), while the oven-dried sample calcined at 700 °C (OD-700) has the lowest area ($47 \text{ m}^2 \text{ g}^{-1}$). Cobalt ferrite samples obtained from the two drying processes were briefly applied to adsorb methylene blue solution as a cationic dye model to know the effect of drying process on the adsorption of dye. The studies showed that all the spray dried samples performed better in adsorbing methylene blue (MB) solution. Energy-filtered TEM (EFTEM) analysis that was carried out on SD-700 ascertained the adsorption of MB on its surface.

1. Introduction

The unique crystal structure of spinel ferrite and its various chemical compositions have made it stand out among other ferrites, thereby attracting the profound interest of the researchers [1–3]. Cobalt ferrite is a typical example of inverse spinel ferrite [4]; found to be an interesting magnetic material that has magnetic properties which encompass large magnetic anisotropy ($1.8\text{--}3 \times 10^5 \text{ J m}^{-3}$) and moderate magnetization saturation (80 emu g^{-1}) [5–8]. It is chemically stable, with encouraging mechanical hardness [9,10]. These properties made cobalt ferrite a useful material for different applications.

Nanocrystalline cobalt ferrite is regarded as an essential material due to its inherent thermal, magnetic, chemical and electrical properties [11]. Various contaminants such as heavy metals and dyes among others have been successfully removed from wastewater by cobalt ferrite [12–14]. It has also been combined with adsorbents and photocatalytic materials in treating wastewater due to its ability to be easily separated from solutions by external magnetic field after being used to remove toxic pollutants [15–18]. A study carried out by Kooti and

Afshari [19] showed that it could act as an excellent catalyst for the conversion of alkenes to aldehydes or epoxides.

Furthermore, it has been proven to be an effective material for drug delivery systems. It is an appropriate magnetic material for hyperthermia application, clinical practice and for isolating and purifying genomic DNA [20–22]. Application of Co-ferrite in drug delivery systems by using hyperthermia method has brought a significant breakthrough and provided a broader view on releasing of drug to a targeted location [23]. Yahya et al. [24], concluded from their research that cobalt ferrite successfully absorbed electromagnetic waves, which resulted to reduction in the oil viscosity and increment in oil recovery.

It was gathered from the literature that characteristics of magnetic nanoparticles depend on the synthesis route and drying process [6]. Given this, several authors have carried out various researches on cobalt ferrite and its synthesis route [25–27]; to provide a well viable and cost-effective means of synthesizing spinel ferrites. Mahboubeh et al. [28], utilized combustion, co-precipitation and Stöber (precipitation) methods to synthesized cobalt ferrite with crystal size (49.5 nm) and saturation magnetization (55.8 emu g^{-1}). Also, Ristic et al. [29], used

* Corresponding author. Universidade Federal de Minas Gerais, Departamento de Química, Laboratório de Materiais Nanoestruturados, Belo Horizonte, Brazil.

** Corresponding author.

E-mail addresses: arewasegun@ufmg.br (S.J. Olusegun), nelcy@ufmg.br (N.D.S. Mohallem).

<https://doi.org/10.1016/j.ceramint.2019.01.197>

Received 26 June 2018; Received in revised form 23 December 2018; Accepted 24 January 2019

Available online 25 January 2019

0272-8842/ © 2019 Elsevier Ltd and Techna Group S.r.l. All rights reserved.

co-precipitation method to synthesized cobalt ferrite and studied the influence of pH and autoclaving time on the crystallite size and magnetic measurement of CoFe_2O_4 . According to their report, both the crystallite size and magnetic saturation increased with the increase in pH.

In view of this, chemical co-precipitation method was used to prepared cobalt ferrite used in this study. This process has been noted to be a suitable method for the synthesis of nanoparticles; it is less time consuming and cost-effective [30]. However, the significant effect of drying process on magnetic, textural, morphological and structural properties of cobalt ferrite and its effectiveness in treating contaminant propelled our curiosity. Therefore, we employed spray drying and conventional oven drying method to dry co-precipitated cobalt ferrite used for the study. Agnese Stunda-Zujeva et al., and Olusegun et al. [31,32], wrote that spray drying method is one of the most amazing, convenient and fast techniques that could be used to produce particles of high surface area. The performance of the oven and spray dried cobalt ferrite on the adsorption of the methylene blue was studied (in brief) before and after calcination process.

2. Experimental details

2.1. Materials

Iron and cobalt sulfate ($\text{FeSO}_4 \cdot 7\text{H}_2\text{O}$ and $\text{CoSO}_4 \cdot 7\text{H}_2\text{O}$) were purchased from Dinamica Quimica Contemporanea Ltd., Brazil, while methylene blue (MB) was from Labsynth.

2.2. Cobalt ferrite synthesis

For this study, CoFe_2O_4 was prepared by chemical co-precipitation method. In this case, $\text{FeSO}_4 \cdot 7\text{H}_2\text{O}$ and $\text{CoSO}_4 \cdot 7\text{H}_2\text{O}$ were mixed in ratio 2:1 and dissolved in distilled water by gently heating the solution and stirred for one hour. An aqueous solution of NaOH was added to the mixture and stirred continuously until the pH reached 12. Digestion was carried out at 90 °C on a hot plate for 2 h, after which the gelatinous precipitate formed was washed with distilled water till pH 7 was attained. Part of the neutralized precipitate was oven dried at 100 °C, while the rest was spray dried.

2.3. Preparation of spray-dried cobalt ferrite

The neutralized cobalt ferrite solution was continuously stirred throughout spray drying period. Spray dryer MSD 0.5 with 1 mm nozzle was used for the drying process. The process was performed by setting an inlet temperature at 120 °C and air flow rate at 50 L min^{-1} pressure. The dried product was collected in a collection bottle.

2.4. Calcination process

The respective oven and spray-dried cobalt ferrite samples were further calcined at 500 and 700 °C for two hours. The scheme of the synthesis is shown in Fig. 1.

2.5. Characterization of the samples

X-ray diffraction (XRD) was performed in an X-ray diffractometer (Shimadzu, XRD 7000) using $\text{CuK}\alpha$ radiation. High spatial resolution morphology, composition, and crystallography were achieved by transmission electron microscopy (TEM), electron energy-loss spectroscopy (EELS), and selected area electron diffraction (SAD) in a non-corrected spherical aberration ($C_s = 2 \text{ mm}$) microscope Tecnai G2-20 SuperTWIN (FEI) with a LaB_6 thermoionic gun and an acceleration voltage of 200 kV, coupled with a Gatan Image Filter (GIF) Quantum System SE (Gatan). The specific surface area was determined by Nitrogen adsorption in a Quantachrome Autosorb, using the Brunauer-

Emmett-Teller (BET) method. The magnetic property was determined by using S700X SQUID magnetometer.

2.6. Adsorption tests

A mass of 0.1 g of cobalt ferrite was added to 12 mL of methylene blue solution (50 mg L^{-1}). The solution was left for 30 min, after which cobalt ferrite was magnetically separated from the solution. The absorbance of the methylene blue in the remaining solution was determined by UV-vis adsorption spectra. The values obtained were plotted against wavelength within the range of 500–700 nm and compared with the original solution (50 mg L^{-1}) of methylene blue.

3. Result and discussion

3.1. X-ray diffraction analysis

The diffractograms of all samples are shown in Fig. 2. The pattern matched with card number 22–1086 of Joint Committee on Powder Diffraction Standards (JCPDS), which is a typical pattern of cubic spinel ferrite having space group of $Fd\text{-}3m$ ($N^\circ 227$). The diffractograms of the as-received samples: OD-100 and SD-100 showed the presence of two phases: CoFe_2O_4 and $\text{Co}_{0.33}\text{Fe}_{0.67}(\text{OOH})$ (card #14–558). Meanwhile, $\text{Co}_{0.33}\text{Fe}_{0.67}(\text{OOH})$ phase disappeared after calcination. Phase transformation was observed after the samples were calcined at 500 °C, leading to the appearance of hematite phase.

Another observation was the slight shift of peak (311) in both OD-100 and SD-100 diffractograms after calcining at 500 °C. The dehydroxylation of Cobalt – iron (oxy) hydroxide ($\text{Co}_{0.33}\text{Fe}_{0.67}(\text{OOH})$) phase at this temperature could have been responsible for the shift. Thermal decomposition of this phase could have initiated the movement of certain amount of Co^{2+} ions from octahedral to the tetrahedral sites, and equivalent transfer of Fe^{3+} ions from tetrahedral to octahedral sites. Rao et al. [33] as well reported a shift in peak due to increase in annealing temperature.

The lattice parameters (a) are itemized in Table 1. The values obtained for both OD-700 and SD-700 are closed to the reported lattice constant of pure cobalt ferrite in the literature ($8.396 \pm 0.001 \text{ \AA}$) [34].

The impure phase, Fe_2O_3 disappeared completely after the samples were calcined at 700 °C, leading to the formation of single-phase cobalt ferrite. This shows that the presence of hematite (an antiferromagnetic) in cobalt ferrite can be thermally decomposed giving rise to pure cobalt ferrite. Calcination process has effect on the purification, crystal growth and crystallization of the synthesized CoFe_2O_4 . This structural change resulted in change in the magnetic properties of the samples. However, the drying process does not have a significant effect on its structure.

3.2. TEM and HRTEM analysis

Transmission electron microscopy (TEM) images of SD-100, SD-500, and SD-700, show distinct agglomeration (Fig. 3). The reason for the agglomeration was due to interaction that exist among the particles. This feature was only observed in the spray dried images.

Bright field TEM images of all the dispersed samples are displayed in Fig. 4. The images are plate-like structure of different orientation and morphology. Some of the plates were lying flat while others were standing.

High resolution-transmission electron microscopy (HR-TEM) images of all the samples show the degree of crystallinity through the appearance of clear lattice fringes of crystalline planes in the particles (Fig. 5). The clear appearance of the fringes (observed at the Fast Fourier Transform in each image) increases with the increase in the calcination temperature. This is in accordance with the X-ray diffractogram results, which show increase in the crystallite size with respect to increase in temperature.

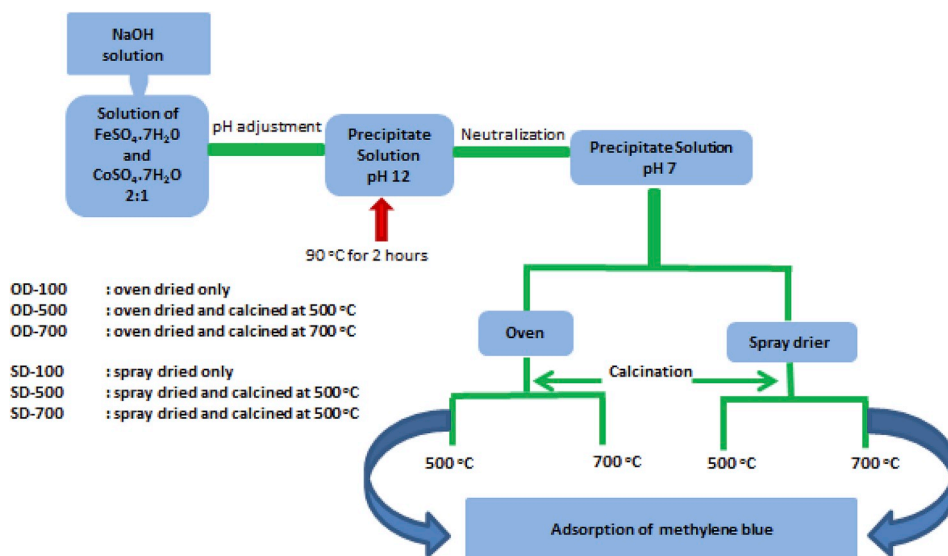


Fig. 1. Scheme of the synthesis.

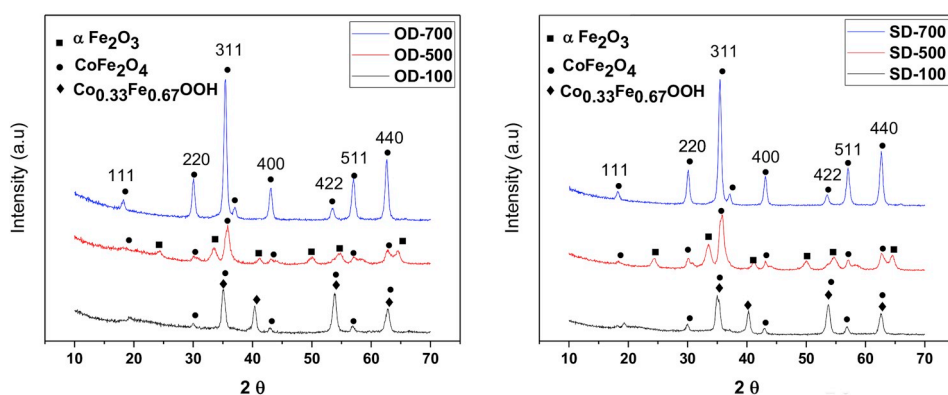


Fig. 2. XRD pattern of cobalt ferrite samples heated at three temperatures.

Table 1
Crystallite size and Lattice constant for cobalt ferrite.

Cobalt ferrite	Crystallite size (nm)	Lattice parameter (Å)
OD-100	8	8.47
OD-100	10	8.32
OD-700	14	8.40
SD-100	9	8.47
SD-500	10	8.36
SD-700	14	8.40

3.3. EELS analysis

Electron energy-loss (EELS) spectra (Fig. 6) showed complementary results of XRD. The spectra of OD-700 and SD-700 are typical of pure cobalt ferrite. The O K-edge at about 532 eV shown in the EEL spectra for OD-700 and SD-700 samples is a fingerprint of cobalt ferrite and accompanying with some features in the energy-loss near edge structure (ELNES) spectrum (e.g., few hundreds above the onset of O K-edge). The pre-peak 1 is due to the O-Fe bond only, followed by a broader peak 2. The 3rd peak (lower) is characteristic for cobalt ferrite as well as the peaks 4 (sharper) and 5, followed by the peak 6 [35]. The cobalt ferrite

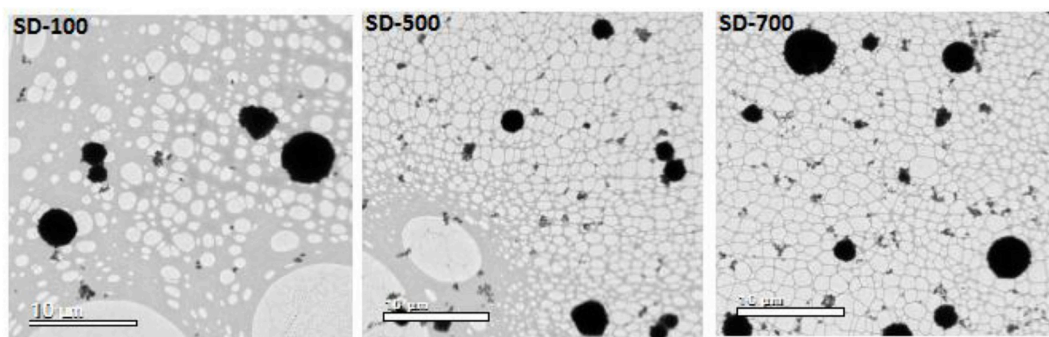


Fig. 3. TEM images of spray-dried cobalt ferrite calcined at different temperature, showing agglomeration.

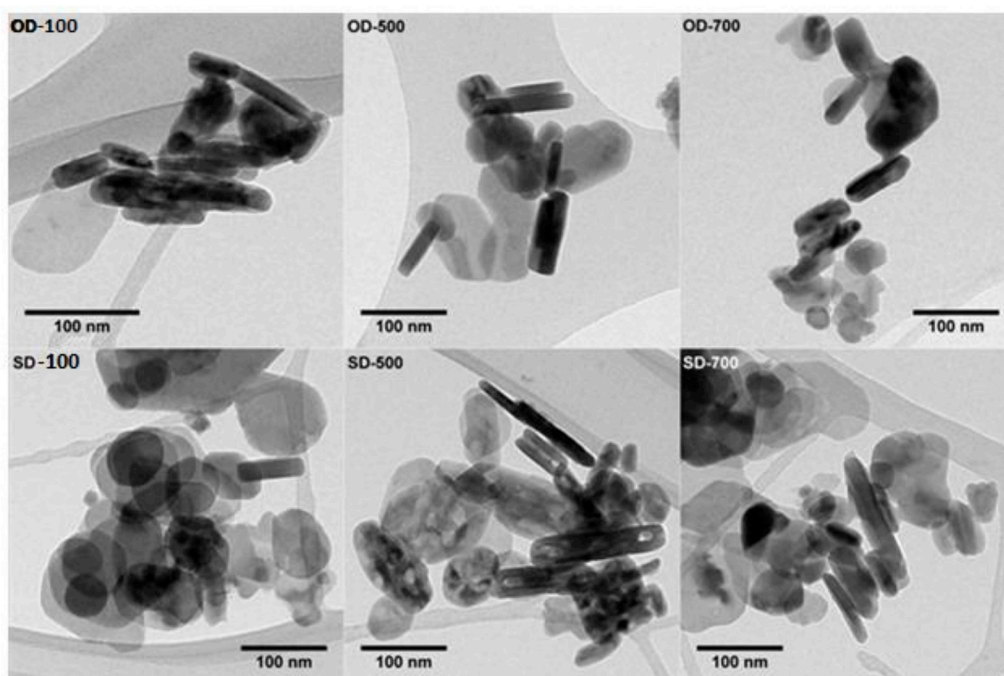


Fig. 4. Bright field TEM images of all the dispersed samples.

phase was also confirmed by XRD and selected area electron diffraction. The peaks 3 and 5 are not present in spectra of OD-100, SD-100, and SD-500 samples as the O K-edge found for particles at OD-500 and SD-500 sample resembles the coordination environment of O atom for α - Fe_2O_3 . It is possible that this phase is a Co-substituted hematite. This is also supported by the XRD data which shows a shift of the peak towards lower d-spaces.

3.4. Scanning electron microscopy (SEM)

Scanning electron microscopy analysis of spray dried samples was

performed to assess the morphology of the agglomerate observed at TEM. Averagely, the image of SD-700 (Fig. 7) shows particles with a spherical shape and a high degree of agglomeration among the fine particles (spray dried powder). It is well documented that particles with the large surface area to volume ratios tend to agglomerate so as to reduce their high surface energies [36].

3.5. BET specific surface area analysis

Nitrogen adsorption and desorption isotherms are shown in Fig. 8, while the specific surface areas (SSA) are itemized in Table 2. The

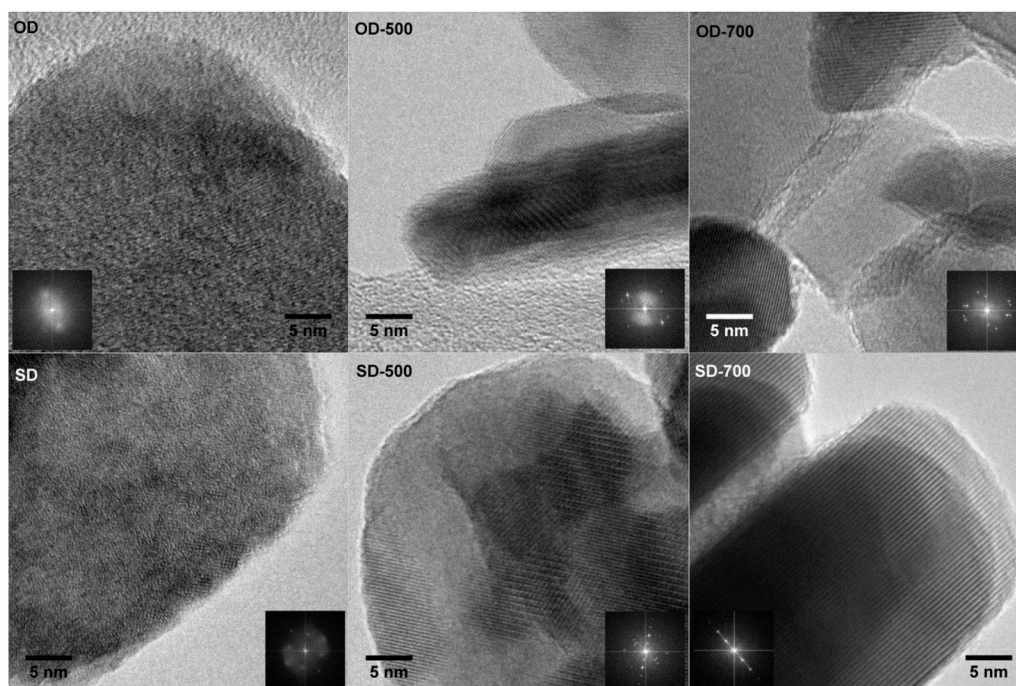


Fig. 5. HRTEM images of various cobalt ferrite samples. The inset in each image shows the Fast Fourier Transform (FFT).

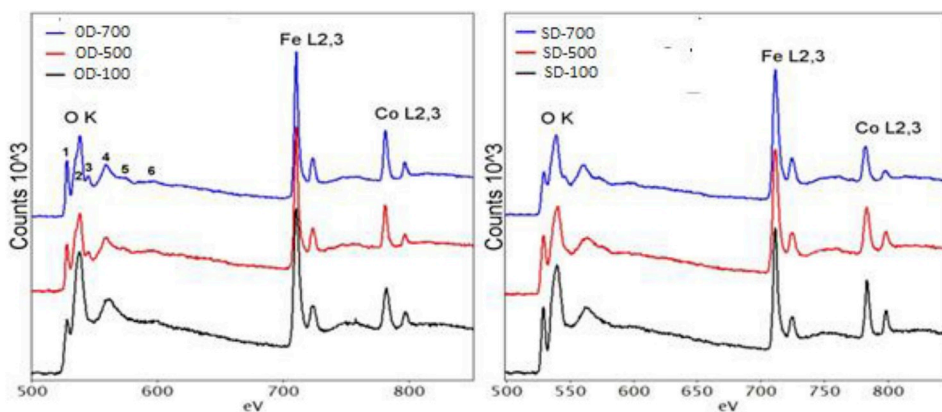


Fig. 6. EEL spectra for various cobalt ferrite samples, showing the ionization edges of O K, Fe L_{2,3} and Co L_{2,3}. The numbers 1 to 6 mark the characteristics features at the O K edge for cobalt ferrite.

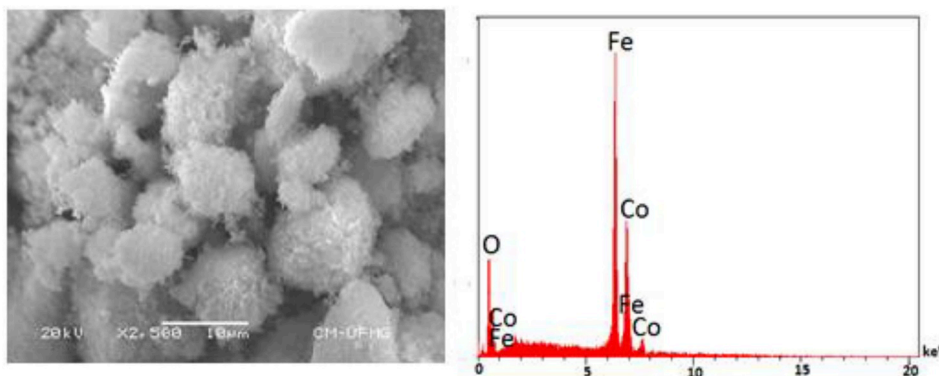


Fig. 7. SEM images of SD-700 (SEM images of SD-100 and SD-500 not shown).

specific surface areas of SD-100, SD-500, and SD-700 are higher than the respective oven-dried samples. This signifies that spray drying can improve the SSA of cobalt ferrite and perhaps other powder samples. More so, the cost of surfactant can as well be reasonably reduced or avoided by employing spray drying process to produce powder of high surface area. The results also show that the values of SSA reduce as the calcination temperature increases, which could be due to phase

transformation as observed in XRD diffractogram. This is expected because calcination leads to lower surface area as decomposition of some compounds could take place. The isotherm is typical of nonporous or macroporous material.

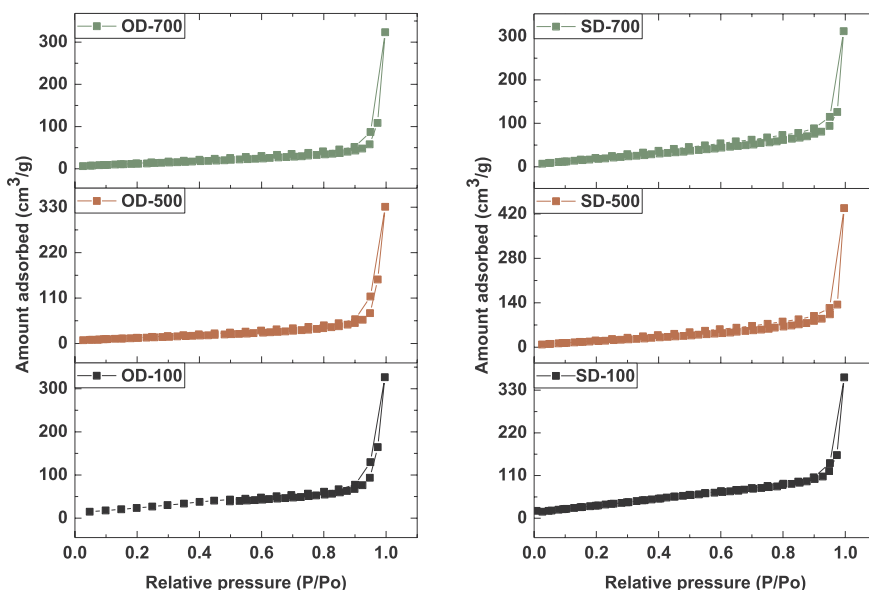


Fig. 8. Nitrogen adsorption-desorption isotherm at 77 K of the for various cobalt ferrite.

Table 2
BET specific surface area.

Cobalt ferrite with different drying process	Parameters	
	SSA ($\text{m}^2 \text{g}^{-1}$)	C constant
OD-100	92	27
OD-500	52	38
OD-700	47	28
SD-100	138	21
SD-500	86	14
SD-700	82	13

3.6. Magnetization versus temperature

The magnetic profile of synthesized cobalt ferrite (OD-100, OD-500, OD-700, SD-100, SD-500 and SD-700) was characterized by measuring the zero-field cooled (ZFC) and field cooled (FC). The results of the measurement are shown in Fig. 9. The maximum point on the ZFC curve is the blocking temperature (T_B) [37]. As shown in the Fig., ZFC of both OD-100 and SD-100 increases with temperature and attained maximum

Table 3
Magnetic anisotropy and squareness ratio at 10 and 300 K.

Cobalt ferrite	10 k		300 K	
	$\text{K} \times 10^3$ (erg cm^{-3})	Rs	$\text{K} \times 10^3$ (erg cm^{-3})	Rs
OD-100 °C	19.27	0.68	2.11	0.34
OD-500 °C	14.21	0.78	2.22	0.39
OD-700 °C	79.06	0.74	6.22	0.35
SD-100 °C	1.49	0.55	1.45	0.3
SD-500 °C	1.73	0.68	3.53	0.35
SD-700 °C	6.81	0.76	4.38	0.37

values (T_B) at 240 and 164 K respectively, after which it decreases with further increase in temperature. This type of behavior is associated with the characteristic behavior of superparamagnetic materials [38], meanwhile considering their coercivity values which are far greater than zero (Fig. 9), they cannot be regarded as pure superparamagnetic.

The presence of cobalt–iron (oxy) hydroxide in the two samples would have influence weak magnetic interaction within the particles hereby leading to attainment of blocking temperature. We infer that the

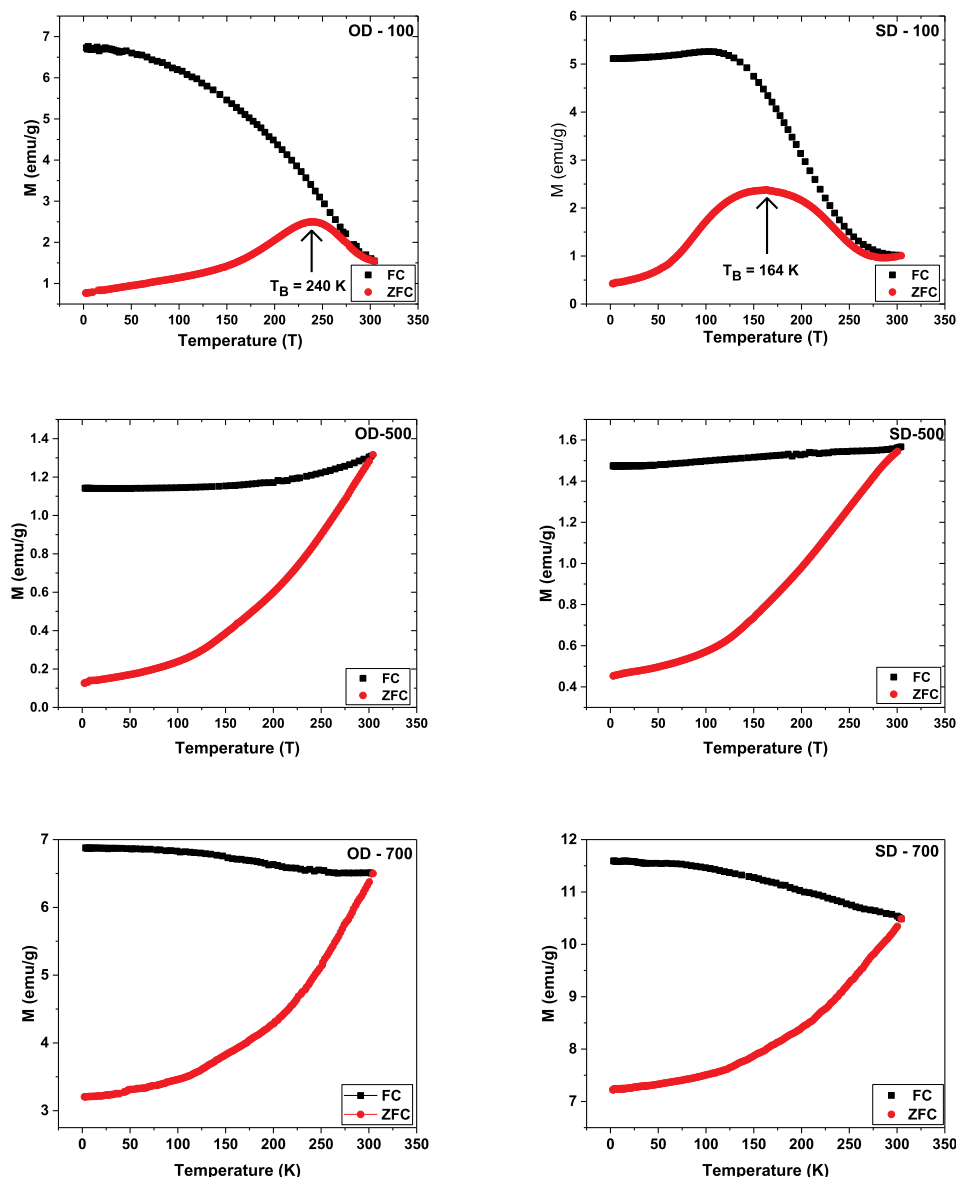


Fig. 9. ZFC and FC magnetic curves of cobalt ferrite under an applied magnetic field of 50 Oe.

presence of cobalt–iron (oxy) hydroxide hindered the response of the magnetic moment to magnetic field which leads to low magnetic anisotropy barrier (Table 3). It has been stated that anisotropy energy acts as an energy barrier that prevents free rotation of the magnetic moments away from the easy axis [39].

The value of T_B corresponds to the particles size interaction; hence for SD-100 to have attained lower T_B than OD-100, it means that the particles have higher interaction and this could have propelled the agglomeration of the particles which was noticed in the electron microscopy images. It was stated that, above the blocking temperature, the interaction between magnetic nanoparticles is very weak, while the interaction between the particles is strong below T_B [40,41]. This implies that the lower the T_B , the higher the magnetic interaction within the nanoparticles. Spray drying process enhanced the magnetic interaction (evidence in the agglomeration) of the particles which resulted to lower T_B .

The decomposition of cobalt–iron (oxy) hydroxide as confirmed from the XRD results, leads to high magnetic anisotropy energy barrier after calcination and became difficult to be overcome by thermal activation within the temperature range (10–300 K). The values of T_B are as well too high to be determined, this indicates that the materials (OD-500, OD-700, SD-500 and SD-700) are still magnetically blocked at room temperature.

3.7. Magnetization versus field

The result of magnetization as a function of applied field (Fig. 10) was carried out at 10 and 300 K. In the curves of hysteresis, the saturation magnetization (M_s) increased with increase in calcination temperature (due to the disappearance of α -Fe₂O₃ and Co_{0.33}Fe_{0.67}(OOH) phase) as listed in Table 4. The M_s of OD-100, OD-500, SD-100 and SD-500 are lower than the bulk M_s of cobalt ferrite (80 emu g⁻¹) [34], meanwhile, values obtained for the SD-700 and OD-700 are closed to the bulk M_s of cobalt ferrite. The lower saturation magnetization values reported for OD-100, OD-500, SD-100 and SD-500 are attributed to the presence of alpha hematite and cobalt–iron (oxy) hydroxide impurities which reduced the number of moments contributing to magnetic saturation.

Increase in crystallite size (itemized in Table 1) could as well be responsible for higher M_s at 700 °C. Magnetic domain size is directly proportional to crystallite size. Whenever the magnetic domain size increases, there will be corresponding increase in the number of atomic spins that align themselves in the direction of the applied magnetic field, thereby enhancing the magnetic saturation of the material [42].

It was also observed from Table 4 that the magnetic saturation of all the samples are higher at 10 K (low temperature) than 300 K (room temperature) because of reduction in thermal vibration [37]. The high values of coercivity (H_C) and a lower value of M_r at 10 K are attributed to the increased in magnetic anisotropy of the particles which prevent magnet moment from aligning in an applied field [43]. At low temperature, magnetic spin freezes and reversal of magnetization becomes difficult, resulting to high anisotropy and coercivity [44]. Coercivity of SD-100, SD-500 and SD-700 are less than their respective oven dried samples due to agglomeration which was caused by mutual interaction within particles. The respective coercivity values of this synthesized cobalt ferrite, make its applications differ at low (10 K) and room (300 K) temperature. The magnetic anisotropy (K) values shown in Table 3 are calculated from equation (1) below [44].

$$K = \frac{M_s \times H_C}{0.96} \quad (1)$$

The squareness ratio (R_S) calculated from equation (2) below is a measure of how easy it is for the direction of magnetization to re-orient to the closet easy axis after withdrawal of the magnetic field [45].

$$R_S = \frac{M_r}{M_s} \quad (2)$$

Squareness ratio obtained at room temperature for all the samples is within 0.3–0.39 implying that at 300 K the magnetic properties of the synthesized cobalt are not direction-dependent (isotropic). This is a typical example of a soft magnet with characteristic of single domain nanoparticles. Meanwhile, at 10 K, R_S range from 0.55 to 0.78, which indicates a hard magnet property, comprising of multi domain nanoparticles with high anisotropy behavior and high coercivity [43].

The difference in drying process did not have a significant effect on the squareness ratio. Comparison of saturation magnetization obtained at room temperature reported by some authors are listed in Table 5.

3.8. Adsorption analysis

The various cobalt ferrite samples were tested for the adsorption of methylene blue. Displayed in Fig. 11 is the UV–Vis spectra of methylene before and after the adsorption process. The absorbance intensity at λ_{max} reduces gradually with increase in calcination temperature of the samples. Considering the drying process, SD and OD-700 performed better than the rest samples. We would recall that it was at the diffractograms of OD-700 and SD-700 that no trace of impurities (α -Fe₂O₃ and Co_{0.33}Fe_{0.67}(OOH)) was noticed. Given this, it could be inferred that the presence of α -Fe₂O₃ and Co_{0.33}Fe_{0.67}(OOH) phase were responsible for the lower adsorption performance in the samples in which they are present. Another interesting observation again was that, although OD-700 and SD-700 have the lower specific surface area, yet due to the absence of impurity, they adsorbed methylene blue solution better than the other samples (related to the same drying process).

Now, comparing the two-drying process, it was also observed that SD-100, SD-500, and SD-700 adsorbed MB better than OD-100, OD-500 and OD-700, respectively. This is due to their higher specific surface areas and the inter-particles pores due to agglomeration of the particles as seen in SEM images. SD-700 adsorbed 93% of the initial methylene blue solution while OD-700 adsorbed 52%. This shows the significant effect that spray drying process has over the texture of the material dried in the oven. The respective pictures of methylene blue solutions before and after adsorption are shown in Fig. 12.

3.9. EFTEM images of SD-700 after adsorption

The adsorption of methylene blue (MB) on the surface of SD-700 (having the highest percentage adsorbed) was confirmed through energy-filtered TEM (EFTEM) images, which was critically examined after the adsorption process. The EELS mapping of the Fe, Co, and C were performed by using the three-window method, in which only the signal above the background at each ionization edge contributed to the EFTEM images (Fig. 13). The C signal outlining the nanoparticle was due to the C from methylene blue. The respective EFTEM images for C, Co and Fe are shown in Fig. 13. This ascertained the adsorption of MB on SD-700.

4. Conclusion

Cobalt ferrite nanoparticles were successfully synthesized by using a co-precipitation method, followed by two different drying processes (oven and spray). Two phases of impurities (α Fe₂O₃ and Co_{0.33}Fe_{0.67}(OOH)) were observed in the samples before they were calcined at 700 °C. These phases drew back the potential of the synthesized cobalt ferrite to adsorb methylene blue. The drying process seems not to have significant effects of the diffractogram, but on the magnetic, specific surface area, morphology of the samples and their ability to adsorb higher percentage of methylene blue solution. Although the calcined samples (oven and spray dried) at 700 °C has the lowest specific surface area, they adsorbed methylene blue better than non-calcined and

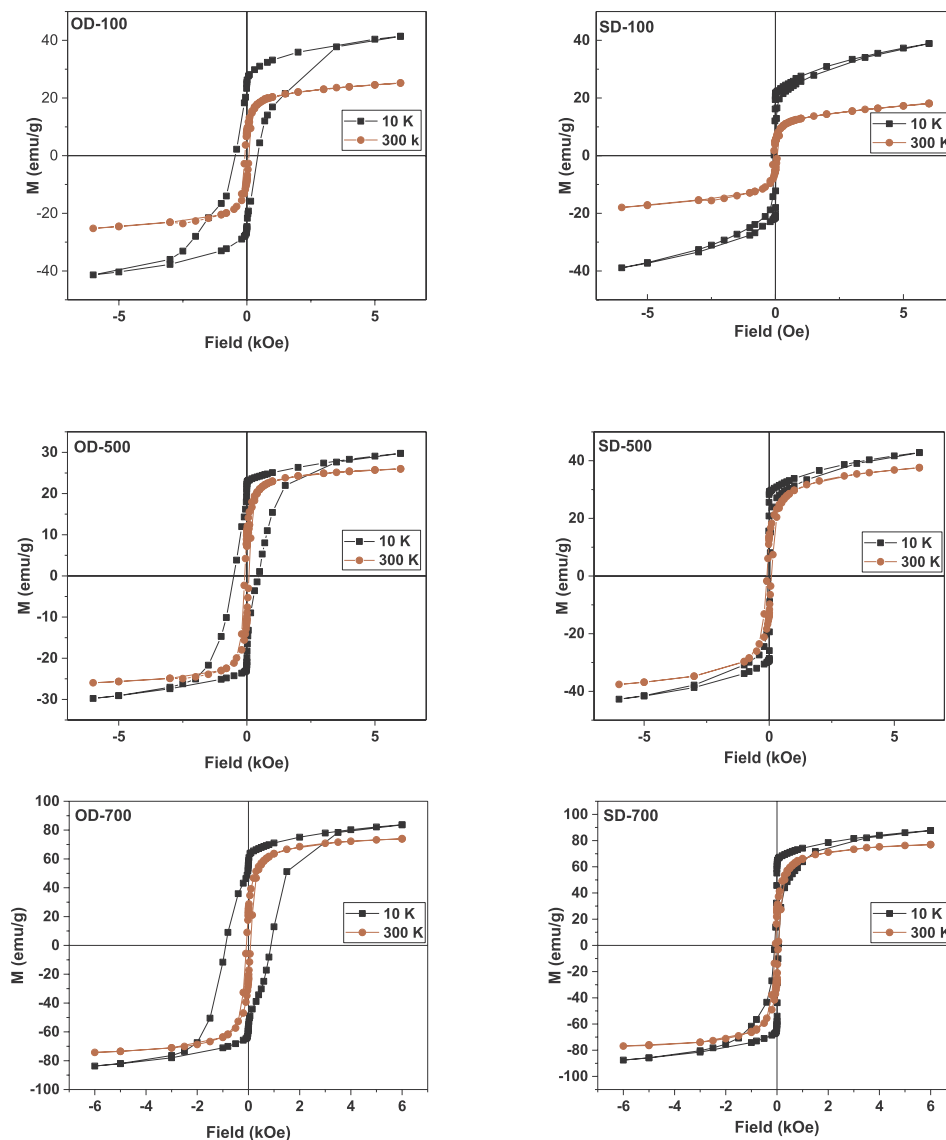


Fig. 10. Magnetization versus applied field at 10 and 300 K for cobalt ferrite samples.

Table 4
Saturation magnetization, coercivity and remanence values obtained at 10 and 300 K.

Cobalt ferrite	10 k			300 K		
	Hc (Oe)	Mr (emu g ⁻¹)	Ms (emu g ⁻¹)	Hc (Oe)	Mr (emu g ⁻¹)	Ms (emu g ⁻¹)
OD-100 °C	449	28.12	41.21	79.95	8.6	25.5
OD-500 °C	465	22.87	29.35	82.36	10.35	25.8
OD-700 °C	913	61.39	83.14	80.8	26.05	73.0
SD-100 °C	36.44	24.13	39.27	65.6	6.29	21.2
SD-500 °C	38.75	29.25	42.86	89.5	13.42	37.8
SD-700 °C	74.7	67.04	87.64	54.6	28.75	77.0

calcined at 500. This was due to the absence of impurities which resulted to single/pure phase CoFe₂O₄. This implies that the crystallite growth of the samples did not have negative effects on their ability to adsorb methylene blue solution. It was also observed that calcination changed the magnetic property from super paramagnetic to ferrimagnetic material. SD-700 has the overall best performance, implying that spray drying method could be employed to produce powder of high surface area and adsorption capacity.

Table 5
Comparison of saturation magnetization (at room temperature) reported by some authors.

Ms (emu g ⁻¹)	Reference
77	This work
73	This work
60.6	[5]
59.4	[19]
54	[23]
20	[43]
56.2	[46]
58.4	[47]
50	[48]
50	[49]
45	[50]
70.4	[51]

Acknowledgments

The authors would like to thank UFMG-Microscopy Center for the structural support, FAPEMIG, CNPq, and TWAS-CNPq for financial support

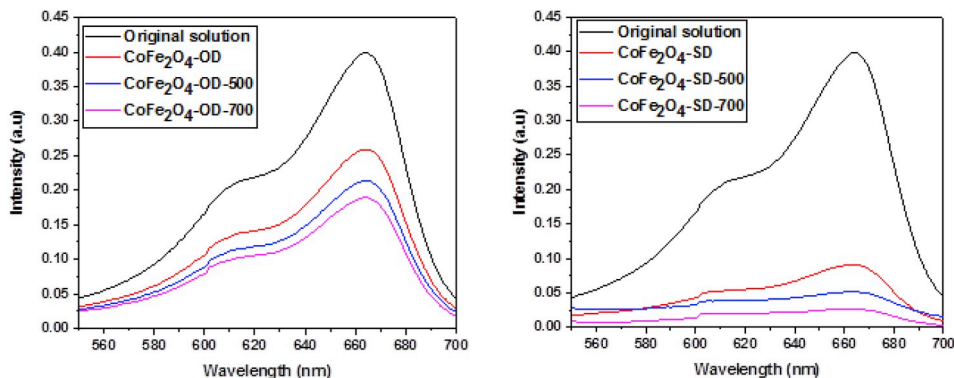


Fig. 11. UV-Vis spectra of the original MB dye solution and the respective MB after adsorption processes.

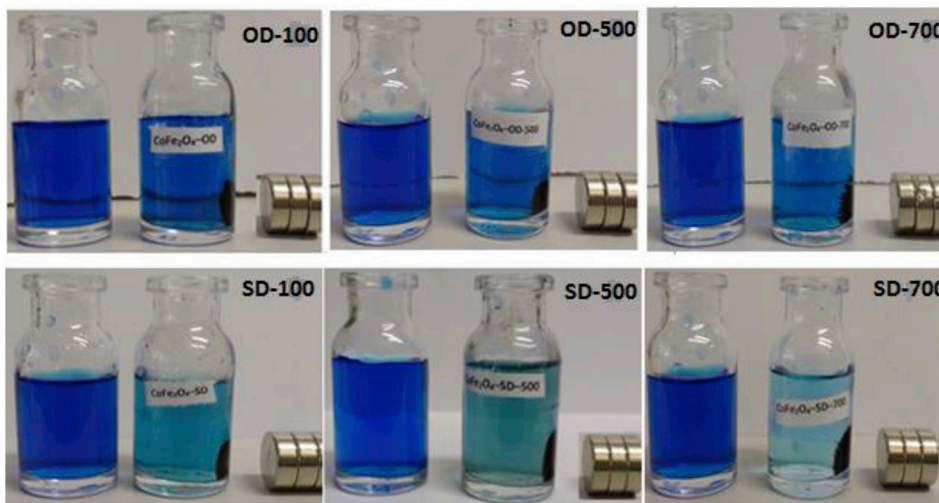


Fig. 12. Methylene blue solution before and after immersion.

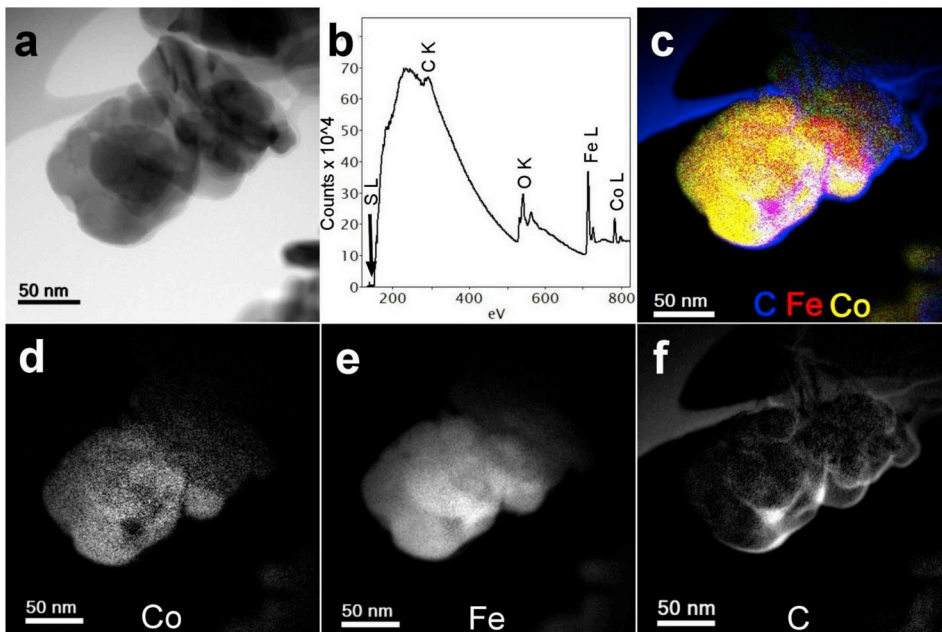


Fig. 13. Bright field TEM image of the cobalt ferrite with adsorbed methylene blue (a). The EEL spectra (b) performed in a particle in (a) under vacuum. The RBG color map (c) show the distribution of each individual element (d–f). (For interpretation of the references to color in this figure legend, the reader is referred to the Web version of this article.)

References

[1] D.H.K. Reddy, Y.S. Yun, Spinel ferrite magnetic adsorbents: alternative future materials for water purification? *Coord. Chem. Rev.* 315 (2016) 90–111, <https://doi.org/10.1016/j.ccr.2016.01.012>.
 [2] X. Liu, H. Wang, B. Lavina, B. Tu, W. Wang, Z. Fu, Chemical composition, crystal structure, and their relationships with the intrinsic properties of spinel-type crystals based on bond valences, *Inorg. Chem.* 53 (2014) 5986–5992, <https://doi.org/10.1021/ic5002013>.

- [3] S. Zhang, Q. Jiao, Y. Zhao, Q. Wu, Preparation of rugby-shaped CoFe₂O₄ particles and their microwave absorbing properties, *J. Mater. Chem. A Mater. Energy Sustain.* 2 (2014) 18033–18039, <https://doi.org/10.1039/C4TA04286G>.
- [4] S.K. Gore, S.S. Jadhav, V.V. Jadhav, S.M. Patange, M. Naushad, R.S. Mane, K.H. Kim, The structural and magnetic properties of dual phase cobalt ferrite, *Sci. Rep.* 7 (2017) 1–9, <https://doi.org/10.1038/s41598-017-02784-z>.
- [5] A.A. and A.B.A.H. 1 Refractory, M.F. Zawrah, M.M. El-Okr, Characterization of sol-gel fabricated cobalt ferrite CoFe₂O₄ nanoparticles, *Middle East J. Appl. Sci. ISSN.* 6 (2014) 362–366.
- [6] J.B. Silva, W. de Brito, N.D.S. Mohallem, Influence of heat treatment on cobalt ferrite ceramic powders, *Mater. Sci. Eng. B* 112 (2004) 182–187, <https://doi.org/10.1016/j.mseb.2004.05.029>.
- [7] S. Yoon, Temperature dependence of magnetic anisotropy constant in cobalt ferrite nanoparticles, *J. Magn. Magn Mater.* 324 (2012) 2620–2624, <https://doi.org/10.1016/j.jmmm.2012.03.019>.
- [8] A. Franco, V. Zapf, Temperature dependence of magnetic anisotropy in nanoparticles of CoxFe(3-x)O₄, *J. Magn. Magn Mater.* 320 (2008) 709–713, <https://doi.org/10.1016/j.jmmm.2007.08.009>.
- [9] N. Sanpo, C.C. Berndt, C. Wen, J. Wang, Transition metal-substituted cobalt ferrite nanoparticles for biomedical applications, *Acta Biomater.* 9 (2013) 5830–5837, <https://doi.org/10.1016/j.actbio.2012.10.037>.
- [10] M.V. Limaye, S.B. Singh, S.K. Date, D. Kothari, V.R. Reddy, A. Gupta, V. Sathe, R.J. Choudhary, S.K. Kulkarni, High coercivity of oleic acid capped CoFe₂O₄ nanoparticles at room temperature, *J. Phys. Chem. B* 113 (2009) 9070–9076, <https://doi.org/10.1021/jp810975v>.
- [11] A. Almasian, F. Najafi, M. Mirjalili, M.P. Gashti, G.C. Fard, Zwitter ionic modification of cobalt-ferrite nanofiber for the removal of anionic and cationic dyes, *J. Taiwan Inst. Chem. Eng.* 67 (2016) 306–317, <https://doi.org/10.1016/j.jtice.2016.07.037>.
- [12] L. Wang, J. Li, Y. Wang, L. Zhao, Q. Jiang, Adsorption capability for Congo red on nanocrystalline MFe₂O₄ (M = Mn, Fe, Co, Ni) spinel ferrites, *Chem. Eng. J.* 181–182 (2012) 72–79, <https://doi.org/10.1016/j.cej.2011.10.088>.
- [13] B. Viltušnik, A. Košak, Y.L. Zub, A. Lobnik, Removal of Pb(II) ions from aqueous systems using thiol-functionalized cobalt-ferrite magnetic nanoparticles, *J. Sol. Gel Sci. Technol.* 68 (2013) 365–373, <https://doi.org/10.1007/s10971-013-3072-z>.
- [14] Z. Ding, W. Wang, Y. Zhang, F. Li, J.P. Liu, Synthesis, characterization and adsorption capability for Congo red of CoFe₂O₄ ferrite nanoparticles, *J. Alloy. Comp.* 640 (2015) 362–370, <https://doi.org/10.1016/j.jallcom.2015.04.020>.
- [15] K.K. Kefeni, B.B. Mamba, T.A.M. Msagati, Application of spinel ferrite nanoparticles in water and wastewater treatment: a review, *Separ. Purif. Technol.* 188 (2017) 399–422, <https://doi.org/10.1016/j.seppur.2017.07.015>.
- [16] Y. Fu, H. Chen, X. Sun, X. Wang, Combination of cobalt ferrite and graphene: high-performance and recyclable visible-light photocatalysis, *Appl. Catal. B Environ.* 111–112 (2012) 280–287, <https://doi.org/10.1016/j.apcatb.2011.10.009>.
- [17] L. Gan, L. Xu, K. Qian, Preparation of core-shell structured CoFe₂O₄ incorporated Ag₃PO₄ nanocomposites for photocatalytic degradation of organic dyes, *Mater. Des.* 109 (2016) 354–360, <https://doi.org/10.1016/j.matdes.2016.07.043>.
- [18] W. Gan, L. Gao, W. Zhang, J. Li, L. Cai, X. Zhan, Removal of oils from water surface via useful recyclable CoFe₂O₄/sawdust composites under magnetic field, *Mater. Des.* 98 (2016) 194–200, <https://doi.org/10.1016/j.matdes.2016.03.018>.
- [19] M. Kooti, M. Afshari, Magnetic cobalt ferrite nanoparticles as an efficient catalyst for oxidation of alkenes, *Sci. Iran.* 19 (2012) 1991–1995, <https://doi.org/10.1016/j.scient.2012.05.005>.
- [20] S. Amiri, H. Shokrollahi, The role of cobalt ferrite magnetic nanoparticles in medical science, *Mater. Sci. Eng. C* 33 (2013) 1–8, <https://doi.org/10.1016/j.msec.2012.09.003>.
- [21] V. Pašukoniene, A. Mlynska, S. Steponkienė, V. Poderys, M. Matulionytė, V. Karabanovas, U. Statkutė, R. Purvinienė, J.A. Iekšandė Kraško, A. Jagminas, M. Kurtinaitienė, M. Strioga, R. Rotomskis, Accumulation and biological effects of cobalt ferrite nanoparticles in human pancreatic and ovarian cancer cells, *Medicina (Kaunas)* 50 (2014) 237–244, <https://doi.org/10.1016/j.medic.2014.09.009>.
- [22] M. Amiri, A. Akbari, M. Ahmadi, A. Pardakhti, M. Salavati-Niasari, Synthesis and in vitro evaluation of a novel magnetic drug delivery system; precocological method for the preparation of CoFe₂O₄ nanostructures, *J. Mol. Liq.* 249 (2018) 1151–1160, <https://doi.org/10.1016/j.molliq.2017.11.133>.
- [23] C. Dey, K. Baishya, A. Ghosh, M.M. Goswami, A. Ghosh, K. Mandal, Improvement of drug delivery by hyperthermia treatment using magnetic cubic cobalt ferrite nanoparticles, *J. Magn. Magn Mater.* 427 (2017) 168–174, <https://doi.org/10.1016/j.jmmm.2016.11.024>.
- [24] N.B. Yahya, M. Kashif, N. Nasir, M.N. Akhtar, N.M. Yusof, Cobalt ferrite nanoparticles: an innovative approach for enhanced oil recovery application, *J. Nano Res.* 17 (2012) 115–126, <https://doi.org/10.4028/www.scientific.net/JNanoR.17.115>.
- [25] N. Dong, F. He, J. Xin, Q. Wang, Z. Lei, B. Su, Preparation of CoFe₂O₄ magnetic fiber nanomaterial via a template-assisted solvothermal method, *Mater. Lett.* 141 (2015) 238–241, <https://doi.org/10.1016/j.matlet.2014.11.054>.
- [26] L.J. Cote, A.S. Teja, A.P. Wilkinson, Z.J. Zhang, Continuous hydrothermal synthesis of CoFe₂O₄ nanoparticles, *Fluid Phase Equilib.* 210 (2003) 307–317, [https://doi.org/10.1016/S0378-3812\(03\)00168-7](https://doi.org/10.1016/S0378-3812(03)00168-7).
- [27] T. Prabhakaran, J. Hemalatha, Combustion synthesis and characterization of cobalt ferrite nanoparticles, *Ceram. Int.* 42 (2016) 14113–14120, <https://doi.org/10.1016/j.ceramint.2016.06.025>.
- [28] M. Houshfar, F. Zebhi, Z.J. Razi, A. Alidoust, Z. Askari, Synthesis of cobalt ferrite (CoFe₂O₄) nanoparticles using combustion, coprecipitation, and precipitation methods: a comparison study of size, structural, and magnetic properties, *J. Magn. Magn Mater.* 371 (2014) 43–48, <https://doi.org/10.1016/j.jmmm.2014.06.059>.
- [29] M. Ristic, S. Krehula, M. Reissner, M. Jean, B. Hannover, S. Musić, Synthesis and properties of precipitated cobalt ferrite nanoparticles, *J. Mol. Struct.* 1140 (2017) 32–38, <https://doi.org/10.1016/j.molstruc.2016.09.067>.
- [30] S. Irfan, M. Ajaz-Un-Nabi, Y. Jamil, N. Amin, Synthesis of Mn_{1-x}ZnxFe₂O₄ ferrite powder by co-precipitation method, *IOP Conf. Ser. Mater. Sci. Eng.* 60 (2014) 012048, <https://doi.org/10.1088/1757-899X/60/1/012048>.
- [31] A. Stunda-Zujeva, Z. Irbe, L. Berzina-Cimdina, Controlling the morphology of ceramic and composite powders obtained via spray drying – a review, *Ceram. Int.* 43 (2017) 11543–11551, <https://doi.org/10.1016/j.ceramint.2017.05.023>.
- [32] S.J. Olusegun, L.F. de Sousa Lima, N.D.S. Mohallem, Enhancement of adsorption capacity of clay through spray drying and surface modification process for wastewater treatment, *Chem. Eng. J.* 334 (2018) 1719–1728, <https://doi.org/10.1016/j.cej.2017.11.084>.
- [33] K.S. Rao, G.S.V.R.K. Choudary, K.H. Rao, C. Sujatha, Structural and magnetic properties of ultrafine CoFe₂O₄ nanoparticles, *Procedia Mater. Sci.* 10 (2015) 19–27, <https://doi.org/10.1016/j.mspro.2015.06.019>.
- [34] A. Franco, V. Zapf, Temperature dependence of magnetic anisotropy in nanospinel, Franco, V. Zapf V. Temperature dependence of magnetic anisotropy in nanoparticles of CoxFe(3-x)O₄, *J. Magn. Magn Mater.* 320 (5) (2008), <https://doi.org/10.1016/j.jmmm.2007.08.009> 709–713. articles of CoxFe(3-x)O₄, *J. Magn. Magn. Mater.* 320 (2008) 709–713.
- [35] V. Gavrilov-isaac, S. Neveu, V. Dupuis, D. Taverna, A. Gloter, V. Cabuil, Synthesis of Trimagnetic Multishell MnFe₂O₄@CoFe₂O₄@NiFe₂O₄ Nanoparticles, (2015), pp. 2614–2618, <https://doi.org/10.1002/sml.201402845>.
- [36] S.P. Yeap, J.K. Lim, B.S. Ooi, A.L. Ahmad, Agglomeration, colloidal stability, and magnetic separation of magnetic nanoparticles: collective influences on environmental engineering applications, *J. Nanoparticle Res.* 19 (2017) 368, <https://doi.org/10.1007/s11051-017-4065-6>.
- [37] A.G. Kolhatkar, A.C. Jamison, D. Litvinov, R.C. Willson, T.R. Lee, Tuning the Magnetic Properties of Nanoparticles, (2013), <https://doi.org/10.3390/ijms140815977>.
- [38] C. Liu, B. Zou, A.J. Rondinone, Z.J. Zhang, Chemical control of superparamagnetic properties of magnesium and cobalt spinel ferrite nanoparticles through atomic level magnetic couplings, *J. Am. Chem. Soc.* 122 (2000) 6263–6267, <https://doi.org/10.1021/ja000784g>.
- [39] S. Yoon, Determination of the temperature dependence of the magnetic anisotropy constant in magnetite nanoparticles, *J. Kor. Phys. Soc.* 59 (2011) 3069–3073, <https://doi.org/10.3938/jkps.59.3069>.
- [40] K. Praveena, K. Sadhana, Ferromagnetic properties of Zn substituted spinel ferrites for high frequency applications, *Int. J. Sci. Res. Publ.* 5 (2015) 1–21.
- [41] K. Rumpf, P. Granitzer, P.M. Morales, P. Poelt, M. Reissner, Variable blocking temperature of a porous silicon/Fe₃O₄ composite due to different interactions of the magnetic nanoparticles, *Nanoscale Res. Lett.* 7 (2012) 445–448, <https://doi.org/10.1186/1556-276X-7-445>.
- [42] L. Kumar, M. Kar, Effect of annealing temperature and preparation condition on magnetic anisotropy in nanocrystalline cobalt ferrite, *IEEE Trans. Magn.* 47 (2011) 3645–3648.
- [43] T. Prabhakaran, R.V. Mangalaraja, J.C. Denardin, J.A. Jiménez, The effect of reaction temperature on the structural and magnetic properties of nano CoFe₂O₄, *Ceram. Int.* 43 (2017) 5599–5606, <https://doi.org/10.1016/j.ceramint.2017.01.092>.
- [44] U. Khan, N. Adeela, K. Javed, S. Riaz, H. Ali, M. Iqbal, X.F. Han, S. Naseem, Influence of cobalt doping on structural and magnetic properties of BiFeO₃ nanoparticles, *J. Nanoparticle Res.* 17 (2015) 429, <https://doi.org/10.1007/s11051-015-3233-9>.
- [45] S. Xavier, S. Thankachan, B. Jacob, E. Mohammed, Effect of sintering temperature on the structural and magnetic properties of cobalt ferrite nanoparticles, *Nanojournal.ifmo.ru* 4 (2013) 430–437 <http://nanojournal.ifmo.ru/en/wp-content/uploads/2013/06/NPCM2013-43P430.pdf>.
- [46] Y.M. Abbas, S.A. Mansour, M.H. Ibrahim, S.E. Ali, Microstructure characterization and cation distribution of nanocrystalline cobalt ferrite, *J. Magn. Magn Mater.* 323 (2011) 2748–2756, <https://doi.org/10.1016/j.jmmm.2011.05.038>.
- [47] I. Sharifi, H. Shokrollahi, M. Mahdi, R. Safi, Magnetic and structural studies on CoFe₂O₄ nanoparticles synthesized by co-precipitation, normal micelles and reverse micelles methods, *J. Magn. Magn Mater.* 324 (2012) 1854–1861, <https://doi.org/10.1016/j.jmmm.2012.01.015>.
- [48] V. Kaliyamoorthy, D.R. Babu, M. Saminathan, Impact of Ignition Temperature on Particle Size and Magnetic Properties of CoFe₂O₄ Nanoparticles Prepared by Self-Propagated Mild Combustion Technique, (2016), pp. 280–288, <https://doi.org/10.1016/j.jmmm.2016.05.025>.
- [49] X.L.C.X.X. Han, Synthesis and Magnetic Properties of Nearly Monodisperse CoFe₂O₄ Nanoparticles through a Simple Hydrothermal Condition, (2010), pp. 1039–1044, <https://doi.org/10.1007/s11671-010-9599-9>.
- [50] T. Shahjuee, S.M. Masoudpanah, S.M. Mirkazemi, Coprecipitation Synthesis of CoFe₂O₄ Nanoparticles for Hyperthermia vol. 50, (2017), pp. 105–110, <https://doi.org/10.22059/JUFNGSM.2017.02.04>.
- [51] M.C.C.N. Anumol, V.A. Baidyanath, S. Subasa, Tailoring magnetic properties of cobalt ferrite nanoparticles by different divalent cation substitution, *J. Mater. Sci. Mater. Electron.* 29 (2018) 813–822, <https://doi.org/10.1007/s10854-017-7976-1>.



Sequestrating anionic and cationic dyes from wastewater using spray dried biopolymeric magnetic composite: Experimental and theoretical studies

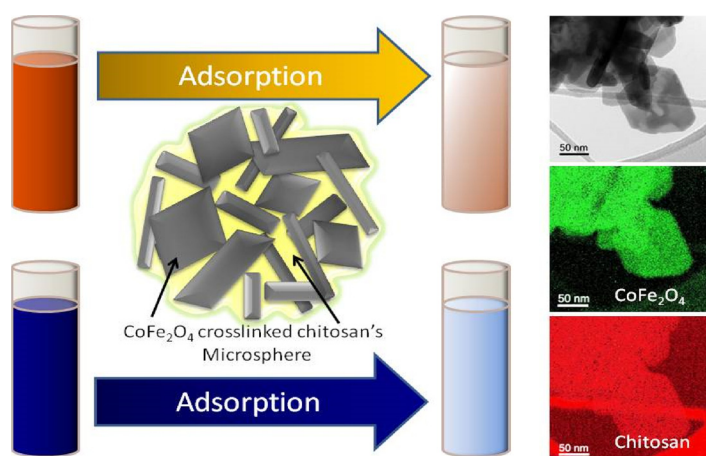


S.J. Olusegun^{a,*}, G.L.S. Rodrigues^a, E.T.F. Freitas^b, L.R.S. Lara^a, W.R. Rocha^a, N.D.S. Mohallem^{a,*}

^a Universidade Federal de Minas Gerais, Departamento de Química, Laboratório de Materiais Nanoestruturados, Belo Horizonte, Brazil

^b Universidade Federal de Minas Gerais, Centro de Microscopia, 31.270-901 Belo Horizonte, Brazil

GRAPHICAL ABSTRACT



ARTICLE INFO

Editor: Xiahong Guan

Keywords:

Acid orange II
Methylene blue
zeta potential
Adsorption mechanism
Computational studies

ABSTRACT

Spray dried cross-linked chitosan/cobalt ferrite composite was synthesized and applied as an adsorbent for the removal of acid orange II and methylene blue. The composite was structurally, thermally, morphologically and magnetically characterized. The result obtained shows that the magnetic composite was in form of microspheres, while cobalt ferrite was encapsulated in the cross-linked chitosan with saturation magnetization of 10.79 emu g⁻¹. Adsorption studies revealed that acid orange II adsorbed more favorably on the composite than methylene blue. The adsorption process is spontaneous and exothermic. Liu isotherm model was found to be applicable for the adsorption process. Computational studies showed that the formation of hydrogen bond between acid orange II and the magnetic composite (at both acidic and alkaline pH) contributed to its better adsorption than methylene blue. Adsorption capacity of acid orange II at pH 3 and methylene blue at pH 12 are 542 and 173 mg g⁻¹ respectively at 303 K based on Liu isotherm model.

* Corresponding authors.

E-mail addresses: arewasegun@ufmg.br (S.J. Olusegun), nelcy@ufmg.br (N.D.S. Mohallem).

<https://doi.org/10.1016/j.jhazmat.2019.120872>

Received 16 February 2019; Received in revised form 27 June 2019; Accepted 5 July 2019

Available online 10 July 2019

0304-3894/ © 2019 Elsevier B.V. All rights reserved.

1. Introduction

The aftermath of rapid growth among industries that use massive volume of water to carry out their day to day activities has led to indiscriminate discharge of wastewater into the environment (Madala et al., 2013). This has resulted to contamination of clean water that is highly demanded by human societies (Zhu et al., 2008; Rodrigues, 2017; Bode-Aluko et al., 2017), and consequently affected the health status of the entire ecosystem. Industrial effluents that contain dyes are among the major sources of water pollutions that has called for immediate concern and attention. Dyes pose great danger to the environment due to their stability and difficulty to degrade biologically (Srinivasan and Viraraghavan, 2010).

Therefore, their removal from wastewater has necessitated prompt action. In view of this, environmentalists have legislated rules that mandate industries that generate hazardous effluents to treat their wastewater before being discharge to waterway, as this will prevent the available clean water from being polluted, and sustain the health condition of the populace (Ali et al., 2011; Naidoo and Olaniran, 2013). Several techniques such as oxidation and ozone treatment (Chen et al., 2009; Osugi et al., 2009; Jana et al., 2011; Gounden et al., 2018), biological (Gümüşdere et al., 2011; Gomez-herrero et al., 2019), ion-exchange (Liu et al., 2007; Xu et al., 2019), coagulation/flocculation (Szyguła et al., 2009; Gaydardzhiev et al., 2006), membrane filtration (Doke and Yadav, 2014; Lin et al., 2014; Jamshidifard et al., 2019) and electron-Fenton (Panizza and Cerisola, 2009; Özcan and Gençten, 2016) have been employed to treat industrial effluents. These techniques have their associated limitation and shortcomings. Due to this, adsorption process has been considered as better/alternative means for the removal of water contaminants. This process is easy to operate, convenient and cost effective (Chen et al., 2017), and it has been widely used to remove different contaminants from industrial effluents (Barakat, 2011).

Among the fundamental characteristics of a good adsorbent is the; presence/availability of adsorption sites, fast adsorption process, should be easily separated from solution and chemically stable among others. Chitosan, a derivative from N-deacetylation of chitin is one of the most abundant biopolymers in nature. It is friendly to the environment, readily available, does not have any toxic effect, biodegradable and cheap to obtain (Huang et al., 2017). These unique features have made it to be an indisputable raw material in the industrial sector.

The usefulness of chitosan in treating wastewater cannot be over-emphasized. However, its solubility in acid solutions is of great concern and this limits its usage in lower pH (Huang et al., 2017). To overcome this challenge, cross linking chitosan with various cross-linking agents has been the way out (Nagireddi et al., 2017). This process improves its mechanical properties, modifies its surface and increases its stability in

acid solution (Zahir et al., 2017). Another challenge with adsorbents is the difficulty of separating them after treatment process. To solve this set-back, magnetic separation has become an alternative technique (Sivashankar et al., 2014), which is achieved by using magnetic composites.

An innovative approach (spray drying process) was used to dry the glutaraldehyde cross-linked chitosan-cobalt ferrite composite used for this study. The obtained spray dried magnetic composite was used to adsorb acid orange II (an azo and anionic dye) and methylene blue (cationic dye) from simulated wastewater. Acid orange II (AO) and methylene blue (MB) are chosen as our target organic dyes due to their usage in textile, cosmetic, paper and food industries (Salima et al., 2012). They are toxic, cause nausea, high blood pressure, and respiratory discomfort in human (Gupta et al., 2006; Zhou et al., 2015). Furthermore, computational chemistry approach was utilized to complement the experimental studies. This is to enable proper understanding of the mechanism of adsorption. The interaction between the dyes molecules and glutaraldehyde cross-linked chitosan-cobalt ferrite composite in the terms of the possibility of charge transferred was unraveled from the quantum chemical descriptors and discussed with respect to the amount of each dye adsorbed.

2. Experimental details

2.1. Materials

Both $\text{FeSO}_4 \cdot 7\text{H}_2\text{O}$ and $\text{CoSO}_4 \cdot 7\text{H}_2\text{O}$ were purchased from Dinamica Quimica Contemporanea Ltd., Brazil, chitosan with degree of deacetylation (87.4%), viscosity (176 cPs at 20 °C), pH (8.7) and apparent density (0.25 g mL^{-1}) was purchased from Polymar/Brazil, while methylene blue and acid orange II were purchased from Labsynth and Sigma Aldrich respectively.

2.2. Preparation of cobalt ferrite/chitosan composite

Firstly, 4 g of chitosan was dissolved in 120 mL of 2% (v/v) acetic acid and sonicated for 30 min. Then, 1 g of cobalt ferrite (prepared according to the method reported by Olusegun et al. (2019) was added and the mixture was sonicated for another 30 min. Subsequently, 1 ml aqueous solution of 25 wt.% glutaraldehyde was added to the mixture and mechanically stirred for 1 h. The resulted magnetic composite was spray dried, characterized and used as adsorbent. The inlet temperature of the spray drier was set at 120 °C and air flow rate at 30 L min^{-1} . Fluxogram of the synthesis is shown in Fig. 1.

2.3. Characterization of the magnetic chitosan composite

X-ray diffraction (XRD) was performed in a X-ray diffractometer

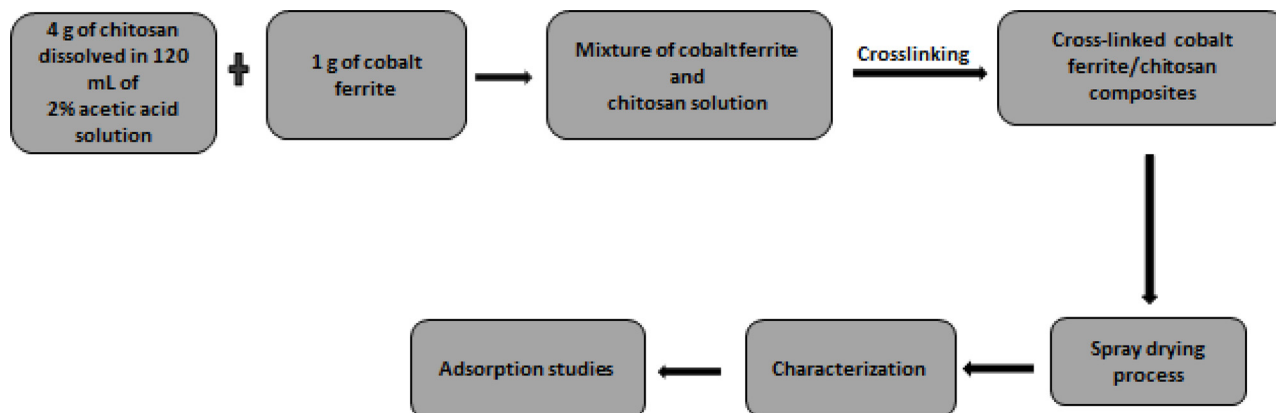


Fig. 1. Scheme of the synthesis.

(Shimadzu, XRD 7000) using CuK α radiation. Thermogravimetric analysis was carried out on Mettler Toledo - TGA/DSC1 – STAR. Morphologies and composition were assessed in a thermionic (W filament) scanning electron microscope (SEM), JEOL JSM 6360 LV coupled with EDX silicon drift detector (Bruker), and in transmission electron microscope (TEM) FEI Tecnai G2-20 (200 kV). S700X SQUID magnetometer was used to determine the magnetic property.

2.4. Adsorption studies

Adsorption studies were performed in duplicate. The pH of the solutions was adjusted using HCl and NaOH. Afterwards, 10 mg of the adsorbent was added to 15 mL of 100 ppm dye solution. Other varying parameters, adsorbent mass, initial concentration of the dyes, contact time and temperature were investigated. After each study, the adsorbent was magnetically separated by an external magnet. Unadsorbed dye concentration in the solution was determined at λ_{max} 664 nm and 485 nm for MB and AO respectively, using UV/Vis Spectrophotometer (U-2010, Hitachi).

2.5. Computational details

To have better understanding of the adsorption mechanism, reactivity and the interactions involving the dyes and chitosan magnetic composite, quantum chemical calculations were carried out at the DFT level theory using the ORCA software (Neese, 2017; Parr and Yang, 1989). Geometry optimizations of the dye molecules which electronic

properties were investigated using the Fukui functions, including the solvation effects are shown in Fig. 2.

Three chitosan models were built as pentameric structures as shown in Fig. 3. The protonated model (charge +5), has the five amino groups in $-\text{NH}_3^+$ form; the neutral model keeps the hydroxyl and amino groups in neutral states and, the deprotonated model (charge -2) has two OH groups deprotonated. These three models simulate the chitosan in acidic, neutral or basic pH respectively. The interaction of the dyes with the chitosan models were investigated through geometry optimization at the DFT/PBE-3c level of theory. Cobalt ferrite in the composite was ignored in the DFT calculations because amount of AO and MB adsorbed by it, is insignificant, however, it has moderate magnetic saturation and is chemically stable (Olusegun et al., 2019).

Hydrogen bond formation of the dyes in water solution was investigated using Monte Carlo (MC) statistical mechanical simulation in an NPT ensemble at 298 K using a classical pair potential composed of Coulomb plus 12-6 Lennard Jones terms (Allen and Tildesley, 1987) in a box with 599 molecules of water described by the TIP3P model (Jorgensen et al., 1983). All MC simulations were done using the DICE (v3.0beta) software developed by Coutinho and Canuto (Cezar et al., 2018).

3. Result and discussion

3.1. Characterization of the magnetic composite

The diffractogram of CoFe_2O_4 and chitosan/ CoFe_2O_4 (magnetic

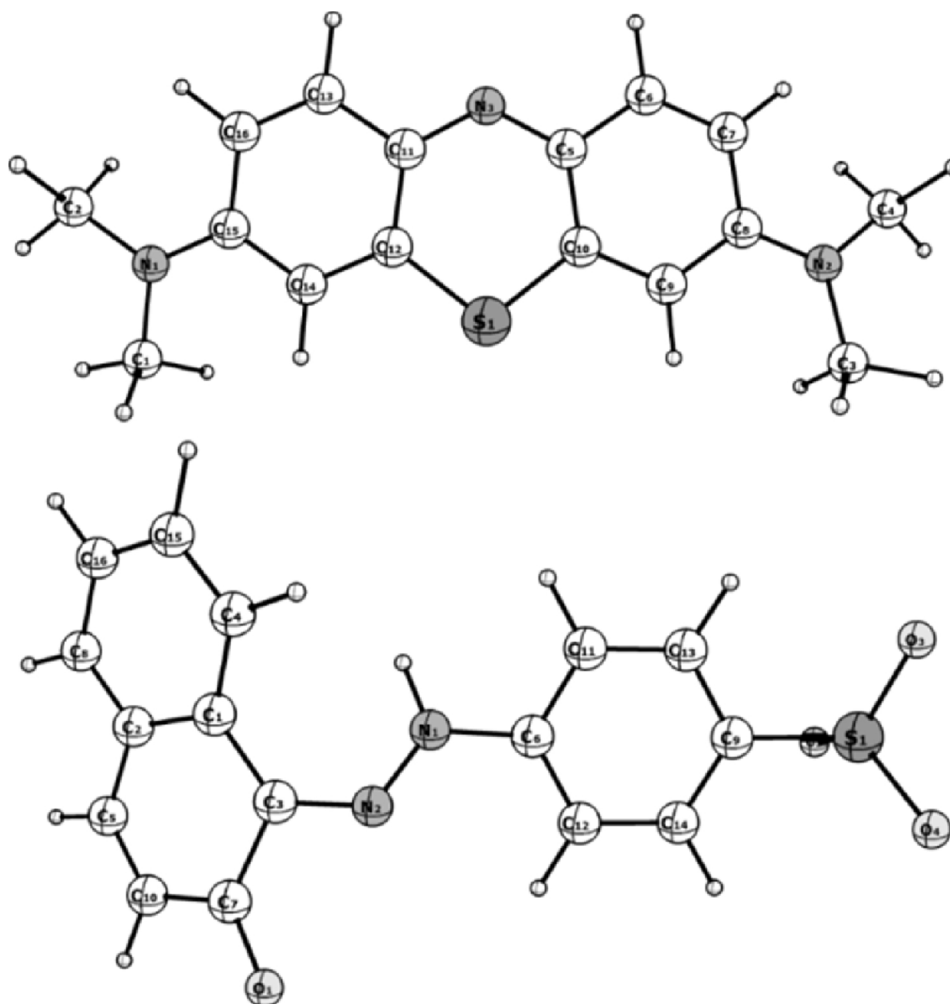


Fig. 2. Optimized structures of MB (top) and AO (bottom) with respective numbering of atoms.

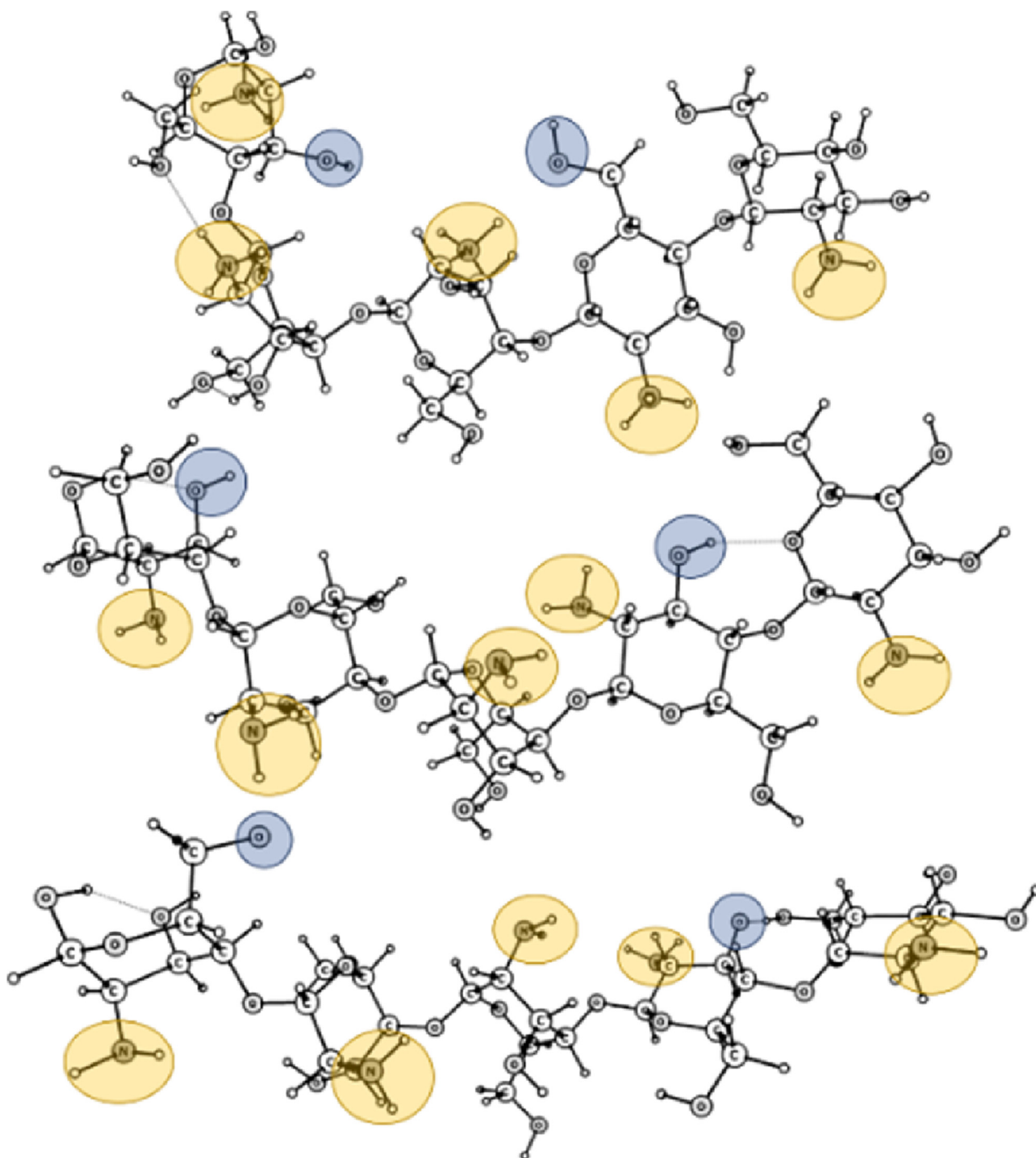


Fig. 3. Protonated (top), non-protonated (middle) and deprotonated (bottom) models to simulate the chitosan polymer. The yellow circles highlight the amino groups that are protonated ($-\text{NH}_3^+$) in the top or non-protonated ($-\text{NH}_2$) in the middle and bottom structures, while the blue circles highlight the OH groups that are protonated ($-\text{OH}$) in top and middle or deprotonated ($-\text{O}^-$) in the bottom structure comprising the three chitosan models. (For interpretation of the references to colour in this figure legend, the reader is referred to the web version of this article.)

composite) presented in Fig. 4 reflects pure cubic spinel crystal structure of CoFe_2O_4 . All the peaks in the pure cobalt ferrite are present in the magnetic composite, this shows that the presence of chitosan did not in any way change the structure of cobalt ferrite. The observed change between 20 and 25° in the pattern of the composite is due to the presence amorphous chitosan. The same observation was reported for amorphous silica with cobalt ferrite (Rohilla et al., 2011).

Scanning electron microscope image of the microspheres magnetic chitosan is shown in Fig. 5. The particles are spherical and their size

ranges from 2 to 5 μm diameter. The secondary electron image suggests that crosslinked chitosan probably formed a coat around cobalt ferrite.

TEM analysis shows that the microspheres of magnetic chitosan are aggregates of nanoparticles (Fig. 6-i). The energy filtered TEM (EFTEM) images in Fig. 6 display the elemental mapping of the composite. Each EFTEM image was recorded by using the three-window method which integrates only the core-loss signal above the background for each of the edges, C-K, Ca-L, O-K, Fe-L and Co-L, shown in the electron energy-loss (EEL) spectrum (Fig. 6-ii). It is clearly seen that the C is

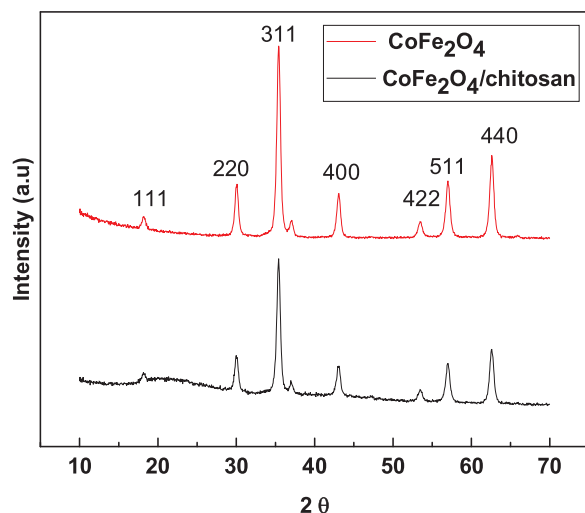


Fig. 4. XRD pattern of CoFe_2O_4 and magnetic chitosan composite.

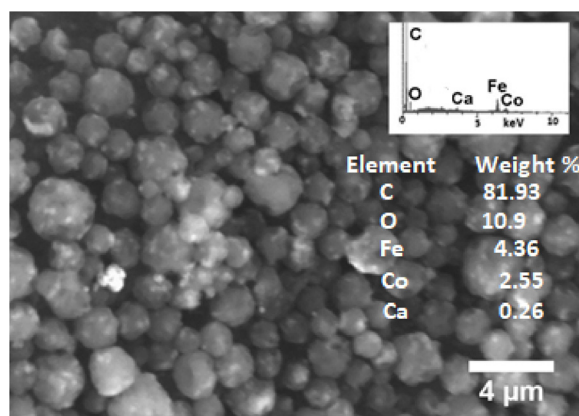


Fig. 5. Secondary electron image and EDX of crosslinked magnetic chitosan composite.

homogeneously distributed within the composite along with O, Co and Fe, thus confirming the covering of crosslinked chitosan onto cobalt ferrite.

The TGA curves of chitosan and magnetic chitosan composite are shown in Fig. 7. The initial mass loss in chitosan up to 100 °C was due to the removal of adsorbed water molecules. After this, it was thermally stable up to 250 °C. More so, there was a significant mass loss from 300 °C to 590 °C due to the complete decomposition of chitosan. However, in the case of magnetic chitosan composite there is a continuous mass loss up to 500 °C. This could be because of loss of water, breaking of bond between chitosan and glutaraldehyde and decomposition of chitosan structure. The estimated amount of cobalt ferrite that was found in the composite after complete decomposition of chitosan was 19.94 wt %, which is approximately equal to the amount in grams of cobalt ferrite that was added to chitosan as mentioned in the experimental section.

The result of magnetization as a function of applied field, carried out at 300 K is shown in Fig. 8. The presence of chitosan on the surface of cobalt ferrite formed a magnetically dead layer and thereby affecting the saturation magnetization. However, the saturation magnetization (10.79 emu g^{-1}) is higher than M_s value of 7.6 emu g^{-1} reported by Ai et al. (2010) for cobalt ferrite/activated carbon composite.

3.2. Adsorption studies

3.2.1. Effect of pH, surface charge and adsorbent dosage on adsorption of acid orange II (AO) and methylene blue (MB)

Fig. 9 shows the influence of pH on the adsorption capacity of the magnetic composite. The result clearly shows that the efficiency of the composite depends on pH, this is because the percentage adsorbed decreases with an increase in the pH of AO solution, whereas it increases with increase in the pH of MB solution. Considering the adsorption of AO, 95% of the initial 100 ppm was adsorbed at pH 2 and 3, while lower value of 30% was adsorbed at pH 10. Whereas for MB a very negligible amount was adsorbed between pH 2 to 10, while 68% was adsorbed at pH 12. Linking this with the result obtained from zeta potential measurement of the adsorbent, which is presented in Fig. 10, insight into the mechanism of the adsorption was obtained. The net charge on the surface of the adsorbent is zero at pH 9, below this pH, zeta potential values are positive while they are negative above it This implies that anionic dye should be favourably adsorbed at lower pH while cationic dye at pH above 9, as shown in Fig. 9. It can be affirmed that electrostatic attraction/repulsion between the composite and the dye molecules contributed to the mechanism of adsorption of the two dyes. At lower pH there is an attraction between the surface of the adsorbent and AO. This attraction decreases as the pH of AO solution increases leading to decrease in amount adsorbed due to the net surface charge that tends towards negative values and vice-versa for MB. The mechanism of adsorption, though mainly due to electrostatic attraction/repulsion for the adsorption of MB, is not limited to this for the adsorption of AO. This is because at pH 10 when the surface was positively charged, approximately 30% of AO was removed, which implies that other mechanism could possibly contribute to the adsorption process. This was further confirmed from the results obtained from theoretical studies. The picture of AO and MB solutions that shows the magnetic separation before and after adsorption is shown in Fig. 11. The result of the effect of dosage on the amount of AO (100 ppm, pH 3) and MB (100 ppm, pH 12) adsorbed are shown in Fig. 12. Amount adsorbed attained equilibrium at 8 mg dosage for AO adsorption, meanwhile MB did not attain equilibrium within the dosage range that was studied. This could be because of better affinity that the composite has for AO. The composite was desorbed and reused for four (4) cycles (Supplementary material).

3.2.2. Adsorption kinetic study

Kinetic investigation was carried out with 100 mg L^{-1} of the adsorbates, 10 mg of adsorbent at 30 min interval for 240 min. The adsorption of AO attained equilibrium at 90 min. whereas, MB adsorption could not attain equilibrium until 210 min. The analysis of the kinetic data was done using pseudo-first order, pseudo-second order and the Elovich kinetic models (Supplementary material). Kinetic parameters are itemized in Table 1, while the nonlinear fit curves of the three models for the two dyes are shown in Fig. 13. It has been established that model with best fit exhibits lowest SD and highest R^2_{adjusted} that is close to unity (Leite et al., 2017). The SD values obtained from pseudo-second order and Elovich for the two dyes are lower than the respective values obtained from pseudo-first order, in addition to this, R^2_{adjusted} for two models are close to unity. The implication of this is that pseudo-second-order and Elovich model are more suitable to explain the kinetic process for the adsorption of the two dyes, and that the rate limiting step of the adsorption is chemisorption, and adsorption rate decreases as the surface coverage increases (Pathania et al., 2017). The lower the SD (obtained from the square root of Reduced Chi-squared), the closer the theoretical q_e to experimental q_e (Kasperiski et al., 2018). See supplementary material for intraparticle diffusion.

3.2.3. Adsorption isotherms

Langmuir, Freundlich and Liu isotherms were employed for the understanding of the adsorption mechanism of the two dyes. Langmuir

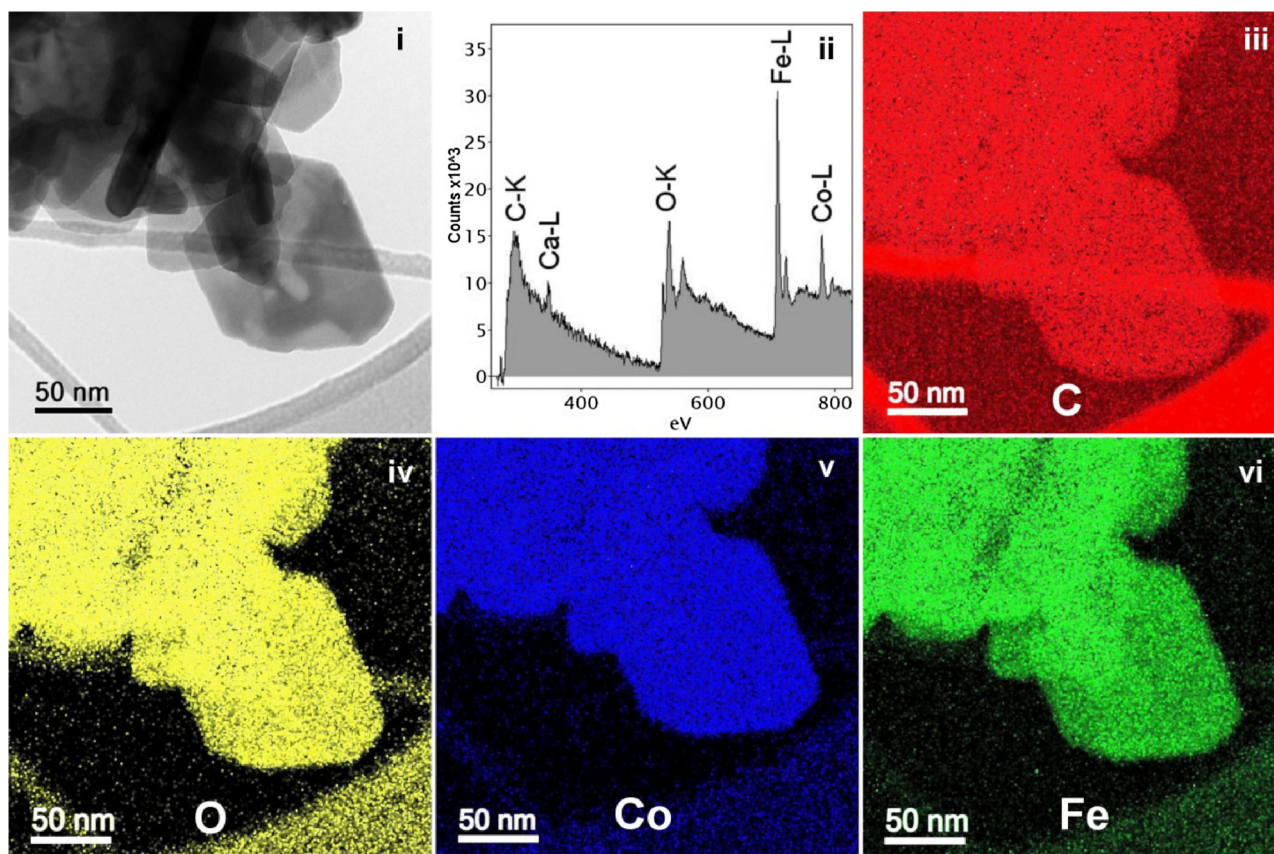


Fig. 6. TEM bright field image (i), EEL spectrum (ii), and EFTEM images of crosslinked magnetic chitosan composite. The EEL spectrum was recorded in a region with no overlapping between the cobalt ferrite and the C-support film.

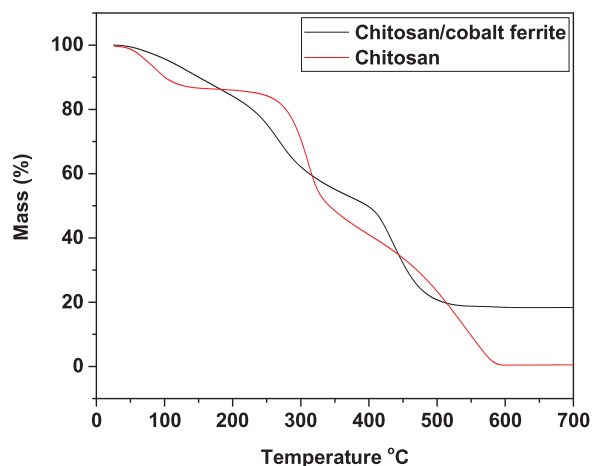


Fig. 7. TGA curves of chitosan and magnetic chitosan composite.

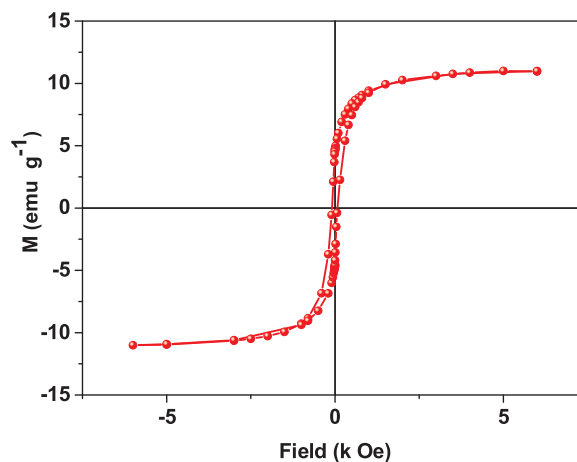


Fig. 8. Magnetization versus applied field at 300 K.

and Liu isotherms help to establish the maximum adsorption capacity of the magnetic chitosan, which is expressed in terms of amount of dye adsorbed per unit mass of the adsorbent. Equilibrium data were analyzed using Langmuir, Freundlich and Liu isotherms (Supplementary material). Figs. 14 and 15 show the experimental data and nonlinear fitting of the isotherms for AO and MB respectively, while their parameters are displayed in Table 2. Based on the values of SD and $R^2_{adjusted}$ for the three isotherms, Liu was found to more fitted to explain the adsorption mechanism which speculate that active sites of adsorbent possess different energy (Lima et al., 2015). The decrease in the values q_{max} , K_g and K_L (as shown in Table 2) with respect to temperature shows that adsorption process is exothermic. The maximum adsorption

capacity for AO are more than the counterpart MB, this signifies that the magnetic composite has better affinity for AO than MB and coupled with the fact that mechanism of AO adsorption was not limited to electrostatic attraction. Comparison of the maximum adsorption capacity (q_{max}) of different adsorbents for the removal of AO and MB are listed in Table 3. The magnetic chitosan used in this study performed better than other adsorbents reported in the literature. The nature of adsorption was determined by linear plot of Dubinin–Radushkevich (D–R) isotherm (Supplementary material). The values of E (mean energy of adsorption) being less than 8 kJ mol^{-1} (Supplementary Table S1) implies that the two dyes were physically adsorbed on the magnetic composite (Darvishi Cheshmeh Soltani et al., 2015).

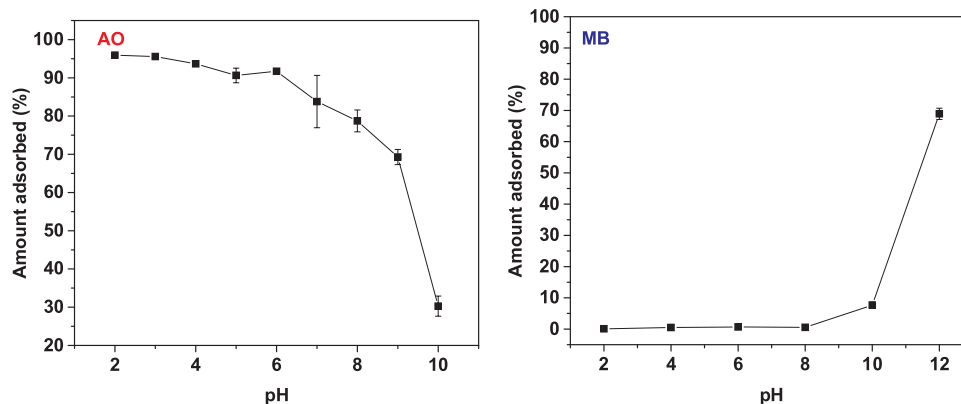


Fig. 9. The effect of pH on the removal of 100 mg L⁻¹ AO and MB using 10 mg of magnetic chitosan.

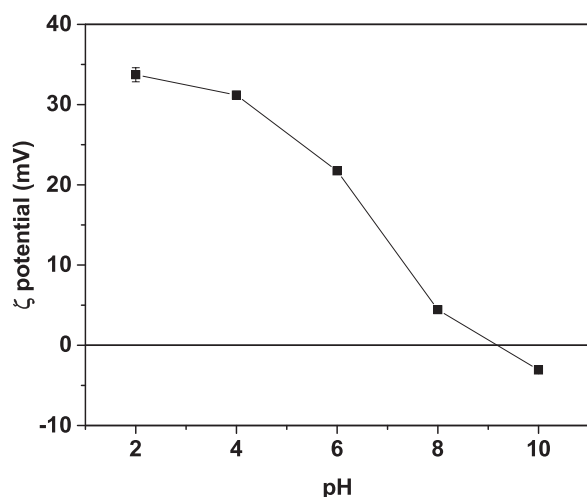


Fig. 10. Zeta potential of cobalt ferrite/chitosan composite as a function of pH.

3.2.4. Adsorption thermodynamics

The values of thermodynamic parameters (free energy (ΔG), enthalpy (ΔH) and entropy (ΔS)) listed in Table 4 were calculated using Eqs. 1 and 3.

$$\log K_e = \frac{\Delta S}{2.303R} - \frac{\Delta H}{2.303RT} \quad (1)$$

It is worthy to note that K_e is a dimensionless thermodynamic equilibrium constant, which was obtained from Liu equilibrium constant (K_g) as shown in Eq. (2) (Kasperiski et al., 2018).

$$K_e = \frac{1000 \cdot K_g \cdot \text{molecular weight of the adsorbate} \cdot \text{standard concentration of the adsorbate}}{\text{activity coefficient of adsorbate}} \quad (2)$$

$$\Delta G^\circ = \Delta H^\circ - T\Delta S^\circ \quad (3)$$

The values of enthalpy (ΔH) are negative for the two dyes which confirms the exothermic nature of the adsorption process. This agrees with the adsorption capacity listed in Table 2, which decreases with increase in temperature. It was also observed that entropy is positive for AO and negative for MB this means that there is an increase and decrease in disorder of the system at the interface of the magnetic chitosan composite and the dye solution respectively (Liu and Liu, 2008). Negative values of ΔG show that the adsorption of the two dyes are feasible and spontaneous. It was obvious that the magnitude of ΔG obtained for AO tends to higher negative values than that of MB. The implication is that the adsorption of AO on the surface of chitosan magnetic composite is more rapid and spontaneous than that of MB.

3.3. Computational studies

3.3.1. Geometry and electronic structure of the Dyes

Table 5 presents the values of common reactivity descriptors related to HOMO and LUMO orbitals for the dye molecules. The data shows that AO and MB have similar HOMO and LUMO energies, and consequently a similar gap $\Delta E_{\text{HOMO-LUMO}}$. This results in very close values of electro affinity, hardness and softness, which in theory describe two molecules with very similar reactivity for covalent interactions. However, the adsorption of AO is much higher than that of MB and this can be explained not only by electrostatic attraction but also by the molecular dipole moment.

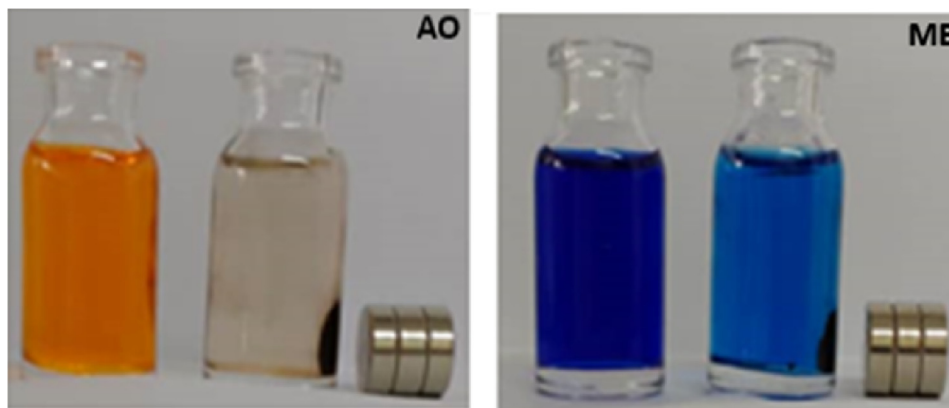


Fig. 11. AO and MB solutions before and after immersion in magnetic chitosan composite.

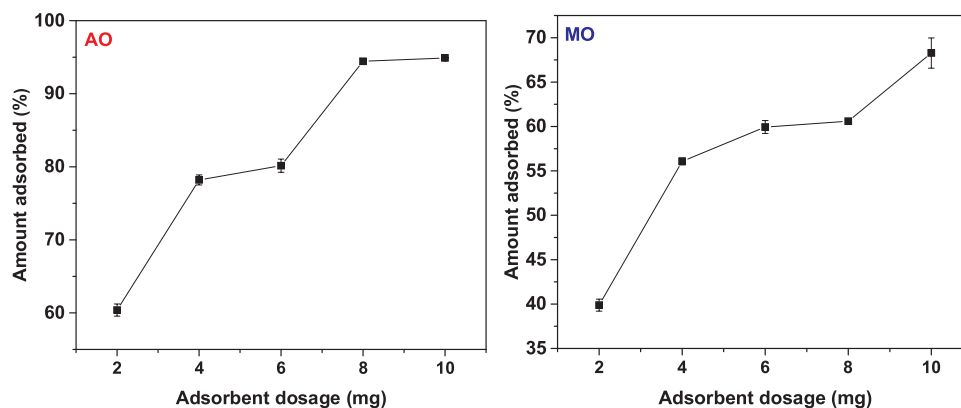


Fig. 12. Variation of amount adsorbed with respect to dosage.

Table 1
Parameters for kinetics models.

Model	parameters	Acid orange II	Methylene blue
Pseudo-first-order	q_e (mg g^{-1})	139.27	94.47
	k_1 (min^{-1})	0.0938	0.03363
	R^2_{adjusted}	0.9981	0.9624
	SD (mg g^{-1})	2.001	6.058
Pseudo-second-order	q_e (mg g^{-1})	159.55	93.39614
	k_2 ($\text{g mg}^{-1} \text{min}^{-1}$)	0.3355	0.0564
	R^2_{adjusted}	0.9994	0.9859
	SD (mg g^{-1})	1.041	3.701
Elovich	α ($\text{mg g}^{-1} \text{min}^{-1}$)	8.36×10^{10}	29.450
	β (g mg^{-1})	0.204	0.06039
	R^2_{adjusted}	0.9998	0.9975
	SD (mg g^{-1})	0.5949	1.5449

Since chemical bonding usually happens by electronic density exchange between the LUMO and HOMO orbitals of the involved species (Liu and Liu, 2008; Gilani et al., 2013), to increase the interactions between two bonding molecules, they usually approach in a way that maximizes the superposition of LUMO and HOMO orbitals of each other. Analysis of Fig. 16, shows that the HOMO and LUMO orbitals of AO and MB are very similar for both molecules, being distributed along the molecule through the π system involving the aromatic rings. Therefore, to increase the interactions, both dye molecules should approach parallel to the surface of the adsorbent through the plane of the aromatic rings, maximizing the surface contact with the adsorbent. As it can be seen from Fig. 17 the yellow to red areas shows regions with more electrophilicity (greater contribution from the $f^+(r)$ function) and the cyan to blue areas shows regions with more nucleophilicity (greater

contribution from $f^-(r)$ function), while blank regions shows small reactivity. The picture shows that many sites with more nucleophilic or electrophilic character are placed in a non-uniform way in both molecules and, adsorption interactions should not have a strong covalent character. Therefore, the weaker inter-molecular interactions should be maximized along the plane of the aromatic rings, increasing the surface contact with the adsorbent.

3.4. Interaction of the Dyes and the magnetic chitosan models

The optimized structures for the interaction of the dye molecules with the chitosan models are shown in Figs. 18 and 19. AO dye interacts with the non-protonated (structure A), protonated (structure B) and deprotonated (structure C) chitosan models. However, MB dye interacts only with the neutral (structure A) and deprotonated (structure B) chitosan models. Interaction of MB with the protonated chitosan model is not favorable and, the optimization leads to separate structures too far from each other. This result is in line with the experimental results since, under experimental conditions, no significant amount of MB is adsorbed in the pH range of 0 to 8, when the composite is positively charged.

Analyzing the structures shown in Fig. 18 it is possible to see that when the chitosan model is very positive the interaction mode between it and the AO changed drastically. The negative SO_3^- group is perpendicular to the polymer surface, being pointed directly towards it to maximize the attractive electrostatic interactions, following the dipole moment vector of the molecule. When the surface changed to neutral or negative the AO molecule interacts with the chitosan along the plane of the aromatic rings, maximizing the weak interactions like hydrogen bonding (hbond), and van der Waals (dispersion forces). However, as expected, for the interaction of the MB dye with the negatively charged model of the chitosan (Fig. 19), the two molecules are close to each

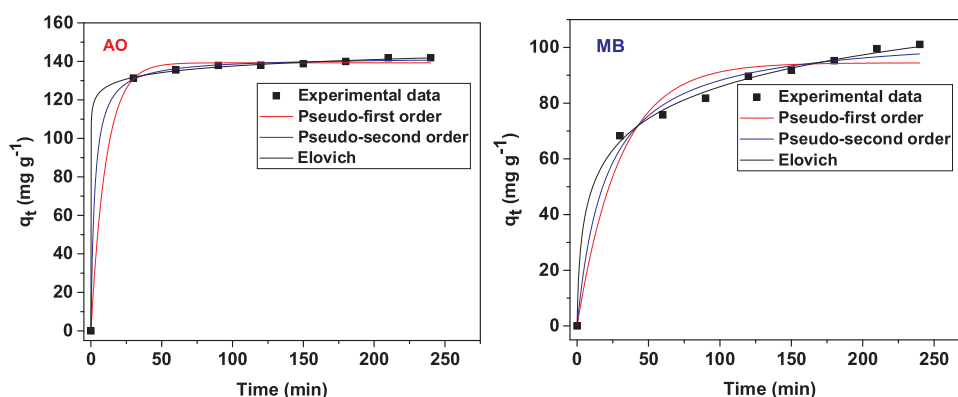


Fig. 13. kinetics plots for AO and MB adsorption.

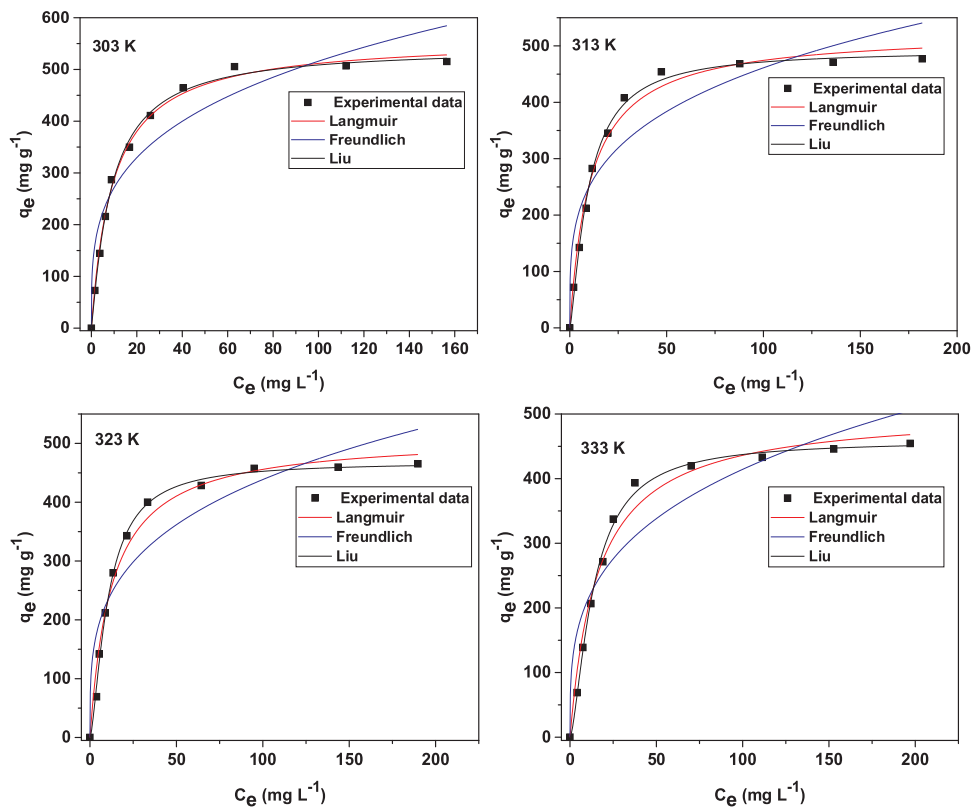


Fig. 14. Langmuir, Freundlich and Liu isotherms for the adsorption of AO.

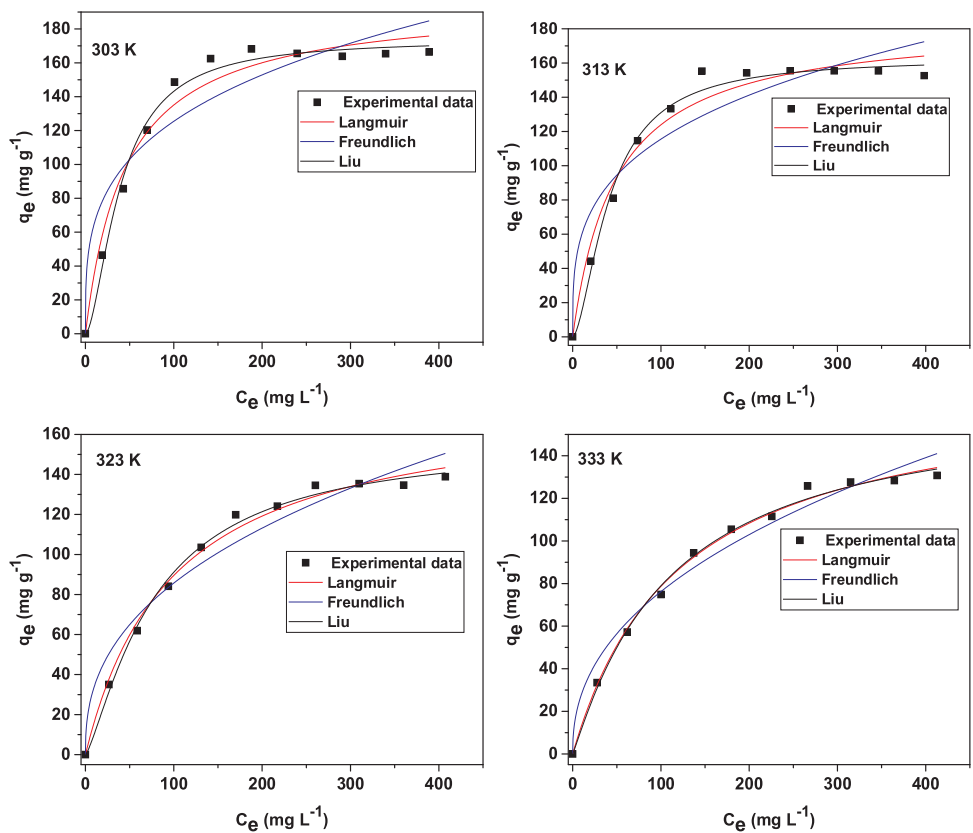


Fig. 15. Langmuir, Freundlich and Liu isotherms for the adsorption of MB.

Table 2
Langmuir and Freundlich isotherms parameters for the adsorption of MB at 303 – 333 K.

Acid orange II	303 K				313 K				323 K				333 K							
	Langmuir																			
q_{max} (mg g ⁻¹)	560.14				525.42				512.71				506.4							
K_L (L mg ⁻¹)	0.1055				0.0929				0.0801				0.0619							
$R^2_{adjusted}$	0.9957				0.9881				0.9826				0.9810							
SD (mg g ⁻¹)	12.08				18.86				22.09				22.41							
Freundlich																				
K_F (mg g ⁻¹ (mg L ⁻¹) ^{-1/nF})	143.01				135.78				122.01				107.27							
n_F	3.588				3.766				3.599				3.407							
$R^2_{adjusted}$	0.9045				0.8769				0.8787				0.8822							
SD (mg g ⁻¹)	57.28				60.85				58.49				55.81							
Liu																				
q_{max} (mg g ⁻¹)	542.89				492.4212				468.5543				458.919							
K_g (L mg ⁻¹)	0.1133				0.10416				0.0967				0.0740							
n_L	1.111				1.328				1.472				1.502							
$R^2_{adjusted}$	0.9965				0.9958				0.9968				0.9966							
SD (mg g ⁻¹)	10.95				11.19				9.38				9.44							
Methylene blue																				
Langmuir																				
q_{max} (mg g ⁻¹)	196.31				184.104				178.2181				173.8338							
K_L (L mg ⁻¹)	0.0220				0.0205				0.0101				0.0083							
$R^2_{adjusted}$	0.9708				0.9720				0.9914				0.9948							
SD (mg g ⁻¹)	9.92				9.01				4.33				3.16							
Freundlich																				
K_F (mg g ⁻¹ (mg L ⁻¹) ^{-1/nF})	33.76				30.38				13.53				10.34236							
n_F	3.507				3.448				2.494				2.305							
$R^2_{adjusted}$	0.8943				0.8991				0.9553				0.9732							
SD (mg g ⁻¹)	18.86				17.12				9.91				7.15							
Liu																				
q_{max} (mg g ⁻¹)	173.83				162.83				157.46				165.78							
K_g (L mg ⁻¹)	0.0252				0.0238				0.0128				0.0092							
n_L	1.664				1.632				1.292				1.075							
$R^2_{adjusted}$	0.9894				0.9887				0.9946				0.9944							
SD (mg g ⁻¹)	5.94				5.71				3.42				3.26							

other due to the electrostatic attraction resulted by the two opposite charges. However, this electrostatic attraction is distributed throughout the entire molecule due to its small dipole moment. This distance can also be quantitatively viewed in Table 6.

Table 6 shows some energy values for the interacting systems. We

Table 3
Comparison of the maximum monolayer adsorption (q_{max}) of different adsorbents for the removal of AO and MB at room temperature.

Dyes	Adsorbents	q_{max} (mg g ⁻¹)	References	
Acid orange	MnO ₂ /MCM-41	218.34	(Yang et al., 2015)	
	CuFe ₂ O ₄ /activated carbon composite	392	(Zhang et al., 2007)	
	ODTMA-palygorskite	99.01	(Sarkar et al., 2011)	
	Iron-benzenetricarboxylate (Fe(BTC))	435	(García et al., 2014)	
	Carbon-modified TiO ₂	24.32	(Jafari et al., 2016)	
	Calcium carbonate/sawdust (AC-1)	310	(Kong et al., 2017)	
	C ₃ H ₉ N treated S. marginatum	71.05	(Kousha et al., 2012)	
	Magnetic graphene chitosan	42.7	(Sheshmani et al., 2014)	
	CoFe ₂ O ₄ /chitosan	542.89	This work	
	Methylene blue	Magnetic cellulose/graphene oxide composite	70.03	(Shi et al., 2014)
		Surface-functionalized silica aerogels	68.15	(Saad et al., 2015)
EDTA-modified bentonite		160	(De Castro et al., 2018)	
RMAC nodules		187.5	(Kunde et al., 2019)	
Activated biochar		33.33	(Wang et al., 2018)	
Acid washed black cumin seEDX		73.52	(Siddiqui et al., 2018)	
CMT nanocomposites		138.1	(Tong et al., 2018)	
CO ₂ -biochar.		161.0	(Franciski et al., 2018)	
CoFe ₂ O ₄ /chitosan		173.83	This work	

Table 4
Thermodynamics parameters for the adsorption of AO and MB at 303 – 333 K.

Adsorbents	ΔH° (kJ mol ⁻¹)	ΔS° (J K ⁻¹ mol ⁻¹)	ΔG° (kJ mol ⁻¹)			
			303 K	313 K	323 K	333 K
AO	-11.22	51.31	-26.77	-27.28	-27.80	-28.31
MB	-30.57	-24.36	-23.19	-22.95	-22.71	-22.46

Table 5
Electronic structure descriptors for MB and AO.

	Acid orange II	Methylene blue
E_{HOMO} (eV)	-5.82	-5.68
E_{LUMO} (eV)	-2.69	-3.30
$\Delta E_{HOMO-LUMO}$ (eV)	3.13	2.39
χ (eV)	4.26	4.49
η (eV)	1.56	1.19
σ (eV ⁻¹)	0.64	0.84
μ (Debye)	32.24	3.46
$\mu^{exp.}$ (Debye ^a)	N.A.	1.63/2.46/3.79

^a Experimental data obtained from absorption and fluorescence shifts in various media using three different methods as explained in reference Gilani et al. (2013). Each value corresponds to one of the methods used.

would emphasize that these come only from the DFT/PBE-3c SCF energies and, thus, have limited quantitative value. Analysis of the data on Table 6 shows that the dispersion energy is similar for all the systems in which the interaction between the dye and the chitosan happens when the two molecules are aligned to each other. This is expected, although we should take into account that the distances between the two molecules are very different from each other considering dispersion forces that are proportional to r^{-6} . So, for the AO with negative chitosan, even though the interaction energy is similar, the much larger distance implies bigger dispersion forces than the MB with negative chitosan, as example. The AO with the protonated chitosan system has a much smaller dispersion energy. This is also expected when we look at the interaction mode, that has low surface contact areas, as was previously discussed. Therefore, most of the interaction in this system should come from the electrostatic energy term, which is roughly covered by the values in the last column of Table 6, that shows the difference between the total interaction energy and the dispersion energy (ΔE_{dif}), if one considers that there is no significant amount of covalent bonding between the two molecules. In fact, a support for this is the observation that ΔE_{dif} is stabilizing for AO with positive chitosan and for MB with

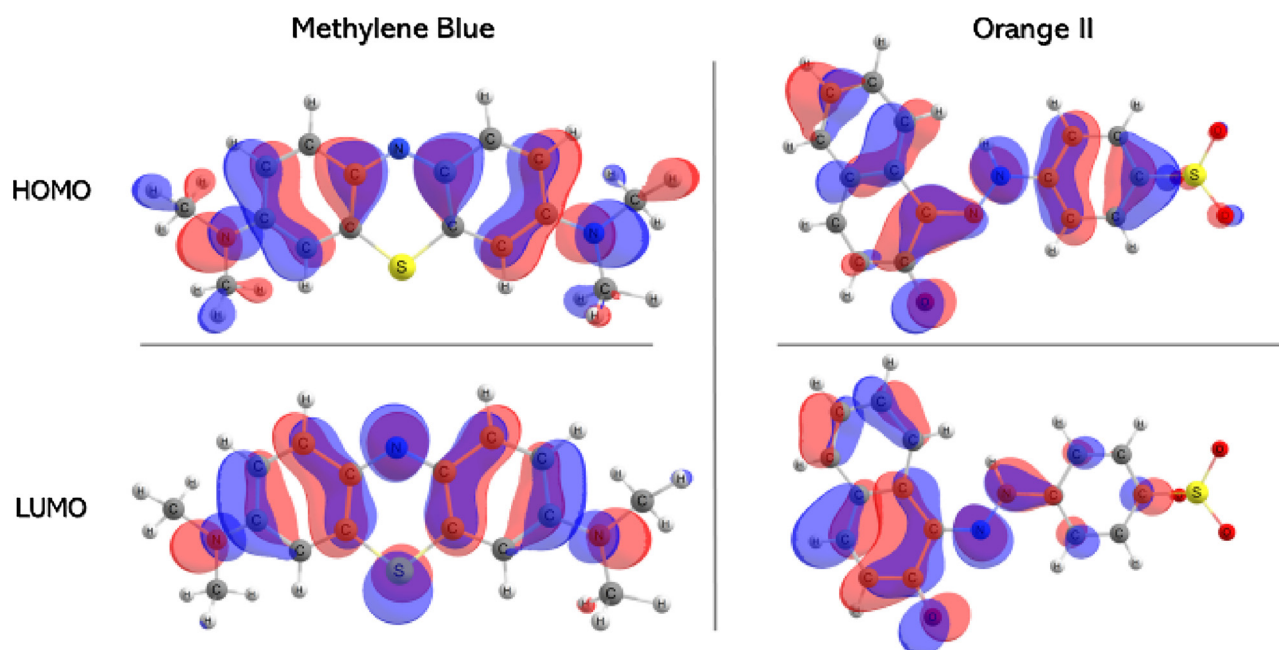


Fig. 16. Frontier Kohn-Sham orbitals obtained with the solvent polarized electronic density for MB and AO molecules.

negative chitosan, which are molecules with opposite charges, and it is destabilizing for AO with negative chitosan and MB with positive chitosan, which are molecules with same charges.

Another observation is that the $r(\text{CM}-\text{CM})$ distance is much smaller for the interaction of AO and the neutral model than for the interaction with negative model, due to the electrostatic repulsion between the molecules in the latter case. However, there are still strong dispersion forces between the AO molecule and the negative chitosan model illustrated by the dispersion energies and the optimized structure, which explains why AO adsorbs on the composite surface even when they have the same charge signal.

The same cannot be said about the interaction of MB with the positive chitosan model since the interaction is not favorable and the system dissociates. Comparing the MB with AO, the CM-CM distances for the interaction with the chitosan models, in the former are larger than in the latter, showing that MB is not able to interact as efficiently as AO with the magnetic chitosan composite. The optimized structures clearly show that there should be no hydrogen bond interactions between MB and the chitosan model as we will discuss. As expected, the $r(\text{CM}_{\text{dye}}-\text{CM}_{\text{chitosan}})$ is smaller for the interaction of MB with the negative model of chitosan than for the interaction with the neutral model, when one should expect stronger and attractive Coulomb interactions due to the opposite charges, confirmed by the larger value of ΔE_{dif} . If we qualitatively use the recommendation from IUPAC for the definition of hydrogen bond (Dannenberg et al., 2011), and the geometric criteria established in the computational details section, the AO molecule can act as a hydrogen bond acceptor through all its oxygens from the SO_3^- group or the $\text{C}=\text{O}$ group, with hydrogen bond distances between 1.8 to 3.0 Å, and also as a hydrogen bond donor through its N-H group, with hydrogen bond distances around 2.3 Å. These observations were further analyzed via Monte Carlo simulations of the isolated dyes in aqueous solution. The hydrogen bond analysis from the MC simulations revealed that while indeed the MB molecule is not capable to form hydrogen bonds in solution, the AO dye is capable of accept multiple hydrogen bonds through its S-O and C=O groups. In all MC simulation configurations, the AO dye formed an average of 6 h-bonds per molecule with an average energy of $-36.54 \text{ kJ mol}^{-1}$. This reinforces the capability of the AO molecule to make stronger and more numerous intermolecular interactions through hydrogen bonding, opposite to MB which is not capable to form these interactions. Furthermore, the larger amount of

intermolecular interactions is what should make AO adsorbs more in most of the situations, especially considering the strong hydrogen bonds that it is able to make with chitosan. The scheme of the overall mechanism of adsorption process is presented in Fig. 20. Mechanism of adsorption had been proposed to be through electrostatic attraction, hydrogen bond, ion exchange among others (Hasan and Jung, 2015; Du et al., 2014). FTIR of the composite before and after adsorption of the two dyes (Supplementary Fig. S3). IR spectra after adsorption of AO revealed new peaks at 1512, 823, and 723 cm^{-1} which correspond to the presence of azo chromophore and fingerprint of AO.

4. Conclusion

Chitosan/cobalt ferrite composite was synthesized and employed as adsorbent for the removal of both acid orange II and methylene blue. The ease of separating the magnetic composite after adsorption was demonstrated by using an external magnet. The results obtained from the characterization of the composite showed that chitosan was well distributed around the surface of cobalt ferrite. Adsorption studies showed that pH of the solution plays a significant role in the removal of the two dyes. Methylene blue adsorption was found to be limited to the surface charge of the composite; this was not the case for the adsorption of acid orange II. The adsorption of the two dyes was spontaneous and exothermic in nature. The theoretical observations of the phenomena are in good agreement with the experimental data. The results from the computational studies showed that the two dyes have similar reactive sites, however, the huge molecule dipole moment and strong dispersion forces of acid orange II enhanced its interaction with the magnetic chitosan. The theoretical results presented here provide a descriptive molecular view of these systems and insight into the mechanism of adsorption.

Declaration of Competing Interest

There are no conflicts of interest.

Acknowledgments

The authors would like to thank UFMG-Microscopy Center for the structural support, FAPEMIG, CNPq, TWAS-CNPq and Coordenação de

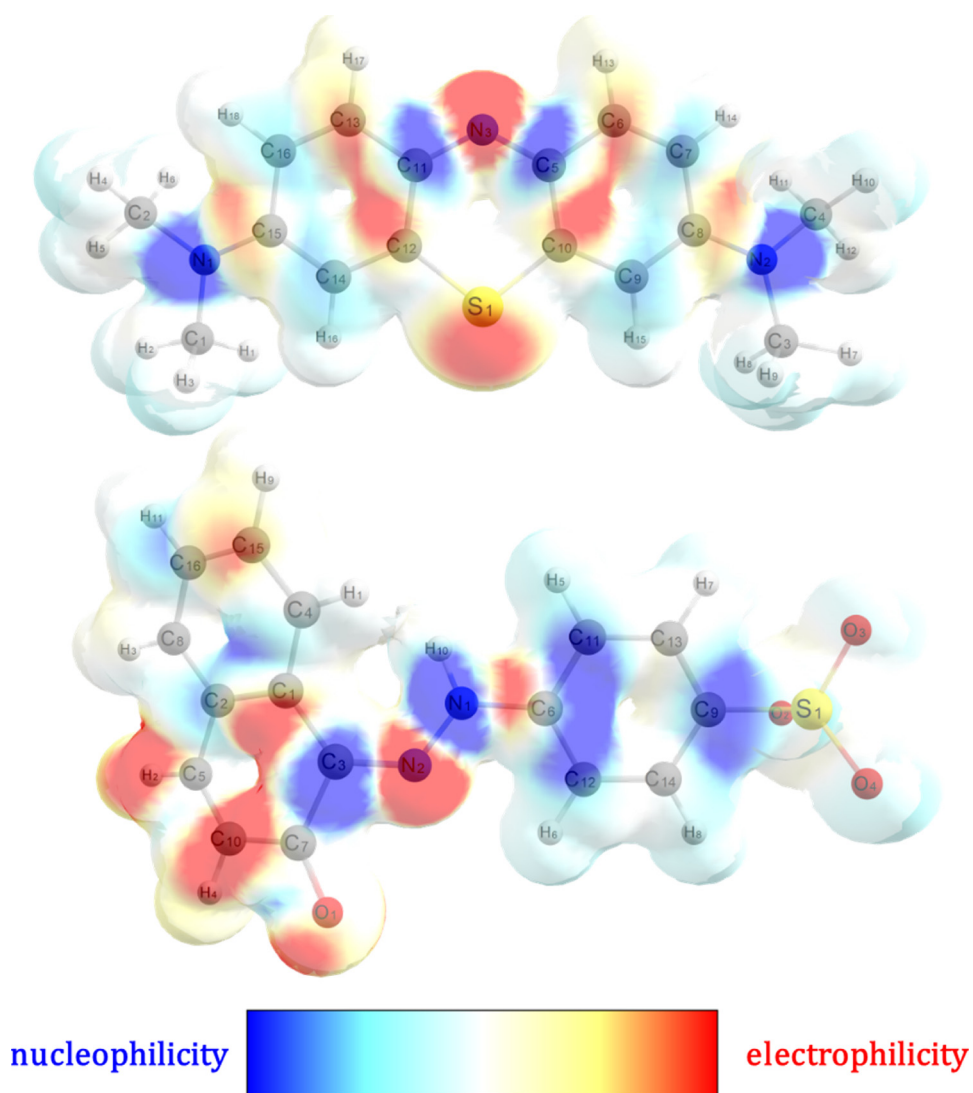


Fig. 17. Electron density plot map of the dual descriptor Fukui function, $\Delta f(r)$, for MB (top) and AO (bottom), obtained from the calculated SCF electronic densities.

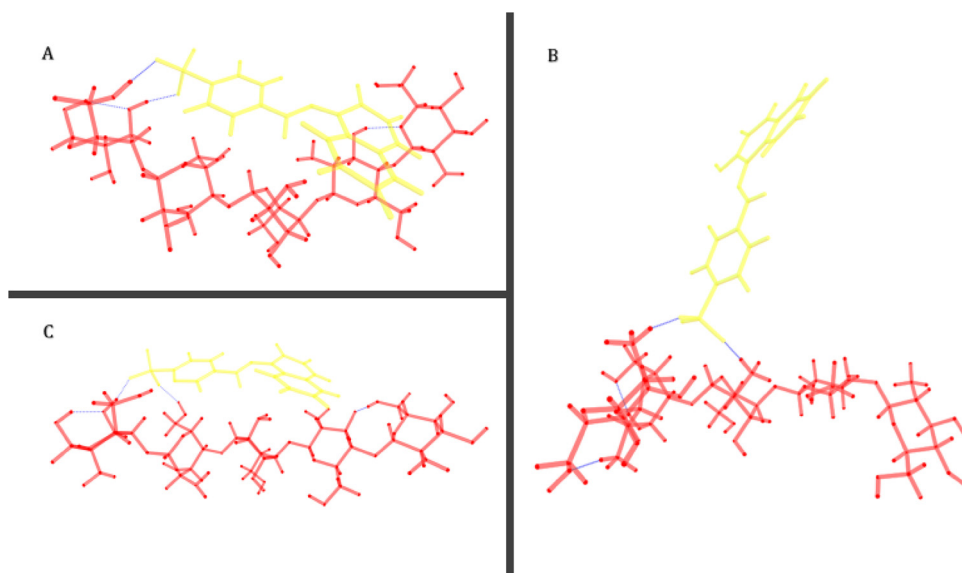


Fig. 18. Optimized structures for the interaction between (A) acid orange II + non-protonated chitosan model, (B) acid orange II + protonated chitosan model and (C) acid orange II + deprotonated chitosan model.

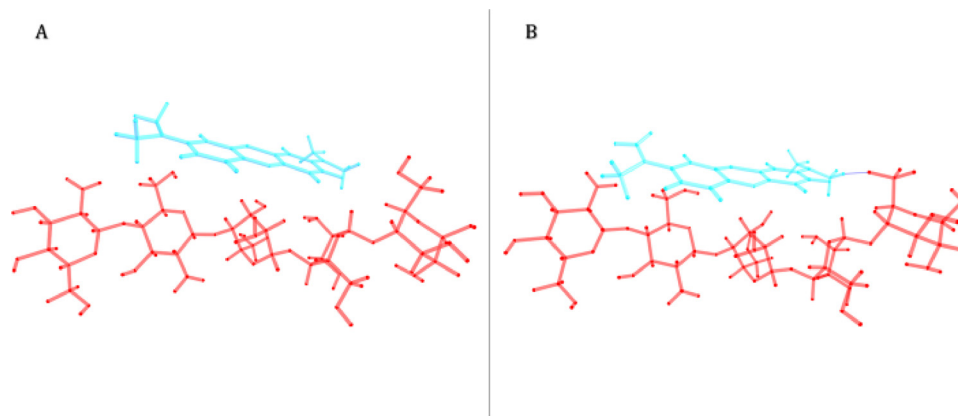


Fig. 19. Optimized structures for the interaction between (A) methylene blue + non-protonated chitosan model and (B) methylene blue + deprotonated chitosan model.

Table 6

Distances (in Å) between the center-of-mass (CM_{dye}) of the dyes molecules and the center-of-mass of the chitosan (CM_{chito}) models, interaction energies (ΔE_{SCF}) and dispersion corrections for the dye-chitosan systems at the optimized geometries. All the energies were calculated using the C-PCM continuum solvation model as detailed in the SI.

System	$r(CM_{dye}-CM_{chito})$ (Å)	ΔE_{SCF} (kcal mol ⁻¹)	$E_{disp.}$ (kcal mol ⁻¹)	$\Delta E_{dif.}^{**}$ (kcal mol ⁻¹)
AO + magnetic chitosan (0)	3.59	-23.86	-12.71	-11.16
AO + magnetic chitosan (+)	9.44	-17.84	-4.30	-13.55
AO + magnetic chitosan (-)	4.91	14.22	-12.06	26.28
MB + magnetic chitosan (0)	4.76	-4.10	-9.96	5.86
MB + magnetic chitosan (+)	-	-	-	-
MB + magnetic chitosan (-)	3.96	-32.84	-12.26	-20.59

* The interaction energies were obtained from the expression $\Delta E_{SCF} = E_{Total} - (E_{dye} + E_{chitosan})$, in which E_{Total} is the dye-chitosan cluster total SCF energy, E_{dye} is the SCF energy of the dye in the cluster geometry and $E_{chitosan}$ is the SCF energy of the chitosan model in the cluster geometry.

** $\Delta E_{dif} = \Delta E_{SCF} - E_{disp.}$

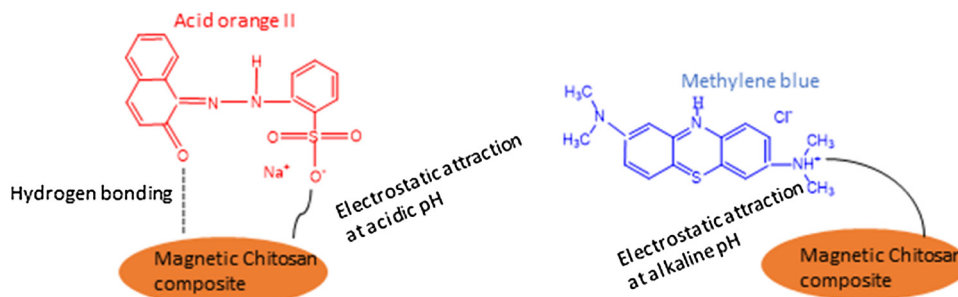


Fig. 20. Proposed mechanism pathway for interactions between magnetic chitosan and the two dyes molecules.

Aperfeiçoamento de Pessoal de Nível Superior - Brasil (CAPES) - Finance Code 001 for financial support.

Appendix A. Supplementary data

Supplementary material related to this article can be found, in the online version, at doi:<https://doi.org/10.1016/j.jhazmat.2019.120872>.

References

- Ai, L., Huang, H., Chen, Z., Wei, X., Jiang, J., 2010. Activated carbon/CoFe2O4 composites: facile synthesis, magnetic performance and their potential application for the removal of malachite green from water. *Chem. Eng. J.* 156, 243–249.
- Ali, S.M., Sabae, S.Z., Fayez, M., Monib, M., Hegazi, N.A., 2011. The influence of agro-industrial effluents on River Nile pollution. *J. Adv. Res.* 2, 85–95.
- Allen, M.P., Tildesley, D.J., 1987. *Computer Simulation of Liquids* 18. Liq. Oxford Univ. Press, New York, pp. 385. <https://doi.org/10.2307/2938686>.
- Barakat, M.A., 2011. New trends in removing heavy metals from industrial wastewater. *Arab. J. Chem.* 4, 361–377.
- Bode-Aluko, C.A., Perea, O., Ndayambaje, G., Petrik, L., 2017. Adsorption of toxic metals on modified polyacrylonitrile nanofibres: a review. *Water Air Soil Pollut.* 228.

- <https://doi.org/10.1007/s11270-016-3222-3>.
- Cezar, H.M., Canuto, S., Coutinho, K., 2018. DICE(v3.0Beta) A General Monte Carlo Program for Liquid Simulation.
- Chen, T.Y., Kao, C.M., Hong, A., Lin, C.E., Liang, S.H., 2009. Application of ozone on the decolorization of reactive dyes - Orange-13 and Blue-19. *Desalination* 249, 1238–1242.
- Chen, X., Wang, X., Wang, S., Qi, J., Xie, K., Liu, X., Li, J., 2017. Furfuryl alcohol functionalized graphene for sorption of radionuclides. *Arab. J. Chem.* 10, 837–844.
- Dannenberg, J.J., Clary, D.C., Klein, R.A., Crabtree, R.H., Hobza, P., Legon, A.C., Alkorta, I., Scheiner, S., Mennucci, B., Desiraju, G.R., Kjaergaard, H.G., Nesbitt, D.J., Sadlej, J., Arunan, E., 2011. Definition of the hydrogen bond (IUPAC Recommendations 2011). *Pure Appl. Chem.* 83, 1637–1641.
- Darvishi Cheshmeh Soltani, R., Khataee, A.R., Godini, H., Safari, M., Ghanadzadeh, M.J., Rajaei, M.S., 2015. Response surface methodological evaluation of the adsorption of textile dye onto biosilica/alginate nanobiocomposite: thermodynamic, kinetic, and isotherm studies. *Desalin. Water Treat.* 56, 1389–1402.
- De Castro, M.L.F.A., Abad, M.L.B., Sumalinog, D.A.G., Abarca, R.R.M., Paoprasert, P., de Luna, M.D.G., 2018. Adsorption of Methylene Blue dye and Cu(II) ions on EDTA-modified bentonite: Isotherm, kinetic and thermodynamic studies. *Sustain. Environ. Res.* 28, 197–205.
- Doke, S.M., Yadav, G.D., 2014. Novelty of combustion synthesized titania ultrafiltration membrane in efficient removal of methylene blue dye from aqueous effluent. *Chemosphere* 117, 760–765.
- Du, Z., Deng, S., Bei, Y., Huang, Q., Wang, B., 2014. Adsorption behavior and mechanism

- of perfluorinated compounds on various adsorbents — A review. *J. Hazard. Mater.* 274, 443–454.
- Francisci, M.A., Peres, E.C., Godinho, M., Perondi, D., Foletto, E.L., Collazzo, G.C., Dotto, G.L., 2018. Development of CO₂activated biochar from solid wastes of a beer industry and its application for methylene blue adsorption. *Waste Manag.* 78, 630–638.
- García, E., Medina, R., Lozano, M., Hernández Pérez, I., Valero, M., Franco, A., 2014. Adsorption of Azo-Dye Orange II from Aqueous Solutions Using a Metal-Organic Framework Material: Iron-Benzenetricarboxylate. *Materials (Basel)* 7, 8037–8057.
- Gaydardzhiev, S., Karthikeyan, J., Ay, P., 2006. Colour removal from model solutions by coagulation–surface charge and floc characterisation aspects. *Environ. Technol.* 27, 193–199.
- Gilani, A.G., Salmanpour, M., Ghorbanpour, T., 2013. Solvatochromism, dichroism and excited state dipole moment of azure A and methylene blue. *J. Mol. Liq.* 179, 118–123.
- Gomez-herrero, E., Polo, A., Rodriguez, J.J., Mohedano, A.F., 2019. Removal of imidazolium-based ionic liquid by coupling Fenton and biological oxidation. *J. Hazard. Mater.* 365, 289–296.
- Gounden, A.N., Singh, S., Jonnalagadda, S.B., 2018. Simultaneous removal of 2,4,6-tribromophenol from water and bromate ion minimization by ozonation. *J. Hazard. Mater.* 357, 415–423.
- Gümüşdere, H.T., Artan, T., Güvenç, A., Dönmez, G., Mehmetoğlu, Ü., 2011. Textile azo dyes decolorization by combined ultrasonication and microbial removal. *Environ. Earth Sci.* 255, 885–892.
- Gupta, V.K., Mittal, A., Gajbe, V., Mittal, J., 2006. Removal and recovery of the hazardous azo dye acid orange 7 through adsorption over waste materials: bottom ash and de-oiled soya. *Ind. Eng. Chem. Res.* 45, 1446–1453.
- Hasan, Z., Jung, S.H., 2015. Removal of hazardous organics from water using metal-organic frameworks (MOFs): Plausible mechanisms for selective adsorptions. *J. Hazard. Mater.* 283, 329–339.
- Huang, R., Liu, Q., Huo, J., Yang, B., 2017. Adsorption of methyl orange onto protonated cross-linked chitosan. *Arab. J. Chem.* 10, 24–32.
- Jafari, S., Tryba, B., Kusiak-Nejman, E., Kapica-Kozar, J., Morawski, A.W., Sillanpää, M., 2016. The role of adsorption in the photocatalytic decomposition of Orange II on carbon-modified TiO₂. *J. Mol. Liq.* 220, 504–512.
- Jamshidifard, S., Koushkbaghi, S., Hosseini, S., Rezaei, S., 2019. Incorporation of UiO-66-NH₂ MOF into the PAN / chitosan nanofibers for adsorption and membrane filtration of Pb (II), Cd (II) and Cr (VI) ions from aqueous solutions. *J. Hazard. Mater.* 368, 10–20.
- Jana, S., Saikia, A., Purkait, M.K., Mohanty, K., 2011. Chitosan based ceramic ultra-filtration membrane: preparation, characterization and application to remove Hg(II) and As(III) using polymer enhanced ultrafiltration. *Chem. Eng. J.* 170, 209–219.
- Jorgensen, W.L., Chandrasekhar, J., Madura, J.D., Impey, R.W., Klein, M.L., 1983. Comparison of simple potential functions for simulating liquid water. *J. Chem. Phys.* 79, 926. <https://doi.org/10.1063/1.445869>.
- Kasperiski, F.M., Lima, E.C., Umpierrez, C.S., Glaydson, S., Silas, P., Ramos, D., Dias, S.L.P., Saucier, C., Janaina, B., 2018. Production of porous activated carbons from *Caesalpinia ferrea* seed pod wastes: Highly efficient removal of captropil from aqueous solutions. *J. Clean. Prod.* 197, 919–929.
- Kong, L., Su, M., Peng, Y., Hou, L., Liu, J., Li, H., Diao, Z., Shih, K., Xiong, Y., Chen, D., 2017. Producing sawdust derived activated carbon by co-calcinations with limestone for enhanced Acid Orange II adsorption. *J. Clean. Prod.* 168, 22–29.
- Kousha, M., Daneshvar, E., Sohrabi, M.S., Jokar, M., Bhatnagar, A., 2012. Adsorption of acid orange II dye by raw and chemically modified brown macroalgae *Stoechospermum marginatum*. *Chem. Eng. J.* 192, 67–76.
- Kunde, G.B., Sehgal, B., Ganguli, A.K., 2019. Synthesis of mesoporous rebar MWCNT/alumina composite (RMAC) nodules for the effective removal of methylene blue and Cr (VI) from an aqueous medium. *J. Hazard. Mater.* 374, 140–151.
- Leite, A.J.B., C.S. A., Thue, P.S., dos Reis, G.S., Dias, S.L., Lima, E.C., Vaghetti, J.C.P., Pavan, F.A., de Alencar, W.S., 2017. Activated carbon from avocado seeds for the removal of phenolic compounds from aqueous solutions. *Desalin. Water Treat.* 71, 168–181.
- Lima, É.C., Adebayo, M.A., Fernando, M.M., 2015. Carbon Nanomaterials As Adsorbents for Environmental and Biological Applications. <https://doi.org/10.1007/978-3-319-18875-1>.
- Lin, C.H., Gung, C.H., Sun, J.J., Suen, S.Y., 2014. Preparation of polyethersulfone/plant-waste-particles mixed matrix membranes for adsorptive removal of cationic dyes from water. *J. Memb. Sci.* 471, 285–298.
- Liu, Y., Liu, Y., 2008. Biosorption isotherms, kinetics and thermodynamics. *Sep. Purif. Technol.* 61, 229–242.
- Liu, C.H., Wu, J.S., Chiu, H.C., Suen, S.Y., Chu, K.H., 2007. Removal of anionic reactive dyes from water using anion exchange membranes as adsorbents. *Water Res.* 41, 1491–1500.
- Madala, S., Nadavala, S.K., Vudagandla, S., Boddu, V.M., Abburi, K., 2013. Equilibrium, kinetics and thermodynamics of Cadmium (II) biosorption on to composite chitosan biosorbent. *Arab. J. Chem.* 10, S1883–S1893.
- Nagireddi, S., Katiyar, V., Uppaluri, R., 2017. Pd(II) adsorption characteristics of glutaraldehyde cross-linked chitosan copolymer resin. *Int. J. Biol. Macromol.* 94, 72–84.
- Naidoo, S., Olaniran, A.O., 2013. Treated wastewater effluent as a source of microbial pollution of surface water resources. *Int. J. Environ. Res. Public Health* 11, 249–270.
- Neese, F., 2017. Software update: the ORCA program system, version 4.0. *Wiley Interdiscip. Rev. Comput. Mol. Sci.*, e1327. <https://doi.org/10.1002/wcms.1327>.
- Olusegun, S.J., Freitas, E.T.F., Lara, L.R.S., Stumpf, H.O., Mohalle, N.D.S., 2019. Effect of drying process and calcination on the structural and magnetic properties of cobalt ferrite. *Ceram. Int.* 45, 8734–8743.
- Osugi, M.E., Rajeshwar, K., Ferraz, E.R.A., de Oliveira, D.P., Araújo, Â.R., Zanoni, M.V.B., 2009. Comparison of oxidation efficiency of disperse dyes by chemical and photo-electrocatalytic chlorination and removal of mutagenic activity. *Electrochim. Acta* 54, 2086–2093.
- Özcan, A., Gençten, M., 2016. Investigation of acid red 88 oxidation in water by means of electro-Fenton method for water purification. *Chemosphere* 146, 245–252.
- Panizza, M., Cerisola, G., 2009. Electro-Fenton degradation of synthetic dyes. *Water Res.* 43, 339–344.
- Parr, R.G., Yang, W.T., 1989. *Density-Functional Theory of Atoms and Molecules*. Oxford University Press, New York. [https://doi.org/10.1016/0306-4549\(89\)90016-9](https://doi.org/10.1016/0306-4549(89)90016-9).
- Pathania, D., Sharma, S., Singh, P., 2017. Removal of methylene blue by adsorption onto activated carbon developed from *Ficus carica* bast. *Arab. J. Chem.* 10, S1445–S1451.
- Rodrigues, A.C.D., do Amaral Sobrinho, N.M.B., dos Santos, F.S., dos Santos, A.M., Pereira, A.C.C., Lima, E.S.A., 2017. Biosorption of Toxic Metals by Water Lettuce (*Pistia stratiotes*) Biomass. *Water Air Soil Pollut.* 228. <https://doi.org/10.1007/s11270-017-3340-6>.
- Rohilla, S., Kumar, S., Aghamkar, P., Sunder, S., Agarwal, A., 2011. Investigations on structural and magnetic properties of cobalt ferrite/silica nanocomposites prepared by the coprecipitation method. *J. Magn. Magn. Mater.* 323, 897–902.
- Saad, N., Al-Mawla, M., Moubarak, E., Al-Ghoul, M., El-Rassy, H., 2015. Surface-functionalized silica aerogels and alcogels for methylene blue adsorption. *RSC Adv.* 5, 6111–6122.
- Salima, A., Ounissa, K.S., Lynda, M., Mohamed, B., 2012. Cationic dye (MB) removal using polymer inclusion membrane (PIMs). *Procedia Eng.* 33, 38–46.
- Sarkar, B., Xi, Y., Megharaj, M., Naidu, R., 2011. Orange II adsorption on polyglysines modified with alkyl trimethylammonium and dialkyl dimethylammonium bromide - An isothermal and kinetic study. *Appl. Clay Sci.* 51, 370–374.
- Sheshmani, S., Ashori, A., Hasanzadeh, S., 2014. Removal of Acid Orange 7 from aqueous solution using magnetic graphene/chitosan: A promising nano-adsorbent. *Int. J. Biol. Macromol.* 68, 218–224.
- Shi, H., Li, W., Zhong, L., Xu, C., 2014. Methylene blue adsorption from aqueous solution by magnetic cellulose/graphene oxide composite: equilibrium, kinetics, and thermodynamics. *Ind. Eng. Chem. Res.* 53, 1108–1118.
- Siddiqui, S.I., Rathi, G., Chaudhry, S.A., 2018. Acid washed black cumin seed powder preparation for adsorption of methylene blue dye from aqueous solution: thermodynamic, kinetic and isotherm studies. *J. Mol. Liq.* 264, 275–284.
- Sivashankar, R., Sathya, A.B., Vasantharaj, K., Sivasubramanian, V., 2014. composite an environmental super adsorbent for dye sequestration - A review *Magnetic. Environ. Nanotechnol. Monit. Manag.* 1–2, 36–49.
- Srinivasan, A., Viraraghavan, T., 2010. Decolorization of dye wastewaters by biosorbents: a review. *J. Environ. Manage.* 91, 1915–1929.
- Szygula, A., Guibal, E., Palacín, M.A., Ruiz, M., Sastre, A.M., 2009. Removal of an anionic dye (Acid Blue 92) by coagulation-flocculation using chitosan. *J. Environ. Manage.* 90, 2979–2986.
- Tong, D.S., Wu, C.W., Adebajo, M.O., Jin, G.C., Yu, W.H., Ji, S.F., Zhou, C.H., 2018. Adsorption of methylene blue from aqueous solution onto porous cellulose-derived carbon/montmorillonite nanocomposites. *Appl. Clay Sci.* 161, 256–264.
- Wang, Y., Zhang, Y., Li, S., Zhong, W., Wei, W., 2018. Enhanced methylene blue adsorption onto activated reed-derived biochar by tannic acid. *J. Mol. Liq.* 268, 658–666.
- Xu, Z., Qin, L., Zhang, Y., Li, X., Nan, J., Guo, X., Zhang, G., 2019. In-situ green assembly of spherical Mn-based metal-organic composites by ion exchange for efficient electrochemical oxidation of organic pollutant. *J. Hazard. Mater.* 369, 299–308.
- Yang, S., Wu, Y., Wu, Y., Zhu, L., 2015. Optimizing decolorization of Acid Fuchsin and Acid Orange II solution by MnO₂ loaded MCM-41. *J. Taiwan Inst. Chem. Eng.* 50, 205–214.
- Zahir, A., Aslam, Z., Kamal, M.S., Ahmad, W., Abbas, A., Shawabkeh, R.A., 2017. Development of novel cross-linked chitosan for the removal of anionic Congo red dye. *J. Mol. Liq.* 244, 211–218.
- Zhang, G., Qu, J., Liu, H., Cooper, A.T., Wu, R., 2007. CuFe₂O₄/activated carbon composite: a novel magnetic adsorbent for the removal of acid orange II and catalytic regeneration. *Chemosphere* 68, 1058–1066.
- Zhou, G., Chen, Z., Fang, F., He, Y., Sun, H., Shi, H., 2015. Fenton-like degradation of Methylene Blue using paper mill sludge-derived magnetically separable heterogeneous catalyst: characterization and mechanism. *J. Environ. Sci. (China)* 35, 20–26.
- Zhu, W., Graney, J., Salvage, K., 2008. Land-use impact on water pollution: elevated pollutant input and reduced pollutant retention. *J. Contemp. Water Res. Educ.* 138, 15–21.



Insight into the adsorption of doxycycline hydrochloride on different thermally treated hierarchical CoFe₂O₄/bio-silica nanocomposite

Sunday J. Olusegun*, Nelcy D.S. Mohallem*

Universidade Federal de Minas Gerais, Departamento de Química, Laboratório de Materiais Nanoestruturados, Belo Horizonte, Brazil



ARTICLE INFO

Keywords:

Doxycycline hydrochloride
Adsorption mechanism
Surface charge
Specific surface area
Isotherm

ABSTRACT

The removal of doxycycline hydrochloride (DOX), a widely used antibiotic, from wastewater by novel CoFe₂O₄/rice husk silica nanocomposite was studied. The adsorbent was synthesized through co-precipitation of iron and cobalt salt mixed with a solution of rice husk silica, whose precipitate was dried in an oven at 100 °C and calcined at 300, 500 and 700 °C. Characterization of the adsorbents showed that calcination did not affect their morphology, although the specific surface area and diffractogram of the nanocomposite were significantly affected at calcination temperature of 700 °C. The as-prepared nanocomposite has the highest surface area (283 m² g⁻¹). The adsorption studies revealed that the synthesized nanocomposite is an excellent material for the removal of DOX. The mechanism of adsorption entails electrostatic and n-π interaction. Adsorption data fitted well with Langmuir isotherm, having the monolayer adsorption capacity of 835.47 and 581.44 mg g⁻¹ for the as-prepared and sample calcined at 700 °C, respectively. The removal of DOX is entropy driven, spontaneous in nature and confirmed by TGA and EFTEM analysis.

1. Introduction

The production of different groups of pharmaceutical products are increasing on daily basis due to geometric increase in population and dwindling health status of the populace. Antibiotics happen to be an important group of pharmaceuticals that are being administered to treat specific kind of ailments, which other drugs could not effectively treat [1]. However, as good as antibiotics are in treating bacterial-related infections in human and animal, the incomplete metabolization of the active ingredients of this class of drug in the body system has led to their releasing into the environment through excretion; thereby increasing the pollutants load in the ecosystem [2]. In view of this, there is a great concern over the detrimental effects that antibiotics, which has been estimated to be averagely consumed more than 100 × 10⁶ kg per year in the entire globe, could have on the environment and various organisms if not treated before being discharged into the environment [3]. Antibiotics are released into the ecosystem from different point sources (such as households, hospitals, and pharmaceutical industries) and leads to the contamination of clean water meant for domestic purpose, rapid spread of bacterial resistant to antibiotics and death or impede of important bacterial in the ecosystem [4].

Doxycycline is among the group of antibiotics that are classified under tetracycline (characterized as broad spectrum antibiotic) [5]. It is

a potent drug that has been tested and confirmed to have satisfactory activity against broad range of Gram-negative and Gram-positive and for the treatment of sexually transmitted diseases, upper respiratory tract infections to mention but a few [6,7]. Just like every antibiotic, the presence of doxycycline in surface water, ground water and sediments is hazardous to the environment hence the need to remove them and make the environment pollutant-free [8].

Meanwhile, the complex structure and the antibacterial nature of this class of drugs make it technically impossible to be degraded by micro-organism, hence resulted to the antibiotics-contaminated environment [9]. To curb this menace, different methods have been used to remove Doxycycline (DOX) from the environment, each of these has one shortcoming or the other. Aqueous photocatalytic oxidation method was used by Klauson et al [10] to treat effluents containing DOX. The studies showed that solution pH does not have significant impact on the photocatalytic oxidation of DOX, meanwhile, increase in concentration increases its potential removal. Furthermore, Zaidi et al [11] performed a research on the removal of DOX from aqueous solution using electrochemical treatment that involved a coupled coagulation and floatation process. According to their report, the optimum pH (7.3) and time (80 min) showed effective removal of 96% of the initial 100 mg DOX concentration. It was further added that efficiency of the process was directly proportional to the space between the electrodes

* Corresponding author.

E-mail addresses: arewasegun@ufmg.br (S.J. Olusegun), nelcy@ufmg.br (N.D.S. Mohallem).

<https://doi.org/10.1016/j.jece.2019.103442>

Received 10 June 2019; Received in revised form 24 September 2019; Accepted 27 September 2019

Available online 29 September 2019

2213-3437/ © 2019 Elsevier Ltd. All rights reserved.

and the time of for electrolysis. Meanwhile this method leads to sludge generation.

Other methods for removing tetracycline class of antibiotics include ozonation [12,13], oxidation Fenton process [14,15], photo-catalytic degradation [16], Electro-adsorption [17], among others. Adsorption process, which entails the transfer of contaminant (adsorbate) in the solution to the surface of adsorbent, is widely used among researchers due to its environmental friendliness, non-toxicity, cost effective and efficiency to mention but a few [18,19]. Different adsorbents have been researched and used to removed various antibiotics (include Doxycycline). However, the specific surface area, pore size, surface charge, affinity for the adsorbate, and molecular structure are among the important characteristics that make an adsorbent to perform effectively [3].

There is a paradigm shift towards the use of spinel ferrite nanocomposite for the treatment of wastewater. Aside its effectiveness in removing pollutants, this magnetic adsorbent can be easily separated from solution through external magnetic field. Silica coating enhances the coulomb repulsion of the magnetic nanoparticles thereby improves its stability, prevents the aggregation of magnetic nanoparticles in solution and promotes the binding of various biological ligands to the surface of the nanoparticles [20]. However chemical route of synthesizing silica is supposedly expensive, environmental hazardous and demands rigorous synthesis conditions [21]. So, having known the limitations of producing silica through chemical route, for the first time we synthesized cobalt ferrite/rice husk silica composite and use it for the removal of doxycycline. Bio-silica from agricultural waste like rice husk has been another source of silica production for different industrial uses [22]. The objectives of this research are to employ adsorption technique to remove DOX from aqueous solution by using synthesized hierarchical cobalt ferrite/rice husk silica nanocomposite. Silica from rice husk is chosen because its extraction process is not as rigorous as chemical route. More so cobalt ferrite is chemically stable [23]. The study examined the influence of specific surface area, surface charge, ionic strength, phosphate, pH and temperature on the adsorption of DOX. We also employed thermal treatment to desorb the DOX-loaded adsorbent which is different from the commonly reported chemical method.

2. Material and methods

2.1. Materials

The rice husk that we used was collected from a local rice mill in Ajaokuta steel city, Kogi State, Nigeria, while $\text{FeSO}_4 \cdot 7\text{H}_2\text{O}$ (assay: 99%) and $\text{CoSO}_4 \cdot 7\text{H}_2\text{O}$ (assay: 98.102%) were purchased from Dinâmica Quimica Contemporanea Ltda., Brazil and Doxycycline (DOX, assay: 98.3, yellow powder, 1.4 to 2.8% water).

2.2. Production of rice husk silica

Silica was extracted from rice husk ash according to the method reported by Daramola et al [24]. The husk was adequately washed using water and dried in oven at 80 °C for 24 h. Firstly, the husk was turned into ash in a muffle furnace programmed at 650 °C for 5 h. Approximately 10 g of the ash was thoroughly mixed with 100 mL of 1 M sodium hydroxide solution, boiled in shaking water bath at 100 °C in a beaker for 1 h, cooled and filtered (using Whatman No 41 ashless filter paper). Concentrated tetraoxosulphate (VI) acid (assay: 97%) was added to neutralize the filtrate and the precipitate obtained was incubated for 48 h to facilitate the formation of silica gel. Vacuum filtration was used to separate the gel from solution, which was dried at above 100 °C in an oven.

2.3. Synthesis of CoFe_2O_4 /rice husk silica

An approximately 1.0 g of rice husk silica was put into 250 mL beaker, containing 100 mL of distilled water. The mixture was sonicated in water bath for 30 min. $\text{FeSO}_4 \cdot 7\text{H}_2\text{O}$ (1.0 g) and $\text{CoSO}_4 \cdot 7\text{H}_2\text{O}$ (0.5 g) were added to the dispersed rice husk silica solution in the beaker and placed on magnetic hot plate stirrer for 30 min, after which the pH was adjusted to 11 using NH_4OH (28% NH_3 , assay 99.99%) and digested for 2 h at 90 °C. The precipitate formed was filtered through vacuum filtration process, washed with distilled water until the pH reached 7. The product formed (CoFe_2O_4 /rice husk silica nanocomposite) was dried in an oven at 100 °C and calcined at 300, 500 and 700 °C for 2 h. Each sample was designated as cobalt ferrite/rice husk silica as-prepared (CFS-100), cobalt ferrite/rice husk silica calcined at 300 °C (CFS-300), cobalt ferrite/rice husk silica calcined at 500 °C (CFS-500), cobalt ferrite/rice husk silica calcined at 700 °C (CFS-700).

2.4. Characterization of the samples

X-ray diffraction (XRD) was performed in a X-ray diffractometer (Shimadzu, XRD 7000) using $\text{CuK}\alpha$ radiation [$\lambda = 1.5418 \text{ \AA}$, scanning step = 0.05°, scanning speed 2° min^{-1}]. The powder samples were prepared by packing them to a flat surface in a separate sample holder [25]. The data obtained were analyzed using Search-match software.

Morphology of the nanocomposite was assessed in a thermionic (W filament) scanning electron microscope (SEM), FEI Quanta 200 FEG coupled with EDX silicon drift detector (Bruker). The powders were put on a stub, fixed with a carbon tape.

The sample for TEM analysis was prepared by dispersing small quantity of the powder inside isopropanol and sonicated for 10 min. A drop of the suspension was pipetted and placed on the carbon-coated copper grid. The solvent evaporates while the particles settled on carbon film. The sample was inserted into the sample holder and the image taken on FEI Tecnai G2-20 (200 kV) coupled with an Si (Li) EDAX detector and a Quantum SE system with Gatan Energy Filter.

The textural characteristics of the samples were determined by nitrogen adsorption in a Quantachrome Autosorb. Approximately, 50–60 mg of the nanocomposite was weighed inside the sample cell and degassed at 200 °C to remove adsorbed gases and water. The sample was cryogenically cooled with liquid nitrogen (77 K), while the adsorbate gas (nitrogen) is dose into the system at the series of reduced pressures. The gas adsorbed and the system is allowed to equilibrate, after which time the resultant pressure over the sample is measured. The amount of gas adsorbed by the sample at each reduced pressure point is then used to construct an isotherm. The data obtained were analyzed using multipoint points BET for the evaluation of specific surface area. The pore size distribution curves were obtained by BJH.

Fourier Transform Infrared (FTIR) spectroscopy was used to study the functional groups that were present in the nanocomposites. The FTIR spectra were recorded via a Varian FTIR 660 spectrometer between 400 and 4000 cm^{-1} , 64 accumulations, and 4 cm^{-1} resolution using the standard KBr method. For this analysis, each sample and KBr powder was dried in an oven at 200 C for 2 h to remove moisture. 200 mg of KBr was mixed with 2 mg of the each sample (CFS-100, CFS-300, CFS-500 and CFS-700), crushed using a mortar and pestle and then pressed to form transparent pellets that were used for the characterization [26]. The pellet was placed in FTIR sample holder and analysis.

NETZSCH– STA 409 EP (Netzsch Inc., Germany)-type thermogravimetric (TGA) was used to detect mass loss with respect to the amount of DOX that was adsorbed as a function of temperature. Before carrying out the test, the samples were evenly distributed in an alumina sample pan. The analysis was performed in synthetic air at 50 $\text{cm}^3 \text{ min}^{-1}$ flow rate starting from 40 °C to 600 °C ± 10 °C with 10 °C/min heating rate.

2.5. Adsorption of DOX

Synthesized CoFe_2O_4 /rice husk silica (as prepared, 300 °C, 500 °C and 700 °C) were used for the adsorption of DOX in batch experiment. Different variables such as pH of the solution, dosage of the adsorbent, time of adsorption and temperature of the solutions were studied [27]. Effect of ionic strength and phosphate on the adsorption were investigated [28]. Each study was carried out in duplicate. After each of the study reasonable quantity of the solution was withdrawn and the final unadsorbed concentration of DOX was measure by a UV-Vis spectrophotometer (U-2010, Hitachi) at λ_{max} 345 nm. The amount adsorbed (mg g^{-1}) was calculated using

$$q = \frac{(C_o - C_e)V}{m} \quad (1)$$

where C_o and C_e are the initial and final concentration (mg L^{-1}) of the dye solutions respectively, m is the mass of composite (g) and V is the volume of the dye solution.

2.6. Materials regeneration and DOX desorption

The material was regenerated after adsorption by thermally treated DOX-loaded adsorbent at 500 °C for 2 h to desorb adsorbed DOX. While the DOX-desorbed adsorbent was reused.

3. Results and discussions

3.1. XRD of CoFe_2O_4 /rice husk silica

The diffractogram of as prepared CoFe_2O_4 /rice husk silica composite and those calcined at 300, 500 and 700 °C are shown in Fig. 1. Calcination of the composite up to 700 °C leads to increase in intensity of peaks of the CoFe_2O_4 phase and the appearance of some peaks which are recessive in the diffractogram below this calcined temperature (700 °C). The diffractogram of CFS-100, CFS-300 and CFS-500 are similar and exhibit nature of nanocrystalline materials. This implies that calcination temperature (below 700 °C) could not promote noticeable movement of atoms within the composite, which could lead to transformation of cobalt ferrite with appearance of designated peaks. The obtained diffractogram of CFS-700 correspond with card number 22-1086 of Joint Committee on Powder Diffraction Standards (JCPDS) which is a typical pattern of cubic spinel ferrite having space group of $Fd-3m$ (N° 227) and devoid of impurities. The crystallite size of CFS-700 calculated from the strongest peak (311) using Scherrer's equation

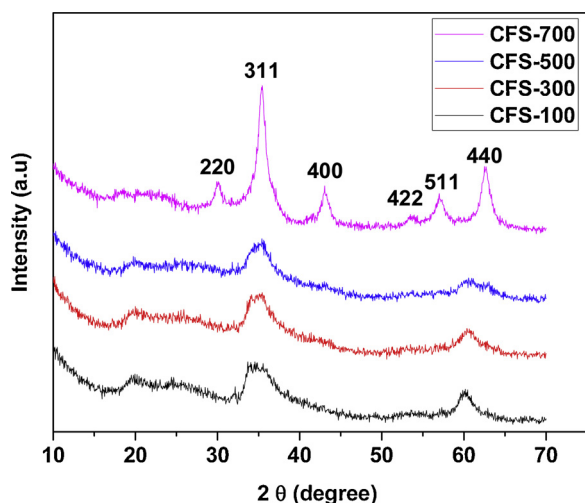


Fig. 1. Diffractograms of cobalt ferrite/ice husk silica: as prepared, CFS-300, CFS-500 and CFS-700.

(equation not shown) is 5 nm. The hump between 17 and 23 (2θ) is due to presence of amorphous rice husk silica.

3.2. Scanning electron microscopy (SEM)

SEM images of CFS-100 (A) CFS-300 (B), CFS-500 (C) and CFS-700 °C (D) are shown in Fig. 2. There seem to be no significant difference in the morphology of the images, meaning that calcination did not have any negative effect on the samples' morphology. Presence of inter particles pores are observed in all the images, which agrees with result obtained from N_2 adsorption and desorption analysis. The shape of the particles is not regular; however, they are agglomerate of particles.

The bright field TEM image of CFS-700 (a representative of the nanocomposite) shown in Fig. 3 reflects agglomerate of particles

3.3. BET specific surface area

The N_2 adsorption and desorption of the nanocomposites and their pore size distribution curves are shown in Fig. 4. The isotherms of the materials are type IIb, which is a characteristic of a mesoporous material with pore diameter > 2 nm. Isotherms with type H3 hysteresis are affirmed not to exhibit any limiting adsorption at high P/Po (P is the pressure of the adsorbate gas (N_2) while Po saturation pressure), the behavior which have been associated with the existence of aggregates of particles forming slit pores with non-uniform shape [29,30]. Regardless of the same isotherm and hysteresis shown by all the samples (CFS-100, CFS-300, CFS-500 and CFS-700), the volume of N_2 adsorbed differs significantly. Table 1 contains the specific surface area (SSA) of the composites. The values of SSA decreases with increase in calcination temperature, close to 50% of the SSA was reduced when the composite was calcined at 700 °C. More so, as the calcination temperature increases, there is a shrinkage and collapsed of pores which as well leads to decrease in pore volumes as shown in Table 1. Positive value of C constant infers interaction between the N_2 molecules and the nanocomposite [31]. The various SSA values obtained in this study are higher than cobalt ferrite that we synthesized without the addition of bio-silica which is a typical example of nonporous nanoparticles [32], the values were as well higher than SSA ($55.4 \text{ m}^2 \text{ g}^{-1}$) of the extracted rice husk silica, the isotherm (not shown).

3.4. FTIR spectra of cobalt ferrite/ice husk silica

The IR spectra of the composite is presented in Fig. 5. The broad band at 3490 cm^{-1} (1) correspond to OH group, which could be due to the presence of absorbed water. However, the intensity of the band decreases with increase in the calcination temperature (CFS-700), because of loss of water (dehydration) during the calcination process. The same observation occurred at peak 1637 cm^{-1} (2) assigned to OH group for CFS-700 as well. The peak at 1023 cm^{-1} (3) is for vibrational band of Si-O-Si [33,34]. The peak at 585 cm^{-1} (4) is attributed to stretching vibration in metal-oxide (CoFe_2O_4) which becomes more distinct in intensity due to increase in temperature. This correlate with the XRD results in Fig. 1, which shows appearance of new peaks and increase in intensity of peaks with respect to temperature. The peak at 490 cm^{-1} (5) present in all the spectra is assigned to Si-O vibrational bond. The 1086 cm^{-1} band with the shoulder at 1160 cm^{-1} (of the sample CFS-700) is due to the asymmetric stretching bonds Si-O-Si of the SiO_4 tetrahedron associated with the motion of oxygen in the Si-O-Si anti-symmetrical stretching which could be promoted by cobalt ferrite [35].

3.5. Adsorption studies

3.5.1. Influence of pH on the adsorption capacity

The results obtained from the effect of pH on the adsorption capacity of cobalt ferrite/ice husk silica nanocomposite calcined at various

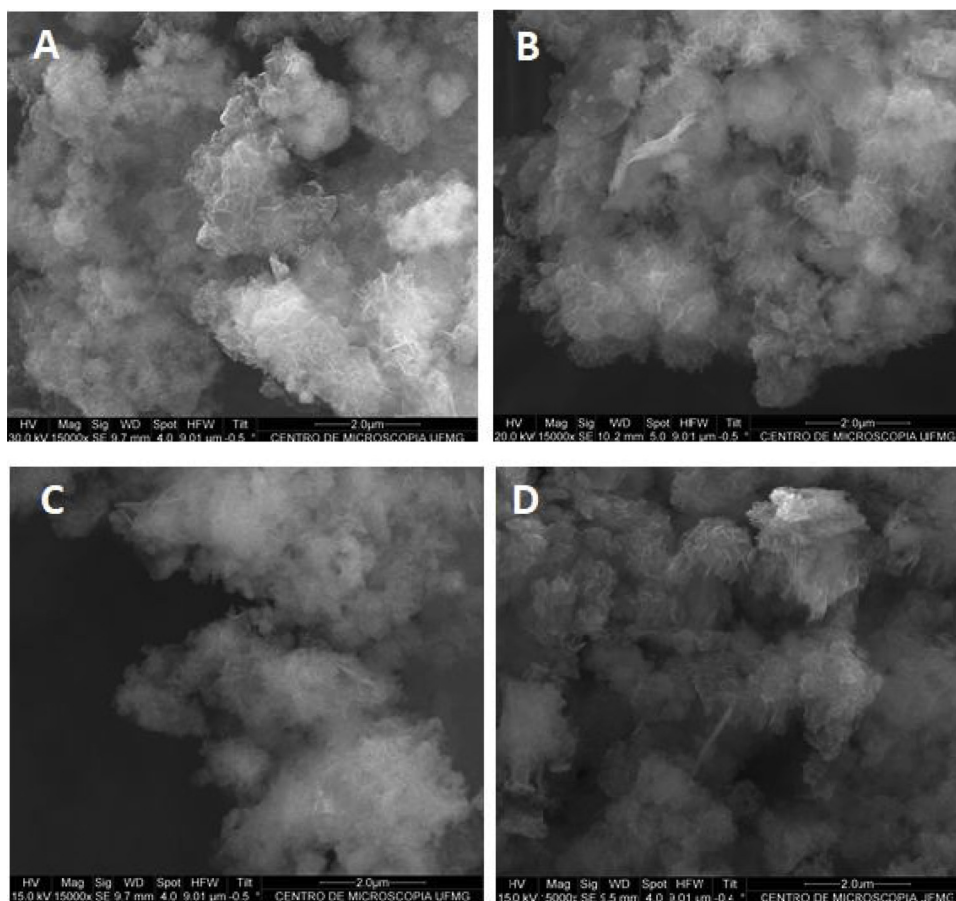


Fig. 2. SEM images of cobalt ferrite/rice husk silica composite: CFS- 100 (A), CFS-300 (B), CFS-500 (C) and CFS-700 °C (D).

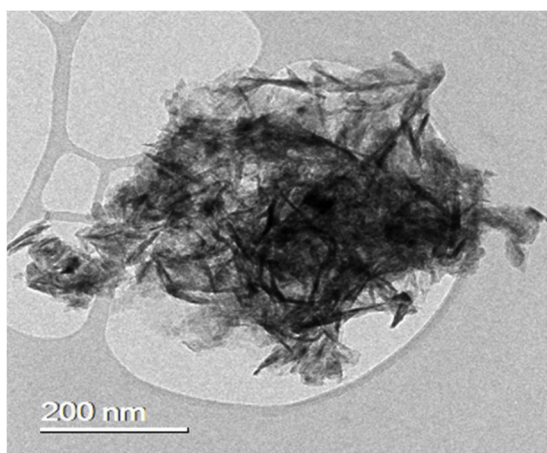


Fig. 3. TEM image of CFS-700.

temperature, rice husk silica only, cobalt ferrite only and zeta potential values are shown in Fig. 6. The trend of the amount of DOX that was adsorbed (with initial concentration of 100 ppm) on the composite is not consistent with variation in the pH of aqueous doxycycline hydrochloride. It increases from pH 2 to 4, maintains equilibrium up till pH 8 and slightly decline at pH 10. The amphoteric nature of DOX molecules (Fig. 7) with different ionizable functional groups such as phenol, alcohol and amino groups, that exist as cations, anions and zwitterion at different pH has made its electrostatic attraction and repulsion between its molecules and the adsorbent to be complex [36]. The surface of the adsorbent is dominated by negative charge (Fig. 6b). At pH \leq 3, DOX is protonated which makes it exists in cationic form (DOX⁺) [37], and

adsorbed on the negative charge surface of the nanocomposites through electrostatic attraction. Meanwhile between pH 4–9 its exists as zwitterions [38] which implies that electrostatic interaction is not the mechanism of adsorption within the range of these pHs. The slight and insignificant decrease in amount adsorbed at pH 10 could be attributed to the repulsion between the negatively charge surface of the adsorbent and the anionic site of some functional groups on DOX. However, electrostatic interaction between the adsorbents and DOX molecules is not enough to explain the mechanism of adsorption of DOX on the synthesized cobalt ferrite/rice husk silica. More so, the reduction in SSA (itemized in Table 1) with respect to calcination temperature did not show a significant effect on the amount of DOX that was adsorbed. The amount of DOX adsorbed by CFS-100, CFS-300 and CFS-500 are almost the same despite the difference in specific surface area (SSA). In addition to this, the SSA of CFS-700 is almost half of CFS-100, ordinarily one would expect the amount adsorbed to follow suit, but this is not the case. It could be stated that the adsorption capacity of the various calcined samples was not completely influence by their SSA. One of the factors that has been documented to favor the adsorption of antibiotics (large molecular size) is the presence of mesopores in the entire bulk of the adsorbent [39], and probably macropores. Samples (CFS-100, CFS-300, CFS-500 and CFS-700) have the presence of meso and macropores, which could promote the adsorption capacity notwithstanding the variation in calcination temperature. Considering the adsorption behavior of cobalt ferrite (COF) and silica (SIL), the amount adsorbed are much lower than those of the composite. Among the reasons for the low values, are non-porosity of COF, micro porosity of SIL and low surface area of both samples. In view of these low values, further studies were focused on the nanocomposite (CFS-100, CFS-300, CFS-500 and CFS-700).

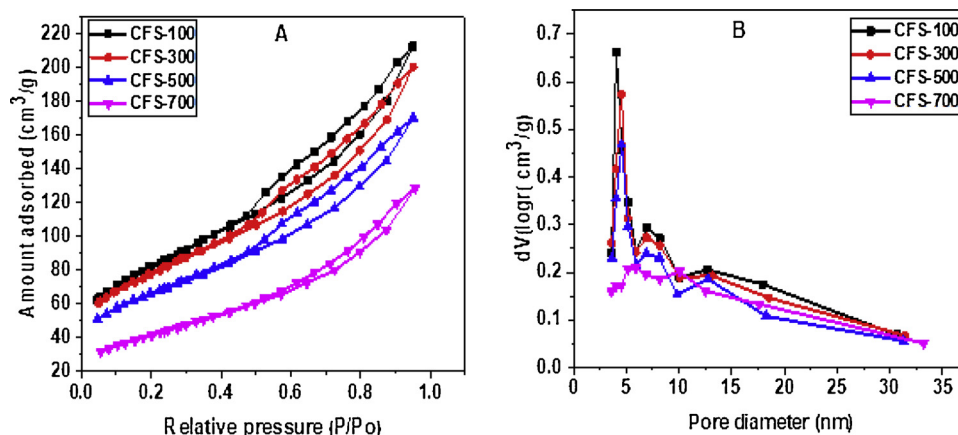


Fig. 4. N₂ adsorption and desorption of the composite (A) and their pore size distribution curves (B).

Table 1
BET specific surface area.

CoFe ₂ O ₄ / rice husk silica	Parameters		
	SSA (m ² g ⁻¹)	*Total pore volume (cm ³ g ⁻¹)	C constant
CFS-100 °C (as prepared)	283	0.33	511
CFS-300 °C	270	0.31	379
CFS-500 °C	229	0.26	389
CFS-700 °C	148	0.2	116

* Single point pore volume was calculated at P/P₀ of 0.95.

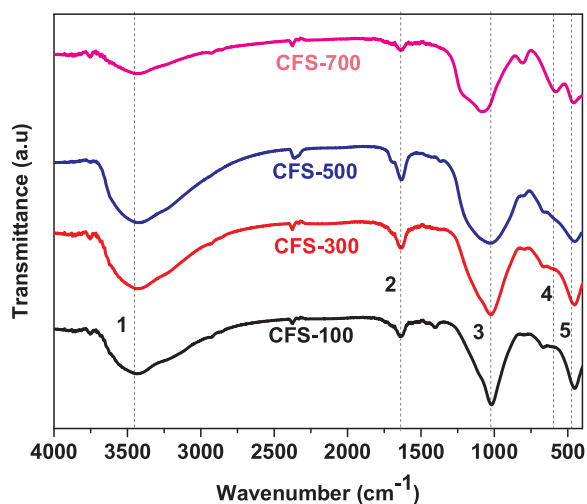


Fig. 5. FTIR spectra of cobalt ferrite/rice husk silica composite.

3.5.2. Effect of contact time

The contact time studies were carried for 10 h as can be seen in Fig. 8. The importance of this study cannot be overemphasised as it helps to know the equilibrium time and how fast the nanocomposite could attain the highest adsorption capacity with respect to the initial concentration. The adsorption of DOX was rapid within 1 h contact time. More than 80 mg g⁻¹ of DOX was adsorbed by all the samples except CFS-700 which adsorbed approximately 50 mg g⁻¹. The availability of active sites at the initial stage of the adsorption process, facilitate rapid adsorption of the antibiotic. Meanwhile, as the time proceeds, less active sites are available for the unoccupied adsorbate, which led to lower rate of adsorption.

3.5.3. Kinetic studies

The data obtained from contact time were further subjected to nonlinear form of pseudo-first order, pseudo-second order and general order kinetic models [40], shown in Eqs. (2), (3) and (4) respectively.

$$q_t = q_e [1 - \exp(-k_1 t)] \quad (2)$$

$$q_t = q_e - \frac{q_e}{[k_2 (q_e) t + 1]} \quad (3)$$

$$q_t = q_e - \frac{q_e}{[k_N (q_e)^{n-1} * t^{n-1} + 1]^{1/n-1}} \quad (4)$$

Where, q_t and q_e are amount of DOX adsorbed at time 't' and at equilibrium time respectively, k_1 , k_2 and k_N are the rate constant of pseudo-first order, second order kinetic and general order models respectively. The plots of these models are shown in Fig. 9, while the respective kinetics parameters are listed in Table 2. Pseudo second order kinetic model is best appropriate for the adsorption process. The R^2_{adjusted} of this model for all the samples are higher than the respective values obtained for pseudo first order and general order. More so, the values of standard deviation (SD) obtain from this model, is lower than that of the other two models. This implies that it is more reliable to relate q_e calculated from pseudo second order to the experimental q_e . The values of q_e obtained from CFS-100, CFS-300 and CFS-500 are within the same range except for CFS-700. This shows that calcination temperature up to 500 °C did not have any significant effect on the amount (mg g⁻¹) of DOX that was removed from the bulk solution. In view of this, further study was carried out on CFS 100 and CFS 700 only.

The shortcomings in relying on R^2_{adjusted} to determine the best model is that it does not take into consideration the number of parameters in each model. Due to this, Bayesian information criterion (BIC) which account for R^2 and number of parameters, is employed. The best model is regarded as the one with lowest BIC. Equation that defines BIC is shown in Eq. (5) [41,42]

$$BIC = N * \ln \frac{RSS}{N} + (P + 1) * \ln N \quad (5)$$

Where N, RSS and p are number of data points, residual sum of squares and number of model parameters respectively. Although the curve fits of general order kinetics model overlapped with pseudo second order, however, pseudo second order has the lowest BIC, this show that it is the best model for this study.

3.5.4. Adsorption isotherm

Langmuir and Freundlich isotherms were used for the understanding of adsorption mechanism in terms of the adsorbate concentration in the bulk solution, the amount adsorbed by the adsorbent as well as nature of adsorption. The maximum capacity of the adsorbent

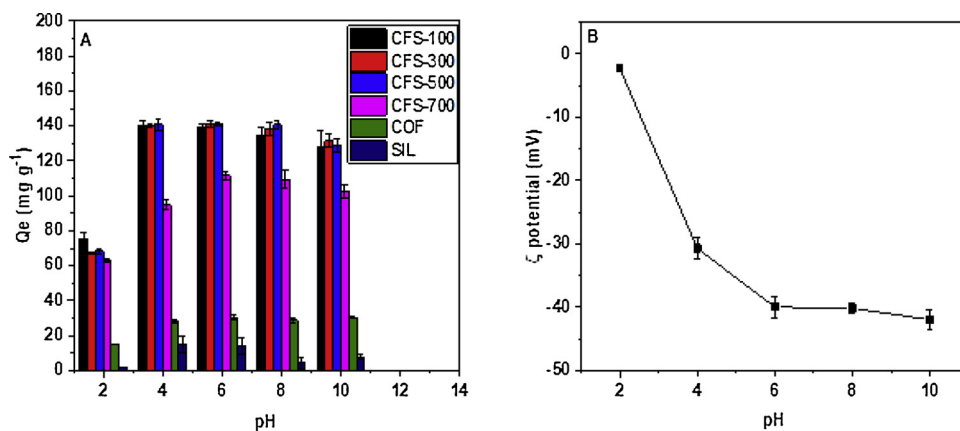


Fig. 6. (A) Effect of pH on the adsorption capacity of CFS-100, CFS-300, CFS-500 and CFS-700; (B) Zeta potential of CFS-100 (a representative of CFS-300, CFS-500 and CFS-700).

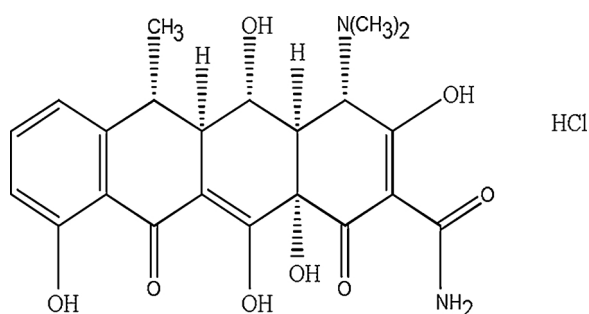


Fig. 7. The structure of doxycycline hydrochloride.

was obtained from Langmuir. Langmuir and Freundlich isotherms are expressed in Eqs. (6) and (7) respectively.

$$q_e = \frac{q_{\max} C_e K_L}{1 + K_L C_e} \quad (6)$$

$$q_e = K_F C_e^{1/n_F} \quad (7)$$

where C_e is the equilibrium concentration in bulk solution (mg L^{-1}), q_e is the amount of DOX that was adsorbed (mg g^{-1}), q_{\max} is the maximum adsorption capacity (mg g^{-1}), K_L is equilibrium constant of Langmuir (L g^{-1}), K_F is the Freundlich constant ($\text{mg g}^{-1} (\text{mg L}^{-1})^{-1/n_F}$), n_F is the dimensionless exponent of Freundlich. The curve fits of the two isotherms for adsorption of DOX on CFS 100 and CFS 700 are shown in Figs. 10 and 11 respectively, while the various isotherms parameters

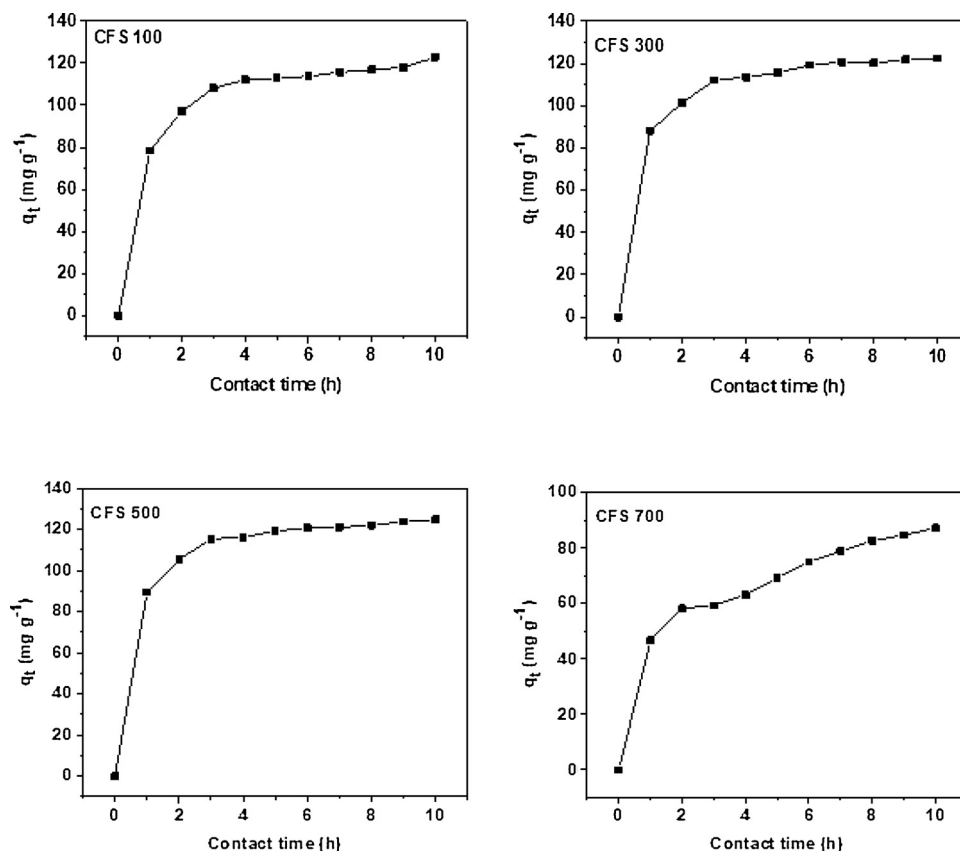


Fig. 8. Effect of contact time on the adsorption of DOX on cobalt ferrite/rice husk silica.

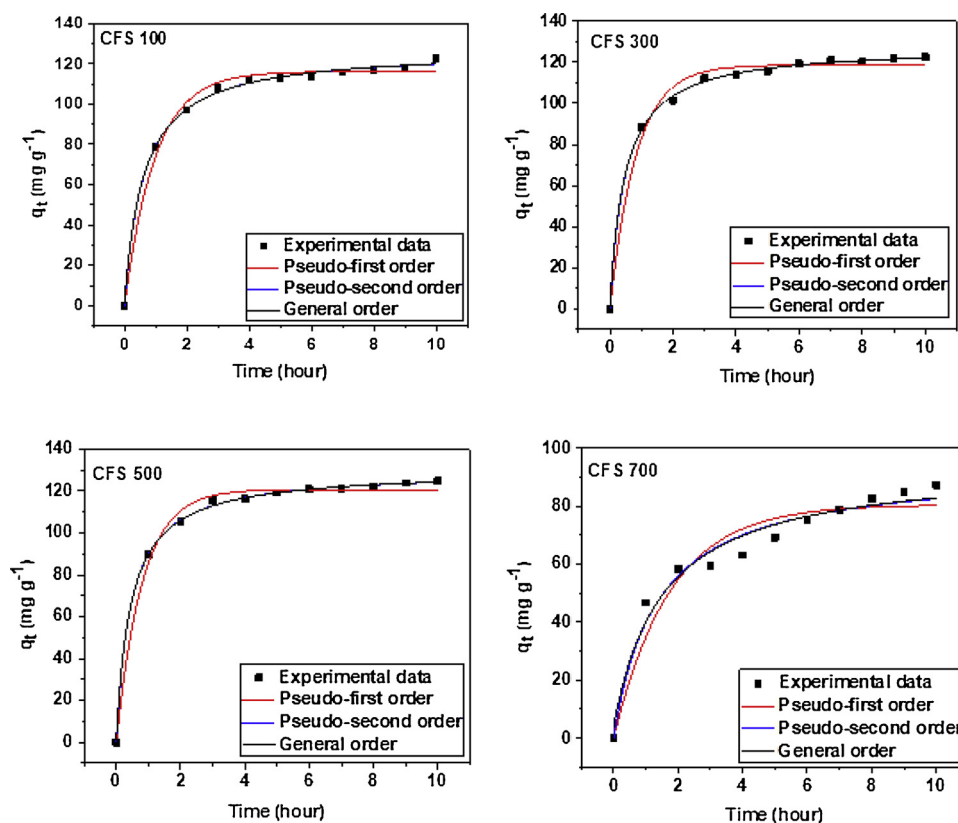


Fig. 9. Kinetic plots of the adsorption of DOX on cobalt ferrite/rice husk silica.

Table 2
Parameters for kinetics models.

Model	Parameters	CFS-100	CFS-300	CFS-500	CFS-700
Pseudo-first-order	q_e (mg g^{-1})	116.09	118.57	120.74	80.49
	k_1 (min^{-1})	1.017	1.203	1.233	0.568
	R^2_{adjusted}	0.9906	0.9881	0.9924	0.9256
	SD (mg g^{-1})	3.414	3.906	3.156	6.763
	BIC	32	34.96	30.27	47.04
Pseudo-second order	q_e (mg g^{-1})	127.16	127.84	129.76	93.72
	k_2 ($\text{g mg}^{-1} \text{min}^{-1}$)	0.013	0.016	0.017	0.007
	q_{max} (mg g^{-1})	0.9977	0.9989	0.9993	0.9654
	SD (mg g^{-1})	1.687	1.191	0.991	4.613
	BIC	16.49	8.82	4.78	38.62
General order	q_e (mg g^{-1})	126.30	126.86	128.83	93.83
	k_N [$\text{min}^{-1} (\text{g mg}^{-1})^{n-1}$]	11.327	5.189	22.614	0.182
	n	1.001	1.003	1.000	1.033
	R^2_{adjusted}	0.9972	0.9986	0.9991	0.9605
	SD (mg g^{-1})	1.840	1.350	1.123	4.928
	BIC	19.50	12.70	8.64	41.17

are itemized in Table 3. The monolayer adsorption capacity obtained from Langmuir isotherm increases with increase in temperature, which is similar to the findings of Brigante and Avena, 2016 [43]. Adsorption of DOX on the adsorbent is favored with increase in temperature which is a typical endothermic adsorption process. Rather than DOX molecule to be desorbed at higher temperature, it was kinetically favored. Its migration and binding to the surface of the adsorbent occurred more faster than desorption which do occur in many adsorption studies. Considering the values of SD and R^2_{adjusted} the experimental data fitted well with Langmuir than Freundlich isotherm. This implies there is monolayer adsorption of DOX on the surface of the nanocomposite without any interaction between the adsorbed species. The adsorption

capacities obtained were further normalized by the surface area of each material (CFS 100 and 700) [44], and the values obtained are 2.95 and 3.93 mg m^2 for CFS 100 and CFS 700 respectively. Based on this normalization result one could opine that the adsorption of DOX on these two nanocomposites was not directly influenced by specific surface. Itemized in Table 4 is the comparison of the adsorption capacity with other adsorbents in the literature for the adsorption of DOX.

3.5.5. Thermodynamic of adsorption

The values of thermodynamic parameters (changes in Gibbs-free energy (ΔG°), changes in enthalpy (ΔH°) and changes in entropy (ΔS°)) listed in Table 5 were calculated using Eqs. (11) and (13).

$$\log K_e = \frac{\Delta S^\circ}{2.303R} - \frac{\Delta H^\circ}{2.303RT} \quad (11)$$

It is worthy to note that K_e is a dimensionless thermodynamic equilibrium constant, which was obtained from Langmuir equilibrium constant (K_L) as shown in Eq. (12), [52].

$$K_e = \frac{1000 \cdot K_L \cdot \text{molecular weight of the adsorbate} \cdot \text{standard concentration of the adsorbate}}{\text{activity coefficient of adsorbate}} \quad (12)$$

$$\Delta G^\circ = \Delta H^\circ - T\Delta S^\circ \quad (13)$$

The values of ΔH° being positive implies that DOX adsorption on the nanocomposite is endothermic process. This depicts that by increasing the temperature of the system, the forces of adsorption that exist between DOX molecules and the adsorbents (CFS-100 and CFS-700) become higher. This is in accordance with the adsorption capacity obtained from Langmuir isotherm which is directly proportional to increase in temperature. Negative values of ΔG° confirms that the process is spontaneous. The values of ΔG° are more negative with increase in the temperature, this implies that spontaneity of adsorption of DOX is stronger [53,54]. The positive values of ΔS° signifies that the

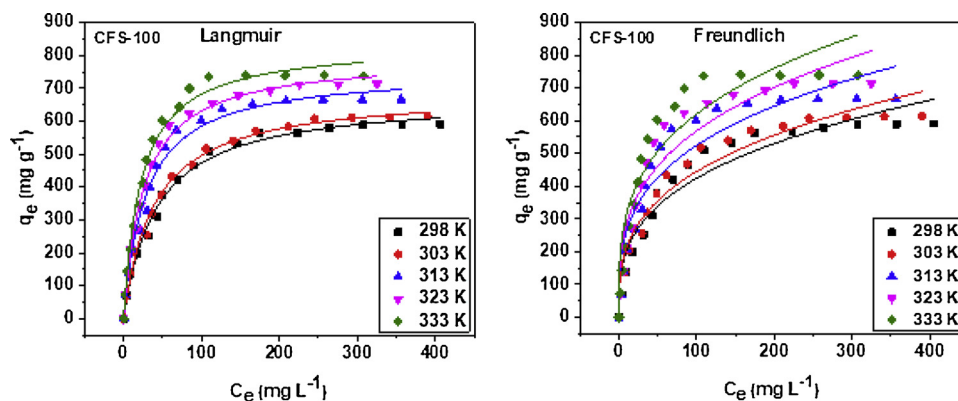


Fig. 10. Langmuir and Freundlich isotherms for the adsorption of DOX on CFS 100.

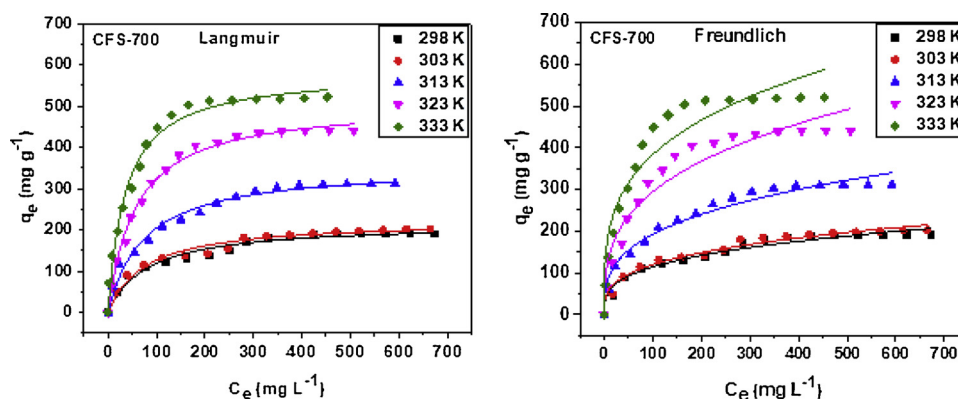


Fig. 11. Langmuir and Freundlich isotherms for the adsorption of DOX on CFS 700.

Table 3

Langmuir and Freundlich isotherms parameters for the adsorption of MB at.303–333 K.

CFS 100					
	298 K	303 K	313 K	323 K	333 K
Langmuir					
q_{max} (mg g ⁻¹)	672.97	689.72	752.31	794.96	835.47
K_L (L mg ⁻¹)	0.024	0.026	0.035	0.038	0.044
$R^2_{adjusted}$	0.9921	0.9933	0.9851	0.9925	0.9888
SD (mg g ⁻¹)	17.81	17.34	28.18	21.12	27.26
Freundlich					
K_F (mg g ⁻¹ (mg L ⁻¹) ^{-1/nF})	96.63	101.43	133.13	141.29	160.83
n_F	3.11	3.11	3.36	3.36	3.41
$R^2_{adjusted}$	0.9321	0.9461	0.8987	0.9111	0.8921
SD (mg g ⁻¹)	52.02	47.92	73.44	72.87	84.93
CFS-700					
Langmuir					
q_{max} (mg g ⁻¹)	216.22	222.98	355.27	507.76	581.44
K_L (L mg ⁻¹)	0.012	0.013	0.014	0.018	0.028
$R^2_{adjusted}$	0.9754	0.9764	0.9806	0.9929	0.9863
SD (mg g ⁻¹)	8.89	9.05	13.47	12.22	20.61
Freundlich					
K_F (mg g ⁻¹ (mg L ⁻¹) ^{-1/nF})	27.48	29.41	44.33	68.32	105.09
n_F	3.22	3.26	3.13	3.15	3.55
$R^2_{adjusted}$	0.9672	0.9748	0.9739	0.9356	0.9272
SD (mg g ⁻¹)	10.27	9.37	15.64	36.83	47.46

adsorption process of the antibiotic is entropy-driven [55]. In addition, the value of ΔS° for CSF-100 being higher than CFS-700 shows increasing randomness.

Table 4

Comparison of the maximum monolayer adsorption (q_{max}) of different adsorbents for the removal DOX.

Adsorbents	q_{max} (mg g ⁻¹)	References
Cu(II) impregnated biochar	93	[45]
MFO-0.5-700	308.51	[36]
Lignin xanthate resin-bentonite clay	438.75	[46]
Electro-generated adsorbents	31.35	[47]
MIL- 53(Fe)/Fe ₃ O ₄	477	[48]
Graphene-MoS ₂ .	555.56	[38]
NaY zeolite	252.12	[49]
Rice straw biochars	170.36	[50]
Fe ₃ O ₄ magnetic nanoparticles	61.35	[37]
graphene nanosheet	110	[51]
CFS-100	835.47	This work
CFS-700	581.44	This work

Table 5

Thermodynamics parameters for the adsorption of AO and MB at.303–333 K.

Adsorbents	ΔH° (kJ mol ⁻¹)	ΔS° (J K ⁻¹ mol ⁻¹)	ΔG° (kJ mol ⁻¹)				
			298 K	303 K	313 K	323 K	333 K
CFS-100	15.76	127.31	-22.17	-22.81	-24.08	-25.36	-26.63
CFS-700	12.21	109.50	-20.96	-22.05	-23.15	-24.24	

3.6. Mechanism of adsorption

FTIR analysis is one of the techniques that helps to understand the mechanism of adsorption through the interaction between the adsorbent and adsorbate. Fig. 12(A) is the FTIR spectra of Doxycycline (DOX), CFS-700 before adsorption and after adsorption (CFS-700 +

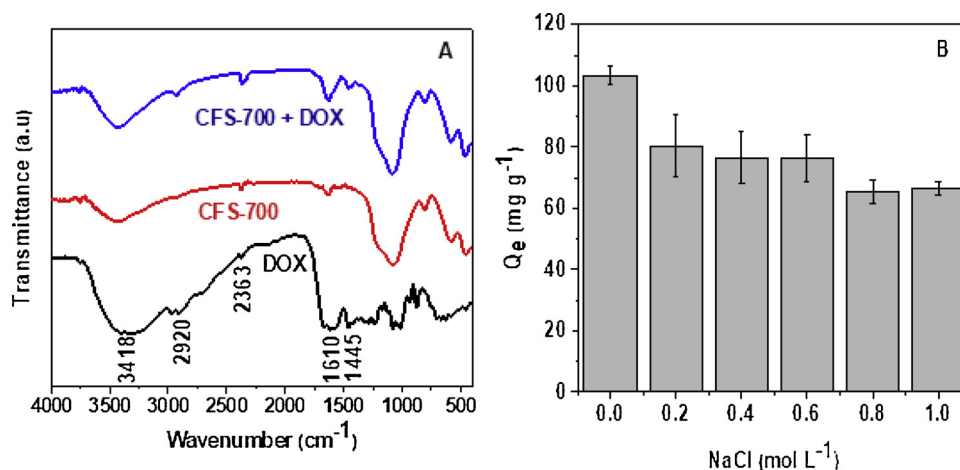


Fig. 12. FTIR spectra of Doxycycline (DOX), CFS-700 before adsorption and after adsorption(A) and effect of ionic strength (B).

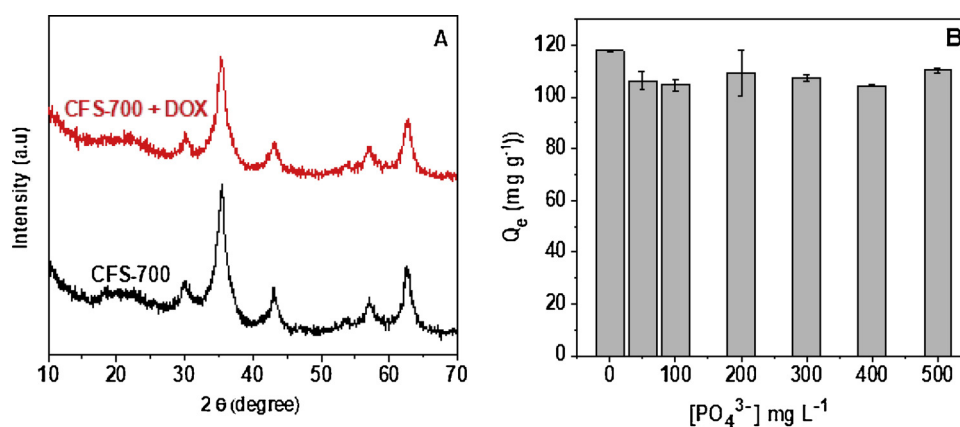


Fig. 13. XRD before and after adsorption (A) and effect of phosphate (B).

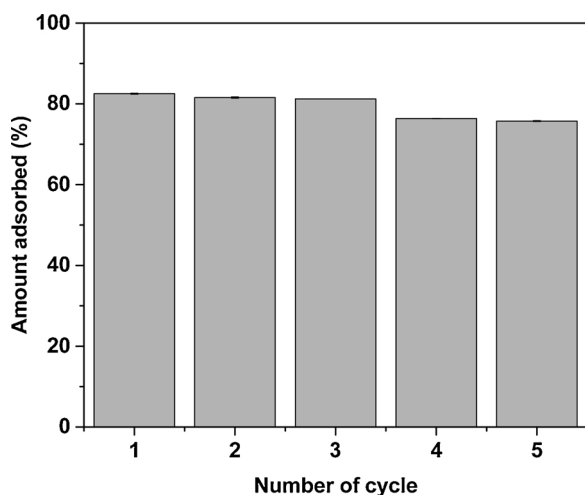


Fig. 14. Reusability of cobalt ferrite/rice husk silica composite.

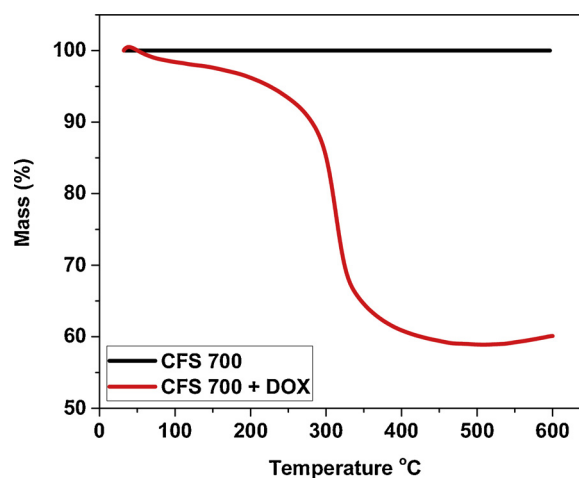


Fig. 15. TGA of CFS-700 before and after adsorption.

DOX). Analyzing the major peaks on the DOX, the broad peak at 3418 cm⁻¹ is assigned to the phenolic -OH stretching, while 2920 cm⁻¹ is attributed to -CH asymmetric stretching. The band at 1610 cm⁻¹ is due to the presence of C=O, while the peak at 1445 cm⁻¹ is attributed to C-C. More so, the band at 1079 cm⁻¹ is assigned to C-O. The peaks at the CFS-700 before adsorption, had been discussed under Section 3.5. The increase in intensity of C=O after adsorption shows that there is interaction between oxygens on the surface of the

nanocomposites and the aromatic rings of DOX which results to n-π interaction [56].

Effect of ionic strength on the adsorption capacity was further investigated for better understanding of adsorption mechanism. This was carried out by adding 0.2–1.0 mol L⁻¹ NaCl to 100 ppm of DOX. The result obtained is presented in Fig. 12(B) and shows that the amount (mg g⁻¹) adsorbed decreases slightly with increase in amount (mol L⁻¹) of NaCl that was added to DOX solution. This confirms that electrostatic interaction also plays a role in the mechanism of

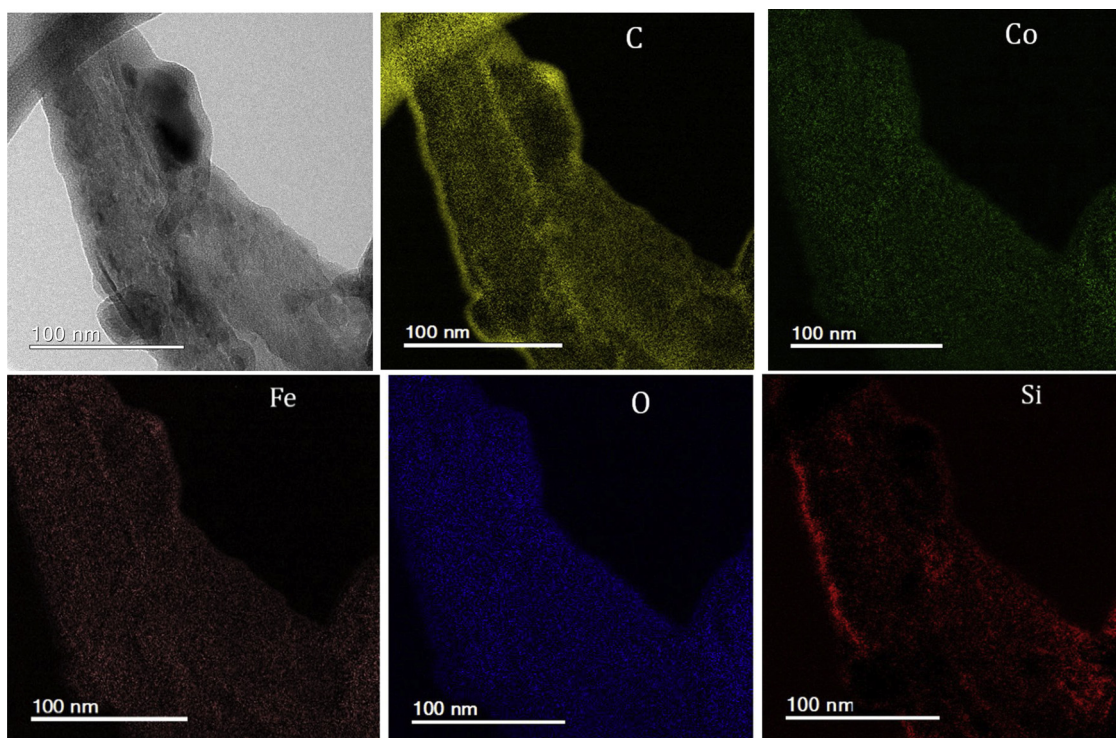


Fig. 16. The RBG color map showing the distribution of each individual element.

adsorption.

The XRD pattern of CFS-700 before and after adsorption presented in Fig. 13(A) are similar. The adsorption of DOX is mainly on the surface of the composite, no ion exchange was involved. The result was similar to what was obtained by [57] in their study on the adsorption of rhodamine 6 G on kaolinite and palygorskite clay minerals. The result obtained from the effects of phosphate on the adsorption of DOX is displayed in Fig. 13(B). Phosphate can be chemically adsorbed on the iron sites through complexation via exchange of ligands and hinder the complexation of other organic ligands on the iron sites [28,58]. The result from this study shows that the presence of phosphate does not have significant effect on the adsorption of DOX despite remarkable concentration of phosphate that was added to fixed concentration (100 mg L^{-1}) DOX solution. This infers that the adsorption of DOX is not through the exchange of ligands on the iron sites as confirm from the XRD.

3.7. Recovery of the adsorbent through thermal treatment

Thermal recovery of the adsorbent (CFS-700) was carried by thermally treating the composite at 500°C for 2 h after each process of adsorption with initial concentration of 500 ppm of DOX. The recovery of the adsorbent (CFS-700) using thermal treatment up to 5 cycles show the reusability of the composites without remarkable reduction in the amount adsorbed in each subsequent cycle (Fig. 14). Economically, the composite is viable to use in industrial scale. The cost of procuring new material will be greatly reduced as the thermally treated composite could be used repeatedly use for the adsorption of the antibiotic. More so, desorbing DOX from DOX-loaded adsorbent by thermal degradation could as well prevent the antibiotic from finding its way into the environment.

3.8. Characterization of CFS-700 after adsorption

Thermogravimetry analysis (TGA) was carried on CFS-700 to confirm the adsorption of DOX. Fig. 15 below shows that there is no weight

loss in the nanocomposite before adsorption this is expected, since it has been earlier calcined at 700°C . However, after adsorption there is an appreciable mass loss which is due to the presence of adsorbed DOX. Approximately 40% of mass loss was recorded. This analysis confirmed adsorption of DOX and that, the adsorbent can be thermally treated and reuse. The initial stage of mass loss up to 200°C is associated with the presence of adsorbed and bound water, while the mass loss from 200 until 450°C is due to the thermal degradation of DOX molecules.

The presence of DOX in the nanocomposite after adsorption was established through energy-filtered-TEM (EFTEM). Elemental mapping of the images is presented in Fig. 16. The Carbon (C) signal is due to the presence of DOX which was adsorbed on the surface of the nanocomposite.

4. Conclusion

We have successfully synthesized a novel cobalt ferrite/bio silica nanocomposite for the first time, with high adsorption capacity and investigated its adsorption capacity for the removal of doxycycline hydrochloride, a hazardous contaminant through batch process. The synthesized nanocomposite was calcined at 300 , 500 and 700°C . The as-prepared nanocomposite has the highest surface area ($283 \text{ m}^2 \text{ g}^{-1}$) while the nanocomposite calcined at 700°C has the lowest ($148 \text{ m}^2 \text{ g}^{-1}$). Optimum pH for the adsorption was found to be 6, while equilibrium time was 10 h. Adsorption process was complexed and affected by temperature which made maximum adsorption capacity of 835.47 and 581.44 mg g^{-1} to be attained by as-received and CFS-700 respectively, at 333 K . Addition of phosphate up to 500 mg L^{-1} did not have any significant effects on the adsorption of DOX, which implies that the mechanism of adsorption is not through complexation with iron species of the nanocomposite. DOX-loaded nanocomposite was desorbed at 500°C , while the DOX-desorbed nanocomposite was reused until 5 cycles. Thermal degradation of the adsorbed DOX was interesting since it could prevent the antibiotic from finding its way to the environment and save cost of procuring new adsorbent. Increased in temperature favored the adsorption process and was spontaneous.

Langmuir isotherm was best applicable to explain the adsorption process among the two isotherms used. TGA and EFTEM analysis clearly ascertain the adsorption of DOX on the nanocomposite.

Declaration of Competing Interest

There are no conflicts of interest.

Acknowledgments

The authors would like to thank UFMG-Microscopy Center for the structural support, FAPEMIG, CNPq and TWAS for financial support.

References

- M.M.A. Hassan, A.K. Hassan, S.S. Allai, Treatment of wastewater contaminated with sulfamethoxazole drug using advanced oxidation processes, *Aust. J. Sci. Technol.* 2 (2018) 72–75.
- R. Shokoobi, A. Dargahi, R. Khamutian, Y. Vaziri, Evaluation of the efficiency of wastewater treatment plants in the removal of common antibiotics from municipal wastewater in Hamadan, Iran, *Avicenna J. Environ. Heal. Eng.* 4 (2017) 1–6.
- L. Nielsen, T.J. Badosz, Analysis of the competitive adsorption of pharmaceuticals on waste derived materials, *Chem. Eng. J.* 287 (2016) 139–147.
- S.D. Costanzo, J. Murby, J. Bates, Ecosystem response to antibiotics entering the aquatic environment, *Mar. Pollut. Bull.* 51 (2005) 218–223.
- M.O. Griffin, E. Fricovsky, G. Ceballos, F. Villarreal, Tetracyclines: a pleiotropic family of compounds with promising therapeutic properties. Review of the literature, *AJP Cell Physiol.* 299 (2010) C539–C548.
- J. Gao, Y. Gao, Z. Sui, Z. Dong, S. Wang, D. Zou, Hydrothermal synthesis of BiOBr/FeWO₄ composite photocatalysts and their photocatalytic degradation of doxycycline, *J. Alloys Compd.* 732 (2018) 43–51.
- N.E. Holmes, P.G.P. Charles, Safety and efficacy review of doxycycline, *Clin. Med. Ther.* (2009) 471–482.
- K. Kümmerer, Antibiotics in the aquatic environment – a review – part I, *Chemosphere* 75 (2009) 417–434.
- Z. Liu, M. Zhu, Z. Wang, H. Wang, C. Deng, K. Li, Effective degradation of aqueous tetracycline using a nano-TiO₂/carbon electrocatalytic membrane, *Materials (Basel)* 9 (2016) 1–14.
- D. Klauson, A. Poljakova, N. Pronina, M. Krichevskaya, A. Moiseev, T. Dedova, S. Preis, Aqueous photocatalytic oxidation of doxycycline, *J. Adv. Oxid. Technol.* 16 (2013) 234–243.
- S. Zaidi, T. Chaabane, V. Sivasankar, A. Darchen, R. Maachi, T.A.M. Msagati, Electro-coagulation coupled electro-flotation process: feasible choice in doxycycline removal from pharmaceutical effluents, *Arab. J. Chem.* (2015) 0–11.
- O.A. Alsager, M.N. Alnajrani, H.A. Abuelizz, I.A. Aldaghmani, Removal of antibiotics from water and waste milk by ozonation: kinetics, byproducts, and antimicrobial activity, *Ecotoxicol. Environ. Saf.* 158 (2018) 114–122.
- X. Liu, Z. Guo, L. Zhou, J. Yang, H. Cao, M. Xiong, Y. Xie, G. Jia, Hierarchical biomimetic BiVO₄ for the treatment of pharmaceutical wastewater in visible-light photocatalytic ozonation, *Chemosphere* 222 (2019) 38–45.
- A.A. Borghi, M.F. Silva, S. Al Arni, A. Converti, M.S.A. Palma, Doxycycline Degradation by the Oxidative Fenton Process, 2015 (2015).
- G. Divyapriya, I. Nambi, J. Senthilnathan, Ferrocene functionalized graphene based electrode for the electro-Fenton oxidation of ciprofloxacin, *Chemosphere* 209 (2018) 113–123.
- M. Khodadadi, M.H. Ehrampoush, M.T. Ghaneian, A. Allahresani, A.H. Mahvi, Synthesis and characterizations of FeNi₃@SiO₂@TiO₂ nanocomposite and its application in photo-catalytic degradation of tetracycline in simulated wastewater, *J. Mol. Liq.* 255 (2018) 224–232.
- N. Li, S. Yang, J. Chen, J. Gao, H. He, C. Sun, Electro-adsorption of tetracycline from aqueous solution by carbonized pomelo peel and composite with aniline, *Appl. Surf. Sci.* 386 (2016) 460–466.
- E. Kristia, R. Pranowo, J. Sunarso, N. Indraswati, S. Ismadi, Performance of activated carbon and bentonite for adsorption of amoxicillin from wastewater: mechanisms, isotherms and kinetics, *Water Res.* 43 (2009) 2419–2430.
- H. Min, S. Yoo, Y. Choi, S. Park, E. Kan, Adsorption isotherm, kinetic modeling and mechanism of tetracycline on Pinus taeda -derived activated biochar, *Bioresour. Technol.* 259 (2018) 24–31.
- S. Laurent, D. Forge, M. Port, a Roch, C. Robic, L.V. Elst, R.N. Muller, magnetic iron oxide nanoparticles: synthesis, stabilization, vectorization, physicochemical characterizations, and biological applications, *Chem. Rev.* 108 (2008) 2064–2110 vol 108, pg 2064, 2008.
- Y. Shen, Rice husk silica derived nanomaterials for sustainable applications, *Renew. Sustain. Energy Rev.* 80 (2017) 453–466.
- J.A. Santana Costa, C.M. Paranhos, Systematic evaluation of amorphous silica production from rice husk ashes, *J. Clean. Prod.* 192 (2018) 688–697.
- N. Sanpo, C.C. Berndt, C. Wen, J. Wang, Transition metal-substituted cobalt ferrite nanoparticles for biomedical applications, *Acta Biomater.* 9 (2013) 5830–5837.
- O.O. Daramola, I.O. Oladele, B.O. Adewuyi, Influence of submicron agro waste silica particles and vinyl acetate on mechanical properties of high density polyethylene matrix composites, *West Indian J. Eng.* 38 (2015) 96–107.
- S.I. Talabi, A.P. Luz, A.A. Lucas, C. Pagliosa, V.C. Pandolfelli, Catalytic graphitization of novolac resin for refractory applications, *Ceram. Int.* 44 (2018) 3816–3824.
- S.I. Talabi, A.P. Luz, V.C. Pandolfelli, A.A. Lucas, Structural evolution during the catalytic graphitization of a thermosetting refractory binder and oxidation resistance of the derived carbons, *Mater. Chem. Phys.* 212 (2018) 113–121.
- S.J. Olusegun, L.F. de Sousa Lima, N.D.S. Mohalle, Enhancement of adsorption capacity of clay through spray drying and surface modification process for wastewater treatment, *Chem. Eng. J.* 334 (2018) 1719–1728.
- P.S. Pinto, T.P.V. Medeiros, J.D. Ardisson, R.M. Lago, Role of [FeOx(OH)y] surface sites on the adsorption of β-lactamic antibiotics on Al₂O₃ supported Fe oxide, *J. Hazard. Mater.* 317 (2016) 327–334.
- P.L. G.M.F. Rouquerol, J. Rouquerol, K.S.W. Sing, Adsorption by Powders and Porous Solids, (2014).
- G. Leofanti, M. Padovan, G. Tozzola, B. Venturelli, Surface Area and Pore Texture of Catalysts 41 (1998), pp. 207–219.
- B. Azom, Calculation of BET Area of Microporous Materials with Automated Software From Quantachrome, (2013), pp. 1–8.
- S.J. Olusegun, E.T.F. Freitas, L.R.S. Lara, H.O. Stumpf, N.D.S. Mohalle, Effect of drying process and calcination on the structural and magnetic properties of cobalt ferrite, *Ceram. Int.* 45 (2019) 8734–8743.
- S. Azat, A.V. Korobeinyk, K. Moustakas, V.J. Inglezakis, Sustainable production of pure silica from rice husk waste in Kazakhstan, *J. Clean. Prod.* 217 (2019) 352–359.
- S. Mor, C.K. Manchanda, S.K. Kansal, K. Ravindra, R.H. Ash, Nanosilica extraction from processed agricultural residue using green technology, *J. Clean. Prod.* 143 (2017) 1284–1290.
- T. Dippong, O. Cadar, E.A. Levei, I. Bibicu, L. Diamandescu, C. Leostean, M. Lazar, G. Borodi, L. Barbu Tudoran, Structure and magnetic properties of CoFe₂O₄/SiO₂ nanocomposites obtained by sol-gel and post annealing pathways, *Ceram. Int.* 43 (2017) 2113–2122.
- J. Li, D.H.L. Ng, R. Ma, M. Zuo, P. Song, Eggshell membrane-derived MgFe₂O₄ for pharmaceutical antibiotics removal and recovery from water, *Chem. Eng. Res. Des.* 126 (2017) 123–133.
- M. Ghaemi, G. Absalan, Fast removal and determination of doxycycline in water samples and honey by Fe₃O₄ magnetic nanoparticles, *J. Iran. Chem. Soc.* 12 (2015) 1–7.
- Y. Chao, W. Zhu, X. Wu, F. Hou, S. Xun, P. Wu, H. Ji, H. Xu, H. Li, Application of graphene-like layered molybdenum disulfide and its excellent adsorption behavior for doxycycline antibiotic, *Chem. Eng. J.* 243 (2014) 60–67.
- A.B. Salviano, M.R.D. Santos, L.M. de Araújo, J.D. Ardisson, R.M. Lago, M.H. Araujo, Iron oxide nanoparticles supported on mesoporous MCM-41 for efficient adsorption of hazardous β-lactamic antibiotics, *Water Air Soil Pollut.* 229 (2018) 59.
- É.C. Lima, M.A. Adebayo, M.M. Fernando, Carbon Nanomaterials as Adsorbents for Environmental and Biological Applications, (2015), <https://doi.org/10.1007/978-3-319-18875-1>.
- B.D. Turner, B.J. Henley, S.B. Sleep, S.W. Sloan, Kinetic model selection and the Hill model in geochemistry, *Int. J. Environ. Sci. Technol.* 12 (2015) 2545–2558.
- G. Schwarz, Estimating the dimension of a model, *Ann. Stat.* 2 (1974) 461–464.
- M. Brigante, M. Avena, Biotemplated synthesis of mesoporous silica for doxycycline removal. Effect of pH, temperature, ionic strength and Ca²⁺ concentration on the adsorption behaviour, *Microporous Mesoporous Mater.* 225 (2016) 534–542.
- M.A. Khan, W.T. Wallace, S.Z. Islam, S. Nagpure, J. Strzalka, J.M. Littleton, S.E. Rankin, B.L. Knutson, Adsorption and recovery of polyphenolic flavonoids using TiO₂-functionalized mesoporous silica nanoparticles, *ACS Appl. Mater. Interfaces* 9 (2017) 32114–32125.
- S. Liu, W. hua Xu, Y. guo Liu, X. fei Tan, G. ming Zeng, X. Li, J. Liang, Z. Zhou, Z. li Yan, X. xi Cai, Facile synthesis of Cu(II) impregnated biochar with enhanced adsorption activity for the removal of doxycycline hydrochloride from water, *Sci. Total Environ.* 592 (2017) 546–553.
- Y. Kong, L. Wang, Y. Ge, H. Su, Z. Li, Lignin xanthate resin-bentonite clay composite as a highly effective and low-cost adsorbent for the removal of doxycycline hydrochloride antibiotic and mercury ions in water, *J. Hazard. Mater.* 368 (2019) 33–41.
- S. Zaidi, V. Sivasankar, T. Chaabane, V. Alonzo, K. Omine, R. Maachi, A. Darchen, M. Prabhakaran, Separate and simultaneous removal of doxycycline and oxytetracycline antibiotics by electro-generated adsorbents (EGAs), *J. Environ. Chem. Eng.* 7 (2019).
- S. Naeimi, H. Faghhihan, Application of novel metal organic framework, MIL-53(Fe) and its magnetic hybrid: for removal of pharmaceutical pollutant, doxycycline from aqueous solutions, *Environ. Toxicol. Pharmacol.* 53 (2017) 121–132.
- M.M.M. Ali, M.J. Ahmed, Adsorption behavior of doxycycline antibiotic on NaY zeolite from wheat (*Triticum aestivum*) straws ash, *J. Taiwan Inst. Chem. Eng.* 81 (2017) 218–224, <https://doi.org/10.1016/j.jtice.2017.10.026>.
- Z. Zeng, X. Tan, Y. Liu, S. Tian, G. Zeng, L. Jiang, S. Liu, J. Li, N. Liu, Z. Yin, Comprehensive adsorption studies of doxycycline and ciprofloxacin antibiotics by biochars prepared at different temperatures, *Front. Chem.* 6 (2018) 1–11.
- R. Rostamian, H. Behnejad, Insights into doxycycline adsorption onto graphene nanosheet: a combined quantum mechanics, thermodynamics, and kinetic study, *Environ. Sci. Pollut. Res.* 25 (2018) 2528–2537.
- F.M. Kasperiski, E.C. Lima, C.S. Umpierrez, S. Glaydson, P. Silas, D. Ramos, S.L.P. Dias, C. Saucier, B. Janaina, Production of porous activated carbons from Caesalpinia ferrea seed pod wastes: highly efficient removal of captopril from aqueous solutions, *J. Clean. Prod.* 197 (2018) 919–929.
- F. Esmaeili, S.A. Gorbanian, N. Moazzezi, Removal of estradiol valerate and progesterone using powdered and granular activated carbon from aqueous solutions,

- Int. J. Environ. Res. 11 (2017) 695–705.
- [54] S.J. Olusegun, G.L.S. Rodrigues, E.T.F. Freitas, L.R.S. Lara, W.R. Rocha, N.D.S. Mohallem, Sequestering anionic and cationic dyes from wastewater using spray dried biopolymeric magnetic composite: experimental and theoretical studies, *J. Hazard. Mater.* 380 (2019) 120872, <https://doi.org/10.1016/j.jhazmat.2019.120872>.
- [55] H.N. Tran, S.J. You, H.P. Chao, Thermodynamic parameters of cadmium adsorption onto orange peel calculated from various methods: a comparison study, *J. Environ. Chem. Eng.* 4 (2016) 2671–2682.
- [56] W. Huang, J. Chen, J. Zhang, Adsorption characteristics of methylene blue by biochar prepared using sheep, rabbit and pig manure, *Environ. Sci. Pollut. Res.* 25 (2018) 29256–29266.
- [57] Z. Li, N. Potter, J. Rasmussen, J. Weng, G. Lv, Removal of rhodamine 6G with different types of clay minerals, *Chemosphere* 202 (2018) 127–135.
- [58] J. Kim, W. Li, B.L. Phillips, C.P. Grey, Phosphate adsorption on the iron oxyhydroxides goethite (α -FeOOH), akaganeite (β -FeOOH), and lepidocrocite (γ -FeOOH): A31P NMR Study, *Energy Environ. Sci.* 4 (2011) 4298–4305.




Synergistic effect of a spinel ferrite on the adsorption capacity of nano bio-silica for the removal of methylene blue

Sunday J. Olusegun, Erico T. F. Freitas, Luciano R. S. Lara & Nelcy D. S. Mohallem

To cite this article: Sunday J. Olusegun, Erico T. F. Freitas, Luciano R. S. Lara & Nelcy D. S. Mohallem (2019): Synergistic effect of a spinel ferrite on the adsorption capacity of nano bio-silica for the removal of methylene blue, Environmental Technology, DOI: [10.1080/09593330.2019.1694083](https://doi.org/10.1080/09593330.2019.1694083)

To link to this article: <https://doi.org/10.1080/09593330.2019.1694083>

 View supplementary material 

 Accepted author version posted online: 20 Nov 2019.
Published online: 01 Dec 2019.

 Submit your article to this journal 

 Article views: 13

 View related articles 

 View Crossmark data 



Synergistic effect of a spinel ferrite on the adsorption capacity of nano bio-silica for the removal of methylene blue

Sunday J. Olusegun ^a, Erico T. F. Freitas ^b, Luciano R. S. Lara ^a and Nelcy D. S. Mohallem ^a

^aDepartamento de Química, Laboratório de Materiais Nanoestruturados, Universidade Federal de Minas Gerais, Belo Horizonte, Brazil;

^bUniversidade Federal de Minas Gerais, Centro de Microscopia, Belo Horizonte, Brazil

ABSTRACT

The synergistic effect of CoFe_2O_4 on the capacity of bio-silica extracted from rice husk for the removal of methylene blue (MB) was investigated. The novel composite of cobalt ferrite/nano bio-silica was prepared by dispersing cobalt and iron salt in ratio 1:2 in a solution containing bio-silica, calcined at 700°C and characterized. The adsorption capacity of the composite (253.6 mg g^{-1}) was higher than that of bio-silica (52.6 mg g^{-1}), and the process was exothermic and spontaneous. Langmuir and Freundlich models were applicable to explain the adsorption isotherm, while pseudo-second-order and Elovich are best applicable for the kinetics mechanism. The amount of MB that was removed, increased with an increase in ionic strength due to dimerization of MB. Regeneration and reusability of the adsorbents showed that they are economically viable. Energy-filtered transmission electron microscopy (EFTEM) and Fourier transformed infrared (FTIR) analysis of MB-loaded adsorbent confirmed the adsorption of MB.

ARTICLE HISTORY

Received 20 August 2019

Accepted 8 November 2019

KEYWORDS

Bio-silica; methylene blue; cobalt ferrite; adsorption; specific surface area



1. Introduction

'Health is wealth' is a common quote that is often used to sensitize people about the importance of health to wealth. Another phrase, that is frequently used, is 'cleanliness is next to godliness'. These two quotes show the importance of maintaining a clean environment for sustainability of healthy lifestyle and enjoyment of wealth. Meanwhile, our environment is being polluted by one pollutant or the other, leading to a decline in health status of rank and file [1,2]. Water, soil and air among others suffer from indiscriminate pollutants whose aftermath effects on the environment are alarming and generally contribute to an increase in death rate [3–6].

Water is an important commodity whose usefulness in day-to-day activities cannot be overemphasized [7]. It is being used at home, school, industries, hospital, for farming, etc. Contamination of both surface- and groundwater is worrisome and thereby requires

prompt attention [8–11]. Dyes, heavy metals and pharmaceuticals wastes are among pollutants that affect the quality of water that is highly required for domestic and industrial uses [12,13]. The source of dyes to waterway has been traced to textile, paper, food and pharmaceutical industries [14,15]. Their presence in small quantity affects the aesthetic beauty of water, prevents sunlight from reaching aquatic organism, results in diseases such as cancer, unpleasant odour and lots more [16–19]. These detrimental effects need enforcing prompt action by a responsible government that could save water from being polluted [20].

Large volumes of water pollutants come from industries [21,22]; due to this, several wastewater treatment techniques are being used, with the single focus of making water free from either micro or macro pollutants. There is growing research in the use of the adsorption technique to remove various contaminants from industrial effluents. Adsorbents with high surface area, viable active sites, high adsorption capacity and eco-friendly

have been developed [23,24], and research is still ongoing on the development of good adsorbents. These adsorbents are either from natural product, biomass, synthetic and agricultural source [25–27]. Silica is one important material that has found its relevance in several applications [28–30] and also as an adsorbent (either as a composite with other materials, raw or functionalized form) for the removal of contaminants from water [31–33]. This versatile material has been synthesized using different methods (sol–gel, hydrothermal process, microwave reactor and combustion process) and sources (sodium silicate and tetraethyl silicate (TEOS)) [34]. The disadvantages of these methods are being expensive, environmental hazardous and time-consuming [35,36]. To combat these menaces, the extraction of silica from the agriculture source has been a safer route.

Littered in the literature is the composite of cobalt ferrite with silica obtained from TEOS [37–40]. So, having known the shortcoming of producing silica through TEOS (synthetic route), for the first time, we produced cobalt ferrite/bio-silica composite for the removal of methylene blue (MB). Nano adsorbents like nano bio-silica with small sizes could be difficult to sort out after attaining their optimum adsorption capacity [41]. Therefore, incorporating magnetic particles into the bio-silica matrix could ease the stress of separation after the adsorption process. Regarding this, synergistic effects of cobalt ferrite, an example of spinel ferrite on the adsorption capacity of nano bio-silica, were investigated. The choice of CoFe_2O_4 is because it has large magnetic anisotropy and remarkable chemical stability [42]. The presence of cobalt ferrite induces magnetic properties on the composite (which is easy to separate after adsorption) and enhances its adsorption capacity.

2. Material and methods

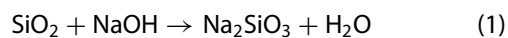
2.1. Materials

Rice husk was collected from a local rice mill in Nigeria, while $\text{FeSO}_4 \cdot 7\text{H}_2\text{O}$ and $\text{CoSO}_4 \cdot 7\text{H}_2\text{O}$ were purchased from Dinâmica Química Contemporânea Ltda., Brazil.

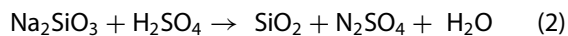
2.2. Production of bio-silica

The extraction of silica from the ash of rice husk was done in line with the method that was outlined by Dar-amola et al [43] without any modification. The summary of the extraction process is shown in Equations (1) and (2) [44]. Ash from rice husk was boiled with sodium hydroxide to produce sodium silicate.

Tetraoxosulphate (VI) was further added to sodium silicate to obtain silica gel precipitate, which was aged for 2 days, filtered and dried.



(ash)



(silica)

2.3. Synthesis of CoFe_2O_4 /rice husk silica

Exactly 0.1 g of Iron (II) sulphate heptahydrate was mixed thoroughly with 0.05 g of cobalt (II) sulphate heptahydrate in a beaker containing 25 mL of distilled water. Bio-silica (0.1 g) was dispersed in a solution containing iron and cobalt salt, stirred for 30 min and precipitated at pH 11 using ammonium hydroxide. The product (bio-silica/cobalt ferrite nanocomposite) obtained was boiled at 100°C for 2 h, filtered and dried. Half of the dried composite was calcined at 700°C and labelled as SCOF700, while the composite that was dried at 100°C in the oven was designated as SCOF100.

2.4. Characterization of the samples

The synthesized materials were characterized by using transmission electron microscope FEI Tecnai G2-20 (200 kV), Zetasizer Nano-Zs model ZEN3600 for zeta potential measurement, S700X SQUID magnetometer for magnetic properties and Fourier transformed infrared (FTIR) spectra measurements were carried out on Perkin–Elmer spectrophotometer using the KBr pellets. The specific surface area (SSA) was determined by nitrogen adsorption in a Quantachrome Autosorb, using the Brunauer–Emmett–Teller (BET) method. X-ray diffraction (XRD) was performed in a X-ray diffractometer (Shimadzu, XRD 7000) using $\text{CuK}\alpha$ radiation.

2.5. Adsorption studies

2.5.1. pH studies

Optimum pH was determined by adding 10 mg of each adsorbent (extracted bio-silica (BSIL), SCOF100 and SCOF700) into separate 50 mL beakers that contain 15 mL of 100 mg L^{-1} of MB. The pH of the dye solution was adjusted to 2, 4, 6, 8 and 10 by adding dilute HCl and NaOH drop-wise and studied for 4 h.

2.5.2. Dosage studies

The amount of each adsorbent was varied from 2, 4, 6, 8 and 10 mg. Each respective mass of the adsorbent was

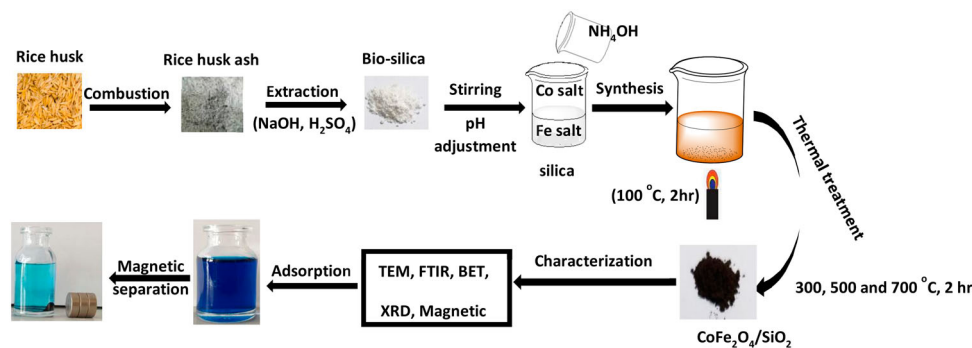


Figure 1. Schematic description of the extraction of bio-silica and synthesis of $\text{CoFe}_2\text{O}_4/\text{bio-silica}$ for the adsorption of MB.

added to 15 mL of 100 mg L^{-1} of MB. Optimum pH was used for this study.

2.5.3. Kinetic studies

Kinetic studies were carried out for 4 h, while the amount adsorbed was measured at 30 min regular intervals to know the optimum time. In this study, optimum pH and dosage were used with 15 mL of 100 mg L^{-1} of MB.

2.5.4. Temperature and concentration studies

The temperature of the solution was varied from 303, 313, 323 and 333 K by placing the beakers containing a fixed volume of the respective initial dye concentration (50, 100, 150, 200, 250, 300, 350, 400, 450 and 500 mg L^{-1}) of MB inside a temperature-controlled water bath and allowed to stay for the optimum time that had been earlier determined.

After each of the study listed above, a reasonable quantity of the solution was withdrawn and the final unabsorbed concentration of MB was measured by a UV-Vis spectrophotometer (U-2010, Hitachi) at a wave-length of $\lambda_{\text{max}} = 664 \text{ nm}$. The amount adsorbed (mg g^{-1}) was calculated using the following equation:

$$q = \frac{(C_o - C_e)V}{m} \quad (3)$$

where C_o and C_e are the initial and final concentrations (mg L^{-1}) of the dye solutions, respectively, m is the mass of the composite (g) and V is the volume of the dye solution (L).

The scheme of the extraction of bio-silica for the adsorption of MB is shown in Figure 1.

3. Results and discussion

3.1. Characterization of the adsorbent

Transmission electron microscopy (TEM) images of the adsorbents are shown in Figure 2. The image of BSIL shows well-dispersed nanoparticles of both spherical

and longitudinal morphology, while those of SCOF 100 and 700 shown typical agglomerates of sponge-like structure. An electron diffraction (ED) image of silica (b) shows that the extracted silica is amorphous and thus silica is used for different applications [29]. There is a remarkable difference in the ED of SCOF 100 and 700. The crystal growth of the composite was prompted by the calcination temperature. The diffraction pattern of SCOF 700 shows distinct d-spacings which are characteristic of cobalt ferrite while fewer d-spacings are seen on SCOF 100, which means that at this temperature, cobalt ferrite has not been fully formed within the composite. More so, the spots on the diffraction pattern of SCOF 700 show that the sample is more crystalline than SCOF 100 whose diffraction pattern shows evenly intensity diffracted rings. This could be a reason for low magnetic saturation value of SCOF 100.

The results of the SSA using the BET method show that BSIL has $55 \text{ m}^2 \text{ g}^{-1}$, while the SSA of SCOF 100 and 700 are 283 and $148 \text{ m}^2 \text{ g}^{-1}$, respectively. Sponge-like structure of SCOF 100 and 700 enhances its SSA. The SSA of cobalt ferrite from our previous work was $47 \text{ m}^2 \text{ g}^{-1}$ [45], lower than that of SCOF 100 and 700. Both silica and cobalt ferrite formed a composite of high surface area which synergistically increase the adsorption capacity for the removal of MB as it will be seen in further discussion.

The crystal phases of the adsorbents were further confirmed by XRD diffractogram (Figure 3). The high-intensity peak of BSIL was between 15° and 32° centred at 22° , confirming the amorphous nature of BSIL as shown from the ED results (Figure 2). The absence of no other sharp peak on the diffractogram of BSIL implies that the extracted silica is pure. The diffractogram of SCFO 100 shows the presence of two peaks; however, when it was calcined at 700°C , there were the appearance of several peaks which corresponds to cobalt ferrite of card number 22-1086 of the Joint Committee on Powder Diffraction Standards (JCPDS) which is

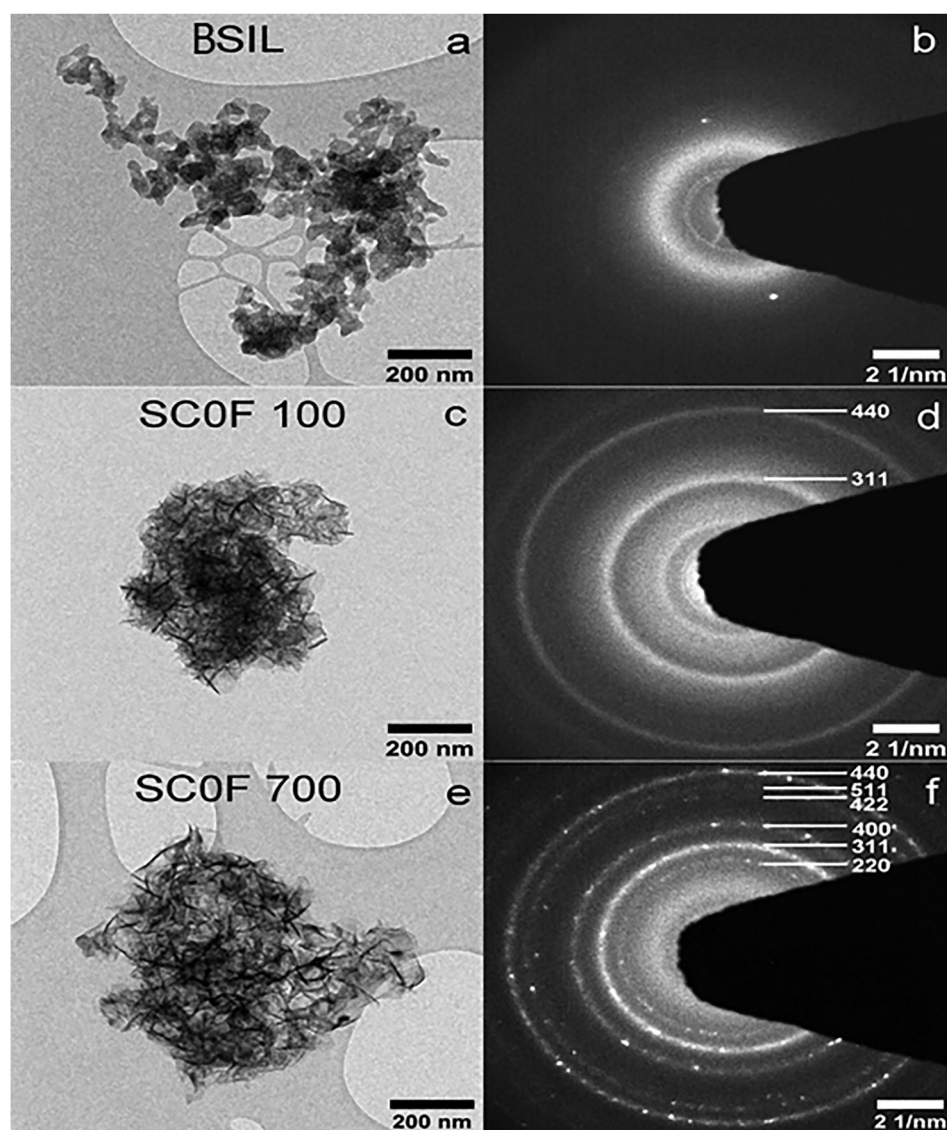


Figure 2. TEM images (a, c and e) with the ED (b, d and f) of BSIL, SCOF-100 and 700.

a typical pattern of cubic spinel ferrite having a space group of $Fd-3m$ ($N^{\circ} 227$) and devoid of impurities. The several sharp peaks at SCOF 700 confirm the results obtained from ED analysis. Crystallite size of SCOF-100 and SCOF-700 at peak 311 calculated using Scherrer's equation is 2 and 5 nm.

The results of magnetic saturation (M_s) values of SCOF-100 and 700 with respect to the applied field are displayed in Figure 4. There is a sharp and noticeable increase in the M_s of the composite after calcined at 700°C, which could be due to the magnitude of thermal vibrations of atoms that increases with the increase in temperature [46]. It is stated that the migration of Fe^{3+} ions to octahedral sites due to an increase in the calcination temperature could induce an increase in magnetic saturation, in addition, the overall magnetic moment of Fe^{3+} ions due to migration is greater than that of Co^{2+} ions [47]. In addition

to this, the sharp increase in M_s could be due to the increase in crystallite size with calcination, as seen in the XRD results. It is stated that a magnetic domain differently proportional to crystallite size results in an increase in magnetic saturation [45]. Both coercivity and magnetic remanence increase with an increase in the calcination temperature. Magnetic parameters are listed in Table 1. Magnetic saturation obtained in this study was compared with those obtained from cobalt ferrite composite with synthetic silica (TEOS, etc.) and listed in Table 2.

4. Adsorption studies

4.1. Influence of pH on amount adsorbed

Solution pH plays an indispensable role in the adsorption process by influencing the adsorbent surface

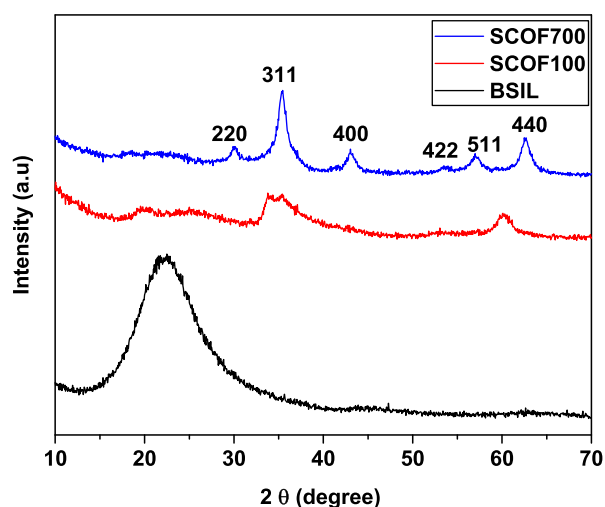


Figure 3. XRD diffractogram of BSIL, SCOF-100 and 700.

charge and ionization of the adsorbate [51,52]. A pH study was carried out by varying the pH of the solution from 2 to 10, and the results obtained are shown in Figure 5. Meanwhile, prior to this, we investigated the zeta potential of BSIL and SCOF 700 (representative of SCOF 100) and found the values to be negative. It was on this premise that MB, a model cationic dye, was used as an adsorbate. The result shows an increase in the amount of MB that was adsorbed on the surface of the adsorbents with respect to pH, which is as a result of electrostatic attraction between MB and the adsorbents. There is an alarming increase in the amount adsorbed by SCOF 100 and 700 compared to BSIL despite the same negative surface charge that both exhibits. In addition to this, the amount adsorbed by both COF (cobalt ferrite) and BSIL are almost the same, and it then implies that the alarming increase

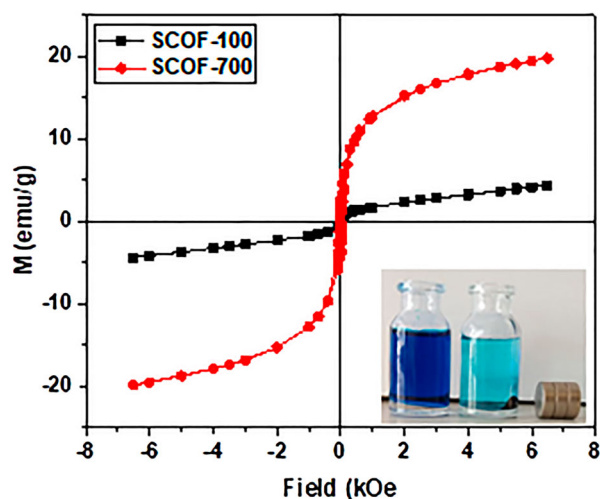


Figure 4. Magnetization versus applied field at 300 K for rice husk silica/cobalt ferrite composite.

Table 1. Saturation magnetization, coercivity and remanence values obtained at 300 K.

	Hc (Oe)	Mr (emu g ⁻¹)	Ms (emu g ⁻¹)
SCOF-100	10.2	0.27	4.38
SCOF-700	34.65	3.01	20.33

Table 2. Comparison of saturation magnetization (at room temperature) of cobalt ferrite with synthetic silica reported by some authors.

Ms (emu g ⁻¹)	Reference
1.26	[48]
18.21	[49]
2.89	[39]
21.09	[40]
21.8	[37]
21.3	[50]
20.33	This study

in the amount adsorbed by the composite is not due to only COF, but due to their synergetic effect. The SSA of the adsorbents shows that the SSA plays an important role in the adsorption on MB. The SSA of SCOF 100 is 5 times more than that of BSIL which is equivalent to 5 times the amount adsorbed by BSIL. Worthy of note is that cobalt ferrite aside offering a magnetic separation to the composite, enhanced the adsorption capacity. Further study was carried out on BSIL, SCF100 and SCOF 700 only.

All silicas have different types of the silanol group (isolated, geminal and vicinal) on their surfaces [53]. Deprotonation of this group occurs in water with increasing pH which leads to negative charge (SiO⁻) [54,55] and becomes an active site for the adsorption of MB through electrostatic attraction (see Supplementary Material Figure S1). Meanwhile, due to the large SSA and negative charge on the surface of the composite, the adsorption of MB was synergistically enhanced.

4.2. Adsorbent dosage

The amount of MB (initial concentration 100 mg L⁻¹ and pH 9) that was adsorbed increases with the dosage of the adsorbents as shown in Figure 6. The dosage of SCOF 100 and 700 was varied from 2 to 10 mg, while that of BSIL was varied from 10 to 100 mg. The amount (%) of MB adsorbed by 2 mg of SCOF 100 was equivalent to that of 10 mg of BSIL. Interesting also is that as the dosage of SCOF 100 and 700 increases, the amount adsorbed also increases, which is due to the availability of more active sites for the adsorption of the dye. SCOF 100 almost attains equilibrium at 8 mg, while SCOF 700 does not. More so, BSIL attained equilibrium at 60 mg of the

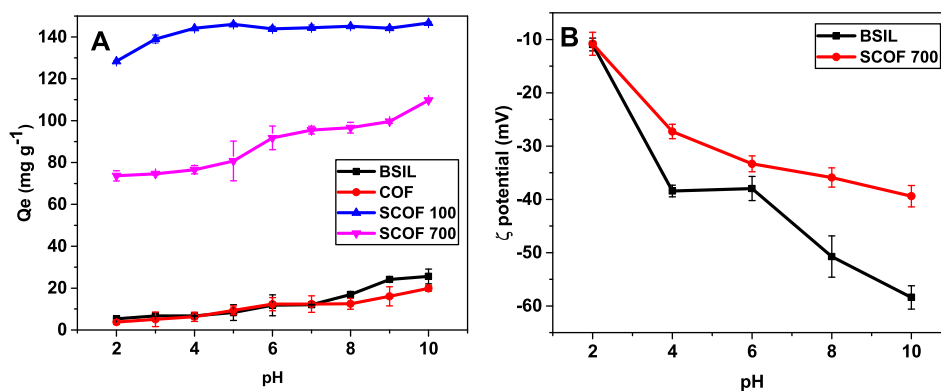


Figure 5. Effect of pH (A) on the adsorption of MB on BSIL, COF, SCOF 100 and SCOF 700, with the zeta potential (B).

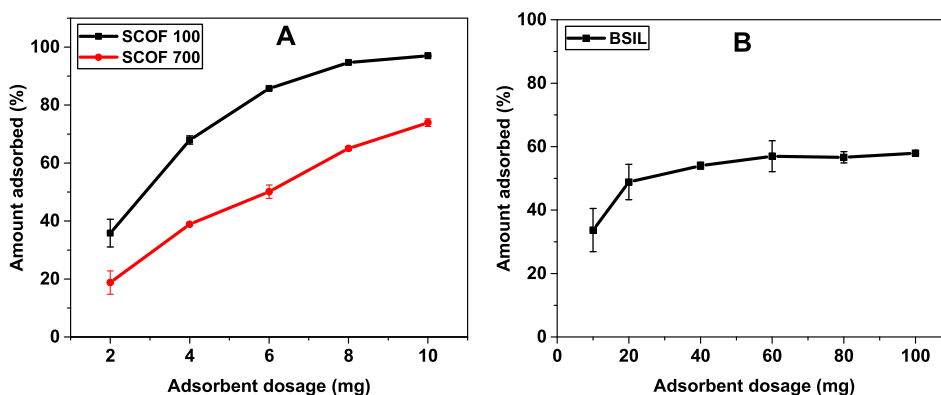


Figure 6. Amount of MB adsorbed with respect to the dosage of the adsorbent SCOF 100 and 700 (A) and BSIL (B).

adsorbent. Overall, both SCOF100 and 700 offer a better adsorption capacity than BSIL.

4.3. Kinetic study

As shown in Figure 7, approximately 133 and 103 mg g^{-1} of MB was adsorbed by SCOF 100 and 700, respectively, while for BSIL, 19 mg g^{-1} was adsorbed after initial 30 min of contact time. After which, the adsorption was slow due to the covering of the active sites by MB molecules. It is economically interesting in wastewater treatment for adsorbents to adsorb the targeted contaminants within a short period of contact time [56]. The optimum time for SCOF 100 and 700 was found to be 120 min.

Three kinetic models were employed for good understanding of adsorption kinetic (see supplementary). The parameters of the models are itemized in Table 3. The respective values of R^2_{adjusted} show that Elovich is probably applicable to explain the adsorption of MB on BSIL, while both pseudo-second-order and Elovich are best suitable for SCOF 100 and SCOF 700. More so, the values of standard deviation (SD) obtained from pseudo-second-order and Elovich models are lower

than pseudo-first-order. In view of this, calculated q_e obtained from pseudo-second-order is more reliable to relate with experimental q_e . This presupposes that the adsorption may likely involve the chemical process [57].

4.4. Adsorption isotherm

The descriptive behaviour of how BSIL, SCOF 100 and 700 interact with different concentrations of MB in the solution at a constant temperature was examined by employing two commonly use isotherms (Langmuir and Freundlich). These two isotherms predict different interactions of the adsorbed molecules with the surface of the adsorbent. While Langmuir supposes single layer adsorption, Freundlich differs by assuming multi-layer sites on the adsorbent surface. The nonlinear equations that define these two models can be found in the supplementary material. Figures 8–10 depict the curve fits of the two isotherms, while their parameters for all the adsorbents are listed in Table 4. The trend of the adsorption capacity which decreases with an increase in the temperature signifies the exothermic adsorption of MB on BSIL and the composites. The higher adsorption capacity of the composites than BSIL is due to the

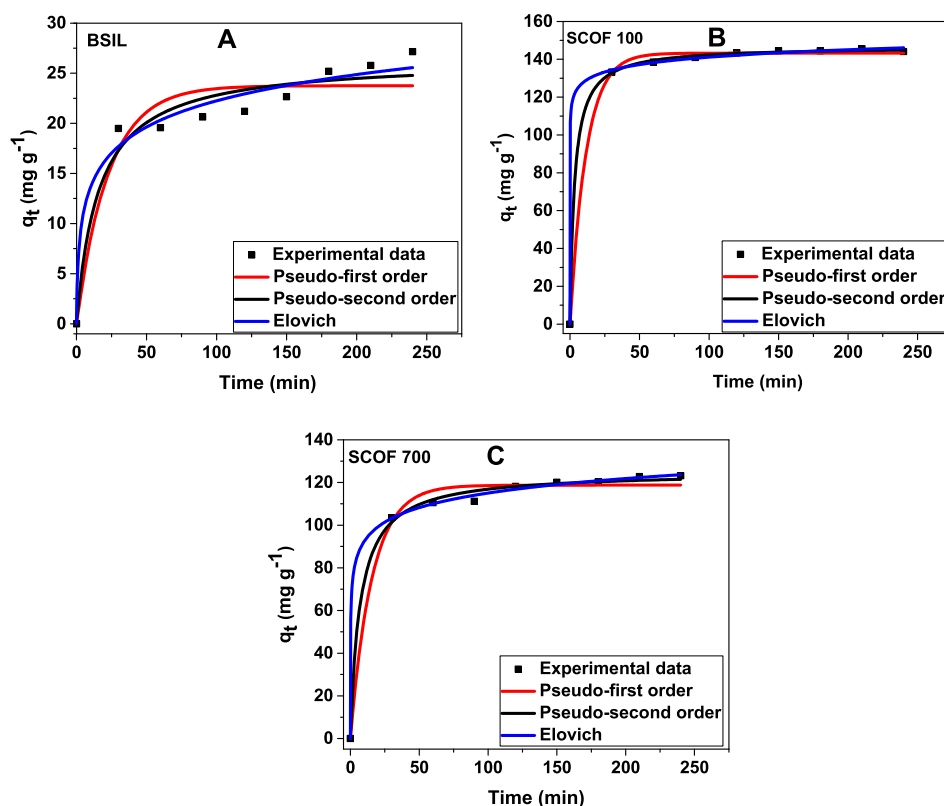


Figure 7. Kinetic plots of the adsorption of MB on BSIL (A), SCOF 100 (B) and SCOF 700 (C).

higher values of the SSA of the composites, which implies the availability of more active sites for adsorption. In addition, Langmuir and Freundlich isotherms are more appropriate to explain the mechanism of adsorption, although we could infer the nature adsorption from the D–R isotherm (see Supplementary Material Figure S2) which predicts the nature of the adsorption to be physisorption if the mean energy of adsorption (E) is less than 8 kJ mol^{-1} . The values of E obtained from this study show that MB is physically adsorbed on SIL, SCOF-100 and 700. A comparison of the maximum

monolayer adsorption (q_{max}) of different adsorbents for the removal of MB is listed in Table 5.

4.5. Effect of temperature and thermodynamic of adsorption

The results of the effects of temperature on the adsorption capacity are shown in Figure 11. The adsorption capacity of the three adsorbents decreased, with an increase in temperature. The amount adsorbed by BSIL, SCOF 100 and SCOF 700 at 303 K are 52.6, 253.6 and 160.48 mg g^{-1} , respectively, meanwhile when the temperature was raised to 333 K, it decreased to 44.07, 236.84 and 141.78 g g^{-1} for BSIL, SCOF 100 and SCOF 700, respectively. The reason can be summarized as follows: there is an increased tendency of MB molecules to escape from the solid phase (adsorbent) to the bulk phase (solution) due to an increase in temperature, more so, with an increase in temperature, MB molecules that are physically adsorbed on the surface of the adsorbent could gain kinetic energy which made them to overcome the electrostatic force of attraction between them and the adsorbents, due to this they get desorbed at higher temperature [70]. This is an example of the exothermic adsorption process in which an increase in temperature results in a decrease in adsorption capacity.

Table 3. Parameters for kinetics models.

Model	Parameters	BSIL	SCOF100	SCOF700
Pseudo-first-order	q_e (mg g^{-1})	23.75	143.26	118.76
	k_1 (min^{-1})	0.0439	0.0868	0.0641
	R^2_{adjusted}	0.9068	0.9981	0.9880
	SD (mg g^{-1})	2.46	2.06	4.30
Pseudo-second-order	q_e (mg g^{-1})	23.32	164.54	130.92
	k_2 ($\text{g mg}^{-1} \text{min}^{-1}$)	0.0716	0.2810	0.1365
	R^2_{adjusted}	0.9386	0.9997	0.9960
	SD (mg g^{-1})	1.99	0.82	2.47
Elovich	a ($\text{mg g}^{-1} \text{min}^{-1}$)	13.38	3.57×10^9	1.18×10^4
	β (g mg^{-1})	0.2638	0.1761	0.1016
	R^2_{adjusted}	0.9713	0.9994	0.9988
	SD (mg g^{-1})	1.36	1.08	1.32

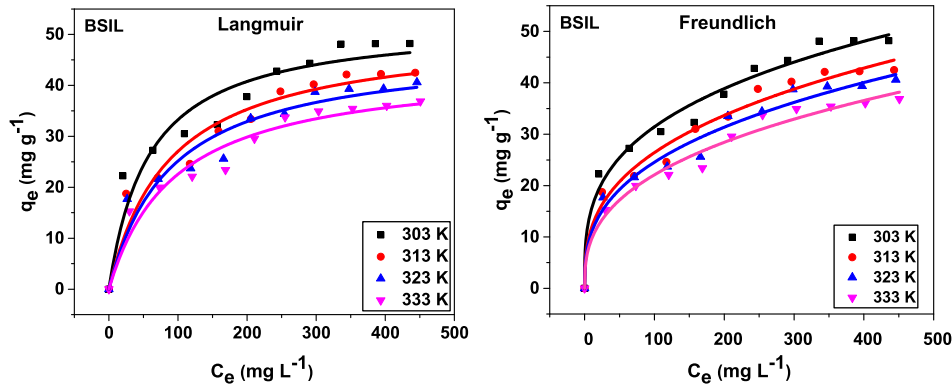


Figure 8. Langmuir and Freundlich isotherms for the adsorption of MB on BSIL.

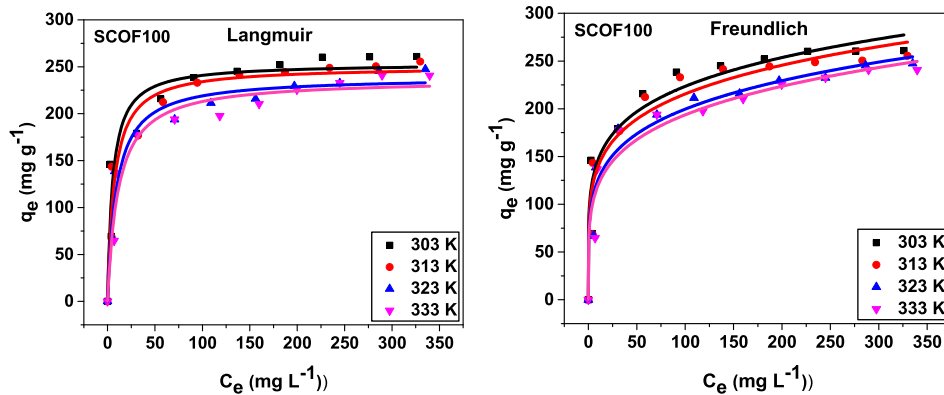


Figure 9. Langmuir and Freundlich isotherms for the adsorption of MB on SCOF100.

The effect of temperature on the adsorption of the MB was further examined by calculating the thermodynamic parameters (changes in Gibbs-free energy (ΔG), changes in enthalpy (ΔH) and changes in entropy (ΔS)) for each adsorbent, through the use of Equations (4)–(6).

show that the adsorption of MB is spontaneous and feasible. Meanwhile, the positive values of ΔS° imply an increase in the randomness of the system due to the high affinity that MB molecules have for the adsorbents.

$$K_e = \frac{1000 \cdot K_L \cdot \text{molecular weight of the adsorbate} \cdot \text{standard concentration of the adsorbate}}{\text{activity coefficient of adsorbate}} \quad (4)$$

$$\log K_e = \frac{\Delta S}{2.303R} - \frac{\Delta H}{2.303RT} \quad (5)$$

$$\Delta G^\circ = \Delta H^\circ - T\Delta S^\circ \quad (6)$$

Based on the values of ΔH° for BSIL, SCOF-100 and SCOF-700 that are negative (Table 6), it implies that the adsorption of MB on three adsorbents is enthalpy driven. This supports the adsorption capacity obtained from the Langmuir isotherm that decreases with an increase in temperature. More so, the values of ΔG° that are negative despite a variation in temperature

4.6. Effect of ionic strength

The effect that ionic strength has on the adsorption capacity of an adsorbate, which may affect electrostatic and hydrophobic interactions, has been documented to be complicated [71]. The results obtained from the effect of ionic strength on the adsorption of MB on BSIL and SCOF-700 are shown in Figure S3. The results show a slight increase (9 mg g^{-1}) in the amount of MB adsorbed on SCOF-700 when the concentration of NaCl was varied from 0.2 to 1 mol L⁻¹. Meanwhile, there is a notable and consistent increase in the adsorption of MB on BSIL with an increase in ionic strength. The

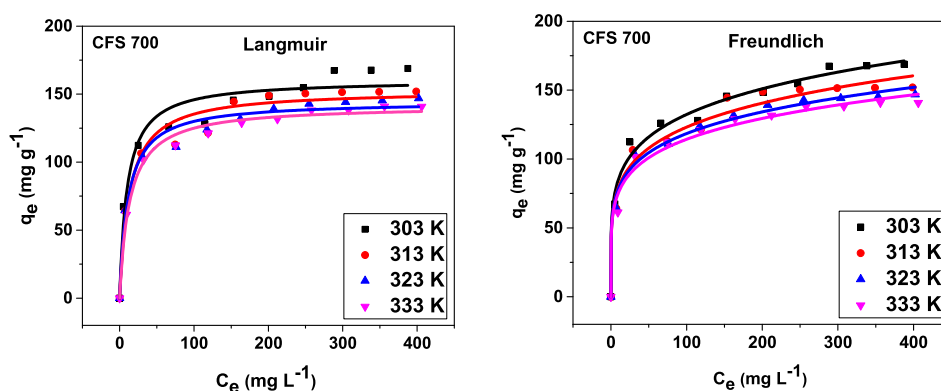


Figure 10. Langmuir and Freundlich isotherms for the adsorption of MB on SCOF 700.

increase in ionic strength modifies the adsorption capacity either by diminishing it (in case of electrostatic attraction) or enhancing it (in case of electrostatic reduction) [72]. However, our results did not follow this assertion. Despite the existence of an electrostatic attraction between MB molecules and the adsorbents (as shown in Section 3.1), the presence of NaCl did not bring about a reduction in the adsorption capacity but rather increases it. The presence of salt in a dye solution increases the intermolecular, van der Waals' forces between dyes' molecules which could lead to the formation of dimers and consequently aggregation of the molecules [73]. The aggregated molecules were adsorbed on the surface of BSIL and SCOF-700, thereby leading to an increase in the adsorption capacity. Monomer and dimers molecules of MB are shown in Figure S4. The good thing about this result is that both adsorbents can perform effectively in a salty dye solution without any reduction in their adsorption capacity.

4.7. Regeneration and reusability of BSIL and SCOF-700

One of the economic interests that adsorbents could offer is their ability to be regenerated and reused after the successive adsorption process without losing much of their active sites and adsorption capacities. The adsorbed MB molecules were desorbed through calcination at 500°C for 2 h after each adsorption process, while the adsorbents (BSIL and SCOF-700) were reused. Images of BSIL before adsorption, after adsorption and calcination are shown in Figure S5, we could not show the images of SCOF 700 because its original colour (dark brown) before adsorption makes it impossible for the colour of MB to be appreciably noticed after adsorption, unlike BSIL that is white. The amount adsorbed remains virtually constant after each successive cycle and till the 5th cycle (Figure 12). SCOF-700 maintains the leading with maximum adsorption capacity. In this

regard, using the adsorbents for the adsorption of cationic dyes is economically viable. It has been documented that silanol groups on the surface of silica are the active adsorption sites, which were not inactive after subjected to calcination following each adsorption test [32]. This made BSIL and SCOF-700 to retain their adsorption capacity after calcination.

4.8. Characterization of BSIL and SCOF-700 after adsorption

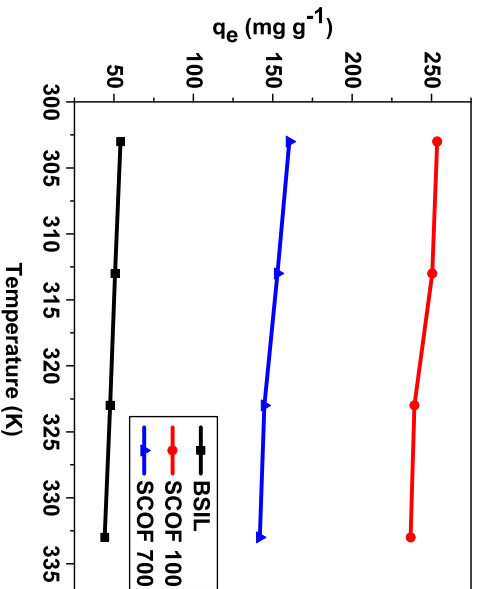
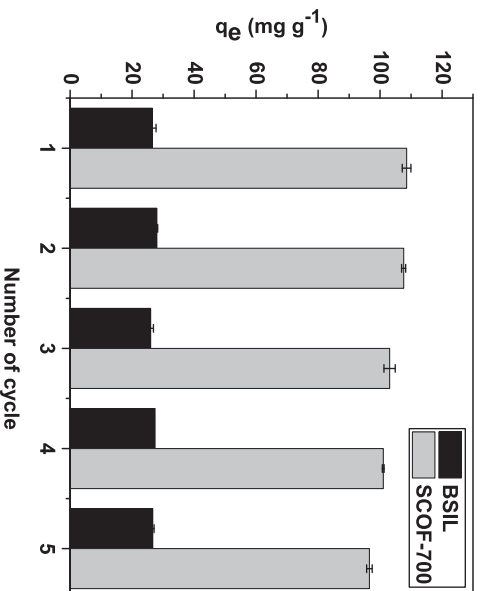
BSIL and SCOF-700 were characterized after adsorption. SCOF-700 was chosen instead of SCOF-100 because of its high value of magnetic saturation and the presence of distinct d-spacings (Figure 3 of TEM) that are characteristic features of cobalt ferrite. These two adsorbents (BSIL and SCOF-700) were characterized using FTIR and TEM techniques. Figure 13 shows their FTIR spectra before and after adsorption, including that of MB. The small peak (A) located at 3791 cm^{-1} is due to the presence of hydrogen bond which was explained to be as a result of interaction between it and silanol groups (Si-OH) [36], while the peaks labelled B and C appearing at 3465 and 1637 cm^{-1} are assigned to be OH (of the adsorbed water molecule) stretching and bending vibration, respectively [35]. The band at 1101 cm^{-1} labelled D is attributed to symmetric stretching vibration of Si-O-Si from SiO_4 [29,34]. Furthermore, the peaks marked E and F at 798 and 498 cm^{-1} are attributed to symmetric Si-O bending [28]. Another obvious peak is at X with wavenumber 635 cm^{-1} , a typical fingerprint of cobalt ferrite [74]. The small peak tag Y at 950 cm^{-1} on BSIL's spectra is due to Si-OH, related to the presence of the high amount of silanol groups [36] This peak could not be found on SCOF-700 spectra, which may affirm an interaction between cobalt ferrite and silica. There is no noticeable peak at the spectra of BSIL after adsorption (probably due to weak interaction between it and MB), on the other hands, peaks labelled as 1 and 2 on

Table 4. Langmuir, Freundlich and D-R isotherms parameters for the adsorption of MB at 303 –333 K.

	BSIL				SCOF-100				SCOF-700			
	303 K	313 K	323 K	333 K	303 K	313 K	323 K	333 K	303 K	313 K	323 K	333 K
Langmuir												
q_{max} (mg g ⁻¹)	52.6	50.6	47.51	44.07	253.6	250.45	239.25	236.84	160.48	152.95	144.67	141.78
K_L (L mg ⁻¹)	0.016	0.012	0.011	0.01	0.187	0.14	0.11	0.089	0.099	0.076	0.088	0.074
$R^2_{adjusted}$	0.9152	0.9433	0.9320	0.9499	0.894	0.9373	0.9596	0.9527	0.9487	0.9625	0.9731	0.9898
SD (mg g ⁻¹)	4.33	3.16	3.24	2.55	28.53	21.32	15.99	16.95	11.66	9.29	7.40	4.39
Freundlich												
K_F (mg g ⁻¹) (mg L ⁻¹) ^{-1/n_F}	7.149	5.296	4.829	4.146	96.30	90.50	79.20	74.39	55.12	51.08	51.75	49.98
n_F	3.11	2.86	2.83	2.75	5.47	5.307	4.982	4.81	5.258	5.234	5.56	5.567
$R^2_{adjusted}$	0.9825	0.9779	0.9726	0.9762	0.9302	0.9333	0.9470	0.9370	0.9873	0.9743	0.9878	0.9803
SD (mg g ⁻¹)	1.96	1.97	2.06	1.76	23.23	21.99	18.32	19.57	5.80	7.70	4.97	6.101
D-R												
q_{DR} (mg g ⁻¹)	40.03	35.20	33.05	30.53	227.14	232.63	221.54	218.19	146.17	137.88	132.20	128.99
K_{DR} (mol ² J ⁻²)	-4.3E-05	-7.1E-05	-7.9E-05	-0.0001	-1.2E-06	-3.2E-06	-6.2E-06	-9.5E-06	-3.9E-06	-7.4E-06	-6.5E-05	-1.1E-05
E (kJ mol ⁻¹)	0.107	0.083	0.079	0.06	0.634	0.396	0.284	0.229	0.357	0.260	0.277	0.212
$R^2_{adjusted}$	0.4341	0.4426	0.4496	0.5357	0.3876	0.7412	0.9254	0.9011	0.7592	0.7724	0.7914	0.8555
SD (mg g ⁻¹)	0.592	0.639	0.626	0.59	0.925	0.592	0.307	0.356	0.387	0.370	0.328	0.274

Table 5. Comparison of the maximum monolayer adsorption (q_{max}) of different adsorbents for the removal of MB.

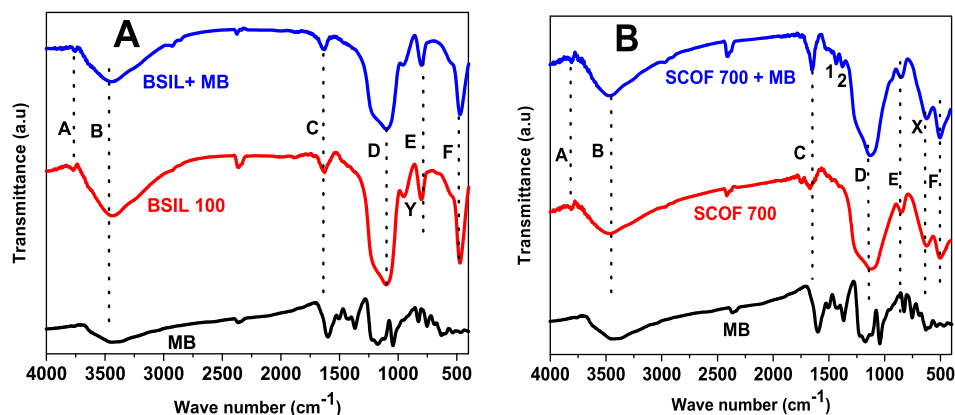
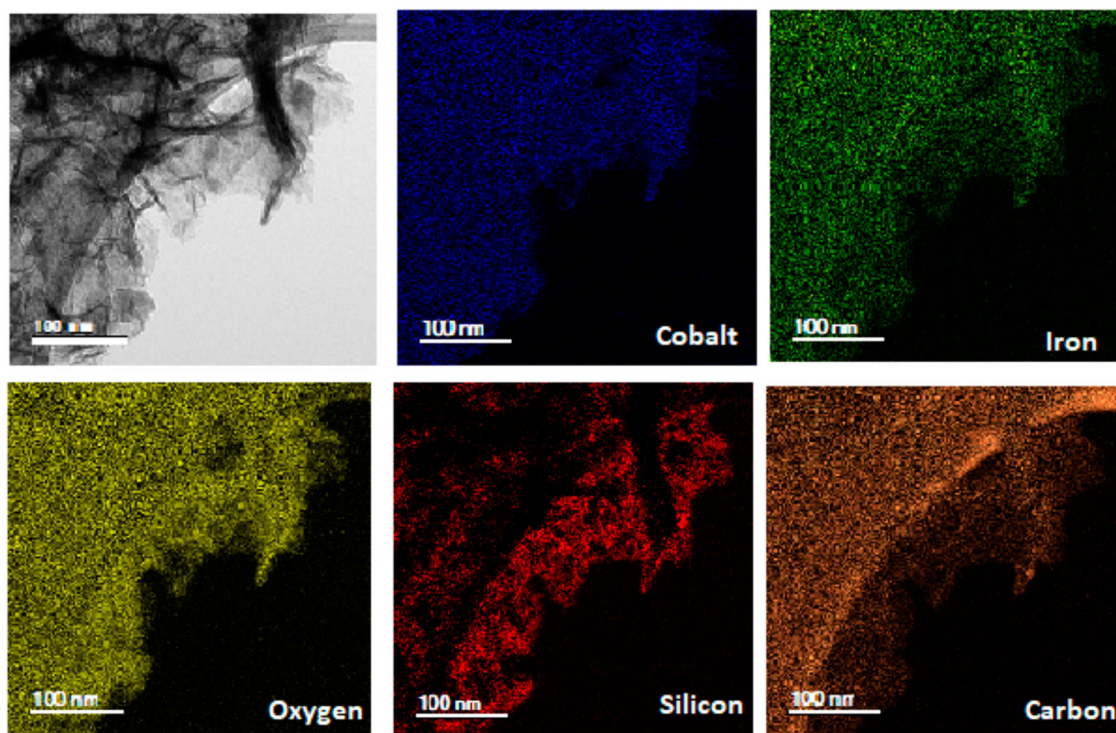
Adsorbents	q_{max} (mg g ⁻¹)	References
nFMB0	72.32	[58]
Magnetic cellulose/GO composite	70.03	[59]
Surface-functionalized silica aerogels	68.15	[60]
Magnetic chitosan	173	[61]
HSC	297.6	[62]
CNT	64.7	[63]
MGS	140.57	[64]
Activated biochar	33.33	[65]
Spray-dried clay	140.64	[66]
Poly-amide modified vermiculite	111.95	[67]
Biochar	33	[68]
Lava	10.32	[69]
BSIL	52.6	This study
SCOF-100	253.6	This study
SCOF-700	160.48	This study

**Figure 11.** Effect of the temperature on the adsorption capacity.**Figure 12.** Reusability.

SCOF-700 after adsorption could be related to the MB. In addition, there is a small increase in the band 1637 cm⁻¹ on the spectrum of SCOF-700 after adsorption,

Table 6. Thermodynamic parameters for the adsorption of MB at 303–333 K.

Adsorbents	ΔH° (kJ mol ⁻¹)	ΔS° (J K ⁻¹ mol ⁻¹)	ΔG° (kJ mol ⁻¹)			
			303 K	313 K	323 K	333 K
BSIL	-12.65	28.81	-27.68	-27.91	-28.14	-28.36
SCOF-100	-20.74	22.91	-28.27	-29.83	-31.39	-32.95
SCOF-700	-6.35	64.802	-25.99	-26.63	-27.28	-27.93

**Figure 13.** FTIR spectra before and after adsorption. BSIL (A) and SCOF-700 (B).**Figure 14.** Elemental mapping of SCOF 700 after adsorption.

suggesting that hydrogen bonding could be involved in the adsorption process.

There are several peaks on the spectrum of MB in the region 1600–610 cm⁻¹. The bands in between 1035 and 610 cm⁻¹ correspond to axial deformation of C–H vibration in polynuclear aromatic rings, while

the peaks in the region between 1600 and 1136 cm⁻¹ were associated with axial deformation C–N vibration in both aromatic and aliphatic rings of MB molecules [75].

Further confirmation of the adsorption of MB on the adsorbents was carried out on SCOF-700 through

energy-filtered-TEM by mapping elements that are present after adsorption. Figure 14 shows images of the elemental mapping of Fe, Co, Si, O and C. The presence of carbon was due to the adsorption of MB.

5. Conclusion

This novel study showed that the adsorption capacity of amorphous nano bio-silica extracted from rice husk for the removal of MB can be synergistically enhanced by compositing it with cobalt ferrite, which also induced magnetic properties on the composite for easy separation after the adsorption process. Both surface charge and the SSA of the adsorbents have a direct influence on their adsorption capacity. The optimum pH and equilibrium time were 9 and 120 min, respectively. Adsorption data are well fitted to isotherms that were proposed by Langmuir and Freundlich, while pseudo-second-order and Elovich are best applicable to explain the adsorption kinetics. SCOF 100 has the highest adsorption capacity of 253.6 mg g⁻¹. An increment in ionic strength led to favourable adsorption which was due to dimerization of MB. The adsorption of MB on the bio-silica and the composite, which was confirmed by FTIR and TEM, was found to be spontaneous and exothermic in nature. Both BSIL and the composite could be effectively reused and regenerated up to 5 cycles.

Acknowledgements

The authors would like to thank the UFMG-Microscopy Center for the structural support.

Disclosure statement

No potential conflict of interest was reported by the authors.

Funding

This study was supported by the FAPEMIG, CNPq and TWAS.

ORCID

Sunday J. Olusegun  <http://orcid.org/0000-0002-2479-0540>
 Erico T. F. Freitas  <http://orcid.org/0000-0002-8509-8662>
 Luciano R. S. Lara  <http://orcid.org/0000-0002-1264-4239>
 Nelcy D. S. Mohallem  <http://orcid.org/0000-0002-9094-4536>

References

- [1] Quesada HB, Takaoka A, Baptista A, et al. Surface water pollution by pharmaceuticals and an alternative of removal by low-cost adsorbents: a review. *Chemosphere*. 2019;222:766–780.
- [2] Yang Q, Li Z, Lu X, et al. A review of soil heavy metal pollution from industrial and agricultural regions in China: pollution and risk assessment. *Sci Total Environ*. 2018;642:690–700.
- [3] João V, Domingues P. Best management practices from agricultural economics: mitigating air, soil and water pollution. *Sci Total Environ*. 2019;688:346–360. doi:10.1016/j.scitotenv.2019.06.199.
- [4] Wang X, Dong X, Fan W, et al. Air pollution terrain nexus: a review considering energy generation and consumption. *Renewable Sustainable Energy Rev*. 2019;105:71–85.
- [5] Azizullah A, Nasir M, Khattak K, et al. Water pollution in Pakistan and its impact on public health — a review. *Environ Int*. 2011;37:479–497.
- [6] Wang Q, Yang Z. Industrial water pollution, water environment treatment, and health risks in China. *Environ Pollut*. 2016;218:358–365.
- [7] Adesina AO, Okoronkwo AE, Mohallem NDS, et al. Adsorption of methylene blue and Congo red from aqueous solution using synthesized alumina – zirconia composite. *Environ Technol*. 2019;0:1–10.
- [8] Li J, Fong K, Chi J. Water resources and water pollution emissions in China's industrial sector: a green-biased technological progress analysis. *J Clean Prod*. 2019;229:1412–1426.
- [9] Kalhor K. Groundwater for sustainable development assessment of groundwater quality and remediation in karst aquifers: a review. *Groundw Sustain Dev*. 2019;8:104–121.
- [10] Hu L, Xia Z. Application of ozone micro-nano-bubbles to groundwater remediation. *J Hazard Mater*. 2018;342:446–453.
- [11] Gonçalves JR. The soil and groundwater remediation with zero valent iron nanoparticles 2 the zero valent iron nanoparticles. *Procedia Eng*. 2016;143:1268–1275.
- [12] Fu J, Chen Z, Wang M, et al. Adsorption of methylene blue by a high-efficiency adsorbent (polydopamine microspheres): kinetics, isotherm, thermodynamics and mechanism analysis. *Chem Eng J*. 2015;259:53–61.
- [13] Li B, Lv JQ, Guo JZ, et al. The polyaminocarboxylated modified hydrochar for efficient capturing methylene blue and Cu(II) from water. *Bioresour Technol*. 2019;275:360–367.
- [14] Yagub MT, Sen TK, Afroze S, et al. Dye and its removal from aqueous solution by adsorption: a review. *Adv Colloid Interface Sci*. 2014;209:172–184.
- [15] Hasan R, Chong CC, Setiabudi HD, et al. Process optimization of methylene blue adsorption onto eggshell-treated palm oil fuel ash. *Environ Technol Innov*. 2019;13:62–73.
- [16] Guo JZ, Li B, Liu L, et al. Removal of methylene blue from aqueous solutions by chemically modified bamboo. *Chemosphere*. 2014;111:225–231.
- [17] Zhang J, Zhou Q, Ou L. Kinetic, isotherm, and thermodynamic studies of the adsorption of methyl orange from aqueous solution by chitosan/alumina composite. *J Chem Eng Data*. 2012;57:412–419.
- [18] Dotto GL, Pinto LAA. Adsorption of food dyes onto chitosan: optimization process and kinetic. *Carbohydr Polym*. 2011;84:231–238. doi:10.1016/j.carbpol.2010.11.028.
- [19] Marzouk Trifi I, Trifi B, Ben Souissi E, et al. Response surface methodology for dyes removal by adsorption onto alginate calcium. *Environ Technol*. 2019;0:1–10.

- [20] He Y, Bin Jiang D, Chen J, et al. Synthesis of MnO₂ nanosheets on montmorillonite for oxidative degradation and adsorption of methylene blue. *J Colloid Interface Sci.* **2018**;510:207–220.
- [21] Raper E, Stephenson T, Anderson DR, et al. Industrial wastewater treatment through bioaugmentation. *Process Saf Environ Prot.* **2018**;118:178–187.
- [22] Keshmirizadeh E, Modarress H, Jahedi F. Removal of acid blue 62 textile dye from aqueous solutions by cerium reagents. *Environ Technol (United Kingdom).* **2018**;0:1–12. doi:10.1080/09593330.2018.1511633.
- [23] Singh NB, Nagpal G, Agrawal S. Water purification by using adsorbents: a review. *Environ Technol Innov.* **2018**;11:187–240.
- [24] Huang Q, Liu M, Mao L, et al. Surface functionalized SiO₂ nanoparticles with cationic polymers via the combination of mussel inspired chemistry and surface initiated atom transfer radical polymerization: characterization and enhanced removal of organic dye. *J Colloid Interface Sci.* **2017**;499:170–179.
- [25] Krstić V, Urošević T, Pešovski B. A review on adsorbents for treatment of water and wastewaters containing copper ions. *Chem Eng Sci.* **2018**;192:273–287.
- [26] Dou J, Gan D, Huang Q, et al. Functionalization of carbon nanotubes with chitosan based on MALI multicomponent reaction for Cu²⁺ removal. *Int J Biol Macromol.* **2019**;136:476–485.
- [27] Liu Y, Huang H, Gan D, et al. A facile strategy for preparation of magnetic graphene oxide composites and their potential for environmental adsorption. *Ceram Int.* **2018**;44:18571–18577.
- [28] Sankar S, Sharma SK, Kaur N, et al. Biogenerated silica nanoparticles synthesized from sticky, red, and brown rice husk ashes by a chemical method. *Ceram Int.* **2016**;42:4875–4885.
- [29] Azat S, Korobeinyk AV, Moustakas K, et al. Sustainable production of pure silica from rice husk waste in Kazakhstan. *J Clean Prod.* **2019**;217:352–359.
- [30] Chen F, Hableel G, Zhao ER, et al. Multifunctional nanomedicine with silica: role of silica in nanoparticles for therapeutic, imaging, and drug monitoring. *J Colloid Interface Sci.* **2018**;521:261–279.
- [31] Brigante M, Avena M. Biotemplated synthesis of mesoporous silica for doxycycline removal. effect of pH, temperature, ionic strength and Ca²⁺ concentration on the adsorption behaviour. *Microporous Mesoporous Mater.* **2016**;225:534–542.
- [32] Tolba GMK, Barakat NAM, Bastaweesy AM, et al. Effective and highly recyclable nanosilica produced from the rice husk for effective removal of organic dyes. *J Ind Eng Chem.* **2015**;29:134–145.
- [33] Darvishi Cheshmeh Soltani R, Khataee AR, Godini H, et al. Response surface methodological evaluation of the adsorption of textile dye onto biosilica/alginate nanobio-composite: thermodynamic, kinetic, and isotherm studies. *Desalin Water Treat.* **2015**;56:1389–1402.
- [34] Mor S, Manchanda CK, Kansal SK, et al. Nanosilica extraction from processed agricultural residue using green technology. *J Clean Prod.* **2017**;143:1284–1290.
- [35] Anh Tuan LN, Kim Dung LT, Thanh Ha LD, et al. Preparation and characterization of nanosilica from rice husk ash by chemical treatment combined with calcination. *Vietnam J Chem.* **2017**;55:455–459.
- [36] Mourhly A, Khachani M, El Hamidi A, et al. The synthesis and characterization of low-cost mesoporous silica SiO₂ from local Pumice Rock. *Nanomater Nanotechnol.* **2015**;5:35. doi:10.5772/62033.
- [37] García-Cerda LA, Torres-García VA, Matutes-Aquino JA, et al. Magnetic nanocomposites: preparation and characterization of co-ferrite nanoparticles in a silica matrix. *J Alloys Compd.* **2004**;369:148–151.
- [38] Dippong T, Cadar O, Levei EA, et al. Structure and magnetic properties of CoFe₂O₄/SiO₂ nanocomposites obtained by sol-gel and post annealing pathways. *Ceram Int.* **2017**;43:2113–2122.
- [39] Amiri M, Salavati-Niasari M, Akbari A, et al. Removal of malachite green (a toxic dye) from water by cobalt ferrite silica magnetic nanocomposite: herbal and green sol-gel autocombustion synthesis. *Int J Hydrogen Energy.* **2017**;42:24846–24860.
- [40] Xiao SH, Luo K, Zhang L. The structural and magnetic properties of cobalt ferrite nanoparticles formed in situ in silica matrix. *Mater Chem Phys.* **2010**;123:385–389.
- [41] Reddy DHK, Yun YS. Spinel ferrite magnetic adsorbents: alternative future materials for water purification? *Coord Chem Rev.* **2016**;315:90–111.
- [42] Mathew DS, Juang RS. An overview of the structure and magnetism of spinel ferrite nanoparticles and their synthesis in microemulsions. *Chem Eng J.* **2007**;129:51–65.
- [43] Daramola OO, Oladele IO, Adewuyi BO. Influence of sub-micron agro waste silica particles and vinyl acetate on mechanical properties of high density polyethylene matrix composites. *West Indian J Eng.* **2015**;38:96–107.
- [44] Sapawe N, Surayah Osman N, Zulkhairi M, et al. Amir Shahab Syed Mohamad Fikry, M. Amir Mat Aris, synthesis of green silica from agricultural waste by sol-gel method. *Mater Today Proc.* **2018**;5:21861–21866.
- [45] Olusegun SJ, Freitas ETF, Lara LRS, et al. Effect of drying process and calcination on the structural and magnetic properties of cobalt ferrite. *Ceram Int.* **2019**;45:8734–8743.
- [46] Pal Singh RP, Hudiera IS, Rana SB. Effect of calcination temperature on the structural, optical and magnetic properties of pure and Fe-doped ZnO nanoparticles. *Mater Sci Pol.* **2016**;34:451–459.
- [47] Purnama B, Wijayanta AT. Effect of calcination temperature on structural and magnetic properties in cobalt ferrite nano particles. *J King Saud Univ - Sci.* **2018**; doi:10.1016/j.jksus.2018.07.019.
- [48] Berger D, Georgescu D, Bajenaru L, et al. Properties of mesostructured silica coated CoFe₂O₄ versus Fe₃O₄-silica composites. *J Alloys Compd.* **2017**;708:278–284.
- [49] Rohilla S, Kumar S, Aghamkar P, et al. Investigations on structural and magnetic properties of cobalt ferrite/silica nanocomposites prepared by the coprecipitation method. *J Magn Magn Mater.* **2011**;323:897–902.
- [50] Abramson S, Dupuis V, Neveu S, et al. Preparation of highly anisotropic cobalt ferrite/silica microellipsoids using an external magnetic field. *Langmuir.* **2014**;30:9190–9200.
- [51] Anantha RK, Kota S. An evaluation of the major factors influencing the removal of copper ions using the egg

- shell (*Dromaius novaehollandiae*): chitosan (*Agaricus bisporus*) composite. *3 Biotech.* **2016**;6:1–16. doi:10.1007/s13205-016-0381-2.
- [52] Heo J, Yoon Y, Lee G, et al. Enhanced adsorption of bisphenol A and sulfamethoxazole by a novel magnetic $\text{CuZnFe}_2\text{O}_4$ –biochar composite. *Bioresour Technol.* **2019**;281:179–187.
- [53] Lowe BM, Skylaris CK, Green NG. Acid-base dissociation mechanisms and energetics at the silica-water interface: an activationless process. *J Colloid Interface Sci.* **2015**;451:231–244.
- [54] Dalstein L, Potapova E, Tyrode E. The elusive silica/water interface: isolated silanols under water as revealed by vibrational sum frequency spectroscopy. *Phys Chem Chem Phys.* **2017**;19:10343–10349.
- [55] Wu H, Li P, Pan D, et al. Interactions between silicon oxide nanoparticles (SONPs) and U(VI) contaminations: effects of pH, temperature and natural organic matters. *PLoS One.* **2016**;11:1–17. doi:10.1371/journal.pone.0149632.
- [56] Liu N, Wu Y, Sha H. Characterization of EDTA-cross-linked β -cyclodextrin grafted onto Fe-Al hydroxides as an efficient adsorbent for methylene blue. *J Colloid Interface Sci.* **2018**;516:98–109.
- [57] Gusmão KAG, Gurgel LVA, Melo TMS, et al. Adsorption studies of etherdiamine onto modified sugarcane bagasses in aqueous solution. *J Environ Manage.* **2014**;133:332–342.
- [58] Lu K, Wang T, Zhai L, et al. Adsorption behavior and mechanism of Fe-Mn binary oxide nanoparticles: adsorption of methylene blue. *J Colloid Interface Sci.* **2019**;539:553–562.
- [59] Shi H, Li W, Zhong L, et al. Methylene blue adsorption from aqueous solution by magnetic cellulose/graphene oxide composite: equilibrium, kinetics, and thermodynamics. *Ind Eng Chem Res.* **2014**;53:1108–1118.
- [60] Saad N, Al-Mawla M, Moubarak E, et al. Surface-functionalized silica aerogels and alcogels for methylene blue adsorption. *RSC Adv.* **2015**;5:6111–6122.
- [61] Olusegun SJ, Rodrigues GLS, Freitas ETF, et al. Sequestering anionic and cationic dyes from wastewater using spray dried biopolymeric magnetic composite: experimental and theoretical studies. *J Hazard Mater.* **2019**;380:120872. doi:10.1016/j.jhazmat.2019.120872.
- [62] Li R, Liang W, Wang JJ, et al. Facilitative capture of As(V), Pb(II) and methylene blue from aqueous solutions with MgO hybrid sponge-like carbonaceous composite derived from sugarcane leafy trash. *J Environ Manage.* **2018**;212:77–87.
- [63] Yao Y, Xu F, Chen M, et al. Adsorption behavior of methylene blue on carbon nanotubes. *Bioresour Technol.* **2010**;101:3040–3046.
- [64] Liu S, Chen X, Ai W, et al. A new method to prepare mesoporous silica from coal gasification fine slag and its application in methylene blue adsorption. *J Clean Prod.* **2019**;212:1062–1071. doi:10.1016/j.jclepro.2018.12.060.
- [65] Wang Y, Zhang Y, Li S, et al. Enhanced methylene blue adsorption onto activated reed-derived biochar by tannic acid. *J Mol Liq.* **2018**;268:658–666.
- [66] Olusegun SJ, de Sousa Lima LF, Mohallem NDS. Enhancement of adsorption capacity of clay through spray drying and surface modification process for wastewater treatment. *Chem Eng J.* **2018**;334:1719–1728.
- [67] Basaleh AA, Al-Malack MH, Saleh TA. Methylene blue removal using polyamide-vermiculite nanocomposites: kinetics, equilibrium and thermodynamic study. *J Environ Chem Eng.* **2019**;7:103–107.
- [68] Chaukura N, Murimba EC, Gwenzi W. Sorptive removal of methylene blue from simulated wastewater using biochars derived from pulp and paper sludge. *Environ Technol Innov.* **2017**;8:132–140.
- [69] Ma J, Zhang J, Li D. Removal of methylene blue by lava adsorption and catalysis oxidation. *Environ Technol.* **2010**;31:267–276.
- [70] Tran HN, You SJ, Chao HP. Thermodynamic parameters of cadmium adsorption onto orange peel calculated from various methods: a comparison study. *J Environ Chem Eng.* **2016**;4:2671–2682.
- [71] Hu Y, Guo T, Ye X, et al. Dye adsorption by resins: effect of ionic strength on hydrophobic and electrostatic interactions. *Chem Eng J.* **2013**;228:392–397.
- [72] Al-degs YS, El-barghouthi MI, El-sheikh AH, et al. Effect of solution pH, ionic strength, and temperature on adsorption behavior of reactive dyes on activated carbon. *Dye Pigment.* **2008**;77:16–23.
- [73] Goftar MK, Moradi K, Kor NM, et al. Spectroscopic studies on aggregation phenomena of dyes. *Eur J Exp Biol.* **2014**;4:72–81.
- [74] Karaagac O, Bilir B, Köçkar H. The influence of synthesis parameters on one-step synthesized superparamagnetic cobalt ferrite nanoparticles with high saturation magnetization. *J Magn Magn Mater.* **2019**;473:262–267.
- [75] Vargas AMM, Cazetta AL, Kunita MH, et al. Adsorption of methylene blue on activated carbon produced from flamboyant pods (*Delonix regia*): study of adsorption isotherms and kinetic models. *Chem Eng J.* **2011**;168:722–730.



Comparative adsorption mechanism of doxycycline and Congo red using synthesized kaolinite supported CoFe_2O_4 nanoparticles[☆]

Sunday J. Olusegun^{*}, Nelcy D.S. Mohallem

Universidade Federal de Minas Gerais, Departamento de Química, Laboratório de Materiais Nanoestruturados, Belo Horizonte, Brazil

ARTICLE INFO

Article history:

Received 14 October 2019

Received in revised form

4 January 2020

Accepted 17 January 2020

Available online 20 January 2020

Keywords:

Doxycycline

Congo red

Adsorption mechanism

Kaolinite

CoFe_2O_4

ABSTRACT

Kaolinite supported CoFe_2O_4 (KCF) was synthesized and employed to adsorb doxycycline (DOX), an antibiotic and Congo red (CR), a dye from aqueous solution. The prepared KCF nanocomposite was treated in a muffle furnace at 300, 500 and 700 °C, and thereafter characterized. X-ray diffractogram revealed structural damage of kaolinite and appearance of distinct peaks of CoFe_2O_4 with an increase in calcination temperature, while transmission electron microscopy (TEM) images showed that CoFe_2O_4 nanoparticles were supported on the lamellar surface of kaolinites. Comparative adsorption mechanism of the two targeted contaminants showed that adsorption of DOX was influenced by hydrogen bond and $n-\pi$ interaction, while that of CR was due to hydrophobic interaction and hydrogen bond. However, the adsorption of the two contaminants was best fitted to the isotherm that was proposed by Langmuir, with a monolayer maximum adsorption capacity of 400 mg g^{-1} at 333 K for DOX, and 547 mg g^{-1} at 298 K for CR. The removal of DOX from aqueous solution was favored by an increase in temperature (endothermic), while that of CR was exothermic. Thermodynamics studies confirmed that the adsorption of the two contaminants is feasible and spontaneous. The presence of natural organic matter (NOM) did not affect the removal of the two contaminants. Regeneration and reusability study showed that KCF is economically viable. Therefore, introducing inorganic particles like cobalt ferrite into the matrix of kaolinites provides a composite with promising adsorption capacity.

© 2020 Elsevier Ltd. All rights reserved.

1. Introduction

Indiscriminate disposal of contaminants such as pharmaceutical wastes, dyes, heavy metals among others into water bodies has been one of the major environmental challenges that is confronting the entire globe (Nghiem et al., 2005). Widespread of these contaminants could be traced to a geometric increase in population growth, rapid industrialization, lack of adequate education on the proper discharge of contaminant and the nonchalant attitude of the populace (Fonseca Couto et al., 2018; Li et al., 2019; Salehi et al., 2016). Wastewater from industries such as chemical manufacturing, mining, pharmaceutical, textile industries, etc. contains high levels of toxic materials, organic pollutants and many other complex compounds that have compromise the integrity of both surface and groundwater (Hasan et al., 2019; Keshmirzadeh et al., 2018; Raper et al., 2018; Zhao et al., 2019).

Among these contaminants are doxycycline (antibiotic) and

Congo red (dye) whose presence in the environment is traced to effluents mainly from pharmaceutical and textile industries respectively. Doxycycline (classified under tetracyclines) is a drug that is widely use for the wellness of humans and animals. In humans, it is effective in curing infections that are related to respiratory trait, poor renal function, lung, among others (Gao et al., 2018). It functions as additives in animals' food to hasten their growth and is often preferred over other tetracyclines (Kogawa et al., 2014). It was stated that very little of the antibiotics administered into humans and animals are consumed by the body while the majority is excreted without modification (Alsager et al., 2018). In addition, the unused antibiotics are discarded to municipal wastewater, and, hence, wastewater treatment plants could not remove antibiotics totally. Then, polluted effluents flow to surface water, seep into groundwater and finally into drinking water (Wang et al., 2019). Congo red is an azo dye commonly used in textile industries. It is credited to be the first dye with the capability of dyeing cotton, it is highly soluble in water and frequently used in textiles, plastics and printing industries (Chawla et al., 2017; Madan et al., 2019; Mahmoud et al., 2018; Purkait et al., 2007). Congo red and doxycycline become contaminants when they are discharged

[☆] This paper has been recommended for acceptance by Baoshan Xing.

^{*} Corresponding author.

E-mail address: arewasegun@ufmg.br (S.J. Olusegun).

to water bodies as industrial effluents without being adequately treated, and due to this, they turn from good to bad products. They are difficult to degrade biologically due to their stable structure, which hereby endangers the environment (Liu et al., 2016; Madan et al., 2019).

The detrimental effects that these contaminants have on both terrestrial and aquatic lives cannot be overemphasized. Their removal is necessary to prevent the environment from deadly consequences (Olusegun et al., 2018). Due to this, proactive measures which have led to the development of different techniques (photocatalytic, chemical degradation, advanced oxidation, adsorption, coagulation, membrane separation, ion exchange, reverse osmosis and bioremediation) for the treatment of wastewater are being utilized (Ganiyu et al., 2018; Khan et al., 2015; Mahmoud et al., 2013; Olusegun et al., 2019a, b, c; Ramlow et al., 2019; Solano et al., 2015; Tagliavini and Schäfer, 2018). Adsorption is one of the viable and economical methods for the treatment of contaminants like doxycycline and Congo red. It entails the use of different materials (adsorbents) to remove contaminants (adsorbates) from aqueous solutions. Among the various materials that have been used to adsorb contaminants are clay minerals (montmorillonite, kaolinite, palygorskite and so on) (Li et al., 2018).

The study carried out on different clay minerals for the removal of Rhodamine shows that kaolinite has low adsorption capacity compared to other clay minerals. This is owing to its low cation exchange capacity and low specific surface area (Li et al., 2018). This has limited the use of kaolinites (in raw form) in comparison with montmorillonites as an adsorbent for the removal of different contaminants (Xu et al., 2018). Introducing inorganic particles like spinel ferrites into the matrix of kaolinites could improve its adsorption capacity and enhance the ease of separation (after removal of contaminants) from aqueous solution by an external magnet (Tadjarodi et al., 2015). This process does not only reinforce the physical and chemical properties of kaolinites, but it also prevents the agglomeration of inorganic nanoparticles leading the nanocomposite to have a high adsorption capacity (Tadjarodi et al., 2015). Coprecipitation of inorganic nanoparticles in the presence of supporting materials like kaolinites helps to prevent agglomeration, which could result from nanoparticle interaction (Peng et al., 2019). Therefore, in this paper, the adsorption mechanism of Congo red (CR) and Doxycycline (DOX) was studied using novel kaolinite supported cobalt ferrite calcined at 300, 500 and 700 °C. The choice of CoFe_2O_4 is due to its chemical stability (Mathew and Juang, 2007). The study examined the effects of pH, ionic strength, contact time and temperature among other things on the adsorption of the CR and DOX. The adsorption mechanism such as hydrophobic interaction, $n-\pi$ interaction and hydrogen bond; of the CR and DOX on the synthesized nanocomposite was affirmed.

2. Material and methods

2.1. Materials

Kaolinite was obtained from Chapada do Norte, Minas Gerais, Brazil, while $\text{FeSO}_4 \cdot 7\text{H}_2\text{O}$ (assay: 99%) and $\text{CoSO}_4 \cdot 7\text{H}_2\text{O}$ (assay: 98.102%) were purchased from Dinâmica Química Contemporânea Ltda., Brazil and Doxycycline (DOX, assay: 98.3, yellow powder, 1.4–2.8% water) from TRB Pharma in Brazil. Congo red (CR) is a product of BDH Chemicals.

2.2. Synthesis and characterization of kaolinite/ CoFe_2O_4 nanocomposite

Kaolinite (2 g) was dispersed in 25 mL solution containing 2 g of

Iron (II) sulfate heptahydrate and 1 g of cobalt (II) sulfate heptahydrate. The mixture was stirred for 30 min and precipitated at pH 11 using ammonium hydroxide (28% NH_3 , assay 99.9%), boiled at 100 °C for 2 h, filtered and dried. Part of the dried nanocomposites was calcined at 300, 500 and 700 °C for 2 h. Each sample was designated as kaolinite/ CoFe_2O_4 nanocomposite as-prepared (KCF-100), kaolinite/ CoFe_2O_4 nanocomposite calcined at 300 °C (KCF-300), kaolinite/ CoFe_2O_4 nanocomposite at 500 °C (KCF-500), kaolinite/ CoFe_2O_4 nanocomposite calcined at 700 °C (KCF-700). The synthesized kaolinite/ CoFe_2O_4 nanocomposites were characterized using Fourier Transform Infra-red (FT-IR), scanning electron microscope/electron dispersed spectroscopy (SEM-EDS), X-ray diffractometer (XRD), transmission electron microscope and N_2 adsorption.

2.3. Adsorption of DOX

Synthesized kaolinite/ CoFe_2O_4 nanocomposites (100 and 700 °C) were used for the adsorption studies in a batch experiment. The first variable was pH which was done by weighing 10 mg of each adsorbent (KCF-100 and 700) into 50 mL beakers that contained 15 mL of 100 ppm of the respective solution of CR and DOX whose pHs were varied from 2 to 12 for CR and 2–10 for DOX. Optimum pH was determined and used for further studies (dosage of the adsorbent, time of adsorption and temperature of the solutions). Each study was carried out in duplicate. After each study, a reasonable quantity of the solution was withdrawn and the final unadsorbed concentration of CR and DOX was measured in a UV–Vis spectrophotometer (U-2010, Hitachi) at λ_{max} 500 and 345 nm respectively.

3. Results and discussion

3.1. Characterization of the synthesized nanocomposites

FTIR spectra of KCF nanocomposites calcined at different temperatures, kaolinite (KAO) and cobalt ferrite (COF) are shown in Fig. 1A. Peaks labeled A (3700 cm^{-1}) and B (3605 cm^{-1}) which gradually decreased with an increase in calcination temperature due to dehydroxylation are assigned to OH stretching of kaolinite (Spence and Kelleher, 2012). The two peaks at 1124 and 1013 cm^{-1} (C and D respectively) were attributed to Si–O stretching. Interestingly these two peaks together with the peak at 915 cm^{-1} became broaden with an increase in temperature. The reason for broadened peaks was as a result of progressive disordering of metakaolin and the increase of the mean bond angle in the Si–O–Si network (Liu et al., 2015). Peak 915 cm^{-1} (E), which is attributed to inner surface Al–OH deformation (Fatimah, 2018), disappeared gradually and completely (on KCF 700), which could due to dehydroxylation at higher temperature. The bands at 698, 541 and 476 cm^{-1} (F, G, H respectively) are characteristic of kaolinites, which are assigned to bending vibration of Al–O, Si–O–Al, and Si–O, respectively. These peaks decreased with an increased in calcination temperature, reason for this has been ascribed to dehydroxylation that was accompanied by the destruction of Al–O–Si linkages of kaolinite (Liu et al., 2015). Cobalt ferrite peak is at 594 cm^{-1} , though seem to have low intensity on the composites.

XRD patterns of the nanocomposite are shown in Fig. 1B and C. The pattern of KCF-100 is predominant of several peaks of kaolinite mineral, which matched with card JCPDS 80–885, with few peaks of alpha-quartz. Meanwhile, the pattern of KCF-700 is dominated by peaks CoFe_2O_4 of card number JCPDS 22–1086. An increase in calcination temperature resulted in to decrease in intensity of peaks 001, 110 and 002 related to kaolinites up till 500 °C. The observation is stated to be as result of decrease in crystal order of

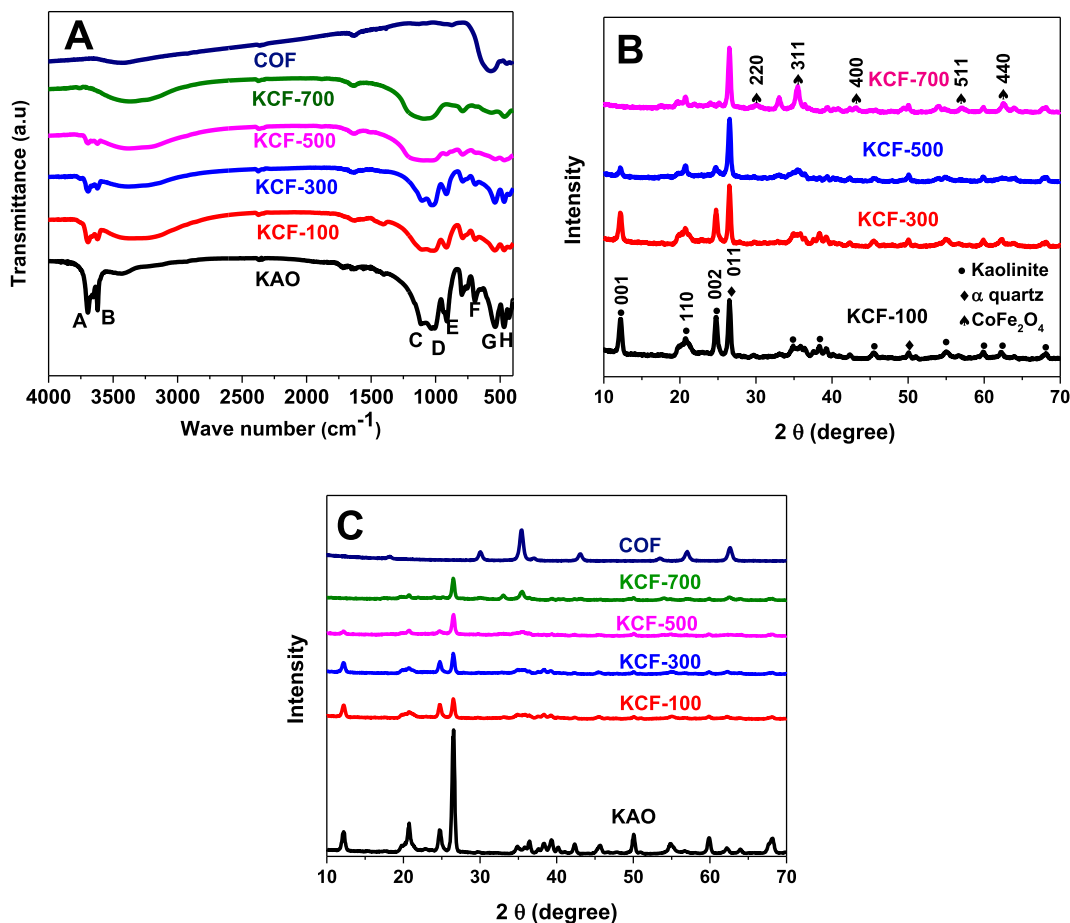


Fig. 1. FTIR spectra (A) and XRD patterns (B) of KCF nanocomposites calcined at different temperatures and XRD patterns (C) of KCF nanocomposites combined with KAO and COF.

the mineral (Liu et al., 2015). The peak 011 related to α -quartz was not affected by calcination. Noteworthy again is the disappearance of kaolinite peaks at the diffractogram of KCF-700. This behavior is ascribed to structural damage of kaolinite ($\text{Al}_2\text{O}_3 \cdot 2\text{SiO}_2 \cdot 2\text{H}_2\text{O}$) through dehydroxylation which resulted in the octahedral layer of kaolinite to reorganize to meta kaolinite ($\text{Al}_2\text{O}_3 \cdot 2\text{SiO}_2$) (Yuan et al., 2017). This confirmed the results of FTIR that has been earlier discussed. While temperature brought structural damage to kaolinite, it leads to the appearance of CoFe_2O_4 peaks. It has been documented that calcination has a positive effect on the crystal growth of cobalt ferrite (Olusegun et al., 2019a, b, c). The itemized d-spacing of the major peaks are shown in Table S1. There is a decrease in d_{002} of kaolinite due to the reorganization of the octahedral layer, while d_{101} of α -quartz remains unchanged. The d_{311} of sample KCF-100 related to cobalt ferrite is lower than of calcined samples, which could be as results of a certain movement of Co^{2+} ions from octahedral to the tetrahedral sites, and equivalent transfer of Fe^{3+} ions from tetrahedral to octahedral sites, which was initiated by thermal treatment (Olusegun et al., 2019a, b, c).

Scanning electron microscopy (SEM) images and energy-dispersive X-ray spectroscopy (EDS) spectra of the synthesized KCF-100 and KCF-700 nanocomposites are shown in Fig. 2. The SEM images of KCF-300 and KCF-500 nanocomposites are displayed in Fig. S1 (Supplementary material). Comparing the images of all the samples, there is no distinct difference in their morphology, likewise in their EDS spectra. Elements present are from kaolinite and cobalt ferrite, devoid of any impurities. More information was obtained from TEM images shown in Fig. 3.

Transmission electron microscopy images of KCF-100 and 700 are presented in Fig. 3. The images showed a lamellar structure of kaolinite that supported cobalt ferrite. The presence of kaolinite increases the dispersion of cobalt ferrite within the matrix. KCF-700 showed distinct particles of cobalt ferrite due to crystal growth. This is in accordance with the XRD diffractogram shown in Fig. 1 B. The images also show that the presence of kaolinite prevents agglomeration of cobalt ferrite nanoparticles, leading to smaller sizes in comparison with the cobalt ferrite that we had earlier synthesized in our research group without kaolinite (Olusegun et al., 2019a, b, c).

The nitrogen adsorption-desorption isotherms of KCF-100 and 700 are shown in Fig. S2 (supplementary material). The amount ($\text{cm}^3 \text{g}^{-1}$) of nitrogen gas that was adsorbed by KCF-100 is more than that of the corresponding KCF-700. This is expected due to the shrinkage of pores due to calcination. BET specific surface area of KCF-100 and 700 are 24 and $11 \text{ m}^2 \text{g}^{-1}$ respectively. Although relatively low, but highly effective for the removal of both studied dye and antibiotic.

3.2. Impact of pH and ionic strength on the removal of Congo red and doxycycline

One of the variables that could affect the interaction between adsorbate and adsorbent is the solution pH. It influences the surface charge of the adsorbent and the ionization of the adsorbate. However, adsorption could as well be influenced by hydrophobic interaction, π - π interaction, n- π interaction, hydrogen bond among

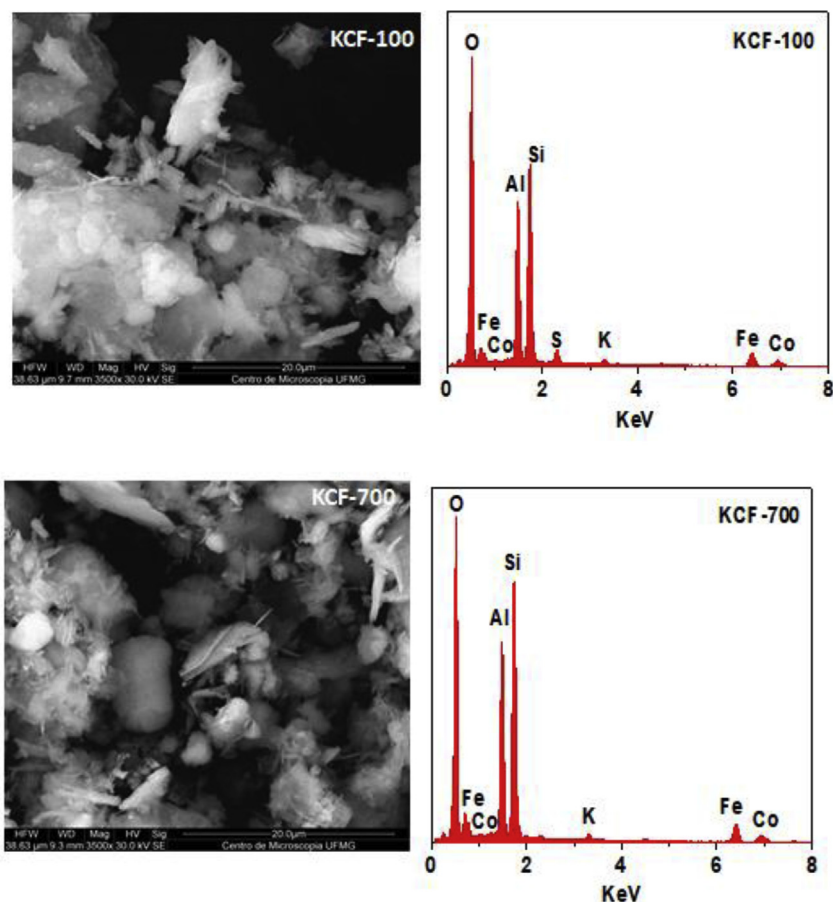


Fig. 2. SEM images and EDS spectra of KCF-100 and KCF-700 nanocomposites.

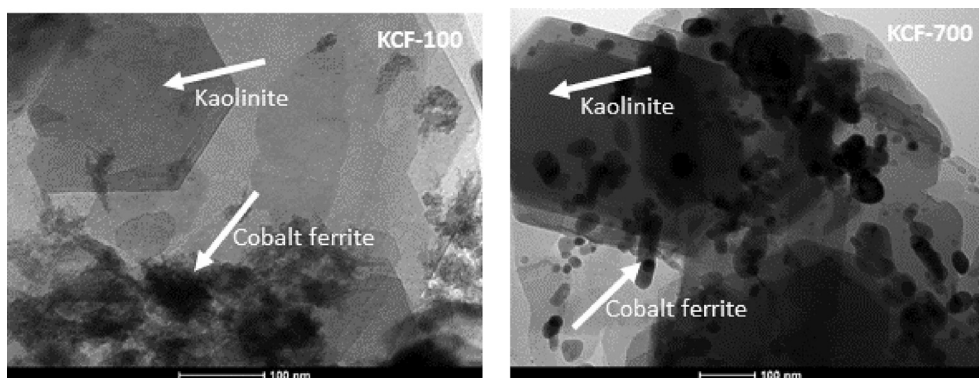


Fig. 3. TEM images of KCF-100 and 700.

others (Hu et al., 2013). In view of this, we investigated the influence of pH on the adsorption capacity of the synthesized nanocomposites (KCF-100 and KCF-700), COF and KAO for the removal of CR and DOX. The results of this study are presented in Fig. 4A and B. Likewise, the surface charge of KCF-100 was studied at the adjusted pH of 2–10 (Fig. S3). Surface charge of the nanocomposite at pH 2 is positive while from pH 4–10, it exhibits negative charge. The adsorption of both CR and DOX is not consistent with increase in solution pH. We observed agglomeration of Congo red at pH 2 before adsorption and due to this, we could not report the result at this pH. This is in accordance with the report of Mozumder and Islam (2010) where Congo red agglomerated at low pH and then

settle down.

The amounts (mg g^{-1}) of CR that were adsorbed at pH 6 and 8 were higher than 4 and 10. The mechanism of adsorption does not seem to be influenced by electrostatic interaction. Congo red being a dipolar molecule will exist in the form of positive charge (cationic) in acidic $\text{pH} < 5.5$ and negative charge (anionic) in alkaline $\text{pH} > 5.5$ (Purkait et al., 2007). Electrostatic attraction between the cationic form of the dye and negative charge surface of the nanocomposites could be responsible for the adsorption at pH at 3 and 4, meanwhile at 6 and 8 that one should expect electrostatic repulsion between the anionic form of the dye and negative charge surface of the adsorbent, this did not occur, but at pH 10 and

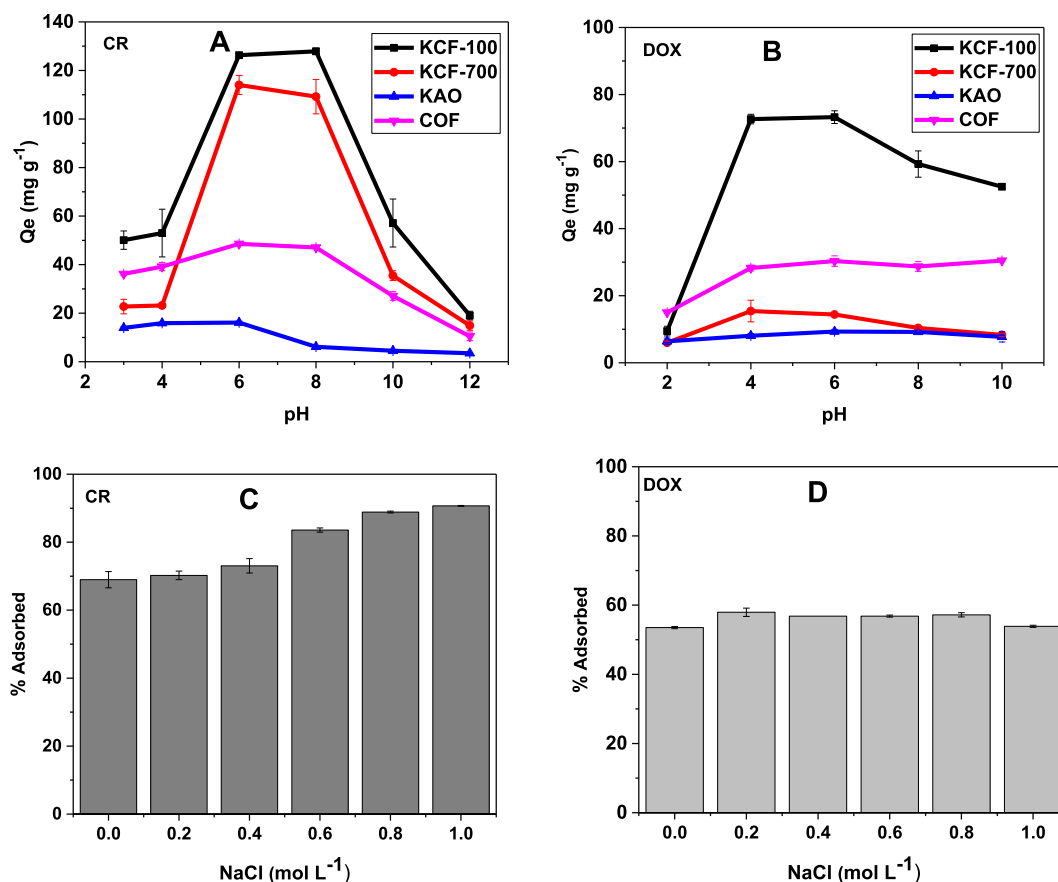


Fig. 4. Effect of pH CR (A), DOX (B) and ionic strength CR (C) and DOX (D) on the adsorption process.

12. This implies that the adsorption of CR on the nanocomposites at pH 6 and 8 is not influenced by the electrostatic interaction. This then led us to further investigation on the adsorption behavior of CR in the presence of ionic strength to ascertain the contribution of hydrophobic interaction to the adsorption process. When adsorption is as a result of electrostatic attraction, increase in ionic strength can diminish the attraction, while it can increase the attraction in case of electrostatic repulsion (Al-degs et al., 2008). The result (effect of ionic strength on the adsorption of CR) as presented in Fig. 4C shows that the addition of NaCl (increase in ionic strength) leads to increase in the adsorption of the dye. This phenomenon has been credited to increase in hydrophobic interaction (attraction between the non-polar groups of the dye with non-polar group of KCF nanocomposite) in which shielding of intermolecular repulsion between the dye and the nanocomposite occurs (Kooch et al., 2016; Samiey and Ashoori, 2012). This result is very advantageous during adsorption process in textile industries where their wastewater contains high amount of salt which is used during pre and post-treatment of fabrics (Kooch et al., 2016).

Considering the influence of pH on the adsorption of DOX, the result was not consistent with pH as well. DOX being an amphoteric molecule has different functional groups that ionize into cations, anions, and zwitterion at different pH (Li et al., 2017). This makes the electrostatic interaction between its molecule and the nanocomposites to be complex and not consistent with pH. The lower amount of DOX (mg g⁻¹) that was adsorbed at pH 2 shows that there is a strong electrostatic repulsion between the positively charged KCF nanocomposites and cationic form of DOX. It is documented that at pH ≤ 3, DOX is protonated, which makes it to exist in cationic form (DOX⁺) (Ghaemi and Absalan, 2015). Meanwhile

between pH 4–9 it exists as zwitterions which implies that electrostatic interaction is not the mechanism of adsorption within the range of these pHs. However, at pH 10, some of the functional groups ionized to anionic form, which resulted in slight electrostatic repulsion. The result gotten from the effect of ionic strength (Fig. 4D) shows that the adsorption of DOX is not influenced by electrostatic interaction and that hydrophobic interaction may not be directly involved in the adsorption process. The alarming sharp difference between the amount adsorbed on KCF-100 and KCF-700 implies that specific surface area of the nanocomposite plays a role in the adsorption of DOX. The case was not the same for the adsorption of CR. Further studies were done at pH 6 for both contaminants. The structures of Congo red and doxycycline are shown in Fig. S4. Relating the amount of CR and DOX adsorbed by the KCF-100 composites with that of COF and KAO one could opine that coprecipitating COF in the presence of KAO led to composites of higher adsorption capacity. The results of the adsorption of the two contaminants also showed that COF adsorbed better than KAO. Meanwhile, it is more economical to use the composites than COF, and, in view of this further studies were carried out on only KCF nanocomposites.

3.3. Adsorbent dose

One of the importance of the study on adsorbent dosage is to avoid wastage of material after equilibrium has been reached. (With respect to the amount of the adsorbent that would be used). The results obtained from the effect of dosage for both CR and DOX are presented in Fig. S5. Examining the impact of dosage variation on the amount of CR that was adsorbed from the initial 100 ppm

concentration of CR, an insignificant amount was adsorbed by 2 and 4 mg of the nanocomposite. There is a sharp increase in the amount adsorbed by 6–8 mg dosage, whereas there is no significant difference in the amount adsorbed within the range of 8 and 10 mg dosage. In the case of DOX, the amount increased from 25 to 50% when the dosage (KCF-100) was increased from 2 to 6 mg. It further increased gradually until it reached equilibrium at 15 mg of the nanocomposite, meanwhile KCF-700 for the absorption of DOX did not attain equilibrium within the dosage variation. 86% was adsorbed from 100 ppm CR solution when 10 mg of the nanocomposite was used, while 68% was adsorbed from 100 ppm of DOX when 20 mg of the adsorbent was used at room temperature. The implication is that the adsorption of CR was more favorable at the room temperature than DOX and that the nanocomposite has better affinity for CR than DOX. Generally, increase in adsorbent dosage, which implies availability of more active sites for the interaction between the contaminants (DOX and CR) and KCF nanocomposite leads to increase in percentage removed from the initial concentration of the dye and antibiotic.

3.4. Contact time and adsorption kinetic

The results obtained from the effect of contact time on the adsorption of CR and DOX on KCF nanocomposites are shown in Fig. S5. This study is important for the purpose of knowing the equilibrium time for the adsorption process. Firstly, for the adsorption of CR, the amount adsorbed within the first 1 h of contact time was almost half of the total amount adsorbed during

the entire duration (12 h). This is due to the collision of CR molecules in the solution which results in their rapid migration to the surface of the nanocomposite hereby leading to high adsorption. After 1 h, the adsorption of CR increases steadily and slowly until equilibrium was attained at 12 h. Since reasonable quantity was adsorbed within the first 1 h, the collision of CR molecules would have reduced, more so, less active sites are available for the unadsorbed molecules. This then could result to slow adsorption rate. The adsorption of DOX within the first 1 h was not as rapid as that of CR. However, the adsorption of DOX attained equilibrium at 12 h. There is a sharp difference in the amount of DOX that was adsorbed by KCF-100 comparing to KCF-700. This is due to the influence of specific surface area; this was not the case for CR.

For a better understanding of the adsorption kinetics, data from the effect of contact time were used to plot nonlinear form of pseudo-first order and pseudo-second-order kinetic models. Presented in Fig. 5 are the plots of the kinetic models. The best model has been described as the one whose values of R^2_{adjusted} is near unity and has lowest standard deviation (SD). Looking at the parameters of the two models listed in Table S2, it is obvious that pseudo-second order is the best to describe the adsorption kinetic. In view of this, it is more reliable to relate q_e (amount adsorbed) calculated from pseudo-second order to the experimental q_e . Although it is well reported in the literature to ascribe chemisorption to adsorption that fits the pseudo-second order model, this should not be affirmed without confirmation from other techniques, such as FTIR. Due to this, we conducted FTIR analysis after adsorption.

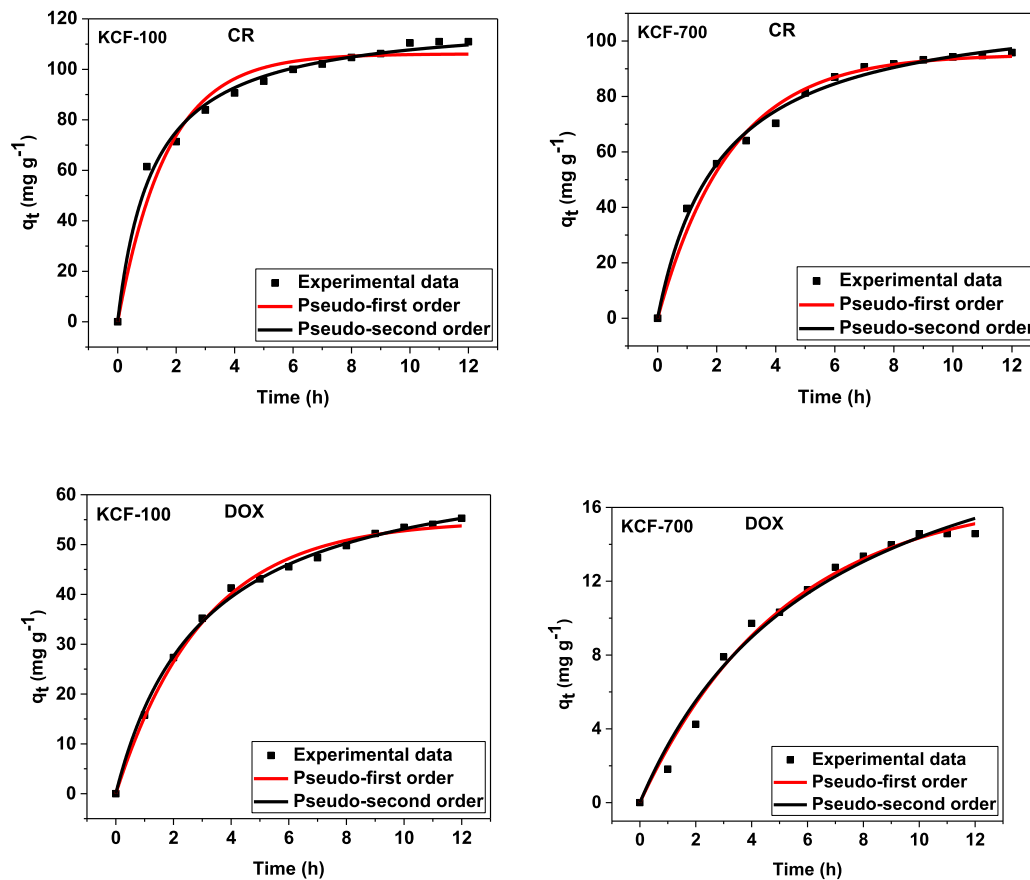


Fig. 5. Kinetic plots of the adsorption of CR and DOX on KCF nanocomposites.

3.5. Adsorption isotherm

The study of adsorption isotherm helps to know the adsorption capacity of the adsorbents (KCF 100 and 700) at various concentrations of the adsorbates (CR and DOX) and at fixed temperature of the system. In addition, the ratio of the quantity adsorbed and amount remaining in the solution at equilibrium is also known. Specifically, maximum adsorption capacity is determined through the isotherm model that was proposed by Langmuir. This model infers that adsorption of adsorbate (CR and DOX in this case) on the adsorbent (KCF nanocomposite) is homogeneous and entails formation of monolayer of adsorbate on the surface of the adsorbent without any interaction between them (Ibrahim, 2019; Zhang et al., 2019). The nearness of R^2 to unity informs whether the experimental data obtained conforms to Langmuir model or not.

Another commonly used isotherm model is the one prescribed by Freundlich. Although Freundlich model is not being used to determine the adsorption capacity, it helps to understand the heterogeneous adsorption process and that the vacant sites on the adsorbent are having distinct energy (Luo et al., 2018; Zahir et al., 2017).

The curve fit of Langmuir and Freundlich isotherms for the two targeted contaminants (CR and DOX) are presented in Fig. S7 – S10.

The parameters of both isotherms are listed in Table 1 (CR and DOX for KCF-100) and Table S3 (CR and DOX for KCF-700). As shown in these tables, the adsorption capacity of CR decreases with the increase in temperature, with maximum adsorption of 547 and 392 mg g^{-1} obtained for KCF 100 and 700 respectively at 298 K. This is a typical exothermic adsorption process in which increase in temperature does not favor the adsorption of the adsorbate on the adsorbent. This occurred because as temperature increases, the adsorbed CR molecules gained kinetic energy which made them to overcome forces of adsorption, and, due to this, desorption of the adsorbed molecule occurred leading to decrease in adsorption capacity (Tran et al., 2016).

In the case of DOX, the adsorption capacity increases with an increase in the temperature of the system, whose maximum adsorption capacity recorded are 400 and 220 mg g^{-1} for KCF-100 and 700, respectively at 333 K. This is opposite to the result obtained for CR. However, for the adsorption capacity of DOX to have

increased as temperature increases, means that the favorable intermolecular forces between DOX and KCF nanocomposites become stronger than those between DOX and water, leading to favorable adsorption with increase in temperature. More so, it could also result from the increase in the mobility of DOX, hereby acquiring enough energy to undergo an interaction with KCF nanocomposites (Doğan and Alkan, 2003). In industrial application of KCF for the adsorption of CR, the cost of energy could be eliminated since it does not involve increase in temperature. However, this would not be the scenario for DOX. Meanwhile, this is not a limitation for the application of KCF nanocomposites for the adsorption of DOX. Most adsorption studies on DOX reported that it was favorably adsorbed at higher temperatures.

Based on the values of adjusted R^2 and standard deviation (SD), the experimental data for the adsorption of the two contaminants is appropriately described by the model prescribed by Langmuir, which implies that the coverage of CR and DOX on the homogeneous surface of the synthesized KCF nanocomposite is monolayer and each adsorbate does not interact with the neighboring one. The adsorption capacity of KCF nanocomposite for the removal of CR and DOX are compared (Table 2) with other adsorbents that were reported in the literature. The synthesized KCF performed better than some of the materials reported in the literature.

3.6. Thermodynamic of adsorption

In other to further establish the response of the adsorption of CR and DOX to changes in temperature, thermodynamic parameters such as changes in Gibbs-free energy (ΔG°), changes in enthalpy (ΔH°) and changes in entropy (ΔS°) were calculated (Table 3).

The values of ΔH° is negative for the adsorption of CR and positive for DOX, showing exothermic and endothermic adsorption processes, respectively. This is in accordance with the adsorption capacity from Langmuir isotherm, which is inversely and directly proportional to increment in temperature for CR and DOX, respectively. While the forces of adsorption of CR on the surface of KCF nanocomposites becomes weaker, not being favored by temperature, it became stronger for the adsorption of DOX. Despite different adsorption behavior of CR and DOX to changes in

Table 1
Langmuir and Freundlich isotherms parameters for the adsorption of CR and DOX for KCF-100.

CR KCF-100					
	298 K	303 K	313 K	323 K	333 K
Langmuir					
q_{\max} (mg g^{-1})	547	543	541	520	497
K_L (L mg^{-1})	0.038	0.037	0.033	0.031	0.026
R^2_{adjusted}	0.971	0.971	0.980	0.977	0.989
SD (mg g^{-1})	32.3	27.8	22.9	23.5	15.4
Freundlich					
K_F ($\text{mg g}^{-1} (\text{mg L}^{-1})^{-1/n_F}$)	81.5	78.7	72.1	68.2	57.1
n_F	2.84	2.81	2.71	2.70	2.59
R^2_{adjusted}	0.885	0.895	0.910	0.908	0.948
SD (mg g^{-1})	56.1	52.8	48.2	46.9	33.3
DOX KCF-100					
Langmuir					
q_{\max} (mg g^{-1})	240	246	389	396	400
K_L (L mg^{-1})	0.013	0.015	0.034	0.059	0.075
R^2_{adjusted}	0.992	0.992	0.954	0.922	0.885
SD (mg g^{-1})	6.12	6.03	25.9	36.2	45.2
Freundlich					
K_F ($\text{mg g}^{-1} (\text{mg L}^{-1})^{-1/n_F}$)	21.2	24.3	69.3	97.6	113
n_F	2.57	2.67	3.35	3.97	4.38
R^2_{adjusted}	0.964	0.962	0.850	0.822	0.781
SD (mg g^{-1})	12.5	13.5	46.7	54.7	62.5

Table 2
Comparison of the maximum monolayer adsorption (q_{max}) of different adsorbents for the removal of Congo red and doxycycline.

Contaminants	Adsorbents	q_{max} (mg g ⁻¹)	References	
Congo red	GM III-5	211	Zhang et al. (2019)	
	Activated carbon	6.72	Namasivayam and Kavitha (2002)	
	Water nut modified carbon	38.8	Ahmad and Mondal (2010)	
	Reagent NiO nanoparticles	39.7	Cheng et al. (2011)	
	Magnetic core–manganese oxide shell	43.0	Zhai et al. (2009)	
	FSP	39.3	Zhang and Hua (2009)	
	ZnO@Ze Composite	161	Madan et al. (2019)	
	NMFO-10	129	Luo et al. (2018)	
	Al ₂ O ₃ –ZrO ₂	57.5	Adesina et al. (2019)	
	KCF-100	547	This work	
	KCF-700	391	This work	
	Doxycycline	Iron loaded sludge biochar	129	Wei et al. (2019)
		Cu(II) impregnated biochar	93.0	Liu et al. (2017)
		MFO-0.5-700	309	Li et al. (2017)
Lignin xanthate resin–bentonite clay		439	Kong et al. (2019)	
Electro-generated adsorbents		31.4	Zaidi et al. (2019)	
MIL- 53(Fe)/Fe ₃ O ₄		477	Naeimi and Faghihian (2017)	
NaY zeolite		252	Ali and Ahmed (2017)	
Rice straw biochars		170	Zeng et al. (2018)	
KCF-100		400	This work	
KCF-700		220	This work	

Table 3
Thermodynamic parameters for CR and DOX.

Adsorbents	ΔH° (kJ mol ⁻¹)	ΔS° (J K ⁻¹ mol ⁻¹)	ΔG° (kJ mol ⁻¹)					
			298 K	303 K	313 K	323 K	333 K	
Congo red								
KCF-100	-8.61	61.7	-26.9	-27.3	-27.9	-28.5	-29.1	
KCF-700	-5.76	57.3	-22.8	-23.1	-23.7	-24.3	-24.8	
Doxycycline								
KCF-100	44.8	222	-21.4	-22.5	-24.8	-26.9	-29.2	
KCF-700	122	15.5	-21.1	-21.7	-22.9	-24.2	-25.4	

temperature, negative values of ΔG° obtained from their adsorption studies confirms that the adsorption process of CR and DOX is feasible and spontaneous. Positive ΔS° for the adsorption of the contaminants implies that there is an increase in the randomness at the solid/solution interface during the process of adsorption (Huang et al., 2017).

3.7. FTIR after adsorption and mechanism of adsorption

FTIR spectra of CR, DOX, and KCF-100 after adsorption are presented in Fig. 6(1) and 6(2). Starting with CR, the peak at 3428 cm⁻¹ is due to the N–H stretching of primary amine, while the peaks at 1587 cm⁻¹ is for N=N stretching vibration of azo group, 1372 cm⁻¹ is for C–N bending, the peak at 1186 and 1036 cm⁻¹ is due to asymmetric vibration of S–O (SO₃–H) group (Jia et al., 2015; Lafi et al., 2019). The shaded portion A shows alteration from broad peak to almost sharp peak at 3463 cm⁻¹ which could possibly due to hydrogen bond between Os from KCF nanocomposite and Hs from NH₂ group of CR. Likewise, also the shaded portion B on the spectrum of KCF-100 + CR after adsorption shows presence of new peaks, more so the two peaks at 1124 and 1013 cm⁻¹ at KCF-100 became one sharp peak after adsorption. This implies that there is a strong interaction between CR and the nanocomposite, possibly a chemical interaction.

Analyzing the major peaks on the DOX, the broad peak at 3475 and 3315 cm⁻¹ are assigned to the phenolic-OH stretching and amino group, respectively, while 2920 cm⁻¹ is attributed to –CH asymmetric stretching. The band at 1675 cm⁻¹ is due to the presence of C=O, while the peak at 1462 cm⁻¹ is attributed to C–C (Li et al., 2017). The shaded portion could also infer interaction between oxygens from the nanocomposite and hydrogens from the

phenolic and amino group of DOX resulting in a hydrogen bond. In addition, there is presence of sharp peak at 1636 cm⁻¹ that corresponds to C=O, implying there is interaction between oxygens on the surface of the nanocomposites and the aromatic rings of DOX, which lead to n- π interaction (Huang et al., 2018).

Based on the result obtained from the pH studies, ionic strength and FTIR, the mechanism of adsorption of Congo red on KCF nanocomposites is mainly due to hydrogen bond and hydrophobic interaction, while that of doxycycline is due to n- π interaction and hydrogen. This is summarized in Fig. 6(3).

3.8. Effect of natural organic matter (NOM) on the adsorption of CR and DOX

The effect of humic acid (HA), an example of NOM, was studied by varying the concentration of HA in the range of 2–10 mg L⁻¹. The result as shown in Fig. S11, implies that the addition of HA to 100 mg L⁻¹ of the respective solution of CR and DOX at pH 6 (optimum pH for the adsorption studies) does not have any significant effect on the adsorption of CR and DOX. This could be due to the electrostatic repulsion between the negatively charge surface of KCF nanocomposite and HA which exist as negative ions in aqueous solution, due to their carboxylic groups (COO⁻). This infers that HA could not block the active sites of KCF nanocomposites either through complexation or electrostatic attraction for the adsorption of CR and DOX.

3.9. Regeneration of KCF composite through thermal process

Thermal process was used to regenerate the KCF nanocomposite. This was done by treating the CR loaded KCF and DOX

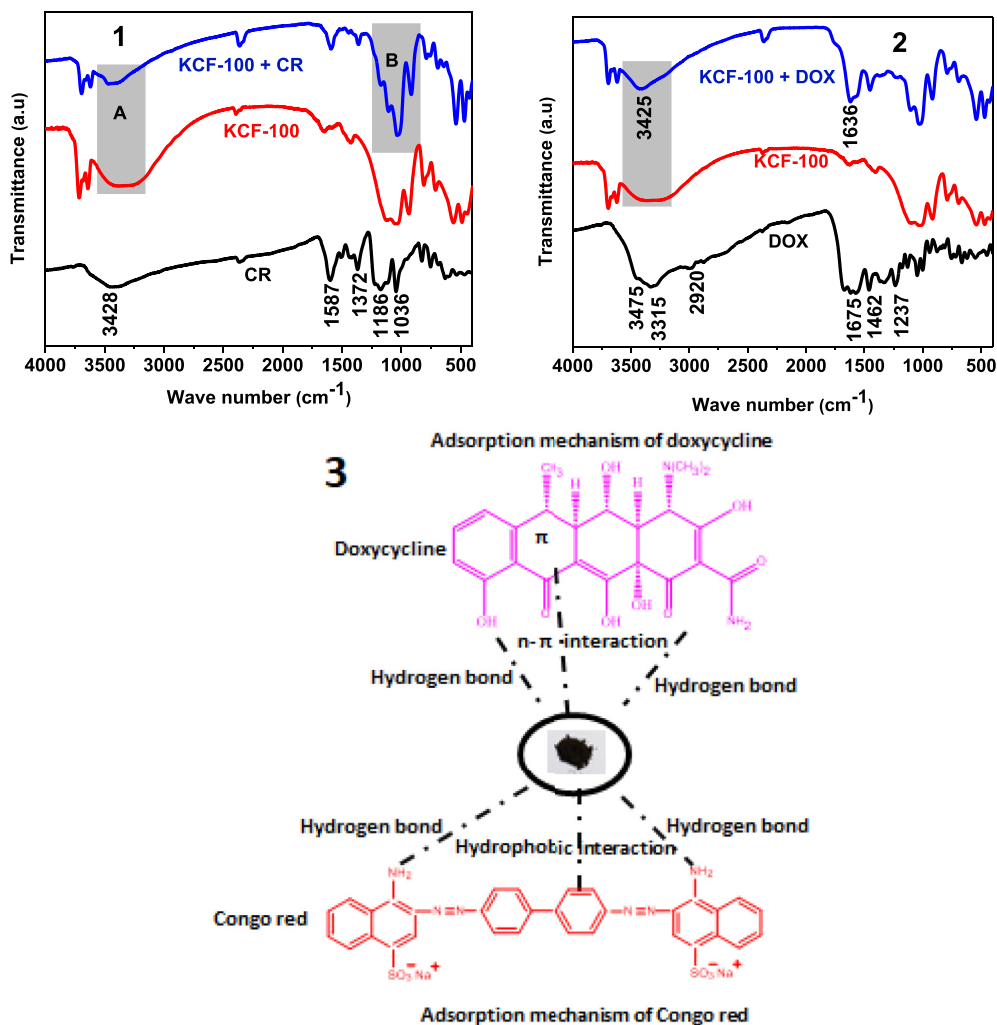


Fig. 6. FTIR spectra of before and after adsorption of CR (1) DOX (2) and adsorption mechanism of CR and DOX (3).

loaded KCF at 500 °C for 2 h. This method was adopted from our previous studies (Olusegun et al., 2019a, b, c). After, each process, the regenerated adsorbent was reused with the initial concentration of 200 ppm of each adsorbate (CR and DOX), at pH 6 for 24 h. The results obtained, as shown in Fig. S12, prove that the regenerated KCF composite can be reused up to 3 cycles without an alarming reduction in the amount adsorbed. This implies that the use of KCF composites for the removal of contaminants, like CR and DOX, is economically viable and the cost of procuring new adsorbent will be greatly reduced as the regenerated adsorbent (through the thermal process) could be reused without losing much of its adsorption capacity. Desorbing antibiotic and dye-loaded adsorbent through thermal degradation could prevent this class of contaminants from finding their ways back to the environment (Olusegun and Mohallem, 2019; Vimonses et al., 2009).

3.10. Photocatalytic activities

Optical band gap value (4.92 eV) of the KCF nanocomposite was obtained by Tauc method (Fig. S13). Photocatalytic activity of KCF for the degradation of CR and DOX was tested under UV light. Prior to the test, the respective 50 mL solutions of CR and DOX containing KCF were left in the dark for 24 h for adsorption process. The concentration of each contaminant in the solution was measured at

1 h interval. Photolysis of CR and DOX under UV light only without KCF composite was also investigated (Fig. S14 A and S14 B). Under dark condition, KCF almost adsorbed all the CR in the solution. The result for CR under UV light shows that no significant amount of CR was degraded by KCF. The result obtained under UV light for the degradation of DOX, when compared with the photolysis, signifies that the degradation of DOX under UV light is due to photodegradation and not solely influenced by the photocatalytic activities of KCF. This shows that KCF composite is a better candidate for the adsorption of CR and DOX than photocatalyst.

3.11. Economic evaluation of KCF adsorbent

One of the important parameters in determining the selection of adsorbent is cost. The economic evaluation of KCF for the treatment of 1 L wastewater containing CR and DOX is calculated as follows (Table S4). Based on the information from the experimental set-up, 0.667 g of KCF will be required to treat 1 L of wastewater containing Congo red and doxycycline. Meanwhile, the production of 0.667 g of KCF, required 0.534 g FeSO₄·7H₂O, 0.267 g CoSO₄·7H₂O, 0.534 g Kaolin and 2.5 mL NH₄OH. The cost of 1 kg of FeSO₄·7H₂O, CoSO₄·7H₂O and 1 L of NH₄OH is listed in Table S4 (supplementary material). The cost of producing 0.667 g of KCF for the treatment of 1 L wastewater containing CR and DOX is 0.131 USD (See

supplementary material). This is less than 0.17 USD reported by Kumari et al. (2019), being the cost evaluation of acid modified alumina for the treatment of 1 L industrial wastewater contaminated by fluoride. Therefore, it can be concluded that KCF composite is economical to treat wastewater that contains DOX and CR.

4. Conclusion

Comparative adsorption mechanism of doxycycline (DOX) and Congo red (CR) using synthesized kaolinite supported CoFe_2O_4 (KCF) nanoparticles have been successfully carried out. KCF nanocomposites, despite having low specific surface areas 24 and 11 mg g^{-1} for KCF-100 and KCF-700 respectively, showed better adsorption capacity for DOX and CR when compared with other adsorbents in the literature. KCF-100 performed better than KCF-700 for the removal of the two contaminants. Basically, the adsorption of the two contaminants was not influenced by electrostatic interaction at optimum pH, but rather by hydrogen bond and $n-\pi$ interaction for DOX, while that of CR was as a result of hydrophobic interaction and hydrogen bond. Calcination temperature up to 700°C resulted in structural damage of kaolinite ($\text{Al}_2\text{O}_3 \cdot 2\text{SiO}_2 \cdot 2\text{H}_2\text{O}$) leading to formation of meta kaolinite ($\text{Al}_2\text{O}_3 \cdot 2\text{SiO}_2$), meanwhile it was favorable for the formation of CoFe_2O_4 with appearance of distinct peaks. Monolayer maximum adsorption capacity of KCF-100 (as prepared) nanocomposites for CR, 547 mg g^{-1} at 298 K was more than that of DOX, 400 mg g^{-1} at 333 K. Adsorption isotherms studies revealed conformation with Langmuir, while the kinetic followed pseudo-second order. Thermodynamics studies confirmed that the adsorption of contaminants are feasible and spontaneous. The adsorption of CR is exothermic while that of DOX is endothermic. The use of KCF nanocomposite for the treatment of wastewater is economically viable and can be regenerated.

Declaration of competing interest

There are no conflicts of interest.

CRedit authorship contribution statement

Sunday J. Olusegun: Conceptualization, Data curation, Formal analysis, Methodology, Writing - original draft, Writing - review & editing. **Nelcy D.S. Mohallem:** Supervision, Writing - review & editing, Funding acquisition, Resources.

Acknowledgments

The authors would like to thank UFMG-Microscopy Center for the structural support, TRB Pharma for the doxycycline, FAPEMIG, CNPq, and TWAS for financial support.

Appendix A. Supplementary data

Supplementary data to this article can be found online at <https://doi.org/10.1016/j.envpol.2020.114019>.

References

Adesina, A.O., Okoronkwo, A.E., Mohallem, N.D.S., Olusegun, S.J., 2019. Adsorption of Methylene blue and Congo red from aqueous solution using synthesized alumina - zirconia composite. *Environ. Technol.* 1–10. <https://doi.org/10.1080/09593330.2019.1652696>, 0.

Ahmad, R., Mondal, P.K., 2010. Application of modified water nut carbon as a sorbent in Congo red and malachite green dye contaminated wastewater remediation. *Separ. Sci. Technol.* 45, 394–403. <https://doi.org/10.1080/01496390903484875>.

Al-degs, Y.S., El-barghouthi, M.I., El-sheikh, A.H., Walker, G.M., 2008. Effect of

solution pH, ionic strength, and temperature on adsorption behavior of reactive dyes on activated carbon. *Dyes Pigments* 77, 16–23. <https://doi.org/10.1016/j.dyepig.2007.03.001>.

Ali, M.M.M., Ahmed, M.J., 2017. Adsorption behavior of doxycycline antibiotic on NaY zeolite from wheat (*Triticum aestivum*) straws ash. *J. Taiwan Inst. Chem. Eng.* 81, 218–224. <https://doi.org/10.1016/j.jtice.2017.10.026>.

Alsager, O.A., Alnajrani, M.N., Abuelizz, H.A., Aldaghmani, I.A., 2018. Removal of antibiotics from water and waste milk by ozonation: kinetics, byproducts, and antimicrobial activity. *Ecotoxicol. Environ. Saf.* 158, 114–122. <https://doi.org/10.1016/j.ecoenv.2018.04.024>.

Chawla, S., Uppal, H., Yadav, M., Bahadur, N., Singh, N., 2017. Zinc peroxide nanomaterial as an adsorbent for removal of Congo red dye from waste water. *Ecotoxicol. Environ. Saf.* 135, 68–74. <https://doi.org/10.1016/j.ecoenv.2016.09.017>.

Cheng, B., Le, Y., Cai, W., Yu, J., 2011. Synthesis of hierarchical $\text{Ni}(\text{OH})_2$ and NiO nanosheets and their adsorption kinetics and isotherms to Congo red in water. *J. Hazard Mater.* 185, 889–897. <https://doi.org/10.1016/j.jhazmat.2010.09.104>.

Doğan, M., Alkan, M., 2003. Adsorption kinetics of methyl violet onto perlite. *Chemosphere* 50, 517–528. [https://doi.org/10.1016/S0045-6535\(02\)00629-X](https://doi.org/10.1016/S0045-6535(02)00629-X).

Fatimah, I., 2018. Preparation, characterization and physicochemical study of 3-amino propyl trimethoxy silane-modified kaolinite for Pb(II) adsorption. *J. King Saud Univ. Sci.* 30, 250–257. <https://doi.org/10.1016/j.jksus.2017.04.006>.

Fonseca Couto, C., Lange, L.C., Santos Amaral, M.C., 2018. A critical review on membrane separation processes applied to remove pharmaceutically active compounds from water and wastewater. *J. Water Process. Eng.* 26, 156–175. <https://doi.org/10.1016/j.jwpe.2018.10.010>.

Ganiyu, S.O., Vieira dos Santos, E., Tossi de Araújo Costa, E.C., Martínez-Huitle, C.A., 2018. Electrochemical advanced oxidation processes (EAOPs) as alternative treatment techniques for carwash wastewater reclamation. *Chemosphere* 211, 998–1006. <https://doi.org/10.1016/j.chemosphere.2018.08.044>.

Gao, J., Gao, Y., Sui, Z., Dong, Z., Wang, S., Zou, D., 2018. Hydrothermal synthesis of $\text{BiOBr}/\text{FeWO}_4$ composite photocatalysts and their photocatalytic degradation of doxycycline. *J. Alloy. Comp.* 732, 43–51. <https://doi.org/10.1016/j.jallcom.2017.10.092>.

Ghaemi, M., Absalan, G., 2015. Fast removal and determination of doxycycline in water samples and honey by Fe_3O_4 magnetic nanoparticles. *J. Iran. Chem. Soc.* 12, 1–7. <https://doi.org/10.1007/s13738-014-0450-6>.

Hasan, R., Chong, C.C., Setiabudi, H.D., Jusoh, R., Jalil, A.A., 2019. Process optimization of methylene blue adsorption onto eggshell-treated palm oil fuel ash. *Environ. Technol. Innov.* 13, 62–73. <https://doi.org/10.1016/j.eti.2018.10.004>.

Hu, Y., Guo, T., Ye, X., Li, Q., Guo, M., Liu, H., Wu, Z., 2013. Dye adsorption by resins: effect of ionic strength on hydrophobic and electrostatic interactions. *Chem. Eng. J.* 228, 392–397. <https://doi.org/10.1016/j.cej.2013.04.116>.

Huang, Q., Liu, M., Mao, L., Xu, D., Zeng, G., Huang, H., Jiang, R., Deng, F., Zhang, X., Wei, Y., 2017. Surface functionalized SiO_2 nanoparticles with cationic polymers via the combination of mussel inspired chemistry and surface initiated atom transfer radical polymerization: characterization and enhanced removal of organic dye. *J. Colloid Interface Sci.* 499, 170–179. <https://doi.org/10.1016/j.jcis.2017.03.102>.

Huang, W., Chen, J., Zhang, J., 2018. Adsorption characteristics of methylene blue by biochar prepared using sheep, rabbit and pig manure. *Environ. Sci. Pollut. Res.* 25, 29256–29266.

Ibrahim, M.M., 2019. Cr 2 O 3/Al 2 O 3 as adsorbent: physicochemical properties and adsorption behaviors towards removal of Congo red dye from water. *J. Environ. Chem. Eng.* 7, 102848. <https://doi.org/10.1016/j.jece.2018.102848>.

Jia, X.J., Wang, J., Wu, J., Du, Y., Zhao, B., Engelsen, D. Den, 2015. Bouquet-like calcium sulfate dihydrate: a highly efficient adsorbent for Congo red dye. *RSC Adv.* 5, 72321–72330. <https://doi.org/10.1039/c5ra11514k>.

Keshmirzadeh, E., Modarress, H., Jahedi, F., 2018. Removal of Acid Blue 62 textile dye from aqueous solutions by cerium reagents. *Environ. Technol. (United Kingdom)* 0 1–12. <https://doi.org/10.1080/09593330.2018.1511633>.

Khan, M.A., AlOthman, Z.A., Naushad, M., Khan, M.R., Luqman, M., 2015. Adsorption of methylene blue on strongly basic anion exchange resin (Zerolit DMF): kinetic, isotherm, and thermodynamic studies. *Desalin. Water Treat.* 53, 515–523. <https://doi.org/10.1080/19443994.2013.838527>.

Kogawa, A.C., Zoppi, A., Quevedo, M.A., Nunes Salgado, H.R., Longhi, M.R., 2014. Increasing doxycycline hyclate photostability by complexation with β -cyclodextrin. *AAPS PharmSciTech* 15, 1209–1217. <https://doi.org/10.1208/s12249-014-0150-7>.

Kong, Y., Wang, L., Ge, Y., Su, H., Li, Z., 2019. Lignin xanthate resin-bentonite clay composite as a highly effective and low-cost adsorbent for the removal of doxycycline hydrochloride antibiotic and mercury ions in water. *J. Hazard Mater.* 368, 33–41. <https://doi.org/10.1016/j.jhazmat.2019.01.026>.

Kooh, M.R.R., Dahri, M.K., Lim, L.B.L., 2016. The removal of rhodamine B dye from aqueous solution using Casuarina equisetifolia needles as adsorbent. *Cogent Environ. Sci.* 2, 1–14. <https://doi.org/10.1080/23311843.2016.1140553>.

Kumari, U., Behera, S.K., Meikap, B.C., 2019. A novel acid modified alumina adsorbent with enhanced defluoridation property: kinetics, isotherm study and applicability on industrial wastewater. *J. Hazard Mater.* 365, 868–882. <https://doi.org/10.1016/j.jhazmat.2018.11.064>.

Lafi, R., Montasser, I., Hafiane, A., 2019. Adsorption of Congo red dye from aqueous solutions by prepared activated carbon with oxygen-containing functional groups and its regeneration. *Adsorpt. Sci. Technol.* 37, 160–181. <https://doi.org/10.1177/0263617418819227>.

Li, B., Guo, J., Lv, K., Fan, J., 2019. Adsorption of methylene blue and Cd(II) onto

- maleylated modified hydrochar from water. *Environ. Pollut.* 254, 113014. <https://doi.org/10.1016/j.envpol.2019.113014>.
- Li, J., Ng, D.H.L., Ma, R., Zuo, M., Song, P., 2017. Eggshell membrane-derived MgFe₂O₄ for pharmaceutical antibiotics removal and recovery from water. *Chem. Eng. Res. Des.* 126, 123–133. <https://doi.org/10.1016/j.cherd.2017.07.005>.
- Li, Z., Potter, N., Rasmussen, J., Weng, J., Lv, G., 2018. Removal of rhodamine 6G with different types of clay minerals. *Chemosphere* 202, 127–135. <https://doi.org/10.1016/j.chemosphere.2018.03.071>.
- Liu, S., Xu, W., Hua, Liu, Guo, Y., Tan, X. fei, Zeng, G. ming, Li, X., Liang, J., Zhou, Z., Yan, Z., li, Cai, xi, X., 2017. Facile synthesis of Cu(II) impregnated biochar with enhanced adsorption activity for the removal of doxycycline hydrochloride from water. *Sci. Total Environ.* 592, 546–553. <https://doi.org/10.1016/j.scitotenv.2017.03.087>.
- Liu, Xiaoxu, Liu, Xiaowen, Hu, Y., 2015. Investigation of the thermal behaviour and decomposition kinetics of kaolinite. *Clay Miner.* 50, 199–209. <https://doi.org/10.1180/claymin.2015.050.2.04>.
- Liu, Z., Zhu, M., Wang, Z., Wang, H., Deng, C., Li, K., 2016. Effective degradation of aqueous tetracycline using a nano-TiO₂/carbon electrocatalytic membrane. *Materials* 9, 1–14. <https://doi.org/10.3390/ma9050364>.
- Luo, T., Hou, X., Liang, Q., Zhang, G., Chen, F., Xia, Y., Ru, Q., Yao, L., Wu, Y., 2018. The influence of manganese ions doping on nanosheet assembly NiFe₂O₄ for the removal of Congo red. *J. Alloy. Comp.* 763, 771–780. <https://doi.org/10.1016/j.jallcom.2018.05.203>.
- Madan, S., Shaw, R., Tiwari, S., Kumar, S., 2019. Adsorption dynamics of Congo red dye removal using ZnO functionalized high silica zeolitic particles. *Appl. Surf. Sci.* 487, 907–917. <https://doi.org/10.1016/j.apsusc.2019.04.273>.
- Mahmoud, M.E., Abdou, A.E.H., Shehata, A.K., Header, H.M.A., Hamed, E.A., 2018. Sustainable super fast adsorptive removal of Congo red dye from water by a novel technique based on microwave-enforced sorption process. *J. Ind. Eng. Chem.* 57, 28–36. <https://doi.org/10.1016/j.jiec.2017.08.004>.
- Mahmoud, M.S., Farah, J.Y., Farrag, T.E., 2013. Enhanced removal of Methylene Blue by electrocoagulation using iron electrodes. *Egypt. J. Petrol.* 22, 211–216. <https://doi.org/10.1016/j.ejpe.2012.09.013>.
- Mathew, D.S., Juang, R.S., 2007. An overview of the structure and magnetism of spinel ferrite nanoparticles and their synthesis in microemulsions. *Chem. Eng. J.* 129, 51–65. <https://doi.org/10.1016/j.cej.2006.11.001>.
- Mozumder, M.S.I., Islam, M.A., 2010. Development of treatment technology for dye containing industrial wastewater. *J. Sci. Res.* 2, 567. <https://doi.org/10.3329/jsr.v2i3.4302>.
- Naeimi, S., Faghihian, H., 2017. Application of novel metal organic framework, MIL-53(Fe) and its magnetic hybrid: for removal of pharmaceutical pollutant, doxycycline from aqueous solutions. *Environ. Toxicol. Pharmacol.* 53, 121–132. <https://doi.org/10.1016/j.etap.2017.05.007>.
- Namasivayam, C., Kavitha, D., 2002. Removal of Congo Red from water by adsorption onto activated carbon prepared from coir pith. *Agric. Solid Waste* 54, 47–58.
- Nghiem, L.D., Schäfer, A.I., Elimelech, M., 2005. Pharmaceutical retention mechanisms by nanofiltration membranes. *Environ. Sci. Technol.* 39, 7698–7705. <https://doi.org/10.1021/es0507665>.
- Olusegun, S.J., de Sousa Lima, L.F., Mohallem, N.D.S., 2018. Enhancement of adsorption capacity of clay through spray drying and surface modification process for wastewater treatment. *Chem. Eng. J.* 334, 1719–1728. <https://doi.org/10.1016/j.cej.2017.11.084>.
- Olusegun, S.J., Freitas, E.T.F., Lara, L.R.S., Mohallem, N.D.S., 2019a. Synergistic effect of a spinel ferrite on the adsorption capacity of nano bio-silica for the removal of methylene blue. *Environ. Technol.* 1–14. <https://doi.org/10.1080/09593330.2019.1694083>.
- Olusegun, S.J., Freitas, E.T.F., Lara, L.R.S., Stumpf, H.O., Mohallem, N.D.S., 2019b. Effect of drying process and calcination on the structural and magnetic properties of cobalt ferrite. *Ceram. Int.* 45, 8734–8743. <https://doi.org/10.1016/j.ceramint.2019.01.197>.
- Olusegun, S.J., Mohallem, N.D.S., 2019. Insight into the adsorption of doxycycline hydrochloride on different thermally treated hierarchical CoFe₂O₄/bio-silica nanocomposite. *J. Environ. Chem. Eng.* 7, 103442. <https://doi.org/10.1016/j.jece.2019.103442>.
- Olusegun, S.J., Rodrigues, G.L.S., Freitas, E.T.F., Lara, L.R.S., Rocha, W.R., Mohallem, N.D.S., 2019c. Sequestering anionic and cationic dyes from wastewater using spray dried biopolymeric magnetic composite: experimental and theoretical studies. *J. Hazard Mater.* 380, 120872. <https://doi.org/10.1016/j.jhazmat.2019.120872>.
- Peng, G., Li, T., Ai, B., Yang, S., Fu, J., He, Q., Yu, G., Deng, S., 2019. Highly efficient removal of enrofloxacin by magnetic montmorillonite via adsorption and persulfate oxidation. *Chem. Eng. J.* 360, 1119–1127. <https://doi.org/10.1016/j.cej.2018.10.190>.
- Purkait, M.K., Maiti, A., DasGupta, S., De, S., 2007. Removal of Congo red using activated carbon and its regeneration. *J. Hazard Mater.* 145, 287–295. <https://doi.org/10.1016/j.jhazmat.2006.11.021>.
- Ramlow, H., Machado, R.A.F., Bierhalz, A.C.K., Marangoni, C., 2019. Dye synthetic solution treatment by direct contact membrane distillation using commercial membranes. *Environ. Technol. (United Kingdom)* 1–12. <https://doi.org/10.1080/09593330.2018.1561758>.
- Raper, E., Stephenson, T., Anderson, D.R., Fisher, R., Soares, A., 2018. Industrial wastewater treatment through bioaugmentation. *Process Saf. Environ. Prot.* 118, 178–187. <https://doi.org/10.1016/j.psep.2018.06.035>.
- Salehi, E., Daraei, P., Arabi Shamsabadi, A., 2016. A review on chitosan-based adsorptive membranes. *Carbohydr. Polym.* 152, 419–432. <https://doi.org/10.1016/j.carbpol.2016.07.033>.
- Samiey, B., Ashoori, F., 2012. Adsorptive removal of methylene blue by agar: effects of NaCl and ethanol. *Chem. Cent. J.* 6, 14. <https://doi.org/10.1186/1752-153X-6-14>.
- Solano, A.M.S., Garcia-Segura, S., Martínez-Huitle, C.A., Brillas, E., 2015. Degradation of acidic aqueous solutions of the diazo dye Congo Red by photo-assisted electrochemical processes based on Fenton's reaction chemistry. *Appl. Catal. B Environ.* 168–169, 559–571. <https://doi.org/10.1016/j.apcatb.2015.01.019>.
- Spence, A., Kelleher, B.P., 2012. FT-IR spectroscopic analysis of kaolinite-microbial interactions. *Vib. Spectrosc.* 61, 151–155. <https://doi.org/10.1016/j.vibspec.2012.02.019>.
- Tadjarodi, A., Imani, M., Salehi, M., 2015. ZnFe₂O₄ nanoparticles and a clay encapsulated ZnFe₂O₄ nanocomposite: synthesis strategy, structural characteristics and the adsorption of dye pollutants in water. *RSC Adv.* 5, 56145–56156. <https://doi.org/10.1039/c5ra02163d>.
- Tagliavini, M., Schäfer, A.I., 2018. Removal of steroid micropollutants by polymer-based spherical activated carbon (PBSAC) assisted membrane filtration. *J. Hazard Mater.* 353, 514–521. <https://doi.org/10.1016/j.jhazmat.2018.03.032>.
- Tran, H.N., You, S.J., Chao, H.P., 2016. Thermodynamic parameters of cadmium adsorption onto orange peel calculated from various methods: a comparison study. *J. Environ. Chem. Eng.* 4, 2671–2682. <https://doi.org/10.1016/j.jece.2016.05.009>.
- Vimonses, V., Lei, S., Jin, B., Chow, C.W.K., Saint, C., 2009. Adsorption of Congo red by three Australian kaolins. *Appl. Clay Sci.* 43, 465–472. <https://doi.org/10.1016/j.clay.2008.11.008>.
- Wang, X., Yin, R., Zeng, L., Zhu, M., 2019. A review of graphene-based nanomaterials for removal of antibiotics from aqueous environments. *Environ. Pollut.* 253, 100–110. <https://doi.org/10.1016/j.envpol.2019.06.067>.
- Wei, J., Liu, Y., Li, J., Zhu, Y., Yu, H., Peng, Y., 2019. Adsorption and co-adsorption of tetracycline and doxycycline by one-step synthesized iron loaded sludge biochar. *Chemosphere* 236, 124254. <https://doi.org/10.1016/j.chemosphere.2019.06.224>.
- Xu, H., Liu, J., Chen, P., Shao, G., Fan, B., Wang, H., Chen, D., Lu, H., Zhang, R., 2018. Preparation of magnetic kaolinite nanotubes for the removal of methylene blue from aqueous solution. *J. Inorg. Organomet. Polym. Mater.* 28, 790–799. <https://doi.org/10.1007/s10904-017-0728-0>.
- Yuan, S., Li, Y., Han, Y., Gao, P., Gong, G., 2017. Investigation on calcination behaviors of coal gangue by fluidized calcination in comparison with static calcination. *Minerals* 7, 19. <https://doi.org/10.3390/min7020019>.
- Zahir, A., Aslam, Z., Kamal, M.S., Ahmad, W., Abbas, A., Shawabkeh, R.A., 2017. Development of novel cross-linked chitosan for the removal of anionic Congo red dye. *J. Mol. Liq.* 244, 211–218. <https://doi.org/10.1016/j.molliq.2017.09.006>.
- Zaidi, S., Sivasankar, V., Chaabane, T., Alonzo, V., Omine, K., Maachi, R., Darchen, A., Prabhakaran, M., 2019. Separate and simultaneous removal of doxycycline and oxytetracycline antibiotics by electro-generated adsorbents (EGAs). *J. Environ. Chem. Eng.* 7. <https://doi.org/10.1016/j.jece.2018.102876>.
- Zeng, Z., Tan, X., Liu, Y., Tian, S., Zeng, G., Jiang, L., Liu, S., Li, J., Liu, N., Yin, Z., 2018. Comprehensive adsorption studies of doxycycline and ciprofloxacin antibiotics by biochars prepared at different temperatures. *Front. Chem.* 6, 1–11. <https://doi.org/10.3389/fchem.2018.00080>.
- Zhai, Y., Zhai, J., Zhou, M., Dong, S., 2009. Ordered magnetic core–manganese oxide shell nanostructures and their application in water treatment. *J. Mater. Chem.* 19, 7030–7035. <https://doi.org/10.1039/b912767d>.
- Zhang, Q.B., Hua, Y.X., 2009. Corrosion inhibition of mild steel by alkylimidazolium ionic liquids in hydrochloric acid. *Electrochim. Acta* 54, 1881–1887. <https://doi.org/10.1016/j.electacta.2008.10.025>.
- Zhang, X., Li, Y., Li, M., Zheng, H., Du, Q., Li, Hong, Wang, Y., Wang, D., Wang, C., Sui, K., Li, Hongliang, Xia, Y., 2019. Preparation of improved gluten material and its adsorption behavior for Congo red from aqueous solution. *J. Colloid Interface Sci.* 556, 249–257. <https://doi.org/10.1016/j.jcis.2019.08.037>.
- Zhao, Y., Cao, B., Lin, Z., Su, X., 2019. Synthesis of CoFe₂O₄/C nano-catalyst with excellent performance by molten salt method and its application in 4-nitrophenol reduction. *Environ. Pollut.* 254, 112961. <https://doi.org/10.1016/j.envpol.2019.112961>.



Enhancement of adsorption capacity of clay through spray drying and surface modification process for wastewater treatment

Sunday Joseph Olusegun^{a,b,*}, Luiz Fernando de Sousa Lima^a, Nelcy Della Santina Mohallem^a

^a Universidade Federal de Minas Gerais, Departamento de Química, Laboratório de Materiais Nanoestruturados, Belo Horizonte, Brazil

^b Department of Metallurgical and Materials Engineering, Federal University of Technology, PMB 704, Akure, Ondo, Nigeria

ARTICLE INFO

Keywords:

Spray dried clay
Adsorption
Specific surface area
Methylene blue
Kinetics
Thermodynamics

ABSTRACT

Nowadays, removal of contaminants like dye from wastewater has become an uncompromising task. In view of this, enhancing the performance of adsorbents so as to facilitate the adsorption technique and reduce the overall cost of the purification process is of great interest to industrial sector. In this study, the adsorption capacity of clay was improved by spray drying a dispersed clay solution and also through its surface modification. Fourier transform infrared spectroscopy (FTIR) confirmed that the surface modification was successful; X-ray diffraction (XRD) analysis showed that surface modification did not affect the crystal structure of the clay, and BET specific surface area results attest that spray dried clay has the highest surface area of 102 m²/g. The adsorption tests were carried out using methylene blue and results showed that the adsorption capacity was influenced by solution pH, with maximum adsorption at pH 10 and 120 min contact time. Adsorption kinetics data were well fitted to pseudo-second order kinetics model. Langmuir and Freundlich adsorption isotherm models were used to investigate the mechanism of adsorption. Freundlich model is more applicable for this process. Spray dried clay performed better than the modified and raw clay with adsorption capacity of 168 mg/g (at 333 K). The calculated thermodynamics parameters revealed that the adsorption process is spontaneous at all the studied temperatures (303–333 K) for spray dried clay.

1. Introduction

Technological advancement, though a driving force behind nation's economic, has led to the generation of urge amount of effluent (especially among industries that use a large volume of water) into the water body and this has brought harmful consequences on the ecosystem [1]. It is noted that due to the cost implication of treating the wastewater, many a time the industries boycott the treatment process and discharge the untreated effluents into the environment, not minding the health implication on human and aquatic lives.

Among these effluents are those generated by textile industries. Dyes are chemical substances that are used in industries such as textile, printing and cosmetic among others [2]. Its discharge into the water body, no matter how small in volume, becomes obvious due to its coloring effects [3]. Researches have shown that the presence of dye in water affects its beauty and depletes the dissolution of oxygen [4]. Furthermore, dyes retard the growth of aquatic lives and hinder photosynthesis due to its ability to absorb and reflect sunlight that enters water body [5,6]. In addition, some ailments in human lives are due to the effects of dye contamination [7].

In view of the enormous dangers that accompany the discharge of dye effluents, stringent regulations have been put in place to ensure its removal from wastewater before discharge into the environment. Different methods of treatment have been employed to treat textile effluents, among which are membrane filtration process, reverse osmosis, coagulation, electrochemical, adsorption, etc [8]. Among these, adsorption is an interesting technique, because is inexpensive, simple to design, does not lead to the production of harmful substances, efficient in removing organic pollutants and lots more [9–11].

Due to the several advantages that adsorption process incorporated, several materials had been tested and proven to be effective in removing dye effluents. Modified bamboo powder had been used to remove methylene blue from simulated effluents by Guo et al. [12]. According to the authors, this adsorbent has maximum capacity of 606 mg/g at 298 K, the data were well fitted into Langmuir isotherm model and the process was found to be exothermic. More so, the effectiveness of fly ash for the simultaneous removal of dyes and heavy metals through adsorption process was critically examined by Visa et al. [13]. They concluded that 60 min contact time between the adsorbent-adsorbate was sufficient to reach optimum efficiencies and that the

* Corresponding author at: Universidade Federal de Minas Gerais, Departamento de Química, Laboratório de Materiais Nanoestruturados, Belo Horizonte, Brazil.
E-mail address: arewasegun@ufmg.br (S.J. Olusegun).

adsorption does not depend on the fraction of the fly ash that was used.

Clay minerals are available naturally on the surface of the earth, economical, pose no threat to the environment and composed of silica and alumina as major components [14,15]. Uddin et al. [16] commented that clay minerals function very well as adsorbents for the removal of harmful materials due to the space between their layers, and they are also more efficient for the removal of cationic dyes because of their negative surface charge. Several works have reported removal of contaminants from solution using different types of clay either in raw or modified form. Anirudhan and Ramachandran [17] investigated the removal of some basic dyes like crystal violet and Rhodamine B by using modified bentonite clay. In their findings, the uptake was found to be sensitive to the solution pH and concentration, while the equilibrium was attained within 2 h.

This research seeks to enhance the adsorption capacity of clay through spray drying process, and surface modification by sodium dodecyl sulfate. The overall idea is to project a highly effective and cost friendly adsorbent. This is interesting because increasing the specific surface area of clay for adequate removal of hazardous materials through spray drying process has not been well reported. The adsorption studies cover the influence of pH, adsorbent dosage, contact time, initial dye concentration and temperature. The results obtained were used to evaluate the kinetic, mechanism and thermodynamic of the adsorption processes.

2. Materials and methods

2.1. Materials

The clay was obtained from Chapada do Norte, Minas Gerais, Brazil, while the sodium dodecyl sulfate (SDS) and methylene blue (MB) were purchased from Labsynth.

2.2. Methods

2.2.1. Preparation of spray dried clay

10 g of raw clay sample was dispersed in 1 L of distilled water containing 0.1 g of dispersant. The mixture was continuously stirred during spray drying period. Spray Dryer MSD 0.5 with 0.7 mm nozzle was used to dry the suspended clay. The process was performed by setting an inlet temperature at 120 °C and air flow rate at 50 L/min pressure. The dried product (spray dried clay) was collected in a collection bottle.

2.2.2. Preparation of SDS-modified raw clay

Sodium dodecyl sulfate (SDS) modified raw clay was prepared according to the method reported by Zhang et al. [18] with little modification. 1 g of raw clay was dispersed into 100 mL of 0.01 M of SDS. The mixtures were stirred for 3 h at 80 °C and left overnight at room temperature. The modified raw clay was centrifuged and dried in the oven at 100 °C.

2.3. Characterization of the samples

All the samples, raw clay (RC), surface modified clay (SMC) and spray dried clay (SDC) were characterized. XRD pattern was obtained by X-ray diffraction (Shimadzu, XRD 7000 diffractometer) using CuK α radiation. Fourier transformed infrared (FTIR) spectra measurements of the adsorbents were carried out on Perkin-Elmer spectrophotometer using the KBr pellets. Morphologies and composition were observed in scanning electron microscope (SEM), Quanta 200 – FEI coupled with EDS probe and in transmission electron microscope (TEM) TECNAI G2 SPIRIT-FEI with an acceleration voltage of 120 kV. Specific surface area was determined by Nitrogen adsorption in a Quantachrome Autosorb, using the BET method and the BJH method was used to determine pore size distribution. The apparent densities were measured by weighing

equal mass (g) of the samples inside 5 mL measuring cylinder. The volume of each clay was recorded and divided by the mass.

The zeta potential of the dispersed (in water) clay particles was measured using a Zetasizer Nano-Zs model ZEN3600.

2.4. Adsorption studies

Adsorption studies were performed using 50 mL of methylene blue solution and the experiment was carried out in triplicate. The pH (2–10) of the solutions was adjusted using HCl and NaOH. Other varying parameters were the adsorbent mass (0.05–0.25 g), the initial concentration of the dye (25–400 mg/L), contact time (30–240 mins) and temperature (303–333 K). After each adsorption study, a reasonable quantity of the solution was centrifuged so as to adequately separate the adsorbent. The unadsorbed dye concentration in the solution was determined using UV/Vis Spectrophotometer. The percentage removal (%R) was calculated using

$$\%R = \frac{C_0 - C_e}{C_0} \times 100 \quad (1)$$

C_0 and C_e are the initial and final concentration of the dye solutions respectively.

Statistical analysis of the variables (i.e. pH and adsorbent dosage; pH and contact time; adsorbent dosage and contact time) was carried out using ANOVA.

3. Results and discussion

3.1. Adsorbents characterization

The XRD patterns of raw clay (RC), surface modified clay (SMC) and spray dried clay (SDC) are shown in Fig. 1. The main mineral components of the studied clay are the kaolinite ($\text{Al}_2\text{Si}_2\text{O}_5(\text{OH})_4$) and alpha-quartz (SiO_2). The peaks at $2\theta = 12.3^\circ$ and 24.7° correspond to the (0 0 1) and (0 0 2) planes of kaolinite (Joint Committee on Powder Diffraction Standards (JCPDS) card number 80-885), and the peak at 26.5° corresponds to the plane (0 1 1) of alpha-quartz (JCPDS card number 89-8937). The SDC diffractogram presents peaks related to alpha-quartz less intense due to the decrease of these particles. The intensity of the peaks 001 and 002 related to kaolinite did not change, showing that the size of the kaolinite plates does not decrease, but it occurs an exfoliation of these plates.

FTIR of the materials is presented in Fig. 2. The two peaks at 3694

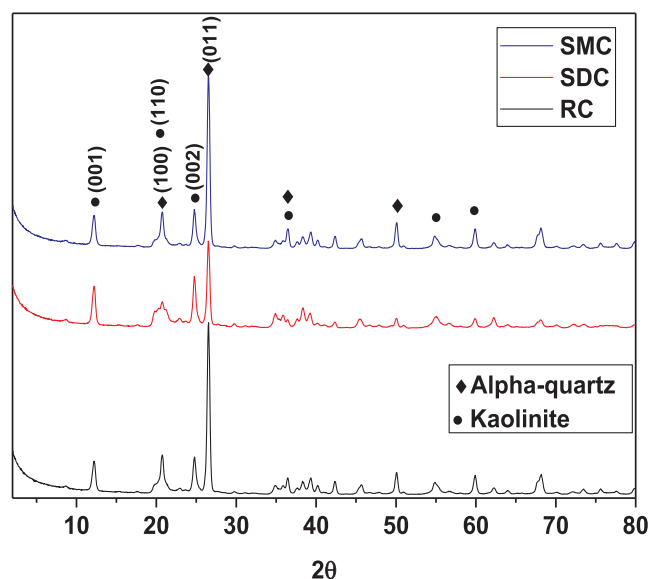


Fig. 1. XRD pattern of raw, surface modified and spray dried clay.

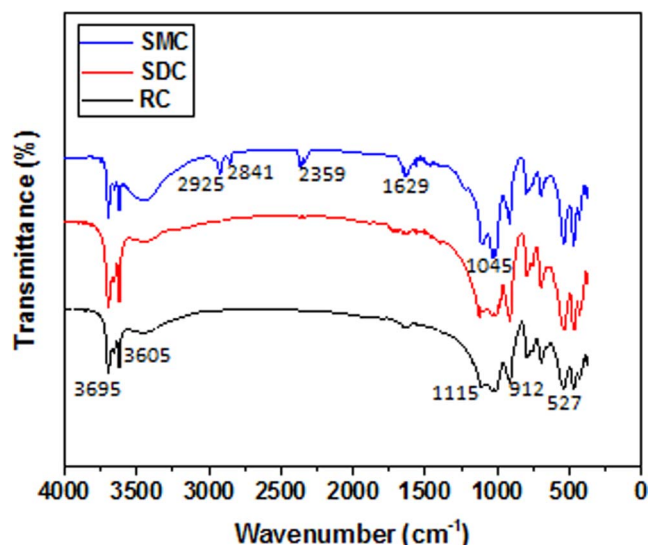


Fig. 2. FTIR spectra of raw, surface modified and spray dried clay.

and 3605 cm^{-1} are assigned to OH stretching of kaolin, while the peaks at 1114 cm^{-1} corresponds to Si–O–Si asymmetric stretching. 912 and 527 cm^{-1} peaks are attributed to Al–OH–Al and Al–O–Si deformation respectively. A similar observation was reported by Aroke et al. [19]. The sharp peak at 1045 cm^{-1} on the modified clay is assigned to Si–O–C stretching. The bands due to 2924 and 2841 cm^{-1} exhibited by the surface modified clay are due to CH_3 asymmetric stretching and CH_2 symmetric stretching.

Fig. 3 shows the nitrogen adsorption-desorption isotherm of RC, SMC, and SDC, whose curves are characteristic of macroporous materials. The formed mesoporous are due to the interstices of the agglomerated material.

The specific surface area of the materials using BET theory is as follow 14 , 35 and $102\text{ m}^2/\text{g}$ respectively. As the raw clay is formed by agglomerate particles, the spray drying process separates part of these agglomerates producing a particulate material with the higher specific surface area. The surfactant used to modify the raw clay also increased the interaction between its surface and nitrogen gas hence leading to the increased in the specific surface area in comparison with the raw clay. These two processes (spray drying and surface modification) have successfully resulted to increase in specific surface area. These results

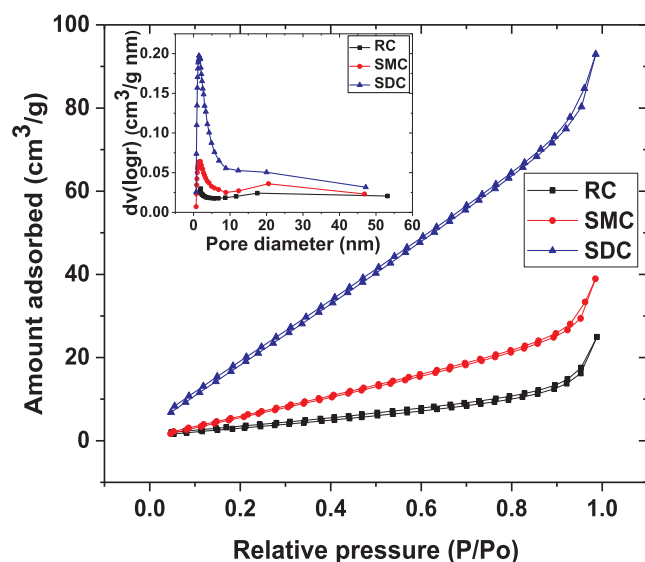


Fig. 3. Nitrogen adsorption-desorption isotherm at 77 K of the adsorbents.

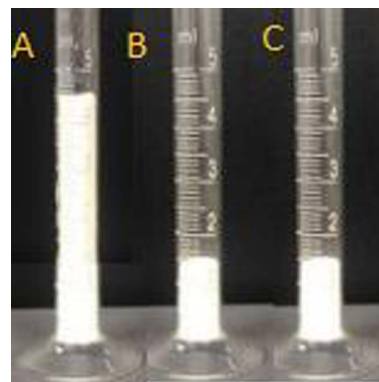


Fig. 4. Volume of equal mass (A) spray dried clay; (B) raw clay; (C) surface modified clay.

are confirmed by the apparent densities of RC, SMC and SDC of 0.824 ± 0.018 , 0.815 ± 0.015 and $0.282 \pm 0.007\text{ g/cm}^3$, respectively, whose volumes measured are shown in Fig. 4.

The respective SEM images with EDS spectra and TEM of the adsorbents are displayed in Figs. 5 and 6 respectively. The images confirm that the RC and SMC are compacted materials, formed by an agglomerate of lamellar (kaolinite) and small particles (alpha-quartz). Meanwhile, SDC consists of exfoliated lamellar kaolinite and smaller particles, confirmed by XRD and SEM images.

The elemental constituents like Al, Si and O shown on the EDS spectra of all samples are in agreement with XRD results, which show that the clay is formed by kaolinite and alpha-quartz minerals, without other contaminants. The presence of Na and S on the EDS spectrum of SMC is an indication of the modification of clay using sodium dodecyl sulfate, in accordance with FTIR results.

3.2. Effect of pH of the dye solution

The study of pH gives an insight about the interaction between the adsorbent and adsorbate. The pH of methylene blue (MB) solutions was varied from 2 to 10, while the amount of adsorbent used was kept constant, $0.1\text{ g}/50\text{ mL}$ of 100 mg/L dye solutions and studied for 4 h. The graphical representation of the results is presented in Fig. 7.

The adsorption of methylene blue was more favorable at $\text{pH} > 4$ and percentage that was removed increases with increase in pH. The variation of the zeta potential of the clay solutions depends highly on the pH of the suspension as displayed in Fig. 8.

Raw clay showed an isoelectric point at pH below 4, while surface modified and the spray dried samples showed an isoelectric point at pH below 2. As the pH increases, the surface charge of the particles becomes more negative. This explains why the adsorption of methylene blue molecules was better at higher pH, and the spray dried clay performed better than others (RC and SMC) because it exhibit higher negative zeta potential values. All the samples have the most negative value of surface charge at pH 10; this implies that adsorption process is basically due to the coulombic attraction between the negatively charged surface and the positive charge of the MB molecules.

Study carried out by Yan et al. [20] revealed that the surface of kaolin is rich in silica with small percentage of alumina. In view of this, its surface charge will likely be Si-OH_2^+ and Si-O^- in acidic and alkaline medium respectively. The adsorption of MB being a cationic dye was favorable at higher pH due to the electrostatic attraction that exists between the MB molecules and the negatively charged clay surface. Spray dried clay (SDC) performed better than raw clay (RC) and surface modified clay (SMC) with the highest MB removal of 72%. This result is due to the increase in the specific surface area related to the disaggregation of the lamellas produced by spray drying process, hereby exposing more of the active surface of the SDC to MB solution.

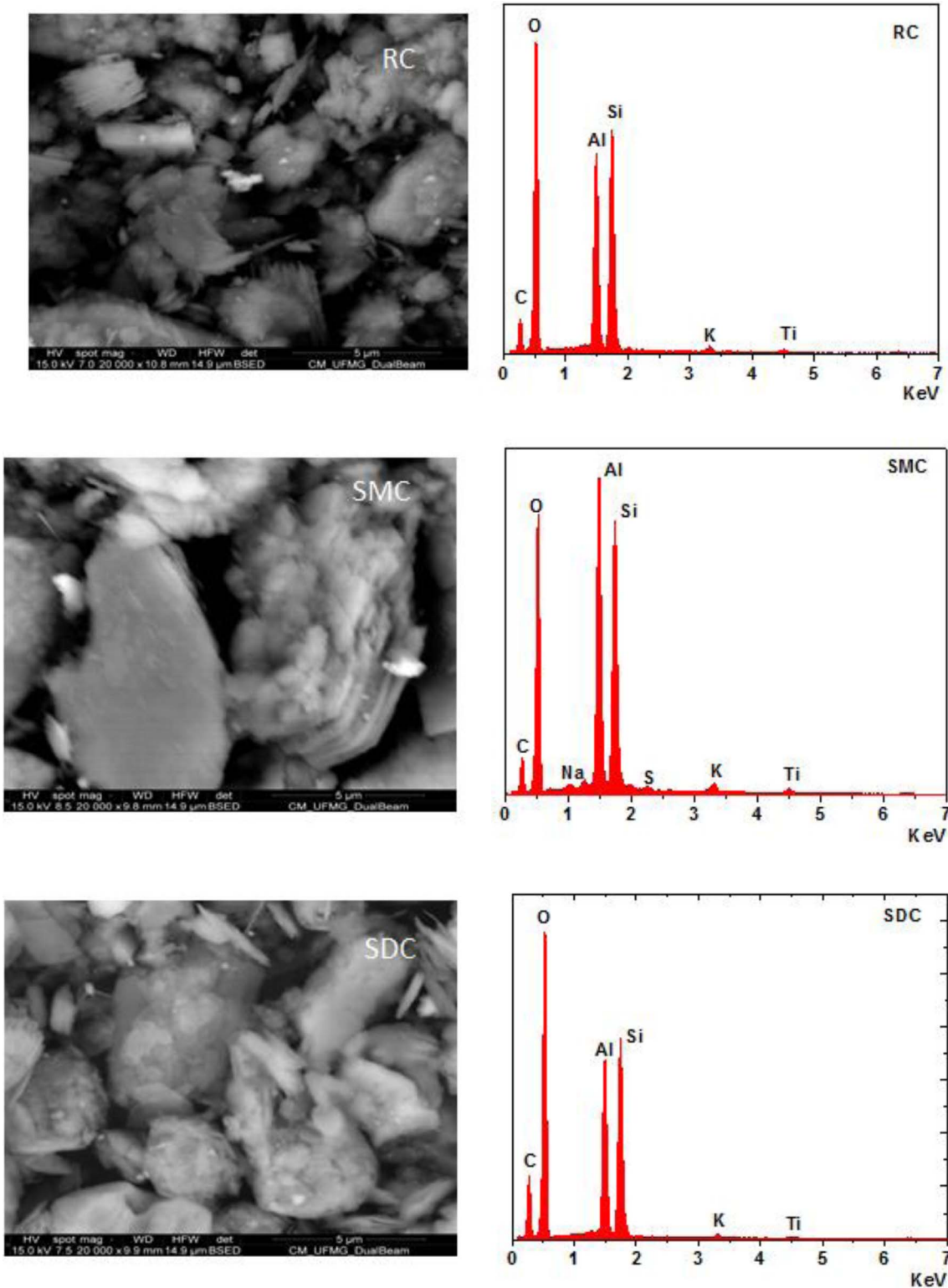


Fig. 5. SEM images with respective EDS spectra.

3.3. Effect of dosage

Fig. 9 represents the influence of adsorbent mass on the removal of MB. The mass of the adsorbent was varied from 0.05 to 0.25 g per 50 mL of the dye solution and maintained for 2 h.

Percentage removal of methylene blue increases as the amount of the adsorbent added to the fixed concentration of the dye solution increases. Spray dried clay takes the lead. The linear behavior of the

adsorption process indicates that the active sites of the adsorbent can still accommodate the dye molecules on its surface. More so, 0.25 g/50 mL of the spray dried clay effectively remove 96% of the dye solution and performed almost more twice than the raw clay.

3.4. Effect of contact time and adsorption kinetics

Fig. 10 illustrates the amount of MB absorbed at the time range of

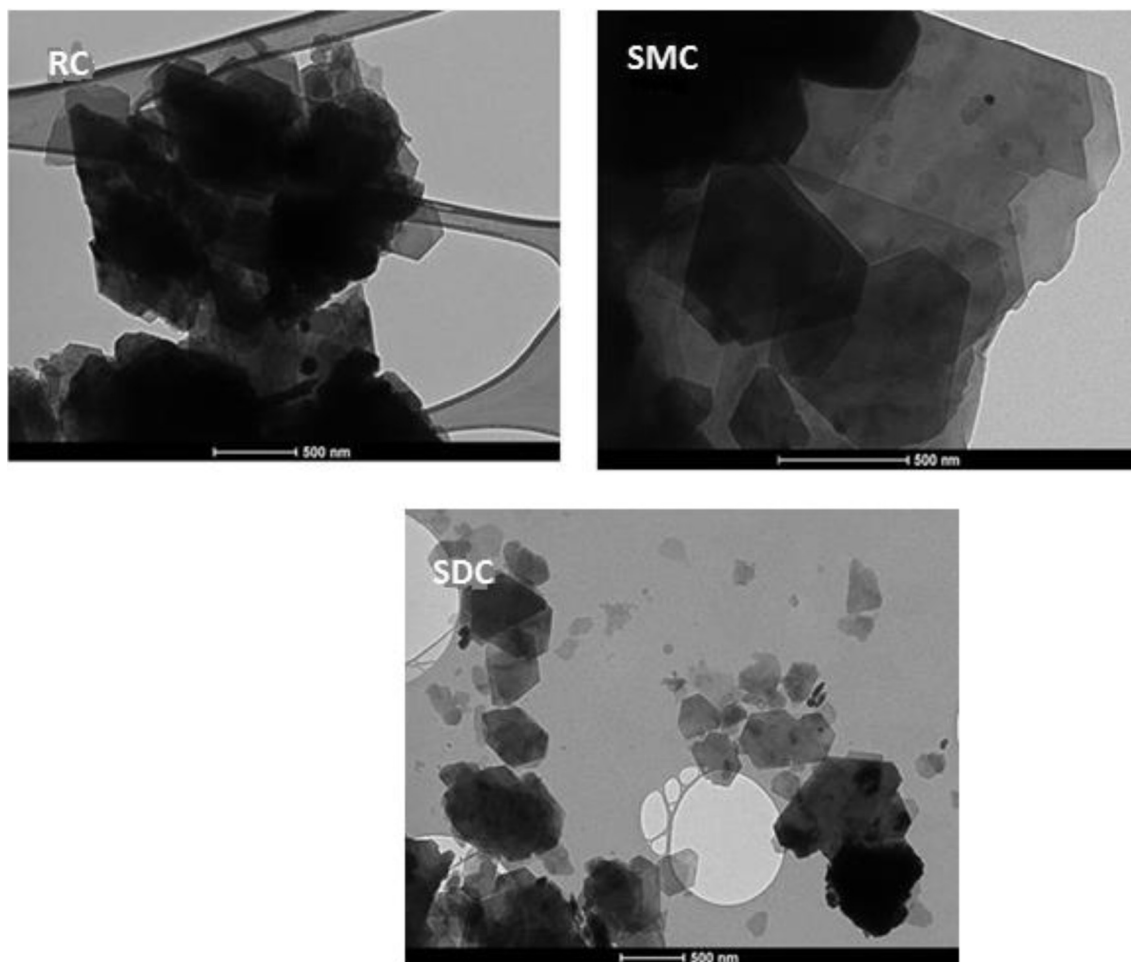


Fig. 6. TEM images.

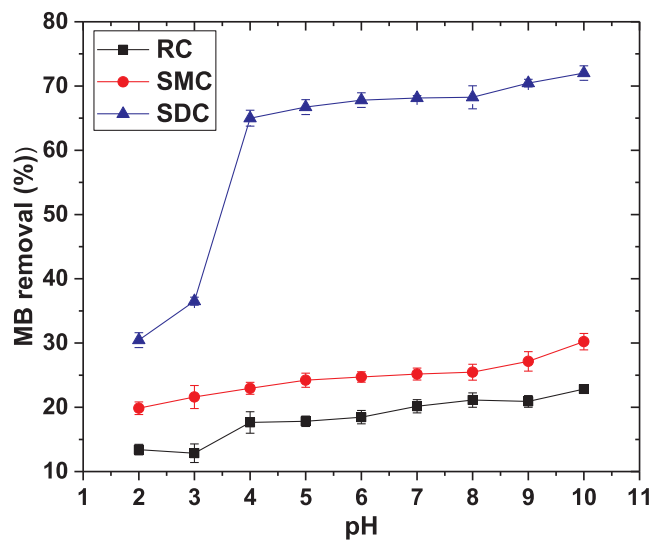


Fig. 7. The effect of pH on the removal of methylene blue.

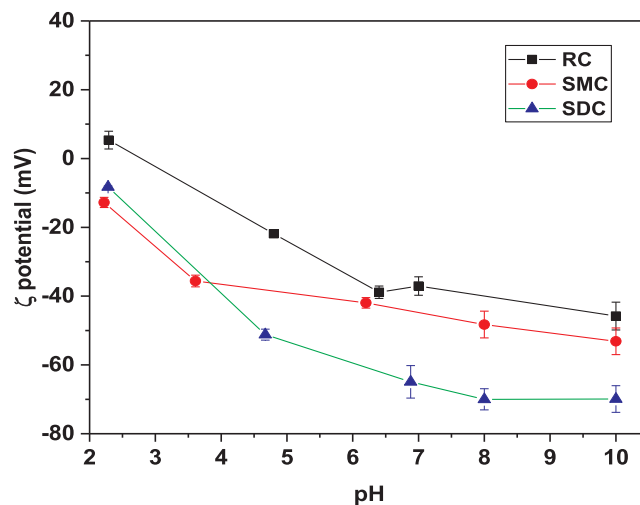


Fig. 8. Zeta potential of the adsorbents as a function of pH.

30–240 mins, initial concentration of 100 mg/g of MB, 0.1 g of the adsorbents and at pH 10. This was to ascertain the adsorption equilibrium time for the removal of MB from the solution. Effective adsorbent must not only have high capacity but, also rapid in removing contaminants. The adsorption process increased rapidly during the first 30 min for spray dried clay. However, all the adsorbents attained equilibrium at 120 min, after which there is no significant uptake in the

percentage of MB that was removed.

The rapid initial stage of the adsorption process shows that a large amount of active vacant sites are available and that concentration gradient between the adsorbate in solution and adsorbate on the adsorbent is high [21]. The concentration gradient becomes almost constant after the attainment of the equilibrium time. This observation has been affirmed to be as a result of a limitation in the mass transfer of MB molecules to the surface of the adsorbent and also reduction in the

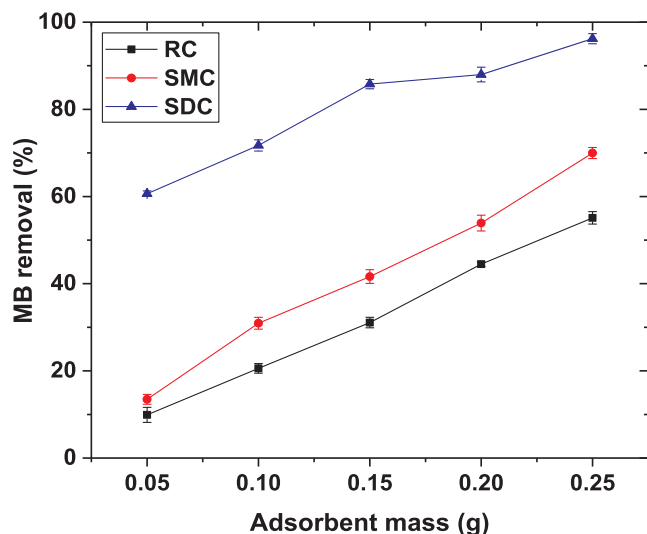


Fig. 9. The plot of adsorbent mass (0.05–0.25 g per 50 mL of the dye solution and maintained for 2 h) for MB adsorption.

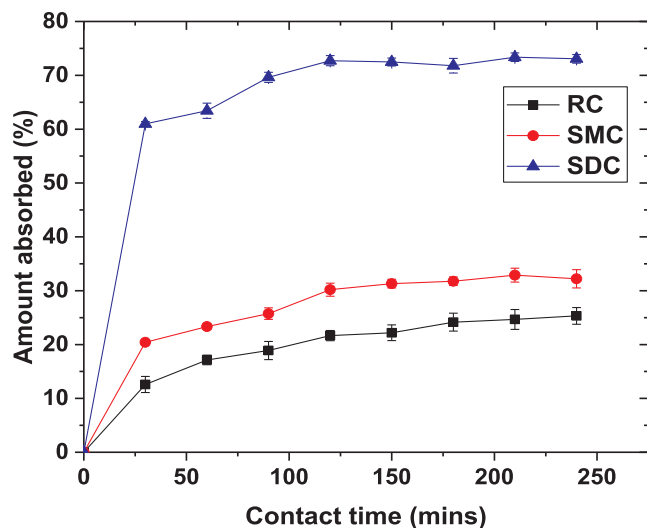


Fig. 10. Amount (%) of MB removed from solution versus contact time (mins).

intra-particle diffusion.

The data obtained were fitted into pseudo-first-order and second-order, and intraparticle diffusion kinetics models. This enabled a proper understanding of the control mechanism of the process of the adsorption.

The linear form of pseudo-first-order is given by the equation below

$$\log(q_e - q_t) = \log q_e - \frac{k_1 t}{2.303} \quad (2)$$

where q_e , q_t , k_1 and t are adsorption capacity at equilibrium (mg/g), amount of MB removed at time t , rate constant and contact time (min) respectively. The plot of $\log(q_e - q_t)$ versus t (not show) is not linear, signifying that the experimental results are not consistent with this model. More so, the large deviation in experimental and calculated q_e , also the values of correlation coefficient showed in Table 1 imply that the model is not applicable for the mechanism. The values of q_e and k_1 are extrapolated from the intercept and the slope respectively.

Pseudo-second-order is expressed by the equation below

$$\frac{t}{q_t} = \frac{1}{k_2 q_e^2} + \frac{t}{q_e} \quad (3)$$

This model proposes adsorption mechanism in which the interaction

Table 1
Parameters for kinetics models.

Model	Parameters	RC	SMC	SDC
Pseudo-first-order	q_e exp (mg/g)	11.27	15.29	35.9
	q_e cal (mg/g)	32.78	18.38	10.89
	k_1	0.0353	0.0278	0.0244
	R	0.8954	0.9280	0.9248
	χ^2	14.1147	0.5194	57.4380
Pseudo-second-order	q_e cal (mg/g)	13.36	17.08	36.85
	k_2	0.0165	0.0051	0.0001
	R	0.9938	0.9964	0.9998
	χ^2	0.3269	0.1875	0.0244
Intra-particle diffusion	k_d	0.5399	0.5461	0.4876
	R	0.9464	0.9407	0.9186

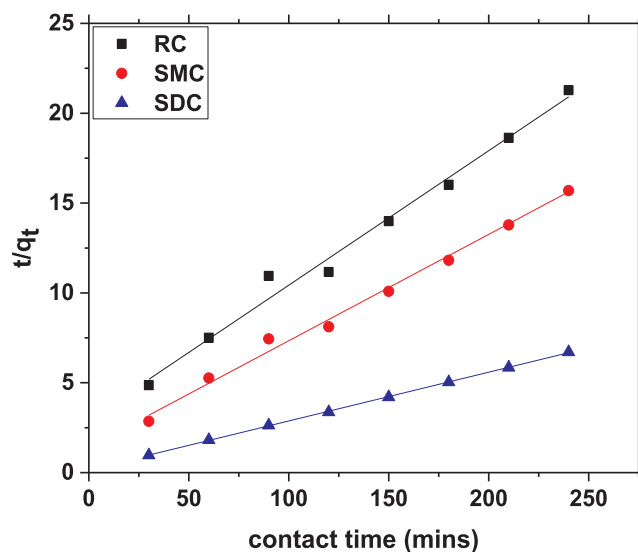


Fig. 11. Pseudo-second-order kinetic plot of MB adsorption on RC, SMC and SDC.

between the adsorbate molecules on the site on the adsorbent is mainly due to the physio-chemical interaction [8,22].

The plot of $\frac{t}{q_t}$ against t is linear (Fig. 11). The respective values of k_2 (pseudo-second-order rate constant) and q_e are obtained from the intercept and slope of the Figure. The calculated values of q_e are considerably closed to the experimental values. The correlation coefficient of the plot is close to unity. Therefore, the experimental data is properly fitted into this model.

To further confirm how suitable these kinetic models (pseudo-first and second order) are in describing the adsorption process, chi-square (χ^2) statistical analysis was also applied [23].

$$\chi^2 = \sum \frac{(q_e \text{exp} - q_e \text{cal})^2}{q_e \text{cal}} \quad (4)$$

$q_e \text{exp}$ is the experimental equilibrium capacity data and $q_e \text{cal}$ is the equilibrium capacity from the model. It was observed from Table 1 that the values of χ^2 obtained from the pseudo-second-order is lower than the pseudo-first-order, this ascertain that the pseudo-second-order is more suitable to describe the adsorption of Methylene blue on RC, SMC and SDC.

The last kinetic model that was used is the intra-particle diffusion, which describes that the adsorption rate mechanism hinges on how quick the adsorbate diffuses towards adsorbent [24]. The model is described by Eq. (4)

$$q_t = k_d t^{1/2} + c \quad (5)$$

The linear plot of q_t versus $t^{1/2}$ is represented in Fig. 12. The

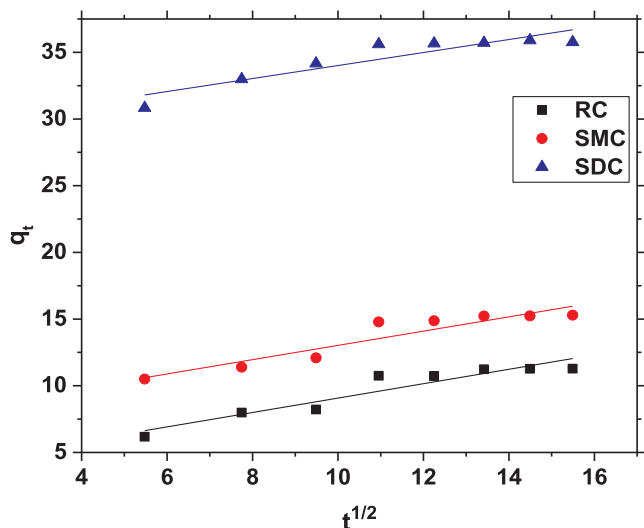


Fig. 12. Intraparticle diffusion plot of MB adsorption on RC, SMC and SDC.

linearity of the plot indicates that process is diffusion-controlled. The value of k_d (rate constant of intra-particle diffusion) for each adsorbent are listed in Table 1.

It has been noted that if the plot of q_t versus $t^{1/2}$ is multi-linear plots, it implies that two or more steps are involved in the adsorption process [25]. The intra particle diffusion plot of this study having two linear plots (Fig. 12) reflects that the adsorption process was accompanied by

two phases. This means that mechanism of MB adsorption on the surface of the adsorbents was fascinated by surface adsorption and intra-particle diffusion.

3.5. Adsorption isotherm

Subjecting experimental data to adsorption isotherms gives adequate insight into the process of adsorption on the surface of the adsorbent, also on the attraction that it has for the adsorbate [26]. In view of these, the suitability of Langmuir and Freundlich adsorption Isotherms was examined. Langmuir adsorption isotherm has been defined to be an adsorption that involves the attachment of only one layer of molecules of the adsorbate to the homogeneous surface of the adsorbent [27]. This isotherm is represented by the equation below.

$$\frac{C_e}{q_e} = \frac{1}{q_{max}b} + \frac{C_e}{q_{max}} \tag{6}$$

where C_e is the equilibrium concentration in solution (mg/L), q_e is the amount of MB adsorbed per unit mass of the adsorbent (mg/g), q_{max} is the maximum adsorption capacity (mg/g) and b is Langmuir equilibrium constant (L/mg). The plot of $\frac{C_e}{q_e}$ against C_e at 303–333 K is presented in Fig. 13. The respective Langmuir parameters are itemized in Table 2.

Freundlich isotherm has been termed as an adsorption of adsorbate molecules on the heterogenous surface of adsorbent, and this is accompanying by non-uniform distribution of heat of adsorption [28]. The equation that describes the isotherm is given as

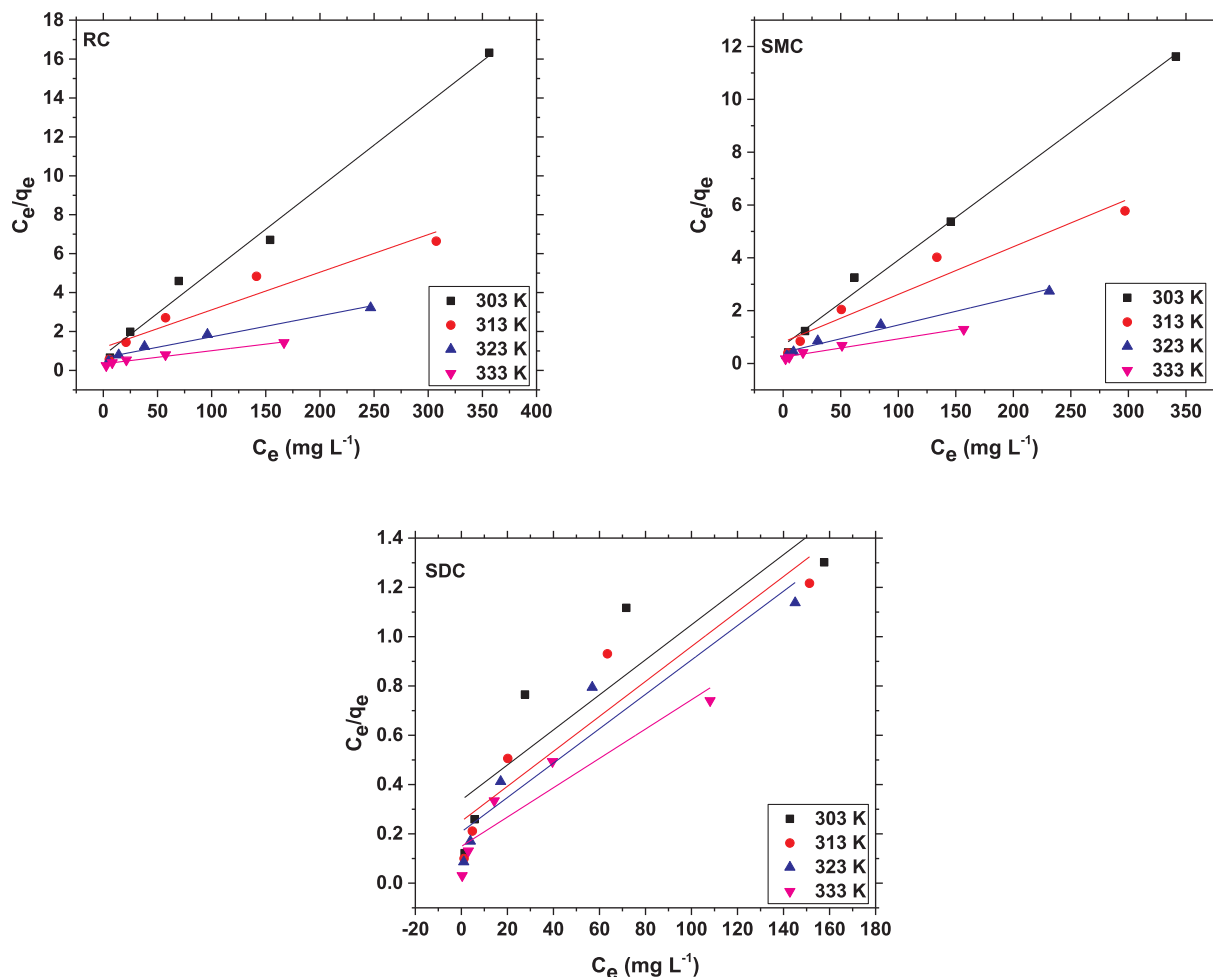


Fig. 13. Langmuir isotherm for the adsorption of MB on RC, SMC and SDC as a function of temperature.

Table 2
Langmuir and Freundlich isotherms parameters for the adsorption of MB at 303–333 K.

Adsorbent	Temp. (K)	Langmuir			Freundlich		
		q_{max} (mg g ⁻¹)	b (mg/L)	R	K_F (mg/L)	$\frac{1}{n}$	R
RC	303	23.13	0.0561	0.995	6.132	0.229	0.965
	313	51.70	0.0164	0.963	4.804	0.378	0.992
	323	92.89	0.0165	0.987	4.601	0.518	0.998
	333	147.98	0.0200	0.986	6.294	0.583	0.998
SMC	303	30.92	0.0476	0.996	7.309	0.245	0.990
	313	55.42	0.0222	0.970	6.400	0.353	0.994
	323	96.32	0.0248	0.989	6.776	0.473	0.997
	333	144.44	0.0289	0.987	8.541	0.539	0.996
SDC	303	140.64	0.0210	0.993	9.352	0.469	0.986
	313	140.98	0.0282	0.938	10.626	0.468	0.995
	323	143.35	0.0335	0.953	11.709	0.464	0.997
	333	168.04	0.0399	0.935	16.290	0.433	0.987

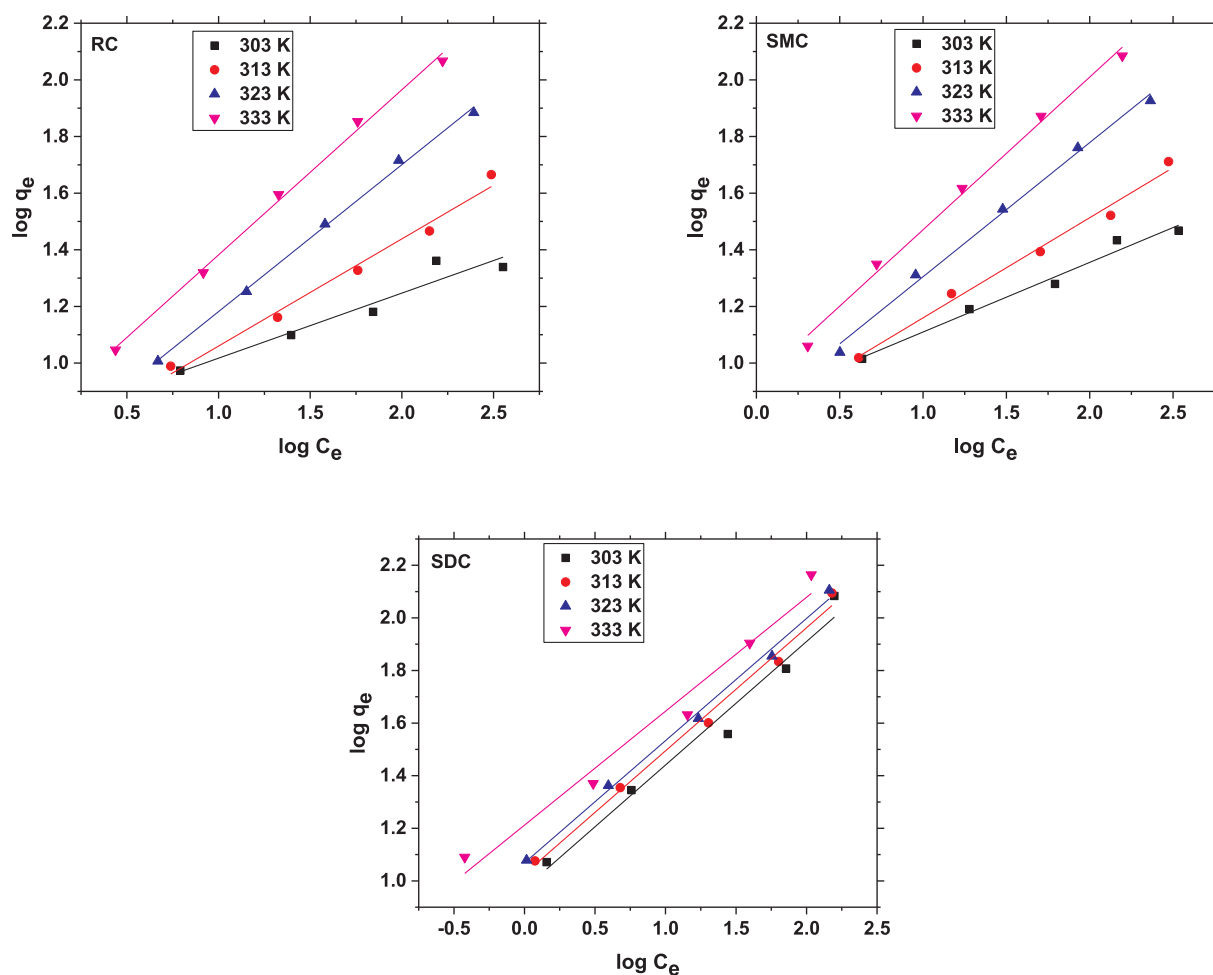


Fig. 14. Freundlich isotherm for the adsorption of MB on RC, SMC and SDC as a function of temperature.

$$\log q_e = \log K_F + \frac{1}{n} \log C_e \quad (7)$$

where K_F is the Freundlich constant and $\frac{1}{n}$ is the heterogeneity factor. The linear plot of $\log q_e$ versus $\log C_e$ at different temperature is shown in Fig. 14. The values of K_F and $\frac{1}{n}$ were obtained from the intercept and the slope respectively.

The isotherms parameters are listed in Table 2. The applicability of the isotherms based on the values of the correlation coefficient (R^2) shows that Freundlich is more applicable than Langmuir because kaolin

has a heterogeneous charge distribution on its surface [29,30]. The Langmuir constant b is not consistent with increase in temperature for RC and SMC, however it increases steadily with temperature for SDC. More so, SDC having the highest surface area, resulted to high q_{max} , adsorption capacity at all temperature. The values of adsorption capacity obtained increases with temperature, signifying the endothermic nature of the adsorption process.

The values of $\frac{1}{n}$ heterogeneity factor in Freundlich isotherm less than 1, is an evidence that the adsorption of MB on the adsorbents is greatly favorable. Zhao et al. [28] affirmed that molecules of an

Table 3
Comparison of the maximum monolayer adsorption (q_{max}) of different adsorbents for the removal of Methylene blue at room temperature.

Adsorbents	q_{max} (mg/g)	References
Montmorillonite/CoFe2O4	97.75	[31]
Palm kernel fiber	95.4	[32]
Graphene/magnetite	43.82	[33]
DNPH- γ -alumina)	32.8	[34]
Kaolin-PDA-PSPSH	96.79	[15]
Modified bamboo	606	[12]
Magnetic Fe3O4@C nanocomposites	52.5	[35]
Spray dried clay (SDC)	140.64	This work
Surface modified clay (SMC)	30.92	This work
Raw clay (RC)	23.13	This work

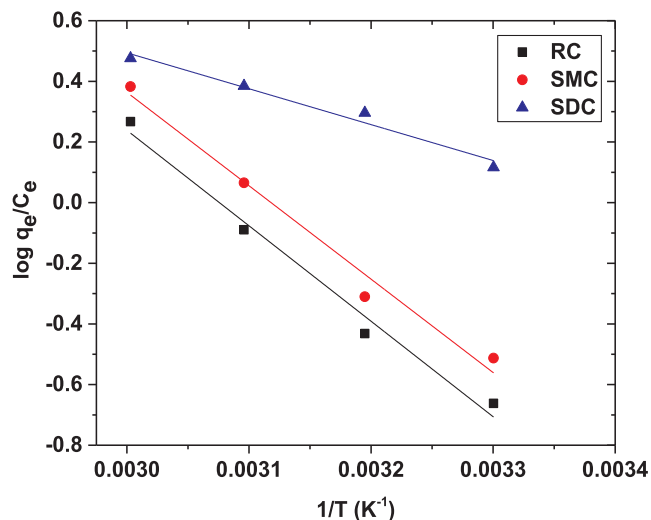


Fig. 15. Plot of $\log \frac{q_e}{C_e}$ versus $\frac{1}{T}$ for the estimation of the thermodynamic parameters for MB the adsorption.

adsorbate can favorably adsorb on the surface on an adsorbent when the value of $\frac{1}{n}$ falls within range of 0.1–0.5, but value of $\frac{1}{n}$ greater than 2 connotes difficulty in adsorption.

Table 3 shows the comparison results of the maximum adsorption capacities of various adsorbents for MB dye reported in literatures. It can be observed that spray dried clay (SDC) exhibit better adsorption capacities for MB in comparison with other adsorbents.

3.6. Adsorption thermodynamic

Thermodynamic parameters like enthalpy, ΔH , (kJ/mol) and entropy, ΔS , (kJ/mol K) were evaluated from Van't Hoff plot by using the equation below.

$$\log \frac{q_e}{C_e} = \frac{\Delta S}{2.303R} - \frac{\Delta H}{2.303RT} \quad (8)$$

While the Gibbs free energy, ΔG (kJ/mol) was evaluated based on Eq. (8)

Table 4
Thermodynamics parameters for the adsorption of MB at 303–333 K.

Adsorbents	ΔH (kJ/mol)	ΔS (kJ/mol K)	ΔG (kJ/mol)				Kc			
			303 K	313 K	323 K	333 K	303 K	313 K	323 K	333 K
RC	60.28	0.1854	4.104	2.249	0.396	–1.458	0.196	0.421	0.863	1.693
SMC	58.98	0.1839	3.258	1.419	–0.418	–2.258	0.274	0.579	1.169	2.261
SDC	22.66	0.0774	–0.792	–1.566	–2.340	–3.114	1.369	1.825	2.390	3.079

Table 5
ANOVA response for interactive effects (A) pH, (B) Adsorbent dose, (C) time.

Adsorbents	Parameters	p-values	t-values	Standard Error
Raw clay	AB	.139	1.640	8.248
	AC	.529	0.658	2.787
	BC	.201	–1.392	8.402
Surface modified clay	AB	.114	1.771	9.793
	AC	.256	1.222	2.799
	BC	.197	–1.405	9.899
Spray dried clay	AB	.081	1.991	9.925
	AC	.310	1.083	7.938
	BC	.133	–1.671	6.683

$$\Delta G = \Delta H - T\Delta S \quad (9)$$

$$\Delta G = -RT \ln Kc \quad (10)$$

where R is the gas constant (8.314 J/mol K), T is the temperature and Kc is the thermodynamic constant.

The plot of $\log \frac{q_e}{C_e}$ against $\frac{1}{T}$ is shown in Fig. 15. The values of ΔH and ΔS are extrapolated from the slope and the intercept respectively.

The enthalpy of adsorption, ΔH , as shown in Table 4 are all positive, affirming that the adsorption process is endothermic in nature.

The enthalpy of SDC is lower than that of RC and SMC; this is due to its high specific surface area which requires less energy for the adsorption to occur. The values of ΔS being positive connotes that the randomness of the MB molecules during the adsorption process increased at the interface of adsorbent/adsorbate solution. The values of Gibbs free energy, ΔG , as listed in Table 4, decrease with increase in temperature, meaning that the adsorption process will become more favorable and spontaneous when the temperature of the system is raised, according to results reported by [36]. Whenever the Gibbs free energy is positive at a specific temperature, it implies that the adsorption process is non-spontaneous and the adsorption capacity will become lower, however increasing the temperature will lead to a spontaneous process [37,38]. The negative value of ΔG obtained for SDC at all temperatures reveal a spontaneous adsorption process of MB.

3.7. Analysis of variance (ANOVA) for percentage removal of MB

Dependent-samples t -test procedure evaluates whether there is a significant difference between the means of the two variables. For instance, if t -test is performed at 95% significance level, a p -value lower than .05 will reject the null hypothesis of a zero coefficient [39]. Hence, the P values that were used as a tool to check the significance of each of the interaction among the variables (i.e. pH and adsorbent dosage; pH and contact time; adsorbent dosage and contact time) were analyzed with one way ANOVA.

The results of the analysis are presented in Table 5. The P values obtained from the interaction effect of the parameters studied were all greater than .05 ($P > .05$), which indicate that the null hypothesis is accepted. This implies that there is no significant difference between means of the amount removed by the adsorbents when two variables (pH and adsorbent dosage, pH and contact time and adsorbent dosage and contact time) are paired.

4. Conclusion

This research has been able to establish that adsorption capacity can be enhanced through spray drying dispersed clay solutions and surface modification of raw clay, although the performance of SDC is better than that of SMC. The higher specific surface area couple with high negative surface charge values exhibited by SDC enhanced its performance over the raw and modified clay. The additional functional group on the surface modified clay was responsible for its better adsorption capacity than raw clay. The removal of methylene blue was sensitive to the pH of the solution. Among the three kinetics models that the experimental data were fitted to, pseudo-second model was best applicable. Adsorption isotherm model proposed by Freundlich was best fitted for the adsorption mechanism. Thermodynamic analysis revealed that adsorption of MB is endothermic and spontaneous at a higher temperature. Among the three adsorbents, spray dried clay is highly efficient in removing methylene blue and is cost effective. This strategy could be employed to produce high surface area adsorbents for the removal of contaminants.

Acknowledgment

The authors would like to thank UFMG-Microscopy Center for the structural support, FAPEMIG, and TWAS-CNPq for financial support.

References

- [1] E. Brillas, C.A. Martínez-Huitle, Decontamination of wastewaters containing synthetic organic dyes by electrochemical methods. An updated review, *Appl. Catal. B Environ.* 166–167 (2015) 603–643.
- [2] S. Banerjee, G.C. Sharma, M.C. Chattopadhyaya, Y.C. Sharma, Kinetic and equilibrium modeling for the adsorptive removal of methylene blue from aqueous solutions on of activated fly ash (AFSH), *J. Environ. Chem. Eng.* 2 (2014) 1870–1880.
- [3] P. Ramachandran, R. Sundharam, J. Palaniyappan, A.P. Munusamy, Potential process implicated in bioremediation of textile effluents: a review, *Pelagia Res. Libr. Adv. Appl. Sci. Res.* 4 (2013) 131–145.
- [4] P.I.M. Firmino, M.E.R. da Silva, F.J. Cervantes, A.B. dos Santos, Colour removal of dyes from synthetic and real textile wastewaters in one- and two-stage anaerobic systems, *Bioresour. Technol.* 101 (2010) 7773–7779.
- [5] N.R. Rane, V.V. Chandanshive, R.V. Khandare, A.R. Gholave, S.R. Yadav, S.P. Govindwar, Green remediation of textile dyes containing wastewater by *Ipomoea hederifolia* L. *RSC Adv.* 4 (2014) 36623–36632.
- [6] Q. Zhang, T. Zhang, T. He, L. Chen, Removal of crystal violet by clay/PNIPAm nanocomposite hydrogels with various clay contents, *Appl. Clay Sci.* 90 (2014) 1–5.
- [7] R. Kant, Textile dyeing industry an environmental hazard, *Nat. Sci.* 4 (2012) 22–26.
- [8] A.E. Okoronkwo, S.J. Olusegun, Biosorption of nickel using unmodified and modified lignin extracted from agricultural waste, *Desalin. Water Treat.* 51 (2013) 1989–1997.
- [9] E.I. Unuabonah, A. Taubert, Clay-polymer nanocomposites (CPNs): adsorbents of the future for water treatment, *Appl. Clay Sci.* 99 (2014) 83–92.
- [10] B. Bi, L. Xu, B. Xu, X. Liu, Heteropoly blue-intercalated layered double hydroxides for cationic dye removal from aqueous media, *Appl. Clay Sci.* 54 (2011) 242–247.
- [11] L.G.C. Villegas, N. Mashhadi, M. Chen, D. Mukherjee, K.E. Taylor, N. Biswas, A short review of techniques for phenol removal from wastewater, *Curr. Pollut. Rep.* (2016) 157–167.
- [12] J.Z. Guo, B. Li, L. Liu, K. Lv, Removal of methylene blue from aqueous solutions by chemically modified bamboo, *Chemosphere* 111 (2014) 225–231.
- [13] M. Visa, C. Bogatu, A. Duta, Simultaneous adsorption of dyes and heavy metals from multicomponent solutions using fly ash, *Appl. Surf. Sci.* 256 (2010) 5486–5491.
- [14] H. Chen, A. Zhong, J. Wu, J. Zhao, H. Yan, Adsorption behaviors and mechanisms of methyl orange on heat-treated palygorskite clays, *Ind. Eng. Chem. Res.* 51 (2012) 14026–14036.
- [15] Q. Huang, M. Liu, J. Chen, K. Wang, D. Xu, F. Deng, H. Huang, X. Zhang, Y. Wei, Enhanced removal capability of kaolin toward methylene blue by mussel-inspired functionalization, *J. Mater. Sci.* 51 (2016) 8116–8130.
- [16] M.K. Uddin, A review on the adsorption of heavy metals by clay minerals, with special focus on the past decade, *Chem. Eng. J.* 308 (2017) 438–462.
- [17] T.S. Anirudhan, M. Ramachandran, Adsorptive removal of basic dyes from aqueous solutions by surfactant modified bentonite clay (organoclay): kinetic and competitive adsorption isotherm, *Process Saf. Environ. Prot.* 95 (2015) 215–225.
- [18] Z. Zhang, J. Zhang, L. Liao, Z. Xia, Synergistic effect of cationic and anionic surfactants for the modification of Ca-montmorillonite, *Mater. Res. Bull.* 48 (2013) 1811–1816.
- [19] U.O. Aroke, A. Abdulkarim, R.O. Ogubunka, Fourier-transform infrared characterization of kaolin, Granite, Bentonite and barite, *J. Chem. Inf. Model.* 53 (2013) 1689–1699.
- [20] Z. Yan, D.I. Gittins, D. Skuse, T. Cosgrove, J.S. Van Duijneveldt, Nonaqueous suspensions of surface-modified kaolin, *Langmuir* 23 (2007) 3424–3431.
- [21] P.S. Kumar, C. Vincent, K. Kirthika, K.S. Kumar, kinetics and equilibrium studies of Pb²⁺ ion removal from aqueous solutions by use of nano-silversol-coated activated carbon, 27 (2010) 339–346.
- [22] Y.S. Ho, G. McKay, Pseudo-second order model for sorption processes, *Process Biochem.* 34 (1999) 451–465.
- [23] A.A. Rahim, Z.N. Garba, Efficient adsorption of 4-Chloroguaiacol from aqueous solution using optimal activated carbon: equilibrium isotherms and kinetics modeling, *J. Assoc. Arab. Univ. Basic Appl. Sci.* 21 (2016) 17–23.
- [24] D. Robati, Pseudo-second-order kinetic equations for modeling adsorption systems for removal of lead ions using multi-walled carbon nanotube, *J. Nanostruct. Chem.* 3 (2013) 55.
- [25] Z.S., L.D. Zhiyan Zou, Highly efficient removal of Cu (II) from aqueous solution using a novel magnetic EDTA functionalized CoFe₂O₄, *RSC Adv.* 7 (2017) 5195–5205.
- [26] Z. Aly, V. Luca, Uranium extraction from aqueous solution using dried and pyrolyzed tea and coffee wastes, *J. Radioanal. Nucl. Chem.* 295 (2013) 889–900.
- [27] K.Y. Foo, B.H. Hameed, Insights into the modeling of adsorption isotherm systems, *Chem. Eng. J.* 156 (2010) 2–10.
- [28] Z. Zhao, X. Wang, C. Zhao, X. Zhu, S. Du, Adsorption and desorption of antimony acetate on sodium montmorillonite, *J. Colloid Interface Sci.* 345 (2010) 154–159.
- [29] J. Liu, R. Gaikwad, A. Hande, S. Das, T. Thundat, Mapping and quantifying surface charges on clay nanoparticles, *Langmuir* 31 (2015) 10469–10476.
- [30] E. Tombácz, M. Szekeeres, Surface charge heterogeneity of kaolinite in aqueous suspension in comparison with montmorillonite, *Appl. Clay Sci.* 34 (2006) 105–124.
- [31] L. Ai, Y. Zhou, J. Jiang, Removal of methylene blue from aqueous solution by montmorillonite/CoFe₂O₄ composite with magnetic separation performance, *Desalination* 266 (2011) 72–77.
- [32] G.O. El-Sayed, Removal of methylene blue and crystal violet from aqueous solutions by palm kernel fiber, *Desalination* 272 (2011) 225–232.
- [33] L. Ai, C. Zhang, Z. Chen, Removal of methylene blue from aqueous solution by a solvothermal-synthesized graphene/magnetite composite, *J. Hazard. Mater.* 192 (2011) 1515–1524.
- [34] W.T. Al-rubayee, O.F. Abdul-rasheed, N.M. Ali, Preparation of a modified nanoalumina sorbent for the removal of Alizarin Yellow R and methylene blue dyes from aqueous solutions, 2016 (2016). doi: 10.1155/2016/4683859.
- [35] S. Wu, J. Huang, C. Zhuo, F. Zhang, W. Sheng, M. Zhu, One-step fabrication of magnetic carbon nanocomposite as adsorbent for removal of methylene blue, *J. Inorg. Organomet. Polym. Mater.* 26 (2016) 632–639.
- [36] K. Chinoue, K. Benteleb, Z. Bouberka, A. Nadim, U. Maschke, Adsorption of reactive dyes from aqueous solution by dirty bentonite, *Appl. Clay Sci.* 123 (2016) 64–75.
- [37] R.M. Schneider, C.F. Cavalin, M.A.S.D. Barros, C.R.G. Tavares, Adsorption of chromium ions in activated carbon, 132 (2007) 355–362.
- [38] L. Cottet, C.A.P. Almeida, N. Naidek, M.F. Viante, M.C. Lopes, N.A. Debacher, Adsorption characteristics of montmorillonite clay modified with iron oxide with respect to methylene blue in aqueous media, *Appl. Clay Sci.* 95 (2014) 25–31.
- [39] D.B. Figueiredo Filho, R. Paranhos, E.C. da Rocha, M. Batista, J.A. da Silva Jr., M.L.W.D. Santos, J.G. Marino, When is statistical significance not significant? *Brazilian Polit. Sci. Rev.* 7 (2013) 31–55.